

DTIC FILE COPY

2

AGARD-CP-407

AGARD-CP-407

AD-A194 686

# AGARD

ADVISORY GROUP FOR AEROSPACE RESEARCH & DEVELOPMENT

7 RUE ANCELLE 92200 NEUILLY SUR SEINE FRANCE

AGARD CONFERENCE PROCEEDINGS No.407

## Terrestrial Propagation Characteristics in Modern Systems of Communications, Surveillance, Guidance and Control

DTIC  
ELECTE  
APR 13 1988

NORTH ATLANTIC TREATY ORGANIZATION



DISTRIBUTION AND AVAILABILITY  
ON BACK COVER

This document has been approved  
for public release and sale; its  
distribution is unlimited.

88 4 11 293

1

# COMPONENT PART NOTICE

THIS PAPER IS A COMPONENT PART OF THE FOLLOWING COMPILATION REPORT:

TITLE: Terrestrial Propagation Characteristics in Modern Systems of Communications,  
Surveillance, Guidance and Control, Proceedings of the Electromagnetic Wave  
Propagation Panel Specialists' Meeting Held in Ottawa (Canada) on 20-24 October 1986.

TO ORDER THE COMPLETE COMPILATION REPORT, USE AD-A194 686.

THE COMPONENT PART IS PROVIDED HERE TO ALLOW USERS ACCESS TO INDIVIDUALLY  
AUTHORED SECTIONS OF PROCEEDING, ANNALS, SYMPOSIA, ETC. HOWEVER, THE COMPONENT  
SHOULD BE CONSIDERED WITHIN THE CONTEXT OF THE OVERALL COMPILATION REPORT AND  
NOT AS A STAND-ALONE TECHNICAL REPORT.

THE FOLLOWING COMPONENT PART NUMBERS COMPRISE THE COMPILATION REPORT:

AD#: AD-P006 731 thru AD#: AD-P006 749.  
AD#: \_\_\_\_\_ AD#: \_\_\_\_\_  
AD#: \_\_\_\_\_ AD#: \_\_\_\_\_

|                    |                                     |
|--------------------|-------------------------------------|
| Accession For      |                                     |
| NTIS GRA&I         | <input checked="" type="checkbox"/> |
| DTIC TAB           | <input checked="" type="checkbox"/> |
| Unannounced        | <input type="checkbox"/>            |
| Justification      |                                     |
| By _____           |                                     |
| Distribution/      |                                     |
| Availability Codes |                                     |
| Dist               | Avail and/or<br>Special             |
| A-1                |                                     |

**DTIC**  
**ELECTE**  
**S** JUL 08 1988 **D**  
**E**

DTIC FORM 463  
MAR 85

A document has been approved  
for public release and using the  
distribution is unlimited.

OPI: DTIC-TID

AGARD-CP-407

NORTH ATLANTIC TREATY ORGANIZATION  
ADVISORY GROUP FOR AEROSPACE RESEARCH AND DEVELOPMENT  
(ORGANISATION DU TRAITE DE L'ATLANTIQUE NORD)

AGARD Conference Proceedings No.407  
TERRESTRIAL PROPAGATION CHARACTERISTICS IN MODERN SYSTEMS OF  
COMMUNICATIONS, SURVEILLANCE, GUIDANCE AND CONTROL

|                    |                                     |
|--------------------|-------------------------------------|
| Accession For      |                                     |
| NTIS GR&I          | <input checked="" type="checkbox"/> |
| DTIC TAB           | <input checked="" type="checkbox"/> |
| Unannounced        | <input type="checkbox"/>            |
| Justification      |                                     |
| By                 |                                     |
| Distribution/      |                                     |
| Availability Codes |                                     |
| Dist               | Avail and/or<br>Special             |
| A-1                |                                     |

DTIC  
COM  
UNCLASSIFIED

Papers presented at the Electromagnetic Wave Propagation Panel Specialists' Meeting held in Ottawa,  
Canada, 20-24 October 1986

This document has been approved  
for public release and sale; its  
distribution is unlimited.

## THE MISSION OF AGARD

The mission of AGARD is to bring together the leading personalities of the NATO nations in the fields of science and technology relating to aerospace for the following purposes:

- Exchanging of scientific and technical information;
- Continuously stimulating advances in the aerospace sciences relevant to strengthening the common defence posture;
- Improving the co-operation among member nations in aerospace research and development;
- Providing scientific and technical advice and assistance to the Military Committee in the field of aerospace research and development (with particular regard to its military application);
- Rendering scientific and technical assistance, as requested, to other NATO bodies and to member nations in connection with research and development problems in the aerospace field;
- Providing assistance to member nations for the purpose of increasing their scientific and technical potential;
- Recommending effective ways for the member nations to use their research and development capabilities for the common benefit of the NATO community.

The highest authority within AGARD is the National Delegates Board consisting of officially appointed senior representatives from each member nation. The mission of AGARD is carried out through the Panels which are composed of experts appointed by the National Delegates, the Consultant and Exchange Programme and the Aerospace Applications Studies Programme. The results of AGARD work are reported to the member nations and the NATO Authorities through the AGARD series of publications of which this is one.

Participation in AGARD activities is by invitation only and is normally limited to citizens of the NATO nations.

The content of this publication has been reproduced directly from material supplied by AGARD or the authors.

Published November 1987

Copyright © AGARD 1987  
All Rights Reserved

ISBN 92-835-0434-8

**Best Available Copy**



Printed by Specialised Printing Services Limited  
40 Chigwell Lane, Loughton, Essex IG10 3TZ



## THEME

This Symposium had the objectives of presentation, discussion and publication of new research results in surface propagation characteristics for modern systems applications in relevant frequency ranges (radio to optical frequencies). System examples are tactical communications, target acquisition, terrain-following instrumentation, etc.

Modern system development requires serious attention to the operational environment and variations it experiences due to natural and artificial influences. Applications based on propagation in the vicinity of the earth surface predominantly depend on characteristics of the near-ground propagation medium as well as on its lower boundary, the ground-surface, or on the "terrestrial propagation characteristics".

Research work carried out during the last few decades has resulted in data banks and other information on average behaviour of parameters concerned, such as ground profiles, vegetation and electrical characteristics. An efficient operation of modern systems of communication, surveillance, guidance and control requires more and more details of ground data and, particularly, of their deviation from average values on account of anthropogeneous effects in addition to seasonal and diurnal variations.

The Symposium covered the topics listed below; the Avionics Panel cooperated in fields of common interest,

1. Ground characteristics, profiles, contours and vegetation,
2. Near-ground tropospheric interface (including modification),
3. Diffraction and shadowing effects,
4. Refraction and reflection at medium boundaries,
5. Measurements, data assembling and processing,
6. Applications in communication systems (including antenna effects),
7. Criteria in surveillance; system aspects in guidance and control.

...

Ce symposium avait pour objectifs la présentation, la discussion et la publication des résultats des dernières recherches dans le domaine des caractéristiques de propagation en surface en vue d'applications dans des systèmes évolués dans un spectre de fréquence significatif (des fréquences radio aux fréquences optiques). Des exemples de tels systèmes sont communications tactiques, acquisitions d'objectif, équipements pour suivi de terrain etc.

Le développement de systèmes modernes demande de prêter une attention particulière à l'environnement opérationnel et à ses variations dues aux influences naturelles et artificielles. Les applications fondées sur la propagation au voisinage de la surface terrestre dépendent principalement des caractéristiques de la propagation moyenne près du sol ainsi que du relief, surface du sol, ou des "caractéristiques de la propagation terrestre".

Les travaux de recherche conduits pendant ces dernières décades ont fourni des banques de données et d'autres informations sur l'environnement moyen des paramètres concernés, tels que profil du sol, végétation et caractéristiques électriques. L'efficacité, opérationnelle des systèmes modernes de communications, surveillance, guidage et contrôle demande de plus en plus de détails sur les données du sol et, plus particulièrement, de leurs écarts par rapport aux valeurs moyennes en tenant compte des effets anthropogéniques à l'addition des variations saisonnières et diverses.

Ce symposium a couvert les sujets ci-dessous et la commission Electronique Aérospatiale a coopéré à tous les domaines d'intérêt commun.

1. Caractéristiques du sol, profils, contours et végétation.
2. Interface troposphérique proche de la surface de la terre.
3. Diffraction et effets d'ombre.
4. Réfraction et réflexion aux limites moyennes.
5. Mesures, ensemble de données et processus de calcul.
6. Applications aux systèmes de communications (comprenant les effets d'antennes).
7. Critères des systèmes de surveillance; aspects système dans le guidage et le contrôle.

# **ELECTROMAGNETIC WAVE PROPAGATION PANEL**

**Chairman:** Dr H. Solcher  
Center for Command Control &  
Communication Systems  
US Army Comm.-Electronics  
Command, ATTN: AMS&L-RD-C3-TA-1  
Fort Monmouth, NJ. 0773-5202  
United States

**Deputy Chairman:** Prof. C. Goutelard  
L.E.T.I.  
Université Paris-Sud  
9, Av. de la Division Leclerc  
94230 Cachan  
France

## **TECHNICAL PROGRAMME COMMITTEE PROGRAMME CO-CHAIRMAN**

Dr H.J. Albrecht  
FGAN  
Bad Neuenahr Strasse 20  
D-5307 Wachtberg-Werthhoven  
Federal Republic of Germany

Dr F.H. Palmer  
Head, Communications E.W. Section  
Defence Research Establishment  
Ottawa Department of National Defence  
Ottawa, Ontario K1A 0Z4  
Canada

## **MEMBERS**

Dr Ing. D. Rother  
Standard Elektrik Lorenz AG (SEL)  
Abt. ERM  
Ostendstrasse 3  
D-7530 Pforzheim  
Federal Republic of Germany

Ing. en Chef L. Boithias  
C.N.E.T.  
38, 40, rue du General Leclerc  
92131 Issy-les-Moulineaux  
France

Mr J.E. Rasmussen  
RADC/EEPS  
Hanscom AFB, MA 01731  
USA

Prof. Dr A.N. Ince  
Burumcek Sok 7-10  
Cankaya  
Ankara  
Turkey

Dr S. Rotherham  
Marconi Research Centre  
West Hanningfield Road  
Great Baddow  
Chelmsford, Essex  
United Kingdom

Ir. H. Vissinga  
Physics and Electronics Lab. TNO  
P.O. Box 96864  
2309 JG The Hague  
Netherlands

## **ELECTROMAGNETIC WAVE PROPAGATION PANEL EXECUTIVE**

**Lt. Colonel M. Stratton**

**From Europe**

**AGARD-OTAN**  
7, rue Ancelle  
92200 Neuilly-sur-Seine  
France

**From the USA and Canada**

**AGARD-NATO**  
APO New York 09777

## PREFACE

With its symposium "Terrestrial Propagation Characteristics in Modern Systems of Communications, Surveillance, Guidance and Control", the Electromagnetic Wave Propagation Panel adhered to its practice of permitting, in intervals of several years, a complete coverage of interim results and of the state of the art reached in a field of continuous interest. The meeting took place in Ottawa, Canada, from 20th to 24th October 1986. The Conference Proceedings contain papers and contributions to discussions. Volume one deals with the unclassified portion of the meeting; volume two contains the materials produced in the classified sessions of the meeting.

In the field of electromagnetic wave propagation, essential limiting conditions may be represented by characteristics and behaviour of upper and lower boundaries of the propagation environment. The performance of propagation paths may depend significantly upon variations in such surface properties. In addition, modern system development requires serious attention to the operational environment and changes it experiences due to natural and artificial influences.

During the symposium, the entire field was dealt with in six sessions, concerning ground characteristics and their effects, diffraction and shadowing effects, refraction and reflection at medium boundaries, general system applications, special system applications, and special experimental results. A round-table discussion at the conclusion of the meeting assisted in clarifying the present state of the art, engineering aspects, and promising areas of research. Examples of Emerging Technologies referred to system adaptation with respect to terrestrial propagation characteristics and their effects on communications, surveillance, and guidance and control.

In summary, this Symposium provided the intended review on the state of the art in this field of research, discussed theoretical and experimental aspects, including system planning, and indicated promising areas for further investigations. The Conference Proceedings give a full account of papers and discussions.

Gratefully acknowledged are the cooperation and assistance rendered by Dr F. Palmer as co-chairman of the programme committee, and by its members, Ing. en Chef L. Boithias, Prof. A. Ince, Mr J. Rasmussen, Dr D. Rother, Dr S. Rotheram, and Ir. H. Vissinga.

Appreciation is furthermore expressed to all who assisted in the organization of the Symposium as well as in the compilation of the Proceedings, to authors and contributors to discussions, to session chairmen, to the host coordinator, to AGARD staff and other collaborators.

H.J. Albrecht  
Editor

## CONTENTS

|   |     |
|---|-----|
| THEME   | iii |
| ELECTROMAGNETIC WAVE PROPAGATION PANEL OFFICERS AND COMMITTEE   | iv  |
| PREFACE   | v   |
| <u>SESSION I - GROUND CHARACTERISTICS AND THEIR EFFECTS</u>   |     |
| AN INVESTIGATION OF TERRAIN RELATED VARIABLES FOR PREDICTING THE MULTIPATH FADE<br>DEPTH DISTRIBUTION ON TERRESTRIAL MICROWAVE LINKS<br>by T.Tjelta, R.L.Olsen and L.Martin | 1   |
| A REVIEW OF THE ROLE OF SURFACE REFLECTION IN MULTIPATH PROPAGATION OVER<br>TERRESTRIAL MICROWAVE LINKS<br>by R.L.Olsen, L.Martin and T.Tjelta                              | 2   |
| DEVELOPMENT OF A GROUND-CONDUCTIVITY MAP FOR THE AREA OF THE FEDERAL<br>REPUBLIC OF GERMANY FROM MEASURED FIELD-STRENGTH CONTOURS<br>by B.Raufmann                          | 3   |
| SCATTERING AND DEPOLARIZATION BY RANDOM ROUGH TERRAIN AND VEGETATION<br>COVERED TERRAIN-UNIFIED FULL WAVE APPROACH<br>by E.Bahar  | 4   |
| <u>SESSION II - DIFFRACTION AND SHADOWING EFFECTS</u>   |     |
| PROPAGATION IN LONGITUDINALLY VARYING DUCTS WITH EMPHASIS ON GUIDING TO<br>ANTIGUIDING TRANSITIONS<br>by L.Felsen   | 5   |
| VHF/UHF PROPAGATION BY DIFFRACTION - CALCULATION BY NUMERICAL INTEGRATION<br>by J.H.Whitaker  | 6   |
| MONO- AND BISTATIC RADAR COVERAGE DIAGRAMS INCLUDING DIFFRACTIVE WAVE<br>PROPAGATION<br>by H.Kuschel  | 7   |
| A DIFFRACTION BASED THEORETICAL MODEL FOR PREDICTION OF UHF PATH LOSS IN CITIES<br>by H.L.Bertoni and J.Wallach   | 8   |
| A PROGRAM FOR THE CALCULATION OF RADIO-WAVE TRANSMISSION LOSS OVER THE<br>SPHERICAL EARTH AND OVER OBSTACLES<br>by M.Ranger, J.L.Régulier, M.Andreu and Y.Le Pape           | 9   |
| CORRECTING RAY FIELD FAILURES CAUSED BY FOCUSING AND SHADOWING IN AN<br>INHOMOGENEOUS DUCT<br>by E.Niver, M.S.Vogel, C.J.Rutz and L.B.Felsen                                | 10  |
| <u>SESSION III - REFRACTION AND REFLECTION AT MEDIUM BOUNDARIES</u>   |     |
| REVIEW OF RECENT DEVELOPMENTS IN EVAPORATION DUCTING ASSESSMENT<br>by J.H.Richter   | 11  |
| IDENTIFICATION OF MICROWAVE LINE-OF-SIGHT MULTIPATH COMPONENTS<br>by A.Hewitt, L.Martin, W.H.Lee, J.Austin, K.H.Craig and E.Vilar   | 12  |
| COINCIDENCE DE REFRACTION, METEOROLOGIE ET AFFAIBLISSEMENTS SUR LES TRAJETS<br>EN VISIBILITE<br>par L.Martin, R.L.Olsen and T.Tjelta  | 13  |

**RADIO AND RADAR "HOLES" AND MULTIPATH ZONES: THE GLOBAL AND LOCAL INFLUENCES ON ATMOSPHERIC REFRACTIVE STRUCTURE AND RESULTING ADVERSE RADIO AND RADAR PERFORMANCE**

by O.R.Côté, J.F.Morrissey and Y.Izumi

14†

**THE CORRELATION BETWEEN METEOROLOGICAL AND LOW-LEVEL ANGLE-OF-ARRIVAL MEASUREMENTS**

by J.Litva, N.R.Fines and P.Bauman

15

**DISCUSSION SUMMARY – SESSIONS I, II AND III**

D1

**SESSION IV – GENERAL SYSTEM APPLICATIONS**

**MM-WAVE PROPAGATION AND APPLICATIONS IN MILITARY COMMUNICATION SYSTEMS**

by D.Rother and E.Müller

16

**SPACE-DIVERSITY EFFECTS IN LINE-OF-SIGHT PROPAGATION PATHS**

by H-G.Giloi, K.Metzger and R.Valentin

17

**SOME MEASUREMENTS OF HEIGHT GAIN AT V.H.F.**

by J.Fairbrother, K.A.Hughes and D.M.Holden

18

**ENVELOPE AND PHASE STATISTICS FOR NON-GAUSSIAN NOISE AND RESULTING ERROR PROBABILITIES FOR DIGITAL COMMUNICATIONS SYSTEMS**

by J.H.Roberts

19

**6GHz PROPAGATION MEASUREMENTS OVER A 51 KM PATH IN THE UK**

by J.E.Leeble

20

**AN EHF TELECOMMUNICATION SYSTEM ENGINEERING MODEL**

by K.C.Allen

20A

**SESSION V – SPECIAL SYSTEM APPLICATIONS**

**MEASUREMENTS ON MULTIPATH PROPAGATION FOR MILLIMETER WAVES**

by H.Essen, E.P.Baars, H.Fuchs and R.Makarushkin

21\*

**THE FORWARD REFLECTION COEFFICIENT OF SNOW, TYPES OF GROUND, VEGETATION AND ROAD SURFACES AT 35 AND 94 GHz AS A FUNCTION OF INCIDENT ANGLE**

by J.Saeder, H.Loch, R.Berger and M.P.J.G.Versloffen

22\*

**MEASUREMENTS ON THE REFLECTIVITY OF SNOW COVERED TERRAIN AT 94 GHz**

by H.Essen, E.P.Baars and H.Schimpf

23\*

**STATISTICAL ANALYSIS OF THE REFLECTIVITY OF LAND CLUTTER AT MILLIMETER-WAVE FREQUENCIES**

by H.Schimpf

24\*

**UNE EXPERIENCE D'ANALYSE BIDIMENSIONNELLE DES TRAJETS MULTIPLES DANS UNE LIAISON VHF**

par F.Christophe

25\*

**SESSION VI – SPECIAL EXPERIMENTAL RESULTS**

**SURVEY OF NATO PROPAGATION CAMPAIGNS IN LORIENT, FRANCE, DURING WINTER 1981/1982 AND WINTER 1984/1985 OVER A 10 KM PATH OVER SEA IN THE FREQUENCY RANGE 10–94 GHz**

by J.Saeder

26\*

**MILLIMETRE- AND CENTIMETRE-WAVE ATTENUATION STATISTICS OVER A 9.7 KM LINE-OF-SIGHT OVERSEA PATH**

by R.Makarushkin

27\*

† Abstract only. Paper not available at time of printing.  
\* Printed in Classified Publication CP 487 (Supplement).

REFLECTION CHARACTERISTICS OF THE SEA AT 10.5, 16, 35, AND 94 GHz  
by W.P.M.N. Kelzer

28\*

UNE CAMPAGNE DE PROPAGATION EN MILIEU MARITIME, UTILISANT UN SYSTEME  
NUMERIQUE A 36 GHz  
par Y. Hurtaud et A. Junchat

29

THE EFFECTS OF SEA SURFACE ON LOW LEVEL PROPAGATION AT 36 GHz  
by Y. Hurtaud, A. Junchat and K.F. Kerdron

30\*

AD-P005 731

# AN INVESTIGATION OF TERRAIN RELATED VARIABLES FOR PREDICTING THE MULTIPATH FADE DEPTH DISTRIBUTION ON TERRESTRIAL MICROWAVE LINKS

by

Terje Tjelta<sup>1</sup>, Roderic L. Olsen<sup>2</sup>, and Louis Martin<sup>3</sup>

<sup>1</sup>Norwegian Telecommunication Administration  
Research Department  
P.O. Box 83  
N-2007 Kjeller, Norway

<sup>2</sup>Communications Research Centre  
Department of Communications  
P.O. Box 11490, Station H  
Ottawa, Canada K2H 8S2

<sup>3</sup>CNET LAB/MER  
Route de Trégastel  
22300 Lannion, France

## SUMMARY

Terrain related variables are shown to be important in an asymptotic prediction equation for the worst-month multipath fade depth distribution. From a fading data base for 47 links in North Western Europe, equations are developed employing up to six variables and an additional variable geoclimatic factor. The best standard error of prediction is 2.8 dB, considerably better than that available from other prediction methods for the same region. A large number of variables are investigated, most of them closely related to the terrain. The results suggest that terrain reflections play an important role in multipath propagation.

## 1. INTRODUCTION

In the design of high capacity line-of-sight digital radio links, there remains a need for a more accurate prediction equation for the multipath fade depth distribution in an average worst month. Single frequency measurements have been conducted by many countries to obtain their own prediction equations. By combining all these measurements it might be possible to develop an accurate equation using simple radio-link parameters under variable geoclimatic conditions [1]. This would improve the prediction of outage time using methods employing the single frequency equation. Indeed, such single frequency models may themselves become even more important in prediction of outage time as equalizers are improved.

From earlier work [2,3,4] it is clear that the terrain plays some role in the multipath fade depth distribution. A terrain roughness parameter has been used with success, for example, in several prediction equations. This was usually assumed to be due to the fact that the terrain appears to have a role in the process in which abnormal atmospheric layers are created and broken up. Even more directly, it now appears that ground reflection is involved in many of the selective fading events. This is discussed in more detail in a companion paper [5].

Using worst month data for 47 links in North Western Europe, in this paper a number of different terrain roughness parameters are analysed in combination with other plausible predictor variables to find their relative importance in an empirical narrow band prediction equation based on the well-known power-law form [6]. Two of these parameters are already in use in the design of line-of-sight links. Others are also considered, one commonly used for ducting transmission loss calculations on transhorizon links [7]. It is found that terrain roughness cannot be discounted as a factor in the physical process causing multipath fading, but that two other variables besides path length and frequency are better predictors. These are the path inclination, and the grazing angle for specular ground reflection.

## 2. EMPIRICAL MODEL AND PROCEDURE

The model investigated in this paper is based on the empirical asymptotic power-law equation for the deep fading range [6] relating the probability  $P$  that fade depth  $A$  (dB) is exceeded as a product of several independent parts:

$$P = k \prod_{i=1}^n f_i(x_i)^{c_i} 10^{-A/10} \quad (1)$$

where  $c_i$  are constants,  $x_i$  are predictor variables,  $f_i$  functions of the variables, and  $k$  a geoclimatic factor in the region in which the prediction equation is used. The Rayleigh slope of 10dB/decade is employed. Linear multiple regression [8] is used, and for this technique eq. (1) is transformed to the logarithmic form

$$A = 0 + c + 10 \log \left( \prod_{i=1}^n f_i(x_i) \right) - 10 \log(P) \quad (2)$$

where the regression coefficients  $a_i = 10a_i$  and  $G+c=10\log(k)$  are constants. For the regressions a fixed reference probability of 0.01% of the time, is chosen and eq. (2) is changed to

$$A_{0.01} - G_j = a_0 + \sum a_i F_i(x_i) \quad (3)$$

where the index  $j$  denotes different geoclimatic groupings of the data and  $a_0 = -c - 10\log(F)$ . The function  $F_i$  is introduced to denote the fact that sometimes a variable is employed directly in the multiple regression, without first taking the logarithm.

To obtain  $G_j$ , iterations are done the following way. Having a set of variables, the first fit is carried out normally with all  $G_j=0$ . A mean prediction error is computed for each geoclimatic group, and the fade depth in the corresponding groups modified by this error. Then a new regression is performed with the modified values of  $A_{0.01}$ . This is continued until the mean errors are negligible in all geoclimatic groups. The technique was introduced in [9], but the single iteration used later found to be insufficient [1].

Some statistical tests [8] are performed on the results to measure statistical significance and goodness of fit. The Student's-t statistic, indicating the significance of each variable is presented. Also given are the variance ratio statistic  $F$  and multiple determination coefficient  $R^2$ , indicating the significance of the overall regression. The critical values for  $t$  and  $F$  statistics for a 5% level of significance are employed. The main measure of the goodness of the fit used is the standard error of regression  $\sigma$ .

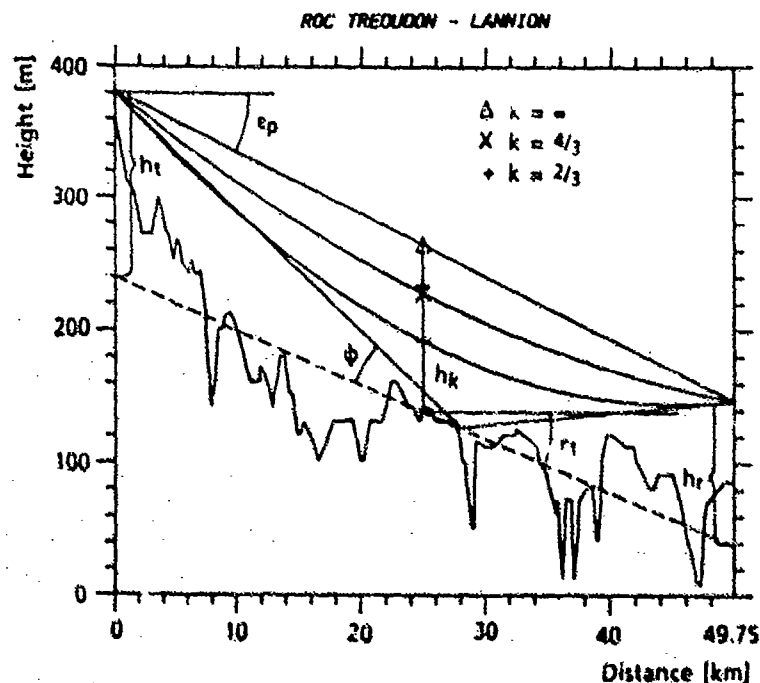


Fig. 1. A typical path profile with some variables indicated.

### 3. CHOICE OF VARIABLES

Many of the variables considered in this paper are related directly to the path terrain profile (Fig. 1). These are as follows:

- $s_j$  - terrain roughness parameters. Four parameters ( $j=1,4$ ) are included, all using or file sample distances of 1 km, 0.5 km, and 0.1 km. In calculating these parameters, a 1 km interval is excluded at both ends of the path.  $s_1$  (in metres) is defined as the rms value of the heights above the mean height;  $s_2$  (in mrad) is the rms value of the terrain slopes between adjacent points on the profile;  $s_3$  (in metres) is the same as  $s_1$ , but with the regression curve through the terrain heights ("average path profile") as a reference instead of the mean height, and  $s_4$  (in metres) is the difference between the 90% and 10% points of the cumulative distribution of the heights.  $s_1$  and  $s_2$  are used in [6] and  $s_3$  in [7].
- $\phi_c$  - the terrain slope (in mrad) obtained from the angle between the average path profile and the horizontal.



$T$  = the profile autocorrelation distance (in metres) [10].  
 $\tan \theta_c = 2s_3/T$ , a diffuse reflection variable that may be interpreted as the mean ratio of the vertical and the horizontal irregularities [10].

Another group of variables determined by both the terrain profile and the path are (Fig. 1):

- $h_k$  = the average path clearance (in metres) taken as the clearance to the mean profile height at midpath for three values of effective earth radius factor  $k=$ , 4/3, and 1.  
 $h_{ob}$  = the clearance (in metres) from the most dominant obstacle, for  $k=4/3$ .  
 $h_{fr}$  = the clearance for the dominant obstacle, in number of Fresnel zones, for  $k=4/3$ .  
 $\epsilon_p$  = the path inclination (in mrad) with respect to the horizontal, for  $k=$ .  
 $a_p$  = the path height (in metres) above the sea level taken at midpath, for  $k=4/3$ .  
 $\psi$  = grazing angle (in mrad) associated with the average path profile, for  $k=4/3$ .  
 $K_\alpha = 2(h_t^2/\theta_t^2 + h_r^2/\theta_r^2)^{1/2}/d$ , a diffuse scattering parameter for the situation when the antenna beams are narrow [10,5].  $\theta_t$  and  $\theta_r$  are the half power beamwidths (in mrad) of the transmitting and receiving antennas, respectively.  
 $K_\beta = (h_t + h_r)/(d \tan(\theta_g))$ , a diffuse scattering parameter for the situation when the antenna beams are wide [10,5]. Here,  $h_t$  and  $h_r$  are the transmitter and receiver antenna heights above the average path profile.  
 $\alpha/\theta_g^2$  = a multiplication factor associated with diffuse scattering [10], where  $\alpha = (\theta_t^2 + \theta_r^2)^{1/2}/2000$ .

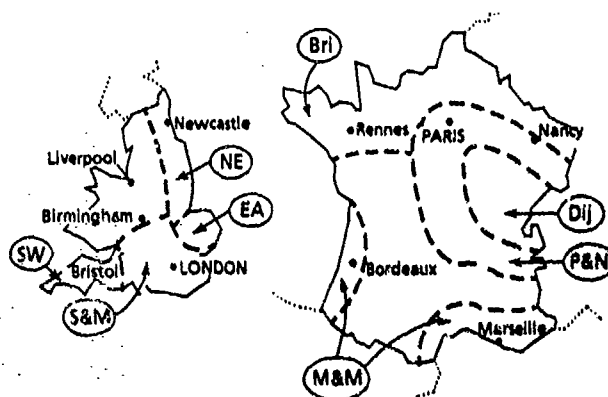
Finally, a third group includes those variables associated only with the link:

- $d$  = path distance (in km).  
 $f$  = radio link frequency (in GHz).  
 $\theta = (\theta_t \theta_r)^{1/2}$ , the geometric mean beamwidth.

In the regressions, the function  $f_1(\epsilon) = 1 + |\epsilon|$  on the variables  $\epsilon_p$  and  $\epsilon_t$  is used rather than the raw variables [1].

#### 4. DATA

The fading data were collected in France [4] and the UK [1] over the past 30 years. The measurement period for nearly all the 47 links used in the analysis is from one year up to five. For four links in France, this period is about half a year, but the worst calendar month is believed to be included. The envelope of all monthly cumulative distributions for a year is taken as the distribution for the worst month, and the mean of these are used in the case when several years of data are available. Two points are chosen from these distributions whenever possible. One is the first point considered to be in the "tail" region, (i.e., having the lowest fade depth). The second is one decade lower in probability. The "tail" region is the part of the distribution which is approximately a straight line and having approximately the Rayleigh slope. The reference tail fade depth  $A_{1,0}$  is obtained by translating the fade depth for the first tail point to 0.01% of the time using the Rayleigh slope.



Number of links in the different geographical groups.

|       |                              |    |
|-------|------------------------------|----|
| NE,   | North East:                  | 8  |
| EA,   | East Anglia:                 | 8  |
| S&M,  | South and Midlands:          | 8  |
| SW,   | South West:                  | 4  |
| Bri,  | Brittany:                    | 5  |
| P&N,  | Paris and Nancy:             | 5  |
| Dij,  | Dijon:                       | 4  |
| M&M,  | Montpellier and Mont Marsan: | 5  |
| Total |                              | 47 |

Fig. 2. Geographical distribution of the links in the analysis.

The geographical distribution of the links is shown in Fig. 2. The map gives the borders for the data groups. The UK links were grouped in the same manner as indicated in [9] using both geographical proximity of the links and residual error trends. The French links were grouped using the contours of refractivity gradient for one summer. These may be changed as additional data become available [4]. The data base currently covers the path length range 7.5-95 km, and the frequency range 2-37 GHz.

## 5. RESULTS OF ANALYSIS

### 5.1 Accuracy of Rayleigh slope assumption.

Since the prediction equation use a 10 dB/decade slope, this is the first assumption to verify. Second tail points are available from the distributions for 38 links. These together with the first tail point give a mean slope  $10.2 \pm 0.5$  dB, where the 95% confidence limits are based on twice the estimated standard error.

### 5.2 Effect of profile sample distance on terrain roughness.

One parameter derived from the path profile is the terrain roughness  $s_1$ , and this is often used as a third variable in the prediction equation in addition to  $d$  and  $f$  [2,3,9]. Shown in Table I are the mean and standard deviations of the differences between the roughness values for 0.5 and 1.0 km sample distances and those for the references 0.1 km sample distance. It is seen that  $s_1$  and  $s_2$  are more sensitive to the sample distance, indicating that at least, 1.0 km samples should be avoided for these two. Since there is little variation for the other two, only 0.5 and 0.1 km sample distances are included in the correlation and regression calculations.

Table I: The mean and estimated standard deviation for the difference between the  $s_1$  values with sample distance of 0.5 and 1.0 km with respect to those for 0.1 km.

|       | mean  |       | standard deviation |          |
|-------|-------|-------|--------------------|----------|
|       | 0.5   | 1.0   | 0.5                | 1.0 [km] |
| $s_1$ | 0.37  | 0.94  | 0.76               | 1.37     |
| $s_2$ | -8.96 | -15.2 | 6.41               | 10.0     |
| $s_3$ | 0.30  | 0.79  | 0.49               | 1.23     |
| $s_4$ | 1.55  | 2.53  | 5.96               | 11.3     |

### 5.3 Cross-correlation coefficients.

Table II gives the correlation matrix of pairwise correlation coefficients for all the variables  $F(x_i)$  and reference fade depth  $A_{0.01}$ . First, in this matrix the absolute value of the correlation coefficients between  $A_{0.01}$  and the variable functions indicate which variable should be the first to enter the regression equation. Secondly, it is of considerable help in interpreting the regression results. If, for example, two variables are highly correlated, it is difficult to distinguish them from each other if they are used in the same equation.

TABLE II: Cross-correlation coefficients in percent for all the variables.

|                 | Logarithm of $d, f, \dots$ |     |     |       |       |       |       |                 |                 |       |       |       |       |       |       |       |       |       |          |          |          |          |          |          |
|-----------------|----------------------------|-----|-----|-------|-------|-------|-------|-----------------|-----------------|-------|-------|-------|-------|-------|-------|-------|-------|-------|----------|----------|----------|----------|----------|----------|
|                 | $A_{0.01}$                 | $d$ | $f$ | $s_1$ | $s_2$ | $s_3$ | $s_4$ | $\tan \theta_0$ | $\frac{u}{h_0}$ | $h_1$ | $h_2$ | $h_3$ | $h_4$ | $h_5$ | $h_6$ | $h_7$ | $h_8$ | $h_9$ | $h_{10}$ | $h_{11}$ | $h_{12}$ | $h_{13}$ | $h_{14}$ | $h_{15}$ |
| $A_{0.01}$      | 100                        |     |     |       |       |       |       |                 |                 |       |       |       |       |       |       |       |       |       |          |          |          |          |          |          |
| $d$             |                            | 56  | 100 |       |       |       |       |                 |                 |       |       |       |       |       |       |       |       |       |          |          |          |          |          |          |
| $f$             |                            | -24 | -65 | 100   |       |       |       |                 |                 |       |       |       |       |       |       |       |       |       |          |          |          |          |          |          |
| $s_1$           |                            | -8  | 47  | -20   | 100   |       |       |                 |                 |       |       |       |       |       |       |       |       |       |          |          |          |          |          |          |
| $s_2$           |                            | 2   | 44  | -35   | 90    | 100   |       |                 |                 |       |       |       |       |       |       |       |       |       |          |          |          |          |          |          |
| $s_3$           |                            | 4   | 69  | -14   | 89    | 99    | 100   |                 |                 |       |       |       |       |       |       |       |       |       |          |          |          |          |          |          |
| $s_4$           |                            | -5  | 44  | -39   | 98    | 87    | 87    | 100             |                 |       |       |       |       |       |       |       |       |       |          |          |          |          |          |          |
| $\tan \theta_0$ |                            | 10  | 71  | -36   | 91    | 93    | 95    | 89              | 100             |       |       |       |       |       |       |       |       |       |          |          |          |          |          |          |
| $\frac{u}{h_0}$ |                            | 4   | 67  | -30   | 86    | 100   | 99    | 87              | 93              | 100   |       |       |       |       |       |       |       |       |          |          |          |          |          |          |
| $h_1$           |                            | -19 | 35  | -9    | 92    | 76    | 78    | 88              | 83              | 75    | 100   |       |       |       |       |       |       |       |          |          |          |          |          |          |
| $h_2$           |                            | 23  | -31 | -4    | -27   | -73   | -75   | -84             | -78             | -72   | -97   | 100   |       |       |       |       |       |       |          |          |          |          |          |          |
| $h_3$           |                            | 18  | 80  | -53   | 73    | 76    | 81    | 69              | 89              | 77    | 70    | -62   | 100   |       |       |       |       |       |          |          |          |          |          |          |
| $h_4$           |                            | -3  | 59  | -80   | 77    | 73    | 77    | 75              | 86              | 73    | 79    | -71   | 95    | 100   |       |       |       |       |          |          |          |          |          |          |
| $h_5$           |                            | -14 | 45  | -31   | 75    | 67    | 71    | 74              | 81              | 67    | 79    | -72   | 87    | 98    | 100   |       |       |       |          |          |          |          |          |          |
| $h_6$           |                            | 8   | -2  | 8     | 9     | -2    | -4    | 14              | -4              | -1    | 1     | 5     | 6     | 11    | 15    | 100   |       |       |          |          |          |          |          |          |
| $h_7$           |                            | -25 | 14  | 13    | 47    | 38    | 42    | -17             | 50              | 37    | 52    | -53   | 50    | 63    | 64    | 2     | 100   |       |          |          |          |          |          |          |
| $h_8$           |                            | 23  | 0   | -48   | -22   | -22   | -26   | -23             | -19             | -22   | -31   | 55    | -3    | -6    | -7    | 21    | -26   | 100   |          |          |          |          |          |          |
| $h_9$           |                            | -3  | 58  | -31   | 69    | 64    | 68    | 67              | 74              | 64    | 71    | -64   | 85    | 89    | 87    | 17    | 55    | -6    | 100      |          |          |          |          |          |
| $h_{10}$        |                            | -50 | -4  | 16    | 49    | 50    | 50    | 51              | 36              | 49    | 43    | -46   | 17    | 25    | 28    | -4    | 18    | -23   | 27       | 100      |          |          |          |          |
| $h_{11}$        |                            | -36 | 18  | 4     | 57    | 70    | 69    | 55              | 49              | 69    | 43    | -53   | 33    | 37    | 37    | 1     | 24    | -26   | 41       | 79       | 100      |          |          |          |
| $h_{12}$        |                            | -51 | -13 | 41    | 64    | 31    | 35    | 44              | 36              | 29    | 61    | -75   | 26    | 43    | 49    | -10   | 55    | -61   | 36       | 43       | 62       | 100      |          |          |
| $h_{13}$        |                            | -8  | -55 | 17    | -84   | -81   | -81   | -82             | -81             | -71   | -88   | 88    | -62   | -59   | -54   | 7     | -30   | 37    | -54      | -35      | -48      | -39      | 100      |          |
| $h_{14}$        |                            | -63 | -42 | 25    | 35    | 11    | 11    | 34              | 20              | 8     | 49    | -45   | 19    | 48    | 61    | 17    | 54    | -7    | 39       | 31       | 20       | 62       | -5       | 100      |

Table II shows that path length has a high correlation coefficient with the fade depth, but not the highest. It is the grazing angle which seems to be most correlated. The correlation coefficient for  $\theta$  was also computed without first taking the logarithm (e.g., eq. 3), and the value of -0.68 is the highest correlation coefficient obtained so far with a single variable. But neither  $\theta$  nor  $\log(\theta)$  gave a lower standard error for the single variable fit after iteration than did  $\log(d)$ . It should be noted that  $\log(d)$  shows a fairly high correlation with several other variables of interest such as roughness and frequency. This expresses the fact that links over rough terrain tend to be longer than average, and that the highest frequency links tend to have shorter than average path lengths. This and other correlations in data for operational links are unavoidable, so that care must be taken in interpreting the regression results.

#### 5.4 Regression equations.

A systematic procedure was followed in the present analysis to obtain regression equations with an increasing number of variables. From the correlation matrix (Table II) some promising variables are picked. An iterative regression is carried out for each of them and the variable giving the lowest standard error  $\sigma$  is chosen to enter the equation. The prediction errors from the model with this variable are then correlated with all the other variables and a new set promising candidates are picked to be added to the regression equation. This process is stopped after the sixth variable. The results are presented in Tables III, IV, and V.

TABLE III: Coefficients and Student's-t statistics from regressions before and after iteration.

| Variables      | Regression coefficients |       |       |       |       |       |       |       |  | Student's-t statistics; theoretical values for 5% significance level are given first. |       |       |       |       |       |       |       |      |
|----------------|-------------------------|-------|-------|-------|-------|-------|-------|-------|--|---|-------|-------|-------|-------|-------|-------|-------|------|
|                | 1                       | 2     | 3     | 4     | 5     | 6a    | 6b    | 6c    |  | 1   | 2     | 3     | 4     | 5     | 6a    | 6b    | 6c    |      |
| Constant       | -1.73                   | 5.47  | -13.3 | 1.74  | 7.93  | -27.6 | 4.07  | 3.81  |  | 2.01  | 2.02  | 2.02  | 2.02  | 2.02  | 2.02  | 2.02  | 2.02  | 2.02 |
| a)             | -17.3                   | -6.91 | -29.1 | -18.2 | -8.97 | -16.2 | -10.4 | -4.40 |  |   |       |       |       |       |       |       |       |      |
| $\log(d)$      | 19.3                    | 16.6  | 25.9  | 20.8  | 15.4  | 21.0  | 17.5  | 15.4  |  | 4.58  | 5.35  | 6.03  | 4.91  | 2.58  | 3.93  | 2.96  | 2.58  |      |
| a)             | 29.0                    | 26.3  | 35.7  | 32.6  | 25.1  | 25.7  | 26.2  | 24.8  |  | 9.30  | 10.9  | 12.7  | 12.4  | 6.97  | 6.86  | 7.14  | 6.94  |      |
| $\log(f(c_p))$ |                         | -12.8 | -14.0 | -11.4 | -13.2 | -11.8 | -7.72 | -12.6 |  |   | -4.70 | -5.38 | -4.53 | -4.50 | -4.68 | -1.89 | -4.33 |      |
| a)             |                         | -12.8 | -14.1 | -11.4 | -13.2 | -12.9 | -11.3 | -13.8 |  |   | -6.76 | -8.29 | -7.36 | -7.60 | -7.33 | -4.45 | -7.87 |      |
| $\log(f)$      |                         | 8.81  | 7.98  | 7.05  | 14.0  | 7.54  | 6.75  |       |  |   | 2.62  | 2.59  | 2.24  | 4.51  | 2.46  | 2.14  |       |      |
| a)             |                         | 8.85  | 9.34  | 7.42  | 9.29  | 7.86  | 7.37  |       |  |   | 4.00  | 4.89  | 3.92  | 4.08  | 4.13  | 3.90  |       |      |
| $\log(\theta)$ |                         |       | -11.5 | -15.4 | -15.2 | -15.2 | -15.8 |       |  |   | -3.15 | -3.24 | -3.71 | -3.29 | -3.33 |       |       |      |
| a)             |                         |       | -12.1 | -16.4 | -16.9 | -15.9 | -16.3 |       |  |   | -5.30 | -5.75 | -5.92 | -5.54 | -5.72 |       |       |      |
| $\log(s_p)$    |                         |       |       |       | 4.53  | 4.98  | 5.00  | 4.05  |  |   |       |       |       | 1.26  | 1.61  | 1.43  | 1.12  |      |
| a)             |                         |       |       |       | 5.64  | 5.85  | 5.14  | 5.97  |  |   |       |       |       | 2.61  | 2.70  | 2.37  | 2.76  |      |
| $\log(\theta)$ |                         |       |       |       |       | 14.7  |       |       |  |   |       |       |       |       | 3.88  |       |       |      |
| a)             |                         |       |       |       |       | 3.53  |       |       |  |   |       |       |       |       | 1.34  |       |       |      |
| $\log(f(s_p))$ |                         |       |       |       |       |       | -7.83 |       |  |   |       |       |       |       |       | -1.83 |       |      |
| a)             |                         |       |       |       |       |       | -3.11 |       |  |   |       |       |       |       |       | -1.17 |       |      |
| $\log(h_{ob})$ |                         |       |       |       |       |       |       | 3.55  |  |   |       |       |       |       |       |       | 1.09  |      |
| a)             |                         |       |       |       |       |       |       | -3.04 |  |   |       |       |       |       |       |       | -1.56 |      |

a) after 20 iterations

Table III presents the regression coefficients and the corresponding Student's-t statistics from before and after the iteration. The order of variables from the top indicates the order of importance down to and including the fifth variable  $s_p$ . As evident from the Student's-t statistics, all five variables are significant, at least after iteration. The results for three possible six variable combinations are also given, but only the geometric mean beamwidth  $\theta$  shows some significance before iteration. The lack of significance of  $\theta$  after iteration may be due to the fact that its distribution from one geoclimatic region to another varies too much. For such variables it might be better to establish the coefficient only from regression without iteration. Investigation is continuing.

TABLE IV: Geoclimatic factors, standard errors ( $\sigma$ ), multiple determination coefficients ( $R^2$ ), and F-test for the regressions in Table III.

| Regr. in<br>Tab. III | Geoclimatic factors for the regions (dB): |     |      |      |     |      |      |     | $\sigma$ [dB] | $R^2$ [%] | F         |
|----------------------|---|-----|------|------|-----|------|------|-----|---------------|-----------|-----------|
|                      | SE  | EA  | SMN  | SV   | SMI | PMN  | RTJ  | MMN |               |           |           |
| 1                    | -4.6                                      | 6.6 | -9.0 | -0.8 | 0.4 | 0.1  | 1.8  | 0.2 | 6.4           | 4.9       | 31.8 65.8 |
| 2                    | -4.1                                      | 6.3 | -1.4 | -7.0 | 4.4 | -2.8 | 0.1  | 2.5 | 5.5           | 3.8       | 54.6 79.5 |
| 3                    | -3.9                                      | 7.5 | -2.0 | -5.7 | 3.8 | -3.3 | -3.0 | 2.4 | 5.1           | 3.6       | 60.8 85.8 |
| 4                    | -3.5                                      | 8.0 | -4.2 | -2.2 | 3.0 | -1.6 | -2.4 | 1.9 | 4.7           | 2.9       | 68.3 90.6 |
| 5                    | -3.5                                      | 7.9 | -4.3 | -2.7 | 2.7 | -2.0 | -0.2 | 1.4 | 4.6           | 2.8       | 69.5 91.1 |
| 6a                   | -3.4                                      | 7.4 | -4.2 | -2.4 | 3.2 | -2.1 | -0.7 | 1.7 | 4.0           | 2.8       | 77.8 91.2 |
| 6b                   | -2.9                                      | 7.4 | -4.2 | -2.1 | 2.3 | -2.1 | -0.1 | 1.1 | 4.5           | 2.9       | 71.9 91.3 |
| 6c                   | -4.0                                      | 7.5 | -4.6 | -2.7 | 3.4 | -1.8 | -0.1 | 1.7 | 4.6           | 2.8       | 70.4 91.5 |

Table IV gives the measures of goodness of the fit for each regression, and the geoclimatic correction factors obtained. (The goodness of fit values without iteration are

listed in the leftmost columns, those with iteration on the right.) As expected from previous results [1], the range in the geoclimatic factor over all regions tends to decrease as additional variables are added.

Table V gives the correlation coefficients between the residuals from each model and the variables. Although even the highest values might appear low at first glance, this is normal in a multivariable problem such as this. The Student-t statistics indicate significance at least to the fifth variable, and the goodness-of-fit statistics indicate an increasingly better fit as more variables are added. The four variable model would seem to represent a good tradeoff between accuracy and practicality, but further investigation is warranted before a final prediction equation (or equations) are suggested for this region of the world.

TABLE V: Results of correlation analysis on residuals. The correlation coefficients are between the residuals for a model (predicted - measured values) with iteration given in Table III and IV and the remaining variables.

| Residuals<br>after a<br>model with | Logarithm of d, f, ..... |     |             |       |       |             |       |    |                             |       |           |       |          |          |          |       |       |       |       |       |     |    |
|------------------------------------|--------------------------|-----|-------------|-------|-------|-------------|-------|----|-----------------------------|-------|-----------|-------|----------|----------|----------|-------|-------|-------|-------|-------|-----|----|
|                                    | d                        | f   | $s_2$<br>km | $s_4$ | $s_1$ | $s_2$<br>km | $s_3$ | s  | $\tan^{-1} \frac{s_2}{s_3}$ | $h_m$ | $h_{4/3}$ | $h_1$ | $h_{0b}$ | $h_{fr}$ | $\theta$ | $a_p$ | $z_p$ | $z_0$ | $K_a$ | $K_p$ | $v$ |    |
| log(d)                             | 0                        | -17 | 22          | 23    | 24    | 20          | 20    | 22 | 24                          | -20   | 27        | 35    | 37       | 0        | 20       | 5     | 34    | 53    | 38    | 23    | -5  | 38 |
| + log(f(s <sub>p</sub> ))          | 0                        | -32 | 0           | 1     | 1     | -6          | 0     | 1  | 5                           | 3     | 19        | 25    | 28       | 12       | 15       | 24    | 23    | 0     | 5     | -1    | 12  | 28 |
| + log(f)                           | 0                        | 0   | 10          | 8     | 8     | 6           | 8     | 7  | 16                          | -15   | 22        | 30    | 32       | 15       | 34       | -3    | 23    | 0     | 10    | 23    | 1   | 34 |
| + log( $\theta$ )                  | 0                        | 0   | -9          | -1    | -2    | -13         | -10   | -1 | -7                          | 5     | 1         | -1    | -2       | 13       | 4        | -7    | -6    | 0     | 10    | 5     | 8   | 0  |
| + log(s <sub>2</sub> )             | 0                        | 0   | 2           | 4     | 2     | 0           | -5    | 5  | 1                           | -4    | 0         | 0     | -1       | 16       | 2        | -9    | -3    | 0     | 7     | 5     | -3  | 0  |

It is noteworthy that the order of variable importance resulting from the systematic approach followed would be slightly different if the t-statistics after iteration were considered: θ and f would be interchanged, and possibly f(s<sub>p</sub>) and d. It must be emphasized, however, that the question of order is less important than the final combination of variables.

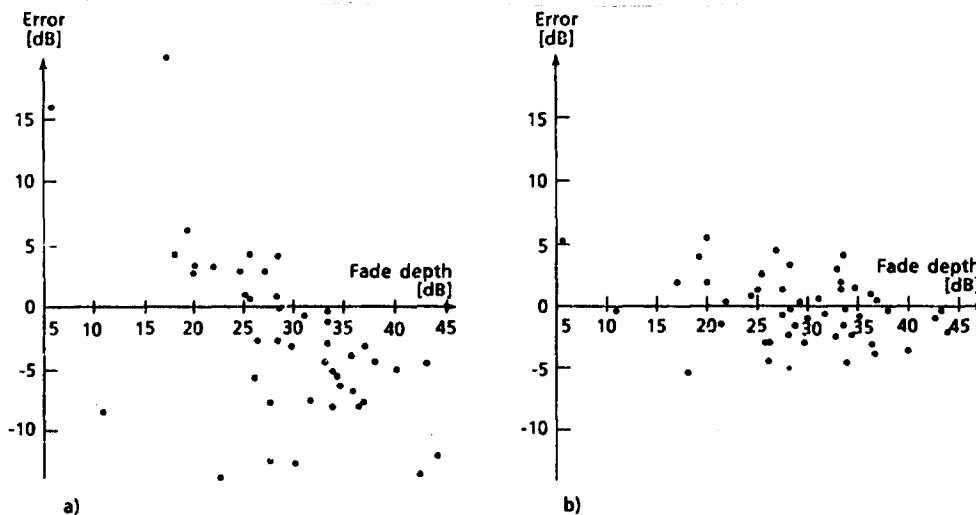


Fig. 3. Prediction errors with respect to 47 first "tail" data points at 0.01% of the time for  
a) the model in [6] for North Western Europe.  
b) the model based on d, f(s<sub>p</sub>), f, θ, s<sub>2</sub> (100m samples), and geoclimatic variation.

The overall improvement for the five variable model in Tables III and IV compared with the existing model presented in [6] for North Western Europe is demonstrated in Fig. 3, with the residuals (predicted - measured values) plotted against the measured values of reference tail fade depth  $A_{0.01}$ . The existing method has a mean error of about -3 dB, and a standard deviation of 6.7 dB when tested on the new expanded tail data base. (The

corresponding standard deviation of error for the five variable model, as distinct from the standard error of regression  $\sigma$  for six degrees of freedom, is 2.6 dB.) This is perhaps not surprising since it is based on only path length and frequency, and does not allow for geoclimatic variation within France and the U.K. It can be seen from Table IV, however, that a good two-variable fit to the new tail data base would give a standard error of slightly less than 5.5 dB. Of course the mean error should be zero.

## 6. DISCUSSION

With the extensive analysis presented in this paper, some interpretation of the physical basis is now possible. The detailed background to this interpretation is presented in one companion paper [5], and the associated meteorological aspects are discussed in another [11].

Considering each variable of the five variable model in turn, path length  $d$  shows itself to be a significant one as in earlier analyses [1,12], and is the first to enter the regression. Its importance would seem to be due to the fact that several mechanisms depend on it in mutually enhancing ways [5]. As  $d$  increases, the amount of flat fading due to defocussing should increase. So also should the amount of fading due to atmospheric multipath when it is the "flat" fading mechanism. At the same time, the relative strengths of both specular and diffuse reflections from the ground tend to increase with increasing path length, increasing the likelihood of deep selective fading resulting from the combination of atmospheric and ground reflected signals. Less important but perhaps still significant, the fading of the atmospheric signal component and the corresponding uncorrelated enhancement of the ground reflected signal component due to scintillation also tend to increase with increasing path length.

The second variable to enter the regression is path inclination, with a fairly high negative coefficient. The significance of this variable is again believed to be due to more than one mechanism. Perhaps most importantly, as the path inclination increases the amount of flat fading due to defocussing should tend to decrease, for a given exceedence probability. However, so also should the amount of fading due to atmospheric multipath when it is the "flat" fading mechanism. Perhaps less importantly on the terrain side, as the path inclination increases the relative strength of the specular reflection will tend to decrease because of the decrease in the combined antenna directivity in the direction of the specular reflection point (which moves closer to one end of the path).

The third most important variable, the frequency  $f$ , has a positive coefficient as in previous analyses for overland paths. A small factor in this may be the increase in atmospheric scintillation with increasing frequency, and the fact that it affects the atmospheric and ground reflected signal components simultaneously. The major factor, however, is believed to be a ground reflected signal that on average over many links tends to increase with increasing frequency, at least for the frequency range considered. Somewhat speculative reasons for this are given in a companion paper [5].

The fourth variable to enter the regression equation is the grazing angle  $\theta$ , with a negative coefficient. This is believed to be a direct indication of the importance of ground reflection, since the smaller the grazing angle, the larger the effective specular reflection coefficient. It is noteworthy that once the grazing angle is used in the regression, the correlation between the residuals and path clearance (e.g.  $h_0$ ,  $h_1$ , and  $h_2$ ) virtually disappears. This suggests that the significance of path clearance discovered in previous analyses [1,12] was due more to the relationship between grazing angle and path clearance than to a possible decrease in the occurrence of abnormal refractive layers with increasing height.

Although the fifth variable to enter the regression,  $s_0$ , increases the accuracy by only a small amount, it still appears to be a significant one on the basis of the  $t$ -statistic. Moreover, as seen from Table V, it is the values of  $s_0$  calculated for a profile interval of 100m that appear to give the best results. The most plausible explanation is that this variable is somehow related to the amount of diffuse reflection occurring from the ground. Further investigation is required [5].

It is interesting that the introduction of geometric mean beamwidth  $\theta$  as a sixth variable reduces the standard error before iteration to 4 dB, and that the  $t$ -statistic indicates significance. The positive regression coefficient is consistent with the fact that the strengths of specular and diffuse reflections will tend to increase with increasing  $\theta$ . As noted in section 5, the effect of the iteration on this variable needs further investigation. The apparent insignificance of  $h_0$  as a sixth regression variable confirms the basic assumption in the analysis that the data base for France and the UK is not significantly contaminated by subrefractive events.

## 7. CONCLUSION

A large number of possible variables have been investigated to determine their potential importance in an asymptotic prediction equation for the fading distribution in an average worst month. The results suggest that a major improvement over existing models is possible by using additional variables that better reflect the complex mixture of mechanisms involved. In particular, it is clear that effects of ground reflection must be recognized explicitly, even for overland paths.

Although further analysis is warranted before a more definitive model is chosen, the prediction equation involving path length, frequency, path inclination, angle of specular

reflection, and variable geoclimatic factor would seem to represent a good compromise between accuracy (2.9 dB standard error) and simplicity. Of course the ultimate accuracy will depend also on how well the climatic variation can be estimated. A geoclimatic factor variation of about 12 dB is indicated from discrete grouping of average worst month fading measurements in France and the UK. Some associated meteorological measurements [11] suggest, however, that the variation among individual paths may be somewhat larger.

#### 8. REFERENCES

- 1 R.L. Olsen, T. Tjelta, L. Martin, and J.E. Doble (1986), Towards a more accurate method of predicting the distribution of multipath fading on terrestrial microwave links, *Electron. Lett.*, Vol. 22, No. 17, pp. 902-903.
- 2 K. W. Pearson (1965), Method for the prediction of fading performance of a multisection microwave link, *Proc. IEE*, Vol. 112, No. 7, pp. 1291-1300.
- 3 A. Vigants (1975), Space-Diversity Engineering, *Bell Syst. Tech. J.*, Vol. 54, No. 1, pp. 103-141.
- 4 L. Martin, R.L. Olsen, and T. Tjelta (1985), Initial analyses of multipath fading measurements for various geographical conditions in France, *Proc. Int. Symp. on Antennas and Propagation*, Kyoto, Japan, pp. 1067-1070.
- 5 R. L. Olsen, L. Martin, and T. Tjelta (1986), A review of the role of surface reflection in multipath propagation over line-of-sight terrestrial microwave links. This symposium.
- 6 CCIR (1986), Rep. 338, Vol. V, ITU, Geneva, Switzerland.
- 7 CCIR (1986), Rep. 569, Vol. V, ITU, Geneva, Switzerland.
- 8 W.R. Draper and H. Smith (1961), *Applied Regression Analysis*, Second edition, New York, John Wiley and Sons.
- 9 J.E. Doble (1979), Prediction of multipath delays and frequency selective fading on digital radio links in the UK, *IEE colloquium digest*, 62.
- 10 P. Beckmann and A. Spizzichino (1963), *The Scattering of Electro-magnetic Waves from Rough Surfaces*, London, Pergamon Press.
- 11 L. Martin, R.L. Olsen, and T. Tjelta (1986), Coindice de réfraction, météorologie et affaiblissement sur les trajets en visibilité, This symposium.
- 12 D. C. Crombie (1983), Prediction of multipath fading on terrestrial microwave links at frequencies of 11 GHz and greater, *NATO/AGARD Conf. Proc. No. 346*, pp. 10 1-9.

#### ACKNOWLEDGEMENT

Although most of the measurements used in the analysis were obtained from the open literature, some additional data and path characteristics were provided by colleagues, notably J. Battesti, J. E. Doble and A. Leclert.

## DISCUSSION

**A.Tenne-Sens**

Please explain the meaning of the "geoclimatic factor". Does it have a physical interpretation?

**Author's Reply**

As explained in the paper the geoclimatic factors are obtained by forcing the mean prediction error to be zero for each of the eight geographical groups of the data. This geographical variation may be caused by different climatic conditions resulting in, for example, more "median depression" in some regions with respect to others. We have assumed in the analysis that the coefficients of the variables such as  $d$ ,  $f$ , etc. are not graphically dependent. Combined meteorological and propagation measurements should help to give a better understanding of the geoclimatic factor (see Martin et al., this symposium).

**A.N.Ince**

Is the (so-called) "geoclimatic factor" related to the distribution of  $k$ -factor and how?

**Author's Reply**

We do not have  $k$ -factor distributions for the different geographical regions. But, the "median depression" indicated by the geoclimatic factor is more likely to happen for ducting situations and therefore it should be related to the  $k$ -factor distribution.

**B.Segal**

I believe that the geoclimatic factor as presented in this paper should be considered as a "residue" after the regression analysis has been carried out for the different variables and for links within a particular geographic region. At this stage of analysis I do not believe it can be given a deeper physical interpretation.

**Author's Reply**

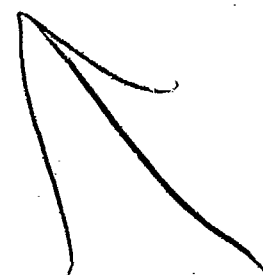
The links are grouped in geographical regions in which the climatic conditions are believed to be approximately constant. Having found the dependency on geoclimatic independent variables such as  $d$ ,  $f$ , etc. for the prediction equation it should be reasonable to interpret the difference between the groups due to climatic conditions resulting in, for example, a variable amount of "median depression".

**L.Bolthius**

1. Vous n'avez pas indiqué la gamme des valeurs des paramètres dans vos formules (fréquence, distance, irrégularité du sol etc.). Ces intervalles ne sont certainement pas indépendants, par exemple la gamme des distance n'est pas la même à 1 GHz et à 20 GHz.
2. Vous ne mentionnez que de liaisons faites dans le même climat. Que deviendraient vos formules par exemple aux Etats Unis, au Japon, en climat équatorial etc.

**Réponse d'Auteur**

- 1- La gamme des valeurs pour les 8 variables utilisée dans les modèles de regression est:  $d$ : 7.5—95 km,  $F(\text{ep})$ : 1.08—24.7 mrad,  $f$ : 1.8—37 GHz,  $f$ : 14—13.4 mrad,  $S_1$  (0.1 km): 3.04—185 mrad,  $h_{\text{eq}}$ : 7.5—61.4 m,  $O$ : 7.1—58 mrad et  $f(\epsilon_f)$ : 1.01—15.0 mrad.
2. Nous n'avons pas comparé les formules de prévision présentées avec d'autres mesures pour le moment. Mais avec la technique présentée, on peut trouver une formule pour toutes les régions du monde où on a donné la mesure en utilisant toutes ces données dans une régression multiple.



AD-P005 732

# A REVIEW OF THE ROLE OF SURFACE REFLECTION IN MULTIPATH PROPAGATION OVER TERRESTRIAL MICROWAVE LINKS

by  
Roderic L. Olsen  
Communications Research Centre  
Department of Communications  
P.O. Box 11490, Station H  
Ottawa, Canada K2H 8S2

Louis Martin  
CNET/LAB/MER  
Route de Trégastel  
22301 Lannion, France

Terje Tjelta  
Norwegian Telecommunication Administration  
Research Department  
P.O. Box 83  
N-2007 Kjeller, Norway

## SUMMARY

It has long been recognized that surface reflection on overwater microwave radio relay paths plays an important role in causing frequency selective multipath fading. However, there has been a tendency among many radio scientists and engineers to assume that similar but less prevalent fading on most overland paths arose mainly from multiple paths through the atmosphere. With the introduction of wide-band digital radio into microwave relay networks, the origin of selective fading has been investigated with renewed interest because of the damaging effects of distortion. There is mounting experimental and theoretical evidence that ground reflection and scattering has an important role in producing much of the selective multipath propagation effects on overland links. This paper reviews both old and new evidence, providing some new insights into the complex mixture of mechanisms involved. Some resulting implications for the design of digital radio links are also discussed.

## 1. INTRODUCTION

Much of the severe fading on terrestrial line-of-sight microwave links has long been recognized to be due to multipath propagation. Its potential to cause thermal noise outages in analog radio systems was discovered early and taken into account in system design. The less significant effect of intermodulation noise resulting from the often frequency selective nature of the most severe fading was more-or-less tolerated, even with increased system bandwidths (Hubbard, 1984). Then with the design and testing of the first wide-band digital radio systems, it was gradually recognized that the distortion resulting from the frequency selective nature of the fading was a more serious source of outage than thermal noise. This resulted in a simultaneous effort by engineers to design radios more immune to this distortion and by propagation researchers to determine more precisely its source and quantify its effect.

It has been known for many years that surface reflection on overwater microwave paths causes deep frequency selective fading. The potential adverse effects on relatively flat overland paths was also recognized and experiments conducted to determine effective reflection coefficients (e.g., Matsuo et al., 1953; Bullington, 1954). However, it appears that deep interference fading on the longer rougher overland paths was usually attributed almost entirely to atmospheric mechanisms, in particular to atmospheric multipath. It is now possible to find many papers in the scientific literature that treat most interference fading on overland links in general as resulting from atmospheric multipath. As late as 1982, even the CCIR (1982) left the impression that the effects of ground reflection were insignificant for the majority of overland paths.

Now with the renewed interest in the effects of multipath propagation on digital radio systems, there is mounting experimental and theoretical evidence that ground reflection and scattering has an important role in producing much of the selective fading on overland paths. Associated with this is the equally important evidence that atmospheric effects, and particularly defocussing, are responsible for reducing the direct signal to a level where the ground reflected signal can interfere destructively with it. The aim of this paper is to review the evidence.

In reviewing the evidence, the authors wish to avoid leaving the impression that the importance of ground reflection on overland paths has been almost totally ignored. There have indeed been a number of works, including those of Beckmann and Spizzichino (1963) and Dougherty (1968), in which its importance has not been overlooked. Fortunately there is now considerably more information from which to make a new assessment. To more quickly advance future investigation, some speculation (possibly incorrect) is included in this assessment.

The various atmospheric and surface mechanisms that have been considered responsible for fading on terrestrial microwave paths are summarized in section 2. The experimental and theoretical results that the authors consider to be evidence for the importance of terrain reflection are then considered in turn in section 3. Section 4 presents some new implications resulting from the importance of terrain reflection, and section 5 presents conclusions.



## 2. PHYSICAL MECHANISMS OF INTEREST

A number of clear-air fading mechanisms on terrestrial microwave paths have been proposed and investigated over about the last four decades. These will be summarized first before presenting the evidence for the important combination of atmospheric fading and surface reflection. Since most of them have been suggested and reviewed previously (Beckmann and Spizzichino, 1963; Dougherty, 1968), the authors will not try to cite all the originators.

Perhaps the most useful classification for the purposes of this paper is the division into atmospheric fading mechanisms, and combined atmospheric and surface mechanisms. Other classifications such as "K-type" fading (earth diffraction fading due to subrefractive bending, or interference fading associated with ground reflection) and "duct type" fading (defocussing and atmospheric multipath fading) (Matsuo et al., 1953), or "power fading" and multipath fading (Dougherty, 1968) have been employed previously. The early one of these seems particularly unfortunate since it does not recognize the combinations that subsequent observations have shown to exist.

### 2.1 Atmospheric fading mechanisms

Several atmospheric fading mechanisms have been investigated:

- (a) Defocussing. This mechanism, which has been variously termed "divergence", "space-wave fadeout" (Bean, 1954) and "diffraction" (Dougherty, 1968), is assumed to be caused by the divergence of waves due to the presence of abnormal refractive layers (usually ducts) in proximity to the path. The fades are often of long duration (several hours), and relatively non-frequency selective. The fading is also fairly non-selective in space, the large zones where it occurs often being termed "shadow regions" or "radio holes". As discussed in section 3, defocussing is considered to be the most prevalent severe atmospheric fading mechanism.

Although as discussed in section 3, regular horizontal ducts either below the path or intermediate between the antenna heights on an inclined path can cause defocussing, another type of defocussing with a finer spatial scale has also been considered. This defocussing could originate from an undulating (wavy) abnormal refractive layer between the terminals on an inclined path (Strickland, 1980). It is particularly indicated from the measurements of severe fading on low elevation angle earth-space paths (Strickland et al., 1977). Further investigation of this likely faster varying type of defocussing is required.

- (b) Atmospheric multipath. This mechanism in which the transmitted wave follows two or more discrete paths is also usually assumed to be due to a duct in proximity to the path. The additional paths are usually assumed to result from gradual refractive bending, but reflection from an elevated layer or a layer below the path have been considered. More generally, other types of abnormal layers can also cause atmospheric multipath fading (Dougherty and Dutton, 1981; Segal, 1985). This mechanism is also discussed in more detail in section 3.
- (c) Antenna decoupling. As a result of abnormal refractivity gradients, the beam can be bent off the axes of the antennas, resulting in non-frequency-selective attenuation. It can be particularly severe for links in which the antennas are mispointed or have beamwidths that are too narrow. Although the levels of this fading can be estimated, given the antenna beamwidths and information on the distribution of angle-of-arrival (Webster, 1982), the uncertainty in antenna pointing accuracy makes its prevalence difficult to assess. It is noteworthy, however, that Webster (1983) has shown that large angles-of-arrival are associated with defocussing layers below the path. Thus, there may be some antenna decoupling loss in many defocussing situations. Again, further investigation is required.
- (d) Scintillation. This very fast frequency selective fading is due to scattering from many small turbulent irregularities in the atmosphere. It is always present to some degree superimposed on the slower deeper fades arising from the other mechanisms. Since its magnitude increases with increasing frequency, it has made the identification of other fast fading mechanisms difficult.

As noted, mechanisms (a) and (b) are usually assumed to arise as a result of ducts in proximity to the path. A detailed review of the meteorological mechanisms that produce ducts is beyond the scope of this paper. It may be noted, however, that surface ducts are caused by advection, evaporation, frontal processes, and radiation, and elevated ducts by advection, subsidence, and advective intrusion. Surface and elevated subrefractive layers that are sometimes involved are caused by some of these and other processes. More detailed information is given elsewhere (Ikegami et al., 1966; Dougherty and Dutton, 1981).

### 2.2 Combined atmospheric and surface fading mechanisms

Several combined atmospheric and surface mechanisms have been considered and investigated to varying degrees:

- (a) Defocussing plus reflection. This would seem to be the most likely mechanism producing the many observed instances of fast frequency selective fading superimposed on slow non-selective fading (see section 3). The combination of the fine-scale type of defocussing noted in the previous sub-section and surface reflection could explain the very severe fading on very low angle earth space paths.
- (b) Atmospheric multipath plus surface reflection. Here the atmospheric multipath is expected to produce relative non-selective ("quasi-flat") fades across the system bandwidths normally in use. As discussed further in section 3, the authors contend that the surface multipath should not be significantly more selective than the interfering atmospheric multipath. The resulting fades, however, can be very deep.

- (c) Antenna decoupling plus surface reflection. On most paths, this mechanism may be more important associated with mechanism (a) than it is on its own.
- (d) Scintillation plus surface reflection. Again this mechanism is most likely when associated with mechanism (a) (see section 3). To be significant on its own, the effective surface reflection coefficient would need to approach unity, a not unlikely situation on overwater paths.
- (e) Earth diffraction resulting from subrefraction. Here a subrefractive layer below the antennas causes the direct wave to intercept the earth ("earth bulge"), with the resulting relatively non-selective diffractive attenuation. The occurrence of significant diffractive attenuation is minimal on well-designed paths with adequate surface clearance.

In mechanisms (a) to (d), the degree to which the surface reflection is "specular" or "diffuse" will depend on many factors (Beckmann and Spizzichino, 1963), which are not all yet well understood, particularly for the relatively long microwave paths of interest here. Some initial consideration to this question is given in section 3.

### 3. EXPERIMENTAL AND THEORETICAL EVIDENCE

There is much experimental and theoretical evidence that surface reflection is an important factor in causing selective fading on terrestrial microwave links. It comes not so much from one or a limited number of investigations, even though some of these have been very productive, as from a synthesis of the results of many. To best make this synthesis, it seems useful to classify the evidence and consider it in some suitable order. Thus, in this section the multitude of observations of fast selective fading superimposed on slow quasi-flat fading are first reviewed. Following this the most likely atmospheric mechanisms (defocussing and atmospheric multipath) that could produce the slow quasi-flat fading are considered. Then to demonstrate that reflection from terrain is sufficiently strong to interfere destructively with these atmospheric fading mechanisms, measurements and calculations of effective ground reflection coefficients are discussed. Finally, to indicate that the fast highly selective interference fading most likely originates from the ground reflected component, the relative delays of atmospheric and surface reflected rays are compared. Following these main sub-sections, two other groups of supporting evidence are discussed (results of correlation and multiple regression calculations on large data bases, and multipath depolarization observations) along with miscellaneous supporting evidence.

Since it is believed that experimental results from overwater paths help clarify those from overland paths, these are considered along with the latter. The main differences between overwater and overland paths are believed to be the more frequent and severe defocussing on overwater paths, the more stable and higher level specular reflection, and lesser amount of diffuse reflection. While combined slow and fast fading events are more frequent on overwater paths they are not greatly different in overall character than those on overland paths.

#### 3.1 Observations of selective fading superimposed on quasi-flat fading

Among the most important evidence that ground reflection and scattering interacts with atmospheric fading mechanisms are the many observations of rapid deep fading superimposed on shallower much slower fading. The slow fading, often referred to as "median depression" or "mean depression", has usually been assumed to result from atmospheric defocussing. The rapid fading has usually been assumed to be interference fading of atmospheric origin, either scintillation or multipath. Among these many experiments have been a few using sophisticated channel probing techniques in which the slow fading component was recognized as relatively non frequency selective (quasi-flat) and the rapid fading as selective.

Crawford and Jakes (1952) in their pioneering swept-frequency experiment were perhaps the first to measure a rapid frequency selective component superimposed on a slow non-selective component (see also Friis (1948)). They noted in fact that reflection from the small water portion of their path was a source of fading in abnormal circumstances, and that it would be desirable to avoid paths with significant ground reflections. However, they seem to have concluded from their associated angle-of-arrival measurements that atmospheric multipath was the most frequent cause of severe fading. Unfortunately as they indicated, the minimum angle-of-arrival in their scan ( $-0.8^\circ$ ) was not sufficiently low that they could be always certain that the surface reflected ray was in range.

Using frequency-sweep equipment similar to that of Crawford and Jakes, Kaylor (1953) produced the first statistics of amplitude selectivity as a function of fade depth (Fig. 1). He noted that no deep interference fading occurred on his 49 km overland path unless the signal was already depressed 10 dB or so across the entire 400 MHz band observed. He concluded that this depression was most likely due to interfering atmospheric rays of slight relative delay, but noted that it could also be due to non-selective attenuation of the direct signal. It is interesting that Kaylor demonstrated that small amplitude components (e.g., levels of -32 dB and -34 dB relative to direct signal level) could have a marked effect on notch shapes, while simultaneously implying that a much larger estimated ground reflection level for his path ( $< -20$  dB) could be ignored. Crawford and Jakes (1952) also arrived at the same seemingly contradictory conclusion in their earlier work.

In their early paper on multipath distortion, Omori and Sato (1958) implicitly recognized from their swept-frequency measurements the superposition of selective and non-selective components, and described a novel technique for measuring the non-selective component. In attempting to explain the three-frequency measurements of Ugal (1961) in which the superposition of selective and non-selective fading was recognized, Ikegami (1967) suggested the possibility of ground reflected waves among others. Unfortunately, as noted previously by Segal (1985), the possibility of a significant ground reflection component in his own pioneering measurements (Ikegami, 1959, 1967; Ikegami et al., 1966) was not considered.

More recent swept- or multi-frequency measurements (e.g., Babler, 1972; Rummier, 1979; Sandberg, 1980; Webster and Ueno, 1980; Stephansen, 1981; Liniger, 1982, 1983; Martin, 1982a, 1984; Sakagami and Hosoya, 1982; Bundrock and Murphy, 1984; Hubbard, 1984; Valentin and Metzger, 1984; Lam and Webster, 1985; Lambers and Marr, 1985) have shed further light on the underlying fading mechanisms and provided more quantitative information on the selective and non-selective signal components. Although he did not consider in detail the possible physical mechanisms involved in his measurements, Rummier (1979) devised a practical channel model that incorporated quasi-flat and selective fading parameters describing his data. Using fairly narrow-band measurements (60 MHz), Sakagami and Hosoya (1982) were nonetheless very successful in proving that their results were due to the combination of a quasi-flat atmospheric signal and a surface reflected signal. They were further able to identify both specular and diffuse components in the reflected signal.

On the basis of wide-band (400 MHz) swept-frequency amplitude and group-delay measurements, one of the authors (Martin, 1982a) concluded for his particular 50 km, 11.5 GHz path that deep selective fading always occurred superimposed on a quasi-flat component. This is illustrated statistically in Fig. 2, which displays three levels of the conditional distribution of peak-to-peak amplitude variation within the band ( $\Delta A$ , in dB) as functions of the peak fade depth ( $A_x$ , in dB). These measurements are discussed further in sub-sections 3.2, 3.3, and 3.4.

Bundrock and Murphy (1984) described the initial results of wide-band (1000 MHz) swept-frequency amplitude and group delay measurements on an overland path specifically chosen to facilitate observation of the effect of ground reflection. They showed the increase in selectivity with increasing fade depth in terms of the amplitude slope statistics within the band, a particularly useful approach for application to digital radio systems. More importantly for this review, they attributed their results to the combination of atmospheric defocussing of the direct signal and ground reflection. They noted, furthermore, an apparent increase in the effective ground reflection coefficient simultaneously with the defocussing of the direct signal (see sub-section 3.3).

Many investigators of overwater paths have had little difficulty in ascribing the superposition of slow, shallow and fast, deep fading to the interaction of an atmospheric mechanism and surface reflection. The conclusion that these are non-selective and selective, and derive respectively from the atmosphere (defocussing) and the sea surface (specular reflection), was particularly clear in the wide-band (1000 MHz) amplitude and angle-of-arrival measurements of Lam and Webster (1985). Interpretation of the mechanisms involved was made difficult, however, by the obstacles partially blocking the surface reflected ray on the two paths investigated. The distributions of direct and reflected signal amplitudes and relative delay for one of the paths, presented in Fig. 3, are discussed further in sub-sections 3.2 and 3.4.

While some investigators using sophisticated channel probing techniques have continued to clarify the propagation mechanisms responsible for combined non-selective and selective fading, others have been constructing models that include the two effects. Pearson (1965) noted the frequent occurrence of median depression associated with multipath fading and partially accounted for it in his model for the single frequency fading distribution. Barnett (1972) described the same phenomenon and tried to account for it in his model by employing a climate-dependent multipath probability occurrence factor. The degree to which the earlier model of Morita (1970) (see also Morita and Kakita, 1958) includes the effect of median depression is unclear, since Morita later introduced a modification (Morita, 1972) designed to take this into account. (In the same paper Morita illustrated the potential importance of including the effect of ground reflection and presented a method designed to do it.) More recently, the combined effect of selective fading superimposed on non-selective fading has been taken into account in channel distortion models (e.g., Rummier, 1978; Martin, 1982a,b; Sakagami and Hosoya, 1982; Sylvain and Lavergnat, 1985; Lavergnat and Sylvain, 1985a).

It is noteworthy that Beckmann and Spizzichino (1963) in their earlier review (Chapter 16) recognized the possibility of very severe fading (40 - 45 dB) when both slow and fast fading are present simultaneously, although they were uncertain as to the cause of the fast fading. They cite, for example, diffuse scattering from the earth or atmosphere. However, they noted the very important result common to this now large body of observations: "the lower the mean (non-selective) level, the greater the amplitude of the rapid (frequency selective) fluctuations".

### 3.2 Atmospheric multipath and defocussing: mechanisms and fade depths

Although mechanisms causing quasi-flat fading have been introduced in section 2, and further background information given in sub-section 3.1, the main mechanisms of defocussing and atmospheric multipath require further consideration. Concerning the mechanisms themselves, the major points of interest are the atmospheric structure under which they occur, their relative frequency of occurrence, and the possibility of simultaneous occurrence. Of course the fading levels attained are also important because this will partially determine the possibility of destructive interference with the ground reflected and scattered waves.

**Mechanisms.** The possible physical bases of defocussing and atmospheric multipath have been a subject of investigation for over four decades. Although an extensive review is beyond the scope of this paper, the important early work of several investigators (Sharpless, 1946; Price, 1948; Doherty, 1952; Crawford and Jakes, 1952; Rivet, 1956; Ikegami, 1959; Dutton, 1961) should be noted. For this paper, the work of Ikegami (1959, 1966, 1967) and more recently Webster (1983) is particularly germane.

A useful illustration of the remarkable work of Ikegami is presented in Figs. 5(a) and 5(b). These show the relationship between fading on two adjacent 55 km, 4 GHz paths (one horizontal and one inclined) and the heights of single and multiple ducts. Fig. 5(a) gives 5-minute mean received power, and Fig. 5(b), the 5-minute fading range (difference between the 10% and 90% levels of the distribution) as functions of height.

On the oblique path, a considerable mean depression and apparently superimposed fast fading is seen to occur when the duct exists near the height of the lower terminal. This occurs on the horizontal path when the duct is near the level of the path. Some fading occurred for duct heights above the paths, and between the terminals on the inclined path, but it was obviously much less severe. On the basis of ray theory, Ikegami explained the depression as due to the divergence of rays, or defocussing that occurs within a large shadow region. He explained the fast fading as due to destructive interference that he felt occurred between two groups of rays within a small "interference region" (see Figs. 6 and 7). Unfortunately, he did not explain for his own data why the mean depression and the faster fading occurred simultaneously, in spite of the fact that his shadow zones and interference zones were not coincident. Explaining this superposition of slow and fast fading in other data (Ugal, 1961), he noted the possibility of a ground reflected signal, as well as the seemingly impossible superposition of zones (Ikegami, 1967).

Fig. 8 displays some of the clarifying ray-tracing results of Webster (1983). Shown for a 50 km horizontal path (100 m antenna heights) are the ray amplitudes, relative delays, and angles-of-arrival as functions of the height of a 100 m thick duct of  $-20$  dB intensity. As evident, when the duct center is below a height just above the path, only a defocussed direct ray exists. The greatest defocussing occurs at about, or just above, the path height. (Since the angle-of-arrival is also greatest at this height, the greatest amount of antenna decoupling would occur simultaneously, the amount depending on the antenna beamwidths and pointing accuracy.) Over a range of greater heights, three-ray atmospheric multipath occurs. (The relative delays associated with the additional paths are discussed in sub-section 3.4.) For the particular "interference region" he investigated, Webster demonstrated that the lower antenna height is critical for inclined paths (i.e., defocussing of the single direct ray occurs below this height). He did not consider the effect of ground reflection although he noted the possibility.

A comparison of these results confirms Ikegami's conclusion that the large mean depression for a layer below the lower terminal height was due to defocussing. It also suggests that the less prevalent and less severe fading for higher duct heights was due to atmospheric multipath. It is interesting to note that in an earlier study similar to the later one of Ikegami, Matsuo et al. (1953) indicated that fading for ducts above the path was of the rapid interference type. Nevertheless, neither Webster's nor Ikegami's theoretical results seem to adequately explain the apparent simultaneous mean depression and faster fading in Ikegami's data. The best explanation would seem to be the presence of a significant ground reflected component. The likelihood of focussing-enhanced ground reflection is discussed in sub-section 3.3.

On the basis primarily of these and other results it is possible to speculate on the relative frequency of occurrence of defocussing and atmospheric multipath. From Fig. 8 it is apparent that significant defocussing should exist over a much greater duct height range than destructive atmospheric multipath. Even though atmospheric multipath occurs over a sizeable duct height range, the main two rays would not be in phase opposition except for a small number of discrete heights (e.g., nine at 4 GHz). A similar conclusion seems possible from Ikegami's theoretical results that show his "interference" regions to be much smaller and at greater distances than shadow (defocussing) regions (see also Dutton, 1961). Furthermore, as implied by Ikegami (1959, 1967), it is only for a small portion of these interference regions (next to the shadow region boundary) that significant atmospheric multipath fading would be possible. (The possibility of signal enhancements caused by the presence of one of these interference regions at the receiving antenna seems more likely.)

The presence of Ikegami's small interference regions for duct heights below the path implies that Webster missed this possibility in his ray-tracing investigation. Ikegami (1967) also noted the possibility of interference regions arising from a subrefractive layer, and Segal (1985) confirmed this. Segal further noted the possibility of atmospheric multipath occurring as a result of a superrefractive layer. Nevertheless, it is important to emphasize that these theoretical results indicate that the regions of the atmosphere where multipath is possible are much less likely to be present at the receiving antenna than the defocussing-inducing shadow zones. The available observations seem to confirm this. Further analysis for multi-layer situations would be desirable.

**Atmospheric multipath fading levels.** Since the presence of atmospheric multipath implies the possibility of destructive interference at microwave frequencies, a wide range of fade levels are obviously possible given rays of approximately equal amplitude. This appears to be confirmed from the small number of observations available that indicate the presence of multipath without median depression. However, it is recognized that likely simultaneous occurrence of atmospheric and surface multipath itself make atmospheric multipath levels difficult to determine from simple measurements. A close scrutiny of swept-frequency amplitude measurements for the presence of rapidly changing quasi-flat fades should make this possible. In any case, it is not difficult to imagine the possibility of atmospheric multipath fades sufficiently deep to cause further destructive interference with the significant surface reflected wave apparently present on many paths (see sub-section 3.3).

**Defocussing fade levels.** Because of the slowly varying nature of defocussing attenuation and probably because of the greater size of shadow regions, measurements of fade depth are more readily available. These are available in three main forms: (i) direct measurements of slow fading, (ii) median depression estimates from data with superimposed slow and fast fading, and (iii) median depression estimates from swept-frequency measurements.

A number of direct measurements of defocussing levels have been made (e.g., Bean, 1954; Barsis and Johnson, 1962; Barsis et al., 1963; Hauteville et al., 1980). In the best of these, the use of multiple frequencies aided the interpretation that these slow fades were relatively non-selective. Estimates of defocussing levels are also available from combined slow and fast fading data obtained over many paths (e.g., Pearson, 1965; Barnett, 1972; Morita, 1972). These all indicate that typical paths in temperate climates can suffer fades of 20 dB for a significant fraction of time. Pearson (1965) noted furthermore that fades of greater than 30 dB had been observed on paths in coastal areas for periods of a few hours. Perhaps the most severe well-documented observations of extreme defocussing levels in tropical regions are

those of Hautefeuille et al. (1980) in Senegal, where 50 dB fades lasting several hours were not considered unusual. The fact that the ground-reflected signal was not observed under these conditions suggests that a shadow region extended over a large portion of the path surface as well.

One of the authors (Martin, 1982a) has estimated median depression statistics for his 50 km, 11.5 GHz path from swept-frequency amplitude and group delay measurements. These are illustrated in Fig. 4 in conditional form versus the relative delay between the two dominant rays (see sub-section 3.4 for further discussion). As evident for this somewhat inclined path, median depressions were of the order of 20 dB during disturbed conditions (i.e., fading greater than 12 dB). The swept-frequency measurements of Law and Webster (1985) (Fig. 3a) indicate defocussing fades approaching 30 dB during disturbed conditions on their 80 km coastal path. (It is recognized that these statistics may include some incidence of atmospheric multipath.)

### 3.3 Measurements and calculations of effective ground reflection coefficients

Another source of evidence for the importance of ground reflection on overland paths is the literature on specular and diffuse reflection from terrain. Unfortunately, little progress appears to have been made in the treatment of microwave reflection and scattering from irregular terrain since the major work by Beckmann and Spizzichino (1963). Although some useful information can be gained from calculations of specular and diffuse reflection parameters at these frequencies, measurements on the type of paths involved would still appear to provide the most reliable evidence.

Calculation of specular reflection parameters. In principle, the effective specular reflection coefficient  $R_s$  over a terrestrial microwave path can be estimated from the well-known relation (Beckmann and Spizzichino, 1963; Hall, 1979; Boithias, 1983)

$$R_s = g_T g_R D R_0 \rho_s \quad (1)$$

where  $g_T$  and  $g_R$  are the directivity reduction factors of the transmitting and receiving antennas in the direction of the specular reflection point,  $D$  is the divergence factor for the earth's surface,  $R_0$  is the Fresnel reflection coefficient, and the scattering coefficient  $\rho_s$  is a reduction factor designed to take into account the terrain roughness. Strictly, the factors in eq. (1) should also be multiplied by another factor that accounts for the amount of surface area reflecting specularly (Hall, 1979; Boithias, 1983). For example, if the specularly reflecting surface were exactly coincident with the first Fresnel zone,  $R_s$  would become a factor of two larger. Unfortunately, accurate estimation of this factor is difficult in practical situations involving real terrain.

In order to clarify the results of correlation and multiple regression analyses of a large 47-link fading data base discussed in a companion paper (Tjelta et al., 1986), some investigation was made of the dependence of  $R_s$  on the various variables involved. From the large amount of information available on the Fresnel reflection coefficient (CCIR, 1986a), it is clear that  $R_0=1$  in the frequency range of interest, except in the rare cases of vertical polarization at grazing angles greater than about  $1^\circ$ . Over the test group of 47 links,  $[20 \log(D)]$  is typically less than 3 dB under the assumption of a spherical reflecting surface having a  $4/3$ -earth radius of curvature.

The directivity reduction factors  $g_T$  and  $g_R$  in the direction of the specular reflection point were calculated using the Gaussian beam approximation

$$g_{T,R} = \exp(-c_{T,R} \theta^2) \quad (2)$$

with the constants  $c_{T,R}$  obtained from the known half-power beamwidths. The overall reduction factor  $g_T g_R$  is a complicated function of several variables including antenna beamwidth, path inclination, path clearance, and path length. Of the 47 links, only three relatively steep ones have reductions  $[20 \log(g_T g_R)]$  greater than 10 dB; half have reductions less than 0.9 dB. Thus, in most cases the specularly reflecting surface is well illuminated by the antenna beams.

Normally the most important overall variable in eq. (1) is the terrain roughness factor  $\rho_s$ . It has commonly been estimated using the Gaussian random surface approximation (Beckmann and Spizzichino, 1963)

$$\rho_s = \exp(-g^2/2) \quad (3)$$

where

$$g = 4\pi f s_h \sin \phi / c \quad (4)$$

with  $s_h$  the standard deviation of surface height about the local mean value within the first Fresnel zone,  $\phi$  the grazing angle,  $f$  the frequency, and  $c$  the speed of light. A more recent derivation of  $\rho_s$  for sea surfaces (Miller et al., 1984) suggests that a better estimate providing agreement with experimental data can be obtained from

$$\rho_s = \exp(-g^2/2) I_0(g^2/2) \quad (5)$$

where  $I_0$  is the modified Bessel function of zero order. It is likely that (5) is also more accurate than (3) for terrain.

As seen from (4) and (5),  $\rho_s$  and thus  $R_s$  would appear to be strongly dependent on the grazing angle  $\phi$ , the surface roughness  $s_h$  within the first Fresnel zone, and the frequency  $f$ . However, there is a complex, somewhat path dependent relationship between  $s_h$  and  $f$ . Since  $s_h$  tends to decrease on

average as the size of the first Fresnel zone decreases, and this size decreases with increasing frequency, the actual average dependence of  $p_s$  on frequency should be different than at first glance.

At UNF,  $p_s$  can be estimated with some accuracy. Here the roughness  $s_h$  is dependent mainly on terrain surface variations. However, at SHF where the size of the first Fresnel zone is much smaller,  $s_h$  decreases to the point where it is difficult to estimate accurately from a single path terrain profile. For example, out of the 47 test links, the ratio of the first Fresnel zone length to the terrain profile correlation distance is less than three for 27 of them. Under such conditions, it is apparent that trees and other small terrain features would become relatively more important than at lower frequencies.

Another difficulty in accurately estimating  $p_s$  at SHF is that, with the reduced first Fresnel zone size, the specular reflection point and hence the grazing angle can no longer be as accurately determined from the antenna heights above the average terrain height. Furthermore, there may be more than one specular reflection zone on the path profile. Despite these various difficulties, effective specular reflection levels  $20\log R_s$  have been estimated for a sample of the smoothest paths among the test group, employing the roughness parameter  $s_3$  (Tjelta et al., 1986) calculated for the entire path (normally an upper bound for the roughness within the first Fresnel zone). The highest of these are in the range -10 dB to -20 dB and correlate well with the group experiencing the worst fading. More tangible statistical evidence that specular ground reflection is important within the overall group of 47 links is presented in a companion paper (Tjelta et al., 1986). Calculations are continuing with more accurate estimates for the surface roughness within the first Fresnel zone.

Calculation of diffuse scattering parameters. Beckmann and Spizzichino (1963) considered two cases relevant to terrestrial microwave links: (i) "glistening surface" (i.e., surface causing diffuse reflection) defined by the ground irregularities, and (ii) glistening surface defined by the antenna beams. To verify that the latter case is the most common with the narrow antenna beams employed at SHF, the parameters  $K_B$  and  $K_a$  corresponding to each of these two cases were calculated for the test sample of 47 links. These parameters are defined

$$K_B = \frac{h_T + h_R}{d \tan \beta_0}, \quad K_a = \frac{1}{d} \left[ \frac{h_R^2}{\sigma_T^2} + \frac{h_T^2}{\sigma_R^2} \right]^{\frac{1}{2}} \quad (7)$$

where  $h_T$  and  $h_R$  are the heights of the antennas above the average terrain height,  $\sigma_T$  and  $\sigma_R$  are the antenna half-beamwidths (i.e., half the half-power beamwidths), and  $d$  the path length. The factor  $\tan \beta_0$  represents a mean-square value of the terrain slope irregularities given by

$$\tan \beta_0 = 2\sigma/d_c \quad (8)$$

where  $\sigma$  is the standard deviation and  $d_c$  the correlation distance of terrain heights. For the calculations it was deemed best to calculate  $\sigma$  and  $d_c$  with respect to the mean terrain profiles as determined by least squares fits to the terrain heights (i.e.,  $\sigma = s_3$ , as employed by Tjelta et al., 1986).

From the calculations, the inequality (Beckmann and Spizzichino, 1963)

$$K_a < K_B/2\sqrt{2} \quad (9)$$

held for only six links. This is indeed an indication that the glistening surface is normally defined by the antenna beams. Since even for these six,  $K_B > 1$  for two and  $K_B > 0.5$  for the remainder, the glistening surface is close to the specular reflection point as in case (ii). For case (i), Beckmann and Spizzichino calculated that diffuse reflection coefficients can range between 0.25 and 1, although they noted that measurements ranged between 0.2 and 0.5.

Of the 41 links for which the glistening surface is limited by the antenna beams (case (ii)),  $0.1 < K_a < 0.5$  for 26 and  $K_a > 0.5$  for the remainder of which most are inclined paths. A few estimates for the most important first group of 26 suggest that significant diffuse reflection must be considered as a distinct possibility. Unfortunately, the theory for case (ii) does not yet appear to have been validated by measurements. Early correlation calculations on the 47-link test sample using the various diffuse reflection parameters are presented in the companion paper (Tjelta et al., 1986) (see also sub-section 3.5).

Measurements of effective specular and diffuse reflection coefficients. Because of the uncertainty in the accuracy of calculations of the effective reflection coefficients for irregular terrain at microwave frequencies, measurements for typical paths may still provide the best evidence for the importance of terrain reflection and scattering. Even though most measurements have been carried out under controlled conditions involving short paths, a few exist for longer paths.

The 4 GHz measurements of Bullington (1954) on many paths over cultivated terrain were classified by Beckmann and Spizzichino (1963) as describing diffuse reflection under conditions when the glistening surface is not defined by the antenna beams, as were the 1 GHz measurements of McGavin and Maloney (1959) over desert terrain. Most of the reflection coefficients measured ranged between about 0.2 and 0.5. Barton (1974) has questioned the validity of this conclusion, and the authors' own calculations for 16 paths at 2 and 4 GHz indicate that only two of them can be considered to have sufficiently non-directional antennas that the glistening surface is defined by the terrain itself. Barton (1974) also appears to question the conclusion that Bullington's measurements did not contain significant specular reflection contributions.

Since the measurements of Bullington (1954) and McGavin and Maloney (1959) were for paths that were expected to pose some reflection problems, it is helpful to observe the results for the rougher ( $s_3 = 33$  m) relatively steep ( $0.3^\circ$ ) path between Roc Tredudon and Lannion in France. Fig. 9 displays the reflection coefficient estimates of Martin (1982a) based on amplitude and group delay measurements in a 400 MHz bandwidth (see also sub-sections 3.1, 3.2, and 3.4). Here,  $R_e = GR$  (expressed in dB), corresponding to  $R_e = ab$  in the well-known model of Rummier (1979). These frequency-sweep measurements are equivalent to the earlier spatial measurements along a vertical or horizontal line, although the specular and diffuse contributions cannot be separated. Unlike the earlier measurements, they were all obtained during disturbed conditions. Nevertheless, they provide two important pieces of information that the previous measurements do not. They show that the effective reflection coefficient is highly variable, with peak magnitudes more than 10 dB higher than the median value of about -25 dB, and that it decreases slightly with increasing delay of the reflected wave. The large variation in the effective reflection coefficient was apparently also observed by Bundrock and Murphy (1984), and thirty years earlier by Matsuo et al. (1953). Although some of the large variation may be due to the two-ray assumption involved (the spatial measurements also contain this assumption), it seems unlikely that departures from this assumption could cause most of this variation.

The fact that the effective reflection coefficient can increase significantly above its median value during disturbed conditions is a very important result. It implies that a rough path can behave like a smoother path for a significant fraction of time. The fact that these enhancements of the reflected signal are sometimes coupled with attenuation of the direct signal, as illustrated by Martin's measurements (see Martin, 1982a) of their relative levels (i.e., the parameter  $R$ , equivalent to  $b$  in the model of Rummier (1979)), illustrates why severe surface multipath fading is so prevalent even on rough paths.

It seems most likely that the significant enhancements in the effective reflection coefficient result from a focussing of incident-wave energy on the reflecting ground surface, and possibly a further focussing of the reflected wave itself. As evident from Fig. 7, the presence of a duct below the path could cause this if the region of dense rays adjacent to the lower apex of the "interference region" coincided with the reflecting surface of the path. Indeed, observation of the calculations of Dutton (1961) of "shadow zone" sizes and "interference region" location, and their ranges of variation, gives heed to the argument that the reflected wave can sometimes undergo a net focussing while the direct wave is simultaneously being defocussed. Since the areas of enhanced surface reflection would move along the path, the proportion of diffusely reflected power with respect to specularly reflected power can be expected to vary considerably. In addition to such large-scale focussing and defocussing, uncorrelated focussing and defocussing (scintillation) due to small scale irregularities could play some role, particularly at higher frequencies.

Regardless of the uncertainties in the average proportion of specular and diffuse reflection involved, the various measurements indicate that terrain reflection and scattering is of sufficiently high amplitude to interfere destructively with faded atmospheric waves for a significant fraction of time. The approximately -6 dB to -14 dB range of ground reflected signals during undisturbed conditions on the highly reflecting paths of Bullington (1954), and McGavin and Maloney (1959), would be sufficient. So also would the approximately -10 dB to -30 dB range during disturbed conditions on the rougher Roc Tredudon - Lannion path ( $s_3 = 33$  m), as observed from the measurements. It might be noted that overall path surface roughnesses in the 47-link sample discussed previously range between  $s_3 = 3$  m and  $s_3 = 62$  m in 42 of these.

#### 3.4 Measurements and calculations of relative path delays

Considerable evidence as to the usual role of surface reflection in selective fading is also available from a comparison of relative path delay measurements and calculations. A brief introduction to some relative delay measurements associated with fading measurements has already been made. Table 1 provides a more complete list of experiments reported, with relative delay and associated amplitude information in summary form.

**Calculations of atmospheric delays.** The information in Table 1 indicates that relative delays as large as several nanoseconds have been observed from most experiments, even on overland paths. Although most of the experimenters on overland paths have assumed these to result from atmospheric multipath, and some erroneous calculations available (e.g., Ruthroff, 1971) appeared to support this, recent calculations suggest that relative atmospheric multipath delays are normally fairly small. (In fact, even some early calculations by Omori and Sato (1958) seem to suggest this.)

The two most relevant and comprehensive works would appear to be those of Webster (1983) and Parl (1983). The ray tracing study of Webster has already been introduced in sub-section 3.2. Referring to the center graph of Fig. 8, it is clear that even for a 50 km path and a layer (100m thickness) with a total refractivity change as large as 20 Nu, the largest relative delays between the two dominant rays (1 and 2) are less than about 1 ns. The relative delay of the third ray is even less since it travels in a height interval where the refractivity is less.

Using a three-layer discrete gradient model, Parl (1983) has analytically derived an expression for the maximum relative delay between atmospheric rays. The solid curves in Fig. 10 display his results as functions of path length for ducts having a -50 Nu intensity and various refractivity gradients. Although the largest refractivity gradients give fairly long delays, it must be emphasized that such large gradients are extremely rare (Bean et al., 1966; Segal and Barrington, 1977; Dougherty and Dutton, 1981). As discussed in the following sub-section, it is more likely that long-delayed rays result from ground reflection.

As demonstrated by Parl, the maximum relative delay varies as  $d^3$  for short path lengths (up to about 30 km) and as  $d$  for longer paths. Earlier workers (Ruthroff, 1971; Sasaki and Akiyama, 1979) had concluded that the dependence was as  $d^3$  for all path lengths. This resulted in very pessimistic early estimates of digital radio performance, as noted by Hubbard (1984).

TABLE 1. RELATIVE DELAY MEASUREMENTS

| Investigators                | Path Location                            | Path Length (km) | Frequency (GHz) | Technique           | Delay Information  | Remarks   |
|------------------------------|--|------------------|-----------------|---------------------|--|---|
| Crawford and Jakes (1952)    | Murray Hill - Holmdel, NJ                | 36               | 3.7 - 4.2       | Frequency sweep     | Delays up to 10 ns estimated with analog simulator                       | Associated angle-of-arrival measurements. See text.             |
|                              | Southard Hill, NJ, USA                   | 27               | "               |                     |  |   |
| DeLange (1952)               | Murray Hill - Holmdel, NJ USA            | 36               | "               | Pulse transmission  | Delays up to 7 ns measured. Usually <3ns                                 | Same path as Crawford and Jakes (1952)                          |
| Headows et al. (1966)        | Widley - Green Halley, U.K.              | 55               | 3.6 - 4.1       | Frequency sweep     | Delay of 2nd ray between 2 and 10 ns                                     | Single event only. See text.                                    |
| Dougherty and Hartman (1977) | Haswell, CO, USA                         | 23               | 13.3, 14.9      | Pseudo random noise | 0.5 ns between 2 paths   | Single event only. Associated meteorological measurements.      |
| Sasaki and Akiyama (1979)    | Shiroyama - Kosuzume, Japan              | 36               | 18 - 22         | Frequency sweep     | 4 ns maximum   | Two-ray model assumed for all paths                             |
|                              | Kawagoe - Musashino, Japan               | 23               | 18 - 22         | "                   | 0.3 ns maximum   |   |
|                              | Warusawa - Mt. Kano, Japan               | 79               | 5.65 - 6.42     | "                   | 6.7 ns max. (0.002%)   | Exponential distribution estimated                              |
|                              | Mt. Hiei - Ohnogi, Japan                 | 62               | "               | "                   | 0.13 ns max.   |   |
|                              | Kawaguchi - Itsukaichi, Japan            | 48               | 3.7 - 4.2       | "                   | 2.3 ns max. (0.05%)  | Exponential distribution estimated                              |
| M. Sandberg (1980)           | Copenhagen, Denmark                      | 75               | 13.5 - 15.0     | Frequency sweep     | <1 ns delay of second ray. Up to 6 ns delay of third small amplitude ray | Second ray comparable in amplitude to first. Single event only. |
| Martin (1982a)               | Roc Tredudon - Lannion, France           | 50               | 11.25 - 11.65   | Frequency sweep     | Delay distribution, with delays of 5 ns (0.01%), 8 ns (0.001%)           | See text  |
| Hubbard (1984)               | Miscellaneous                            | 40 - 160         | 8.6             | Pseudo random noise | Delays up to 18 ns   | See text  |
| Lam and Webster (1985)       | Otter Lake - Aylesford, N.S., Canada     | 60               | 9.5 - 10.5      | Frequency sweep     | Delays up to 5 ns (0.01%) in distribution                                | See text  |
|                              | Otter Lake - Miramichi S., N.S., Canada  | "                | "               | "                   | Delays up to 14 ns (0.01%) in distribution                               | See text  |
| Laomers and Marr (1985)      | Saddle back Mt. - Prospect Hill, MA, USA | 73               | 16 GHz          | Pseudo random noise | Estimated delays up to 4 ns  | Two events only. Associated angle-of-arrival measurements       |



The major difference between the single layer models of Webster and of Parl is that Webster assumed a smooth transition whereas Parl did not. The advantage of Parl's approach is that the ray equations can be solved analytically, allowing equations to be obtained for the maximum relative delay and other useful quantities. The maximum relative delay calculations of Parl, however, would seem to be comparable to those of Webster, if perhaps slightly less. Parl also showed that higher order rays which crisscross the layer lower boundary are theoretically possible (see also Dougherty, 1981). It is clear from his analysis, however, that any additional relative delay of these higher order rays is negligible by comparison with the results of Fig. 10. Further detailed comparisons between the various models, including those of Webster and Parl, would be useful.

Webster (1983) also calculated the relative delay that would result from total reflection by an elevated subsidence layer in which an abrupt change in refractivity occurs within a very small height interval. The results are displayed in Fig. 11, along with the observations of Meadows et al. (1966). Such an explanation for the results of Meadows et al. seems plausible, particularly in view of the associated refractivity profiles that they presented. It should be noted, however, that this was a single isolated event during a one-year period. The bulk of the fading that Meadows et al. observed on their very rough path was flat fading indicative of defocussing.

Hubbard (1984) also discussed some relative delay measurements and associated refractivity profiles that from his calculations seemed indicative of reflection by an elevated ducting layer well above his path. He also noted other measurements on the same day that appeared to be due to ground reflection. The relative frequency of both types of event would be of interest.

**Calculation of surface multipath delays.** Various investigators have assumed that the relative delay of ground reflected rays is quite small. Meadows et al. (1966), for example, calculated a relative ground delay of 2 ns for their experimental path. Such a calculation assumes, however, that the refractivity profile below the path is normal or near normal (i.e., 4/3-earth profile with gradient of -40 Nu/km). If a layer with an abnormally high negative gradient exists below the path, the situation can be quite different.

This is illustrated beautifully in the ray-tracing curves of Lam and Webster (1985) corresponding to their most elevated 80 km overwater path (Fig. 12b). When the duct (-40 Nu intensity and 100m thickness) is at the surface (the center of the duct that eventually becomes elevated, in this case), the direct ray, and for the most part the surface reflected ray, travel in an atmosphere with normal gradient. The relative delay calculated is almost exactly equal to that obtained for a normal atmosphere (4.4 ns), shown by the cross added to the graph of Lam and Webster. As the duct rises, an increasing portion of the path traveled by the surface reflected ray is in the much higher refractivity region below the duct. As evident, the relative delay increases almost linearly as the duct rises. Once the duct rises above the path and the direct ray no longer travels in a less "dense" medium above, the relative delay drops quickly back to the value for a normal atmosphere. As also illustrated in Fig. 12b, the relative delays of the atmospheric rays that arise once the duct is above the path (6 ns maximum) are considerably smaller than the maximum value for the surface ray occurring when the duct is just below the path (12 ns maximum).

Unlike the calculation of maximum relative delays of atmospheric multipaths, which appear to require a rigorous analysis such as that of Webster (1983) or Parl (1983), an approximate estimate of the maximum relative delay of the surface reflected ray can be obtained more simply. Under the assumption that a defocussing layer is just below the path, then the relative delay can be calculated as the sum of two contributions. The contribution  $\Delta\tau_1$  from the region of constant gradient below the layer can be estimated in the normal way from the equation (Boithias, 1983)

$$\Delta\tau_1 = \frac{2d_T d_R}{c} \frac{dR}{d} (h_T + h_R)^2 [1 - m(1+b^2)] \quad (10)$$

where  $d_T$  and  $d_R$  are the distances from the transmitting and receiving terminals to the specular reflection point, and  $m$  and  $b$  are coefficients in a third-order equation. The contribution resulting from the fact that the direct wave travels in the lower refractivity region above the layer can be estimated from

$$\Delta\tau_2 = (|\Delta N| \times 10^{-6}) d/c \quad (11)$$

where  $\Delta N$  is the duct intensity. The total relative delay,  $\Delta\tau_m = \Delta\tau_1 + \Delta\tau_2$ , of course assumes that the layer is infinitely thin.

The accuracy of this simple procedure is illustrated in Fig. 12b. As already noted, the value  $\Delta\tau_1 = 4.4$  ns for a normal refractivity gradient is virtually identical to the ray tracing calculation for a ground-based layer half the thickness of the elevated layer. The value of  $\Delta\tau_2 = 10.7$  ns for the -40 Nu layer gives a total relative delay of 15.1 ns. This is the approximate value that would be obtained if the approximately linear curve in Fig. 12b were extrapolated to the average path height. The 20% lower ray tracing calculation of 12 ns for a layer just below the path is due to the fact that it accounts for finite duct thickness. Lam (1983) showed the variation of maximum delay for finite duct thickness on his Bay-of-Fundy path as a function of duct intensity  $\Delta N$ . From his delay statistics, he estimated that maximum  $|\Delta N|$  values for his path seldom exceed 40 Nu.

The contribution  $\Delta\tau_1$  to the maximum relative delay is usually much smaller than the additional contribution  $\Delta\tau_2$  during the presence of fairly extreme ducts (e.g.,  $\Delta N = -40$  Nu). For the test sample of 47 links discussed earlier,  $\Delta\tau_1$  ranges between 0.2 ns and 5.5 ns for 44; for the steepest path,  $\Delta\tau_1 = 11$  ns. However, for 35 links this contribution is less than 2 ns.

Eq. (11) therefore provides a good approximate upper bound to the maximum delay under the worst-case condition that the layer is just below the path. The curve based on eq. (11) with  $\Delta N = -50$  Nu is superimposed on the atmospheric multipath delay graph of Parl in Fig. 10. As evident, it gives larger relative delays than occur under worst-case conditions where the same layer is above the path, even in the case of very extreme gradients. For more normal relatively extreme gradients in temperate climates (e.g.,  $-400$  Nu/km), the difference is quite large. As for atmospheric multipath at longer path lengths, the maximum delay is approximately linear in  $d$ .

As evident from this analysis, the maximum relative delay depends much more on the layer characteristics, in particular the intensity  $\Delta N$ , than on the path height above the reflecting surface. The approximate distribution of  $\Delta t$  could be estimated, given the distributions of  $\Delta N$  and abnormal layer heights. For horizontal paths, and layer heights  $h$  less than the mid-path height  $h_p$ , eq. (11) can be generalized to

$$\Delta t_2 = (|\Delta N| \times 10^{-6}) dh / h_p c \quad (12)$$

For inclined paths, little error would be introduced by employing the height at path center also, particularly since abnormal layers tend to be inclined with the average terrain slope (e.g., Lammers and Marr, 1985). Eq. (12) could be multiplied by some suitable factor (e.g., 0.8) to allow for the fact that it assumes infinitely thin layers.

**Discussion.** As evident from the calculations of surface multipath delays, (e.g., Fig. 12a,b) the greatest delays occur along with the greatest amount of defocussing attenuation of the direct signal. This is confirmed by the results of Martin (1982a) displayed in Fig. 4, and also by the observations of Lam and Webster (1985), described in more detail by Lam (1983). It is significant that the maximum defocussing loss in Fig. 12a (25 dB) and the maximum relative delay in Fig. 12b (12 ns) were both exceeded for the same percentage of time (about 0.3%) in the experimental measurements of Lam and Webster shown in Fig. 3. Thus, the single uniform layer model used to obtain the results of Fig. 12 would seem to be an excellent one, at least statistically. As indicated previously, the observations of Lam and Webster were complicated by the presence of a ridge partially obstructing the surface reflection path. Also displayed in Fig. 12a is the estimated amplitude of the surface reflected wave without the additional diffraction loss (Lam, 1983). It is noteworthy that, for this particular path geometry and layer characteristics, there is some indication of focussing of the reflected wave associated with the defocussing of the direct wave.

Of the main two main mechanisms causing significant median depression, defocussing and "refractive" atmospheric multipath, it is evident that the largest relative delays will be associated with defocussing layers just below the path. This is also the situation for which the greatest frequency selectivity of the deep fades will occur. The large relative delays occurring in this manner for both specular and diffuse ground reflection should have approximately the same value, except when the propagation distances for these two components are very different (e.g., the path of Sakagami and Hosoya, 1982). When refractive atmospheric multipath due to a layer above the path is the mechanism causing median depression, the relative delays of surface multipath will be comparable to those during undisturbed conditions (i.e.,  $\Delta t_1$ ). These are of approximately the same magnitude as the maximum relative delays due to refractive atmospheric multipath.

No information appears to be available for refractive atmospheric multipath delays associated with abnormal layers below the path (i.e., the interference regions of Ikegami (1959)). In view of the geometry of this situation, however, these are considered unlikely to be larger than those for layers just above the path. A similar speculative conclusion might be made for refractive atmospheric multipath arising from a subrefractive layer below the path. Further investigation is needed for these and various multi-layer situations.

The sole atmospheric multipath situation that would seem to produce relative delays comparably large to those for surface multipath is that of an elevated duct from which a reflection occurs (i.e., "refractive" atmospheric multipath, Fig. 11). All available observations, however, suggest that this highly frequency selective fading situation without median depression is extremely rare.

### 3.5 Correlation and multiple regression analyses

Usually the statistical analyses of large fading data bases are not considered to provide much information on the underlying clear-air mechanisms. Nevertheless, the type of detailed correlation and multiple regression analyses of many variables, discussed in a companion paper (Tjelte et al., 1986), has begun to do this.

The clearest indication that specular ground reflection is important in the 47-link test sample is that the grazing angle  $\theta$  has emerged as one of the most significant variables in the asymptotic multiple regression equation for the large fade depth range of the fading distribution. The negative regression coefficient obtained for  $\theta$  is in general agreement with eqs. (1) to (5) which give a specular reflection coefficient increasing with decreasing  $\theta$ . It is fairly clear from the results of Tjelte et al. (1986) that earlier indications of the importance of path clearance in asymptotic models for the fading distribution (Crombie, 1983; Olsen et al., 1986) were an imperfect indication of the importance of grazing angle, and hence of specular reflection.

A clear indication of the importance of diffuse reflection is not as easily obtained from the analysis. Perhaps the most tangible indication is that the surface roughness parameter  $s_2$  involving the terrain elemental slopes also emerged as a significant regression variable, and particularly that  $s_2$  values for a path profile interval of 100 m produced the best results. The positive regression coefficient for  $s_2$  indicates in effect that the greater the roughness, the greater the amount of diffuse reflection. This result is in agreement with results observed for diffusely reflecting water surfaces in the lowest range of surface roughnesses (CCIR, 1986a). The high correlation between the diffuse

reflection parameter  $K_0$  and the reference tail fade depth  $A_{0.01}$  may also be an indication of diffuse reflection, as may the correlations with the other two diffuse reflection parameters  $\tan \theta_0$  and  $\alpha/\theta_0$ . It is evident, however, that there is a functional similarity between eq. (7) for  $K_0$  and the expression (Boithias, 1983) for the grazing angle  $\phi$  (i.e., both  $K_0$  and  $\phi$  are approximately proportional to the path clearance and inversely proportional to the path length). Thus, the correlation between  $K_0$  and  $A_{0.01}$  may be more an imperfect indication of the importance of specular reflection. Further analysis is required.

The strong relationship between fade depth (or probability of exceeding a given fade depth) in the tail range of the distribution and path length, also evident in previous analyses (Morita and Kekita, 1958; Pearson, 1965; Morita, 1970; Barnett, 1972; Boithias, 1979, 1981; Martin et al., 1985; Olsen et al., 1986), is believed to be due to the fact that several mechanisms, including specular and diffuse reflection, are dependent on path length in mutually enhancing ways. Perhaps most importantly on the atmospheric side, as path length increases, the amount of flat fading due to defocussing would tend to increase. However, so also would the likelihood of refractive atmospheric multipath (Webster, 1983), and therefore the probability of exceeding a given atmospheric multipath fade depth. On the terrain side, the relative strengths of both specular and diffuse reflections from the ground tend to increase with increasing path length. Finally, on both atmospheric and terrain sides, the uncorrelated components of atmospheric fade depth and ground reflected signal enhancement due to scintillation tend to increase with increasing path length. The degree to which the importance of path length in the analysis is a measure of the importance of each of these mechanisms is as yet unclear. It is clear, however, that path length alone cannot describe the fading contributions of each mechanism nearly as well as combinations of variables that account for other aspects of these mechanisms also.

The importance of path inclination in the analysis of Tjelta et al. is believed to indicate the importance primarily of the atmospheric contribution to the fading. In particular, defocussing attenuation of the atmospheric signal component would tend to increase with increasing path inclination. (So also would atmospheric multipath fading, as indicated by the work of Webster (1983) and of Parl (1983).) An effect not unimportant on the terrain side, however, is the fact that an increasing path inclination will tend to cause a decreasing effective specular reflection coefficient as a result of the decreasing antenna directivity product (see sub-section 3.3).

The overall increase in fading with increasing frequency evident in the overland-path analyses of Tjelta et al. and others is believed to be another indication primarily of the importance of terrain reflection. The positive regression coefficient, however, would suggest that the strength of the specular reflection tends to increase with increasing frequency, the opposite of what would be expected at first glance from eqs. (4), (5), and (1). One reason may be that on most paths the surface roughness within the first Fresnel zone decreases sufficiently quickly with increasing frequency (because the size of this zone decreases with increasing frequency, reducing the proportion of large surface irregularities - see sub-section 3.3) to outweigh the normal decrease in the effective specular reflection coefficient with increasing frequency. Another not unrelated reason may be the fact that finite terrain reflecting elements can reflect more energy as the frequency is increased (e.g., Hall, 1979; Boithias, 1983). Recently, Lavergnat and Sylva (1986b) have cited another possible reason associated with the constant phase shifts of the various multipath components. It does not appear that the 180° phase shift associated with at least specular reflection, however, would produce a significant frequency variation.

At microwave frequencies, the decrease in fade levels with increased surface roughness has been commonly attributed to the lessened probability of stable atmospheric layering over rough terrain (e.g., Vigants, 1975). The results of Tjelta et al. might be taken to suggest that the importance of large scale surface roughness parameters (such as  $s_1$ ) in previous analyses (Pearson, 1965; Morita, 1970; Barnett, 1972; Vigants, 1975; Olsen et al., 1986) was an imperfect indication of the importance of path inclination (which is fairly highly correlated with surface roughness), since path inclination appears to be a better predictor variable. However, an effect of surface roughness on layer stability might be sufficiently well described by a variable such as path inclination that accounts for other effects as well. Some small effect of surface roughness may also be included in the geoclimatic factors determined by Tjelta et al., because of somewhat different distributions of surface roughness from one geoclimatic region to another. The whole question of surface roughness effects on both atmospheric and surface mechanisms is a complex one, and requires further investigation.

It is well known that single-frequency fading distributions have a tail region of 10 dB/decade slope that normally begins at fade depths of about 10 or 15 dB (CCIR, 1986b). The results of this and previous sub-sections suggest that this tail region arises mainly from the complex interaction of atmospheric fading and surface reflection that begins at about these fade depths.

### 3.6 Depolarization theory and measurements

It is fairly well established that deterioration in cross polarization discrimination (XPD) on dual polarized links results primarily from a combination of fading of the copolarized signal and multipath coupling into the crosspolarized patterns of the antennas (Morita, 1971; Martin and Casanova, 1974; Rooryck and Martin, 1977; Morita et al., 1979; Olsen, 1981; CCIR, 1986c). While the different effect of the copolar and crosspolar antenna patterns on the multipath signals poses a problem for operating radio systems, it provides another source of information on the multipath mechanisms involved.

The results of several clear-air crosspolarization experiments have shown that conditional XPD statistics  $XPD_c$  (mean, median, rms, or equiprobable value) can be related to the copolar attenuation (CPA) in the deep fading range by the empirical relation (Olsen, 1981; CCIR, 1986c)

$$XPD_c = -CPA + C \quad (dB) \quad (13)$$

Here,  $C$  is a parameter for each path and frequency that has virtually always been observed to be greater than  $XPD_0$ , the value of  $XPD_0$  during undisturbed conditions (i.e., when  $CPA = 0$ ), sometimes by more than 20 dB. This has been expressed as (Morita et al., 1979)

$$C = XPD_0 + Q \quad (\text{dB}) \quad (14)$$

where  $Q$  is an "improvement factor" that determines at what value of  $CPA$  the relation (13) begins to apply. Thus,  $Q$  has virtually always been observed to be positive, with values ranging beyond 20 dB.

One of the authors (Olsen, 1985) has theoretically verified eq. (13) and developed expressions for the parameter  $C$  for each of two of the combined fading mechanisms introduced in sub-section 2.2:

(a) atmospheric defocussing plus surface reflection;

(b) atmospheric multipath plus surface reflection.

These are the only copolar fading mechanisms for which eq. (13) would appear to apply. For mechanism (a) and the conditional mean statistic  $XPD_s$ ,  $C$  is of the approximate form

$$C = \overline{XPD_s} + \bar{A}_s \quad (\text{dB}) \quad (15)$$

where  $\overline{XPD_s}$  is the mean relative crosspolar response of the two antennas to the dominant surface reflected wave and  $\bar{A}_s$  is its mean relative fade depth for a conditional value of  $CPA$ . Similarly, for mechanism (b),

$$C = \overline{XPD_a} + \bar{A}_a \quad (\text{dB}) \quad (16)$$

where  $\overline{XPD_a}$  is the mean relative crosspolar response of the two antennas to the dominant atmospheric ray (not including the direct ray), and  $\bar{A}_a$  is its mean relative fade depth for a conditional value of  $CPA$ . Both  $\overline{XPD_s}$  and  $\overline{XPD_a}$  depend on the crosspolar patterns of the antennas and the distributions of ray angles-of-arrival and launch. For most crosspolar patterns used experimentally in which there is a notch on or near the axis and higher sidelobes off axis,  $\overline{XPD_s} < XPD_0$  and  $\overline{XPD_a} < XPD_0$ . This just expresses the fact that the  $XPD$  of the antennas usually degrades off axis.

The value of  $Q$  for combined mechanism (a) is therefore

$$Q_s = \overline{XPD_s} - \overline{XPD_0} + \bar{A}_s \quad (17)$$

Since  $\overline{XPD_s} < XPD_0$ ,  $\bar{A}_s$  must be positive (i.e., the amplitude of the reflected wave must be less than that of the direct wave) and greater than this difference. This is the normal situation, and the lower the mean level of the reflected signal, the larger is  $Q_s$ .

In combined mechanism (b), in order that  $CPA$  be sufficiently large for eq. (13) to apply, the atmospheric ray and the direct ray must be of approximately the same amplitude so that they interfere destructively. Thus  $\bar{A}_a = 0$ , and

$$Q_a = \overline{XPD_a} - XPD_0 \quad (18)$$

For the crosspolar patterns usually applicable experimentally,  $Q_a$  would be negative or approximately equal to zero. Hence, the crosspolar performance of the link would tend to be much worse during atmospheric multipath and surface reflection than it would during defocussing and surface reflection. This just expresses the physically understandable fact that large amplitude atmospheric rays arriving off axis cause the link  $XPD$  to degrade more than do normally much lower amplitude surface reflected rays.

As discussed previously, mechanisms (a) and (b) both occur for some fraction of the time. Measured values of  $Q$  will reflect the relative occurrence. The fact that measured values are virtually always positive is a further indication that defocussing plus surface reflection is the dominant mechanism on most paths.

### 3.7 Other miscellaneous evidence

There are a number of other miscellaneous pieces of evidence that surface reflection is a component of multipath fading superimposed on a quasi-flat median depression. One is the observation that tilting the antennas slightly upwards reduces the severity of deep fading (e.g., Hartman and Smith, 1977; Liniger, 1982). In the experiment of Liniger (1982), the degree of frequency selectivity was also seen to reduce accordingly. Quarta (1966) in his earlier experiment essentially demonstrated the same effect, but using two antennas of different beamwidth. In the experiments of both Quarta and Liniger, the interpretation that the severity of the fading depended on the strength of the surface reflected signal was easily made because the reflecting surface was water.

Quarta's observation that horizontal polarization produced worse fading than vertical polarization was another demonstration of the same effect, made easy by the nature of his path. Again, Liniger (1984) demonstrated that the degree of selectivity of the horizontally polarized signal was greater than that of the vertically polarized signal, but this time on an overland path. He noted, furthermore, that the "notch" frequencies for the two polarizations were slightly displaced. However, he did not interpret these polarization differences for his overland path as due to the effects of ground reflection.

In a more recent experiment, Gardina and Lin (1985) demonstrated that horizontally spaced antennas with different beamwidths could provide a significant diversity improvement factor against distortion in their digital radio link. They interpreted this very important result as due to the different gain reductions of the two antennas to long-delayed atmospheric multipath signals arriving at large positive angles. In view of the large amount of evidence presented in this paper, it seems more likely that the long-delayed signals observed were from the ground, and that the median depression was caused not by two atmospheric signals of slight delay, but by defocussing of the direct signal.

It is believed that the collective multitude of all the space and frequency diversity experiments that have been carried out on overland paths provides another major source of evidence that ground reflection remains important on these paths. Such an interpretation has been made difficult, however, by several factors: the high degree of spatial correlation associated with defocussing coupled with the low degree of correlation associated with surface reflection, the differences in the relative phase and amplitudes of the specularly and diffusely reflected waves at different antenna positions, and probably by the fact that different parts of the ground reflect differently at different times as layer-focussed energy is directed at one point and then another.

#### 4. SOME IMPLICATIONS OF THE EVIDENCE

An extensive discussion of the practical implications of these findings is beyond the scope of this paper. Many of them have already been known for years, since highly reflecting paths were avoided where possible, and diversity or other techniques normally applied otherwise. Some discussion is warranted, however, particularly with respect to recent attempts to obtain better models of wide-band propagation channel behaviour.

It is apparent that even on links having approximately the same path length, frequency, and path inclination, the statistics of the propagation channel transfer function will be quite variable because of the variation in ground reflection characteristics from one path to another. These statistics include the probability of significant fading (such as associated with single-frequency fading distributions, as discussed by Tjelta et al. (1986)), and the conditional distribution of transfer function shape variables (e.g., Lavergnat and Sylvain, 1985a). Associated with this, the proportion of minimum phase and non-minimum phase fading, a subject of speculation by systems engineers, will as a result vary somewhat from one path to another.

Several investigators have considered it necessary to employ three-phaser (usually assumed to correspond to three physical paths) models for the channel transfer function in wide-band studies (e.g., Martin, 1980; Sakagami and Hosoya, 1982; Lee and Lin, 1985; Shafi and Taylor, 1986). The utility of such models has been demonstrated by Lee and Lin (1985) and Shafi (1986a) in recent Monte Carlo simulations of frequency diversity performance of digital radios. These investigators used a model realization corresponding to two strong atmospheric rays of small relative delay and a third small amplitude ray of large delay (explicitly corresponding to a ground reflected ray in the study of Shafi). Unfortunately, as discussed in preceding sections, this approximate physical situation for realizing median depression seems to be far less prevalent than that involving defocussing attenuation of the direct wave. The importance of slight variations in the small atmospheric delay noted by Shafi and Taylor (1986) seems to be a consequence of this particular model realization, and the fact that insufficiently large bandwidths were considered to see the full effect of the large surface-reflected signal delay. More recently, Shafi (1986b) has obtained initial simulation results corresponding to a flat fade of the direct wave and two ground reflected waves.

As a consequence of the evidence presented in this paper and the results of these various early analyses, in wide-band applications there would seem to be a need for three-phaser ("simplified four-phaser") models of the form

$$H(j\omega) = a_0 + a_1 e^{j(\omega\tau_1 + \phi_1)} + a_2 e^{j(\omega\tau_2 + \phi_2)} \quad (19)$$

or

$$H(j\omega) = a_0 \left[ 1 - b_1 e^{j(\omega\tau_1 + \phi_1)} - b_2 e^{j(\omega\tau_2 + \phi_2)} \right] \quad (20)$$

in which there are five variables as follows:

- (i)  $a_0$  is the amplitude of the quasi-flat atmospheric attenuation resulting from defocussing, atmospheric multipath, or antenna decoupling,
- (ii)  $a_1$  and  $\tau_1$  are the amplitude and relative delay of the surface specularly-reflected wave,
- (iii)  $a_2$  and  $\tau_2$  are the amplitude and relative delay of the surface diffusely-reflected wave.

The phase shifts  $\phi_1$  and  $\phi_2$  are the physically real but essentially frequency independent quantities associated with the surface reflection. Lavergnat and Sylvain (1985b) have recently discussed their physical necessity in general. Rummler (1979) in effect employed a phase shift  $\phi_1$  in his simplified three-ray model, although he let it vary and fixed the delay, a mathematically justifiable approach.

The explicit separation into specular and diffuse reflection contributions in (19) and (20) would seem to be necessary for at least space diversity applications, because of the great variability of the diffuse contribution with spatial variation. Unfortunately, suitable distributions for the ray amplitudes, relative delays, and their corresponding means and standard deviations, remain uncertain because of the lack of both experimental results and theoretical calculations. The small amount of evidence suggests that  $a_0$  is lognormally distributed (e.g., Rummler, 1979; Lam and Webster, 1985), and  $\tau_1$  Gaussian distributed (e.g., Lam and Webster, 1985). The data of Martin (1982a) indicate that the

distribution of  $2N\log(a_1)$  is at least symmetric. The results of many controlled experiments in undisturbed conditions discussed by Beckmann and Spizzichino (1963) indicate that  $a_2$  is Rayleigh distributed. However, with the apparent atmospheric-focussing enhancements in both  $a_1$  and  $a_2$  occurring during disturbed conditions, these are more likely to be approximately lognormally distributed.

Simulations have so far been based on the assumption of statistical independence between the various ray amplitudes and phases. However, the investigations discussed in section 3 have shown that there is some correlation between  $a_0$  and  $\tau_1$ ,  $a_0$  and  $a_1$ , and  $\tau_1$  and  $\tau_2$ . The effect of such correlations on the several applications of the simulation results needs to be investigated. In general, care must be taken to avoid models that are physically fairly realistic but impractical.

Finally, although ground reflection might be considered as a problem to be minimized as much as possible, there is some indication that its presence may help avoid outages when in rare instances the atmospheric signal fades beyond the flat fade margin of a system.

## 5. DISCUSSION AND CONCLUSIONS

This paper has attempted to classify and present the diverse evidence for the important role of terrain reflection at SHF in a systematic way such that the conclusion is clear. At the same time, it has tried to show that defocussing, and not atmospheric multipath, is the most prevalent mechanism reducing the atmospheric signal to a level where it can interfere destructively with the terrain-reflected signal. The authors do not claim that this combined atmospheric/surface mechanism is the only one responsible for the observed frequency selectivity of fading - only that it is the most frequently occurring one.

Much further research needs to be done in order to improve the understanding of the complex mixture of mechanisms interacting in the clear-air propagation channel. Both "microscopic" and "macroscopic" approaches in this research are required. Detailed microscopic investigations should include:

- (i) the conduct of more sophisticated channel probing experiments, along with simultaneous in-situ atmospheric measurements. There is a dearth of information on individual ray amplitudes (both polarizations), relative delays, and angles-of-arrival. There is even less such information in association with overall fade levels, group delays, and XPD's. Simultaneous meteorological measurements from which to interpret such transmission measurements are similarly lacking, although the availability of modern instrumentation and data processing equipment is encouraging (Segal, 1986). More attention needs to be paid to the terrain in controlled experiments.
- (ii) more ray-tracing calculations, and full-wave analyses where necessary. These must include rays reflected from the ground, and even real path profiles in some instances. Statistical ensembles of refractivity profiles should be used where possible (e.g., Costa, 1986). Ray amplitudes, delays, and angles-of-arrival need to be calculated in addition to ray paths. Subrefractive, superrefractive, and multi-layer situations require consideration.

More macroscopic investigations should include:

- (iii) further statistical analyses of large single-frequency fading and associated meteorological data bases (e.g., Schiavone, 1986; Tjelta et al., 1986; Martin et al., 1986), and wide-band data bases as they become available (e.g., Lavergnat and Sylvain, 1985a);
- (iv) further Monte Carlo and associated theoretical analyses of the consequences of various channel models on amplitude slope distributions, diversity improvement factors, etc. (e.g., Lee and Lin, 1985; Shafi and Taylor, 1986; Shafi, 1986a,b).

## REFERENCES

- Babler, G.M. (1972), A study of frequency selective fading for a microwave line-of-sight narrowband radio channel, Bell Syst. Tech. J., Vol. 51, No. 3, pp. 731-757.
- Barnett, W.T. (1972), Multipath propagation at 4, 6, and 11 GHz, Bell Syst. Tech. J., Vol. 51, No. 2, pp. 321-361.
- Bersis, A.P. and M.E. Johnson (1962), Prolonged space-wave fadeouts in tropospheric propagation, J. Res. NBS, Vol. 66D, No. 6, pp. 681-694.
- Bersis, A.P., A.F. Barghaussen, and R.S. Kirby (1963), Studies of within-the horizon propagation at 9300 MHz, Vol. AP-11, No. 1, pp. 24-38.
- Barton, D.K. (1974), Low-angle radar tracking, Proc. IEEE, Vol. 62, No. 6, pp. 687-704.
- Bean, B.R. (1964), Prolonged space-wave fadeouts at 1.046 Mc observed in Cheyenne Mountain propagation program, Proc. IRE, Vol. 42, No. 8, pp. 848-853.
- Bean, B.R., B.A. Cahoon, C.A. Samson, and G.D. Thayer (1966), A World Atlas of Radio Refractivity, U.S. Department of Commerce, Washington, D.C., U.S.A., ESSA Monograph No. 1.
- Beckmann, P. and A. Spizzichino (1963), The Scattering of Electromagnetic Waves from Rough Surfaces, New York, Pergamon Press.
- Boithias, L. (1979), Multipath propagation on line-of-sight links, Electron. Lett., Vol. 15, No. 7, pp. 209-210.
- Boithias, L. (1981), Distribution statistique des niveaux reçus en propagation par trajets multiples troposphériques, Ann. Télécommun., Vol. 36, No. 6-8, pp. 329-337.

- Boithias, L. (1983), Propagation des Ondes Radioélectriques dans l'Environnement Terrestre, Paris, Dunod.
- Bullington, K. (1954), Reflection coefficients of irregular terrain, Proc. IRE, Vol. 42, No. 8, pp. 1258-1262.
- Bundrock, A.J. and J.V. Murphy (1984), A broad-band 11 GHz radio propagation experiment, IEEE Trans. Antennas Propag., Vol. AP-32, No. 5, pp. 449-455.
- CCIR (1982), Propagation data required for line-of-sight radio relay systems, International Telecommunication Union, Geneva, Switzerland, Report 338-4, CCIR Vol. V, pp. 279-313.
- CCIR (1986a), Reflection from the surface of the earth, International Telecommunication Union, Geneva, Switzerland, Report AB/5 (MOD F) [Doc. 5/1011], CCIR XVth Plenary Assembly.
- CCIR (1986b), Propagation data and prediction methods required for line-of-sight radio-relay systems, International Telecommunication Union, Geneva, Switzerland, CCIR Report 338-5, CCIR Vol. 5.
- CCIR (1986c), Cross polarization due to the atmosphere, International Telecommunication Union, Geneva, Switzerland, CCIR Report 722-2, CCIR Vol. 5.
- Costa, E. (1986), A simulation of multipath effects on the cross-polarization discrimination in microwave line-of-sight links, Ann. Télécomm., Vol. 41, No. 3-4, pp. 197-211.
- Crawford, A.B. and W.C. Jakes, Jr. (1952), Selective fading of microwaves, Bell Syst. Tech. J., Vol. 31, No. 1, pp. 68-89.
- Crombie, D.D. (1983), Prediction of multipath fading on terrestrial microwave links at frequencies of 11 GHz and greater, in Proc. NATO/AGARD Conf., North Atlantic Treaty Organization, Paris, No. 346, pp. 10/1-8.
- DeLange, O.E. (1952), Propagation studies at microwave frequencies by means of very short pulses, Bell Syst. Tech. J., Vol. 31, No. 1, pp. 91-103.
- Doherty, L.H. (1952), Investigation of air-to-air and air-to-ground electromagnetic propagation, School of Electrical Engineering, Cornell University, Ithaca, NY, U.S.A., Research Report EE 138.
- Dougherty, H.T. (1968), A survey of microwave fading mechanism, remedies and applications, U.S. Department of Commerce, Washington, D.C., U.S.A., ESSA Report ERL-WPL4.
- Dougherty, H.T. (1981), Electromagnetic wave trajectories at VHF and higher frequencies, U.S. Department of Commerce, Washington, D.C., U.S.A., NTIA Report CR-81-14.
- Dougherty, H.T. and W.J. Hartman (1977), Performance of a 400 Mbit/s system over a line-of-sight path, Trans. IEEE Communicat., Vol. COM-25, No. 4, pp. 427-432.
- Dougherty, H.T. and E.J. Dutton (1981), The role of elevated ducting for radio service and interference fields, U.S. Department of Commerce, Washington, D.C., U.S.A., NTIA Report 81-69.
- Dutton, E.J. (1961), On the climatology of ground-based radio ducts and associated fading regions, U.S. Department of Commerce, Washington, D.C., U.S.A., NBS Technical Note 96.
- Friss, H.T. (1948), Microwave repeater research, Bell Syst. Tech. J., Vol. 27, No. 2, pp. 183-246.
- Gardina, M.F. and S.H. Lin (1985), Measured performance of horizontal space diversity on microwave radio path, in Proc. IEEE Global Communications Conference.
- Hall, M.P.M. (1979), Effects of the Troposphere on Radio Communication, London, Institution of Electrical Engineers.
- Hartman, W.J. and D. Smith (1977), Tilting antennas to reduce line-of-sight microwave link fading, Trans. IEEE Antennas Propag., Vol. AP-25, No. 5, pp. 642-645.
- Hautefeuille, M., A.W. Boyle, A.G.W. Timmers, and J.S. Shannon (1980), Duct fading - is Senegal an isolated case?, Telecommunication Journal, Vol. 47, No. 8, pp. 517-525.
- Hubbard, R.W. (1984), A review of atmospheric multipath measurements and digital system performance, in Proc. NATO/AGARD Conf., North Atlantic Treaty Organization, Paris, No. 363, pp. 10/1-18.
- Ikegami, F. (1959), Influence of an atmospheric duct on microwave fading, IRE Trans. Antennas Propag., Vol. AP-7, No. 3, pp. 252-257.
- Ikegami, F. (1967), Analyses of microwave fading due to laminar structure of the atmospheric refractive index, Rev. Elec. Comm. Lab. (Japan), Vol. 15, Nos. 7-8, pp. 483-506.
- Ikegami, F., M. Haga, T. Fukuda, and H. Yoshida (1966), Experimental studies on atmospheric ducts and microwave fading, Rev. Elec. Comm. Lab. (Japan), Vol. 14, Nos. 7-8, pp. 505-533.
- Kaylor, R.L. (1953), A statistical study of selective fading of super-high frequency radio signals, Bell Syst. Tech. J., Vol. 32, No. 9, pp. 1187-1202.
- Lam, W.I. (1983), The propagation of microwaves on line-of-sight oversea paths, Faculty of Engineering Science, University of Western Ontario, London, Canada, Ph.D. Thesis.



- Lam W.L., and A.R. Webster (1985), Microwave propagation on two line-of-sight oversea paths, IEEE Trans., Antennas Propag., Vol. AP-33, No. 5, pp. 510-516.
- Lammers, U.H.W., and R.A. Marr (1985), Atmospheric multipath propagation over a long terrestrial line-of-sight path, U.S.A.F. Rome Air Development Center, Griffiss Air Force Base, NY, U.S.A., Report RADC-TR-85-79.
- Lavergnat, J. and M. Sylvain (1985a), Statistiques de la fonction de transfert par trajets multiples pour des largeurs de bande moyennes, Application à la prévision de la qualité, Ann. Télécommun., Vol. 40, No. 11-12, pp. 604-616.
- Lavergnat, J. and M. Sylvain (1985b), Analyse théorique d'un canal de propagation en présence de trajets multiples, Ann. Télécommun., Vol. 40, No. 11-12, pp. 572-583.
- Lee, T.C. and S.H. Lin (1985), More on frequency diversity for digital radio, in Proc. IEEE Global Communications Conference.
- Liniger, M. (1982), Sweep measurements of the transferfunction of a RF-channel and their representation by polynomials, in Proc. IEEE International Conference on Communications.
- Liniger, M. (1983), One year results of sweep measurements of a radio link, in Proc. IEEE International Conference on Communications.
- Martin, L. (1980), Étude de la sélectivité des évanouissements dus aux trajets multiples, Ann. Télécommun., Vol. 35, No. 11-12, pp. 482-487.
- Martin, L. (1982a), Statistical results on selective fading, in Proc. IEEE International Conference on Communications, Session 7B.
- Martin, L. (1982b), Computing method of outage time for high bit rate digital radiolinks, IEEE International Conference on Communications, Session 7B.
- Martin, L. (1984), Phase distortions of multipath transfer functions, in Proc. IEEE International Conference on Communications.
- Martin, L. and G. Casanova (1974), Études des variations du découplage de polarisation à 7 GHz sur une liaison de 50 km, Centre National d'Études des Télécommunications, Lannion, France, Note. Tech. TML/ETL/72.
- Martin, L., R.L. Olsen, and T. Tjelta (1986), Initial analyses of multipath fading measurements for various geographical conditions in France, in Proc. Symp. on Antennas and Propagation, Kyoto, Japan.
- Martin, L., R.L. Olsen, and T. Tjelta (1986), Coïncide de réfraction, météorologie et affaiblissements sur les trajets en visibilité, this conference.
- McGavin, R.E., and Maloney (1959), Study at 1.046 Gc/s of the reflection coefficient of irregular terrain at grazing angles, J. Res. NBS, Vol. 63D, pp. 235-248.
- Matsuo, S., S. Ugai, K. Kakita, F. Ikegami, and Y. Kono (1953), Microwave fading, Reports of Elec. Comm. Lab. (Japan), Vol. 1, No. 3, pp. 38-47.
- Meadows, R.W., R.E. Lindgren, and J.C. Samuel (1966), Measurement of multipath propagation over a line-of-sight radio link at 4 Gc/s using frequency-sweep technique, Proc. IEE, Vol. 113, No. 1, pp. 41-48.
- Miller, A.R., R.M. Brown, and E. Vagh (1984), New derivation for the rough-surface reflection coefficient and for the distribution of sea-wave elevations, Proc. IEE, Vol. 131, Pt.H, No. 2, pp. 114-116.
- Morita, K. (1970), Prediction of Rayleigh fading occurrence probability of line-of-sight microwave links, Rev. Elec. Comm. Lab. (Japan), Vol. 18, No. 11-12, pp. 810-821.
- Morita, K. (1971), Fluctuations of cross polarization discrimination ratio due to fading, Rev. Elec. Comm. Lab. (Japan), Vol. 19, pp. 549-552.
- Morita, K. (1972), Prediction of equivalent Rayleigh fading occurrence rate on line-of-sight reflected-wave path, Rev. Elec. Comm. Lab. (Japan), Vol. 20, No. 7-8, pp. 589-598.
- Morita, K. and K. Kakita (1958), Fading in microwave relays, Reports of Elec. Comm. Lab. (Japan), Vol. 6, No. 9, pp. 352-370.
- Morita, K.S. Sakagami, S. Murata, T. Mukai, and M. Ohtani (1979), A method for estimating cross polarization discrimination ratio during multipath fading (in Japanese), Trans. IECE (Japan), Vol. 62-B, No. 11, pp. 998-1005.
- Olsen, R.L. (1981), Cross polarization during clear-air conditions on terrestrial links: A review, Radio Sci., Vol. 16, No. 5, pp. 631-647.
- Olsen, R.L. (1985), unpublished notes on crosspolarization.
- Olsen, R.L., T. Tjelta, L. Martin, and J.E. Dobie (1986), Towards a more accurate method of predicting the distribution of multipath fading on terrestrial microwave links, Electron. Lett., Vol. 22, No. 17, pp. 902-903.



- Omori, T. and R. Sato (1958), Multipath propagation of microwaves, Reports of Elec. Comm. Lab. (Japan), Vol. 6, No. 1, pp. 1-11.
- Pearson, K.W. (1965), Method for the prediction of the fading performance of a multi section microwave link, Proc. IEE, Vol. 112, No. 7, pp. 1291-1300.
- Price, W.L. (1948), Radio shadow effects produced in the atmosphere by inversions, Proc. Phys. Soc., London, Vol. 61, pp. 59-78.
- Parl, S. (1983), Characterization of multipath parameters for line-of-sight microwave propagation, IEEE Trans. Antennas Propag., Vol. AP-31, No. 6, pp. 938-948.
- Quarter, P. (1966), Propagation tests on an oversea path (Mt. Verrugoli - Mt. Portofino), Alta Frequenza, Vol. 33, No. 1, pp. 22-30.
- Rivet, P. (1956), Essais de diversité et étude de l'effet de focalisation sur des liaisons longues en visibilité, l'Onde Électrique, Vol. 36, No. 346, pp. 23-31.
- Rooryck, M. and L. Martin (1977), Disponibilité des liaisons hertziennes numériques utilisant des polarisations croisées à la même fréquence, Ann. Télécomm., Vol. 32, No. 11-12, pp. 560-564.
- Rummler, W.D. (1979), A new selective fading model : Application to propagation data, Bell Syst. Tech. J., Vol. 58, No. 5, pp. 1037-1071.
- Ruthroff, C.L. (1971), Multiple-path fading on line-of-sight microwave radio systems as a function of path length and frequency, Bell Syst. Tech. J., Vol. 50, No. 7, pp. 2375-2398.
- Sakagami, S. and Hosoya, Y. (1982), Some experimental results on in-band amplitude dispersion and a method for estimating in-band linear amplitude dispersion, IEEE Trans. Commun., Vol. COM-30, No. 8, pp. 1875-1888.
- Sandberg, J. (1980), Extraction of multipath parameters from swept measurements on a line-of-sight path, IEEE Trans. Antennas Propag., Vol. AP-28, No. 6, pp. 743-750.
- Sasaki, O. and Y. Akiyama (1979), Multipath delay characteristics on line-of-sight microwave system, IEEE Trans. Communicat., Vol. COM-27, No. 12, pp. 1876-1886.
- Schiavone, J.A. (1986), Predicting the geographical distribution of microwave fading from ground-based climatological measurements, in Proc. IEEE International Conference on Communications.
- Segal B. (1985), The measurement of tropospheric refractive index relevant to the study of anomalous microwave propagation - Review and recommendations, Communications Research Centre, Ottawa, Canada, CRC Report No. 1387.
- Segal, B. and R.E. Barrington (1977), The Radio Climatology of Canada, Tropospheric Refractivity Atlas for Canada, Communications Research Centre, Ottawa, Canada, CRC Report No. 1315-E.
- Shafi, M. (1986a), Statistical analysis/simulation of a three ray model for multipath fading with applications to outage prediction, Faculty of Engineering, McMaster University, Hamilton, Canada, CRL Report No. 168.
- Shafi, M. (1986b), Final report on the simulation of a general three ray channel model for microwave LOS applications, Faculty of Engineering, McMaster University, Hamilton, Canada, CRL Report No. 172.
- Shafi, M. and D.P. Taylor (1986), Influence of terrain induced reflections on the performance of high capacity digital radio systems, in Proc. IEEE International Conference on Communications.
- Sharpless, W.M. (1946), Measurement of the angle of arrival of microwaves, Proc. IRE, Vol. 34, No. 11, pp. 837-846.
- Stephensen, E.T. (1981), Clear-air propagation on line-of-sight radio paths : A review, Radio Sci., Vol. 16, No. 6, pp. 609-629.
- Strickland, J.I. (1981), Site-diversity measurements of low-angle fading and comparison with a theoretical model, Ann. Télécomm., Vol. 36, No. 7-8, pp. 457-463.
- Strickland, J.I., R.L. Olsen, and H.L. Werstik (1977), Measurements of low angle fading in the Canadian arctic, Ann. Télécomm., Vol. 32, No. 11-12, pp. 530-535.
- Sylvain, M. and J. Lavergnat (1985), Modelling the transfer function in medium bandwidth radio channels during multipath propagation, Ann. Télécomm., Vol. 40, No. 11-12, pp. 584-603.
- Tjelte, T., R.L. Olsen, and L. Martin (1986), An investigation of terrain related variables for predicting the multipath fade depth distribution on terrestrial microwave links, this symposium.
- Ugai, S. (1961), Characteristics of fading due to ducts and quantitative estimation of fading, Rev. Elec. Comm. Lab. (Japan), Vol. 9, No. 5-6, pp. 319-360.
- Valantin, R. and K. Metzger (1984), Wideband line-of-sight channel measurements and simulation : application to digital radio links, in Proc. NATO/AGARD Conf., North Atlantic Treaty Organization, Paris, No. 363, pp. 14/1-11.

Vigants, A. (1975), Space-diversity engineering, Bell Syst. Tech. J., Vol. 54, No. 1, pp. 103-141.

Webster, A.R. (1982), Angle-of-arrival considerations in microwave communication systems, IEEE Trans. Antennas Propag., Vol. AP-30, No. 4, pp. 796-800.

Webster, A.R. (1963), Angles-of-arrival and delay times on terrestrial line-of-sight microwave links, IEEE Trans. Antennas, Propag., Vol. AP-31, No. 1, pp. 12-17.

Webster, A.R. and T. Ueno (1980), Tropospheric microwave propagation - an X-band diagnostic system, IEEE Trans. Antennas Propag., Vol. AP-28, No. 5, pp. 693-699.

#### ACKNOWLEDGEMENTS

The first author gratefully acknowledges helpful discussions with Drs. W.I. Lam, S. Segal, M. Shaff, and A.R. Webster during the preparation of this paper.

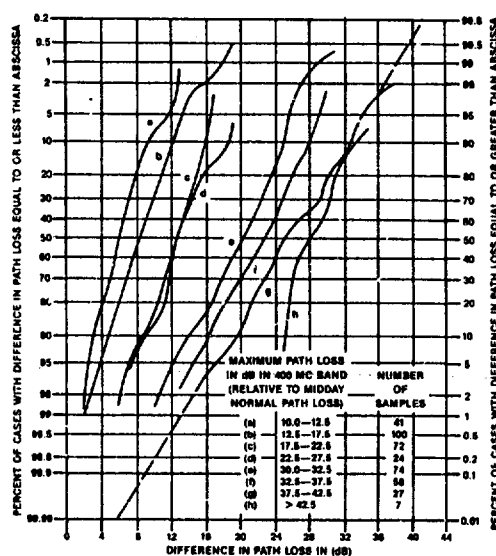


Fig. 1. Statistical distribution of differences between maximum and minimum fade depth in 400 MHz bandwidth, 49 km, 4 GHz path in Iowa, U.S.A., July and August, 1950. [reproduced from Kaylor (1953), Copyright, American Telephone and Telegraph Company, Reprinted by permission]

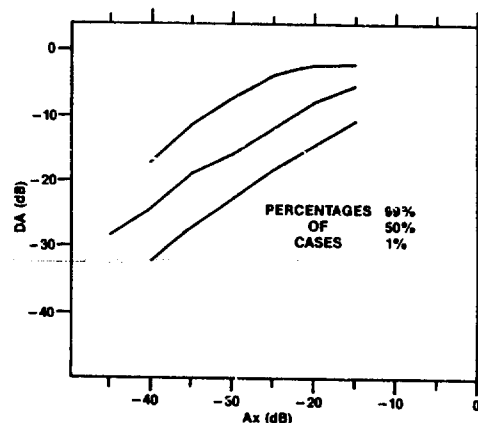


Fig. 2. Variation of 99%, 50%, and 1% levels of conditional distribution of maximum fade depth differences (DA) in 400 MHz bandwidth with maximum fade depth ( $A_x$ ), 50 km, 11.5 GHz path in France, July 1979. [reproduced from Martin (1982a)]

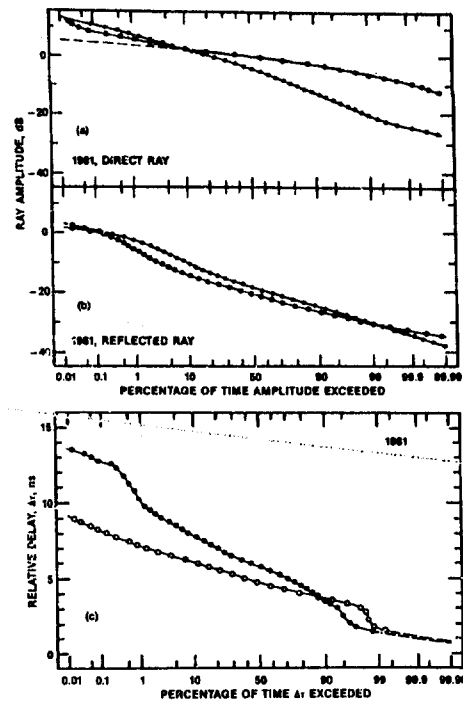


Fig. 3. Distributions of (a) direct ray amplitude, (b) reflected ray amplitude, and (c) relative delay, for quiet (—o—) and disturbed (—•—) periods. 80 km path (9.5–10.5 GHz) in Canada, July and August, 1981. [reproduced from Lam and Webster (1985)]

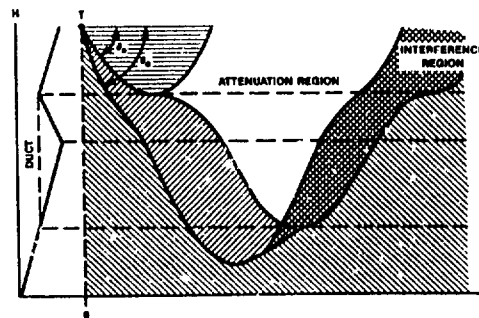


Fig. 6. "Attenuation" and "interference" regions for transmitter situated above a duct (shown by M-profiles). [reproduced from Ikegami (1967)]

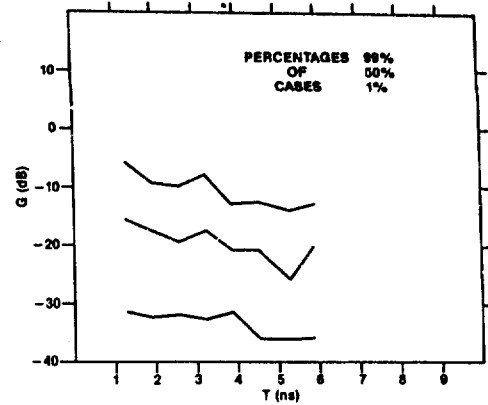


Fig. 4. Variation of 99%, 50%, and 1% levels of conditional distribution of quasi-flat fade depth ( $G$ ) in 400 MHz bandwidth with relative delay ( $T$ ) between direct and dominant secondary rays. 50 km, 11.5 GHz path in France, January 1980. [reproduced from Martin (1982a)]

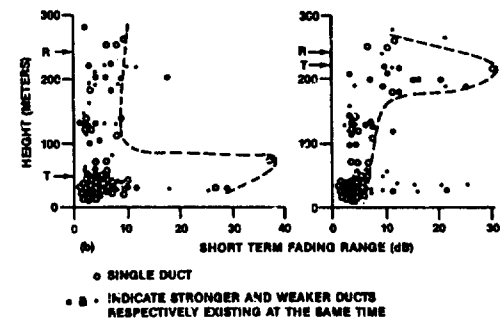
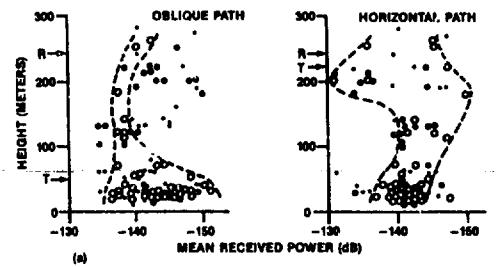


Fig. 5. Comparison of (a) 5-minute mean received power, and (b) 5-minute fading range, with duct height. 55 km, 4 GHz co-located horizontal and inclined paths in Japan, 1–15 November 1954. [reproduced from Ikegami (1959)]

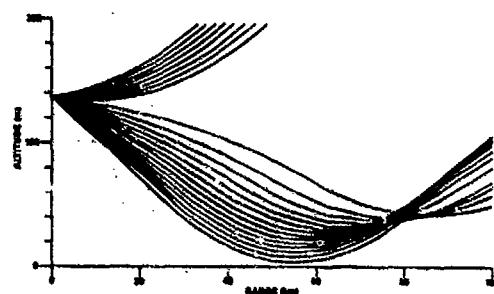


Fig. 7. Example of ray paths for transmitting antenna situated above a duct. [after Segal (1985)]

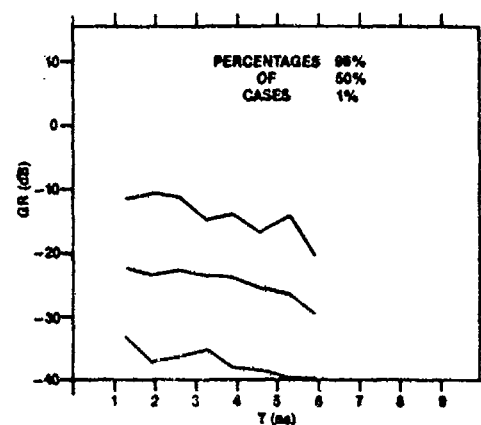


Fig. 9. Variation of 99%, 50%, and 1% levels of conditional distribution of effective reflection coefficient ( $G \cdot R$ ) with relative delay ( $T$ ) between direct and dominant secondary rays. 50 km, 11.5 GHz path in France, January 1980. [reproduced from Martin (1982a)]

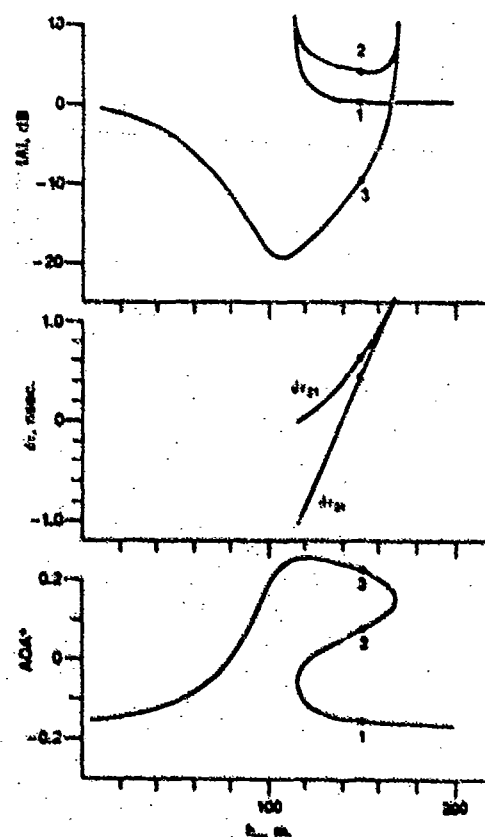


Fig. 8. Variation of ray amplitude  $|A|$ , relative delay  $\Delta T$ , and angle-of-arrival  $AOA$ , with anomalous layer ( $-20$  M $\mu$  intensity, 100 m thickness) height  $h_a$ . 50 km path length, 100 m antenna heights,  $-47$  M $\mu$ /km refractivity gradient outside layer. [reproduced from Webster (1983)]

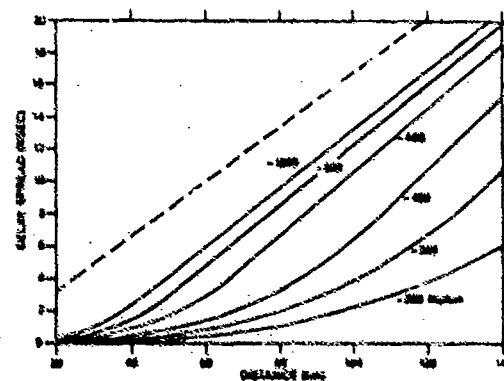


Fig. 10. "Maximum" atmospheric (—) and surface (---) multipath relative delays ("delay spread") versus path length for a duct of intensity  $\Delta N = -50$  M $\mu$ . Refractivity gradient of  $-40$  M $\mu$ /km outside the duct. Various duct refractivity gradients for atmospheric multipath. [partially reproduced from Farl (1983)]

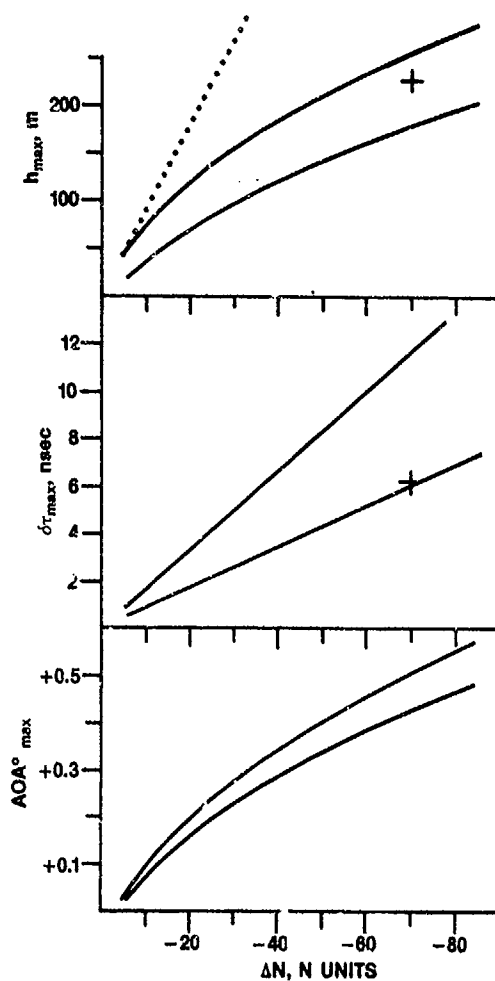


Fig. 11. The maximum anomalous layer height ( $h_{max}$ ), associated relative delay ( $\sigma_{Tmax}$ ), and angle-of-arrival ( $AOA_{max}$ ) versus intensity ( $\Delta N$ ) for "reflective" multipath. 50 km path, 100 m antenna heights, -40 NU/km refractivity gradient outside layer. Lower curve - layer thickness  $\Delta h = 100$  m; upper curve -  $\Delta h = 0$ ; dotted curve - maximum height for layer to support strong reflection. The crosses represent the values quoted by Meadows et al. (1966). [reproduced from Webster (1983)]

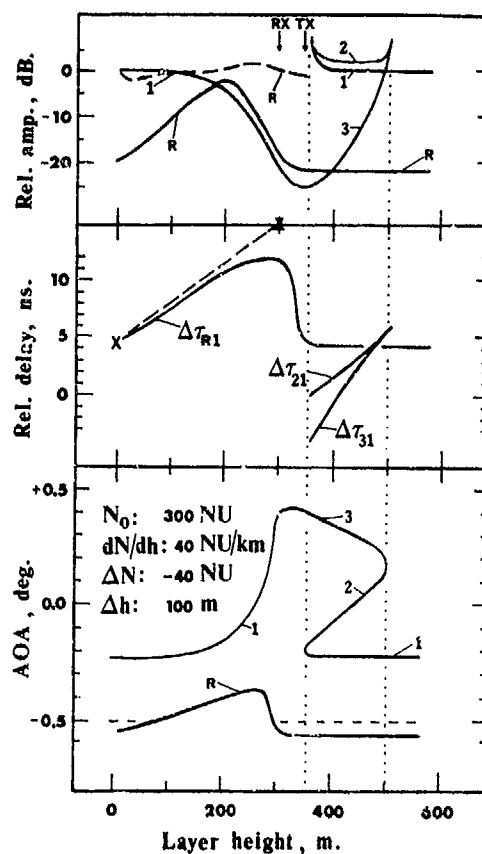


Fig. 12. Variation of ray (a) relative amplitude, (b) relative delay, and (c) angle-of-arrival with height of a single anomalous layer (characteristics indicated on Fig. 12c). Subscripts: 1 main ray; 2,3 - additional atmospheric rays; R - reflected ray with (—) and without (---) obstacle diffraction. [reproduced from Lam and Webster (1985), and Lam (1983)]

## DISCUSSION

**L.Felsen**

You have made the statement that experiments for propagation loss and fading are more reliable than theory. If that is true, what is missing from the theoretical models? Are the experiments sufficiently controlled to isolate the various effects which you designated as being important? If not, then the data are the result of so many interacting parameters that systematic modeling for prediction is well nigh impossible.

**Author's Reply**

My statement was really that experimental results for the specular and diffuse reflection coefficients from terrain are more reliable than theoretical results. I hope the reasons for this given in sub-section 3.3 of the paper are sufficiently clear. To answer your more general question, fading models at the moment are fairly highly empirical and I don't see any prospect of this changing significantly even in the long term. On the other hand, I believe that experiments have been sufficiently well controlled that systematic modelling is possible, even if the empirical component is fairly high (e.g., Tjelta et al., 1986).

**L.Boithias**

Le phénomène de "trou radioélectrique" (RADAR) et le phénomène de baisse du niveau moyen (liaison point à point) sont liés. Ils correspondent au cas où le récepteur (ou la cible) est situé du côté de la caustique où, d'après la théorie des rayons, aucun rayon venant de l'émetteur ne peut passer. Le concept de caustique serait donc préférable aux concepts de focalisation et de défocalisation qui sont plutôt obscurs et non clairement définis.

**Author's Reply**

In some respects I prefer the terms "divergence" and "convergence" to "defocussing" and "focussing", because I think they are a little more physically descriptive. However, I have used the latter because they are more entrenched in the literature, and they are also somewhat descriptive of the physical situation. The fact that a stratified medium is causing the focussing and defocussing, rather than a lens-like medium should present no insurmountable difficulty. I find that the mathematical term "caustic" does not immediately convey enough physical meaning to qualify as part of a term for the type of loss involved, but to each his own preference.

**T.E.Doble**

Your work indicates that there should be some correlation between multipath delay and flat fade depth. Lam and Webster found this to be so on an overwater path, but has this been supported on a wider basis?

**Author's Reply**

As far as I know, Martin (1982 a) is the only one to have analyzed wide-band data in a way that gives an explicit statistical relationship between the median depression depth and the relative delay between the main two rays. Lam and Webster (1985) found a correlation also but did not present a statistical relationship in their paper. However, their associated ray-tracing calculations show a clear relationship between the defocussing attenuation resulting from a duct below the path and the corresponding relative delay between the direct and surface-reflected waves.



# DEVELOPMENT OF A GROUND-CONDUCTIVITY MAP FOR THE AREA OF THE FEDERAL REPUBLIC OF GERMANY FROM MEASURED FIELD-STRENGTH CONTOURS

by

Bernd Raufmann  
Institut für Rundfunktechnik GmbH  
Floriansmühlstr. 60  
D - 8000 München 45

AD-P005 733

## SUMMARY

Resolution 73 of the International Radio Consultative Committee (CCIR) urgently requests ground-conductivity information at 1 MHz for planning purposes in form of suitable maps. Following that request 1201 propagation paths with a total length of 92578 km were derived from daytime field-strength contours of 47 MF-transmitters at 33 transmitter sites in the Federal Republic of Germany. Assuming a constant antenna efficiency of 70 % the field-strength values at the receiving terminals of these propagation paths were normalized to the conditions which form the base for the propagation curves in the Annex of CCIR Recommendation 368-4. From the propagation curves mentioned before the related ground-conductivity values were taken for the given values of receiving distance and field-strength. A comparison of ground-conductivity values found for 14 transmitter sites with two frequencies showed a linear relation between the effective ground conductivity and the frequency. On this basis all conductivity values were normalized to a frequency of 1 MHz. The average ground-conductivity values for each transmitter were associated with four different geographical zones. As there were only slight differences among the average values in three neighbouring zones the conductivity data of this area were unified as a whole. So the final result of the evaluations was a ground-conductivity map with only two areas of different ground conductivity. The paper presents detailed explanations of the methods applied in the developing process of the conductivity map and discusses the limits of these methods as well as the statistical distribution of the results obtained.

## PREFACE

The electrical characteristics of the surface of the earth play an important role in field-strength prediction techniques, especially in the VLF-/LF- and MF-bands. An internationally agreed field-strength prediction method for the frequency range between 10 kHz and 30 MHz is given in CCIR-Recommendation 368 /1/. Its application requires data of the ground conductivity  $\sigma$  and the relative permittivity  $\epsilon_r$ . Such values are given in Recommendation 527 for different types of the soil, however as explicitly stated in CCIR Report 229 /1/ they refer to homogeneous sub-surface soil structures. For their application in CCIR-Recommendation 368 it is suggested in CCIR-Report 229 to introduce the concept of effective parameters whereby the inhomogeneous sub-surface structures are replaced by an equivalent homogeneous structure. In many cases, however, these sub-surface structures are very complex or even unknown and it is impossible to evaluate these effective parameters. Methods for estimating effective electrical characteristics of the surface of the earth are given in CCIR-Report 879 /1/.

Considering the lack of ground conductivity data in large areas of the world the CCIR Study Group 5 entrusted its Interim Working Party (IWP) 5/1 by CCIR Decision 3 to provide conductivity maps for use in a world Atlas of ground conductivity. This could not have been accomplished without help of the member administrations of the International Telecommunication Union (ITU) which have been requested by Resolution No. 73 of the CCIR to supply ground-conductivity information in form of suitable maps. IWP 5/1 of the CCIR had set a deadline for the incoming information on the 1st of April in 1985.

For the area of the Federal Republic of Germany two old ground conductivity maps did exist, probably produced in the 3rd decade of this century. In spite of slight differences in the areas of given ground-conductivity values they seemed to be derived from the same data. It was, however, impossible to identify the type of data from which the maps had been deduced or any authorship of these maps. For these reasons the reliability of the maps was to be called into question.

## 1. METHOD OF ESTIMATING THE EFFECTIVE GROUND CONDUCTIVITY

A new approach for mapping the ground conductivity parameter within the area of the F.R. of Germany was necessary. A consequent application of one of the methods described in the above mentioned CCIR Report 879 would have required a large amount of measured data which could not have been obtained in the short time available. However, use could be made of a number of field-strength contours of MF-transmitters measured in 1931. Fig. 1 shows an example of such a set of field-strength contours

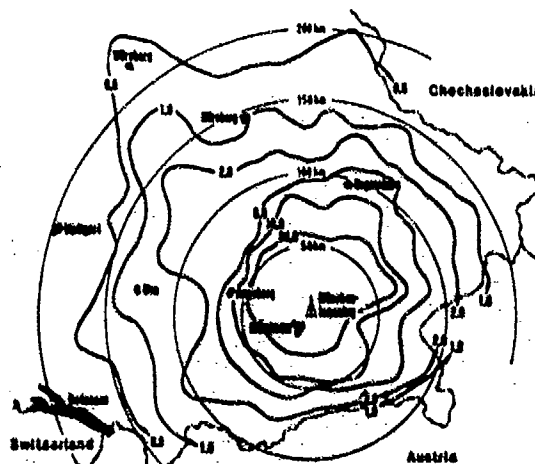


Fig. 1 - Field-strength contours of MF-transmitter  
München - Ismaning

related to the MF-transmitter of München-Ismaning. The outer field-strength contours of 47 MF-transmitters formed the base to the evaluation of average ground-conductivity values for 1201 transmission paths. Fig. 2 shows the distribution of MF-transmitters over the area of the Federal Republic of Germany in 1951.

For each of the outer field-strength contours propagation paths were constructed in azimuthal steps of 10 degrees as schematically demonstrated in Fig. 3. The field-strength value of each field-strength contour in question was normalized in relation to an effectively transmitted power of 1 kW assuming the antenna efficiency being of the order of 70 %.

For each propagation path a set of field-strength values being a function of the ground conductivity was taken from CCIR-Recommendation 368-4 and compared with the normalized field-strength value of the field-strength contour. By this means and the additional application of a linear interpolation procedure the most appropriate value of the ground conductivity for the propagation path in question was chosen. The relative permittivity  $\epsilon_r$  could be neglected because it is handled in CCIR-Recommendation 368 as a function of the ground conductivity  $\sigma$ . Under practical aspects this procedure is correct because the method for finding the effective ground conductivity values is in fact the complete inversion of the field-strength prediction method of CCIR-Recommendation 368. Physical values of ground-conductivity, however, cannot be deduced from these data.

## 2. FREQUENCY DEPENDENCE OF GROUND CONDUCTIVITY VALUES

Following the request of CCIR-Resolution 73 data relative to the MF part of the spectrum should be standardized to 1 MHz. Therefore comparisons were made at transmitter sites where two or more frequencies had been radiated. The results turned out that in fact a linear relation between frequency and effective ground conductivity did exist. A correction process taking account of this effect was applied to all ground conductivity data.

## 3. ASSOCIATION OF THE EFFECTIVE GROUND CONDUCTIVITY VALUES TO GEOGRAPHICAL AREAS

Being aware of CCIR-Resolution 73 which states that the data to be submitted should serve in frequency planning procedures for telecommunication services, it was necessary to associate the effective ground-conductivity values found for the various propagation paths to geographical areas. For the same reason there was no necessity for a very detailed mapping of the data and it seemed to be appropriate to average all ground conductivity values belonging to the service area of the same transmitter. These average ground-conductivity values of each transmitter were associated with four different geographical zones. As there were only slight differences among the average values in the three zones south of 53° N it was justified to unify the conductivity data for this area as a whole (see Table I). For this case the average effective ground conductivity was found to be 5.9 mS/m with a standard deviation of 1.8 mS/m or 31 %, respectively.

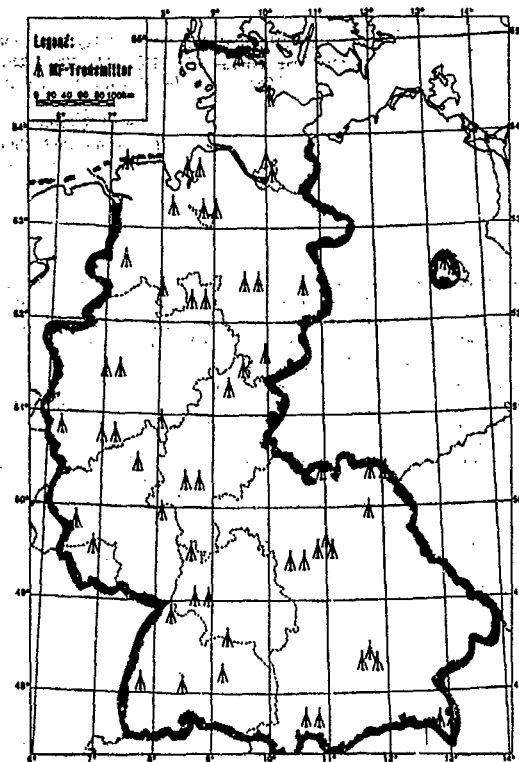


Fig. 2 - Distribution of MF-transmitters in 1951

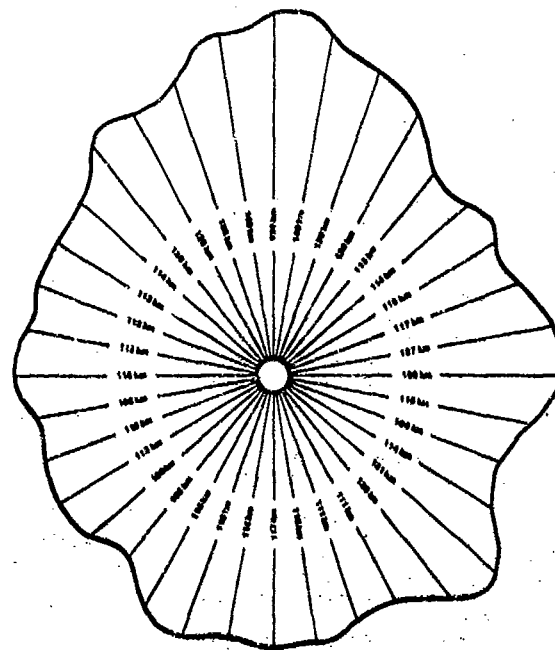


Fig. 3 - Construction of propagation paths



Table 1 - Results of ground-conductivity evaluations for various geographical zones

| Geographical latitude | Average ground conductivity | Standard deviation |    | Number of transmitters | Number of transmitter sites | Number of transmission paths | Total length of transmission paths |
|-----------------------|-----------------------------|--------------------|----|------------------------|-----------------------------|------------------------------|------------------------------------|
| North                 | mS/m                        | mS/m               | %  | -                      | -                           | -                            | km                                 |
| 50                    | 6,1                         | 1,7                | 28 | 12                     | 8                           | 344                          | 35 598                             |
| 50 - 52               | 5,6                         | 1,7                | 30 | 10                     | 7                           | 298                          | 24 169                             |
| 52 - 53               | 6,0                         | 2,3                | 38 | 7                      | 5                           | 202                          | 11 468                             |

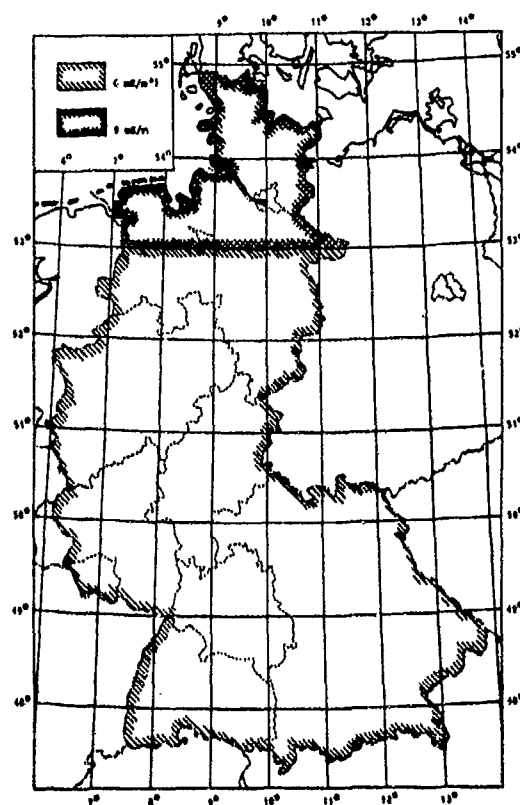
These data are based on 29 transmitters at 20 different transmitter sites. 844 transmission paths having a total length of 71 235 km were taken into account. The data available from some low power transmitters situated in particularly mountainous regions were omitted as in these regions the effective ground-conductivity was found to be well below 1 mS/m. This applies, however, only to a very small percentage of the investigated area.

North of 53° N the average effective ground conductivity was evaluated as 9.1 mS/m with a standard deviation of 2.6 mS/m or 29 %, respectively. Data of 9 transmitters at 8 different transmitter sites were taken into account. The number of transmission paths was 220 having a total length of 16 835 km. For practical reasons it was desirable to round the above mentioned average values of effective ground conductivity to become 6 mS/m or 9 mS/m, respectively. The consequential effects on the accuracy of field-strength predictions are very small and in fact negligible.

Fig. 4 shows the map of the Federal Republic of Germany with the two areas of different ground conductivity as it was submitted to the CCIR.

#### 4. CONCLUSIONS

The above described method for estimating the effective ground conductivity does not claim to be a very sophisticated one. It is in fact a simplified application of the attenuation method given in section 4.2 of CCIR Report 879 which is, as already mentioned, the complete inversion of the field-strength prediction method of CCIR-Recommendation 368. It does, however, claim like the full attenuation method to be a method the results of which are totally compatible with the field-strength prediction method of CCIR Recommendation 368. Considering that prediction method to be a purely theoretically based one it is obvious that its prediction accuracy is improved if the input data are obtained by inversion of the method in question.



Effective ground conductivity  $f = 1 \text{ MHz}$

\*in particularly mountainous regions well below 1 mS/m

Fig. 4 - Conductivity map

Another advantage of the method is that it takes account of several propagation factors like ground conductivity, relative permittivity, topographical and morphographical structure of the surface of the earth, sub-surface structure, and penetration depth of the radio waves in the single parameter of effective ground conductivity.

The final result of the mapping process for the area of the Federal Republic of Germany with in practice only two areas of different effective ground conductivity is not only due to the chosen kind of averaging procedure but also due to the relatively small variations of the more detailed intermediate results, which of course with some more efforts also could have been mapped. It was the feeling, however, that this would have complicated frequency planning procedures without gaining improvements in accuracy.

It seems worth while to be mentioned that the propagation curves in CCIR Recommendation 368 are arranged in that way, that for each given value of ground conductivity a frequency dependent set of propagation curves is given. This made the finding of the proper conductivity value for each propagation path from the couple of distance and field strength very time consuming. Therefore, it had been proposed to CCIR Study Group 5, to rearrange the propagation curves of CCIR Recommendation 368 in that way that conductivity dependent sets of propagation curves are drafted for given frequency values in steps of 100 kHz. CCIR Study Group 5 did not yet follow the proposal with respect to CCIR Recommendation 368. The World Atlas of ground conductivity, however, which is to be published in the near future, will contain an arrangement of propagation curves as proposed. An example is shown in Fig. 5. By that the estimation of the effective ground-conductivity parameter from measured field-strength values will be essentially facilitated.

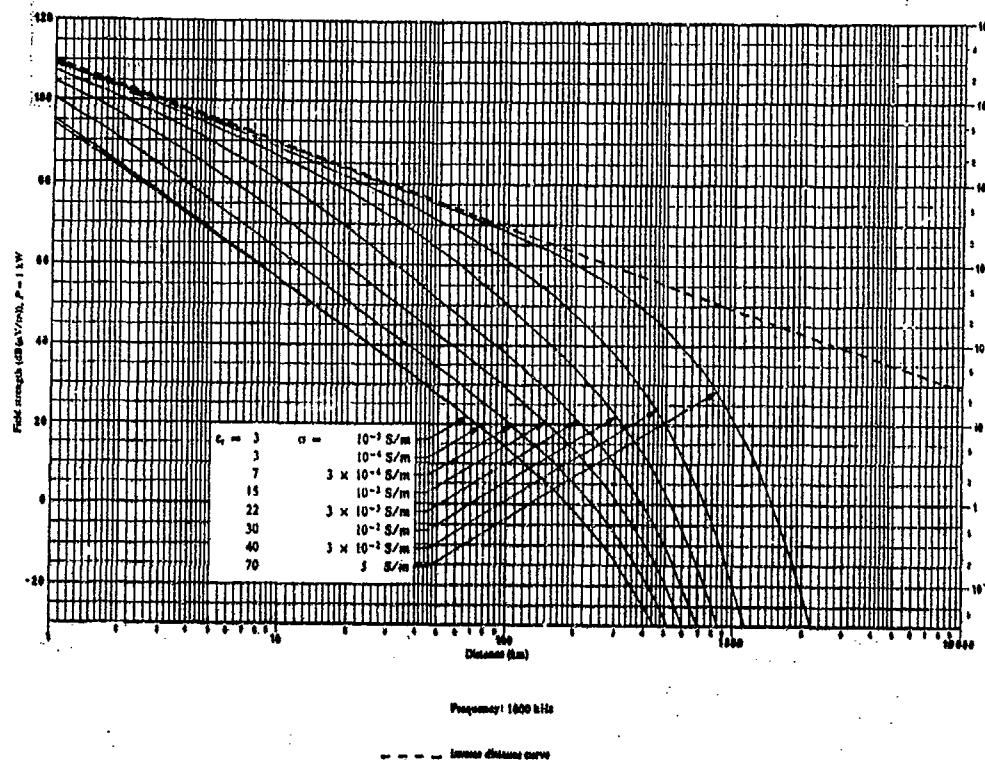


Fig. 5 Ground-wave propagation for different values of  $\sigma$  and  $\epsilon_r$ .

#### REFERENCE

- /1/ Recommendations and Reports of the CCIR, 1982, Volume V, Propagation in non-ionized media, Geneva 1982, ISBN 92-61-01431-3


## DISCUSSION

**H. Vissinga**

The differences in the conductivities you have mentioned seem to be relatively small, from about 6 as the lower value and 9 as the higher value. Now these CCIR curves, I think, go in steps of 10 or, maybe, 3. What are the consequences for, say, the predicted field strengths if you have such small differences in conductivity, in view of the relatively short distances involved in these MF broadcast bands?

**Author's Reply**

If you have small differences in the ground conductivity, the consequence is a simplification of field strength prediction in frequency planning for distance ranges of the ground wave from about 100 km to 500 km, in these frequency bands. And this was the intention of the CCIR, i.e. to provide information for frequency planning purposes, not for transmitter-site selection. It is a very complicated matter to find a method which is capable to present precise data for transmitter-site selection. Also the wave-tilt method, which is a point measurement, does not work if there are many changes in ground conductivity, along the entire length of the propagation path. If you have a good station at the transmitter site, this will follow the propagation the whole way and you will measure wrong data at a special point where you apply the wave-tilt method.



AD-P006 734

4-1

SCATTERING AND DEPOLARIZATION BY RANDOM ROUGH TERRAIN AND  
VEGETATION COVERED TERRAIN-UNIFIED FULL WAVE APPROACH

Ezekiel Bahar

Department of Electrical Engineering  
University of Nebraska-Lincoln  
Lincoln, NE 68588-0511

## ABSTRACT

In this paper the principal elements of the full wave approach to problems of scattering and depolarization by rough terrain and vegetation covered terrain are presented. Scattering by random rough surfaces is considered in detail and the full wave solutions are compared with earlier solutions based on geometric optics, physical optics and perturbation theories. It is shown that since the full wave approach accounts for both specular point scattering as well as Bragg scattering in a self-consistent manner, it resolves the discrepancies between the physical optics and perturbation solutions and bridges the wide gap between them. Thus, on applying the full wave approach to scattering by composite random rough surfaces it is not necessary to adapt a two-scale model of the rough surface.

The analytical procedures that account for the effects of vegetation on radio wave propagation over a terrestrial path are also presented. They are based on the full wave solutions to scattering by finitely conducting irregularly shaped objects with rough surfaces.

The full wave solutions satisfy duality, reciprocity and realizability relations in electromagnetic theory and the results are invariant to coordinate transformations. The full wave approach also accounts for coupling between the radiation fields, the lateral waves and the surface waves that constitute the complete expansions of the fields and it can be applied directly to problems of scattering at near grazing angles.

## 1. INTRODUCTION

Terrestrial radio wave propagation characteristics can be derived from the terrain and vegetation covered terrain like and cross polarized scattering cross sections for both vertically and horizontally polarized excitations. Traditionally physical optics and perturbation theories have been used to derive the like and cross polarized scattering cross sections for composite random rough surfaces (Beckmann and Spizzichino 1963, Rice 1951). To this end two-scale models have been adopted and the rough surfaces are regarded as small scale surface perturbations that are superimposed on large scale, filtered surfaces (Wright 1968, Valenzuela 1968, Barrick and Peake 1968). Thus the scattering cross sections are expressed as sums of two cross sections. The first accounts for specular point scattering. It is given by the physical optics cross section for the filtered surface consisting of the large scale spectral components. The second accounts for Bragg scattering. It is given by the cross section for the surface consisting of the small scale spectral components that ride on the filtered surface.

On applying the perturbed-physical optics approaches it is necessary to specify the wavenumber  $k_d$  where spectral splitting is assumed to occur between the large and small scale spectral components of the rough surface. Thus Brown (1978), who applied a combination of Burrows' perturbation theory (1967) and physical optics (Beckmann 1968), to obtain the scattering cross sections for perfectly conducting random rough surfaces, specified  $k_d$  on the basis of the characteristics of the small scale surface ( $8\pi k_d^2 \langle h_s^2 \rangle = 0.1$ , where  $k_0$  is the electromagnetic wavenumber and  $\langle h_s^2 \rangle$  is the mean square height of the small scale surface). However, using the approaches of Hagfors (1966) and Tyler (1976) the specification of  $k_d$  is assumed to be based on the characteristics (radius of curvature) of the large scale surface. In general the restrictions on both the large and small scale surfaces cannot be satisfied simultaneously and using the perturbed-physical optics approaches the evaluation of the scattering cross sections critically depend on the specification of  $k_d$  (Brown 1978).

More recently the full wave approach has been used to determine the scattering cross sections for composite random rough surfaces of finite conductivity (Bahar 1981b, Bahar and Barrick 1983). Since the full wave solutions account for Bragg scattering and specular point scattering in a self-consistent manner, it is not necessary to decompose the surface into two surfaces with small and large roughness scales. However, when such a decomposition is implemented, the full wave solutions for the scattering cross sections is expressed in terms of a weighted sum of two cross sections (Bahar 1981b, Bahar and Barrick 1983). Thus on adopting a two-scale model, the full wave solution resolves the discrepancies between Valenzuela's (1968) solution (mostly based on physical considerations) and Brown's solution (1978). Furthermore, in an attempt to draw more definite conclusions regarding the choice of  $k_d$ , it was varied over a wide range of values (Bahar et al 1983). It was shown that while, as expected, the individual cross sections associated with the large and small scale surfaces critically depend upon the choice of  $k_d$ , the weighted sum of the like polarized cross sections remain practically insensitive to variations in  $k_d$  for  $2.0 > \beta > 1.0$ . Thus, provided that the large scale surface satisfies the radii of curvature criteria (associated with the Kirchhoff approximations for the surface fields) and the condition for deep phase modulation, the full wave solutions for the like polarized scattering cross sections based on the two-scale model are practically independent of the specified value of  $k_d$ .

On applying the full wave approach to evaluate the like and cross polarized scattering cross sections for two-scale models of composite rough surfaces, several assumptions were made to facilitate the computations. The first assumption was that the large and small scale surfaces were statistically independent (Brown 1978). It would seem reasonable to make such an assumption if the two surfaces are results of independent processes. For the general case, however, one cannot assume statistical independence of the large and small scale surfaces.

The second simplifying assumption that was made was that the mean square slope  $\sigma_s^2$  for the total

surface was approximately equal to the mean square slope  $\sigma_{\text{FS}}^2$  for the filtered large scale surface.

The third assumption was that the mean square height of the total rough surface is large compared to a wavelength, and the surface height characteristic function for the total surface is negligibly small compared to unity.

Finally, the physical optics approximation for the cross polarized backscatter cross section is zero (Brown 1978). As a result, the cross polarized backscatter cross section for the filtered surface is set equal to zero when the two-scale model is used. However, for backscatter, only the specular points on the rough surface do not depolarize the incident wave.

A unified formulation has also been derived for the like and cross polarized cross sections for all angles of incidence. These solutions are compared with earlier solutions based on a two-scale model of the random rough surface (Bahar and Fitzwater 1984). Thus, the simplifying assumptions, that are common to all the earlier solutions based on two-scale models of the rough surface, are carefully examined. It is shown that while the full wave solutions for the like polarized scattering cross sections based on the two-scale model are in reasonable agreement (within 3 db) with the unified full wave solutions, the two solutions for the cross polarized cross sections differ very significantly (about 15 db).

The full wave approach has also been applied recently to problems of scattering and depolarization by arbitrarily shaped discrete scatterers of finite conductivity characterized by their rough surface height spectral density functions (Bahar and Fitzwater 1983, Bahar and Chakrabarti 1985). The co-polarized and cross polarized diffuse specific intensities (related to the Stokes parameters) scattered by a layer of randomly distributed arbitrarily shaped particles are shown to be significantly different from the specific intensities scattered by particles with smooth surfaces (Bahar and Fitzwater 1986a,b).

Using the unified full wave approach it is therefore possible to analyze more realistic models of propagation paths over the earth's surface without resorting to the artificial decomposition of the irregular terrain into large and small scale surfaces. Moreover, at microwave frequencies the vegetation that covers the terrain can be represented by random distributions of discrete scatterers of arbitrary shape rather than by a dielectric layer with an "effective complex permittivity" or an "effective surface impedance."

Two important extensions to the present form of the unified full wave solutions (Bahar and Fitzwater 1984, 1985), can be made. The present form of the solution is based on a second order iteration of the rigorous telegraphists' equations for the wave amplitudes. Higher order iterations can be considered in order to account for multiple scattering by the rough surface. In addition, contributions to the scattered fields from the non-illuminated or non-visible portions of the rough surface were ignored. The contributions from these shadow regions (Morse and Feshbach 1953) can also be taken into account using the full wave approach. They are of particular significance for scattering near grazing angles.

## 2. REVIEW OF THE FULL WAVE APPROACH

Rigorous closed form solutions for the reflection and transmission of electromagnetic waves have been derived for multilayered dielectric structures of uniform thickness (Wait 1962). (See Fig. 1). However, in a large variety of pertinent radio wave propagation problems the thicknesses of the layers are nonuniform and the height of the interface between two adjacent dielectric layers is a random function. (See Fig. 2). In these cases the incident waves are depolarized and scattered into both propagating and evanescent waves. Furthermore, an incident radiation field may be coupled into guided surface waves and lateral waves of the structure.

Often the problem that is actually solved is a highly idealized version of the original problem and concepts such as "effective dielectric coefficient" and "effective surface impedance" are introduced in order to make the solution of the original problem more tractable. However, the validity of such approximations is very limited and often questionable and they do not necessarily satisfy reciprocity (Schlak and Wait 1967, 1968).

Using a full wave approach it is possible to analyze more realistic models of the original physical structure without introducing simplifying approximations that cannot be justified a priori (Bahar 1973c,d).

The principal properties of the full wave solution and its relationships to earlier solutions of scattering problems are also summarized here (Bahar 1981a). This summary is also presented schematically in Figs. 3 and 4. The reader of this manuscript who is not familiar with the full wave approach will find this summary useful even though the details of the full wave method have been reported earlier (Bahar 1973a,b,c,d, 1974, 1981a).

### A. Principal Elements of the Full Wave Approach (See Fig. 3)

(a) The electromagnetic fields are expressed in terms of complete expansions of vertically and horizontally polarized waves. These include the radiation fields, the lateral waves and the surface waves (Bahar 1973c,d, 1974).

(b) Exact boundary conditions are imposed at the irregular surface.

(c) Using the orthogonal properties of the basis functions appearing in the complete expansions of the fields, Maxwell's equations are integrated over the transverse plane  $(y,z)$  (Bahar 1973c,d, 1974). Green's theorems are used to avoid term-by-term differentiation of the field expansions.

(d) Maxwell's equations for the electromagnetic fields are converted into coupled first order ordinary differential equations for the forward and backward traveling wave amplitudes which are only functions of the variable  $x$  (Bahar 1973c,d, 1974). (In view of the integration in the transverse plane  $(x,z)$  the telegraphists' equations are only function of  $x$ ). The coupled equations for the wave amplitudes are referred to the generalized telegraphists' equations (Bahar 1981a).

(e) Closed form second order iterative solutions for the radiation fields are obtained from the telegraphists' equations on neglecting multiple scattering from the rough surface. These second order iterative solutions account for wave scattering in arbitrary directions.

(f) A variable coordinate system that conforms with the local features of the irregular boundary is introduced and the resulting solutions for the scattered fields are shown to be invariant to coordinate transformations.

(g) The full wave solutions are compared with earlier geometric optics, physical optics and perturbation solutions. On adopting a two-scale model of the rough surface the unified full wave solution is decomposed into a weighted sum of two cross sections.

#### B. Principal Properties of the Full Wave Approach (See Fig. 4)

(a) The full wave solutions are shown to satisfy the reciprocity, realizability and duality relationships in electromagnetic theory and they are invariant to coordinate transformations.

(b) The full wave approach not only accounts for scattering and depolarization of the radiation fields but also accounts for coupling between the surface waves, the lateral waves and the radiation fields.

(c) The versatility of the full wave approach is demonstrated by determining its relationship to earlier solutions. Thus, on using a stationary phase approach to evaluate the integrals for the scattered fields, the full wave approach is shown to reduce to the geometric optics solutions (Bahar 1981a).

(d) If the vector  $\bar{n}$  normal to the rough surface is replaced by its value at the specular points  $\bar{n}_s$ , the full wave expressions for the scattered fields are shown to reduce to the physical optics solutions. Thus, the physical optics approach is valid only if the contributions to the scattered fields come primarily from the neighborhood of specular points on the rough surface.

(e) In a survey of the technical literature one finds several different forms of physical optics solutions. The discrepancies between the different physical optics solutions and the appearance of the so-called "edge effect" have been shown to be the result of premature truncation of the closed surface integrals.

(f) If one assumes that the height and the slopes of the rough surface are small, it is shown that the full wave solutions reduce to the perturbation solutions.

(g) The physical optics solutions for the backscattered fields become singular for near grazing angles. Thus in this case, even if the rough surface satisfies the radii of curvature criteria (associated with the Kirchhoff approximations of the surface fields), the physical optics solutions cannot be used and the far fields cannot be represented by plane waves at grazing angles. This is because at near grazing angles, the principal contributions to the backscattered fields do not come from specular points of the rough surface. (In this case specular points, if they existed, would be on vertical portions of the rough surface). It is shown that the full wave solutions for the backscattered fields remain valid as one approaches grazing angles (Bahar 1982).

(h) The full wave solutions have been compared with the hybrid perturbed-physical optics solutions (Bahar and Barriok 1983, Bahar et al, 1983) based on a two-scale model of the rough surface. It is shown that while the solutions based on the perturbed-physical optics approach critically depend upon the wave-number  $k_1$  where spectral splitting is assumed to occur, the solutions based on the full wave approach are relatively insensitive to the choice of  $k_1$  for the like polarized case (Brown 1978). However, for the cross polarized case, the results based on the two-scale model are incorrect (particularly for backscatter for near normal incidence). This is because the physical optics contribution to backscatter from the large scale surface is assumed to be zero.

(i) The full wave approach can be applied to problems of scattering by scatterers of irregular shape with rough surfaces even when the roughness parameter  $\rho = k_1 \langle h^2 \rangle > 1$  (Bahar and Fitzwater 1983, Bahar and Chakrabarti 1985).

### 3. FORMULATION OF THE PROBLEM

For the convenience of the reader the principal steps in the derivation of the full wave approach are summarized in this section. It is assumed that both electric and magnetic sources ( $J, \rho$  and  $M, \rho_m$ ) are present in any of the  $m+1$  layers of the structure. A suppressed  $\exp(i\omega t)$  time dependence is assumed in this work. The  $i$ th layer of the structure is characterized by the complex electromagnetic parameters  $\epsilon_i$  and  $\mu_i$  and the interface between medium  $i$  and  $i+1$  is given by the surface (See Fig. 2).

$$y = h_{i,i+1} \quad (1)$$

Maxwell's equations for the transverse components of the electric and magnetic fields,  $E_T$  and  $H_T$  respectively are (Bahar 1973c,d).

$$-\frac{\partial E_T}{\partial x} = i\omega\mu(\bar{H}_T \times \bar{a}_x) - \frac{1}{i\omega\epsilon} \nabla_T \nabla_T \cdot (\bar{E}_T \times \bar{a}_x) + \bar{E}_T \times \bar{a}_x + \frac{1}{i\omega\epsilon} \nabla_T J_x \quad (2)$$

$$-\frac{\partial H_T}{\partial x} = i\omega\epsilon(\bar{a}_x \times \bar{E}_T) - \frac{1}{i\omega\mu} \nabla_T \nabla_T \cdot (\bar{a}_x \times \bar{H}_T) + \bar{a}_x \times \bar{H}_T + \frac{1}{i\omega\mu} \nabla_T M_x \quad (3)$$

in which the operator  $\nabla_T$  is given by

$$\nabla_T = \bar{a}_y \frac{\partial}{\partial y} + \bar{a}_x \frac{\partial}{\partial x} \quad (4)$$

and the transverse vectors are

$$\vec{A}_T = \vec{a}_y A_y + \vec{a}_z A_z, \quad \vec{A} = \vec{E}, \vec{H}, \vec{J} \text{ or } \vec{H} \quad (5)$$

The following field transform pairs provide the basis for the complete expansion of the transverse electric and magnetic fields into vertically (V) and horizontally (H) polarized waves:

$$\vec{E}_T(x, y, z) = \int_{-\infty}^{\infty} \int_{-\infty}^{\infty} [\vec{E}^V(x, v, w) \vec{e}_T^V + \vec{E}^H(x, v, w) \vec{e}_T^H] dv, \quad (6)$$

where

$$\vec{E}^P(x, v, w) = \int_{-\infty}^{\infty} \vec{E}_T(x, y, z) \cdot (\vec{e}_P^T \times \vec{a}_x) dy dz, \quad P=V \text{ or } H, \quad (7)$$

where

$$\vec{E}_T(x, y, z) = \int_{-\infty}^{\infty} [\vec{E}^V(x, v, w) \vec{e}_T^V + \vec{E}^H(x, v, w) \vec{e}_T^H] dv, \quad (8)$$

$$\vec{H}^P(x, v, w) = \int_{-\infty}^{\infty} \vec{H}_T(x, y, z) \cdot (\vec{a}_x \times \vec{e}_P^T) dy dz, \quad P=V \text{ or } H, \quad (9)$$

The basis functions for the vertically polarized waves are

$$\vec{e}_T^V = Z^V (\vec{a}_y \psi^V(v, y) - \frac{\vec{a}_z i v}{u^2 + v^2} \frac{\partial \psi^V(v, y)}{\partial y}) \phi(v, z) \quad (10)$$

and

$$\vec{E}_T^V = \vec{a}_z \psi^V(v, y) \phi(v, z) \quad (11)$$

and the complementary basis functions for the vertically polarized waves are

$$\vec{e}_V^T = Z^V N^V (\vec{a}_y \psi^V(v, y) + \frac{\vec{a}_z i v}{u^2 + v^2} \frac{\partial \psi^V(v, y)}{\partial y}) \phi^C(v, z) \quad (12)$$

and

$$\vec{H}_V^T = \vec{a}_z N^V \psi^V(v, y) \phi^C(v, z). \quad (13)$$

For the horizontally polarized waves, the basis functions and the complementary basis functions are respectively,

$$\vec{e}_T^H = \vec{a}_z \psi^H(v, y) \phi(v, z), \quad (14)$$

$$\vec{E}_T^H = Y^H (-\vec{a}_y \psi^H(v, y) + \frac{\vec{a}_z i v}{u^2 + v^2} \frac{\partial \psi^H(v, y)}{\partial y}) \phi(v, z), \quad (15)$$

and

$$\vec{e}_H^T = \vec{a}_z N^H \psi^H(v, y) \phi^C(v, z), \quad (16)$$

$$\vec{H}_H^T = Y^H N^H (-\vec{a}_y \psi^H(v, y) - \frac{\vec{a}_z i v}{u^2 + v^2} \frac{\partial \psi^H(v, y)}{\partial y}) \phi^C(v, z). \quad (17)$$

in which  $N^P$  are normalization coefficients,  $Z^P$  and  $Y^P$  are the wave impedance and admittance and

$$\phi(v, z) = \exp(-ivz) \text{ and } \phi^C(v, z) = (1/2\pi) \exp(ivz) \quad (18)$$

The scalar basis functions are

$$R_{PO}^{Dh, P}(v, y) = \begin{cases} \exp(iv_y y) + R_{PO}^{Dh} \exp(-iv_y y), & \text{for medium 0,} \\ \prod_{q=1}^r \frac{T_{Pq-1}^D}{T_{Pq}^{Dh}} \exp(i \sum_{q=1}^r v_{p-1, q}^h v_{q-1, q}^h) \\ \times [\exp(iv_y y) + R_{Pr}^{Dh} \exp(-iv_y y)], & \text{for medium } r = 1, 2, 3, \dots, m, \end{cases} \quad (19)$$

$$R_{Pm}^{Uh, P}(v, y) = \begin{cases} \prod_{q=1}^{m-r} \frac{T_{Pq+1}^U}{T_{Pq}^{Uh}} \exp(i \sum_{q=1}^{m-r} v_{m-q, m+1-q}^h v_{m-q, m+1-q}^h) \\ \times [\exp(-iv_y y) + R_{Pr}^{Uh} \exp(iv_y y)], & \text{for medium } r = 0, 1, 2, \dots, m-1 \\ \exp(-iv_y y) + R_{Pm}^{Uh} \exp(iv_y y), & \text{for medium } m, \end{cases} \quad (20)$$

$$\psi_s^{Pn}(v, y) = \psi_s^{Pn}(v, h_{0,1}) = \begin{cases} \exp[-iv_0^n(y-h_{0,1})], & \text{for medium 0,} \\ \frac{1}{\tau_{P1}^{DH}} \exp(-iv_1^n h_{0,1}) [\exp(iv_1^n y) + R_{P1}^{DH} \exp(-iv_1^n y)], & \text{for medium 1,} \\ \frac{1}{\tau_{P1}^{DH}} \exp(-iv_1^n h_{0,1}) \prod_{q=2}^m \frac{\tau_{Pq}^D}{\tau_{Pq}^{DH}} \times \\ \times \exp(i \sum_{q=2}^m v_{q-1,q}^n h_{q-1,q}) [\exp(iv_m^n y) + R_{Pm}^{DH} \exp(-iv_m^n y)], & \\ \text{for medium } m=2,3,\dots,m, \end{cases} \quad (21)$$

where

$$[\psi_s^{Pn}(v, h_{0,1})]^2 = \left[ u / iZ_0^P v_0 \frac{d}{du} \frac{1}{R_{P0}^D} \right]_{v=v_n} \quad (22)$$

The scalar functions for vertically and horizontally polarized waves  $\psi^V(v, y)$  and  $\psi^H(v, y)$ , are given by (19), (20), and (21), on replacing the letter P in all the expressions by V and H respectively. The reflection coefficient at the  $i, i+1$  interface for waves incident from above is  $R_{Pi}^D$  and  $R_{Pi}^U$  is the reflection coefficient at the  $i-1, i$  interface for waves incident from below (See Fig. 1). Thus, for  $P=V$  or  $H$ ,

$$R_{Pm}^D = 0, \quad R_{Pi}^D = \frac{(R_{i+1,i}^P + R_{Pi+1}^{DH})}{(1 + R_{i+1,i}^P R_{Pi+1}^{DH})}, \quad i = 0, 1, \dots, m-1,$$

and

$$R_{P0}^U = 0, \quad R_{Pi}^U = \frac{(R_{i-1,i}^P + R_{Pi-1}^{UH})}{(1 + R_{i-1,i}^P R_{Pi-1}^{UH})}, \quad i = 1, 2, \dots, m, \quad (23)$$

where  $R_{i+1,i}^V$  and  $R_{i+1,i}^H$  are the two medium Fresnel reflection coefficients for vertically and horizontally polarized waves respectively, and

$$\begin{aligned} R_{Pi}^{DH} &= R_{Pi}^D \exp(-i2v_i h_{i,i-1}), & R_{Pi}^{Dh} &= R_{Pi}^D \exp(i2v_i h_{i,i-1}) \\ R_{Pi}^{UH} &= R_{Pi}^U \exp(-i2v_i h_{i,i-1}), & R_{Pi}^{Uh} &= R_{Pi}^U \exp(i2v_i h_{i,i-1}). \end{aligned} \quad (24)$$

The transmission coefficients are

$$\begin{aligned} T_{Pi}^D &= 1 + R_{Pi}^D, & T_{Pi}^U &= 1 + R_{Pi}^U \\ T_{Pi}^{DH} &= 1 + R_{Pi}^{DH}, & T_{Pi}^{UH} &= 1 + R_{Pi}^{UH} \end{aligned} \quad (25)$$

and  $N^P$  are normalization coefficients. The symbol  $\sum_v$  denotes summation over the entire wavenumber spectrum  $v$ . The generalized Fourier transform consists of two infinite integrals (continuous parts of the wavenumber spectrum) which are associated with the radiation and the lateral wave terms and a finite set of surface wave terms (discrete part of the wavenumber spectrum). The infinite integrals in the  $v$  plane are associated with branch cut integrals  $\text{Im}(v_0) = 0$  and  $\text{Im}(v_m) = 0$  in the complex  $v$  plane, while the surface wave terms are associated with the residues of the poles at  $1/R_{P0}^D = 0$  (or  $1/R_{Pm}^U = 0$ ). The model equation which determines the surface wave parameters  $v^n (\text{Im}(v) \leq 0)$ , is given by

$$1 - R_{Pi}^U R_{Pi}^D \exp(-i2v_i h_i) = 0, \quad v_i \in (k_1^2 - u^2 - v^2)^{1/2}, \quad v_{i-1,i} = v_{i-1} - v_i \quad (26)$$

for  $P$  equals  $V$  or  $H$  and  $i = 1, 2, 3, \dots, m-1$ .

The irregular interfaces  $y = h_{i,i+1}$  are assumed here to be continuous functions of  $x$  only. Thus, the exact boundary conditions at  $y = h_{i,i+1} = h(x)$  can be expressed exclusively in terms of the transverse field components

$$\left[ \frac{1}{i\omega\epsilon} \nabla_T \cdot (\bar{E}_T \times \bar{a}_x) \right]_{h^-}^{h^+} = -\bar{E}_y \frac{dh}{dx} \Big|_{h^-}^{h^+}, \quad \left[ \bar{E}_y \right]_{h^-}^{h^+} = 0 \quad (27)$$

$$\left[ \frac{1}{i\omega\mu} \nabla_T \cdot (\bar{a}_x \times \bar{H}_T) \right]_{h^-}^{h^+} = -\bar{H}_y \frac{dh}{dx} \Big|_{h^-}^{h^+}, \quad \left[ \bar{H}_y \right]_{h^-}^{h^+} = 0. \quad (28)$$

The complete field expansions are substituted into Maxwell's equations for the transverse field components and use is made of the orthogonality relationship, Green's theorem, and the exact boundary conditions, to obtain the differential equations for the field transforms  $\bar{E}^P$  and  $\bar{H}^P$ . These may be expressed in terms of the forward and backward wave amplitudes  $a^P$  and  $b^P$ , respectively, as follows:



$$E^P = a^P \pm b^P \text{ and } H^P = a^P \mp b^P, P = \begin{cases} V, & \text{upper sign} \\ H, & \text{lower sign} \end{cases} \quad (29)$$

Thus Maxwell's equations are converted into the following rigorous set of generalized telegraphists' equations for  $P=V$  or  $H$  (Bahar 1973c,d)

$$-\frac{da^P}{dx} - iua^P = \sum_Q \int_V \int_V (s_{PQ}^{BA} a^Q + s_{PQ}^{BB} b^Q) dw' - A^P, \quad (30)$$

and

$$-\frac{db^P}{dx} + iub^P = \sum_Q \int_V \int_V (s_{PQ}^{AA} a^Q + s_{PQ}^{AB} b^Q) dw' + B^P. \quad (31)$$

Explicit closed form expressions for the reflection and the transmission scattering coefficients have been derived (Bahar 1973d).

Excitations of vertically and horizontally polarized waves (with respect to the reference  $(x,z)$  plane) are considered. The terms  $A^P$  and  $B^P$  appearing in (30) and (31) account for the electric and magnetic sources  $J, \rho$  and  $\bar{M}, \rho$ .

A similar set of generalized telegraphists' equations can also be derived for two dimensionally rough surfaces  $h(x,z)$  (Bahar 1974). They can be solved numerically to obtain rigorous solutions that account for multiple scattering from two dimensionally rough surfaces. However if multiple scattering from the rough surfaces and the edge effects are negligible, then through a judicious choice of the coordinate system, it is sufficient to assume, at this phase of the analysis, that the normal to an element of the rough surface  $\bar{n}$  is in the  $x,y$  plane. This procedure is followed here since it simplifies the intermediate steps of the analysis considerably. The introduction later of a coordinate transformation from a fixed reference system (See Fig. 5) to a local coordinate system that conforms with the rough surface (See Fig. 6) permits the application of these results to elements of the rough surface with arbitrary orientations (Bahar 1981a).

The first-order iterative solutions for the wave amplitudes  $a^P$  and  $b^P$  are obtained by neglecting the transmission and reflection scattering coefficients in (30) and (31). These first-order solutions are substituted on the right side of (30) and (31), and the resulting equations are solved to obtain the second-order iterative solution for the wave amplitudes. These second-order iterative solutions are used in the complete expansions for the electromagnetic fields to obtain the desired iterative solutions for the scattered radiation fields through the use of the steepest descent method. Thus the first-order solutions to (30) and (31) are the unperturbed vertically and horizontally polarized fields excited by the vertical electric and magnetic dipoles respectively. The second-order iterative solutions which account for depolarization and scattering in arbitrary directions are suitable when multiple scattering can be ignored. Since the full wave expressions for the fields (6), (8) are valid for all points in space, they can also be used to determine the surface fields. The above iterative procedure can be extended to account for multiple scattering. In Section 4 the specific case of scattering and depolarization by a random rough interface between two semi-infinite media is considered.

#### 4. SCATTERING BY ROUGH SURFACES--UNIFIED AND TWO-SCALE FORMULATION

The full wave solution for the radiation fields scattered by two dimensionally rough surfaces  $f(x,z) = y - h(x,z) = 0$  (See Fig. 5) is expressed as follows in matrix notation

$$G^f = G_0 \int_{A_{iv}} D(\bar{n}^f, \bar{n}^i) \exp[i\bar{v} \cdot \bar{r}] dA G^i = G_0^i \quad (32)$$

in which  $\bar{n}^i$  and  $\bar{n}^f$  are unit vectors in the directions of the incident and scattered fields and the vector  $\bar{v}$  is

$$\bar{v} = (\bar{n}^f - \bar{n}^i)k_0 = v_x \bar{a}_x + v_y \bar{a}_y + v_z \bar{a}_z \quad (33)$$

where  $k_0 = \omega \sqrt{\mu_0 \epsilon_0}$  is the free space wavenumber of the electromagnetic wave. The integration is over  $A_{iv}$  the illuminated and visible portions of the rough surface and

$$\int dA = \int_{-L_x}^{L_x} \int_{-L_y}^{L_y} dx dy \bar{n} \cdot \bar{a}_y = A_y \cdot \int dA = \int_{A_{iv}} dA \quad (34)$$

where  $\bar{n}$  is the unit vector normal to the surface  $f(x,z) = 0$

$$\bar{n} = \nabla f / |\nabla f| = \frac{-h_x \bar{a}_x + \bar{a}_y - h_z \bar{a}_z}{(1 + h_x^2 + h_z^2)^{1/2}}, \quad n_x = \frac{-h_x}{\sqrt{1 + h_x^2 + h_z^2}}, \quad n_z = \frac{-h_z}{\sqrt{1 + h_x^2 + h_z^2}} \quad (35)$$

and  $\bar{r}$  is the position vector to a point on the rough surface. The elements of the  $2 \times 1$  column matrix  $G^i$  are the incident vertically and horizontally polarized complex wave amplitudes  $G^{vi}$  and  $G^{hi}$  at the origin with  $\bar{n}^i \times \bar{a}_y$  defined as the vector normal to the plane of incidence. Similarly  $G^f$  is a  $2 \times 1$  column matrix whose elements are the vertically and horizontally polarized complex wave amplitudes  $G^{vf}$  and  $G^{hf}$  (with  $\bar{n}^f \times \bar{a}_y$  defined as the vector normal to the scatter plane) at the point given by the position vector (See Fig. 5)

$$G^f = x^f \bar{a}_y + y^f \bar{a}_y + z^f \bar{a}_z = r^f \bar{n}^f \quad (36)$$

Thus

$$G^i = \begin{pmatrix} G^{Vi} \\ G^{Hi} \end{pmatrix} = \begin{pmatrix} E^{Vi} \\ E^{Hi} \end{pmatrix} = \eta_0 \begin{pmatrix} H^{Vi} \\ H^{Hi} \end{pmatrix} \quad (37a)$$

and

$$G^r = \begin{pmatrix} G^{Vr} \\ G^{Hr} \end{pmatrix} = \begin{pmatrix} E^{Vr} \\ E^{Hr} \end{pmatrix} = \eta_0 \begin{pmatrix} H^{Vr} \\ H^{Hr} \end{pmatrix} \quad (37b)$$

where  $\eta_0 = \sqrt{\mu_0 \epsilon_0}$  is the free space wave impedance. The coefficient  $G_0$  is given by

$$G_0 = k_0^2 \exp[-ik_0 r^2] / 2 \pi i k_0 r^2 \quad (38)$$

and a suppressed  $\exp(i\omega t)$  time dependence is assumed in this work. The like and cross polarized local scattering matrix  $D(\bar{n}^i, \bar{n}^i)$

$$D(\bar{n}^i, \bar{n}^i) = \begin{pmatrix} D^{VV} & D^{VH} \\ D^{HV} & D^{HH} \end{pmatrix} = (-\bar{n}^i \cdot \bar{n}) T^i T^i \quad (39)$$

is derived as follows: (a) The 2x2 matrix  $T^i(\bar{n}^i, \bar{n}^i)$  is used to transform the incident vertically and horizontally polarized wave from its representation in the fixed reference coordinate system  $(\bar{a}_x, \bar{a}_y, \bar{a}_z)$  to its representation with respect to the local coordinate system  $(\bar{n}_1, \bar{n}_2 = \bar{n}, \bar{n}_3)$  (the unit vector  $\bar{n}^i$  is the representation of the vector  $\bar{n}^i$  in the local coordinate system (See Fig. 6)). (b) The 2x2 local scattering matrix  $(-\bar{n}^i \cdot \bar{n}) \cdot P(\bar{n}^i, \bar{n}^i) dA$  is used to account for like and cross polarized scattering by an element  $dA$  of the rough surface ( $\bar{n}^i$  is the representation of the vector  $\bar{n}^i$  in the local coordinate system). The elements of the scattering matrix  $P(\bar{n}^i, \bar{n}^i)$  are obtained from the second-order iterative solution of the generalized telegraphists' equations (30) and (31). Finally, (c) The 2x2 matrix  $T^i(\bar{n}^i, \bar{n}^i)$  is used to transform the scattered vertically and horizontally polarized wave from its representation in the local coordinate system to its representation in the reference coordinate system. The full wave solutions (32) are invariant to coordinate transformations and they satisfy the duality and reciprocity relationships in electromagnetic theory. In (32) it should be recalled that multiple scattering by the rough surface is neglected. Explicit expressions for the local scattering matrix  $D(\bar{n}^i, \bar{n}^i)$  (39) are found in the published literature (Bahar 1981a).

The full wave solution for the scattered field can be applied to random rough surfaces (Bahar 1981b). Thus the scattering cross sections per unit projected area  $A_y$  for an incident wave with polarization  $Q=V$  or  $H$  and scattered wave with polarization  $P=V$  or  $H$  are given by

$$\langle \sigma^{PQ} \rangle = \frac{k_0^2}{\pi} \frac{D^{PQ}(\bar{n})}{\bar{n} \cdot \bar{n}_y} \frac{D^{PQ}(\bar{n}')}{\bar{n}' \cdot \bar{n}_y} P_2(\bar{n}^i, \bar{n}^i | \bar{n}, \bar{n}') \exp(i\bar{v} \cdot (\bar{r} - \bar{r}')) \frac{dx dx' dz dz'}{A_y} \quad (40)$$

in which the symbol  $\langle \rangle$  denotes the statistical average over the heights  $h, h'$  and the slopes  $\bar{n}, \bar{n}'$ . The evaluation of the scattering cross section is considerably simplified if the probability density functions for the random slopes  $\bar{n}, \bar{n}'$  and random heights  $h, h'$  are assumed to be independent, i.e.,  $p(\bar{n}, \bar{n}', h, h') = p(\bar{n}, \bar{n}') p(h, h')$ . In addition, if it is assumed that the slopes are more strongly correlated than the heights;  $p(\bar{n}, \bar{n}') = p(\bar{n}) \delta(\bar{n}' - \bar{n})$ . In this work, it is also assumed for simplicity that the rough surface is assumed to be isotropic (independent of direction) and its characteristics are independent of position ( $\bar{r}$ ). Thus the rough surface height characteristic function

$$\chi(v_y, h) = \langle \exp(iv_y h) \rangle = \int \exp(iv_y h) p(h) dh \quad (41)$$

is independent of position while the rough surface height joint characteristic function

$$\chi_2(v_y, h-v_y, h') = \langle \exp[iv_y(h-h')] \rangle = \int \exp[iv_y(h-h')] p(h, h') dh dh' \quad (42)$$

is only a function of distance  $\tau$  measured in the  $(x, z)$  reference plane

$$\bar{r}_d = (x-x')\bar{a}_x + (z-z')\bar{a}_z, \quad |\bar{r}_d| = \tau = [(x-x')^2 + (z-z')^2]^{1/2} \quad (43)$$

In (40)  $P_2(\bar{n}^i, \bar{n}^i | \bar{n})$  is the probability that points  $\bar{r}$  and  $\bar{r}'$  on the rough surface are both illuminated ( $\bar{n}^i$ ) and visible ( $\bar{n}^i$ ) given the value of the slopes ( $\bar{n}$  and  $\bar{n}'$ ) at these points (Bahar and Barrick 1983). It is related to the probability  $P_2(\bar{n}^i, \bar{n}^i | \bar{n})$  derived by Sancer (1968).

Since the full wave solution (40) accounts for both specular point (physical optics) scattering as well as diffuse scattering in a self-consistent manner there is no need to adopt an artificial two-scale model. However, when the two-scale model is adopted in order to compare the full wave solutions with earlier results, it is assumed that the surface  $h_1(x, z)$  consisting of the large scale components of the surface height spectral density function  $W(v_x, v_z)$  is statistically independent of the surface  $h_2(x, z)$  consisting of the small scale components of the surface height spectral density function. This assumption in addition to the assumptions that the height and slope probability densities are statistically independent and that multiple scattering is negligible are made for all the earlier rough surface scattering solutions based on the two-scale models (Wright 1968, Valenzuela 1968, Barrick and Peake 1968, Brown 1978). The surface height spectral density function is the two dimensional Fourier transform of the rough surface height autocorrelation function  $\langle hh' \rangle$ . Thus

$$\begin{aligned} \frac{W(v_x, v_z)}{4} &= \frac{1}{4\pi^2} \int_{-\infty}^{\infty} \langle hh' \rangle \exp(i\vec{v} \cdot \vec{r}_d) d\vec{r}_d \\ &= \frac{1}{2\pi} \int_0^{\infty} \langle hh' \rangle J_0(kr) r dr \end{aligned} \quad (44a)$$

where  $J_0$  is the Bessel function of order zero and the spatial wavenumber  $k$  is

$$k = v_{xz} = \sqrt{v_x^2 + v_z^2} \quad (44b)$$

in which use has been made of the fact that  $\langle hh' \rangle$  is only a function of  $r$ . Similarly,

$$\begin{aligned} \langle hh' \rangle &= \int_{-\infty}^{\infty} \frac{W(v_x, v_z)}{4} \exp(-i\vec{v} \cdot \vec{r}_d) d\vec{v}_x d\vec{v}_z \\ &= 2\pi \int_0^{\infty} \frac{W(k)}{4} J_0(kr) k dk = R(\tau) \langle h^2 \rangle \end{aligned} \quad (45)$$

in which  $|R(\tau)| \leq 1$  is the normalized correlation coefficient and  $\langle h^2 \rangle$  is the mean square height

$$\langle h^2 \rangle = \langle hh' \rangle_{\tau=0} = 2\pi \int_0^{\infty} \frac{W(k)}{4} k dk \quad (46)$$

Thus using the two-scale model, it is assumed that the large scale surface  $h_L$  is associated with the surface height spectral density function  $W(k)U(k_d - k)$  and the small scale surface  $h_s$  is associated with the surface height spectral density function  $W(k)U(k - k_d)$  in which  $U(\cdot)$  is the unit step function and  $k_d$  is some arbitrary value of  $k$  where spectral splitting is assumed to occur (Brown 1978). Brown chooses  $k_d$  such that the parameter

$$\beta = 4k_d^2 \langle h_s^2 \rangle = 0.1 \quad (47)$$

satisfies the perturbation condition for the small scale surface. However, he shows that the computed value of the scattering cross sections critically depends on the choice of  $\beta$  and therefore the specified value of  $k_d$ . Bahar and Barrick (1983) considered the two-scale model using the full wave approach. It is shown that if  $k_d$  is chosen such that deep phase modulation occurs it is necessary to choose  $\beta > 0.1$ . For a range of values of  $k_d$  corresponding to  $\beta$  between 0.5 and 2 it is shown (Bahar et al. 1983) that the values of the scattering cross sections do not significantly depend on  $k_d$ .

For problems of scattering by random rough surfaces the dimensions of the projected area  $A_y = 4L_x L_z$  are such that  $L_x \gg \tau_c$  and  $L_z \gg \tau_c$  (where  $R(\tau_c) = \exp(-1)$  and  $\tau_c$  is the correlation length). For distances  $\tau \gg \tau_c$ ,  $X_2 \sim |X|^2$  since  $\langle hh' \rangle \sim \langle h^2 \rangle$ . Thus assuming statistical independence between the surface  $h_L$  and  $h_s$  ( $p(h_L, h_s) = p(h_L)p(h_s)$ ) the characteristic and the joint characteristic functions of the total surface are expressed as

$$X = X^L X^s; \quad X^s \equiv X^s(\vec{v} \cdot \vec{n}), \quad X^L \equiv X^L(v_y), \quad X_2^s \equiv X_2^s(\vec{v} \cdot \vec{n}), \quad X_2^L \equiv X_2^L(v_y) \quad (48a)$$

$$X_2 = X_2^L X_2^s = (X_2^L - |X^L|^2) |X^s|^2 + (X_2^s - |X^s|^2) X_2^L + |X^L X^s|^2 \quad (48b)$$

in which the superscripts  $L$  and  $s$  denote quantities associated with the large and small scale surfaces, respectively. Using the two-scale model, it is also assumed that the slopes for the small scale (perturbation) surface are small such that slope probability density function for the total surface is equal to the slope probability function for the large scale surface  $p(\vec{n}) = p(\vec{n}_L)(\vec{n}_s = \nabla f_s / |\nabla f|)$  and  $f_s = y - h_s$ . Thus the unified (U) and two-scale (T) expressions for the scattering cross sections (40) are respectively,

$$\langle \sigma^{PQ} \rangle_U = \int A^{PQ}(\vec{n}^f, \vec{n}^i, \vec{n}) p(\vec{n}) d\vec{n} [Q(\vec{n}^f, \vec{n}^i) + \frac{1}{A_y} |v_y X^L \exp(i v_x x + i v_z z) dx dz|^2] \quad (49a)$$

where

$$Q(\vec{n}^f, \vec{n}^i) = v_y^2 \int (X_2^L - |X^L|^2) \exp(i\vec{v} \cdot \vec{r}_d) d\vec{r}_d d\vec{r}_d \quad (49b)$$

$$A^{PQ}(\vec{n}^f, \vec{n}^i, \vec{n}) = \frac{1}{\pi} \left| \frac{k_D P^{PQ}}{v_y \vec{n} \cdot \vec{a}_y} \right|^2 P_2 \quad (49c)$$

$$p(\vec{n}) d\vec{n} = p(h_x, h_z) dh_x dh_z \quad (49d)$$

and

$$\begin{aligned} \langle \sigma^{PQ} \rangle_T &= |X^s|^2 A^{PQ}(\vec{n}^f, \vec{n}^i, \vec{n}_s) [Q_L(\vec{n}^f, \vec{n}^i) + \frac{1}{A_y} |v_y X^L \exp(i v_x x + i v_z z) dx dz|^2] \\ &\quad + \int A^{PQ}(\vec{n}^f, \vec{n}^i, \vec{n}) \vec{n} \cdot \vec{a}_y Q_s(\vec{n}^f, \vec{n}^i, \vec{n}, p(\vec{n})) d\vec{n} \\ &\equiv |X^s|^2 \langle \sigma^{PQ} \rangle_L + \langle \sigma^{PQ} \rangle_s \end{aligned} \quad (50a)$$

where

$$Q_2(\vec{n}^f, \vec{n}^i) = \frac{1}{v_y} \int (\chi_2^f - |\chi^f|^2) \exp(i\vec{v} \cdot \vec{r}_d) dx_d dz_d \quad (50b)$$

$$Q_3(\vec{n}^f, \vec{n}^i, \vec{n}) = \frac{1}{v_y} \int (\chi_2^f - |\chi^f|^2) \exp(i\vec{v} \cdot \vec{r}_{ld}) dx_{ld} dz_{ld} \quad (50c)$$

In (49b), (50b) and (50c) the integration limits are  $(-\infty, \infty)$  since  $L_x, L_z \gg \tau_c$  and  $A^{PQ}(\vec{n}^f, \vec{n}^i, \vec{n})$  is defined in (49c).

To derive the first term in (50a), the slope dependent function  $A^{PQ}(\vec{n}^f, \vec{n}^i, \vec{n})$  is replaced by its value at the specular point where

$$\vec{n} + \vec{n}_s = \vec{v}/v, \quad v = |\vec{v}| = \vec{v} \cdot \vec{n}_s \quad (51)$$

For surface height probability density functions that are Gaussian

$$|\chi^f|^2 = \exp(-v_y^2 \langle h^2 \rangle) \quad (52)$$

$$\chi_2^f = \exp(-v_y^2 \langle h^2 \rangle + v_y^2 \langle h_x h_x \rangle) = \exp(v_y^2 \langle h_x h_x \rangle) |\chi^f|^2 \quad (53)$$

Thus for  $v_y^2 \langle h^2 \rangle \gg 1$  it can be shown that the two dimensional Fourier transform (50b) is given

$$Q_2(\vec{n}^f, \vec{n}^i) = 4\pi^2 p(\vec{n}_s) \quad (54)$$

in which  $p(\vec{n}_s)$  is the slope probability density function at the stationary phase points (Bahar 1981a)

$$p(\vec{n}_s) = p(h_x, h_z) = \frac{1}{2\pi\sigma_n^2} \exp\left[-\frac{v_{xz}^2}{2\sigma_n^2 v_y^2}\right] = \frac{1}{2\pi\sigma_n^2} \exp\left[-\frac{(h_x^2 + h_z^2)}{2\sigma_n^2}\right] \quad (55)$$

in which the value of the slope at the specular point is

$$(h_x^2 + h_z^2)_{\vec{n}_s} = \tan^2 \gamma_s = v_{xz}^2 / v_y^2, \quad \vec{n}_s \cdot \vec{a}_y = \cos \gamma_s \quad (56a)$$

and the mean square slope  $\sigma_n^2$  is half the total mean square slope  $\sigma_{nt}^2$

$$\sigma_n^2 = \frac{\pi}{h} \int_0^\infty W(k) k^3 dk = \sigma_{nt}^2 / 2 \quad (56b)$$

Thus the first term in (50a) is given by

$$|\chi^f|^2 \langle \sigma^{PQ} \rangle_s = |\chi^f|^2 A^{PQ}(\vec{n}^f, \vec{n}^i, \vec{n}_s) [4\pi^2 p(\vec{n}_s) + A_y |v_y \chi^f|^2 \text{sinc}^2(v_x L_x) \text{sinc}^2(v_z L_z)] \quad (57)$$

in which  $\text{sinc} = \sin(\alpha)/\alpha$  and  $A_y = 4L_x L_z$  is the projected area of the rough surface on the  $x, z$  plane. In (57)  $\langle \sigma^{PQ} \rangle_s$  is precisely the physical optics solution for scattering by the large scale (filtered surface). Thus the coefficient  $|\chi^f|^2 < 1$  accounts for the degradation of the physical optics (specular point) contribution due to the small scale surface.

To derive the second term in (50), it is assumed that over a correlation length of the small scale surface, the large scale surface is approximately flat and that the small scale (perturbed) surface height is measured normal to the large scale surface. Thus,

$$\vec{v} \cdot (\vec{r} - \vec{r}') = \vec{v} \cdot (\vec{r}_d - \vec{r}'_d) + \vec{v} \cdot (h - h') \vec{n}_s = \vec{v} \cdot \vec{r}_{ld} + \vec{v} \cdot \vec{n} (h - h') \quad (58)$$

in which the distance  $\vec{r}_{ld}$  is measured along the large scale surface in the local coordinate system ( $\vec{e}_1, \vec{e}_2 = \vec{e}, \vec{e}_3$ )

$$\vec{r}_{ld} = x_{ld} \vec{e}_1 + z_{ld} \vec{e}_3, \quad |\vec{r}_{ld}| = r_{ld} = (x_{ld}^2 + z_{ld}^2)^{1/2} \quad (59)$$

Thus in the expression for  $\langle \sigma^{PQ} \rangle_s$ , the integration is with respect to distances measured along the large scale surface and not the reference surface. This is in agreement with the expressions obtained intuitively by Wright and Valenzuela "mostly based on physical considerations" (Wright 1968, Valenzuela 1968). Thus  $\langle \sigma^{PQ} \rangle_s$  can be regarded as an average of the scattered power from patches of slightly rough surfaces that ride the large scale surface. Brown's (1978) solutions which are based on a combination of Burrows' perturbation theory (Burrows 1967) and physical optics (Beckmann 1963) are in agreement with the full wave expressions for  $\langle \sigma^{PQ} \rangle_s$  only in the limit of very small slopes since in his work  $\vec{n}_s$  is measured normal to the reference plane. However, in Burrows' perturbation theory (upon which Brown's solution is based) the small scale surface height  $h_s$  is measured normal to the large scale surface  $h_l$ .

The two dimensional Fourier transform (49b) can be expressed as

$$Q(\vec{n}^f, \vec{n}^i) = 2\pi v_y^2 \int_0^\infty (\chi_2(v_y) - |\chi(v_y)|^2) J_0(r_{xz} r) r dr \quad (60)$$

since the surface height correlation function  $\langle hh' \rangle$  is only a function of  $\tau = r_d = |\vec{r}_d|$ . The corresponding expression for the Fourier transform (50c) is dependent on the slope. Thus

$$Q_s(\vec{n}^f, \vec{n}^i, \vec{n}) = 2\pi v_y^2 \int_0^\infty (\chi_s^2(\vec{v} \cdot \vec{n}) - |\chi_s^2(\vec{v} \cdot \vec{n})|^2) J_0(v_{xz} \tau) \tau d\tau \quad (61)$$

in which

$$\vec{v} \cdot \vec{n} = \vec{v} \cdot (x_{ld} \vec{n}_1 + z_{ld} \vec{n}_3) = v_{xl} x_{ld} + v_{zl} z_{ld} \quad (62a)$$

$$\vec{v} \cdot \vec{n} \equiv v_{yl}, \quad v_{xz} = [v_{xl}^2 + v_{zl}^2]^{1/2} \quad (62b)$$

and  $v_{xl}$ ,  $v_{zl}$  and  $v_{yl}$  are the components of  $\vec{v}$  in the local coordinate system  $(\vec{n}_1, \vec{n}_2, \vec{n}_3)$ . Thus the scattering cross sections can be expressed as follows for the unified and two-scale models

$$\langle \sigma^{PQ} \rangle_U = \int A^{PQ}(\vec{n}^f, \vec{n}^i, \vec{n}) p(\vec{n}) d\vec{n} [Q_s(\vec{n}^f, \vec{n}^i) + A_y |v_y \chi|^2 \text{sinc}^2(v_{xx} L_x) \text{sinc}^2(v_{zz} L_z)] \quad (63)$$

and

$$\begin{aligned} \langle \sigma^{PQ} \rangle_T = & |\chi_s|^2 A^{PQ}(\vec{n}^f, \vec{n}^i, \vec{n}_s) [Q_s(\vec{n}^f, \vec{n}^i) + A_y |v_y \chi|^2 \text{sinc}^2(v_{xx} L_x) \text{sinc}^2(v_{zz} L_z)] \\ & + \int A^{PQ}(\vec{n}^f, \vec{n}^i, \vec{n}) \vec{n} \cdot \vec{a}_y Q_s(\vec{n}^f, \vec{n}^i, \vec{n}) p(\vec{n}) d\vec{n} \end{aligned} \quad (64)$$

To facilitate the computations in (64) in which  $Q_s$  is a function of  $\vec{n}$ , for a given  $\vec{v}$  and  $R(\tau)$ , a set of values of  $Q_s/v_y^2$  are first computed and stored as a function of

$$\vec{v} \cdot \vec{n} = (-v_x h_x + v_y - v_z h_z) / (1 + h_x^2 + h_z^2)^{1/2} \quad (65)$$

The integration with respect to  $d\vec{n} = dh_x dh_z$  is performed using values of  $Q_s$  interpolated from the stored set. For Gaussian surface height probability density functions (52) and (53)

$$\begin{aligned} Q_s(\vec{n}^f, \vec{n}^i, \vec{n}) = & 2\pi v_y^2 \int \exp(-v_y^2 \langle h_s^2 \rangle) [\exp(v_y^2 \langle h_s^2 \rangle R(\tau)) - 1] J_0(v_{xz} \tau) \tau d\tau \\ = & v_y^2 r(\vec{n}^f, \vec{n}^i, \vec{v} \cdot \vec{n}) \xrightarrow{\beta \ll 1} v_y^2 v_y^2 |\chi_s^2(\vec{v} \cdot \vec{n})|^2 W(v_{xz}) \end{aligned} \quad (66)$$

Thus for  $\vec{n} \rightarrow \vec{a}_y$  and  $\beta \ll 1$  the last term in (64)  $\langle \sigma^{PQ} \rangle_J$  reduces to the perturbation solution (Bahar 1981c)

$$\langle \sigma^{PQ} \rangle_J \rightarrow \langle \sigma^{PQ} \rangle_P = \pi k_0^2 v_y^2 |\chi_s^2(v_y) (-\vec{n}^i \cdot \vec{n}) F(\vec{n}^f, \vec{n}^i)|^2 W(v_{xz}) \quad (67)$$

Note that (64) reduces to (63) if we set  $\langle h_s^2 \rangle \rightarrow 0$  and (63) reduces to (64) if we set  $\langle h_s^2 \rangle \rightarrow \infty$  and replace  $A^{PQ}(\vec{n}^f, \vec{n}^i, \vec{n})$  by  $A^{PQ}(\vec{n}^f, \vec{n}^i, \vec{n}_s)$ . The term containing the product of the sinc functions is coherent scattered field. This term vanishes as  $|\chi(v_y)|^2 \rightarrow 0$ .

For cases in which the physical optics solutions are valid the corresponding geometrical optics expressions for  $\langle \sigma^{PQ} \rangle_J$  are obtained by replacing  $\vec{n}$  by  $\vec{n}_s$  in (32) and integrating over the area  $A_{1v}$  (using the stationary phase method) before the expectations  $\langle \dots \rangle$  are evaluated. Thus in the neighborhood of a stationary phase point  $\vec{r} = \vec{r}_{op}$ , where  $v_x + v_y h_x$  and  $v_z + v_y h_z = 0$  (Barrick 1970, Bahar 1981b) it can be shown that

$$\begin{aligned} \int \exp(i\vec{v} \cdot \vec{r}) \frac{dx dz}{h \cdot \vec{a}_y} &= \int \exp(i\vec{v} \cdot \vec{r}_{op}) \exp\left(-\frac{i\vec{v} \cdot \vec{n}_s}{2} (h_{xx} x_p^2 + h_{zz} z_p^2)\right) dx_p dz_p \\ &\rightarrow \frac{\exp(i\vec{v} \cdot \vec{r}_{op})}{\vec{v} \cdot \vec{n}_s} \frac{(2\pi i)}{\sqrt{h_{xx} h_{zz}}} \quad \vec{v} \cdot \vec{n}_s = 2k_0 (-\vec{n}^i \cdot \vec{n}_s) \end{aligned} \quad (68)$$

in which the integral has been expressed in terms of the local coordinate  $(x_p, z_p)$  of the stationary phase point  $(x_{op}, z_{op})$  associated with the unit vectors  $(\vec{n}_1, \vec{n}_2 = \vec{n}, \vec{n}_3)$  and  $\vec{n}_1$  and  $\vec{n}_2$  the vectors in the tangent plane, are chosen such that the principal radii of curvature  $r_{xx} = |1/h_{xx}|$  and  $r_{zz} = |1/h_{zz}|$  are measured along the  $\vec{n}_1$  and  $\vec{n}_2$  directions. As seen by an observer in the region  $v > h$  ( $\vec{n}, \vec{s}$ ), the curvatures  $h_{xx}$  and  $h_{zz}$  are positive when the surface is concave. They are negative when the surface is convex. When  $h_{xx}$  or  $h_{zz}$  are negative, they are expressed as  $\sqrt{h_{xx}} = i/\sqrt{r_{xx}}$  and  $\sqrt{h_{zz}} = i/\sqrt{r_{zz}}$ . Thus the geometric optics contribution to the normalized cross section from  $N$  randomly located specular points per unit surface area is

$$(\sigma^{PQ})_{op} = \pi r_{xp} r_{zp} \left| \left( \vec{r}^f \cdot \vec{r}^i \right) \frac{PQ}{\vec{n}_s} \right|^2 P_s(\vec{n}^f, \vec{n}^i, \vec{n}_s) \quad (69)$$

in which

$$P(\vec{n}^f, \vec{n}^i)_{\vec{n}_s} = \begin{bmatrix} R_v(\theta_{op}^i) & 0 \\ 0 & R_h(\theta_{op}^i) \end{bmatrix} \quad (70)$$

and  $R_V(\theta_{op}^i)$  and  $R_H(\theta_{op}^i)$  are the Fresnel reflection coefficients at the specular points where the local angles of incidence and scatter are  $-\hat{n}^i \cdot \hat{n} = \hat{n}^f \cdot \hat{n} = \cos \theta_{op}^i$ . Note however, that the surface will depolarize the incident wave if the triple products  $(\hat{n} \cdot \hat{n}^i \cdot \hat{a}_y)$  and  $(\hat{n} \cdot \hat{n}^f \cdot \hat{a}_y)$  do not vanish. (When  $(\hat{n} \cdot \hat{n}^i \cdot \hat{a}_y)$  and  $(\hat{n} \cdot \hat{n}^f \cdot \hat{a}_y)$  vanish  $T^i$  and  $T^f$  become identity matrices).

The expectation of  $(r_{xp} r_{zp})$  in (64) (Barrick 1972, Barrick and Bahar 1981) is

$$\langle r_{xp} r_{zp} \rangle = p(\hat{n}_s) / (\hat{n}_s \cdot \hat{a}_y) \quad , \quad \hat{n}_s \cdot \hat{a}_y = v_y / (\hat{v} \cdot \hat{n}_s) \quad (71)$$

thus

$$\langle \sigma^{PQ} \rangle_\infty = \frac{\pi}{(\hat{n}_s \cdot \hat{a}_y)^4} p(\hat{n}_s) |T^f T^i|_{PQ}^2 P_2(\hat{n}^f, \hat{n}^i | \hat{n}_s) \quad (72)$$

in agreement with  $\langle \sigma^{PQ} \rangle_\infty$ . Thus for backscatter geometric optics theory predicts no depolarization and for the like polarized case

$$\langle \sigma^{PP}(\hat{n}^f = -\hat{n}^i) \rangle_\infty = \frac{\pi}{(\hat{n}_s \cdot \hat{a}_y)^4} p(\hat{n}_s) P_2(-\hat{n}^i, -\hat{n}^i | \hat{n}_s) |R_P(\theta_o = 0)|^2 \quad (73)$$

## 5. EFFECTS OF VEGETATION ON THE SCATTERING CROSS SECTIONS

The full wave approach has been applied to problems of scattering by arbitrarily shaped rough conducting flakes that scatter both specularly and diffusely (Bahar and Fitzwater 1983, Bahar and Chakrabarti 1985). Thus, rather than model the vegetation by a dielectric layer with an "effective surface impedance" the large leaves can be modeled more realistically as random distributions of arbitrarily oriented scattering facets that are characterized by their complex permittivity and their surface height spectral density functions.

For terrain that is covered by vegetation, the cross sections are evaluated in five steps.

**Step One:** The scattering cross sections  $\langle \sigma^{PQ}(\hat{n}^f, \hat{n}^i) \rangle_1$  for individual scatterers (such as leaves and stems) are determined. These scatterers cannot be adequately characterized as objects of idealized shape such as disks or cylinders. They are characterized by their complex permittivity and their surface height autocorrelation functions and the probability density functions of the surface height and slopes. The full wave approach is used here to account for both specular and diffuse scattering from the individual scatterers (Bahar and Fitzwater, 1983).

**Step Two:** Appropriate transformations are employed to obtain the corresponding cross sections  $\langle \sigma^{PQ}(\hat{n}^f, \hat{n}^i | \hat{n}_o) \rangle_1$  for the individual scatterers with arbitrary orientation  $\hat{n}_o$  in a fixed reference coordinate system (Bahar and Fitzwater, 1983).

**Step Three:** Using the statistical data on the orientational distribution,  $p(\hat{n}_o)$ , of the individual scatterers, the average scattering cross sections for an ensemble of randomly oriented scatterers  $\langle \sigma^{PQ}(\hat{n}^f, \hat{n}^i) \rangle_e$  are derived. (Information on orientational distribution of leaves for instance is collected in studies related to photosynthesis.)

**Step Four:** To account for shadowing by the individual scatterers, the results obtained in step three are modified by a factor referred to as the "sunlit leaf area." It is defined as the (radar) illuminated area of individual scatterer per unit area of ground. The "sunlit leaf area" is also used in studies of photosynthesis.

**Step Five:** If the vegetation covers a flat surface and the vegetation canopy can be regarded as horizontal, steps one through four will suffice for the evaluation of the scattering cross sections. However, for rough terrain, the undulating nature of the canopy must be taken into account especially for targets near grazing incidence. To this end, it is necessary to determine the "fractional illuminated area of the canopy." It is defined as the (radar) illuminated area of the canopy per unit area of the ground. This quantity can be determined from the slope probability density function of the terrain  $p(\hat{n}_t)$ .

When the attenuation of the incident wave by the vegetation layer is not large and the intensity of the wave incident upon the ground is not negligible, scattering by the vegetation as well as by the rough terrain must be taken into account. Thus, it is necessary to evaluate the extinction cross sections of the scatterers in order to determine the reduced intensities impacting upon the earth's surface. Since the random terrain and vegetation characteristics are uncorrelated scattering by the rough terrain and the foliage can be treated separately.

## 6. CONCLUDING REMARKS

The solutions for the backscatter like and cross polarized cross sections based on the unified full wave solutions has been compared with geometric optics, physical optics and perturbation solutions and the solutions based on the two-scale model. For the two-scale model the wavenumber  $k_1$  where spectral splitting is assumed to occur is chosen such that  $\delta = 4k_1^2 \langle h^2 \rangle = 1$ , (Bahar et al. 1983). It is also assumed that the two surfaces  $h_1$  and  $h_2$  are statistically independent, and the slope of the small scale surface was neglected ( $\hat{u} \approx \hat{n}_t$ ). Except for near grazing angles the two solutions for the like polarized cross sections are in good agreement. For the cross polarized case, the difference between the two solutions is most significant near normal incidence. The large discrepancy near normal incidence is due to the fact that elements of the rough surface that are oriented specularly do not depolarize the backscattered wave. The depolarization comes from the neighborhood of these specular points and even the filtered large scale surface depolarizes the incident waves (Bahar and Fitzwater 1984). However, the physical optics contribution to cross polarization is zero.

The discrepancy between the full wave and physical optics solutions near grazing angles is due to the fact that for  $\theta^i \rightarrow \pi/2$ , there are practically no specular points on the surface and again the physical optics approximations are invalid.

The analytical procedures that account for the effects of vegetation on radio wave propagation over a terrestrial path are given in Section 5. It is based on the full wave solutions to scattering by finitely conducting irregularly shaped objects with rough surfaces.

#### 7. ACKNOWLEDGMENTS

This investigation was sponsored by the U. S. Army Research Office Contract DAAG-29-82-K-0123. The author wishes to thank M. A. Fitzwater and E. Everett for their assistance in the preparation of this manuscript.

#### 8. REFERENCES

1. Bahar, E., (1973a), "Electromagnetic Wave Propagation in Inhomogeneous Multilayered Structures of Arbitrary Thickness-Generalized Field Transforms," *J. Math. Phys.*, Vol. 14, No. 8, pp. 1024-1029.
2. Bahar, E., (1973b), "Electromagnetic Wave Propagation in Inhomogeneous Multilayered Structures of Arbitrary Thickness-Full Wave Solutions," *J. Math. Phys.*, Vol. 14, No. 8, pp. 1030-1036.
3. Bahar, E., (1973c), "Depolarization of Electromagnetic Waves Excited by Distributions of Electric and Magnetic Sources in Inhomogeneous Multilayered Structures of Arbitrarily Varying Thickness-Generalized Field Transforms," *J. Math. Phys.*, Vol. 14, No. 11, pp. 1502-1509.
4. Bahar, E., (1973d), "Depolarization of Electromagnetic Waves Excited by Distributions of Electrical Magnetic Sources in Inhomogeneous Multilayered Structures of Arbitrarily Varying Thickness-Full Wave Solutions," *J. Math. Phys.*, Vol. 14, No. 11, pp. 1510-1515.
5. Bahar, E., (1974), "Depolarization in Nonuniform Multilayered Structures--Full Wave Solutions," *J. Math. Phys.*, Vol. 15, No. 2, pp. 202-208.
6. Bahar, E., (1981a), "Full-Wave Solutions for the Depolarization of the Scattered Radiation Fields by Rough Surfaces of Arbitrary Slope," *IEEE Transactions on Antennas and Propagation*, Vol. AP-29, No. 3.
7. Bahar, E. (1981b), "Scattering Cross Sections from Rough Surfaces--Full Wave Analysis," *Radio Science*, Vol. 16, No. 3, pp. 331-341.
8. Bahar, E., (1981c), "Scattering Cross Sections for Composite Random Surfaces--Full Wave Analysis," *Radio Science*, Vol. 16, No. 6, pp. 1327-1335.
9. Bahar, E., (1982), "Scattering and Depolarization by Rough Surfaces Near Grazing Angles--Full Wave Solutions," *IEEE Transactions on Antennas and Propagation*, Vol. AP-30, No. 4, pp. 712-719.
10. Bahar, E. and D. E. Barrick, (1983), "Scattering Cross Sections for Composite Rough Surfaces that Cannot be Treated as Perturbed Physical Optics Problems," *Radio Science*, Vol. 18, No. 2, pp. 129-137.
11. Bahar, E., D. E. Barrick and M. A. Fitzwater, (1983), "Computations of Scattering Cross Sections for Composite Surfaces and the Specification of the Wavenumber Where Spectral Splitting Occurs," *IEEE Transactions on Antennas and Propagation*, Vol. AP-31, No. 5, pp. 698-709.
12. Bahar, E. and S. Chakrabarti, (1985), "Scattering and Depolarization by Large Conducting Spheres with Rough Surfaces," *Applied Optics*, Vol. 24, No. 12, pp. 1820-1825.
13. Bahar, E. and M. A. Fitzwater, (1984), "Scattering Cross Sections for Composite Rough Surfaces Using the Unified Full Wave Approach," *IEEE Transactions on Antennas and Propagation*, Vol. AP-32, No. 7, pp. 730-734.
14. Bahar, E. and M. A. Fitzwater, (1985), "Like and Cross Polarized Scattering Cross Sections for Random Rough Surfaces--Theory and Experiment," *Journal of the Optical Society of America*, Special Issue on "Wave Propagation and Scattering in Random Media," Vol. 2, pp. 2295-2303.
15. Bahar, E. and M. A. Fitzwater, (1986), "Multiple Scattering by Irregular Shaped Particles of Finite Conductivity at Infrared and Optical Frequencies," *Radio Science*, in press.
16. Bahar, E. and M. A. Fitzwater, (1986), "Scattering and Depolarization of Linearly Polarized Waves by Finitely Conducting Particles of Irregular Shape," *Journal of Applied Physics*, in press.
17. Barrick, D. E., (1970), "Rough Surfaces," in *Radar Cross Section Handbook*, Chapter 9, Plenum Press, New York.
18. Barrick, D. E., (1972), "Remote Sensing of Sea State by Radar," in *Remote Sensing of the Troposphere*, V. E. Derr, Ed., Washington, D.C.: U. S. Government Printing Office, pp. 12.1-12.24.
19. Barrick, D. E. and E. Bahar, (1981), "Rough Surface Scattering Using Specular Theory," *IEEE Transactions on Antennas and Propagation*, Vol. AP-29, No. 5, pp. 798-800.
20. Barrick, D. E. and W. H. Peake, (1968), "A Review of Scattering from Surfaces with Different Roughness Scales," *Radio Science*, Vol. 3, No. 8, pp. 865-868.
21. Beckmann, P., (1968), *The Depolarization of Electromagnetic Waves*, Golem Press, Boulder, Colorado.
22. Beckmann, P. and A. Spizzichino, (1963), *The Scattering of Electromagnetic Waves from Rough Surfaces*, MacMillan, New York.
23. Brown, G. S., (1978), "Backscattering from a Gaussian-Distributed Perfectly Conducting Rough Surface," *IEEE Transactions on Antennas and Propagation*, Vol. AP-26, No. 3, pp. 472-482.
24. Burrows, M. L., (1967), "On the Composite Model for Rough Surface Scattering," *IEEE Transactions on Antennas and Propagation*, Vol. AP-21, No. 2, pp. 241-243.
25. Hagfors, T., (1966), "Relationship of Geometric Optics and Autocorrelation Approach to the Analysis of Lunar and Planetary Radar," *Journal of Geophysical Research*, Vol. 71, pp. 279-383.
26. Morse, P. M. and H. Feshbach, (1953), *Methods of Theoretical Physics*, McGraw-Hill Book Company, Inc., New York.
27. Rice, S. O. (1951), "Reflection of Electromagnetic Waves from a Slightly Rough Surface," *Communication of Pure and Applied Math.*, Vol. 4, pp. 351-378.
28. Sancer, M. I. (1968), "Shadow-Corrected Electromagnetic Scattering from a Randomly Rough Surface," *IEEE Transactions on Antennas and Propagation*, Vol. AP-17, No. 5, pp. 577-585.
29. Schlak, G. A. and J. R. Wait, (1967), "Electromagnetic Wave Propagation Over a Nonparallel Stratified Conducting Medium," *Can. J. Phys.*, Vol. 45, pp. 3697-3720.
30. Schlak, G. A. and J. R. Wait, (1968), "Attenuation Function for Propagation Over a Nonparallel Ground," *Can. J. Phys.*, Vol. 46, pp. 1135-1136.

31. Tyler, G. L., (1976), "Wavelength Dependence in Radio-Wave Scattering and Specular Point Theory," *Radio Science*, Vol. 11, No. 2, pp. 83-91.
32. Valenzuela, G. R., (1968), "Scattering of Electromagnetic Waves from a Tilted Slightly Rough Surface," *Radio Science*, Vol. 3, No. 11, pp. 1051-1066.
33. Wait, J. R., (1962), *Electromagnetic Waves in Stratified Media*, MacMillan, New York.
34. Wright, J. W., (1968), "A New Model for Sea Clutter," *IEEE Transactions on Antennas and Propagation*, Vol. AP-16, No. 2, pp. 217-223.

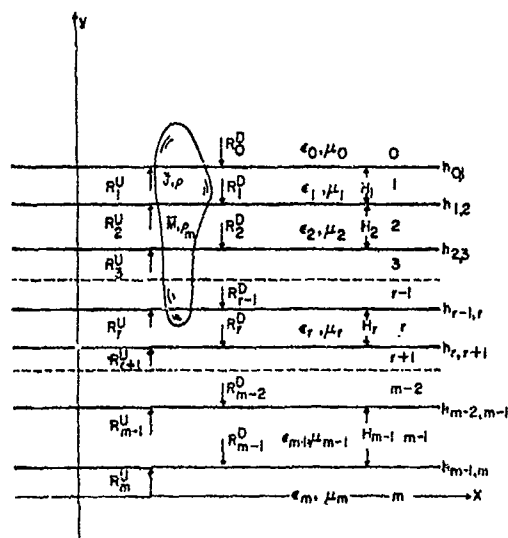


Fig. 1. Electric and magnetic sources distributed in the layers of a uniform multilayered structure.

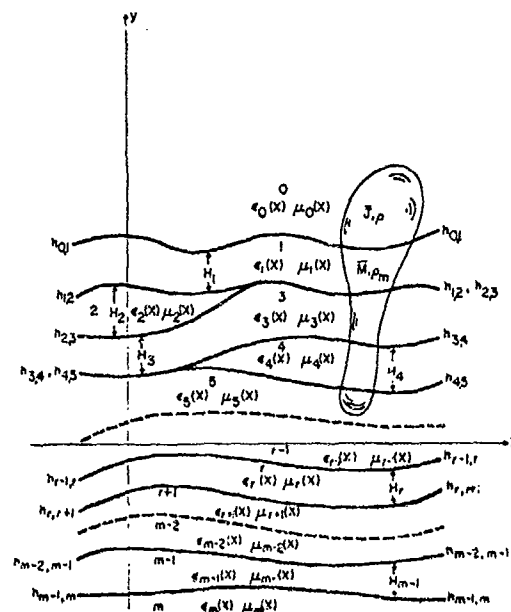


Fig. 2. Electric and magnetic sources distributed in the layers of a nonuniform multilayered structure.

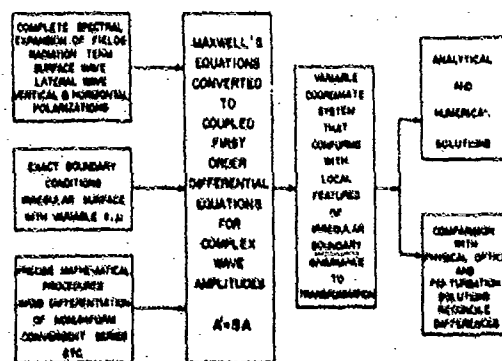


Fig. 3. Principal elements of the full wave approach.



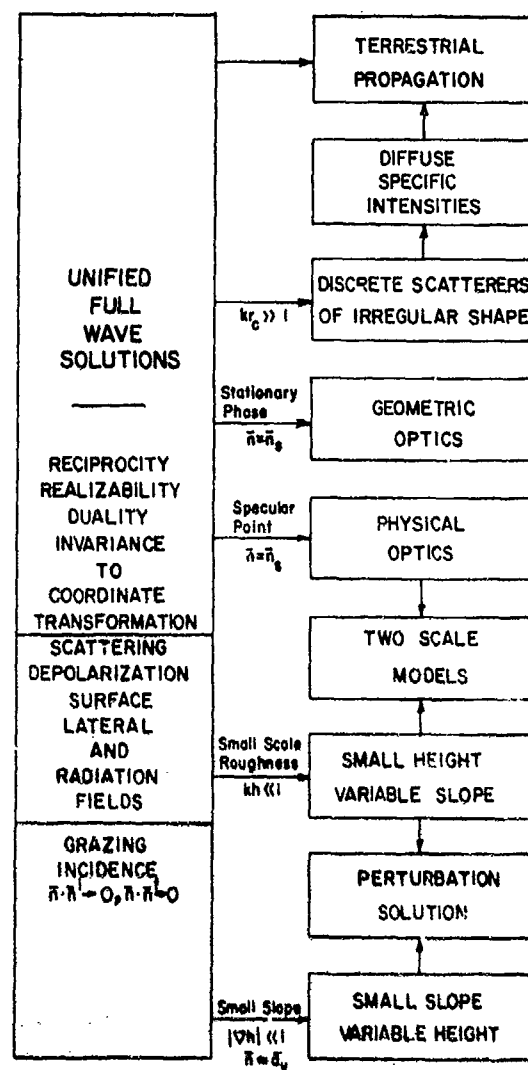


Fig. 4. Principal properties of full wave approach.

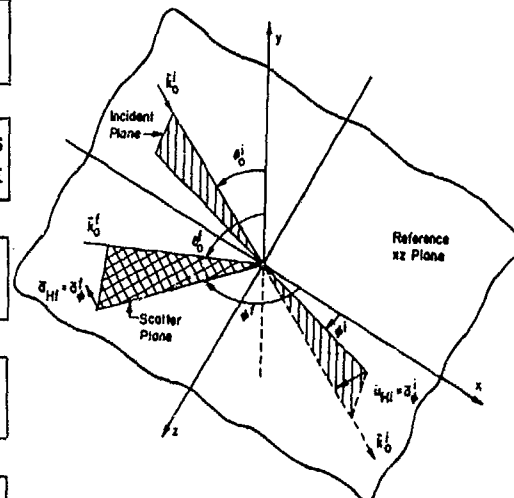


Fig. 5. Planes of incidence and scatter with respect to the reference coordinate system. Mean (reference plane for rough surface is  $y = 0$ ).

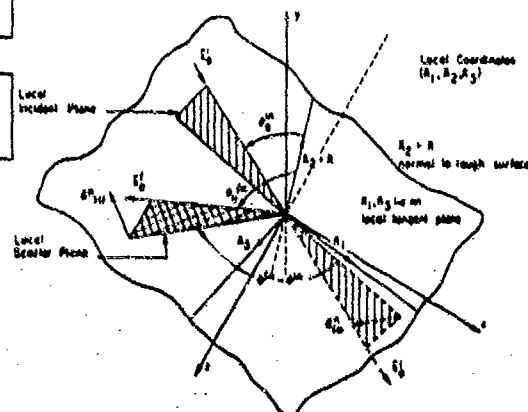


Fig. 6. Local planes of incidence and scatter and local coordinate system  $(\vec{n}_1, \vec{n}_2, \vec{n}_3)$ .

## DISCUSSION

**T.R. Carlson**

Over what frequency range would a hybrid solution normally be applied? Where (frequency range) does any optical approach become significant? (neglecting  $X =$  polarization boundary condition).

**Author's Reply**

In using the full-wave approach, we do not need the hybrid approach; we did it artificially, just to compare with earlier two-scale models. Early two-scale models had a lot of problems with it because you had to select the spatial spectral point at which you were going to split. There was a lot of discussion and disagreement of how you decompose it. What is nice about the full-wave, you do not have to decompose.



AD-P005 735

## Propagation in Longitudinally Varying Ducts, With Emphasis on Guiding to Antiguiding Transitions

Leopold B. Felsen

Department of Electrical Engineering and Computer Science/Weber Research Institute  
Polytechnic University, Route 110, Farmingdale, NY 11735 USA

Naturally occurring ducting environments (for example, tropospheric elevated or surface ducts) may exhibit continuous longitudinal changes that progressively decrease the guiding capability and eventually destroy it altogether. This circumstance has evident implications for systems employing such ducts as communication or surveillance channels. Recent developments in the theory of propagation in longitudinally varying ducts are reviewed, with emphasis on gradual guiding to antiguiding transitions that convert an initially well-trapped mode field smoothly (adiabatically) into a leaky mode. The connection between the trapped and leaky mode regimes is provided by a parabolic equation or, in certain cases, by an "intrinsic mode" spectral integral. Numerical implementation for different examples confirms the phenomenology predicted by the analysis and reveals the beaming of initially trapped modal energy into the exterior after the duct disappears. Some consideration is also given to incorporating these concepts into a synthesis of the field excited by a radiating source inside the duct.

## I. Introduction

Electromagnetic wave propagation in the terrestrial environment is affected by the physical parameters that characterize the propagation channel. Of special interest for communication are environmental conditions that cause trapping of the electromagnetic energy, thereby making it possible for a distant observer to receive signals that would have been weakened beyond recognition, or even blocked by shadowing, along a direct propagation path. We shall be concerned here generically with refractive index profiles that may describe an atmospheric duct, an ionospheric duct, the earth-ionosphere waveguide, or any other trapping environment. The discussion will be focused on basic phenomena, on recent advances in the mathematical modeling of these phenomena, on numerical implementation, and on physical interpretation.

Ducting implies the existence of refractive index variations transverse to the propagation path from source to receiver such that signals along directions deviating from that path are returned back to the preferred direction by continuous refraction or by reflection. This generates a multiplicity of refracted and/or reflected rays, which can be advantageously reorganized collectively into the guided modes of the duct. These modes will be trapped, with minimal propagation loss, if the rays which generate them are confined to the duct, and they will be leaky, with consequent attenuation, if the rays which generate them escape partially or totally from the duct. The quantitative description of these phenomena, and especially the interpretation by ray fields, mode fields, and ray-mode combinations, requires solution of the electromagnetic field equations subject to complicated constitutive and boundary conditions, which are generally intractable. Therefore, analytical modeling has principally been confined to coordinate separable configurations, wherein duct boundaries and/or refractive index variations are constrained to follow constant-coordinate contours, as exemplified by radial stratification in the presence of a spherical earth, or by planar stratification in the equivalent earth flattened model. In these geometries, the duct profile may be relatively arbitrary in the cross section transverse to the duct axis but it retains this profile at all axial locations. With these assumptions, exact formal field solutions can be constructed, which then form the basis for various physically incisive approximations as well as numerical implementation. From a thorough study of these "canonical" problems, much knowledge and insight has been gained concerning a diversity of fundamental wave phenomena, and the possibility of modifying these so as to account for more general "non-canonical" conditions.

A principal constraint in these coordinate separable models is their inability to account for smooth longitudinal variations in the refractive index profile, particularly important among which are those that eventually lead to the disappearance of the duct. Examples are a gradual narrowing of an essentially homogeneous duct whose transverse boundaries are formed by an abrupt change in refractive index, or a duct with a smooth transverse profile that changes with propagation range gradually from guiding to antiguiding. In both cases, initially trapped electromagnetic fields become less strongly trapped as they proceed along the duct axis, and eventually undergo a radiative transition into directions that deviate markedly from the one desired, if the duct had remained intact.

When longitudinal changes of the type described above occur only over a limited range, mode coupling schemes may be employed (both analytically and numerically [1]) to chart the transitional behavior. However, such schemes become analytically and numerically intractable when the changes are gradual and extended over long distances. It is then possible to appeal to "adiabatic" concepts that seek to adapt a particular wavefield defined in the longitudinally homogeneous channel smoothly to the changing conditions without causing it to couple strongly with other wavefields. The foundation of these concepts is a smoothly changing wave spectrum that synthesizes the observable field. General aspects of this modern perspective of spectral theory have been discussed in several comprehensive reviews [2-4], to which the interested reader is referred. Here, we deal with the above two examples, which illustrate the general features.

## II. Formulation

The field  $G$  excited by a line source located at  $(y', z')$  in a two-dimensional  $(y, z)$  ducting environment satisfies the wave equation

$$\left[ \frac{\partial^2}{\partial y^2} + \frac{\partial^2}{\partial z^2} + k_0^2 n^2(y, z) \right] G(y, z, y', z') = -\delta(y-y')\delta(z-z') \quad (1)$$

with  $n(y, z)$  representing the transversely and longitudinally varying refractive index. We assume the medium to be unbounded so that a radiation condition must be satisfied at  $(y, z) \rightarrow \infty$ . The index function  $n(y, z)$  is assumed to be smooth, but if it has abrupt changes across a surface  $S$ , one may easily incorporate the required continuity conditions for the field on either side of  $S$ . The scalar field  $G$  is the  $x$ -component of the electric field; for the other polarization,  $n(y, z)$  would be replaced by an equivalent refractive index  $\tilde{n}(y, z)$ .

We shall deal specifically with index profiles of the type shown in Fig. 1. Assuming sufficiently high frequencies, the propagation properties of the field emanating from a source in the ducting environment can be schematized in terms of rays. The amplitude and phase of the local plane wave fields transported along each ray can be calculated by geometrical ray theory. The ray paths can be divided into those which are trapped inside the duct, and those which leave the duct (Fig. 2a). The fields carried along the former can be summed collectively into trapped modes [2] (see Fig. 2b for a typical modal ray pattern consisting of upgoing and downgoing congruences), while the fields corresponding to the latter synthesize leaky modes. Because of the slowly varying conditions along the duct axis  $z$ , the mode profile (see Fig. 2b) adapts continuously to fill the changing transverse cross section without appreciable coupling to other modes. Our special concern is with index variations that cause the initially trapped modal field to become leaky because of a cutoff transition in a narrowing duct profile, or those that lead to disappearance of a duct because of guiding to antiguiding index transitions. In both cases, the local mode model fails and must be augmented by a uniform transition field that charts continuously the conversion from the trapped to the radiative state. The ray model also fails in these transitional domains, making a uniformized treatment unavoidable here as well.

The ray picture in Fig. 2a suggests, in fact, a scenario that can be expected to be most effective for treating this class of transitional ducting problems. The initially trapped ray events should be treated collectively by converting them into trapped local modes. This can be accomplished by filling the angular spectrum spanned by these rays, and also the transitional rays, with modal fields. The spectral machinery for accomplishing this has been discussed elsewhere [2]. The leaky ray fields are to be kept intact. This hybrid ray-mode approach thus accommodates both the trapping as well as the leaky regime in the region not too far away from the source. As the observer moves along the duct axis, the changing conditions are taken into account by the uniform tracking of the local mode fields  $u_m(y, z)$ ,  $m$  being the mode index, including the region that causes the mode to become radiative. Our emphasis here is on this latter aspect, which forms an essential ingredient in a comprehensive treatment of this complicated class of propagation problems. The examples presented have been introduced in other disciplines but the techniques of analysis and the conclusions are applicable as well to the problems considered here.

### III. Examples

#### A. Narrowing duct

The narrowing duct depicted in Fig. 1a is analogous to what is encountered in a tapered dielectric or optical waveguide, and it has also served as a model for underwater acoustic propagation in a shallow ocean with sloping bottom. Here, we shall consider a wedge-shaped duct whose refractive index is constant and changes abruptly to lower values across the (straight) duct boundaries (see Fig. 1a, with rectangular index profile). In the wider portion, a mode is assumed to be trapped and to propagate toward the narrower portion. In this adiabatic regime, the trapped mode can be expressed locally as though it exists in a plane parallel duct with the same local cross section. This model fails if the mode passes through cutoff and becomes leaky. The previously trapped mode energy is then redistributed, part of it being transmitted along the duct but most of it being leaked into the exterior. The entire wave process can be described by synthesis of plane waves which are multiply reflected inside the duct and then superposed self-consistently to satisfy the source-free wave equation and boundary conditions. The resulting spectral object has been termed an *intrinsic mode* because it has mode-like properties in this nonseparable guiding channel. Details for constructing the intrinsic modes may be found in the literature [5,6]. For a wedge-shaped duct bounded by different refractive index media on its two sides as in Fig. 3, their analytic form is given by [7]:

$$u_m(y, z) = \int_C f(\theta, y) \exp(iQ(\theta, z)) d\theta \quad (2)$$

where

$$f(\theta, y) = \begin{cases} \cos\left[\frac{1}{2}\phi_2(\theta + \alpha)\right] \exp(-k_1 y [\cos^2(\theta + \alpha) - \cos^2\theta_{c2}]^{1/2}), & \text{Region 2} \\ \cos\left[\frac{1}{2}\phi_3(\theta) + k_1 r \sin\theta \sin\phi\right], & \text{Region 1} \\ \cos\left[\frac{1}{2}\phi_3(\theta)\right] \exp(-k_1 y [\cos^2\theta - \cos^2\theta_{c3}]^{1/2}), & \text{Region 3} \end{cases} \quad \begin{matrix} (3a) \\ (3b) \\ (3c) \end{matrix}$$

and

$$Q(\theta, z) = \begin{cases} S(\theta) + \frac{1}{2}\phi_3(\theta) - k_1 z \cos(\theta + \alpha), & \text{Region 2} \\ S(\theta) - \frac{1}{2}\phi_2(\theta + \alpha) - k_1 r \cos\theta \cos\phi, & \text{Region 1} \\ S(\theta) - \frac{1}{2}\phi_2(\theta + \alpha) + k_1 z \cos\theta, & \text{Region 3} \end{cases} \quad \begin{matrix} (4a) \\ (4b) \\ (4c) \end{matrix}$$

with

$$S(\theta) = \frac{1}{2\alpha} \int_{\theta_{c2}}^{\theta} \phi_2(\theta' + \alpha) d\theta' + \frac{1}{2\alpha} \int_{\theta}^{\theta_{c3}} \phi_3(\theta') d\theta' - (m-1) \frac{\pi\theta}{\alpha} \quad (5)$$

Here  $h(z) = r \sin \alpha$  is the local taper thickness,  $\alpha$  is the taper angle,  $k_{1,2,3}$  are the wavenumbers in media 1, 2, 3, respectively, and

$$\phi_{2,3}(\theta) = -2 \tan^{-1} \{ [\cos^2 \theta - \cos^2 \theta_{c,2,3}]^{1/2} / \sin \theta \} \quad (\text{TE case}) \quad (6)$$

are the phases of the plane wave reflection coefficients at the upper and lower interfaces, respectively, with  $\theta_{c,2,3}$  denoting the critical angles. The intrinsic mode spectral integral in (2), in which the integration variable is the plane wave spectral angle  $\theta$ , is taken over an infinite path which, for numerical purposes, can be approximated by the real axis interval  $0 < \theta < \pi$ . Numerical integration of (2) has been implemented and furnishes mode shapes as in Fig. 4 which hold uniformly from the well trapped into the leaky regime through the cutoff transition. It can be shown [5] that well before cutoff, the spectral integral in (2), for small taper angle  $\alpha$ , can be evaluated asymptotically by the saddle point method ( $1/\alpha$  being the large parameter), yielding a result which agrees with the local (adiabatic) trapped mode. However, the explicit adiabatic mode form fails with the approach to cutoff. One observes that the transition occurs smoothly, with the mode energy being transferred from the duct into the upper and lower exterior along two "beams". When media 2 and 3 have different refractive indices, the trapped mode and leaky beam shapes exhibit asymmetries with respect to the duct axis.

The analysis leading to (2) can be generalized to accommodate refractive index profiles within the duct, and to non-planar duct boundaries. Details concerning these extensions may be found in references [8,9].

### B. Disappearing duct

Referring to Fig. 1b, we assume a V-type refractive index profile

$$n(y,z) = n(0,z) \exp[-|y|b(z)] \quad (7)$$

wherein the slowly varying profile function  $b(z)$  describes the smooth transition from a duct, with  $b(z) > 0$ , to an antiduct, with  $b(z) < 0$ . The duct disappears at  $z = z_c$  defined by  $b(z_c) = 0$ . In the well-guided region  $z < z_c$ , the field  $\psi_m(y,z)$  can be expressed as a local adiabatic mode. For the profile in (7), the transverse local mode pattern  $\psi_m(y,z)$ , with  $z$  representing the local dependence, is given by Airy functions (similar to the case of the linear V-type profile), and the variable propagation coefficient of the local

mode is incorporated in the phase integral  $\exp[ik \int_{z_c}^z n(0,\zeta) d\zeta]$ , which multiplies  $\psi_m(y,z)$ . Again, this simple description fails in the duct-antiduct transition near  $z = z_c$ , and the adiabatic mode field must be replaced by a transitional field. The uniform transition can be effected by deriving for  $\psi_m(y,z)$  a parabolic equation [10], which can be approximated for  $z < z_c$  to a form that yields as a solution the adiabatic mode shape for  $\psi_m(y,z)$ . However, the full parabolic equation must be employed for  $z = z_c$ . No explicit solution of this equation has as yet been found but numerical integration can be effected by the split-step algorithm [10]. This procedure has been used effectively to chart acoustic signal propagation in the longitudinally and transversely varying ocean environment, and the results presented below have, in fact, been derived in that context [11].

The analytical details yielding the results in Fig. 5 may be found in reference [11]. Summarized briefly, the local Airy-type mode serves as input to the parabolic equation algorithm in the region  $z < z_c$ , where the duct is well established. The algorithm then "marches" the solution through cutoff at  $z = z_c$  into the antiguiding region  $z > z_c$ . For  $z \gg z_c$ , the parabolic equation can again be simplified to yield an explicit Airy-type solution that expresses a leaky local mode with complex propagation coefficient. The plots in Fig. 5 reveal clearly how the previously trapped modal energy gets "beamed" away from the duct axis in the antiguiding region.

### Summary

Longitudinal changes along a ducting environment for electromagnetic propagation have serious implications when these changes are such as to cause the signal to escape from the duct. In this presentation, two models have been examined that incorporate such effects: a narrowing duct with relatively sharply defined boundaries, and a transversely smooth duct whose refractive index profile changes gradually from guiding to antiguiding. These models, which can be generalized away from the specific prototypes chosen for numerical evaluation, accommodate a representative class of physical environments that may be encountered in this regard. Emphasis has been placed here on the guided mode behavior: source fields can be synthesized by a hybrid approach that includes rays and modes. Solution strategies for these phenomena are already being pursued in other disciplines, notably underwater acoustics, and they deserve consideration as well for electromagnetic propagation. It is hoped that the examples presented here will provide an impetus for moving in that direction.

### References

1. J.R. Wait, "Coupled Mode Analysis for a Non-Uniform Tropospheric Waveguide", *Radio Sci.* **15**(1980), pp. 667-673.
2. L.B. Felsen, "Progressing and Oscillatory Waves for Hybrid Synthesis of Source Excited Propagation and Diffraction", Invited Paper, *IEEE Trans. on Antennas and Prop.*, **AP-32**(1984), pp. 775-796.
3. L.B. Felsen, "Novel Ways for Tracking Rays", Invited Paper, *J. Opt. Soc. Am. A*, **2**(1985), pp. 956-963.
4. L.B. Felsen, "Real Spectra, Complex Spectra, Compact Spectra", *J. Opt. Soc. Am. A*, Vol. 3, No. 4 (1986), pp. 486-496.
5. J.M. Arnold and L.B. Felsen, "Intrinsic Modes in a Nonseparable Ocean Waveguide", *J. Acoust. Soc. Am.* **76**(1984), pp. 850-860.
6. E. Topuz and L.B. Felsen, "Intrinsic Modes: Numerical Implementation in a Wedged-Shaped Ocean", *J. Acoust. Soc. Am.* **78**(5), (1985), pp. 1735-1745.

7. F. Xiang, M. Cada and L.B. Felsen, "Numerical Study of Tapered Optical Waveguides Using the Intrinsic Mode Approach", Proceedings of the IEEE Montech '86 Conference on Antennas and Communications, Montreal, Canada, September 29-October 1, 1986.
8. J.M. Arnold and L.B. Felsen, "Local Intrinsic Modes: Layer with Nonplanar Interface", Wave Motion 8 (1986), pp. 1-14.
9. I.T. Lu and L.B. Felsen, "Adiabatic Transforms for Spectral Analysis and Synthesis of Weakly Range Dependent Shallow Ocean Green's Functions", submitted to J. Acoust. Soc. Am.
10. F.D. Tappert, "The Parabolic Approximation Method", in Wave Propagation and Underwater Acoustics (J.B. Keller and J.S. Papadakis, editors), Springer Verlag, New York, 1977.
11. T. Ishihara and L.B. Felsen, "High Frequency Acoustic Propagation in a Range Dependent Guiding to Antiguiding Ocean Channel Transition", Proceedings of the International Conference on Acoustics, Speech and Signal Processing, Tokyo, Japan, April 7-11, 1986.

#### Acknowledgement

The results reported here were obtained under sponsorship by the U.S. Army Research Office, Contract No. DAAG-29-85-K-0180 and the Joint Services Electronics Program, Contract No. F-49620-85-C-0078. The author expresses his appreciation to Dr. M. Cada for providing him with prepublication numerical data for the intrinsic modes.

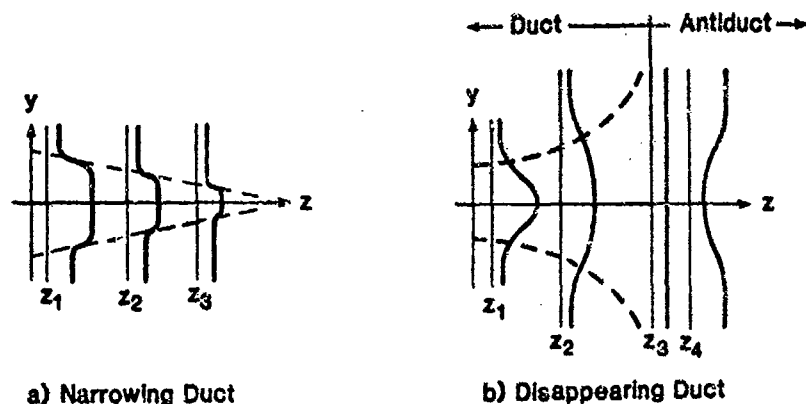
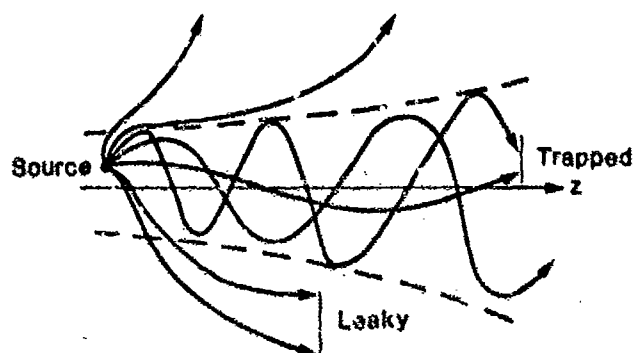
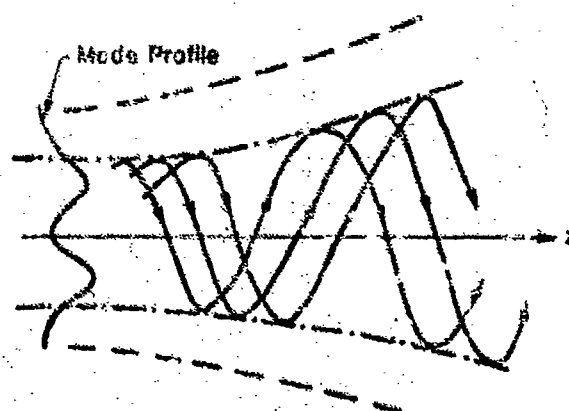


Fig. 1 - Refractive index profiles at various locations  $z_1$  along the axis of a narrowing and disappearing duct. Duct boundaries are shown dashed.



a) Ray Paths



b) Ray Paths and Profile for Trapped Local Mode

Fig. 2 - Ray schematization of source excited and source-free (modal) fields. Transient rays are sketched.

- - - duct boundaries defined by refractive index of Fig. 1.
- boundaries of duct for typical mode (modal caustics).

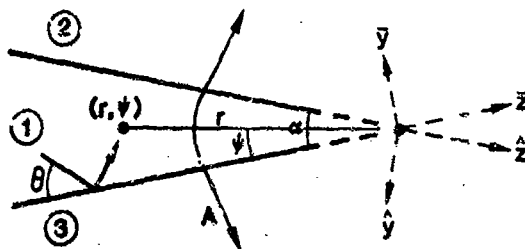


Fig. 3 - Wedge tapered duct geometry. Interior coordinates are cylindrical  $(r, \psi)$ ; external coordinates are rectangular  $(y, z)$  and  $(\bar{y}, \bar{z})$ .  $\theta$  is the plane wave propagation angle for spectral synthesis. "A" is a typical cross section.

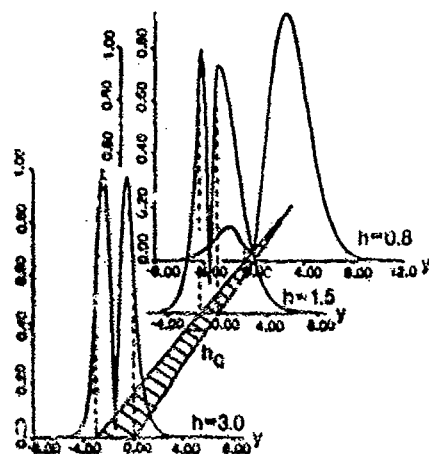


Fig. 4 - Field magnitude profiles for TE mode  $u_0$ ,  $m=2$ , plotted along cross sections "A" as in Fig. 1, in arbitrary units. Parameters:  $a = 1.55$ ,  $n_1 = 1.54$ ,  $n_2 = 1.47$ ,  $n_3 = 1.5$  (asymmetrical media). The dashed lines identify the total duct width  $h$ ;  $h_c = 1.60$  is the width corresponding to the local mode cutoff.

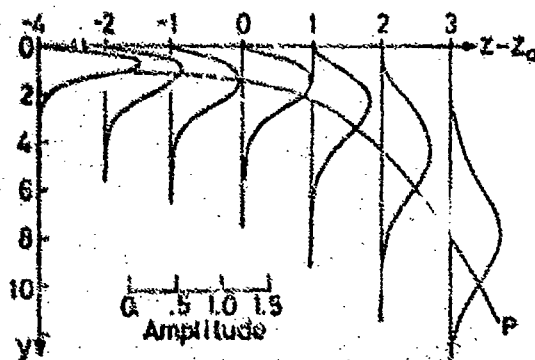


Fig. 5 - Field magnitude profiles (arbitrary units) for TE mode field  $u_0$ ,  $m=2$ , in V-type exponential duct with  $h(z) = (z-z_0) \ln(2)$ , computed from parabolic equation algorithm. The profile peak follows the trajectory labeled P. Only the  $y > 0$  portion is shown; the total profile is symmetrical about the  $y$ -axis.



## DISCUSSION

**K.C.Yeh**

We have heard two papers this morning, one by you and one by Bahar which seem to deal with some realistic problems. My question is this: do these two methods solve the same class of problems? If they do, could there be a comparison made in terms of ease of computation and the physical understanding of the results?

**Author's Reply**

This is a very good question. As I mentioned, the main burden on the analytical modeller is to extract observables. One can extract observables from both a physical or a numerical experiment. In fact, some of the impetus to this whole wedge-type propagation was done by a strictly numerical experiment. The people of underwater acoustics put the problem on a computer with a parabolic equation algorithm and the algorithm ground out a certain set of contour plots that looked extremely intriguing. Before that came out, one did not know how to do it, because one did not know whether the phenomenology in the transition region required strong coupling between the different modes. And since one did not know that, people just stopped doing anything about it. But because the numerical experiments showed that it is not coupling between modes that is important but it is rather of a given mode to its non-focussed spectrum, basically from the discrete to the continuous spectrum, the transition from being trapped to being not trapped. That could be done on a one-to-one basis. And that has pushed now the analysis tremendously in terms of pursuing these observables. A good experiment will do the same job. Now, talking to Bahar, I would ask him: to what extent has his theory been parameterized in terms of extractable observables? If it has, it could be extremely valuable. But then, these must be identified and one must show that these are indeed stable ones with respect to perturbation, because in a global theory, in principle, everything is in there. In a real environment, things keep changing from one type to another and one has to have extreme flexibility and to do this all under a global umbrella is numerically impossible, and analytically formally ok but you do not get answers out of it.

**E.Bahar**

I had been motivated into this full-wave solution by a very simple problem that one of Wait's students had done together with us. The problem was, again propagating in a wedge-region, a three layer medium with a wedge, and there they had used ray-optics techniques to obtain the expression for the surface impedance, which they needed in order to solve that propagation problem. They realized that reciprocity did not hold. So this really had projected me into getting this so-called exact approach of the complete expression where you do not neglect anything. We found that the reason that they were not getting reciprocity was some excitation between the radiation fields and the waveguide modes that were accounted for in one direction. So we saw that this approach did give us reciprocity completely and did account for the problems they had.

**Author's Reply**

Reciprocity obviously has to be satisfied in any true and real problem. But if it comes to implementation I am willing to sacrifice reciprocity as long as I get a good approximate expression for the field. I would not insist on reciprocity as a matter of principle. If you want to test a numerical algorithm, it is another matter. If you want to test the accuracy of a numerical algorithm that is supposed to be good you have to build all that in, but when you want to construct actual fields then one has to be locally adaptive. I would ask you again: the question of reciprocity was an important one but now, have you formulated it in such a way that it can be patched in locally where it is really critically needed in order to explain phenomena. If that can be done, this would be extremely useful. That is, it is basically the matter of localization, because in the extremely complicated environments that we deal with we have to deal locally with the phenomena that are important in the local region.

**E.Bahar**

If you have noticed I have mentioned before that if you take the first-order iteration one gets so-called localized intrinsic modes exactly, the same as the intrinsic modes that you use. And as long as then one can ignore the coupling, the coupling between those modes and the reflections of those modes, you can do anything you want but you have the expression to examine, you do not a priori ignore reflections. So you can, without ignoring a priori examine exactly where coupling is important and where it is not important.

**Author's Reply**

You are going to have to do it in such a way that it gives essentially a recipe that when I get into such and such a regime I do that localization and when I get into such and such a regime, I do that and patch it together.



AD-P005 736

VHF/UHF PROPAGATION BY DIFFRACTION  
- CALCULATION BY NUMERICAL INTEGRATION

by  
J.H. Whitteker

Communications Research Centre, Department of Communications  
3701 Carling Avenue, Box 11490, Station H  
Ottawa, CANADA K2H 8S2

SUMMARY

Since precise mathematical solutions of the diffraction problem exist only for simple shapes (knife edge, cylinder, sphere), most methods of estimating path loss idealize the terrain as a small number of such shapes, and then apply the solutions to those shapes. The method proposed here, instead of using solutions already worked out, applies approximate diffraction theory to a terrain model that retains most of the complexity of the real terrain, and finds a numerical solution to the diffraction problem for each particular transmission path profile. The method is to find the radiowave field as a function of height above each terrain point by integrating over the field above the preceding terrain point, using Huygen's principle. The integration is done not only for direct rays, but also for earth-reflected rays. Such a detailed calculation is demanding of computer time, but an attempt is being made to keep the computer time short enough so that the calculation can reasonably be done on line.

1. INTRODUCTION

At VHF and UHF, propagation by diffraction over terrain obstructions can be important at ranges greater than line-of-sight, but less than about 100 km. Estimating the diffraction attenuation over complex terrain is a difficult problem, since diffraction theory provides us with solutions only for certain shapes such as knife edges and rounded obstructions with uniform curvature. The best methods now in use for estimating diffraction attenuation idealize the terrain profile along the transmission path as a small number of simple obstructions, and then apply these solutions.

Such methods often work well, but there is room for improvement in two respects: (1) Choosing an appropriate representation of the terrain profile is not always straightforward. In particular, a hill with a complex shape may be represented as either a single rounded hill or two or more smaller hills close together. The calculated path loss will usually depend on this choice. (2) Although theory provides accurate solutions for individual simple obstructions, it does not provide accurate solutions for several such obstructions on the same path, unless all these obstructions are knife edges. There are methods for combining the attenuations due to individual obstructions, but they are accurate only in the limit of high, well-separated obstructions. For a series of obstructions that are either not high or not well separated, empirical correction factors must be introduced.

The method proposed here represents an attempt to avoid the necessity of oversimplifying the terrain, with the associated difficult choices. It applies theory in a relatively raw form to the terrain, rather than using results already worked out for particular shapes. In this way it is a kind of numerical simulation.

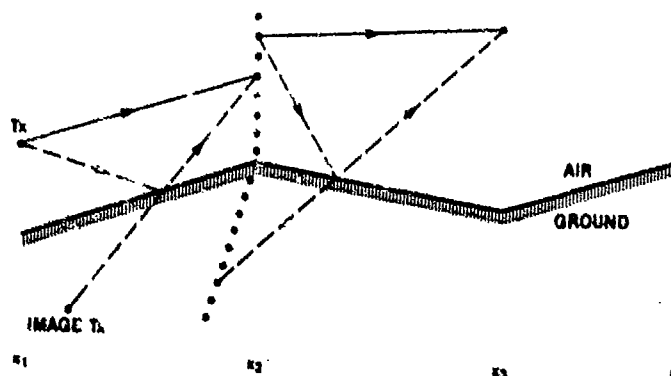


Figure 1. A terrain profile, rays, and field points. Direct rays are indicated with solid lines and reflected rays with broken lines. Source points are assumed to appear as plane-mirror images below the ground surface.

## 2. THEORY

The terrain profile of the transmission path is modelled as a series of connected line segments, usually just lines joining the points that specify the path profile. See Figure 1. The terrain is assumed to be uniform in a direction perpendicular to the plane of the diagram. Suppose that there is a transmitter (a point source) at the origin of coordinates. We wish to find the radiowave field at any point above the ground, using Fresnel diffraction theory.

The field at distance  $x_2$  is easily found. It is composed of two parts: the direct wave from the transmitter with only the free-space transmission loss, and a wave reflected from the (plane) surface of the ground between the transmitter and the field point. The two waves interfere to produce interference fringes. To avoid these fringes extending to a great height, the ground surface is assumed to be rough on a small scale, so that the reflected wave becomes attenuated for reflection angles that are not close to grazing.

Finding the wave field at  $x_3$  is more difficult, since the wave source is distributed vertically at  $x_2$  rather than being concentrated at a point. Use is made of Huygen's principle, which, as applied here, states that the field at distance  $x_3$  may be found by treating the wave field at each point on the surface at  $x_2$  as a source of radiation, and by integrating over these sources. As before, each point source gives rise to both a direct wave and a reflected wave. The principle may be applied repeatedly. That is, the field at distance  $x_j$  may be found from the field at distance  $x_{j-1}$ .

The field at distance  $x_4$  is found by the following formula, which is a variant of the Fresnel-Kirchhoff diffraction formula:

$$u(P) = \left( \frac{kx_j}{2\pi i x_{j-1}(x_j - x_{j-1})} \right)^{1/2} \int_h^\infty A(y) e^{i\phi(y)} dy \quad (1)$$

Here,  $u(P)$  is the field relative to the free-space field at  $P(x=x_4)$ , and  $k$  is the propagation constant. The leading factor depends only on the wavelength and on horizontal distances, and is easily evaluated. The integral contains  $A(y)$ , the amplitude of the wave at  $x_j$  as a function of vertical distance  $y$ , and a phase  $\phi(y)$ . This phase is the sum of the phase of the wave at  $y$  and the phase path from  $y$  to  $P$ .

Since  $A(y)$  and  $\phi(y)$  are arbitrary functions, defined numerically, since the real and imaginary parts of the integrand oscillate, and since the integral goes to infinity, the integration is not straightforward. Various approaches are possible. The one adopted here is to introduce a change of variable that makes the phase variation simple by folding any non-simple variation into the amplitude factor. A dimensionless variable  $t$ , analogous to  $y$ , is defined as

$$t = \pm \sqrt{\phi(y) - \phi_0} \quad (2)$$

where  $\phi_0$  is the minimum phase. The lower sign is chosen for  $y$  below the point of minimum phase, and the upper sign for  $y$  above. The lower limit of the integral becomes

$$t = \pm \sqrt{\phi(h) - \phi_0} \quad (3)$$

The integral over  $y$  then becomes an integral over  $t$ :

$$\int_h^\infty A(y) e^{i\phi(y)} dy = e^{i\phi_0} \int_t^\infty A'(t) e^{it^2} dt \quad (4)$$

where

$$A'(t) dt = A(y) dy \quad (5)$$

This particular transformation is chosen because the phase function is often approximately a quadratic, and because the resulting integral resembles the well-known Fresnel integral.

According to Eq. (5), finding the new amplitude  $A'(t)$  involves finding  $dt/dy$ . In dealing with numerically defined functions, differentiation can be troublesome, and in any case we can only use a finite number values of  $A'$ , each of which should represent a small interval rather than just one point. If the limits of this small interval are chosen to be  $t_1$  and  $t_2$  in the  $t$  domain with the corresponding values  $y_1$  and  $y_2$  in the  $y$  domain, Eq. (5) becomes

$$\int_{t_1}^{t_2} A'(t) dt = \int_{y_1}^{y_2} A(y) dy \quad (6)$$

$A'(t)$  is then a function whose integrals over a number of small intervals is given. If these intervals are chosen to be equal in length, it is not too difficult to find a function  $A'$  which is continuous and which satisfies Eq. (6) for these intervals. After some experimentation, it was decided to represent  $A'(t)$  as piecewise quadratic, with a different quadratic function for each of the intervals  $-\infty$  to  $-1.2$ ,  $-1.2$  to  $-0.8$ , ...,  $1.2$  to  $\infty$ . The interval length 0.4 was chosen as a compromise between accuracy and speed.

The choice of  $\pm 1.2$  as the boundary between the finite and infinite parts of the integral is based on the following considerations: Integration is a smoothing procedure, provided that the integrand does not oscillate about zero. That is, irregularities in the integrand tend to be smoothed out. On the other hand, where the integrand oscillates about zero, the integration becomes sensitive to amplitude differences of successive swings away from zero. In the integral of Eq. (4), it is therefore appropriate to integrate in steps where the phase changes slowly, up to about  $t = (\pi/2) = 1.253$ , i.e. over half of the first Fresnel zone. Beyond there, it is safer to model the amplitude of the integrand as a smooth curve and integrate in one step to infinity.

With  $A'(t)$  in polynomial form, the integral in Eq. (4) can be evaluated. In particular, for powers up to  $t^2$ ,

$$\int_{-\infty}^{\infty} e^{it^2} dt = P(\tau)$$

$$\int_{-\infty}^{\infty} te^{it^2} dt = \frac{1}{2} e^{i\tau^2} \quad (7)$$

$$\int_{-\infty}^{\infty} t^2 e^{it^2} dt = \frac{1}{2} [te^{i\tau^2} + P(\tau)]$$

where  $P$  is the complementary Fresnel integral. (Strictly speaking, the second two integrals of (7) do not converge. However, if  $i$  is replaced with  $i - \epsilon$  in the integrand, where  $\epsilon$  is a positive real number, the integral converges for arbitrarily small  $\epsilon$ . Eqs. (7) represent the limit as  $\epsilon \rightarrow 0$ .)

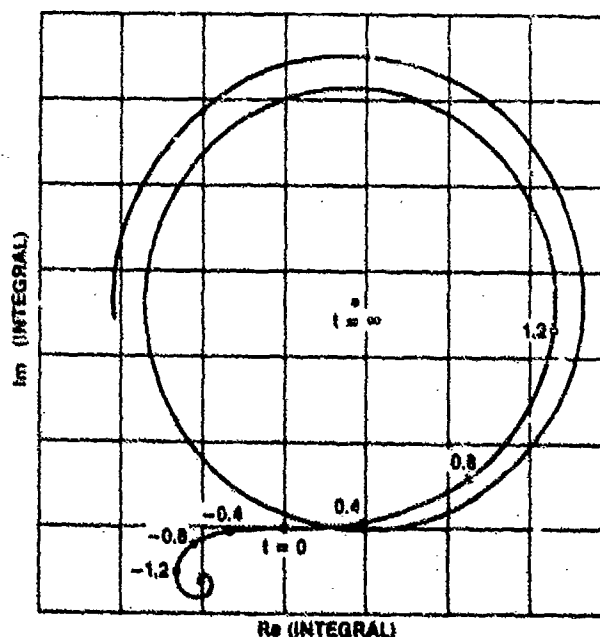


Figure 2. An example of a field integral for the direct wave over a spherical earth. The imaginary part of the integral is plotted against the real part, and the integration parameter  $t$  is indicated along the curve. The location of any point on the curve is given by  $\int_{-\infty}^t A'(t) \exp(it^2) dt$ .

### 3. CALCULATION

The integration is done in steps of 0.4 in for  $t$  between -1.2 and 1.2, and in a single step to infinity outside of these limits. For the integration to infinity, a quadratic is fitted to the integrals of Eq. (6) between  $t = 1.2$  and  $t = 3.2$ . An example in the case of propagation over a spherical earth is shown in Figure 2. Only the direct-wave integration is shown. The curve is a Cornu spiral, but greatly distorted from the spiral found in textbooks on physical optics because the source intensity increases with height. That is, the positive spiral is much larger than the negative spiral.

In finding the field amplitude of the reflected wave, an amplitude and phase must be found for the reflected ray from each element of the source field. The phase path may be found by considering the ray to come from the reflection image of the surface on which the source field is defined. The phase and amplitude of the wave component along the ray are changed according to the reflective properties of the surface of the ground. The reflection coefficient is given, for example, by Hall<sup>6</sup>. In addition, since the surface is considered to be rough, there is a further attenuation  $\rho$  given by<sup>7</sup>

$$|\rho| = \exp - \frac{1}{2} \frac{4\pi\sigma\sin\psi}{\lambda}^2 \quad (8)$$

where  $\sigma$  is the rms roughness of the reflecting surface, and  $\psi$  is the angle between the ray and the surface.

The rms roughness of the ground is assigned according to the type of ground and the roughness in the profile. In the present version of the algorithm, a default roughness for smooth ground is assigned as

$$\sigma = \frac{10\lambda h}{5\lambda + h} \quad (9)$$

where  $h$  is the height of the transmitting antenna or of a diffracting ridge above the smooth ground. This assignment is arbitrary; it is one that results in good agreement with spherical diffraction results. Changing the roughness by a factor of two changes spherical-earth path losses by a few decibels.

### 4. COMPARISON WITH EXACT THEORY

For most of the development of the computer program, a spherical earth was used as the test terrain. The program is ultimately intended for use on irregular terrain, but the spherical earth has the advantage that the results of rigorous diffraction theory are available for comparison. Figure 3 shows four examples of comparative results for different antenna sizes and polarizations. In order to obtain the close agreement seen here, appropriate roughness values had to be chosen, since the algorithm cannot handle a completely smooth surface. On the other hand, it was necessary to assume that the surface of the ground is locally smooth. That is, the roughness is set at zero for finding the field at ground level, and gradually increased to its assigned value in the first few meters above ground. This apparent variation with height may make some sense physically, since the first Fresnel zone for reflection is small for field points close to the ground and therefore may not encompass large variations in terrain height.

The agreement between the two sets of curves is not trivial, since the theories on which they are based are quite different. For example, in the rigorous theory, the wave polarization is part of the boundary condition at the ground surface. In the approximate theory used here (Huygens' principle), polarization enters only in its effect on the reflection coefficient.

### 5. COMPARISON WITH MEASUREMENTS

A limited number of comparisons with measured field strengths have been done. Figure 4 illustrates measured and calculated values of path loss as function of distance along three radials from Resolute Bay in the Canadian Arctic. These propagation paths are of interest because the terrain is both irregular and treeless. In operational propagation predictions, trees must often be included, but in the development of a new algorithm, they are an unwanted complication. In the comparisons shown here, there are not enough measured data points to assess the accuracy of the calculation, but they show at least that the algorithm behaves reasonably in irregular terrain. The curves of calculated loss rise and fall with the terrain roughly as expected, and they pass close to most of the measured values. Further testing is planned.

### 6. COMPUTER TIME

The time taken to find the path attenuation along a radial from a transmitter is roughly ten times greater than for methods now in use. For on-line use, such an increase in waiting time is unacceptable, and an effort is being made to reduce it. Major reductions can only be made by reducing the number of points for which the field

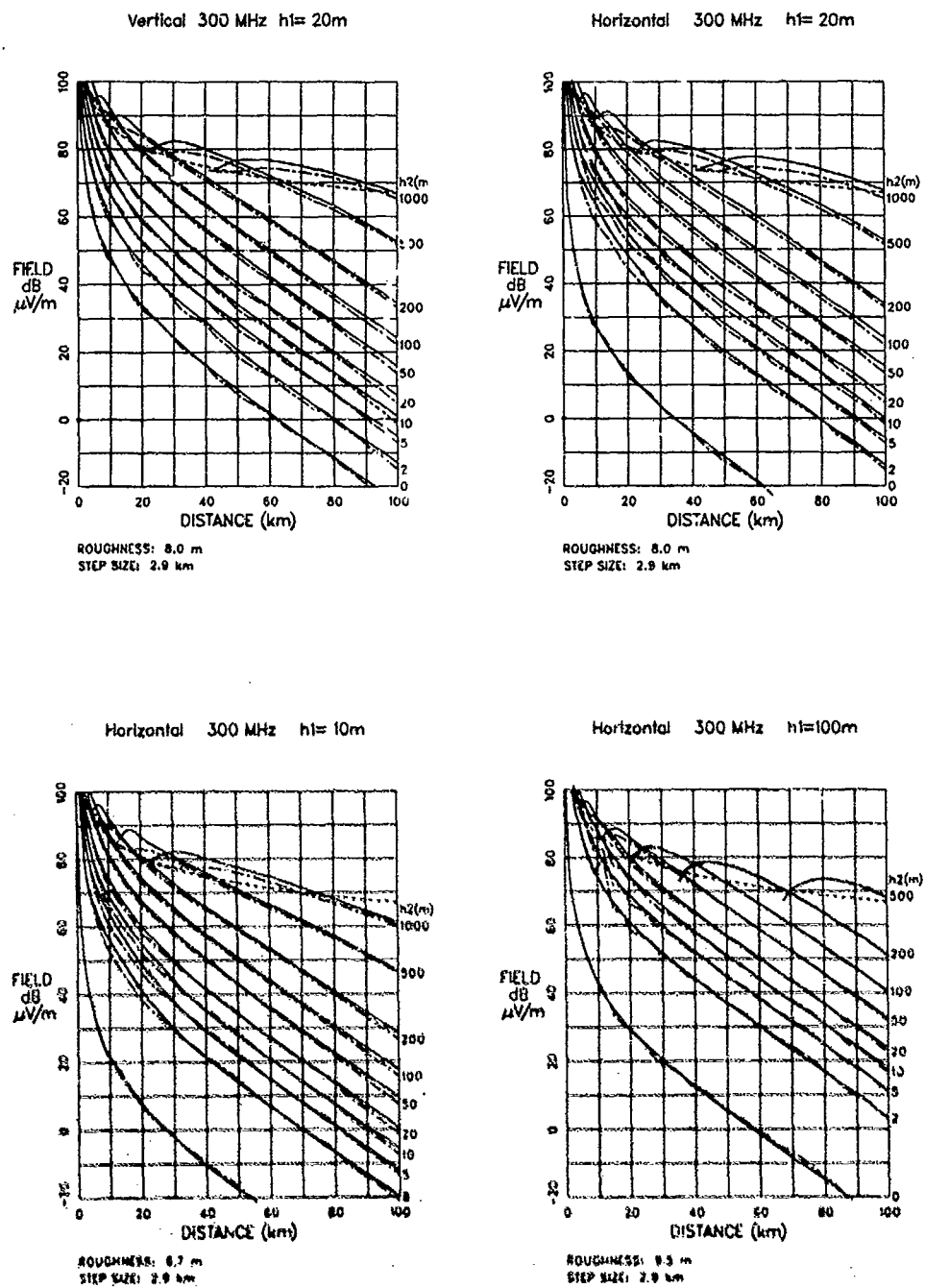


Figure 3. Field strength over a spherical ( $4/3$ ) earth from a 1 kW transmitter. Each diagram corresponds to a particular transmitter polarization and antenna height, indicated at top of diagram. Curves are labelled according to the height of the receiving antenna. Solid curves are from a CCIR Atlas. Broken curves were calculated by the method described in this paper.

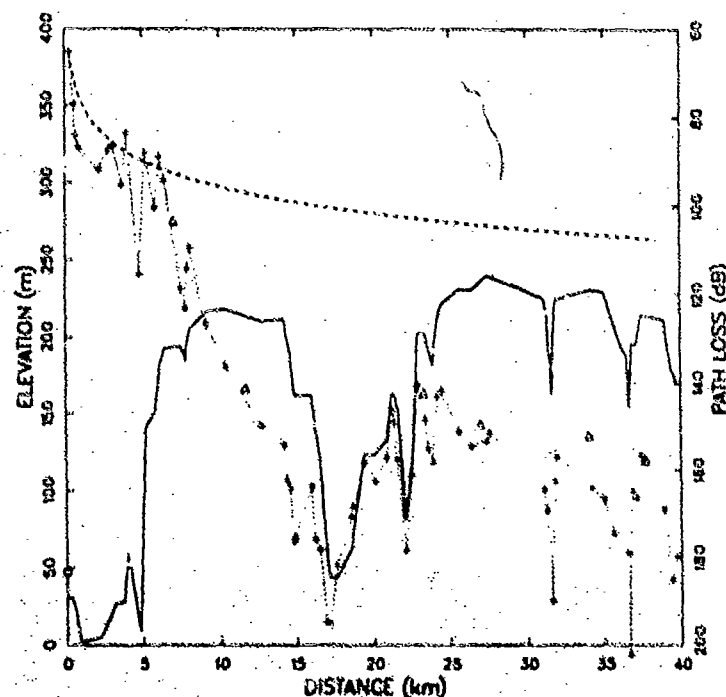
must be evaluated. In particular, it may be possible to find the field at points well clear of the ground without finding it first at all the intermediate points between the transmitter and the field point in question.

#### 7. CONCLUSION

A new algorithm for the calculation of diffraction attenuation over irregular terrain exists in preliminary form. It applies approximate diffraction theory to a detailed model of the terrain profile. Comparison with spherical diffraction theory and with some measured data have demonstrated that diffracted fields can be calculated in this way. Much more testing remains to be done, and modifications will likely be made as a result. The most severe remaining problem appears to be the computer time required, which must be reduced if the program is to be acceptable for on-line use. It is planned to do this by reducing the number of field points, retaining a high density of points only close to the ground.

#### 8. REFERENCES

- [1] Epstein, J., and D.W. Peterson, "An experimental study of wave propagation at 850 Mc", *Proc. IRE*, 41(5), 595-611, 1953.
- [2] Deygout, J., "Multiple knife-edge diffraction of microwaves", *IEEE Trans. Antennas Propag.*, AP-13(4), 480-489, 1965.
- [3] Hacking, K., "Approximate methods for calculating multiple-diffraction losses", *Electron. Lett.*, 2(5), 179-180, 1966.
- [4] de Assis, M.S., "A simplified solution to the problem of multiple diffraction over rounded obstacles", *IEEE Trans. Antennas Propag.*, AP-19, 292-295, 1971.
- [5] Born, M., and E. Wolf, "Principles of Optics", 808 pp., Pergamon, New York, 1965.
- [6] Hall, M.P.M., "Effects of the Troposphere on Radio Communications", 206 pp., Peregrinus, Stevenage UK, 1979.
- [7] Beckmann, P., and A. Spizzichino, "The Scattering of Electromagnetic Waves from Rough Surfaces", Pergamon, Oxford, 1963.
- [8] Palmer, F.H., "Measurements of VHF/UHF propagation characteristics over arctic paths", *IEEE Trans. Antennas Propag.*, AP-28(6), 733-743, 1980.
- [9] Atlas of Ground-Wave Propagation Curves of Frequencies between 30 Mc/s and 300 Mc/s, ITU, Geneva, 1955.



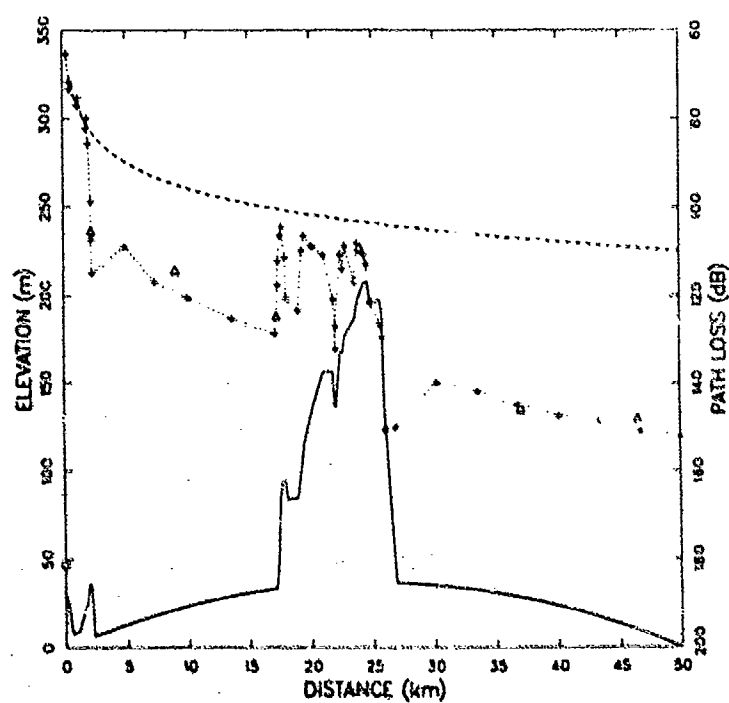
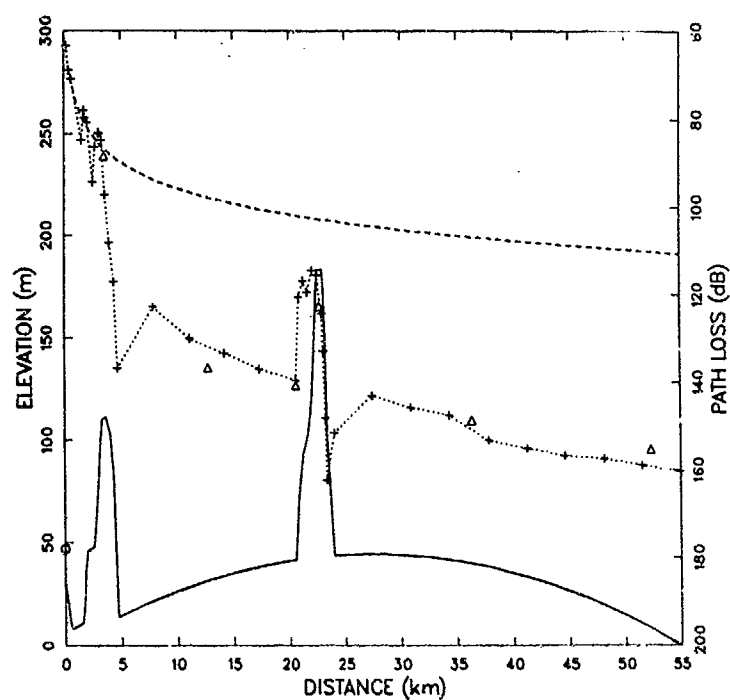


Figure 4. Terrain profiles and path attenuations at 148 MHz on three transmission paths. The left-hand end of each path is near Resolute Bay, North-West Territories. A small circle shows the location of the base antenna, 17 m above ground. The mobile antenna is 3 m above ground. The calculated path loss is indicated by + signs joined by a broken line. The measured path loss is indicated by triangles.



## ERRATUM

## DISCUSSION

## H.L. Bertoni

I have a two-part question. First, how large is the integration interval  $Y_2-Y_1$ , as compared to wavelength, and is it small enough to allow for accurate approximation of the amplitude function  $A(y)$ ? Second, how many times did you repeat the numerical integration to compute field strength on the path you showed for the arctic?

## Author's Reply

The integration interval  $Y_2-Y_1$  is related to the wavelength through the Fresnel-Zone radius, which depends on the horizontal scale of the problem. At the edge of the first Fresnel-Zone integration variable  $t = \sqrt{R} = 1.77$ , about 4.4 times the integration of  $t_2-t_1 = 0.4$ .

Apparently this interval is just small enough for accurate computation. It was found by trying several values and choosing the largest for which the calculated fields did not depend on  $t_2-t_1$ . The number of steps in the calculation is equal to the number of vertices in the terrain profile, about 66 for the first arctic (Resolute Bay) path shown. On the smooth-earth paths, 35 steps were used. The number of numerical integration is much larger, since at each step the field is found at about 20 points.

AGARD Conference Proceedings N° 407 on  
Terrestrial Propagation Characteristics in Modern Systems of  
Communications, Surveillance, Guidance and Control.

Please insert this page before page 7-1



AD-P005 737

7-1

## Mono- and Bistatic Radar Coverage Diagrams Including Diffractive Wave Propagation

by

Heiner Kuschel  
Forschungsinstitut für Hochfrequenzphysik der FGAN e.V.  
Neuenahrer Str. 20  
D-5307 Wachtberg-Werthhoven  
F.R.G.

### SUMMARY

Coverage patterns of radar sites, providing information on the terrain masked situation of a radar, are of great importance, particularly for the detection of low flying targets. Digital terrain maps can be used as a powerful base for a computer supported calculation of highly reliable coverage patterns for different kinds of radar sites.

Here, a digital terrain database, the Digital Landmass System (DLMS), having high horizontal and vertical resolution, is used to obtain optical coverage patterns, as well as physical coverage plots. Physical coverage calculations are based on the consideration of wave propagation phenomena such as diffraction and refraction using a multiple knife edge propagation model in combination with the above mentioned terrain database. Both, the propagation model and the terrain database have been verified by measurements.

### 1. INTRODUCTION

Approaching a ground based target at low altitude is a commonly used tactics to avoid detection by air defense radars suffering from clutter and terrain masking. This is why the knowledge of coverage gaps is of viable interest for a ground based surveillance system. Today, digital terrain databases provide a means to obtain coverage diagrams, which is much cheaper and easier to handle than checking the radar coverage by measuring a reference aircraft at particular heights and directions of interest.

Having the gaps once identified, the question arises, what could be done to improve the coverage performance of ground based radars. To investigate this question, wave propagation effects are considered in addition to line of sight calculations, to allow for diffraction phenomena, which are of increasing importance at larger wavelengths. The influence of radar frequency and radar antenna height is observed using fictive radar sites in real terrain for the monostatic case as well as for the bistatic one.

### 2. THE TERRAIN DATA BASE

The reliability of the prediction of field strengths behind an obstacle is strongly dependent on the accuracy of terrain height information, especially if target heights are in the order of magnitude of surface structures, like forests.

Hence, a terrain database of high accuracy as well as of high reliability is required. The DLMS is a database which can meet these demands. It consists of two general parts. The first part contains the topographic height data which are subdivided into blocks of 1 degree longitude by 1 degree latitude. Depending on the geographic latitude of the block, the number of terrain height samples varies from 201 to 1201 for a constant value of latitude on one block, while the number of terrain height samples for a constant value of longitude is always 1201; this leads to an approximate distance between two samples of 100 meters.

A second level is being developed which will have a resolution of about 30 m. The height accuracy is dependent on the type of terrain, where 10 m is a typical value for hilly regions. The height resolution, however, is given by the digitized height steps of 1 m in all types of terrain.

In addition to the topographic height information, surface structure information is available. This includes features like buildings, settlements, forest, and others, where characteristic parameters are predominant height of the feature, surface material, and surface roughness. The corners of a polygon, forming the boundary of the feature, are digitized in longitude and latitude with an accuracy of 0.1 seconds. Figure 2.1 shows a 3D-plot of typical terrain in the center of Europe, while figure 2.2 is a plan view of forested areas inside a geographical block as an example.

Both, topographic and surface structure information can be used separately, but are combined for the coverage calculations. Forested areas are modelled as solid obstacles, i.e. the average vegetation height is added to the topographic height. Although this is a very simple forest model and, of course, more precise and sophisticated models are available, it has shown good results at least for radar coverage applications. Earlier work [1] has shown that for forest depths greater than a few hundred meters, the electromagnetic energy, penetrating through a forest, is negligible compared to the energy diffracted at the forest edge. This result shows, of course, strong frequency dependence but justifies the application of the solid obstacle forest model in most cases.



Fig. 2.1

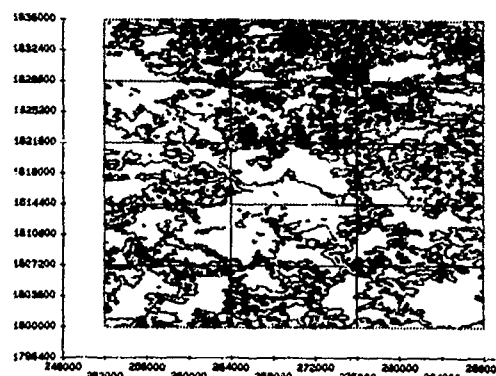


Fig. 2.2

### 3. THE FLIGHT PATH MODEL

The following calculations, ending up with mono- and bistatic coverage diagrams are dependent on the basic assumptions of the targets flight behaviour. Since the terrain following capability is different from aircraft to aircraft or from one missile to another and will presumably increase in future, a target flight path model is adopted, which is very easy to handle and, even more important, independent of the target type. The model target is always assumed to fly at constant height above ground and thus ideally follows the terrain.

This assumption is of course an idealized one, which can only be interpreted as a worst case. Real target aircraft or missiles are usually limited in mobility and manoeuvrability by the maximum normal acceleration. Hence, a real terrain following flight profile will be smoother than the one derived from the model assumptions. In the coverage diagrams this will lead to fewer and smaller gaps but hardly to larger line-of-sight ranges. The quantification of this effect, however, is strongly dependent on the actual terrain following algorithm and device.

### 4. LINE-OF-SIGHT COVERAGE DIAGRAMS

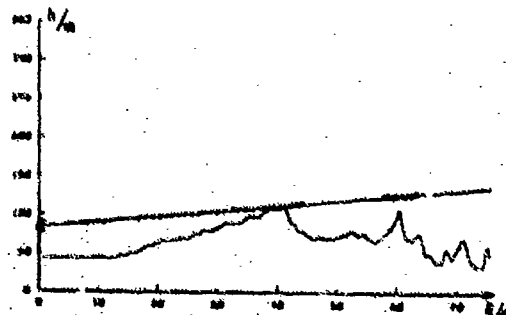
Since the intention of radar coverage diagrams is the description of the terrain masked site of a radar, in this case line-of-sight means radio line-of-sight and hence includes the consideration of a modified earth radius to allow for refraction effects in the earth's atmosphere. The correction factor  $k$  is dependent on air pressure, temperature and humidity and can vary with place and time from 0.7 to 10.

To obtain line-of-sight coverage diagrams of polar geometry, a number,  $n$ , of terrain profiles is extracted from the database in equidistant angular spacing. Thus the observed area is a circular one, limited by the maximum range of interest. The terrain profiles are corrected for earth curvature and refraction in the earth's atmosphere and scanned for the identification of regions, where a target at constant height above ground has a line-of-sight to the radar antenna. Figure 4.1 shows a typical terrain profile, with those areas indicated, where a target at constant height above ground is within the line-of-sight region.

Line-of-sight diagrams for the bistatic case are generated similarly but for an area which is limited by a so called Cassini curve of constant range product  $R_1 \cdot R_2$ , where  $R_1$  is the distance from transmitter to target and  $R_2$  is the distance from receiver to target. Such bistatic diagrams are derived from superpositions of two monostatic ones relating the polar geometry to a best fit cartesian one, which gives the best areal resolution.

Figures 4.2 to 4.4 show line-of-sight diagrams for two monostatic sites and the corresponding bistatic diagram, indicating those areas, where a line-of-sight from target to both transmitter and receiver exists.

Fig. 4.1 path profile



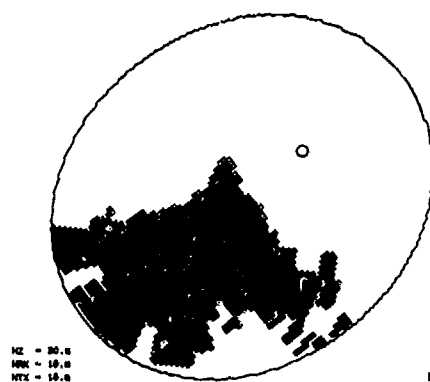


Fig. 4.2 monostatic

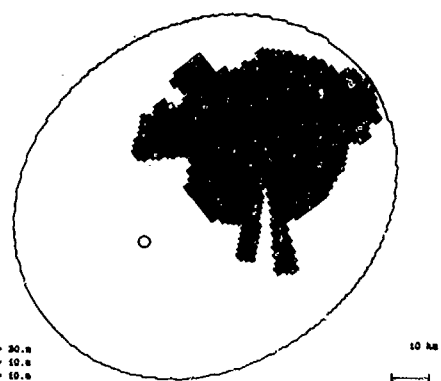
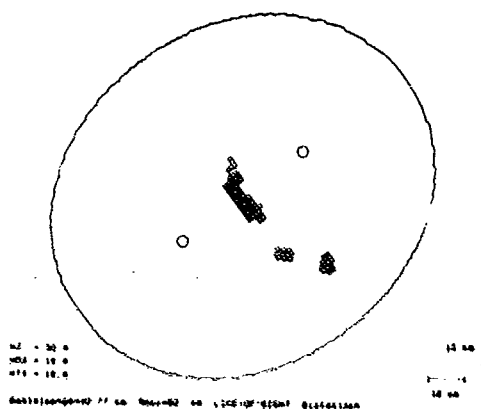


Fig. 4.3 monostatic

Fig. 4.4 bistatic



#### 5. THE PROPAGATION MODEL

The propagation model, which is here used for radar application is valid for frequencies from VHF to X-band. It is mainly based on diffraction and refraction effects in the atmosphere. For this so called multiple knife edge diffraction model, the precise knowledge of the propagation path is necessary. In the terrain profile, corresponding to the propagation path, those edges building the horizon for a fictive source located on top of the previous edge, are modelled by ideally conducting screens of actual obstacle height and infinite extension. An example for a terrain profile and the corresponding propagation path are given in fig. 5.1 and fig. 5.2.

Since the wavefront is assumed to be planar at the point of diffraction, the whole problem is reduced to a 2 dimensional one. Based on the previous assumption, the single knife edge diffraction attenuation along the partial paths  $R K_1 K_2$  and  $K_1 K_2 Z$  are calculated based on the well known Fresnel Kirchhoff theory. Fig. 5.3 shows the geometry for the calculation of the diffraction attenuation, caused by a single knife edge.



Fig. 5.1

Fig. 5.2

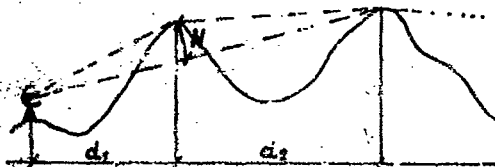
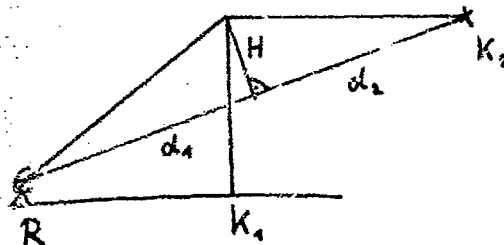


Fig. 5.3



Let R be the location of a source, generating an electromagnetic field of the form

$$E = \int X e^{ikd} d', \quad (5.1)$$

where X is the location of the transmitter in the plane of the first diffraction screen  $K_1$  and d is the distance from R to  $K_2$ . The ratio of actual received field strength E to free space field strength  $E_0$  at the given location  $K_2$  can be calculated using Kirchhoff's equation

$$\frac{E}{E_0} = \frac{e^{-j\pi/4}}{\sqrt{2}} \left[ \frac{e^{j\pi/4}}{\sqrt{2}} + [C(v) + jS(v)] \right], \quad (5.2)$$

where

$$C(v) = \int_0^v \cos\left(\frac{\pi}{2}t^2\right) dt \quad (5.3)$$

and

$$S(v) = \int_0^v \sin\left(\frac{\pi}{2}t^2\right) dt \quad (5.4)$$

are the well known Fresnel integrals.

The argument v describes the geometric properties of the propagation path, it is given by

$$v = H \sqrt{2/\lambda} \left( \frac{1}{d_1} + \frac{1}{d_2} \right) \quad (5.5)$$

where H is the height, by which the obstacle exceeds the straight line between R and  $K_2$ ,  $d_1$  the distance R  $K_1$ ,  $d_2$  the distance  $K_1 K_2$  and  $\lambda$  the radio wave length. H is negative for transhorizon paths and thus v becomes negative, as well. The actual values for  $d_1$ ,  $d_2$  and H are extracted from the path profile, which is derived from the terrain database.

The logarithmic attenuation, defined by the ratio of diffracted to free space field strength,

$$L = -20 \cdot \log_{10} |E/E_0| \quad (5.6)$$

is evaluated using the following approximation:

$$L = 5.42 + 0.11 \cdot v - 1.27 \cdot v^2 \text{ for } v = 2.4 \quad (5.7)$$

and

$$L = 17.951 + 20 \cdot \log_{10} (v) \text{ for } v > 2.4 \quad (5.8)$$

which are valid for regions short beyond the horizon and far beyond the horizon, respectively. In the case of propagation paths with more than one diffraction edge, the total path loss, relative to

free space, is the sum of the single diffraction losses  $L_i$ .

$$L = \sum_{i=1}^n L_i \quad (5.9)$$

From (5.6) and (5.9) follows

$$L = -20 \cdot \sum_{i=1}^n \log_{10} |(E/E_0)_i| \quad (5.10)$$

$$= -20 \cdot \log_{10} \left( \prod_{i=1}^n |(E/E_0)_i| \right) \quad (5.11)$$

An additional correction factor, which was derived from measurements, done by the RSRE (UK) is included. This correction factor leads to an increase of the path loss at wavelengths  $< 50$  cm resulting from the wavelength being in the order of magnitude of the surface fine structure. At wavelengths  $> 50$  cm the correction factor leads to a decrease of total path loss to allow for increased influence of ground wave propagation.

Since the one way propagation loss is defined to be

$$L = -10 \log_{10} |(E/E_0)^2| \quad (5.12)$$

we can define a one way attenuation factor  $\alpha_0(v)$

$$\alpha_0(v) = |(E/E_0)|^2 \quad (5.13)$$

which can be included in the radar equation to allow for diffraction influences. The argument  $v$  is defined by equation (5.5).

Thus the radar equation for monostatic radar is

$$P_{e(\min)} = \frac{P_t \cdot G_t \cdot A_r \cdot \sigma}{(4\pi)^2 R_{\max}^4} \cdot \alpha_0^2(v) \quad (5.14)$$

with  $\alpha_0(v) < 1$ .

For a bistatic radar configuration, different attenuation factors will occur for the transmitter and receiver path, respectively. Hence for the bistatic case the transceiver radar equation will be

$$P_{e(\min)} = \frac{P_t \cdot G_t \cdot A_r^2 \cdot \sigma_{br}}{(4\pi)^2 \cdot (R_t^2 \cdot R_r^2)_{\max}} \cdot \alpha_0 : (v_t) \cdot \alpha_0 : (v_r) \quad (5.15)$$

In free space,  $\alpha_0$  and  $\alpha_{br}$  both equal 1 and thus  $P_{e(\min)}$  is given by the maximum possible product of target ranges to transmitter and receiver. Curves with

$$R_t^2 \cdot R_r^2 = \text{const} \quad (5.16)$$

are the so called Cassini curves.

## 6. MONOSTATIC PHYSICAL COVERAGE PATTERNS

Similar to the line-of-sight case, where a target can be detected at ranges less than  $R_{\max}$ , for locations beyond the radio horizon, a condition for detectability can be defined as follows:

Let  $R_{\max}$  be the maximum free space radar range for given parameters like probability of detection, false alarm rate and target radar cross section, for example, then an energy surplus will be available at ranges less than  $R_{\max}$ . Hence, as long as the product of target range and propagation factor is less than or equal to the maximum free space range, the target will be detectable even beyond the horizon, according to energy calculations.

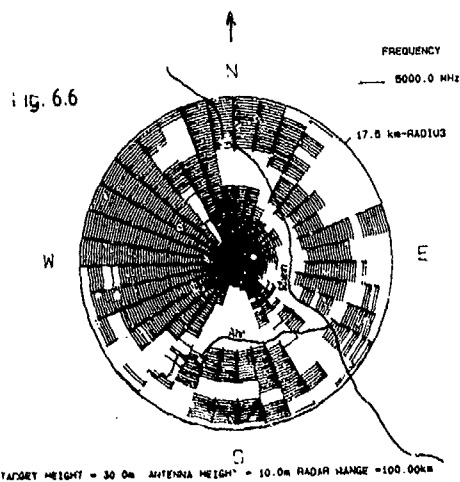
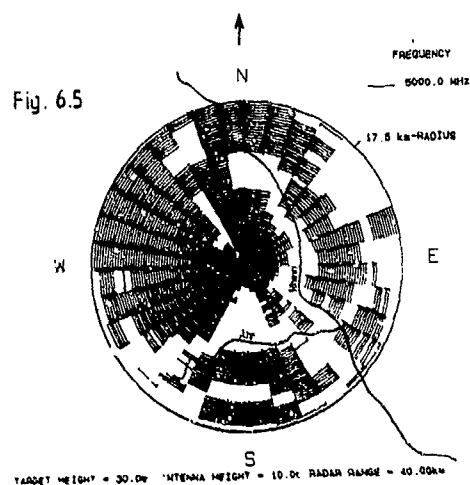
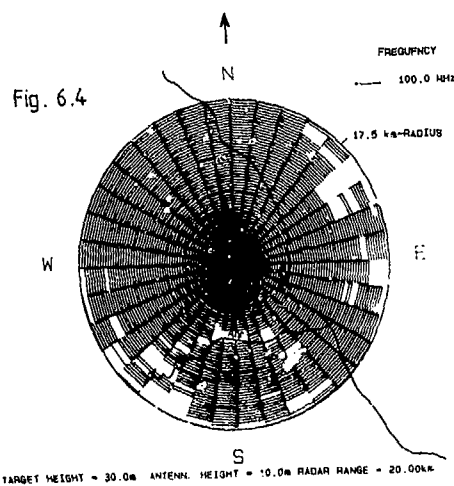
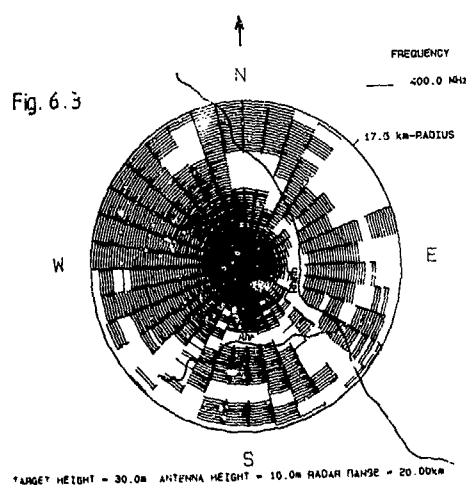
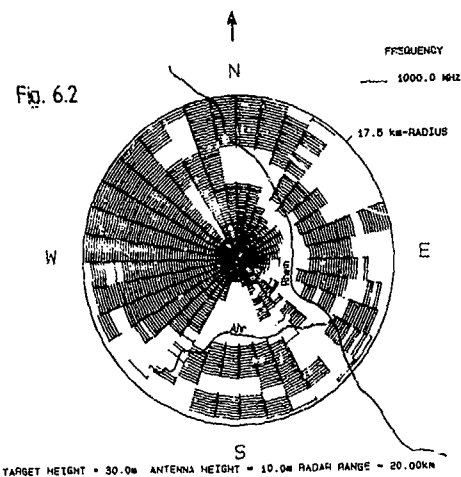
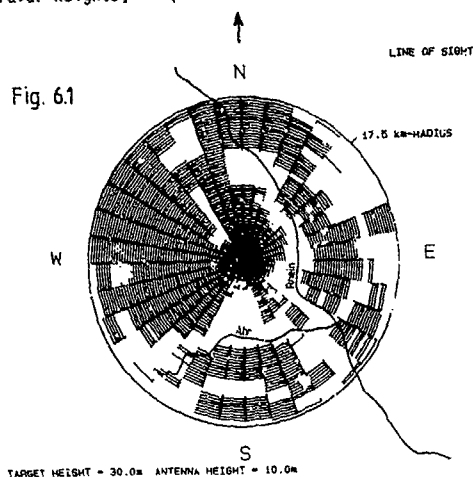
$$R \cdot \sqrt{\alpha_0} = R_{\max} \quad (6.1)$$

Atmospheric refraction is taken into account via the refraction index, influencing the k-factor and thus the effective earth radius. Since  $k$  can vary from 0.7 to about 1.5, the effective earth radius, for which straight ray geometry can be applied, can vary from 4460 km to 6370 km  $k = 4/3$  is an often used mean value.

It was out of the scope of this paper, to include the examination of clutter problems. Diffraction effects above line-of-sight are excluded as well as multipath effects.

In analogy to the procedure used for line-of-sight patterns, terrain profiles in equidistant angular spacing are extracted from the terrain database. Each path is examined for those ranges, where the condition for detectability of a target at given height is met, i.e. in equidistant range steps, the attenuation caused by diffraction is calculated and the detectability condition is checked using equation (6.1).

In figures 6.1 to 6.6, the dark areas indicate zones, where a target can be detected for different radar heights, frequencies and free space radar ranges.



## 7. BISTATIC PHYSICAL COVERAGE PATTERNS

In the bistatic case the condition for detectability appears to be a bit different. Similarly to the monostatic case, the radar parameters like transmitter power, antenna gain and detection probability and the target RCS can be combined in a fictive maximum free space range limiting the area of observation to the Cassini curves (5.16). Inside this area, a target can be detected, if

$$\sqrt{R_1 \cdot R_2 \cdot 1/\alpha_{D_T} \cdot \alpha_{D_R}} \leq R_{\max} \quad (7.1)$$

the square root of the product of ranges  $R_1$ ,  $R_2$  to the target divided by the product of corresponding attenuation factors  $\alpha_{D_T}$ ,  $\alpha_{D_R}$ , is less than or equal to the fictive maximum free space range. Different from monostatic radar, there are locations, in addition to masked and unmasked target situations, where the target is masked for either the transmitter or the receiver and within line-of-sight for the other. For a configuration like this, one of the attenuation factors  $\alpha_{D_R}$  or  $\alpha_{D_T}$  is 1. The following figures show bistatic coverage patterns for different combinations of antenna heights, frequency and target height. The effect of varying bistatic RCS for different bistatic angles is neglected.

Fig. 7.1 and 7.2 show the monostatic LOS coverage patterns for receiver and transmitter indicating a very good transmitter (T) location, fig. 7.3 shows the corresponding bistatic LOS pattern. Physical coverage patterns are shown in figs. 7.4 to 7.5 indicating increased coverage of areas, where there is line-of-sight to the transmitter, while the receiver is masked. Only at very low frequencies (400 MHz) there is a small region, where a target, which is masked for the receiver, as well as for the transmitter ( $\leftarrow$ ), can be detected.

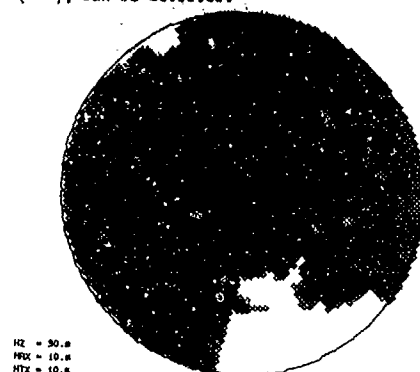


Fig. 7.1 monostatic (T)

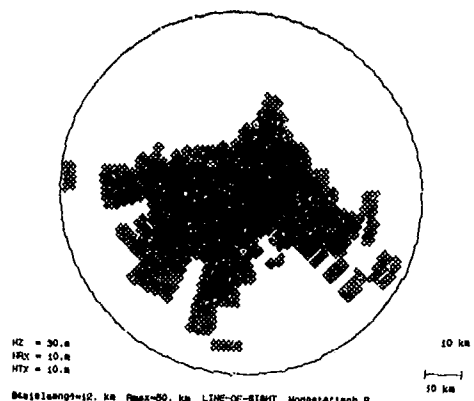


Fig. 7.2 monostatic (R)

Fig. 7.6 shows the increase in LOS area coverage if the receiver is elevated to 100 m.

Figs. 7.7 to 7.10 indicate the frequency dependent increase in radar coverage for the monostatic case i.e. a monostatic radar is assumed to be installed at the locations of transmitter and receiver, respectively. Figs. 7.11 and 7.12 show, how radar coverage increases with wave length for a bistatic configuration at the same locations as above. Though both monostatic radars together provide a much better coverage, the increase in radar coverage with wave length is more significant in the bistatic case.

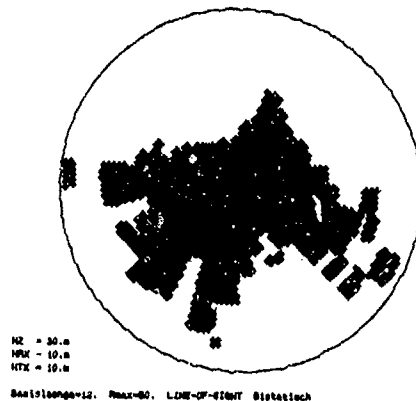


Fig. 7.3 bistatic

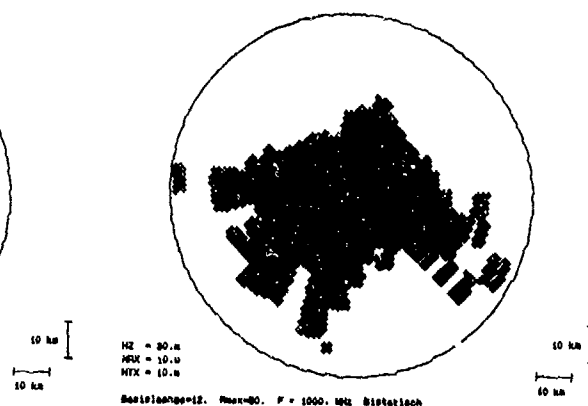


Fig. 7.4



Fig. 7.5

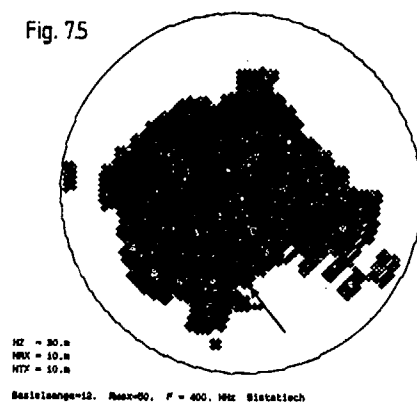


Fig. 7.6

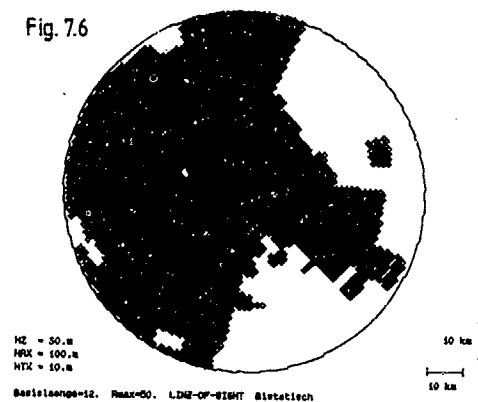


Fig. 7.7

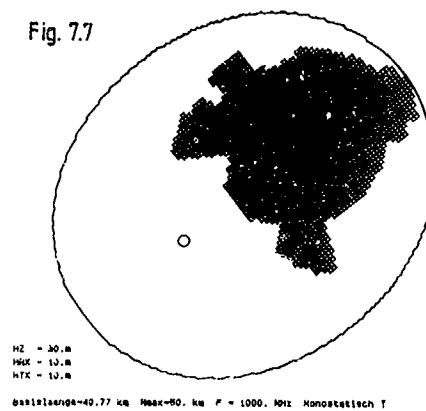


Fig. 7.8

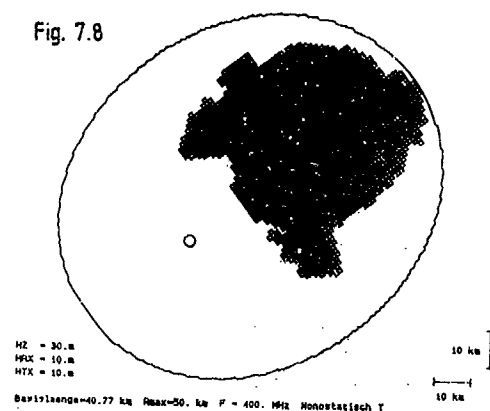


Fig. 7.9

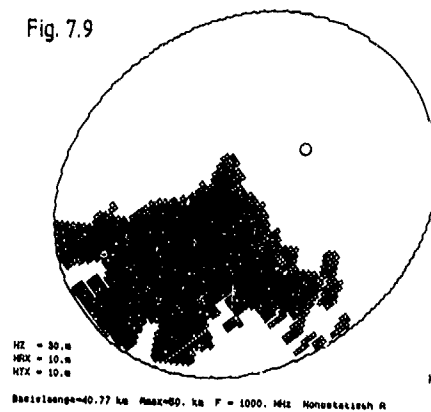


Fig. 7.10

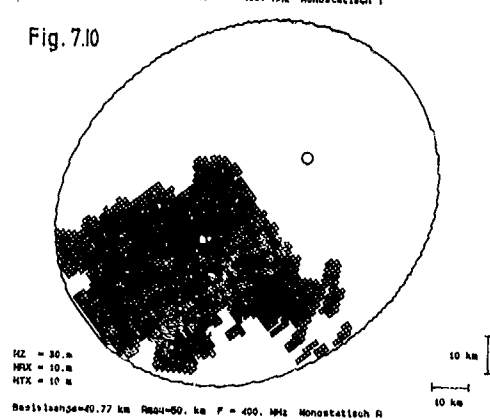


Fig. 7.11

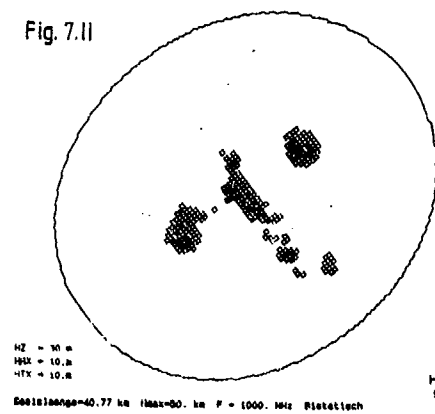
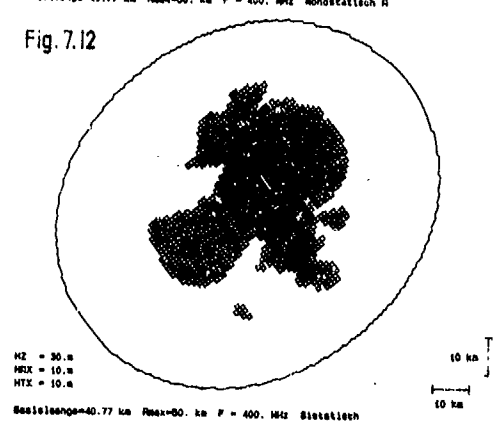
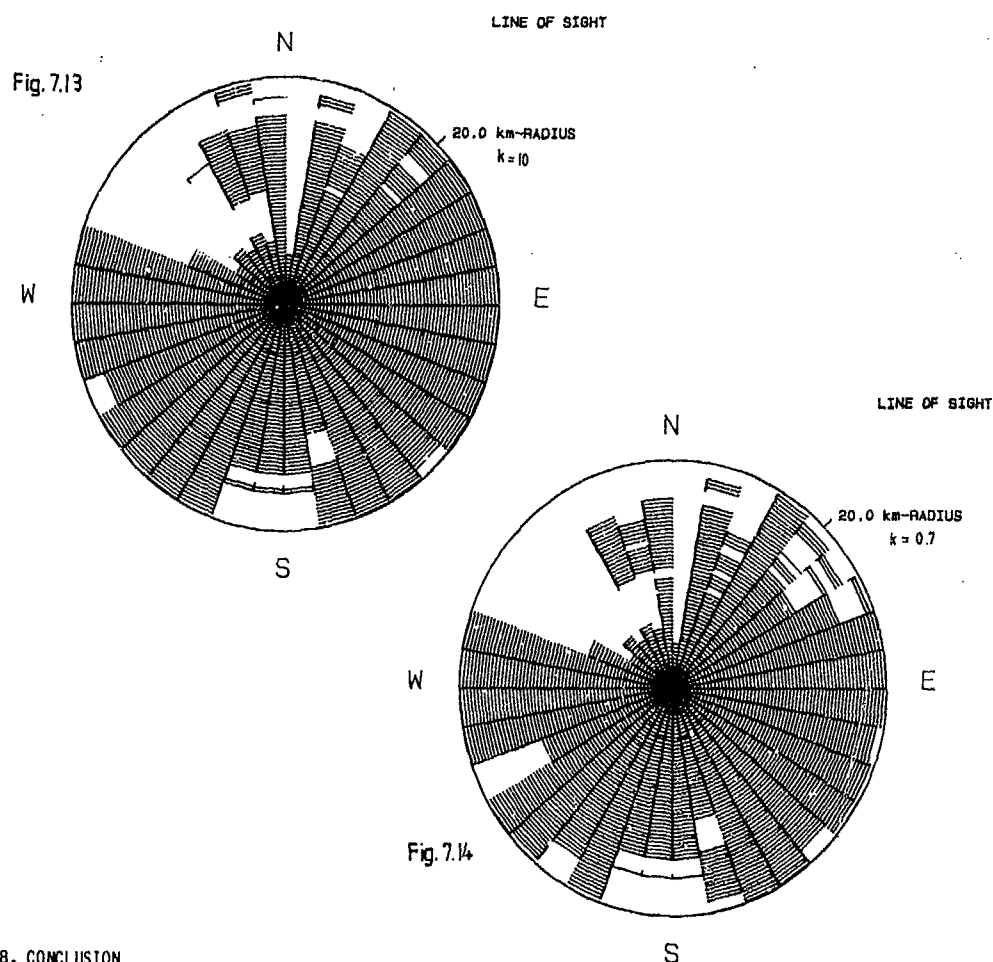


Fig. 7.12



In figures 7.13 to 7.14, the influence of atmospheric refraction is shown for the examples  $k = 0.7$ , and  $k = 10$ .



## 8. CONCLUSION

Simulations and measurements have shown that the combination of a digital terrain database with a physical wave propagation model is an appropriate tool to provide monostatic as well as bistatic radar coverage diagrams dependent on target height, antenna height, frequency and free space radar range. Such coverage patterns, including effects of wave propagation phenomena like diffraction and refraction provide useful information for the radar operator as well as for the radar design engineer. As a result of the simulations shown in chapter 7, wave propagation phenomena, providing beyond the horizon detectability at low frequencies, seem to be more likely in the bistatic case, especially if there exists a line-of-sight to either the transmitter or the receiver. In most situations, however, a combination of monostatic radars show greater coverage at line-of-sight as well as at low frequencies.

## REFERENCES

- /1/ H. Kuschei Methoden zur Berücksichtigung von Bewuchs und Bebauung auf Funkstreckendämpfungsschätzungen Kleinheubacher Bericht, Band 26, 1982, S. 501 - 511
- /2/ J. Grosskopf Wellenausbreitung I und II Hochschultaschenbücher 141/141a, 1970
- /3/ H.T. Dougherty, The Application of Diffraction by Convex Surfaces to Irregular Terrain Situations, 1964 L.J. Malony
- /4/ J.R. Wait Wave Propagation Theory Programm Press 1981
- /5/ CCIR Atlas of ground wave propagation curves for frequencies between 30 Mc/s and 300 Mc/s ITU, Geneva

## DISCUSSION

**L.Felsen**

In Kuschel's procedures (paper 7) dealing with edge diffraction by a stack of half planes, each edge is treated as though it were illuminated by the incident field alone. Whittaker's approach (paper 6), which requires much more computational effort, accounts for the modification of the incident field by each preceding diffraction. To what extent do the results of paper 6 justify those of paper 7? Can you give recommendations where the method of paper 7 is inadequate?

**Author's Reply**

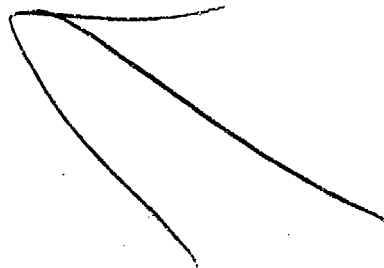
In the multiple "knife edge diffraction model", which I used, the diffraction attenuation is calculated for each edge along the path from the preceding to the succeeding edge including transmitter or receiver, respectively. The single attenuations are then superposed and thus the modification at the incident field by each preceding diffraction is, of course, included.

**J.Fairbrother**

Terrain data bases have reached the stage where any improvement must include environment category, e.g. urban or rural etc. For effective standardization such categories must be numerically defined.

**Author's Reply**

D.L.M.S. includes in each square % roof cover and % tree cover + surface material, e.g. concrete.



AD-P005738

# A DIFFRACTION BASED THEORETICAL MODEL FOR PREDICTION OF UHF PATH LOSS IN CITIES\*

Henry L. Bertoni and Joram Walisch  
Center for Advanced Technology in Telecommunications  
Brooklyn, N.Y. 11201

Cellular mobile radio and other urban communication systems working in the UHF band (30MHz - 3GHz) are based on propagation from an elevated fixed antenna to a mobile at street level. The requirement for cellular systems for coverage in one area, and isolation from other areas, makes prediction of path loss in cities an important aspect of system design. To date, the only bases for predicting path loss are the measurements made in various cities. This paper presents a theory for predicting path loss in urban areas outside of the high-rise urban core. In such areas, the buildings are of nearly uniform height and form nearly parallel rows. Each row has the appearance of a cylinder lying on the ground, so that propagation is a process of diffraction past many cylinders. Using this approach, we develop a model for predicting average path loss that is in good agreement with measurements.

## I. Introduction

The development and design of cellular mobile radio systems has made use of propagation path loss models based on measurements made in various cities. These measurements show a dependence of the average signal on the range  $R$  from the fixed antenna of the form  $1/R^M$  with  $M$  between 3 and 4 [1-7]. The influence of building height, street, width, etc. is not well understood, and is usually accounted for by experimentally obtained correction factors [1,2,8]. To date, no theoretical model has been developed that explains why the presence of buildings results in the observed range dependence and amplitude. Such a theoretical model could be used to clarify the range of application of measurements based models, and extend path loss prediction to new situations, such as fixed antennas at or below roof-top level.

We have constructed a theoretical model for predicting average path loss in the UHF frequency band for areas of cities where the buildings are of relatively uniform height. In many cities the high-rise buildings are clustered in a core region. Surrounding this core is a much larger area where the buildings have relatively uniform height, except for occasional tall buildings. In this surrounding area the buildings are organized by the street system into nearly parallel rows. Even when neighboring buildings are not physically joined together, the passageways between them are typically smaller than the building width. Except for the special cases when the passageways are aligned with transmitter, propagation must take place through the buildings or over them. Because of reflection and attenuation by exterior and interior walls, propagation through the buildings can, at most, be significant only for the last row in front of the mobile.

The foregoing considerations lead to modeling a row of buildings by an opaque rectangular cylinder lying on the ground. Propagation then takes place over the cylinders, as suggested by path 1 in Figure 1 for the case when the elevated fixed antenna is the source. Here a few rows of buildings are shown in cross-section. For  $R$  in the range 1-10 km the actual number of rows goes from about 20 to over 200. At each cylinder a

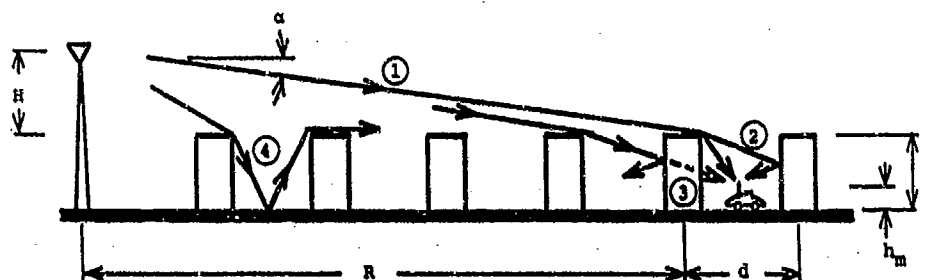


Figure 1. Various ray paths for UHF propagation in the presence of buildings.

\*This work was supported in part by a contract from GTE Laboratories Inc., and in part by a grant from the New York State Science and Technology Foundation.

portion of the field is diffracted down to the ground. The diffracted and subsequently reflected rays in the vicinity of the mobile, which are indicated by 2 in Figure 1, account for the well known multipath, or wavelength scale, variations of the field [9,10].

The field reaching the ground can rejoin that above the buildings after multiple reflections and refractions, as suggested by path 3 in Figure 1. In addition to a loss in amplitude, these fields lose phase coherence with the original field above the building, and become part of the incoherent background. For these reasons the fields reflected from the ground are neglected, so that the height of the buildings does not influence propagation over their roofs, but only influences the final diffraction down to street level.

For small glancing angles  $\alpha$ , the forward diffracted field will maintain coherence with the incident field even when the tops of the buildings are irregular. However, fields that are multiply back-diffracted at the tops of the buildings will lose coherence with the phase and direction of the incident field due to irregularities of the buildings. Because of this loss of coherence, the back-diffracted fields are neglected. Since only forward diffraction is included in our model, and since for small angles this diffraction is not strongly dependent on the cross-section or electrical properties of the diffracting obstacle, we replace each row of buildings by an absorbing screen of vanishing thickness. Finally, because reflections from the ground are not important, the screens are assumed to be semi-infinite.

A further simplification is achieved by using the local plane wave approximation to find the influence of the buildings on the spherical wave radiated by the elevated antenna. We first determine the amplitude  $Q(\alpha)$  of the field at the roof tops due to a plane wave of unit amplitude incident at the glancing angle  $\alpha$  on an array of building rows. The roof top fields due to the spherical wave are then the product of  $Q(\alpha)$ , with  $\alpha$  as shown in Figure 1, and the spherical wave amplitude, which is inversely proportional to the range  $R$  in Figure 1. This plane wave approximation is similar to that used when finding the field above a homogeneous earth. Here the spherical wave amplitude is multiplied by the factor  $[1 + \Gamma(\alpha)]$ , where  $\Gamma(\alpha)$  is the plane wave reflection coefficient. Moreover, this approximation is consistent with the concept of effective antenna height introduced by Lee [11].

When computing the range dependence of the average signal, all buildings are assumed to have the same height  $h$  equal to the average height of the actual buildings. The use of uniform height buildings to find the average signal strength is justified by the agreement obtained with measurements. Computations made assuming the height of the rows to be randomly distributed also confirm the validity of this approach.

## II. Diffraction Past a Series of Half Screens

To find the plane wave amplitude factor  $Q(\alpha)$  we consider the diffraction of a plane wave by a series of half screens labeled  $n=0,1,2,\dots$ , as shown in Figure 2. Diffraction

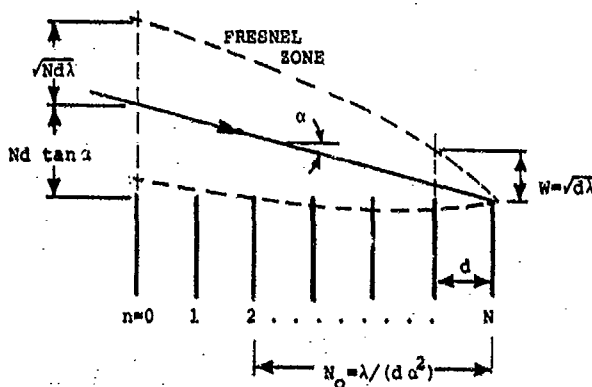


Figure 2. Ray reaching the edge  $n=N$  and the Fresnel zone about it.

past all preceding screens will alter the field incident on plane of the  $n$ th screen. Let  $H_n(y)$  be the field incident on the plane of the  $n$ th screen. The field incident on the edge of the  $n$ th screen  $H_n(0)$  will vary as  $n$  increases, but can be expected to settle to the constant value  $Q(\alpha)$  independent of  $n$  for  $n$  large enough, since the plane wave is incident from above the edges.

An estimate of the number of half screens that must be considered in order to achieve settling can be obtained from the Fresnel zone for the plane wave field reaching the edge  $n=N$  in Figure 2. For  $N$  large enough, the edges of  $N_0$  half screens will lie within the

Fresnel zone about the ray reaching the edge  $n=N$ . For small  $\alpha$ ,  $N_0$  is the integer part of  $d/(\lambda\alpha^2)$ , so that

$$N_0 \approx d/(\lambda\alpha^2) \quad (1)$$

Because the edges for screens with  $n < N - N_0$ , do not lie in the Fresnel zone, they should not significantly effect the field incident on the  $n=N$  edge. Thus one expects settling to be achieved after about  $N_0$  half screens. These observations confirmed by the numerical results described below.

#### A. Kirchhoff-Huygens Evaluation

In studying diffraction over hills, the forward diffraction approximation has been employed [12-14]. Vogler [15] has developed a method for treating diffraction by a series of half screens, starting with an approximate solution that may be obtained by repeated application of the Kirchhoff integral to the plane of each screen. He further approximates this solution into an infinite summation of terms. Besides being difficult to work with, the approximation appears to be valid only for plane wave incidence from below the horizon, rather than from above, as in Figure 2.

Because no strictly analytic method appears to exist for the diffraction problems posed in Figure 2, a method based on direct numerical evaluation of the Kirchhoff-Huygens integrals is adopted here. We assume that the incident plane wave has unit amplitude magnetic intensity  $H$  polarized along  $z$  in Figure 2, and time dependence  $\exp(j\omega t)$ . When there is no variation along  $z$ , the field  $H_{n+1}(y)$  incident on the plane of the  $n+1$  half screen due to the field  $H_n(y')$  above the  $n$ th half screen is [16]

$$H_{n+1}(y) = \frac{e^{j\pi/4}}{2\sqrt{\lambda}} \int_0^\infty H_n(y') \frac{e^{-jkr}}{\sqrt{r}} (\cos \delta + \cos \alpha) dy' \quad (2)$$

where

$$r = \sqrt{d^2 + (y-y')^2} \quad ; \quad \cos \delta = d/r \quad (3)$$

and  $d$  is the separation between the screens.

Numerical evaluation of (1) requires that the integration be broken into discrete intervals over which the integration can be approximated by an algebraic expression. Furthermore, the integral must be truncated at some finite value of  $y'$ . Since the integration aperture is large compared to wavelength, choice of the discrete interval length  $\Delta$  must be as large as possible for realistic computing times. An integration rule has been developed by making separate linear approximations for the phase and amplitude of the integrand in (2) that allows  $\Delta$  to be chosen as large as the wavelength  $\lambda$  [17].

The principal contribution to (2) come from points within the Fresnel zone shown in Figure 2 [18]. Thus the termination of the integration must be made outside of this region. Abrupt termination of the integration will also result in a numerical error, even when the termination point is well outside the Fresnel zone. To avoid this error, a termination strategy has been developed [17], in which the integrand of (2) is brought smoothly to zero before the integration is stopped. The details of the integration rule and termination strategy are omitted here, and only the numerical results are presented.

#### B. Field Variation From Edge-to-Edge

Corresponding to the UHF band,  $d/\lambda$  is in the range 30 to 600 for incidence normal to the edges in plane view. For oblique incidence, the effective  $\lambda$  is greater by  $1/\cos \psi$  where  $\psi$  is the angle between the plane of incidence and the normal to the screens, thereby reducing  $d/\lambda$ . The calculations reported here have been carried out for the four cases  $d/\lambda = 200, 100, 50, 25$ .

The results of the calculations for the field incident on the edge of the  $n$  half screen for an incident plane wave of amplitude  $|H| = 1$  are given in Figure 3 for  $d/\lambda = 50$ . Similar results have been obtained for  $d/\lambda = 200, 100$  and 25. While the calculations are made only for integer values of  $n$ , a continuous curve has been drawn through the points to help in visualizing the results. Each curve corresponds to a particular value of incidence angle  $\alpha$ . The dependence of the calculated curves on  $\alpha$  and  $d/\lambda$  is such that, to an accuracy of better than about 2%, the same curve is obtained for the same value of  $\alpha^2 d/\lambda$ , which is the inverse of  $N_0$  in (1).

For  $\alpha = 0$  and an incident plane wave of unit amplitude,  $|H| = 0.5$  at the edge of the  $n=1$  half screen. As  $\alpha$  increases, the edge of the  $n=1$  half screen lies above the shadow boundary, so that  $|H| > 0.5$  there. In the illuminated region of the diffraction pattern of a single half screen, the field has maxima greater than the amplitude of the incident field. Thus for  $\alpha$  large enough, the diffracted field at one edge will lie along a maximum of the diffraction by the previous edge, so that  $|H|$  can be greater than unity, as seen in Figure 3.

The pervasive behavior of the curves in Figure 3 is the fact that for  $\alpha \neq 0$  the field

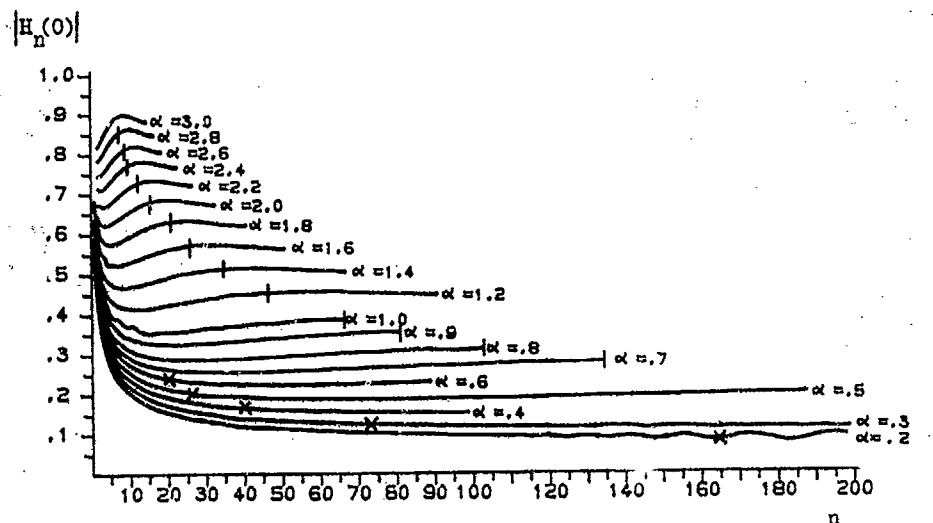


Figure 3. Variation of the field incident on the edges of the half screens as a function of screen number  $n$  for screen spacing  $d=50\lambda$  and various values of  $\alpha$ .

amplitude settles to a nearly constant value for  $n$  large enough. [Undulations for large  $n$  are thought to result for numerical error due to the use of too small an integration aperture.] The ratio  $Q(\alpha)$  of this settled field amplitude to the incident field amplitude gives the influence of the buildings on the roof top fields.

The angles  $\alpha$  of interest for cellular mobile radio are generally below  $20^\circ$ , so that settling involves diffraction past many half screens. Due to the long running time of the program for a large number of screens (several hours for one value of  $\alpha$  on a VAX computer), it is essential to have a good estimate of the number of screens that must be treated to find the settled value of the field. The settling process is illustrated in greater detail in Figure 4 for  $d/\lambda = 50$   $\alpha = 1.20^\circ$ .

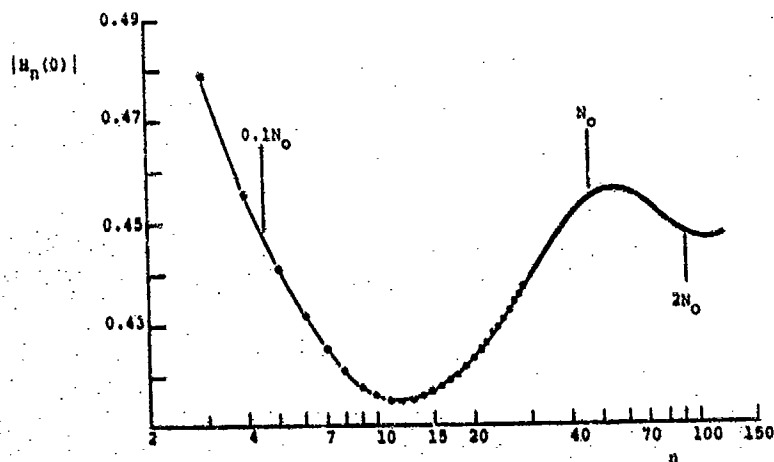


Figure 4. Settling behavior of the field incident on the edges of the half screens shown in expanded scale for  $d=50\lambda$  and  $\alpha = 1.20^\circ$ .

As  $n$  increases, the field in Figure 4 initially drops to a minimum, and gradually increases again, after which it oscillates with decreasing amplitude about the settled value  $Q(\alpha)$ . It is seen that the value of the field incident on the  $n=N_0$  screen is close to the maximum but still within  $2\%$  of the settled value. The value of the field incident

on an edge  $n = 0.1N_0$  is also within 2% of the settled value, and at all edges in between the field is within about 2% of the settled value. In other words, to within an accuracy better than 1db, the settled value is obtained after the abbreviated number of half screens  $0.1N_0$ . Thus for low angles  $\alpha$ , where the number of half screens  $N_0$  is beyond our computational capabilities, the settled value can be obtained from the much less time consuming calculation for  $0.1N_0$  half screens. In Figure 3 we have indicated  $N_0$  for each value of  $\alpha$  by the verticle stroke crossing the corresponding curve, while  $0.1N_0$  is indicated for some curves by cross. For many of the lower angles we have computed for  $n$  beyond  $0.1N_0$ , but not out to  $N_0$  itself.

Another significance of the abbreviated settlings number is that the number of rows of building that must be passed over to achieve the settled field is only  $0.1N_0$ , rather than  $N_0$ . For small angles, the distance  $N_0 d$  may be larger than the range  $R$  between fixed antenna and mobile. However, the distance  $0.1N_0$  is typically a fraction of  $R$ . For undulating terrain, the abbreviated settling distance gives the foreground that should be used to define the local slope at the mobile.

The value of the settled field, taken to be the value at  $N_0$  or at  $0.1N_0$ , is plotted in Figure 5 versus the parameter  $\alpha\sqrt{d/\lambda}$ , using logarithmic scales to make clear the power

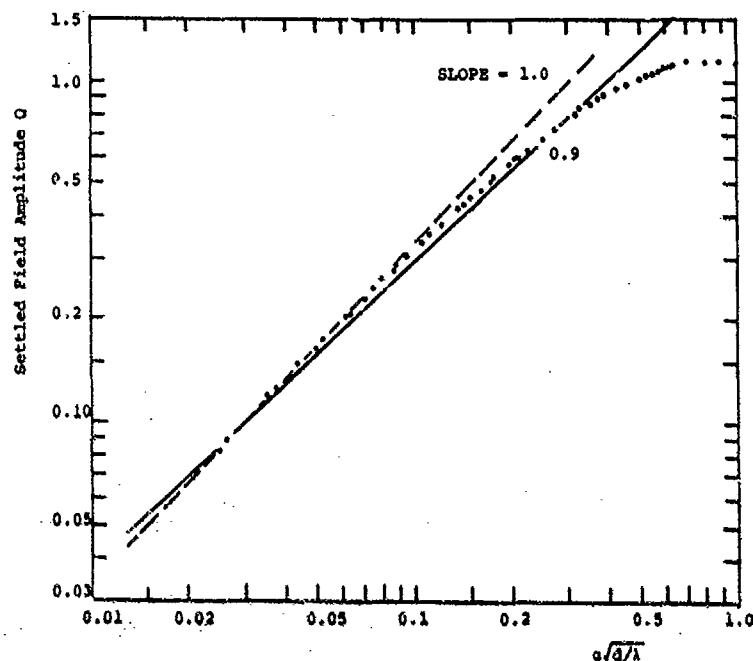


Figure 5. Dependence of the settled field  $Q$  on the parameter  $\alpha\sqrt{d/\lambda}$ . Solid line has slope 0.9, dashed line has slope 1.0.

law dependence. The series of points are the values of field taken from the calculations for various values of  $d/\lambda$ . These points lie along a curve having small curvature for  $\alpha\sqrt{d/\lambda} < 0.4$ . Between 0.4 and 1.0, the curvature is seen to be substantial. For  $\alpha\sqrt{d/\lambda} > 1$ ,  $N_0$  is unity and the settled field is found from diffraction past a single half screen.

Two straight lines are drawn through the point (0.1, 0.03). The dashed line has unity slope, and appears to be tangent to the curve (not drawn) defined by the points. However, for  $\alpha\sqrt{d/\lambda} > 0.15$  the straight line deviates from the points by more than 10%. The solid straight line has slope 0.9 and is seen to lie within 10% or 0.8dB of the curve defined by the points for  $\alpha\sqrt{d/\lambda}$  up to 0.4. If  $d=40m$ ,  $f=1$  GHz and  $0.10 < \alpha < 2.0$ , as is typical for cellular mobile radio, then  $\alpha\sqrt{d/\lambda}$  ranges from 0.02 to 0.4. As a result, the solid straight line may be used as a fit to the settled field, so that

$$Q = 0.1 \left[ \frac{\alpha\sqrt{d/\lambda}}{0.03} \right]^{0.9} \quad (4)$$

In Figure 1,  $\alpha=H/R$  which implies that  $Q$  of (4) varies as  $1/R^{0.9}$  for fixed  $H$ . This range variation is in addition to the  $1/R$  dependence of the spherical wave, so that the overall range dependence of the field is  $1/R^{1.9}$ . Thus received power will vary as  $1/R^{3.8}$ , which is in good agreement with many measurements [3,4,6]. In the limit as  $H/R \rightarrow 0$ ,  $Q$  is proportional to  $1/R$  giving the field variation of  $1/R^2$ , in agreement with the dependence found by Volger [15].



### III. Propagation Path Loss

The propagation model developed in the foregoing sections can be used to predict the average path loss between the elevated antenna and the mobile. Path loss consists of three factors: 1) the path loss between antennas in free space; 2) the reduction  $Q(\alpha)$  of the roof top fields due to settling; and 3) diffraction of the roof top fields down to ground level.

#### A. Path Loss Model

Not accounting for antenna gain, i.e., for isotropic antennas, the ratio of received power to transmitted power for antennas in free space is given by  $(\lambda/2\pi R)^2$ . Expressing this ratio in dB gives the free space path loss  $L_0$ . If  $f_c$  the frequency in MHz and  $R_k$  is the range in km, then

$$L_0 = 32.4 + 20 \log f_c + 20 \log R_k. \quad (5)$$

Equation (4) is used to find  $Q(\alpha)$ , and through the definition of  $\alpha$  it is possible to account for terrain slope at the mobile and for the earth's curvature, provided that  $R$  is not close to the radio horizon. For level terrain,  $\alpha$  in radians is given by

$$\alpha = \frac{H}{R} - \frac{R}{2R_e} \quad (6)$$

where  $R_e = 8.5 \times 10^3$  km is the effective earth radius.

Path loss associated with diffraction down to street level depends on the shape and construction of the buildings in the vicinity of the mobile. A simple approximation to this process for receiving antennas near street level is obtained by assuming diffraction to occur at the center of the row of buildings before the mobile. In this case the path loss is given by [19].

$$\frac{\sqrt{\lambda}}{2\pi} \frac{1}{\left[\left(\frac{d}{2}\right)^2 + (h-h_m)^2\right]^{3/4}} \left[ \frac{-1}{\gamma - \alpha} + \frac{1}{2\pi + \gamma - \alpha} \right] \quad (7)$$

where  $h$  is the height of the building before the mobile and  $h_m$  is height of the mobile antenna, as indicated in Figure 1. The angles  $\gamma$  and  $\alpha$  are in radians with

$$\gamma = \tan^{-1} [2(h-h_m)/d] \quad (8)$$

Expression (7) may be further simplified by neglecting  $1/(2\pi + \gamma - \alpha)$  as compared to  $1/(\gamma - \alpha)$ , and assuming that  $\alpha$  is small. Finally, to account for reflections from buildings, shown in Figure 1, and other sources of multipath, a factor of  $\sqrt{2}$  is included to arrive at the average field.

Combining (4), (6)-(8), and including the factor  $\sqrt{2}$ , we obtain an expression for the reduction of the field over that experienced by the same antennas separated by a distance  $R$  in free space. When expressed in dB, this expression is the excess path loss  $L_{ex}$ , and is given by

$$L_{ex} = 63.1 + \log f_c + A - 18 \log H + 18 \log R_k - 18 \log \left[ \frac{R_k^2}{1 - 17H} \right] \quad (9)$$

The last term in (26) accounts for the curvature of the earth, while the term

$$A = 5 \log \left[ \left(\frac{d}{2}\right)^2 + (h-h_m)^2 \right] - 9 \log d + 20 \log \left[ \tan^{-1} [2(h-h_m)/d] \right] \quad (10)$$

results from diffraction down from the roof tops.

The overall path loss  $L_p$  is found by adding  $L_{ex}$  to the free space path loss  $L_0$  for isotropic antennas. Received signal strength can be found by subtracting  $L_p$  from the radiated power plus antenna gains, expressed in dB.

#### B. Comparison With Measurements

Measurements of average received signal were made in Philadelphia by Ott and Plitkins [14]. Six fixed antenna locations were used with antenna heights ranging between 45 and 235 feet above the curb. The measurements were carried out at 820 MHz with radiated power and antenna gains totaling 23.3 dB. The maximum building height in the vicinity of the mobile locations was reported to be 30 feet. For calculations we have assumed an average building height of 25 feet in determining the transmitter height  $H$  above the roof tops. The height of the mobile antenna was 5 feet, or about 1.5m, and the separation

between rows was taken to be  $d=40\text{m}$ . Finally, the earth's curvature was ignored in expression (9).

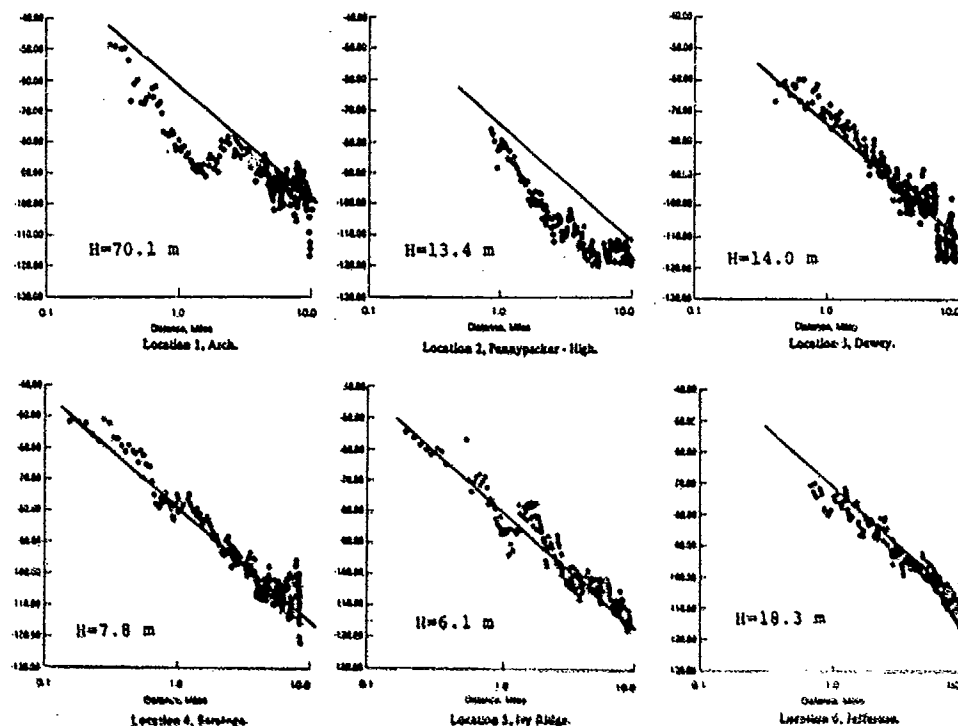


Figure 6. Comparison of sector-averaged signal strength for various transmitter sites, as measured by Ott and Plickins (4), with theoretical predictions (solid lines). Signal level is in dBm, the range is in miles, and the value of  $H$  is indicated in meters.

Figure 6 reproduces the measurements of reference (4) for the six locations. The dots represent sector averages of the received signal level in dBm plotted as a function of range in miles from the transmitter. Transmitter height above the assumed roof top level is indicated for each site. Superimposed on the data we have drawn a straight line representing the received signal predicted by our theory.

The first two sites are located near down-town Philadelphia, whose tall buildings may be responsible for the reduction in the signal below the predicted values. The remaining four sites are away from the down town region. For these sites the average has range dependence that is in good agreement with our theory. Combining the data for sites 2-6, Ott and Plickins obtain a range dependence of  $36.8\text{ dB}$  per decade, as compared to the  $36\text{ dB}$  per decade given by our model.

An alternative way of comparing theory with measurements is to plot excess attenuation as a function of the angle of incidence  $\alpha$  given by (6). Okumura et al (1) have measured path loss for various frequencies and antenna heights. We have subtracted the free space path loss  $L_0$  of (3) from their measurements and used (6) to convert range into angle. The resulting plots of excess attenuation versus  $\alpha$  are shown as the broken curves in Figures 7(a) - (c) for antenna heights between 30 and 140m. In Figure 7(a), data for  $f_c=1317$  and  $1430\text{ MHz}$  have been superimposed, while Figure 7(b) is for  $f_c = 922\text{ MHz}$ . Data at  $433\text{ MHz}$  for heights 30, 45 and 60m deviate by less than  $1\text{ dB}$  from the single curve used to plot them in Figure 7(c).

When excess loss is plotted versus  $\alpha$ , antennas 140 and 30-60m high are seen to have the same excess loss, to within  $3\text{ dB}$ . This agreement supports the assumption that excess path loss is a function of  $\alpha$ , rather than of  $R$  and  $H$  separately. The observed variation of excess path loss with  $H$  for a given  $\alpha$  may be due to the fact that since  $R \propto H$ , the measurements were made in different portions of Tokyo.

The solid curves in Figure 7 represent excess path loss computed from our model.

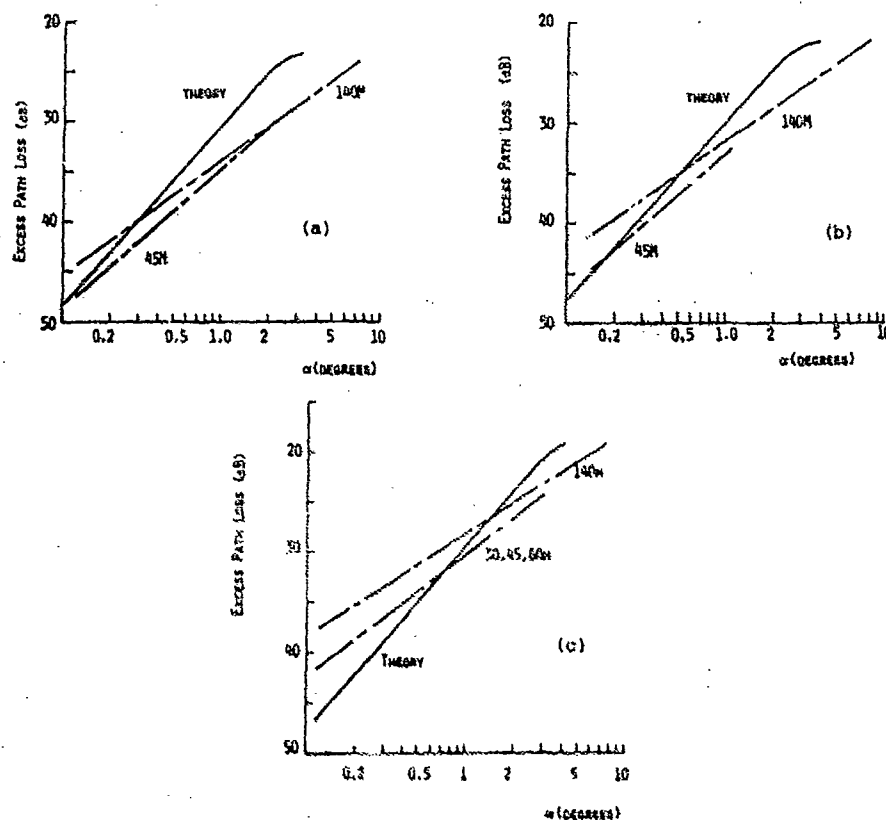


Figure 7. Comparison of excess path loss from measurements by Okumura, et al (1) with theoretical predictions for: a)  $f_c = 1,117$  and  $1,430$  MHz; b)  $f_c = 922$  MHz; and c)  $f_c = 453$  MHz. The broken curves are based on measurements for the fixed antenna heights indicated, and the solid curve is from the theory.

Bending of these curves for larger values of  $\alpha$  results from the fact that the simple approximation (4) is not valid for  $Q(\alpha)$ , and it is necessary to resort to values of  $Q$  taken from Figure 5 in the region where curvature is significant. The computations have been made assuming  $h_b = 3m$ , which is the value used in making the measurements. We have also assumed that  $d = 33m$  and building height  $h = 12m$ .

The predicted excess loss for  $f_c = 1400$  MHz is seen from Figure 7(a) to be within about 5dB of the measured value over the range of  $\alpha$  shown. At  $f_c = 922$  MHz the agreement is about 4dB, as seen from Figure 7(b). However, at 453 MHz the deviation is seen from Figure 7(c) to be greater than 5dB for a high antenna and low  $\alpha$ . The primary disagreement is the difference in slope between the measurements curve and the model.

#### IV. Conclusion

A theoretical model of UHF propagation in urban environments has been developed to predict the range dependence of the average signal strength, and is found to be in good agreement with measurements. The model shows how the building height and separation influences signal strength. Because the excess attenuation is found to depend on  $W$  and  $R$  only through the glancing angle  $\alpha$ , variations of ground elevation and slope can be accounted for through the definition of  $\alpha$ . When finding the local tangent to the terrain, one need only take into account the terrain in the abbreviated settling distance  $0.1 N_{0.5}$  in front of the mobile.

#### References

1. Y. Okumura, E. Ohmori, T. Kawano and K. Fukuda, "Field strength and its Variability in UHF and Land-Mobile Radio Service", Review of the Electrical Communications Laboratory, 16, (1964) pp. 825-873.

2. M.Hata, "Empirical Formula for Propagation Loss in Land Mobile Radio Services", IEEE Trans., VT-29, (1980), pp.317-325.
3. R.K.Kelly, "Flat Suburban Area Propagation at 820 MHz", IEEE Trans. VT-27, (1978), pp. 198-204.
4. G.D.Ott and A.Plitkina, "Urban Path-Loss Characteristics at 820 MHz", IEEE Trans., VT-27, (1978), pp. 189-197.
5. V.Graziano, "Propagation Correlations at 900 MHz", IEEE Trans., VT-27, (1978), pp. 182-189.
6. M.Allsebrook and J.D.Parson, "Mobile Radio Propagation in British Cities at Frequencies in the VHF and UHF Bands", IEEE Trans., VT-26, (1977), pp 313-322.
7. A.P. Borgia, "Determination of Service Area for VHF/UHF Land Mobile and Broadcast Operations Over Irregular Terrain", IEEE Trans, VT-22, (1973), pp. 21-29.
8. S.Kozono and R.Watanabe, "Influence of Environmental Buildings on UHF Land Mobile Radio Propagation". IEEE Trans, COM-25, (1977) pp. 1133-1145.
9. F.Ikegami and S.Yoshida, "Analysis of Multipath Propagation Structure in Urban Mobile Radio Environments", IEEE Trans. AP-28 (1980), pp. 531-537.
10. F.Ikegami, S.Yoshida, T.Takeuchi and M.Umehira "Propagation Factors Controlling Mean Field Strength on Urban Streets", IEEE Trans , AP-32, (1984), pp. 822-829.
11. W.C.Leo, "Studies of Base-Station Antenna Height Effects on Mobile Radio", IEEE Trans., VT-29, (1980), pp. 252-260.
12. R.S.Kirby, H.T.Dougherty and P.L.McQuate, "Obstacle Gain Measurements Over Pikes Peak at 60 to 1,046 Mc", Proc. IRE, 43, (1955), pp. 1467-1472.
13. G.Millington, E.Hewitt and F.S.Immirzi, "Double Knife-Edge Diffraction in Field Strength Predictions", Proc. IEEE Monograph No. 507E, (1962), pp. 419-429.
14. J.Beygout, "Multiple Knife-Edge Diffraction of Microwaves", IEEE Trans., AP-14, (1966), pp. 480-489.
15. L.E.Vogler, "The Attenuation of Electromagnetic Waves by Multiple Knife-Edge Diffraction", U.S. Dept. of Commerce NTIA Report 91-96, (1941).
16. M.Born and E.Wolf, Principles of Optics, Second Ed. Pergamon Press, New York, (1964), pp. 171-182.
17. J.Walfish and R.L.Bertoni, "Diffraction of Plane Waves Past a Series of Absorbing Half-Screens", 1986 National Radio Science Meeting, Philadelphia, June 1986.
18. R.L.Bertoni, L.O.Felsen and A.Hessel, "Local Properties of radiation in Lossy Media", IEEE Trans., AP-19, (1971), pp. 226-237.

## DISCUSSION

**J.H. Whitteker**

Two questions:

- (1) Could you explain how it is that the field settles down to a constant value in spite of the fact that the diffracting screens continue to remove energy from the wave?
- (2) If houses are arranged in straight rows, the distance from one row to the next in the radial direction will depend on azimuth. Does this result in a field strength that varies with azimuth as well as distance?

**Author's Reply**

- (1) Because we are treating the case of a plane wave incident from above the away of edges, the incident wave brings energy down to the edges to replenish that scattered and absorbed by the screens. At the settling point and beyond, an equilibrium is established between the incident energy and that removed by the screens.
- (2) For oblique propagation over rows, the solution can be obtained by replacing the wavelength  $\lambda$  by  $\lambda/\cos \psi$ , where  $\psi$  is the angle between the plane of incidence and normal to the rows (screens). Since  $\lambda$  enters as a square root, the effect is not strong. We have not examined the implications of this dependence.

**J.S. Belrose**

Mr Bertoni presented a theoretical model for predicting UHF path loss where the geometry was such that the propagation path was across streets perpendicular to the path. He commented that a cosine factor would have to be taken into account for other propagation directions.

In the orthogonal direction the propagation mode is radically different from diffraction down into and multiple reflections from buildings on both sides of the street. The waves can be trapped or channelled down the street.

The signal amplitudes, the correlation distances and the amplitude probability distributions are quite different in those situations. In the geometry Dr Bertoni analysed, the signal correlation distance is so short that a so-called gain antenna at 800 MHz, a half-wave which has a gain 4dB over a quarter wave, can exhibit no gain at all (0dB over a quarter wave). There is clearly a need to extend the model for other geometries.

**Author's Reply**

Many measurements have shown significant differences for signal strength along streets aligned with the transmitter, as opposed to streets at an angle to the transmission direction. However, for a transmitter located in an urban environment, only a few streets are oriented in the direction of the transmitter. At street level in the vicinity of buildings it is rarely possible to see the transmitter.

Dr Belrose is correct in that the city is complex and the theory needs to be extended to cover different geometrical conditions.

AD-P005 739

9-1

# A PROGRAM FOR THE CALCULATION OF RADIO-WAVE TRANSMISSION LOSS OVER THE SPHERICAL EARTH AND OVER OBSTACLES

by

Michel Ranger, Jean-Louis Régnier  
Marc Andreu, Yves Le Pape  
translated by Margaret A. Hanson  
CELAR (Division ITES)  
35170 Bruz, France

The Centre d'Electronique de l'Armement (CELAR), located near Rennes, Ile et Vilaine (FRANCE) has created a new computer program to evaluate the radioelectric wave propagation loss around the earth in the frequency range of 30 - 40 MHz up to 10 - 12 GHz. The name of this program is CARDIF.

## CONTENTS

1. Why this program ?
2. The CARDIF Program
  - 2.1 Theoretical bases
  - 2.2 Intervening physical phenomena
  - 2.3 Parameters of program entry
  - 2.4 Earth Surface Representation
  - 2.5 Use of Deygout's Method
  - 2.6 Use of Boudouris' Method
  - 2.7 Summation of the two methods
3. Adjustment of the CARDIF Program
  - 3.1 Adjustment relative to existing programs
  - 3.2 Adjustment relative to measurements
4. Conclusion

## Bibliography

Appendix I : Results of comparisons between CARLOS and GRWAVE

Appendix II : Results for different terrains

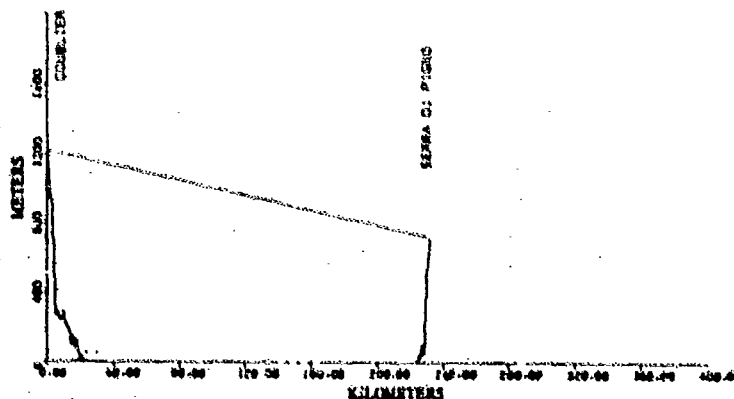
## 1. WHY THIS PROGRAM ?

The calculation of radioelectric wave propagation loss is at the heart of all modern study concerning the diffraction and conception of telecommunication systems be it radio support, radio link or satellite communication.

Furthermore, the present multiplicity of such systems - civil as well as military, fixed or mobile - along with an increasing limit of authorized frequential space, makes it necessary to consider from the outset of the study all problems related to the electromagnetic compatibility studied as compared to existing systems on the terrain.

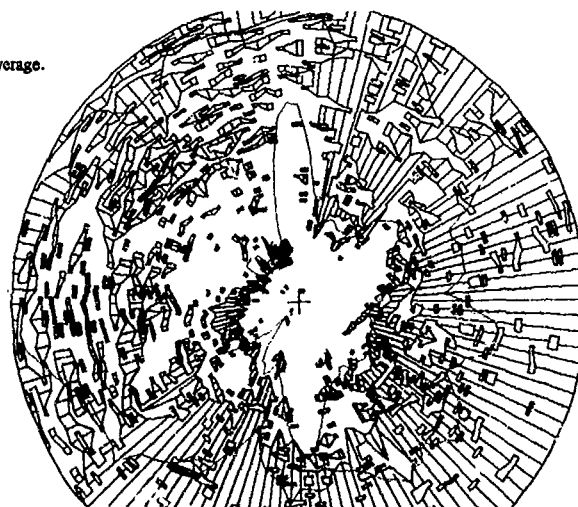
Due to such «systems» needs, CELAR was led to develop the following kinds of tools for this study :

- those for point to point links, with representation of terrain cross-section.



Editor's Note:  
The original figures used in the preparation of this paper were in colour but are not suitable for reproduction in that form and have therefore been printed in black in this publication.

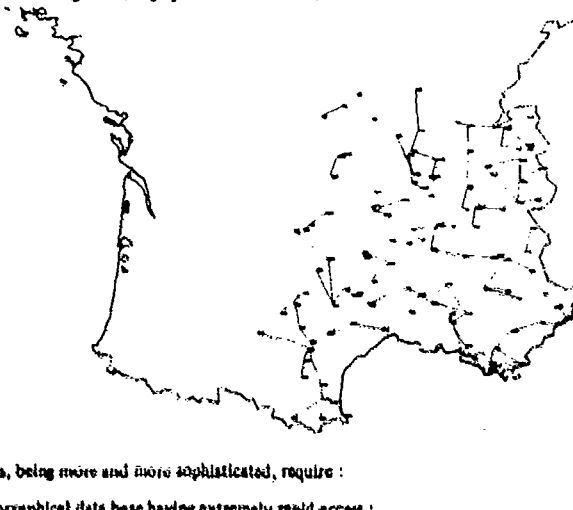
— those for radioelectrical coverage.



radioelectrical coverage  
around a transmitter.

NB : The plot of this kind of zone requires around 12,000 iterations of the propagation loss calculation program.

— those for defining hertzian graphs and interference risks



Colors are used to classify the qualities  
of the different calculated hertzian links.

Such tools, being more and more sophisticated, require :

- 1) a topographical data base having extremely rapid access :

CELAR now possesses an «altimetric» data base on magnetic disk which has an interval of 12" x 9" (280 m x 260 m). The information is extracted by administering a graded data base. This base is taken directly from a national file of topographical data bases on the GMEDTN standard (Groupe Multinational d'Echange de Données de Topographie Numérique) and implemented in France at an interval of 3" x 3" following agreement by the Institut Géographique National (IGN) and The Délégation Générale pour l'Armement (DGA).

- 2) Different models for evaluating radioelectric propagation loss :

These models can be of the following nature :

- **determinist** : the terrain is then precisely known and after a somewhat lengthy computation time, these models give the propagation loss in dB for the link under study. For a given area, this loss can be valid for 50%, 90% or 99% of the time.
- **statistical** : these models which are somewhat sophisticated and thus rather rapid in execution, give results with a confidence degree (average error value, variance, ...) related to the characteristics of the terrain (flat, hilly...).

During the five years that these studies have been carried out, CELAR was led to conceive and put into effect a new determinist model. This model, known as CARDIF (Calcul d'Affaiblissement Radioélectrique par Diffraction), has an average computation time of 50 ms (including terrain cross-section) and will be better adapted than existing programs to needs in the range of 10 - 40 MHz - 10 - 12 GHz.

## 2. THE CARDIF PROGRAM

### 2.1 Theoretical bases

Maxwell's equations lead to the equation of wave propagation, which is expressed as :

$$\Delta \vec{\pi} + k^2 \vec{\pi} = \frac{\vec{J}_0}{j 2 \pi \epsilon f} \quad (1)$$

$\vec{\pi}$  is called the hertzian vector and is linked to the electric potential  $V$  and to the vector  $\vec{A}$  potential by the following equations :

$$\vec{A} = \frac{d \vec{\pi}}{dt} \quad (2)$$

$$V = - \text{div} \vec{\pi} \quad (3)$$

Knowledge of the  $\vec{\pi}$  vector enables us to reconstitute the entire wave structure. Wave determination at transmission and reception allows us to establish the path's transmission loss.

In Formula 1, the density of current  $\vec{J}_0$  (no density outside the antenna), the wave vector module  $\|\vec{k}\| = k$  and the constant dielectrical complex  $\epsilon = \epsilon_0 \epsilon_r$  intervene as well,

$$\text{where } \epsilon_r = \epsilon_{r1} + j 60 \sigma \frac{c}{f}$$

$$\text{and the ratio } R = \frac{\text{Im}(\epsilon_r)}{\text{Re}(\epsilon_r)} = \frac{60 \sigma \lambda}{\epsilon_{r1}}$$

This ratio is characteristic of the area in which the wave is propagated :

If  $R \gg 1$  the area is conductive

If  $R \ll 1$  the area is dielectrical

Wave reflection and absorption thus depend on the nature of the ground.

The solution of Equation 1 is an integral and rarely applicable except in special cases :

- where the earth is smooth and flat
- where the earth is smooth and spherical.

CARDIF is the outcome of Equation 1 in these special cases.

If the theory is well-backed up for all problems of diffraction, reflection and absorption by the ground, there is nevertheless no general theory concerning diffraction problems on the earth's relief for somewhat complex forms. A new approach has therefore been adapted which uses Fresnel's ellipsoid concept. This ellipsoid corresponds to an ellipse in the cross-section plan ; if the ellipse is not engaged in the ground, there will be no diffraction by the ground, and the different phenomena such as reflection, atmospheric refraction and absorption can be isolated. In the opposite case, we must consider diffraction on the ground or on obstacles. Deygout's method is used for diffraction on obstacles.

### 2.2 Intervening physical phenomena

This new program takes the following physical phenomena into account :

- tropospheric refraction : the atmosphere is viewed as a sphere with a vertical gradient of refraction index  $\left(\frac{3 N}{2 h}\right)$  which is constant and equal to  $-29 \text{ uN/km}$ .
- diffraction on smooth and spherical earth : the mathematical developments of this phenomenon are presented in the works of Boudouris [2] and Boithis [1].
- reflection on smooth, flat or spherical earth : a two-ray model in the cross-section plan explains this phenomenon for «weak» distances. The curvature of the earth can be integrated into the program with the aid of a coefficient of spherical reflection.
- diffraction on obstacles : Deygout's method, presented in 1966 [4], is rapidly and originally programmed in this model.



### 2.3 Parameters of program entry

$\epsilon, \sigma$  dielectrical permittivity and conductivity of the area

$h_e, h_r$  aerial heights

$f$  frequency

IPOL wave polarisation

transmitter position, receiver position

CARDIF does not take random phenomena into account, such as :

- scintillation
- multiple atmospheric paths
- existence of atmospheric conducts.

It determines an average loss in time starting with an average value  $\frac{\partial N}{\partial h}$  equal to  $-39 \text{ uN/km}$ . This value applies to temperate climates. The preceding random phenomena for calculation of losses for percentages of given time, will be the subject of subsequent statistical studies.

### 2.4 Earth Surface Representation

#### A. Use of a Topographical Data Base (TDB)

To determine the relief between the transmitter and the receiver, a cross-section of terrain is extracted by following the direct geodesical path between these two points. This geodesic is calculated by a simple algorithm using a spherical representation of the earth.

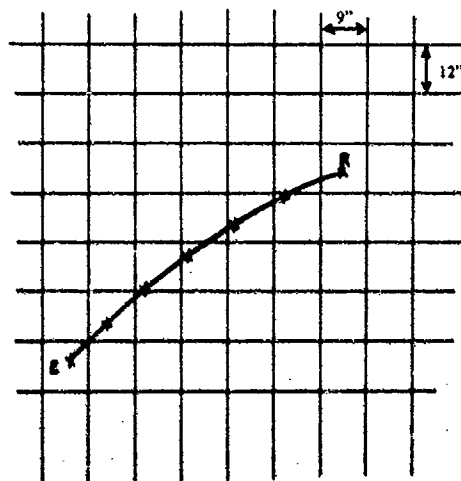


fig. Geodesic on the 12" x 9" grid

The geodesic is studied at a constant distance of 12"x9". The precision with which the points are adjusted is greater than 50 m for distances less than 400 km.

The altitude of each point is obtained by interpolating the values of the four nearest nodes of the network.

Use of this kind of data base in telecommunications brings up three points :

- the positions of the transmitter and receiver ought to be known with a precision greater than 100 m so that the cross-section of terrain is compatible with the precision of the geodesic and the TDB grid.
- the actual altitude should also be verified because it can differ considerably from the one obtained by the TDB, especially on an extremal point (generally a high point).
- vegetation or urbanization is not represented. As opposed to the altitude, this deals with data changing in time. The insertion of these factors will most likely constitute a future data base (TDB adapted for Telecommunications Science). Their importance for the user depends on the desired goal :
  - minimum loss for a coverage diagram,
  - maximum loss for a coordination diagram,
  - average loss for a fixed link.

### B. The earth's atmosphere taken into account

The influence of the earth's atmosphere on radioelectric propagation is expressed by a curvature of the rays' path, which is linked to the refractive index  $n$  or to the coindex  $N = 10^6 (n - 1)$ . The rays can be described as a straight line if one introduces a fictive earth radius connected to the gradient  $\frac{\partial N}{\partial h}$  by the relation

$$R = k R_0$$

$$\text{where } k = \frac{1}{1 + R_0 \frac{\partial N}{\partial h}}$$

Here  $R_0$  stands for the actual earth radius.

NB: If  $\frac{\partial N}{\partial h} = -39 \mu\text{N/km}$ , then  $k = 4/3$  and  $R = 8500 \text{ km}$ .

Thus, the altitude on the transmitter-receiver path ought to be modified by raising each point a value, the value representing the roundness. This follows a parabolic formula which is very adequate for the distances considered.

The actual altitude  $h_i$  is replaced by :

$$h'_i = h_i + \frac{X_i (D - X_i)}{2 R}$$

where  $D$  = transmitter-receiver distance  
 $R$  = modified earth radius  
 $X_i$  = distance from point  $i$  to the transmitter

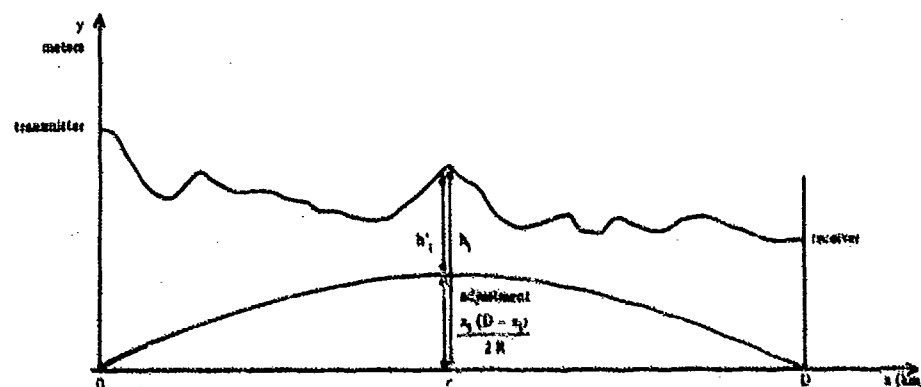
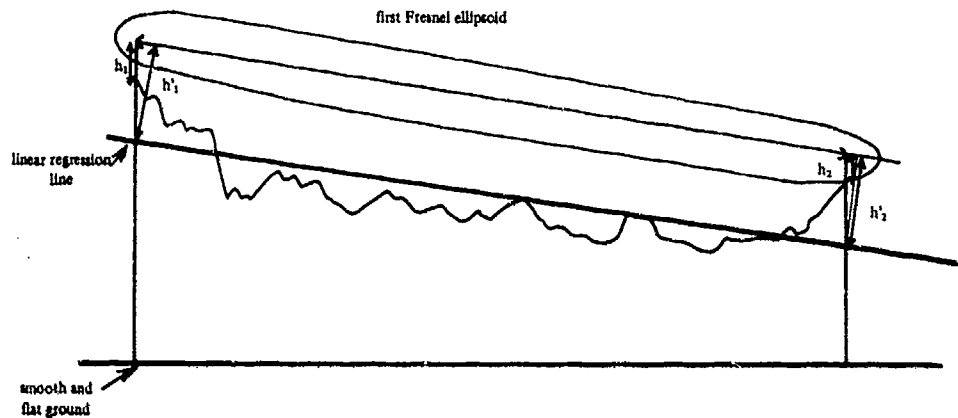


fig. Altitudinal adjustment due to roundness

### C. Representation of actual relief by Boudouris' smooth earth model

Boudouris' theory is used for smooth and spherical earth. The following approach has been adapted for using this model in instances where there is no significant obstacle penetrating Fresnel's first ellipsoid.

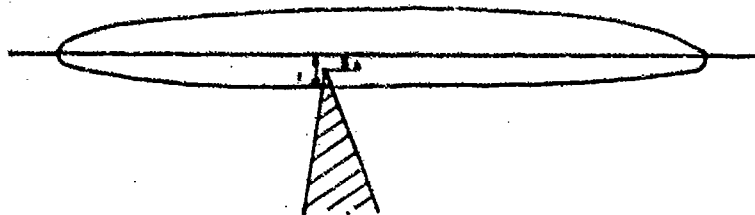


The parameters  $h_1$  and  $h_2$  are the actual antenna heights. The goal is to find a plan that best represents the profile link. To do this a regression is carried out on 80% of the points on the profile between the transmitter and the receiver. The equivalent smooth model plan will thus take the aerial heights  $h'_1$  and  $h'_2$  into account, which are referenced to this plan. By proceeding this way, an antenna having an actual height of  $h_1$  situated on a peak is transformed into a height  $h'_1 > h_1$  above the smooth ground plan.

### 2.5 Use of Deygout's method

A program of Deygout's algorithm formed by the National Research Center of Telecommunications at Lannion (CNET LAB/MER : Dr Meyer) in collaboration with the University of Upper Brittany - Rennes (UNB : Prof. Pihan) served as reference.

The obstacles caught in Fresnel's ellipse are sorted out according to an increasing obstruction (the parameter  $h/r$ , algebraically counted by comparison to the ellipse axis, is maximum).



The most penetrating obstacle is thus the principal obstacle here, and from this point secondary, tertiary, etc. obstacles are constructed.

Each obstacle is then approximated by a knife edge obstacle and the loss compared to free space is shown by :

$$\alpha_{dB} = 6.4 + 20 \log \left[ \sqrt{2 \left( \frac{h}{r} \right)^2 + 1} + 1.4 \left( \frac{h}{r} \right) \right], \text{ formula of absorption by an obstacle.}$$

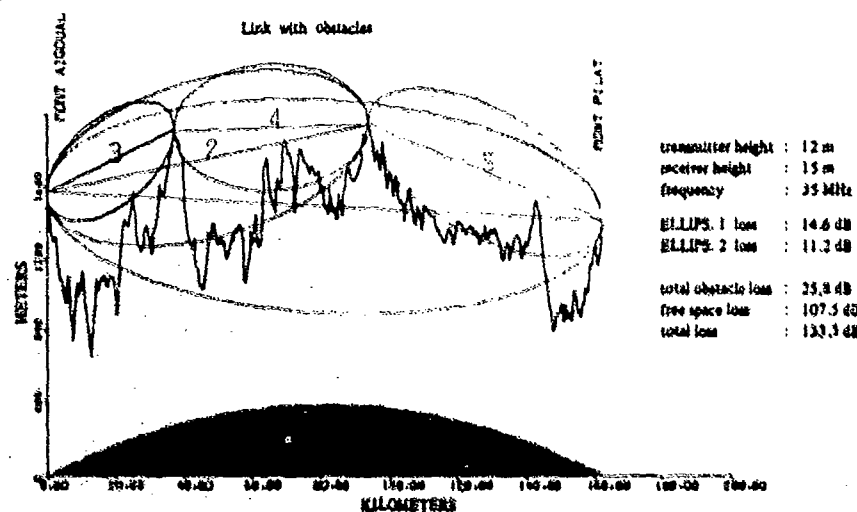
If  $N$  stands for the number of identified obstacles in the preceding method, the total diffraction loss caused by obstacle diffraction is shown by

$$\alpha_{dB} = \sum_{i=1}^{i=N} \alpha_{i,dB}$$

This method requires the following remarks :

- Fresnel's ellipsoid is reduced to a simple ellipse in the cross-section plan. This is justified because the dimensions of the ellipsoid are weak considering the sampling step of the TDB.
- the obstacle, whatever its form may be at the peak is reduced to a knife edge obstacle ; considering a rounded obstacle would lead to a longer computation time.
- the approximations (not the acquisition of terrain) create imprecisions.
- a value  $\left( \frac{h}{r} \right)_{min}$  is introduced, which determines the presence or absence of an obstacle.
- a parameter fixes the maximum number of obstacles.

For the last two points, subsequent measurements and diffusion of the program to a large number of users will permit us to improve parameter values.



## 2.6 Use of Boudouris' method

The calculations conducted by Poincaré to determine the field created by wave diffraction on the earth and followed up by Watson, Van der Pol and others, lead to a series that converges too slowly. New approximations introduced from the beginning of calculations lead to a solution that can be applied directly. Boudouris synthesized the work conducted on this subject to make a practical application of it possible. To this end, the wave is separated into two terms :

$$\vec{E} = \vec{E}_{space} + \vec{E}_{surface}$$

The space wave stands for the sum of the wave propagated in free space and of the wave reflected by the ground. The surface wave stands for the wave diffracted on the ground.

By some simple considerations on aerial heights he managed to isolate those cases where only the space wave exist and those where only the ground wave interference.

Under these circumstances, the discriminant parameter is the numerical height of antenna  $q$  :

$$q = \frac{2\pi h}{\lambda_0} \left| \sqrt{\frac{e'_r - \cos^2 \psi_1}{e'_r}} \right| \quad \text{where } e'_r = e_r + j 60 \sigma \lambda$$

This parameter is dimensionless and quantitatively measures the ratio  $\frac{\text{antenna height}}{\text{wave length}}$  while keeping in mind electrical characteristics of the ground ( $e, \sigma$ ).

In the same way, the distance between two aerials is counted in wave lengths, and is called the numerical distance.

$$P = \| \vec{P} \| = \frac{\pi d}{\lambda (1 + e_r)} \sin \left[ 2 \operatorname{Arctg} \frac{e_r}{60 \sigma \lambda} - \operatorname{Arctg} \frac{e_r - 1}{60 \sigma \lambda} \right]$$

Approximations arising from various values of numerical height helps us to identify some simple formulas that allow for rapid calculation by approximating residue series.

CARDIF applies these results. However, by replacing most of the charts presented by Boudouris with numerical solutions, we were able to improve calculation precision and certain parameter validity ranges considerably.

## 2.7 A well-balanced summation of the two methods

Deygout's algorithm treats situations where knife edge obstacles penetrate Fresnel's first ellipsoide.

Boudouris' algorithm treats wave diffraction on smooth and spherical earth.

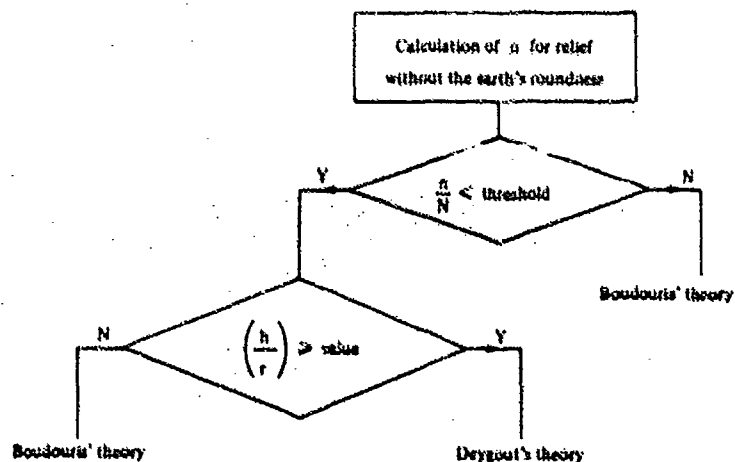
Each of these theories needs to be considered in most of the cases where propagation loss is evaluated. Combining them sensibly is thus of great importance in order to obtain a correct and global evaluation. Numerous adjustments will allow us to carry out a well-balanced summation of the two methods. The coefficients of ponderation can depend on the frequency ( $f$ ), the distance ( $d$ )... For the time being, the following approach has been adopted :

$n$  is the number of profile points seen simultaneously by the transmitter and the receiver.

If  $N$  is the total number of profile points, the relation  $\frac{n}{N}$  characterizes the nature of the relief on the path.

Thus  $\frac{n}{N} \rightarrow 1$  for a flat profile, and  $\frac{n}{N} \rightarrow 0$  for an uneven profile

This results in the following organigram :



N.B.  $\text{value}$  and  $\text{threshold}$  are two parameters to be adjusted by measurements. The notion of visible and invisible points eliminates the risk of confusing the spherical earth with an obstacle for sufficiently long distances (relative to aerial heights) above a flat terrain or in a sea path.

### 3. ADJUSTMENT OF THE CARDIF PROGRAM

#### 3.1 Adjustments relative to existing programs

CELAR has two programs permitting comparisons with the results of CARDIF :

- GRWAVE (Ground Wave) originates from Marconi Laboratories and was conceived by Dr Rotheram and his team. GRWAVE is the result of research done on a residue series analogous to that done by Van der Pol. The validity range announced for this program is in the area of [10 kHz ; a few GHz] but its computation time remains high. This program takes into account an exponential atmosphere, but a parametric study on the refractive index  $n$  showed that it was possible to compare the results with CARDIF (spherical atmosphere).
- WAGNER comes from the Research Center at Boulder (Colorado). WAGNER integrates the spherical earth and relief at the same time, but presents the following limitations :
  - prohibitive computation time
  - a restricted frequency range ( $f \leq$  a few MHz) due to required sampling step.

Results of comparisons between CARDIF and GRWAVE are presented in appendix I.

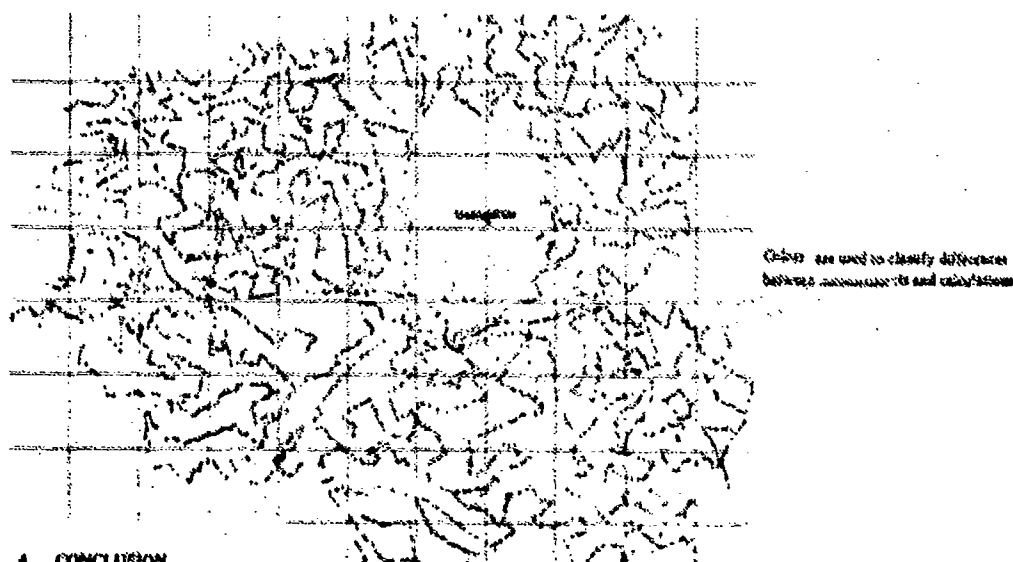
#### 3.2 Adjustment relative to measurements

In the framework of national exchanges, CELAR assembles multiple results on measurements (land, sea...). The measurements, whether obtained automatically or not, give the following conclusions for different frequency ranges (40 MHz, 70 - 80 MHz, 160 MHz, 400 MHz, 900 MHz...):

- certainty that programming of both algorithms is coherent and got worked enough while considering the multiple cases encountered.
- adjustment of parameters where there is doubt today ( $\frac{h}{r}$ /min, threshold, ...).
- a well-balanced summation of the two algorithms used in the CARDIF program (Dygonet and Boudouris) by minimizing the differences between CARDIF and the measurement.

The first results are very encouraging and are presented for different frequencies and terrains in appendix II.

Comparisons between measurements and theoretical calculations :



### 4. CONCLUSION

The creation of CARDIF is essentially the fruit of an excellent collaboration between various national organizations such as CNET, CEA, the Ministry of Equipment, UHB and EDF. Moreover, it demonstrates the absolute necessity for exchanges and collaboration between designers and experimenters, while also taking into consideration required expenses and investments. There is no doubt that collaboration will allow us to go even further in statistical studies of such effects as :

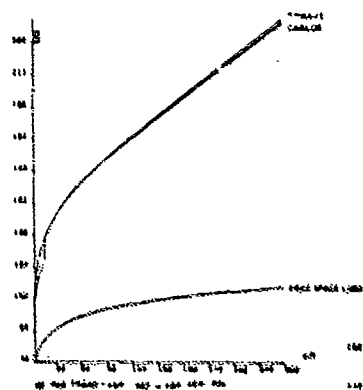
- influence of certain types of vegetation and urban zones represented in the telecommunications data base,
- random phenomena

## BIBLIOGRAPHY

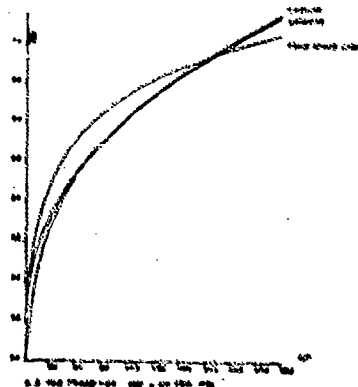
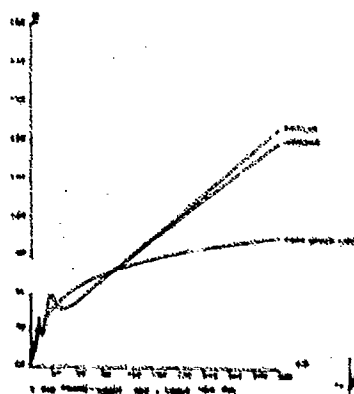
- |  |                           |
|--|---------------------------|
| 1 - Radioelectric wave propagation in the earth's environment  | Lucien Boithias - 1983    |
| 2 - Tropospheric wave propagation  | G. Boudouris -            |
| 3 - Radioelectric wave propagation / sections 1 and 2  | J.-C. Pellissolo - 1970   |
| 4 - Multiple knife edge diffraction of microwaves -<br>IEEE transactions, Volume AP - 14, n° 4, pages 480 et suivantes | J. Deygout - Juillet 1966 |
| 5 - Notices and reports by CCIR, volume V, propagation in nonionized areas   | 1978                      |
| 6 - Telecommunications by hertzian beam  | M. Mathieu - 1979         |
| 7 - Tropospheric propagation and transhorizon wireless beams   | F. du Castel - 1961       |

## APPENDIX I: RADIOELECTRICAL LOSS OVER A SMOOTH AND SPHERICAL EARTH

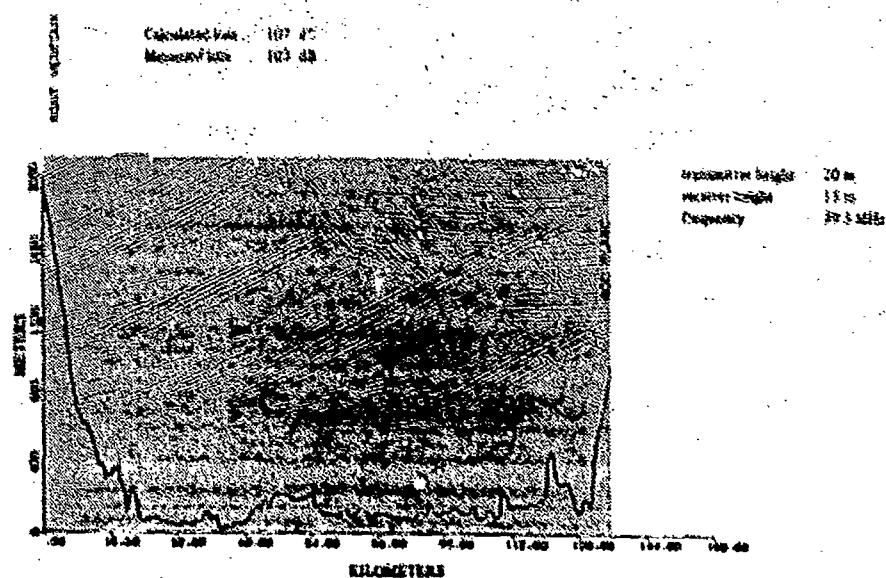
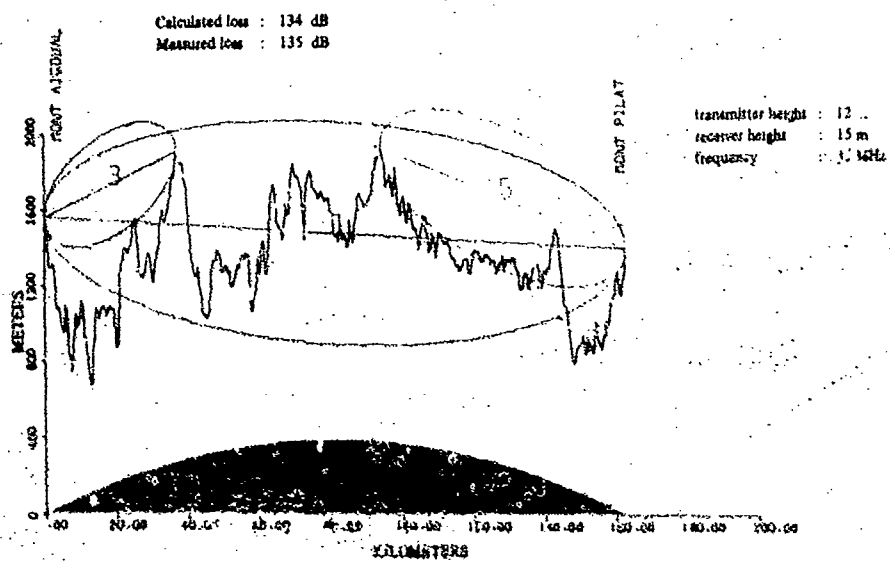
## RESULTS OF COMPARISONS BETWEEN CARLOS AND GRWAVE



\* CARLOS, developed by CELAR, is the program name of Boudouris' algorithm.



## APPENDIX II : COMPARISON BETWEEN THEORETICAL CALCULATIONS AND MEASUREMENTS



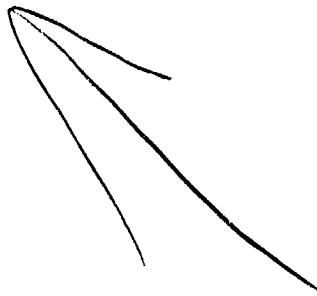


## DISCUSSION

**H.Kuschel**

There exists a data base including surface structure information, the DLMS (= digital landmass system), which has a resolution of about 1/10 of a geographic second for man-made obstacles, like buildings and power lines, and for forests.

I suppose you did compare your theoretical model to that of A.G.Longley and P.L.Rice, who developed the "Transmission loss prediction model for tropospheric radio links" in 1967 based on the same theoretical considerations of Bremmer, van der Pol, Norton, Fresnel et al.?



AD-P005 740

10-1

# CORRECTING RAY FIELD FAILURES CAUSED BY FOCUSING IN AN INHOMOGENEOUS DUCT: A CRITICAL LOOK AT THE GAUSSIAN BEAM METHOD

by

E. Niver, M.S. Vogan, C.J. Ruiz  
Department of Electrical Engineering,  
New Jersey Institute of Technology,  
Newark, New Jersey 07102 USA

and

L.B. Felsen  
Department of Electrical Engineering/Computer Science  
Weber Research Institute,  
Polytechnic University,  
Farmingdale, New York 11735 USA

## SUMMARY

Ducting due to an inhomogeneous refractive index profile affects the propagation of electromagnetic signals in various regions of the earth's environment. At high frequencies ray methods afford a versatile, and numerically easily implementable, method for predicting the field at the receiver. However, when ducting occurs, multiple refractions of the confined rays cause field enhancement due to focusing, and when there is an abrupt change in the ducting profile, critically incident and glancing rays cause diffraction and shadowing. The ray algorithm fails in these transition regions. To repair these deficiencies, one may eliminate the troublesome ray fields and fill the spatial spectral interval vacated thereby with guided modes and remainder fields. This technique has previously been incorporated in a hybrid ray-mode theory, which accomplishes the desired objective and also furnishes important physical insight into the associated propagation phenomena, but its implementation requires calculation of the relevant guided modes and remainders, which may be inconvenient. By a new alternative approach, first introduced into seismology, we explore here the effectiveness of filling the transitional spectral intervals with Gaussian beams. Gaussian beam fields, because of their smoothed profile, do not experience the violent transitional behavior of ray fields. Moreover, in the usually employed paraxial approximation, they are tracked by simple modification of the ray algorithm. However, due to the smoothing, the fields synthesized by Gaussian beams may lead to inaccuracies, and due to an inherent arbitrariness in the beam superposition, the method does not as yet have a priori predictive capability. Specific aspects pertaining to the Gaussian beam method are explored here on a model surface duct with exponential refractive index profile in height, bounded on one side by a perfect boundary. In this model environment, emphasis is placed on wave phenomena pertaining to multiple reflected rays, particularly phenomena near caustics generated thereby. These problems have not been exposed previously to treatment by Gaussian beams. Detailed numerical comparisons of the asymptotic conventional ray and the Gaussian beam options with an exact generalized ray reference solution can lead to an assessment of the advantages and drawbacks of the Gaussian beam method. The first phase of these investigations is reported here.

## 1. INTRODUCTION

In the earth's natural environment, the physical parameters may vary in a manner so as to form ducts for the propagation of electromagnetic waves. Examples are provided by the temperature induced refractive index variations in the atmosphere and by aligned ionization in the ionosphere. Especially at short wavelengths compared to duct dimensions, propagation in such ducts, whose properties may vary longitudinally and laterally as well as in height, can be described effectively in terms of ray fields, which can be tracked by numerical algorithms even under complicated conditions. An inconvenience in these calculations is the need to correct for ray field failures in convergence zones near caustics and foci, and also the absence of ray fields in refraction shadow zones. Moreover, in long range ducted propagation, ray caustics pile up at the source and conjugate source levels so that correction for individual caustics, even if it could be performed, would be inadequate [1]. Thus for reliable and continuous field tracking, it is necessary to treat the troublesome ray field regions in another manner.

One remedy has been to fill the angular spectrum interval occupied by the troublesome rays with modes. This gives rise to a rigorous hybrid ray-mode algorithm comprising legitimate rays, modes and remainder fields (usually small) to ensure smooth blending of the ray-mode mix [2,3]. While this scheme furnishes some basic insights into the propagation mechanisms and works effectively in analytical test profiles, it remains to be extended to more general environments, especially those specified numerically instead of analytically. Even for analytic profiles, it is necessary to calculate certain mode groups which may be numerically inconvenient. This does not imply by any means that the hybrid ray-mode formulation is found wanting but merely that its full potential for general propagation environments remains to be further explored.

An alternative method, designed especially to cope with complicated environmental conditions [4], replaces the ray fields with paraxial Gaussian beams. Gaussian beams have the advantage that they remained defined along their entire trajectories, even in focusing regions of the conventional rays. In the paraxial regime, they can be traced

like real rays, but with wavefronts whose curvature is complex. Algorithms [5] have been developed to track the phase and amplitude of individual paraxial beam fields, and to use them in discretized superposition to cover the vicinity of a given observation point. This technique was first introduced, and is now widely used, in seismology. A major difficulty with its implementation is that although its theoretical foundation, based on continuous spectrum asymptotics, can be justified, the numerical implementation in discretized form involves arbitrarily assignable free parameters describing the beams and their location. Moreover, the smoothing inherent in replacing rays by paraxial beams may remove spectral content with consequent loss of resolution. Thus, the Gaussian beam method (GBM) is deficient in that it does not as yet have a priori predictive capability. It has been necessary to "tune" the parameters by comparison with test problems solved by other methods. Nevertheless, the procedure holds sufficient promise to warrant its further investigation. Rigorous techniques, though at the expense of greater complexity, are being developed to put the method on a sound footing but this stage has only just been initiated [6,7].

Because of the above-noted potentially desirable features, it is worth investigating GBM also for electromagnetic propagation modeling. The present paper explores this contingency for a model ducting environment that has been analyzed previously by ray and by hybrid ray-mode methods, with the latter invoked to repair the failures of asymptotic ray theory (ART) in ray caustic and other transitional domains. Because discretized GBM is not as yet a rigorous discipline, it is necessary to explore the spectral characteristics of different beam stacking arrangements to assess their basic properties and limitations. The present study is a first step in this direction. We ask very specifically how well particular beam arrangements in a given angular spectrum interval in a surface bounded duct predict the field along ray trajectories after successive multiple reflection, in the presence of caustics. The reference solution is calculated numerically along a "generalized ray", which is given by an exact traveling wave field integral, the asymptotic solution of which generates the conventional ray field. Although our test environment is idealized, the spectral behavior of the beams found therein is expected to characterize as well the behavior in more realistically modeled tropospheric channels [7]. Because of our previous experience with "exponential surface ducts", this test environment was a logical choice.

In what follows, we state the assumed model, show the ray paths pertaining to it, list the previously derived full field and generalized ray spectral integrals, and briefly summarize the hybrid ray-mode formulation. We then proceed to the Gaussian beam method, discuss its properties, list the relevant equations, and define the question which is to be addressed. Numerical results, as yet incomplete, nevertheless allow us to draw certain conclusions.

## II. MODEL CONFIGURATION

We shall explore the questions posed in the Introduction on the model duct shown in Fig. 1, which is comprised of a medium with exponentially decaying refractive index along the height coordinate  $x$ , away from a reflecting boundary at  $x=0$ . Excitation is from a time harmonic line source of magnetic current located at  $(x', z')$  so that the magnetic field component  $H_y = G$  satisfies the two-dimensional Green's function equation

$$\left[ \frac{\partial^2}{\partial x^2} + \frac{\partial^2}{\partial z^2} + k^2 n^2(x) \right] G(x, z, x', z') = -\delta(x-x')\delta(z-z') \quad (1)$$

where  $k=\omega/v$  is the wavenumber.

$$n(x) = \exp(-x/a) \quad x \geq 0 \quad (2)$$

is the refractive index, and "a" is a constant which determines the rate of variation of the profile. At  $x=0$ ,  $G$  satisfies the boundary condition  $\partial G / \partial x|_{x=0} = 0$ . A time dependence  $\exp(-i\omega t)$  is suppressed. By constructing an image profile  $n(x) = \exp(x/a)$ ,  $x \leq 0$ , and placing an image source at  $x=-x'$ , one produces a model problem for a full duct with a V-type profile, which resembles realistic conditions.

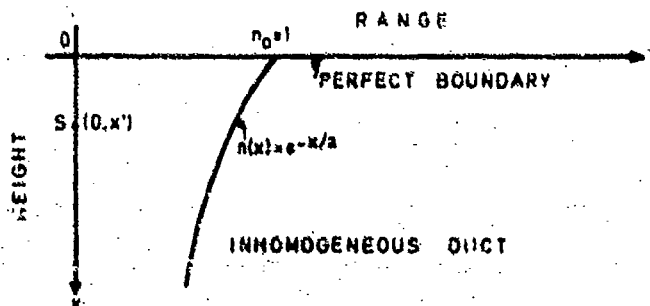
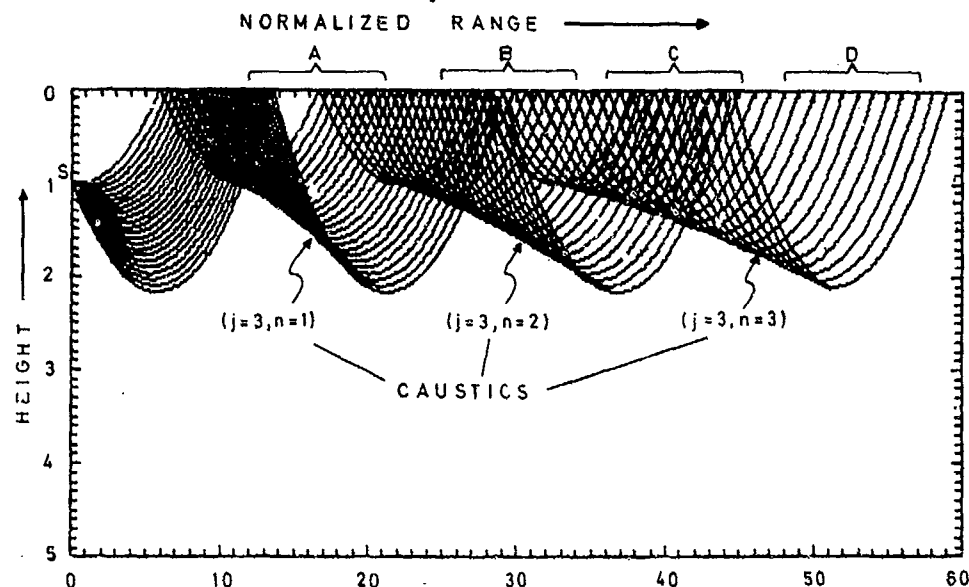


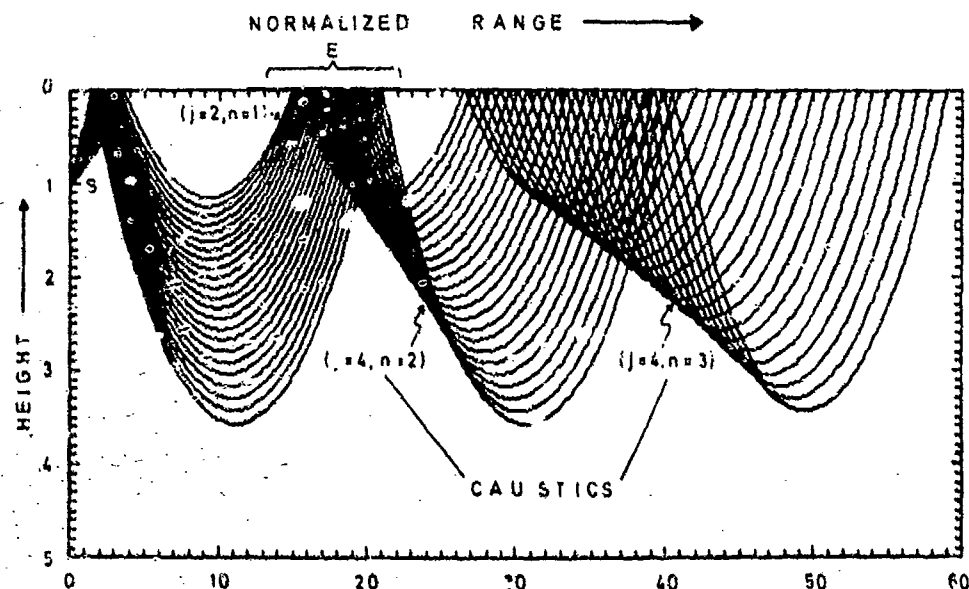
Fig. 1. Inhomogeneous duct geometry. Line source S is located at height  $x'$ , range  $z=0$ . By imaging, the solution applies also in a full V-type duct.

### III. RAY FORMULATION

Ray paths computed from a dynamic ray tracing program [9] for the duct of Fig.1 are shown in Fig.2. The formation of multibranched caustics after multiple reflection is evident. With increasing number of reflections and range distance  $x$ , one branch of these caustics approaches the horizontal direction, and successive branches therefore pile up near the height coordinate  $x'$  that defines the source location. The other branch of the caustics is directed toward the boundary and intersects it.



(a) downgoing rays at the source; ray species  $j=1$  (upgoing at observer) and  $j=3$  (downgoing at observer).



(b) upgoing rays at the source; ray species  $j=2$  (upgoing at observer) and  $j=4$  (downgoing at observer).

Fig.2. Ray paths and caustics for surface reflector rays, with identical normalization used for height and range coordinates. For clarity, only a portion of the rays corresponding to various reflection indices  $n$  has been plotted. Also shown are the intervals covered by the numerical results in Fig.5 and Fig.6. The profile gradient  $a=1865$ .

The generalized ray integral, which describes the complete spectral object whose asymptotic approximation yields the geometrical ray field, can be derived from the spectral representation of  $G$  [3]

$$G(x, s, x', s') = \frac{ika}{8} \int_{-\infty}^{+\infty} \left[ H_v^{(1)}(q_x) + R_u H_v^{(2)}(q_x) \right] \left[ H_v^{(1)}(q_{x'}) + H_v^{(2)}(q_{x'}) \right] e^{ik\zeta s} d\zeta \quad (3)$$

where the reflection coefficient from the upper boundary is

$$R_u = -H_v^{(1)}(q_0)/H_v^{(2)}(q_0) \quad (4)$$

and the argument of the Hankel function is  $q_u = ka \exp(-u/a)$ ,  $u=x, x'$ .

The desired representation leading to the asymptotic and generalized ray series may be developed by expanding the denominator in (3) as

$$(1-R_u)^{-1} = \sum_{n=0}^{\infty} R_u^n + R_u^{(N+1)}/(1-R_u) \quad (5)$$

with subsequent regrouping. A typical generalized ray field is then given by [10]

$$G(x, s, x', s') = \frac{ika}{8} \int_{C_{nj}} R_u^{(\tau+n)} v_j(x, x') \exp(ik\zeta s) d\zeta, \quad x \neq x' \quad (6)$$

where

$$v_j(x, x') = \begin{cases} H_v^{(1)}(q_x) H_v^{(j)}(q_{x'}) & \text{for } j=1 \text{ and } 2 \\ H_v^{(2)}(q_x) H_v^{(j-2)}(q_{x'}) & \text{for } j=3 \text{ and } 4 \end{cases} \quad (7)$$

$(\tau+n)$  is the number of surface reflections, with  $\tau=(0,0,1,1)$  for  $j=1,2,3$  and 4. The index  $j$  orders ray species according to their directions of departure from the source and arrival at the observer. For an observer on the upper boundary, the number of species reduces to two because of the merging of species (1,3) and (2,4) (see Fig.2). The integration contour  $C_{nj}$  passes through the saddle point  $\zeta_{s,nj}$  as shown in Fig.3.

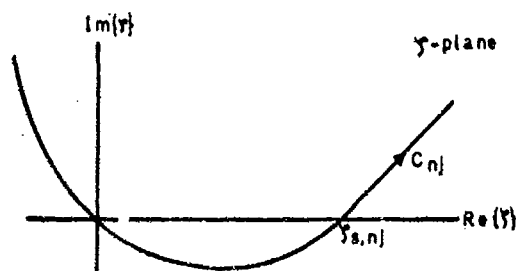


Fig.3. Integration path in the complex  $\zeta$ -plane.

Asymptotic evaluation of (6) by the method of steepest descents, with Hankel functions approximated by their Debye asymptotic forms whenever  $|y - q| > 0(y^{1/3})$ , yields the first order saddle point contribution, i.e., the APT field [3],

$$G_{nj} \approx \sqrt{\frac{2\pi}{ka|q_{nj}'(\zeta_{s,nj})|}} f_j(\zeta_{s,nj}) \exp[ikaq_{nj}(\zeta_{s,nj}) \pm i\pi/4], \quad q_{nj}'(\zeta_{s,nj}) \neq 0 \quad (8)$$

with phase function

$$q_{nj}(\zeta) = 2(\tau+n)\zeta(0,\zeta) + 1_j\zeta(x,\zeta) + s_j\zeta(x',\zeta) + s\zeta/a \quad (9.a)$$

and amplitude term

$$f_j(\zeta_{s,nj}) = \frac{1}{4\pi} \frac{q_j(-1)^{\tau+n}}{(e^{-2x/a} - \zeta^2)^{1/4} (e^{-2x'/a} - \zeta^2)^{1/4}} \quad (9.b)$$

Here,  $l_j = (+1, +1, -1, -1)$ ,  $m_j = (+1, -1, +1, -1)$  and  $n_j = (-1, 1, 1, +1)$  for  $j = (1, 2, 3, 4)$ , and

$$\zeta(x, \zeta) = \sqrt{e^{-2x/a} - \zeta^2} - \zeta \cos^{-1}(\zeta/e^{-x/a}) \quad (10)$$

The saddle point  $\zeta_{s,nj}$  is determined from,

$$q_{nj}^1(\zeta) = 0 \quad (11)$$

and together with the following second derivative yields the equation for the caustics

$$q_{nj}^2(\zeta_{s,nj}) = \frac{2(\tau+n)}{\sqrt{1-\zeta^2}} + \frac{l_j}{\sqrt{e^{-2x/a} - \zeta^2}} + \frac{m_j}{\sqrt{e^{-2x'/a} - \zeta^2}} \quad (12)$$

Eqs. (8)-(12) have been employed in our calculations of the ART fields along the rays of Fig. 2, and the results agree with those from our implementation of the dynamic ray trace code SHISS [9]. Near a caustic, where  $q_{nj}^1(\zeta_{s,nj}) \rightarrow 0$ , the failure of ART requires a correction algorithm. Although it is possible to perform such corrections near isolated caustics by uniform (Airy type) transition functions, this procedure breaks down when caustics pile up. Moreover it requires careful bookkeeping of each ray encounter with a caustic, which becomes cumbersome in the presence of the multiple reflections.

#### IV. HYBRID RAY-MODE FORMULATION

A different alternative for repairing the transition region failure of ART is to employ the rigorous equivalence [2] between a group of ray fields and a group of modal fields (with an appropriate remainder field) to construct a hybrid ray-mode algorithm for the total field. The modes, which have no convergence problems near ray caustics, serve to replace the angular spectrum of troublesome caustic forming rays. The hybrid combination must be updated for different observer locations but it has the advantage that a fixed number of surface guided modes can account for the transitional behavior with range distance if the motion of the observer is confined to heights not too far from the boundary. The rays are used to describe the fields far from the boundary.

Although the hybrid method is useful for the present problem if source and observer are located not too far from the boundary, it requires calculation of the relevant mode (and remainder) fields, in addition to the ray fields (see [1,3] for various strategies). The Gaussian beam algorithm, to be discussed next, could avoid the need for hybrid decomposition but, as noted earlier, its predictive capability and accuracy are as yet open to question.

#### V. GAUSSIAN BEAM METHOD (GBM)

##### A. General Remarks.

A principal motivation for the present study is the performance of the Gaussian beam method when a wavefield in an inhomogeneous ducting environment undergoes multiple caustic-forming reflections. This goes beyond the encounter of direct rays with a single caustic, which has received much attention [4]. As mentioned previously, a major advantage of GBM is the use of dynamic ray tracing without regard to caustics because the paraxial beam fields do not diverge and are continuous there. However, establishing accuracy is another matter. Before exploiting this question here we review briefly the foundation of the method.

By the GBM, the fields radiated by the source are modeled along rays which serve as trajectories of paraxial Gaussian beams. The paraxial beam fields are computed via the parabolic equation method which yields beam like solutions of the wave equation concentrated in the vicinity of central rays. The total wave field at any observation point is then determined as the discrete superposition of individual Gaussian beams which have traversed the propagation environment on their way from source to observer. The basic theory was developed by Babich [11], Babich and Buldyrev [12], and Babich and Pankratova [13]; the latter suggested expansion of a high frequency wave field as a Kirchhoff-type integral over beams centered on rays. Based on this study, Popov [14] proposed a discretized version for computation, now known as the Gaussian Beam Method (GBM).

The method has been applied extensively to seismic wave fields, utilizing primarily the basic numerical code SHISS [9], which we have modified to accommodate beams. Previous seismic results have been reported in [4] and [15]-[18]. A recent comprehensive paper [19] summarizes the impact of GBM on seismology. Still lacking is a systematic and predictive approach [20] to determine the various parameters in the Gaussian beam algorithm, i.e., the number of beams, widths of individual beams and the required width of a beam bundle.

Two-dimensional paraxial beam propagation is based on the parabolically reduced wave equation [4],

$$\frac{2i}{v} u_{zz} + u_{yy} - \frac{v^2}{v_0} u_{xx} = 0 \quad (13)$$

whose solution  $u$  along ray-centered coordinates  $(s, n)$  (see Fig. 4) generates the wavefield

$$G(s,n) = \sqrt{v(s)} \exp \left\{ i\omega \int_{s_0}^s \frac{ds}{v(s)} \right\} W(s,n) \quad (14)$$

where  $v = \sqrt{2n}$ . In (13), subscripts denote partial derivatives. In explicit form,

$$G(s,n) = \left[ \frac{v(s)}{q(s)} \right]^{1/2} \exp \left\{ i\omega \int_{s_0}^s \frac{ds}{v(s)} + i \frac{\omega}{2} \frac{p(s)}{q(s)} n^2 \right\} \quad (15)$$

where  $p(s)$  and  $q(s)$  are solutions of the dynamic ray tracing system. The parameters  $p$  and  $q$  are real for conventional ART ray tracing but they are complex for Gaussian beams. Following [4], the wave field at a point  $P$  due to a given source distribution is represented as a continuous superposition of angularly distributed Gaussian beams,

$$G(P) = \int_0^{2\pi} \Phi(\psi) G_\psi(s,n) d\psi \quad (16)$$

with  $\Phi$  denoting a complex weighting function that ensures that the asymptotic evaluation of the integral agrees with what is obtained by ART outside ray transition regions.

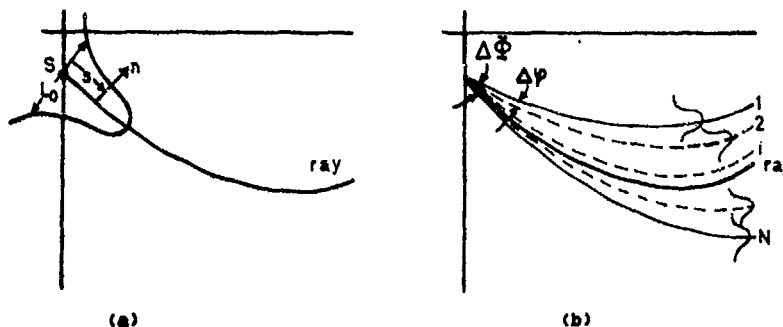


Fig. 4. (a) Ray centered coordinates  $(s,n)$  and Gaussian beam of width  $L_0$  at the source. (b) Various parameters applicable to the GBM.

For a line source, (16) becomes

$$G(P) = \frac{-i}{4\pi} \left[ \frac{r}{v_0} \right]^{1/2} \int_0^{2\pi} G_\psi(s,n) d\psi, \quad r = -iL_0^2 \quad (17)$$

The discretized version for computation is

$$G(P) = \sum_{j=1}^N \Phi(\psi_j) G_{\psi_j}(s,n) \Delta\psi, \quad N\Delta\psi = 2\pi \quad (18)$$

where  $\psi_j$  are the beam axis locations and  $\Delta\psi$  is the angular interval between them.

### B. Application

To test one aspect of the quality of Gaussian beam stacking for the multiple reflection environment of Fig. 2, we pose a very specific problem. We specify a particular angular spectrum interval  $\Delta\psi$  and fill this interval at equal angular increments  $\Delta\psi_j = (\Delta\psi)/N$  with  $N$  beams having beamwidths  $L_0$  at the source. The parameters  $\Delta\psi$ ,  $\Delta\psi_j$ ,  $N$  and  $L_0$  (see Fig. 4) are selected by numerical experiment such that the stack of beams reproduces correctly the ART field where that is valid. Both, in turn, are compared with the numerically evaluated generalized reference ray field in (6). We now seek to determine how the fields generated by a beam stack "optimized" around a ray in a particular reflection domain behave when that ray passes on to another reflection domain. Placing the source at  $x=1.0$  and the observer on the boundary, we have surrounded each relevant ray in Fig. 2 symmetrically with a bundle having  $N=27$  equally spaced beams with waist located at the source point. The beam width  $L_0$  and the beam spacing  $\Delta\psi = (\Delta\psi)/N$  are adjusted for optimization.

The results are shown in Figs. 5 and 6 for  $j=1$  and  $j=2$ , respectively. In Fig. 5(a), covering case A of Fig. 2(a), optimizing the direct ray field  $n=0$  ( $j=1$ ) with beam bundle parameters  $L_0/\lambda=3.4$ ,  $\Delta\psi=0.60$  radians, yields excellent agreement with ART and the numerical integration of the ray integral (NI) for  $s>13$ . When a ray in this group passes on to

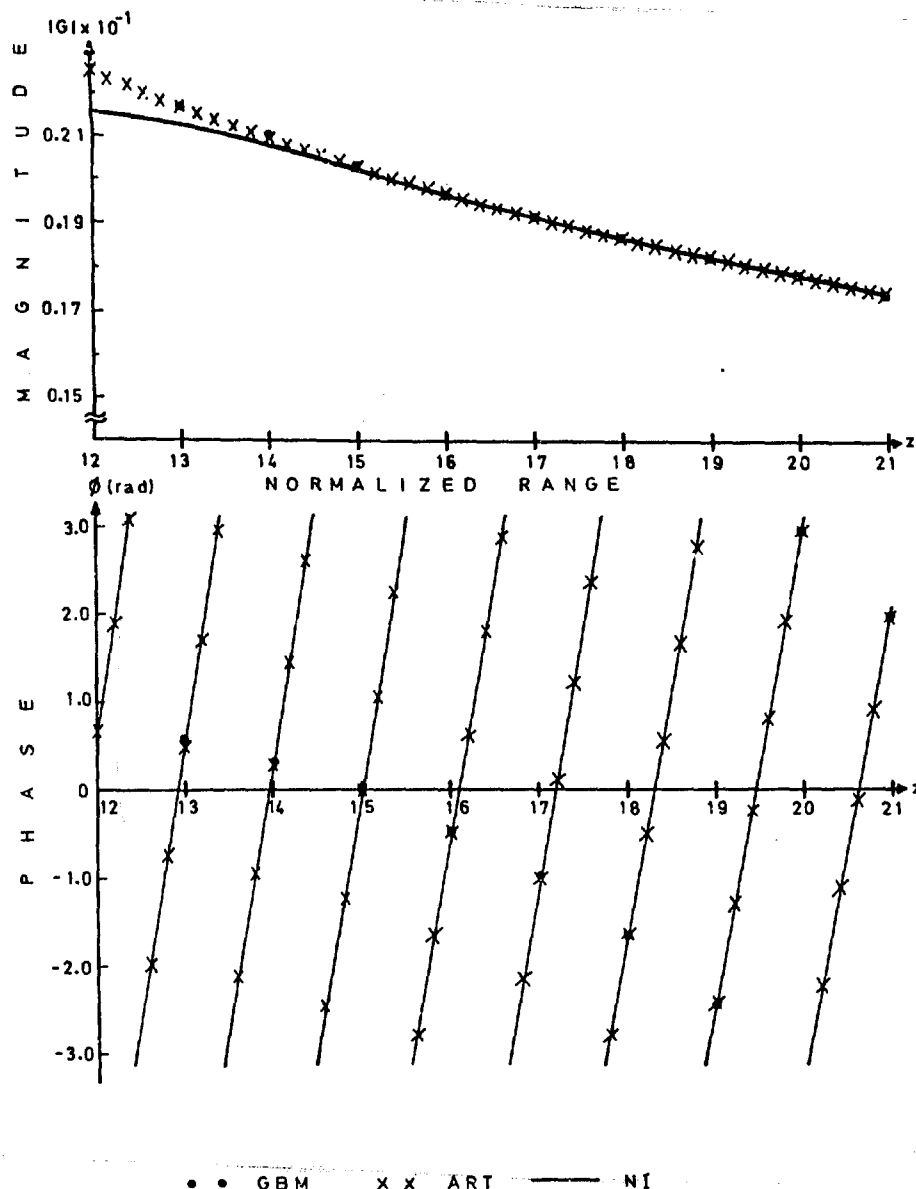
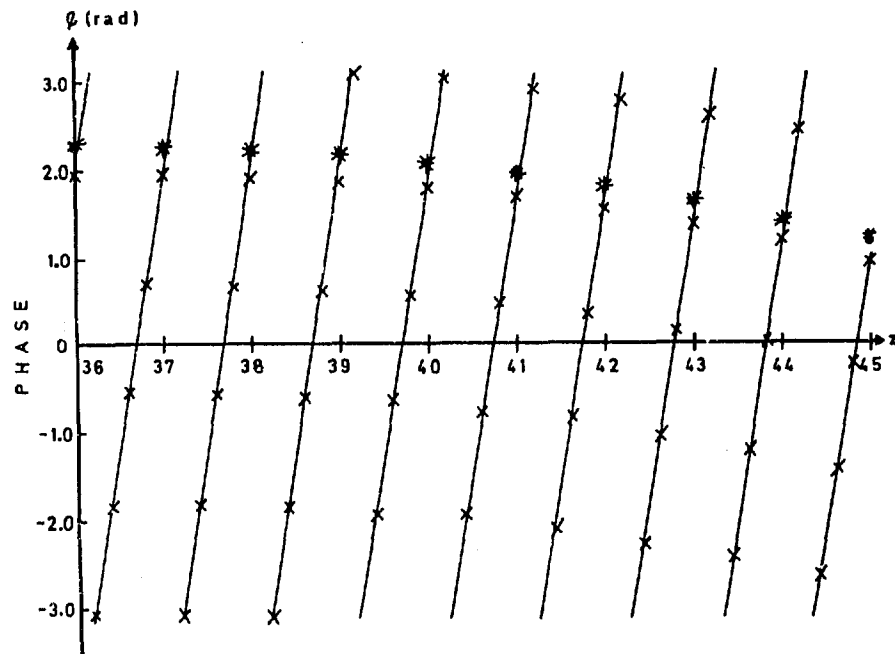
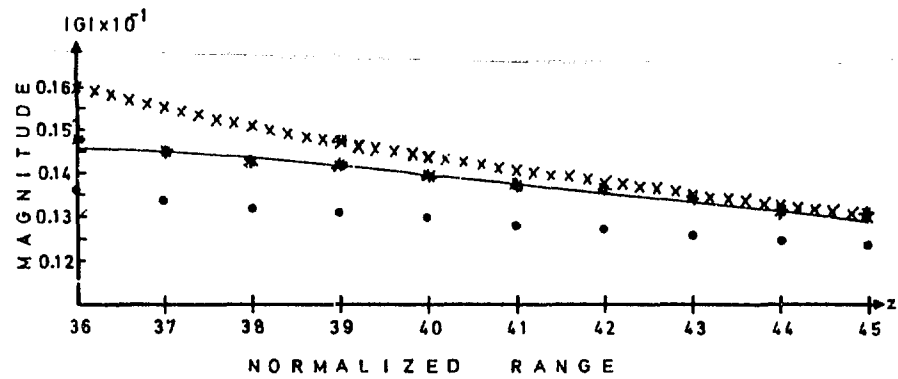


Fig.5(a). Magnitude and phase of the field  $G$  on the surface in the various observation regions of Fig.2(a) for ray species  $j=1$ . Beam stack parameters:  $M=27$ ,  $\Delta\theta=(\Delta\theta)/M$  for given  $\Delta\theta$ , beam waists at source location. Beam stacks optimized for  $n=0$  are compared with beam stacks optimized for  $n=2,3$  in their respective domains. Other parameters:  $n=0$  (Region A of Fig.2(a)), with optimized values  $L_0/\lambda=3.4$  and  $\Delta\theta=0.4$  radians.

successive reflections  $n=1,2,3$  ( $j=1$ ) corresponding to cases B,C,D of Fig.2(a), with the beam bundle unaltered, the agreement deteriorates steadily. This is shown in Fig. 5(b) for  $n=2$  ( $j=1$ ). It is to be noted that for  $j=1$ , ray caustics do not intercept the surface. Therefore, all rays in this category define ordinary ray fields, for which the reference solution (NI) is generated without difficulty and ART is valid as long as the ray direction at the source is not nearly horizontal; when ART deviates from NI, this implies proximity to horizontal launching. Also plotted in Fig. 5(b) are the much better results obtained when the beam bundle at the source is optimized for  $n=2$  ( $j=1$ ); the parameters here are  $L_0/\lambda=3.4$ ,  $\Delta\theta=0.446$ . Passing on to  $n=3$  ( $j=1$ ) in Fig. 5(c) and comparing with





\* \* \* \* \* (  $L_0/\lambda=3.4$ ,  $\Delta\phi=0.446$  ) } GBM      x x x    ART      ———    NI  
 • • • • • (  $L_0/\lambda=3.4$ ,  $\Delta\phi=0.400$  )

Fig. 5(b). Captions as in Fig. 5(a). Other parameters:  $n=2$  [Region C in Fig. 2(a)], with optimized values  $L_0/\lambda=3.4$  and  $\Delta\phi=0.446$  radians.

Fig. 5(b), one observes the further deterioration of the beam bundle optimized for  $n=0$ , but the much better agreement for the beam bundle optimized for  $n=3$ , with parameters  $L_0/\lambda=4.0$ ,  $\Delta\phi=0.60$ . Conversely, our calculations show (figure not included here) that the  $n=3$  ( $j=1$ ) optimized beam bundle performs rather poorly on the direct ray  $n=0$  ( $j=1$ ). For ray species  $j=2$  in Fig. 2(b), the multiple reflected ray caustics intercept the boundary  $x=0$ . As the caustic is approached from the illuminated side, ART grows without bound and yields no penetration into the caustic shadow. The Gaussian beams traverse the caustic transition smoothly but with inconsistent accuracy. Typical results are shown in

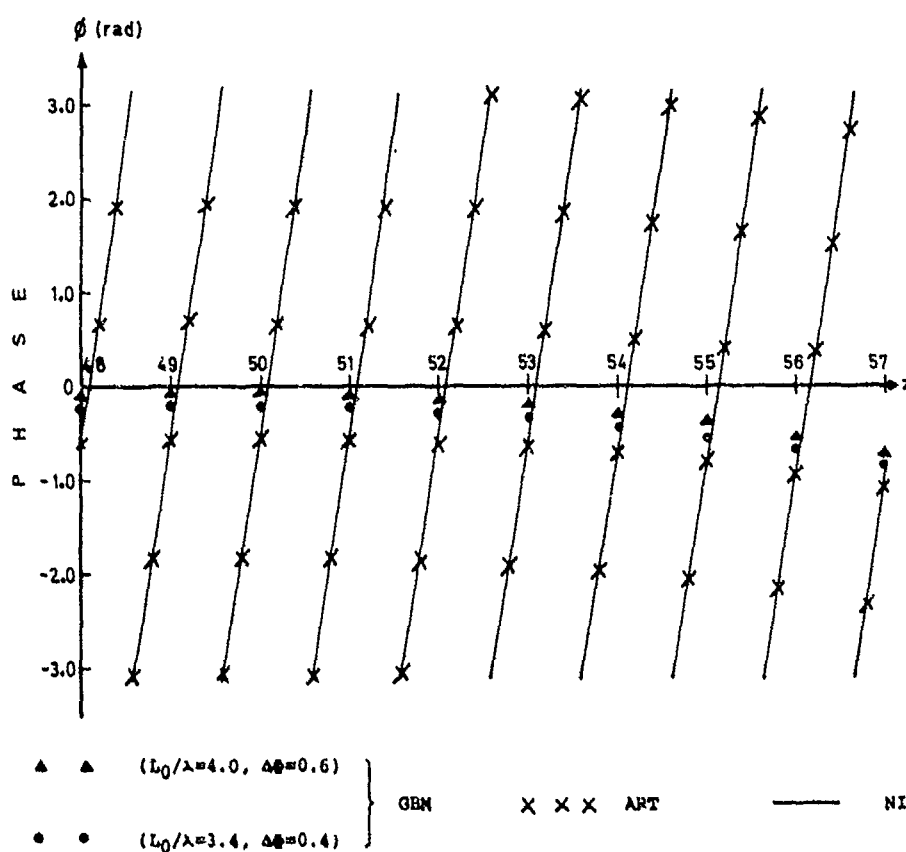
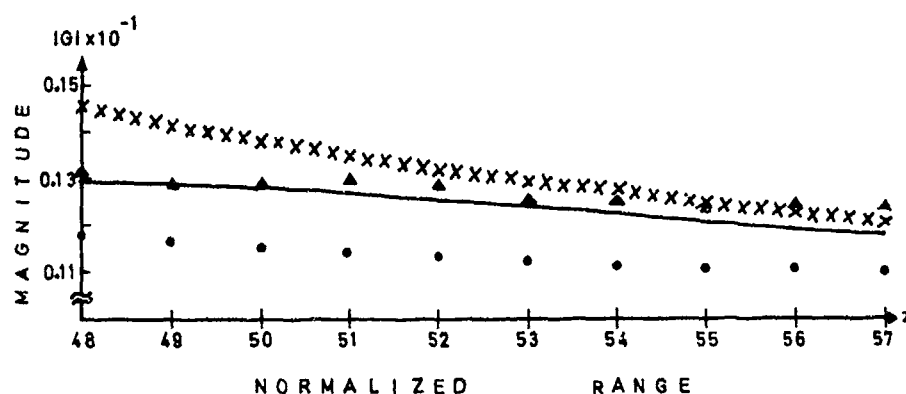


Fig.5(c). Captions as in Fig.5(a). Other parameters:  $n=3$  (Region D in Fig.2(a)), with optimised values  $L_0/\lambda=4.0$  and  $\Delta\phi=0.6$  rad/ans.

Fig.6 for  $n=1$  ( $j=2$ ), corresponding to Case E in Fig.2(b). Using the beam stack optimised for  $n=0$  ( $j=1$ ) as in Fig.5(a) yields poor agreement here, the much better behaved optimised stack being one with parameters  $L_0/\lambda=3.4$ ,  $\Delta\phi=0.6$ . The reference solution NI is shown only for  $s \geq 21.0$ ; numerical difficulties (which persisted up to the manuscript submission deadline but can undoubtedly be removed) were encountered for smaller  $s$  values. Other calculations, not included here, present a picture consistent with the observations above.

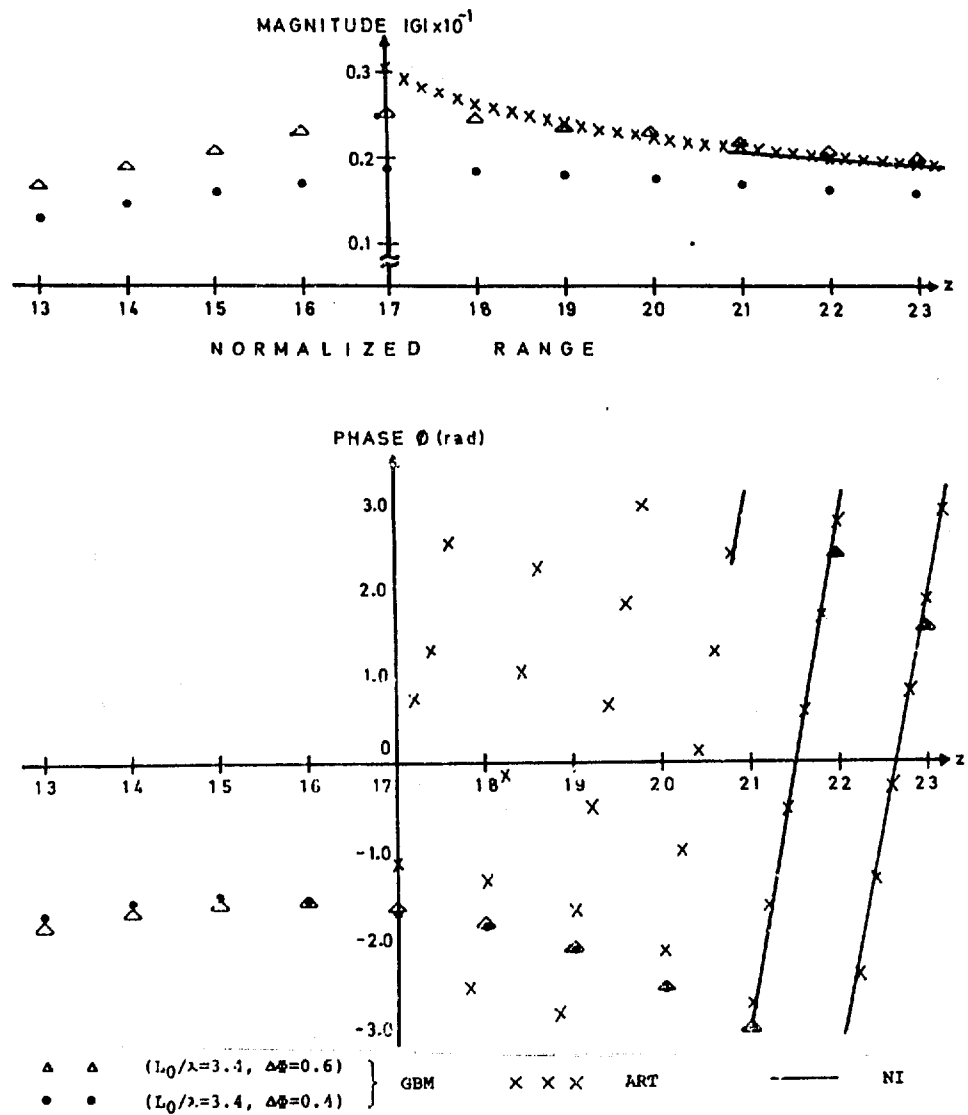


Fig. 6. As in Fig. 5, but for ray species  $j=2$  in Region E of Fig. 2(b), with  $n=1$ .

#### CONCLUSIONS

In this study, we have investigated the Gaussian beam method (GBM) for multiple reflected ray fields in a model surface duct (or equivalently, a symmetrically excited full duct with a V-type refractive index profile). The purpose has been to ascertain whether a beam stack that adequately represents the field at observation points along a particular ray segment corresponding to a certain number of reflections continues to be adequate along ray segments with a different number of reflections. To standardize the choice of beam parameters, the beams have been equally spaced, their waist has been placed at the source point, and their number kept constant. This made the beam width at the waist and the spacing interval the free parameters. By comparing with ART, when valid, and with a reference solution NI obtained by numerical integration of the exact ray integral, it has been found that the beam stack could be optimized for each reflection order but that a stack optimized for one reflection order does not remain optimized for other reflection orders. Optimization here was achieved by numerical experiment; the "optimized" parameters give good agreement but should not be regarded as absolute.

The results described above point out the dilemma of the GBM. The GBM is attractive because of its smooth behavior across caustics; however its a priori predictive capability is an open question. The "numbers game" can always be played against a reference

solution to a particular observation domain along a ray, but there is no guarantee that the beam stack established in this manner remains adequate in other observation domains along that ray. This has been demonstrated here for multiple reflections or refractions in a refracting duct. It remains to be seen whether this defect is fundamental in the GBM or whether it can be attributed to the paraxial approximation. In other tests [5], it has been found that tracking beam stacks with full complex spectra restores accuracy where the paraxial approximation fails. It is intended to perform such a study here.

#### ACKNOWLEDGEMENT

Authors at NJIT would like to acknowledge the SBR support provided by the Foundation at the New Jersey Institute of Technology. The last author (L.B.F.) acknowledges support from the Army Research Office under Contract No. DAAG-29-85-K-0180 and from the Joint Services Electronics Program under Contract No. F49620-85-C-0078.

#### REFERENCES

- [1] Topus, E. and L.B. Felsen, "Hybrid Representation of Long Range Sound Pulse Propagation in an Surface Duct," J. Acoust. Soc. Amer., Vol. 78, pp. 1746-56, 1985.
- [2] Kamel, A. and L.B. Felsen, "On the Ray Equivalent of a Group of Modes," J. Acoust. Soc. Amer., Vol. 71, pp. 1445-1452, 1982.
- [3] Niver, E., Kamel A. and L.B. Felsen, "Modes to Replace Transitional Asymptotic Ray Fields in a Vertically Inhomogeneous Earth Model," Geophys. J. Roy. Astron. Soc. Vol. 80, pp. 289-312, 1985.
- [4] Carveny, V., M.M. Popov and I. Paencik, "Computation of Wave Fields in Inhomogeneous Media-Gaussian Beam Approach," Geophys. J. Roy. Astron. Soc. Vol. 70, pp. 109-128, 1982.
- [5] Lu, I.T., L.B. Felsen and Y.Z. Ruan, "Spectral Aspects of the Gaussian Beam Method: Reflection from an Isovelocity Half Space," to be published in Geophys. J. Roy. Astron. Soc.
- [6] Einsinger, P.D., S. Raz and M. Shapira, "Gabor Representation and Aperture Theory," J. Opt. Soc. Am. A, Vol. 3, pp. 508-522, 1986.
- [7] Einsinger, P.D., Y. Harnamty and L.B. Felsen, "Complex Rays for Radiation from discretized Aperture Distributions," to be published in IEEE Trans. Antennas Propagat.
- [8] Pappert, R.A. and C.L. Goodhart, "Case Studies of Beyond-the-Horizon Propagation in Tropospheric Duct Environment," Radio Science, Vol. 12, pp. 75-88, 1977.
- [9] Carveny, V. and I. Paencik, "Gaussian Beams in 2-d Laterally Varying Layered Structures," Geophys. J. Roy. Astron. Soc., Vol. 82, pp. 63-91, 1984.
- [10] Niver, E., S.H. Cho and L.B. Felsen, "Rays and Modes in an Acoustic Channel with Exponential Velocity Profile," Radio Science, Vol. 16, pp. 963-970, 1981.
- [11] Babich, V.M., "Eigenfunctions Concentrated in the Vicinity of Closed Geodesics," in Mathematical Problems of Theory of Propagation of Waves, Vol. 9, pp. 15-63, Nauka, Leningrad (in Russian), 1986.
- [12] Babich, V.M. and Buldyrev, V.S., Asymptotic Methods in Problems of Diffraction of Short Waves, Nauka, Moscow (in Russian), 1972.
- [13] Babich, V.M. and Pankratova, T.F., "On Discontinuities of the Green Function of Mixed Problem for Wave Equation with Variable Coefficients," in Problems of Mathematical Physics, Vol. 6, pp. 9-27, Leningrad University Press (in Russian), 1973.
- [14] Popov, M.M., "A new Method of Computation of Wave Fields in the High Frequency Approximation," Preprint LOMI-AM USSR, E-1-81, Leningrad, 1981.
- [15] Carveny, V. and I. Paencik, "Gaussian Beams in two Dimensional Elastic Inhomogeneous Media," Geophys. J. Roy. Astron. Soc., Vol. 72, pp. 417-433, 1983.
- [16] Nowack, R. and K. Aki, "The 2-d Gaussian Beam Synthetic Method Testing and Application," J. Geophys. Res., Vol. 89, pp. 1466-94, 1984.
- [17] Yomogida, K., "Gaussian Beams for Surface Waves in Laterally Slowly Varying Media," Geophys. J. Roy. Astron. Soc., published.
- [18] Muller G., "Efficient Calculation of Gaussian Beam Seismograms for Two Dimensional Inhomogeneous Media," Geophys. J. Roy. Astron. Soc., Vol. 79, pp. 153-166, 1984.
- [19] Carveny, V., "Gaussian Beam Synthetic Seismograms," Journal of Geophysics, Vol. 58, pp. 44-72, 1983.
- [20] Felsen, L.B., "Geometrical Theory of Diffraction, Evanescent Waves, Complex Rays and Gaussian Beams," Geophys. J. Roy. Astron. Soc., in press.

AD-P005 741

11-1

## REVIEW OF RECENT DEVELOPMENTS IN EVAPORATION DUCTING ASSESSMENT

by

JUERGEN H. RICHTER  
OCEAN AND ATMOSPHERIC SCIENCES DIVISION  
NAVAL OCEAN SYSTEMS CENTER  
SAN DIEGO, CA 92152-5000  
USA

## SUMMARY

Continued interest in accurately assessing and exploiting evaporation ducting effects has resulted in some recent work summarized in this paper.

Available evaporation duct height and path loss models are compared (ref-1). This includes both sensitivities of duct height values to meteorological inputs and agreements between different path loss models. The models compared are those developed by Jaske (ref-2), Hiney (ref-3), and Rotherham (ref-4). Reasonable agreement of duct height calculations and path loss values derived from the different models was obtained when applied to statistically averaged meteorological inputs. Commonly used point measurements were found inadequate for reliable evaporation duct assessment. This led to the suggestion of a new shipboard deployable sensor using a single temperature sensor for air-sea temperature measurements.

Both long time statistical duct height averages and individual data sets often contain unusually high duct heights not supported by propagation measurements. Paulus (ref-5) analyzed the meteorological conditions and found a bias in commonly used measurement techniques toward stable conditions. He proposed a correction algorithm and demonstrated its utility convincingly on a set of radiometeorological measurements.

The optimum frequency for utilization of the evaporation duct for long range surface detection appears to be in the 10-20 GHz band. This is illustrated by calculating surface detection ranges for hypothetical radars equivalent in performance parameters but operating at different frequencies (ref-6).

## PREFACE

The vertical decrease of relative humidity from 100% at the air-sea boundary results in a rapid vertical decrease of the refractive index. Electromagnetic waves traveling close to the water surface may be significantly influenced by such a refractive index distribution and in extreme cases may be very efficiently ducted. This oceanic evaporation duct, which is found to some degree nearly all the time over all oceanic areas, is of particular importance for over-the-horizon, surface-to-surface radar coverage. It is an important factor in the low flying ship-to-ship missile problem. To illustrate some fundamental properties of the effect of the oceanic evaporation duct on radio propagation, two vertical distributions of the modified refractivity profile are shown in figure 1. (Modified refractivity  $M = (n-1) \cdot 10^6 \cdot h/a \cdot 10^3$ ;  $n$  = refractive index,  $h$  = height above the surface,  $a$  = earth's radius.) The dashed line represents no evaporation ducting while the solid line is representative of good ducting conditions. Figure 2 shows the vertical distribution of path loss for the two refractivity distributions assuming a 19-nmi, 9.6 GHz over-water propagation path with one terminal at 16 feet above the water (path loss is the ratio in dB of transmitted to received power assuming isotropic antennas). The dashed curve in figure 2 indicates a decrease of path loss (or an increase of signal) with height. The solid curve corresponding to the solid M-curve in figure 1 shows a minimum in path loss (or a maximum in received signal) at a height of about 15 feet. At this height the signal enhancement over no ducting conditions is 62 dB. Signal enhancements of such a magnitude emphasize the importance of the oceanic evaporation duct. (The solid curve in figure 2 must not be extrapolated beyond the height plotted. It will not cross the "no ducting" curve but, depending on horizon range, increase with altitude.) The presentation of figure 2 may also be used to determine antenna heights for optimum utilization of ducting conditions. For example, an antenna at a height of 66 feet would receive 11 dB less signal than an antenna at 15 feet. Nonetheless, the signal enhancement from evaporation ducting would be 30 dB for the high antenna. A fact frequently overlooked is that signal enhancements from evaporation ducting are usually encountered for all possible antenna heights on board ship.

A convenient parameter for the description of ducting conditions is "duct height" defined as the height at which the M-curve attains its minimum value. Thus, the solid curve in figure 1 has a duct height of 47 feet. In general, greater duct heights will result in higher signals. However, this duct height parameter should not be misinterpreted as a height limit above which signal enhancements cannot occur. As shown in figure 2, 30 dB signal enhancements are experienced well above the duct height.

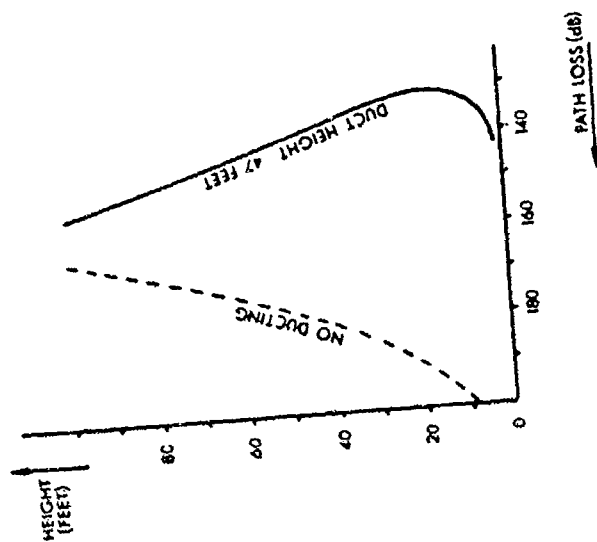


Figure 2. Path loss profiles for a 9.6 GHz, 19-nmi path with a terminal height 16 feet. The dashed curve is for no ducting and the solid curve is for a 47-foot duct height.

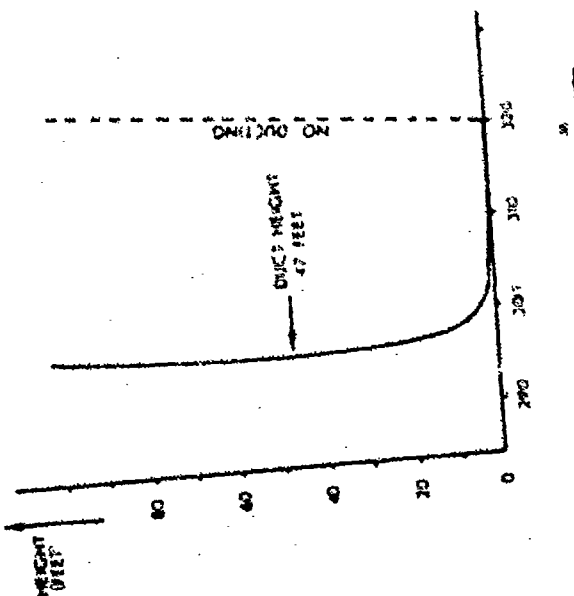


Figure 1. Modified refractivity profile N for no ducting (dashed curve) and for a 47-foot duct height (solid curve).

## REFRACTIVITY PROFILES

The vertical distribution of the refractive index must be known for propagation calculations. A direct measurement of the refractive index profile under operational conditions is impractical. For instance, the profile in figure 1 changes 20 M-units within the first 4 feet above the water and only an additional 4 M-units between 4 and 47 feet. Even for moderate winds and ocean waves it would be very difficult to make measurements that close to the water surface. In addition, profiles based on single measurements usually show strong variations which often make the true profile shape unrecognizable. These variations are smoothed out only if mean values are derived by averaging over several minutes. If the functional relationship is known which governs the vertical distribution of the refractive index, then only measurements at the sea surface and at a convenient reference height are needed. Such measurements are called bulk measurements. Advances in boundary layer research have made it possible to derive profile descriptions which are adequate to describe radio propagation conditions. Those profiles are dependent on turbulent transfer processes and assume different shapes depending on the thermal structure in the boundary layer. Under thermally neutral conditions (adiabatic lapse rate) a logarithmic profile describes the vertical distribution of the meteorological parameters of interest. For non-neutral temperature conditions (diabatic lapse rate) the vertical gradient of the meteorological parameters is modified by a function which depends on stability. According to Jeske (ref 2), in the stable region a stability function first proposed by Monin and Obukhov (ref 7) should be used which results in a logarithmic-linear profile. Under intense thermal stratifications the turbulence theories used are no longer valid. Therefore, for stabilities exceeding a bulk Richardson's number of one, no general functional relationship for the vertical distribution of the meteorological parameters is presently available. Bulk Richardson's number can be determined from the temperature difference  $\Delta T$  (in K) between the surface and a reference height  $z_1$  (in m) and the wind speed  $u$  (in knots, measured at  $z_1$ ) according to

$$R_{1b} = 1.3z_1 \frac{\Delta T}{u^2} \quad (1)$$

The logarithmic-linear profile also provides the satisfactory profile descriptions in the unstable region ( $R_{1b} < 0$ ). However, a different stability function provides more accurate profiles for superadiabatic lapse rates (ref 2). Based on the two stability functions for stable and unstable conditions duct height DH (in m) may be calculated according to the following formulas.

Stable region ( $0 < R_{1b} < 1$ ):

$$DH = \Delta N / (b_1 B - \Delta N \alpha / L') \quad (2)$$

where

$$B = \ln(z_1/z_0) + \alpha z_1/L'$$

$\Delta N$  is the refractivity difference between surface and reference height,  $z_1$ ,  $b_1$  is a constant with the value of -0.125 m, the hydrodynamic roughness of the sea  $z_0 = 1.5 \times 10^{-5}$  m,  $\alpha = 4.5$ , and  $L'$  is the so-called Monin-Obukhov length. The Monin-Obukhov length can be determined from an empirical relationship between bulk Richardson's number and a so called profile coefficient (ref 2).

Unstable Region ( $R_{1b} < 0$ ):

$$DH = [(b_1 B / \Delta N)^4 - 4\alpha (b_1 B / \Delta N)^3 / L']^{-1/4}$$

where

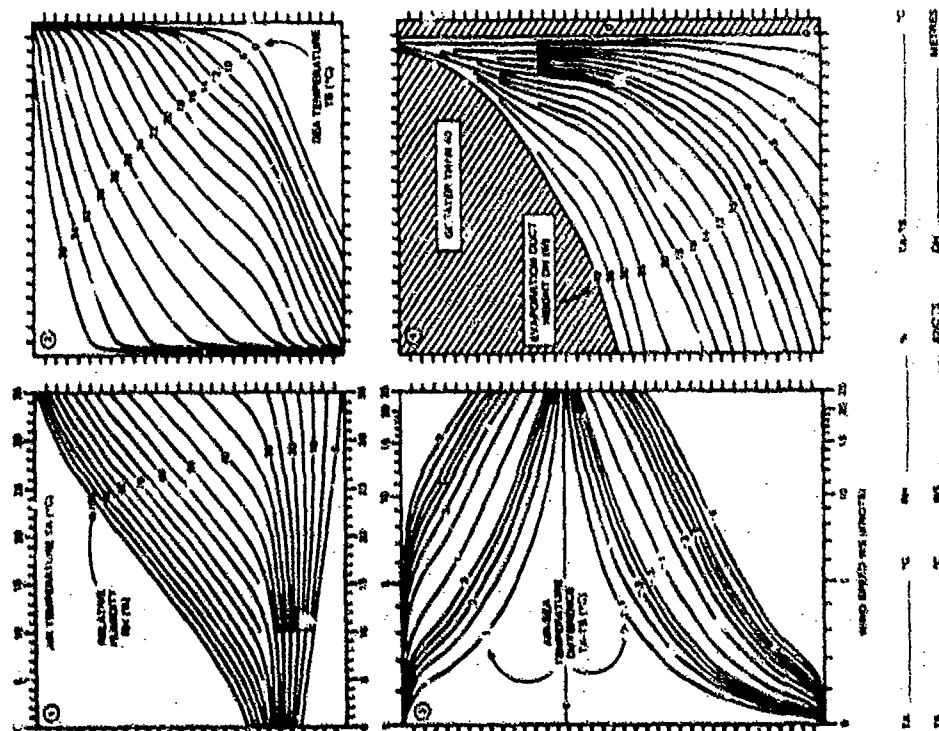
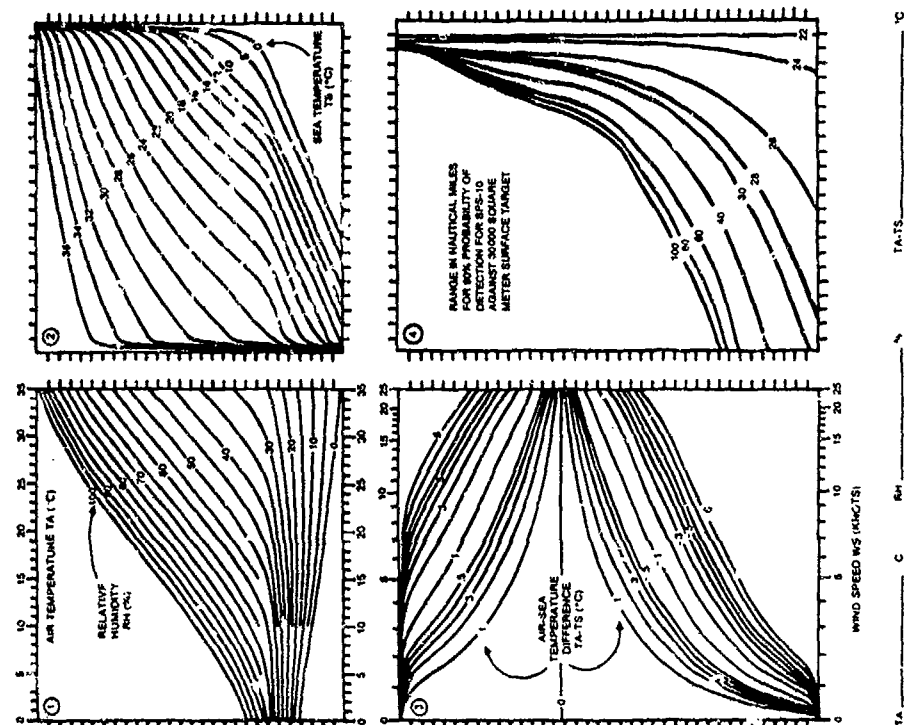
$$B = \ln(z_1/z_0) - \psi \quad (3)$$

The function  $\psi$  may be found in ref 8. Further refinements of boundary layer models have been attempted based on the so-called Businger-Dyer stability function (ref 9-10).

## DUCT HEIGHT NOMOGRAMS

The measurements necessary for duct height calculations according to equations (1) - (3) are surface water temperature  $T_S$  and, at some convenient reference height, air temperature  $T_A$ , relative humidity  $RH$ , and wind speed  $WS$ . Refractivity  $N$  is calculated from

$$N = \frac{77.6 P}{T} + \frac{3.73 \times 10^6 e}{T^2} \quad (4)$$





Where  $P$  is atmospheric pressure in millibars,  $T$  is temperature in Kelvins, and  $e$  is water vapor pressure in millibars. A simple nomogram (figure 3) was developed which provides an easy means for deriving evaporation duct height based on simple bulk meteorological measurements. Starting at graph 1 in figure 3, a horizontal line is drawn for the measured RH and TA values until it intersects the appropriate TS curve in graph 2. From this intersection a vertical line is drawn into graph 4 where the intersection with a horizontal line starting at the measured TA-TS and WS values of graph 3 gives the duct height DH. Since evaporation duct height by itself does not give quantitative systems performance data, additional nomograms have been developed in which the graph for duct height is replaced by, for instance, a radar detection range graph. In figure 4 the range of detecting a 30000 m<sup>2</sup> target with a 90% probability using an SPS-10 radar is shown (graph 4). Besides eliminating cumbersome and lengthy calculations, figures 3 and 4 illustrate also the sensitivity of evaporation ducting assessment to the measurement accuracy of the input parameters. For example, small changes to air-sea temperature differences values may significantly change duct heights and detection ranges. Both nomograms shown in figures 3 and 4 are based on models and their verification described by Hitney (ref 3) and Richter and Hitney (ref 11).

#### MODEL SENSITIVITIES

Patterson (ref 1) recently compared the relative performance of evaporation duct and path loss models. He found that the models performed reasonably well when considering statistically averaged meteorological inputs but, not surprisingly, were extremely sensitive to point-observed meteorological input parameters. He concluded that the measurement techniques employed by naval and transiting commercial vessels are not of sufficient quality to calculate individual evaporation duct heights. Figures 5 and 6 illustrate the spread between measured and calculated 9.624 GHz path loss data based on the models used by Rotheram (ref 4) and by the Integrated Refractive Effects Prediction System (IREPS) (ref 2, 11, 12, 13). (The measured data are from ref 11, November period, path length 19 nmi, transmitter antenna height 5 m). Since small uncertainties in air-sea temperature differences (see figure 3) may cause significant changes in duct height, an evaporation ducting sensor development program is being conducted at the Naval Ocean Systems Center, which uses a single sensor for TA and TS measurement. This eliminates the need of accurate cross calibration for different sensors. A very fast response thermistor probe, connected by wire to a shipboard processing unit, is thrown from a convenient shipboard location into water undisturbed by the moving ship. During the fall the probe measures TA and, subsequently, TS when entering the water. The probe may be retrieved or made expendable. Initial tests showed that air-sea temperature differences of 0.1 Celsius are obtainable. This, by far exceeds, commonly achievable accuracies and should improve individual evaporation duct height measurements significantly.

#### CORRECTION ALGORITHM

Examining evaporation ducting statistics like the one shown in figure 7 (for Marsden Square 88, Hawaii), one often finds high percentages of duct height occurrences for large duct heights (all duct heights in excess of 40 m are combined in the column 40-42 m). Such large evaporation duct heights are difficult to explain from a micrometeorological interpretation, are not supported by radio propagation observations and are not found in meteorological measurements for which special care has been taken like meteorological buoy observations (ref 5). The most likely error source is surface heating in TA measurements which leads to erroneous high thermal stabilities. Paulus (ref 5), based on a number of careful arguments, introduced a modified duct height calculation algorithm in which stable, high humidity conditions are accepted and stable, low humidity conditions are assumed to be in error and defaulted to unstable. This algorithm applied to the data of figure 7 produces a much more reasonable distribution and is shown in figure 8. Even more convincing is an application of Paulus' (ref 5) technique to 18 GHz propagation measurements over an 81 km over-water path (transmitter and receiver heights were 19 m and 11 m, respectively). The solid curve in figure 9 is the calculated path loss for this geometry and the dots are measured values. When Paulus' technique (ref 5) was applied to the measured values of figure 9, a significantly better agreement was obtained as shown in figure 10. From the evidence so far it appears that Paulus' modified duct height calculations are capable of dramatically improving evaporation ducting statistics.

#### SURFACE DETECTION RANGES

Based on measurements described in ref 11, it appears that signal enhancements from evaporation ducting are largest in the 10-20 GHz frequency range. For higher frequencies molecular absorption, scattering from the rough ocean surface, inhomogeneities in the evaporative duct and scattering from aerosols counteract the otherwise increased effectiveness of the wave guiding mechanism. Anderson (ref 6) compared four hypothetical radars with equivalent performance characteristics but operating at frequencies of 3, 6, 10, 18 GHz. He used a global refractivity climatology (ref 14) and propagation models discussed in ref 15 to calculate the probability of detecting surface targets at ranges well beyond the normal radar horizon. The results are displayed in figure 11 and show both a latitude dependence, i.e., the evaporation ducting effect is stronger in lower latitudes, and the superior performance for frequencies in the 10-20 GHz frequency band.

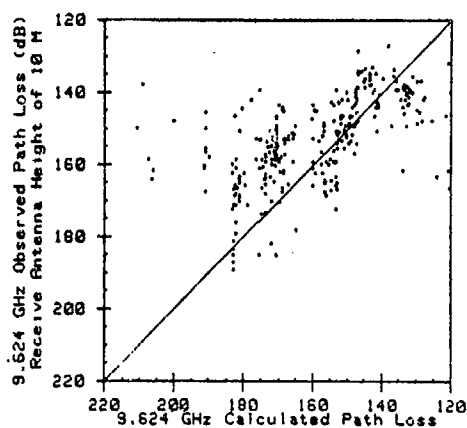


Figure 5. Observed calculated path loss for Rotheram models (ref 4).

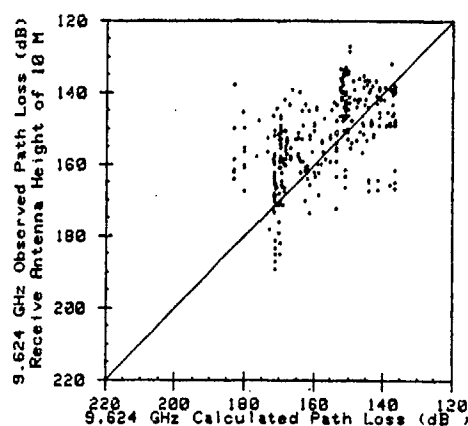


Figure 6. Observed versus calculated path loss for IREPS (ref 2, 11, 12) models.

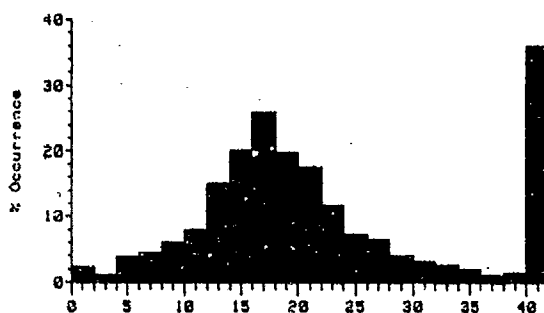


Figure 7. September IREPS duct height distribution for MS 88.

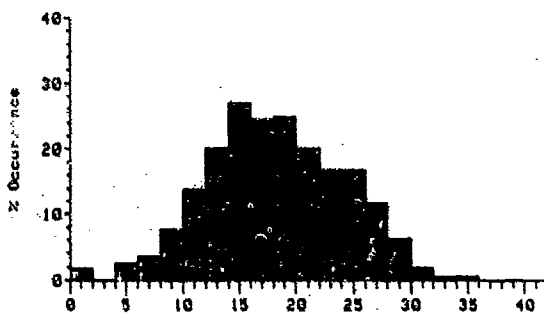


Figure 8. September modified duct height distribution for MS 88.

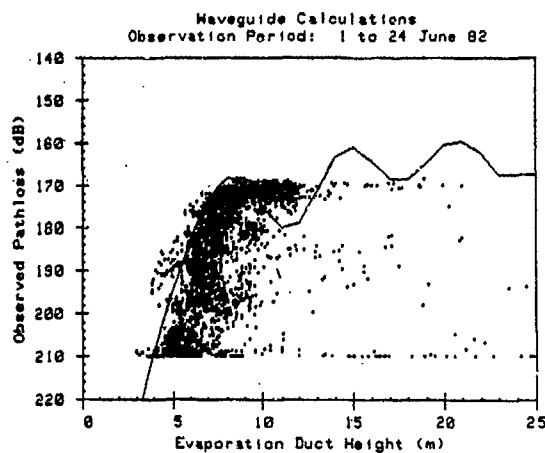


Figure 9. Comparison of experimental measurements to waveguide predictions.

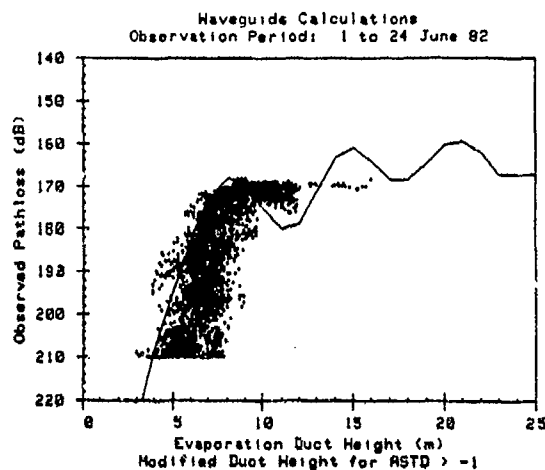


Figure 10. Comparison of experimental measurements to waveguide predictions in which all data points based on an air-sea temperature difference greater than  $-1^{\circ}\text{C}$  were subjected to a modified duct height calculation.

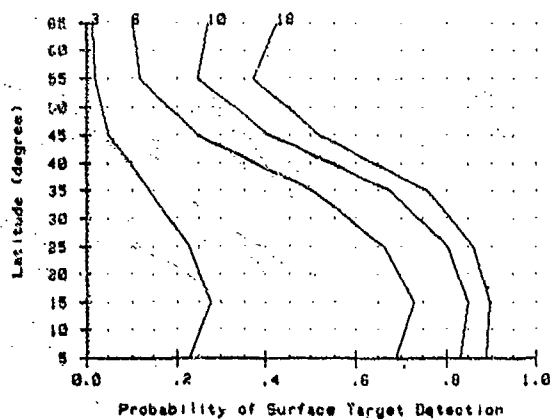


Figure 11. Geographic influence of the evaporation duct on shipboard radar surface-target detection capabilities. The target is well beyond the normal horizon and the increased detection range is solely due to the evaporation duct. Predictions are for four radar frequencies; 3, 6, 10, and 18 GHz.

## CONCLUSIONS

Evaporation ducting is an important propagation enhancement mechanism over the oceans of continued scientific interest. Recent efforts have shown that presently used models appear adequate for statistical assessments. An important correction algorithm was developed to remove erroneously high duct heights. A new air-sea temperature probe is under development which is expected to improve in-situ evaporation ducting assessment. Future work should address propagation modeling under horizontally inhomogeneous conditions, investigation of sensing techniques for the three-dimensional evaporation ducting structure and development of meteorological forecasting techniques.

## ACKNOWLEDGMENT

This work was supported by the Office of Naval Technology under the Atmospheric Effects on EM/EO Propagation program.

## REFERENCES

1. Patterson, W.L., "Comparison of Evaporation Duct and Path Loss Models," Radio Science, 20 (5), pp 1061-1068, 1985.
2. Jeske, H., "The State of Radar Range Prediction Over Sea," AGARD Conf. Proc., 70 (2), pp 50.1-50.10, 1971.
3. Hitney, H.V., "Propagation Modeling in the Evaporation Duct," Naval Electronics Laboratory Center TR 1947, 1975.
4. Rotheram, S., "Radiowave Range Prediction Over the Sea in Evaporation Ducting Conditions," Marconi Research Laboratory, TR 77/37, 1977.
5. Paulus, R.A., "Practical Application of an Evaporation Duct Model," Radio Science, 20 (4), pp 887-896, 1985.
6. Anderson, K.D., "Surface-Search Radar Performance in the Evaporation Duct: Global Predictions," Naval Ocean Systems Center TR 923, Rev A, 1983.
7. Monin, A.S. and A.M. Obukhov, "Basic Laws of Turbulent Mixing in the Ground Layer of the Atmosphere," Akad. Nauk. USSR Geofiz. Inst. Tr., (151), pp 163-187, 1954.
8. Lumley, J.L., and H.A. Panofsky, "The Structure of Atmospheric Turbulence," New York, Interscience Publishers, 1964.
9. Businger J.S., J.C. Wyngaard, Y. Izumi, and E.F. Bradley, "Flux-profile Relationships in the Atmospheric Surface Layer," J. Atm. Sci., (28), pp 181-189, March 1971.
10. Rotheram, S., "Radio Propagation in the Evaporation Duct," the Marconi Review, XXXVII, No. 192, pp 18-40, 1974.
11. Richter, J.H. and H.V. Hitney, "The Effect of the Evaporation Duct on Microwave Propagation," Naval Electronics Laboratory Center, TR 1949, 1975.
12. Hattan, C.P., "Propagation Models for IREPS Revision 2.0," Naval Ocean Systems Center, TR 771, 1982.
13. Hitney, H.V. and J.H. Richter, "Integrated Refractive Effects Prediction System," Nav. Eng. J. 88 (2), pp 257-262, 1976.
14. Patterson, W.L., "Climatology of Marine Atmospheric Effects," Naval Ocean Systems Center, TD 573, 1982.
15. Hitney, H.V., J.H. Richter, R.A. Pappert, K.D. Anderson, and G.B. Baumgartner, "Tropospheric Radio Propagation Assessment," Proc. IEEE 73 (2) pp 265-283, 1985.

## DISCUSSION

**E.Vilar**

- (1) You presented results obtained in the early 70s at several frequencies, X-band in particular, between two Greek islands. Could you tell us the transhorizon path length?
- (2) We are currently concerned in Europe with transhorizon interference over-sea paths (part of Eurocop COST 210). Could you please comment about the desirability and minimum sample of meteorological data to correlate our observations with the existence of an evaporation duct?

**Author's Reply**

- (1) Path length was 19 nmi with terminal heights of 5 m (see figure 16 of reference 15).
- (2) The parameters describing the evaporation duct must be carefully measured as described in the preceding paper. In addition, upper air soundings should be taken to differentiate between ground-based ducting effects caused by elevated refractive layers and evaporation ducting effects.

**L.B.Felsen**

Because the physical environment presents a multiparameter problem, where the parameters themselves are not well defined, no progress can be made on analytical and numerical modelling unless some sort of error bars can be put on the parameters. Those tolerances then can guide the modeller as to whether attempts at improving presently available predictive algorithms are likely to bear fruit. Do you feel that more can or *must* be done to sharpen the question, or have we reached an impasse?

**Author's Reply**


More can and must be done in providing experimental data to validate existing models and guide the development of new ones. The problem in obtaining good experimental data is cost and time. Measurement of all relevant physical parameters is expensive and encountering a sufficient large range of the uncontrolled variables may require long measurement periods or many repetitions. Once acquired and properly documented, good experimental data can and have been used for many decades in various model validation purposes.

**H.Vissinga**

Can you elaborate somewhat on the physics of the evaporation duct in the presence of a rough sea surface. In view of the fact that duct height and wave height are not that different in magnitude can an evaporation duct exist over a rough sea?

**Author's Reply**

As one can see from figure 3, duct height increases with increasing surface winds under unstable conditions. Since surface winds are directly related to sea surface roughness, one would not expect the simultaneous occurrence of rough seas and small duct heights. Extremely high winds will create a well mixed atmosphere with no evaporation duct. In our measurements, sea surface roughness affected path loss values only for frequencies well above X-band.



AD-P005 742

IDENTIFICATION OF MICROWAVE LINE-OF-SIGHT MULTIPATH COMPONENTS

A Hewitt, I Martin(\*), WH Lau, J Austin, KH Craig(#), E Vilar

Department of Electrical and Electronic Engineering,  
 Portsmouth Polytechnic,  
 Anglesea Road,  
 Portsmouth, PO1 3DJ,  
 England.

\* - C.N.E.T.,  
 Lab / Mer,  
 Route de Tregastel, BP 40,  
 22301, Lannion Cedex,  
 France.

# - Rutherford Appleton Laboratory,  
 Chilton,  
 Didcot,  
 Oxon, OX11 0QX,  
 England.

Summary

Fading due to multipath propagation is frequency-selective. Given a wideband measurement of the channel transfer-function, it is of interest to estimate the delays and amplitudes of the multipath rays. Fourier techniques suffer from limited resolution and "sidelobes". Alternative parametric methods are available and one, the Prony algorithm, has been used in this research. The algorithm has been tested against a database of laboratory-generated "fades" involving known delays and amplitudes. The capabilities and limitations of the method are outlined. Results obtained using real "in-the-field" measurements are illustrated and discussed as are the areas of applicability of this approach.

Keywords: multipath fading, selective fading, autoregression, Prony algorithm

1. Introduction

This paper describes research work carried out into ways of analysing multipath transfer-functions in order to study the underlying propagation phenomena. Attention is focused particularly on ways of estimating the delays and amplitudes of the discrete set of rays which are assumed to constitute the propagation.

The particular algorithm which has been utilised in this research, the Prony algorithm, is described in Section 2, after a general discussion of the problem being considered and of ways of tackling it. Section 3 of the paper outlines some research carried out into the functioning of the Prony algorithm by applying it to transfer-function measurements made using a network containing known delays and amplitudes. After this, the algorithm is applied in Section 4 to real "in-the-field" measurements made in the UK and in France. Certain limitations of the algorithm become apparent in these cases, and some of the lines of continuing research in this area are mentioned. Section 5 summarises the results of the paper and discusses the applicability of the approach adopted in this research.

2. Processing of Multipath Measurements

In this paper we assume that a measurement has been made, in amplitude and phase / group-delay, of a frequency-selective fading multipath channel over a wide bandwidth. Such a measurement is of interest in its own right, but the interest of the research described in this paper is in the use of such measurements in studying the underlying propagation phenomena by estimating the delays and amplitudes of the rays which constitute the multipath.

2.1 Possible Approaches

Since the change from transfer-function to delays and amplitudes is a transformation from frequency-domain to time-domain, the obvious approach to consider is the Fourier transform. Unfortunately, the transfer-function data is generally sampled and of finite extent so that the appropriate form is the discrete Fourier transform (DFT). This suffers from problems of limited resolution and sidelobes which have been well documented by, for example, Harris [1]. The resolution available is limited to  $4.84 \text{ ns}$  for  $250 \text{ MHz}$  data (the  $6\text{-dB}$  width of the main lobe:  $1.21 \times \text{bandwidth}$ ) with a first sidelobe only  $-13 \text{ dB}$  down on

the main lobe. Windowing can reduce the sidelobe levels, but at the price of worsened resolution.

The reason why the DFT is not a very successful method for processing multipath is that there is an inherent mismatch between the implicit model of the DFT and the actual structure of a multipath transfer-function. In particular, the DFT attempts to fit a "harmonic" model of a large number of evenly-spaced terms whereas the multipath data is due to a small number of arbitrarily-spaced terms, a discrepancy perhaps not as widely appreciated as it should be. However, there are a number of methods available which involve fitting a more appropriate parameterised model to the data and these are known as parametric methods. Unlike the Fourier transform, they are inherently nonlinear in that the output model parameters (delays, amplitudes etc.) are not linear functions of the input data.

There are a wide variety of modern nonlinear spectral analysis techniques available [2], but the one chosen for this research is a version of a method first developed by Prony in the late 18th century. In fact, the modern Prony algorithm bears little resemblance to the original. It has been chosen for this research because it yields a discrete set of delay amplitude pairs.

## 2.2 The Prony Algorithm

When modelling multipath at microwave frequencies, the received signal is generally assumed to consist of a finite set of delayed, attenuated copies of the original transmitted waveform. This is a consequence of the discrete raypaths that result from a geometrical optics propagation model. The channel impulse response is therefore:

$$h(t) = \sum_{k=1}^N a_k \delta(t - \tau_k) \quad (1)$$

i.e.  $N$  "rays" with delays  $\{\tau_k\}$  and amplitudes  $\{a_k\}$ . The transfer-function samples which would result from this at frequencies  $\{f_n\}$  are:

$$H_n = \sum_{k=1}^N a_k e^{-j2\pi f_n \tau_k} \quad (2)$$

Now, if the frequencies are evenly spaced with spacing  $f_s$  so that:

$$f_n = f_s + n f_s \quad (3)$$

then we can write each transfer-function sample  $H_n$  as:

$$H_n = \sum_{k=1}^N b_k Z_k^n \quad (4)$$

where

$$b_k = a_k e^{-j2\pi f_s \tau_k} \quad (5)$$

and

$$Z_k = e^{-j2\pi f_s \tau_k} \quad (6)$$

Given equation (4), it can be shown [e.g. 3] that the  $\{H_n\}$  transfer-function samples have an autoregressive structure:

$$H_n = -\sum_{k=1}^N \lambda_k H_{n-k} \quad (7)$$

with each sample being a linear combination (weighted sum) of its predecessors. Equally,  $H_n$  can be expressed as a linear sum of its successors. The weighting factors  $\{\lambda\}$  can be shown to be the coefficients of a polynomial  $P(z)$ , defined as that polynomial whose roots are the  $Z_k$  terms of equation (6):

$$P(z) = \prod_{k=1}^N (z - Z_k) = \sum_{k=0}^N \lambda_k z^{N-k} \quad (8)$$

with  $\lambda_0 = 1$ .

The Prony algorithm utilises this inherent structure of multipath transfer-functions so as to deduce the delays and amplitudes of the constituent rays. This is done in three stages:

- (1) solve the system of equations (7) for the autoregressive coefficients  $\{\lambda\}$ ;

(ii) factorise  $P(z)$  to obtain the  $z_k$ 's and hence, by (6), the  $\tau_k$ 's;

(iii) solve equation (4) for the complex amplitudes  $\{b_k\}$ .

Stage (i) of this process, the autoregression, can, in principle, be implemented using standard techniques for solving overdetermined systems of linear equations. However, the high degree of mutual dependence of the various terms in the equations can lead to severe numerical problems. Fortunately, algorithms have been found, such as that due to Marple [4], which turn the special structure of the equation to advantageous use. Similarly, a variety of reliable algorithms have been published for stage (ii): the polynomial factorisation. The algorithm used in this research is that of Grant & Hitchins [5]. Work on these two stages has been previously published in initial form in [6].

The amplitude estimation (iii) is another overdetermined system which, unlike (i), is amenable to standard methods utilising the pseudo-inverse of a rectangular matrix. In this research, we do not attempt to derive the real amplitudes  $\{a_k\}$  from the complex  $\{b_k\}$  since the uncertainty in  $\tau_k$  is too large to be able to determine the sign of  $a_k$  from equation (6).

A further stage (iv) is added to the algorithm to assist in the evaluation of the effectiveness of the method. This involves substituting the deduced amplitudes and delays into equation (4) so as to produce a set of "reconstructed" transfer-function samples  $\{H^r\}$  which can then be compared with the original  $\{H_n\}$ .

A variety of practical problems arise when using the algorithm. Of particular significance are the effect of added noise in the data and the associated difficulty of selecting an appropriate model order  $N$ . Empirical solutions to these problems have been adopted [3] and they are the subject of continuing research.

### 3. Laboratory Results

In order to test the operation of the algorithm, it was first applied to a set of measurements made on a network consisting of known delays and amplitudes. This was done at Portsmouth using the PP/RAL experimental equipment and a hardware "multipath simulator" (both outlined in Appendix A). The relative delays available were 0 ns, 2.25 ns, 5.75 ns and 10.75 ns, and a database of measurements was produced containing 38 files each applying distinct patterns of attenuation to the four delays. Of particular interest were the files which made use of the two rays separated by only 2.25 ns which, for the 250 MHz bandwidth used, are much closer than the Fourier resolution limit of 4.84 ns quoted above.

Each file contained eight "scans" (transfer-function measurements) with constant parameters but independent noise. Consequently we can calculate means and standard deviations for the results obtained using the Prony algorithm. These statistical parameters have been studied to elucidate the behaviour of the algorithm.

As well as the statistical studies, the capabilities of the algorithm were examined visually, using the "reconstruction" operation discussed in Section 2. As an example of the results obtained, consider Figures 1 and 2. These show a transfer-function (in amplitude and group-delay) generated using the 0 ns, 2.25 ns and 10.75 ns "rays" together with the reconstructions (solid line = original; broken line = reconstruction). It will be seen that the reconstructions are very good even though this file contains delays which the Fourier transform would be totally incapable of resolving. The impulse response associated with this reconstruction is shown in Figure 3 where it is clear that the two close "rays" have been successfully resolved.

The capabilities of the algorithm which have been deduced using this and many other similar laboratory results can be summarised as:

(i) the Prony algorithm can consistently resolve delays whose separation (2.25 ns) is less than half the Fourier limit (4.84 ns);

(ii) the Prony algorithm can allocate amplitudes to the delays so as to yield accurate reconstructions of the original measurement.

At this stage of the research it is not possible to give detailed quantitative measures of the algorithm's accuracy since this will depend on several factors (e.g. signal-to-noise ratio) which have not been thoroughly explored but are the subject of continuing study, using new laboratory measurements. However, the statistical analysis of the laboratory results has indicated certain problems. For example, although the standard-deviation of the delay estimates is generally small, the mean does not coincide exactly with that expected: i.e. the delay estimator is to some extent a biased estimator. Typically the biases are of the order of 0.5 ns for this database. The amplitude estimators are also biased.

A study of the correlation between various factors within the database has given some insight into the mechanism of these biases. For example, the estimates for a given ray seem to be affected by the strength of that ray and also by the strength of the other rays present in the measurement. Unfortunately, the estimates are also affected by the measurement hardware, particularly the operation of looking onto one of the rays as the "direct ray". It is therefore difficult, at the present stage of the study, to readily



distinguish between biases due to the algorithm and those due to the measurement equipment. This is the subject of continuing research, but a more detailed account of the results thus far can be found in [3].

#### 4. Field Results

Having investigated the capabilities and limitations of the Prony algorithm in the laboratory using known delays and amplitudes, it is of obvious interest to see what sort of results can be obtained when using real "in-the-field" experimental data. Some initial studies have been carried out using data obtained in the UK and in France.

##### 4.1 UK Results

The UK results were obtained during the initial field trials of the PP/RAI experimental equipment in 1984. The link was 29.05 km, across the Thames valley and the path was inclined at  $0.25^\circ$  to the horizontal. Due to problems with equipment reliability, only a few files were produced that were not attributable to system malfunction and the first scan from one of these is shown together with its reconstruction in Figures 4 and 5. It is clear that the overall curvature of the dB graph (indicative of a pair of rays with a small separation) is well reproduced. The medium-scale ripple (due to a longer delay) is also generally matched, except in the middle of the band where there is a mismatch of about 2 dB. The extremely rapid fluctuations, most noticeable on the group-delay curve, are not reproduced. This is because the implementation of the Prony algorithm used here eliminates excessively long delays. In this particular case, the Prony algorithm finds four "real" rays together with several "spurious" rays which are of small amplitude and are associated with the noise content of the data.

##### 4.2 French Results

The Prony algorithm of Section 2 has also been applied to measurements, made in France as part of a long-running experiment [7]. Unlike the other measurements presented in this paper, these have been obtained using a frequency sweeping system, described in Appendix B, which gives amplitude and group-delay rather than the complex Fourier components of the UK experiment. Also unlike the UK field and laboratory results, the Prony algorithm so far yields only moderate success when applied to a limited selection of French data.

Figures 6 and 7 show a typical measurement (solid line) together with its reconstruction (broken line). This is one of the more successful analyses. The main discrepancy on the amplitude plot is that the reconstructed nulls (one of them just off the left-hand edge of the plot) are too close together: i.e. the predominant pair of rays have been estimated too far apart. The discrepancy on the group-delay plot is more apparent than real. Away from the nulls the reconstruction is quite good whilst in the region of the nulls the polarity of the group-delay is reversed. This is not indicative of a serious error; a small change in a ray's delay or amplitude can have this effect.

By contrast, Figures 8 and 9 show one of the less successful analyses, though by no means the worst. It is clear that although the algorithm has managed to correctly locate the null, the match between the two sets of curves is not all that good. It is suspected that this imperfect reconstruction may result from a mismatch between the propagation model assumed by the algorithm and that which actually occurred, resulting in the frequency-selective fading. In particular, if the actual propagation incorporated a ground-reflection then it is possible that the contribution to the impulse response of that ray would become diffuse and would not match the delta-function assumed by the algorithm.

In a recent Portsmouth / CNET collaboration, a refinement to the algorithm has been considered which takes the delay and amplitude estimates from the Portsmouth Prony program and uses them as initial values in a CNET optimisation program. The aim is to obtain the best possible fit between the discrete ray model and the data. In some initial investigations this refinement gave a consistent minus sign on the amplitude estimate for one of the rays, strongly suggesting the presence of a reflection with its associated phase-reversal. The optimisation also showed an improvement in null-location for data similar to that in Figure 6. This aspect of the research is a very recent development which shows great promise.

#### 5. Conclusions

The research outlined in this paper has indicated the usefulness of nonlinear spectral analysis techniques, such as the Prony algorithm, for the study of multipath propagation via the analysis of wideband fade measurements. Using these modern numerical methods it is possible to resolve rays whose spacing is significantly less than the Fourier limit. With the addition of a further stage of processing (an optimisation developed by CNET) the approach holds out the promise of extremely accurate estimation of both delays and amplitudes provided the propagation fits the model assumed in the algorithm being used.

Were the algorithms of sufficient computational efficiency, one might envisage using them in adaptive equalisation on real links. Unfortunately, the computational complexity of the algorithms would prohibit this at present. Thus the clearest areas of applicability of the work are those for which the need for off-line non-real-time processing are not a hindrance. For example, an accurate knowledge of the delays and amplitudes underlying a real multipath fading sequence would be useful for the prediction of the effect on new digital radio systems etc. It would also enable the simulation of the frequency-selectivity which could occur in frequency bands other than that in which the measurement was originally made, subject to the provision of the applicability of the geometrical optics model of propagation. There are probably many other potential applications, but it is expected that they would generally fall into the category of simulation / prediction.

#### 6. Acknowledgements

The research at Portsmouth is being sponsored by the UK Science and Engineering Research Council; the authors are grateful for a research grant and one scholarship.

#### 7. References

- [1] Harris FJ : " On the Use of Windows for Harmonic Analysis with the Discrete Fourier Transform ", Proc IEEE, vol 66, no 1, June 1978
- [2] Kay SM, Marple SL : " Spectrum Analysis - A Modern Perspective ", Proc IEEE, vol 69, no 11, November 1981
- [3] Hewitt A : "Theoretical and Experimental Study of LOS Refractive Multipath at 18 GHz ", Ph.D Thesis, Department of Electrical and Electronic Engineering, Portsmouth Polytechnic, UK, October 1986
- [4] Marple SL : " A New Autoregressive Spectrum Analysis Algorithm ", IEEE Trans ASSP-28, no 4, August 1980
- [5] Grant JA, Hitchins GD : " An Always Convergent Minimisation Technique for the Solution of Polynomial Equations ", J. Inst Maths. Applics., vol 8, 1971
- [6] Hewitt A, Moulisley TJ, Austin J, Vilar E, Craig KH, Whitehead N, Barton SK, Norbury JR : " An 18 GHz Wideband LOS Multipath Experiment ", IEE International Conference MTTs '85, London UK, November 1985
- [7] Martin L : " Statistical Results on Selective Fading ", ICC '82, pp 7B.3.1-5
- [8] Vilar E, Moulisley TJ, Austin J, Hewitt A, Norbury JR, Barton SK : " A System to Measure LOS Atmospheric Transmittance at 19 GHz ", AGARD Conference Proceedings no. 346, Spatind Norway, October 1983

#### 8. Appendixes

##### A: PP/RAL wideband experimental system [8]

This system uses a spread spectrum technique together with cross-correlation to probe the channel characteristics. The schematic diagram of the system is shown in Figure A1. In order to investigate the wideband channel characteristics, a high speed pseudo random binary sequence (PRBS) is used to cover a bandwidth of 250 MHz in the 18 GHz region.

In the transmitter, the 250 MHz PRBS bi-phase modulates a 750 MHz I.F. which is then up-converted to 18 GHz. Optionally a multipath simulator (M.S.) may be inserted at the output of the I.F. stage permitting the creation of a database of simulated multipath events.

The multipath simulator splits the incoming I.F. signal into four equal parts by a passive power splitter. The signal is then passed through four equal-length coaxial cables to a set of independent voltage controlled attenuators. Four unequal-length coaxial cables from these attenuators are connected to a power combiner. The different lengths of the cables represent the different delays, with the attenuators controlling the amplitudes, of the four rays.

The receiver system consists of three main parts: the receiver, correlator and data acquisition computer. All the receiver operations, such as synchronisation and locking, are under the control of a logic unit which in turn is supervised by the PDP 11 computer. The received signal is brought down to 750 MHz I.F. and correlated with a locally generated PRBS, a replica of the transmitted PRBS. Coherent demodulation is used to provide the equivalent quadrature components I & Q. Digitisation of these two components is carried out by a low noise, purpose built ADC unit. The computer is responsible for the on-line signal processing, in particular the removal of the system characteristics by a Fourier-based de-calibration using previously recorded calibration data. This data can be obtained by performing a system back-to-back test or an on-site test under suitable weather conditions. The captured data is transferred into magnetic tape for subsequent

off-line processing, such as that described in this paper.

#### B: French CNET measurement system

This system applies the frequency sweeping technique to probe the channel characteristic. In general, systems using such a technique will provide information of amplitude and phase (or rather the group delay) of the spectral components over the band of interest. The block diagram of the system is shown in Figure B1. This system can cover a bandwidth of 20 MHz up to 1.4 GHz in 11 GHz region.

In the transmitter, the main component is the frequency sweeper and it provides a sweeper range from 2.3 GHz to 3.7 GHz. The I.F., obtained by mixing the frequency sweep and 4.2 GHz master, has a maximum range of 0.5 GHz to 1.9 GHz. The nominal I.F. centre frequency will typically be about 1.2 GHz which will be subsequently up-converted to 11 GHz. To facilitate the measurement of the group delay, a small excursion high frequency FM is superimposed onto the sweep.

In the tracking receiver, the received signal is down-converted to the first I.F. of about 1.2 GHz. The main loop tracks the sweep of the received signal. The YIG oscillator is steered by the frequency discriminator and detector and its output is mixed with the 4.2 GHz master to follow the transmitter sweeper with an offset of 70 MHz. This second I.F. is used for the A.G.C. and fed into the microwave link analyser (M.L.A.). The output of the A.G.C. provides the amplitude data of spectral components. The M.L.A. uses the rapid FM, which is on the I.F. because it is too fast for the main loop to track, to obtain the group delay data. Finally the data is stored for subsequent off-line processing.

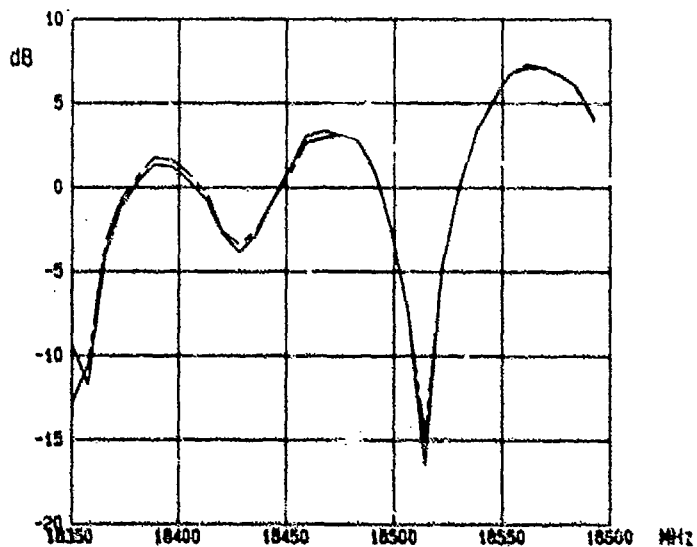


Figure 1: Original and reconstructed amplitude (laboratory)

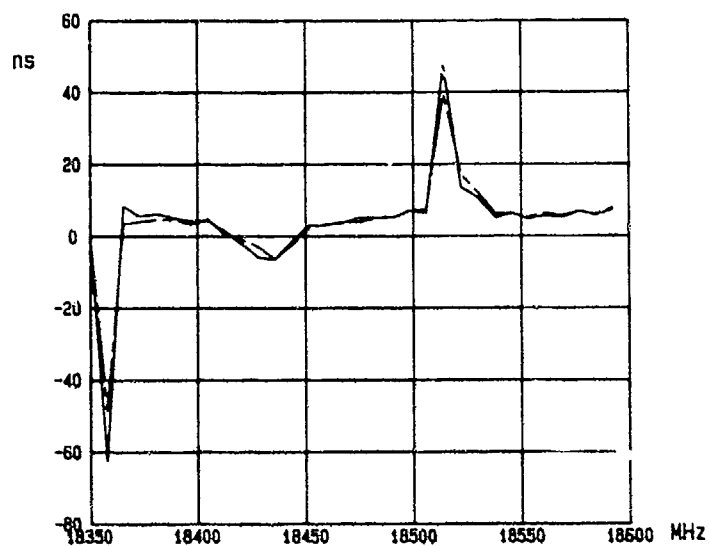


Figure 2 : Original and reconstructed group delay (laboratory)

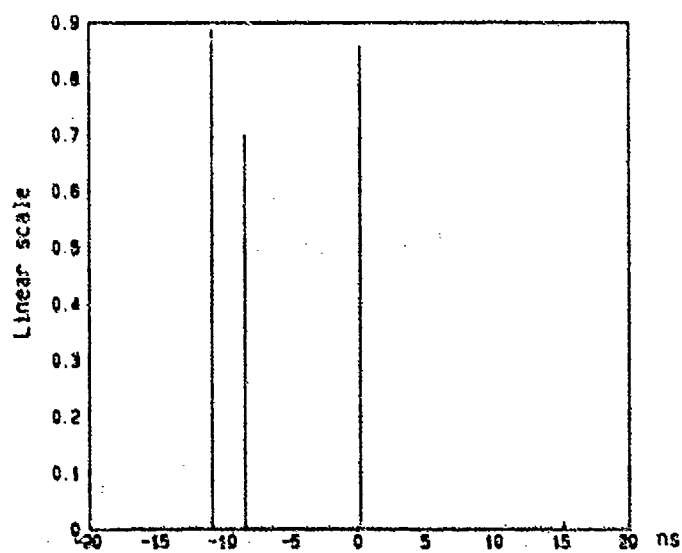


Figure 3 : Impulse response derived from Figure 1

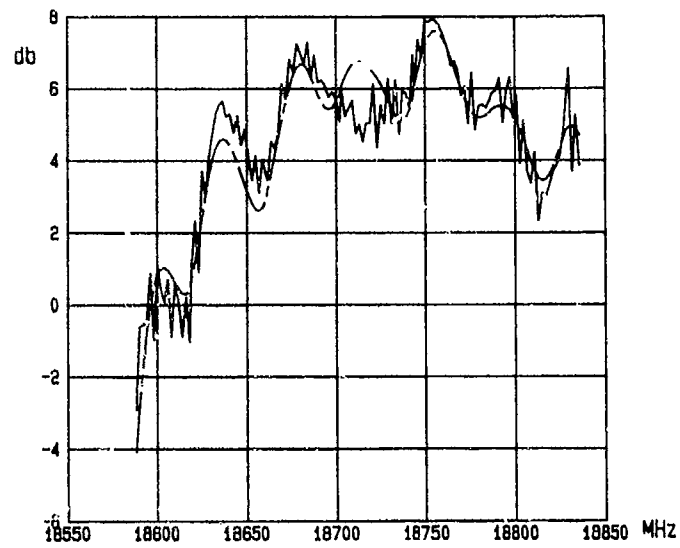


Figure 4 : Original and reconstructed amplitude (UK Field)

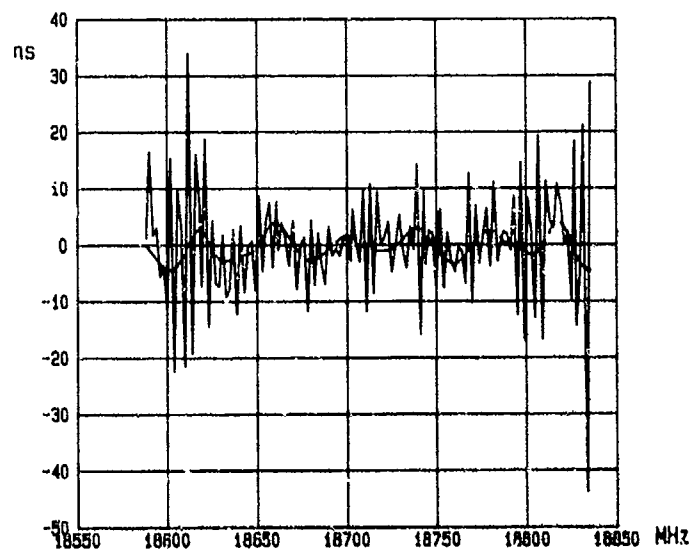


Figure 5 : Original and reconstructed group delay (UK field)

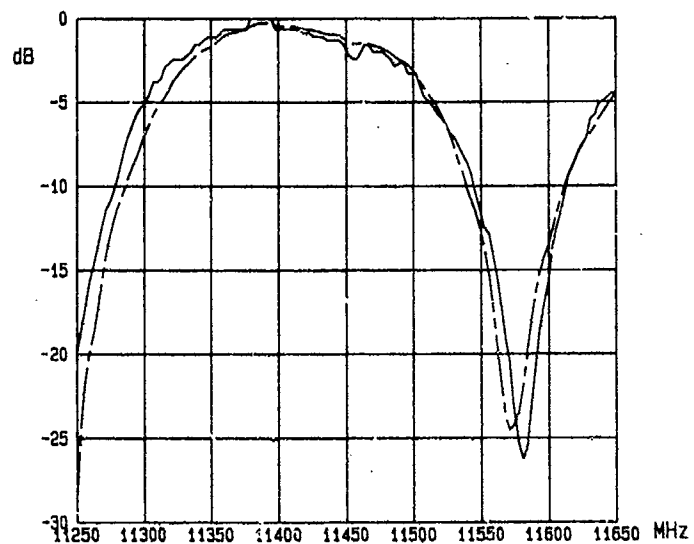


Figure 6 : Original and reconstructed amplitude (France field)

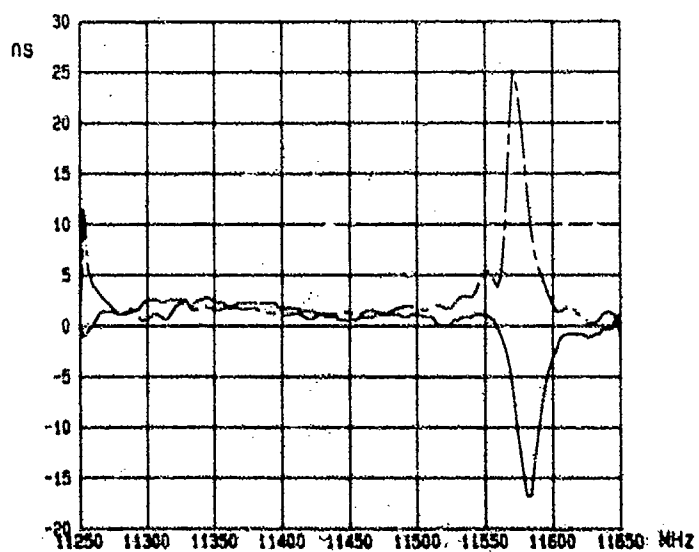


Figure 7 : Original and reconstructed group delay of Figure 6

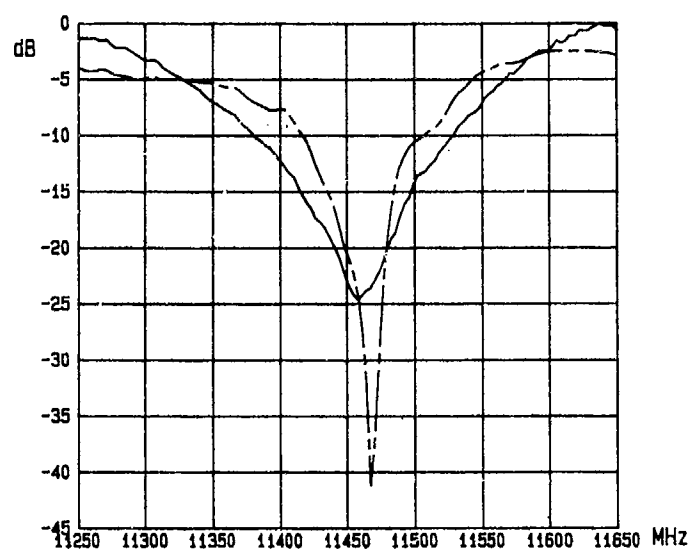


Figure 8 : Original and reconstructed amplitude (France field)

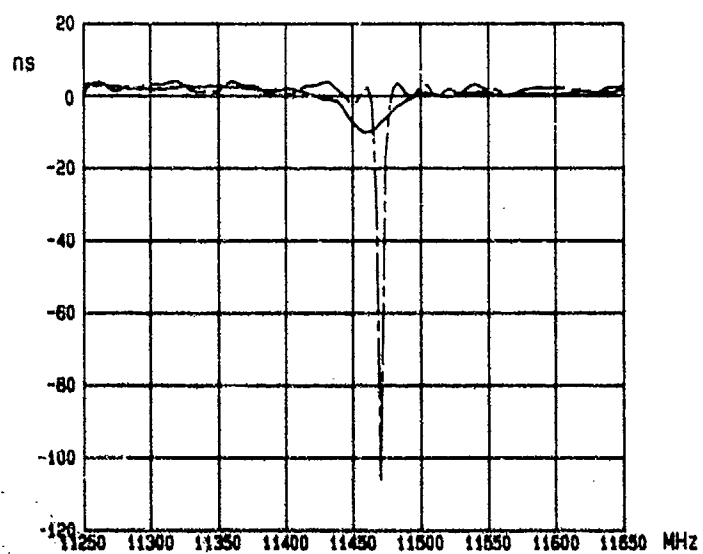


Figure 9 : Original and reconstructed group delay of Figure 8

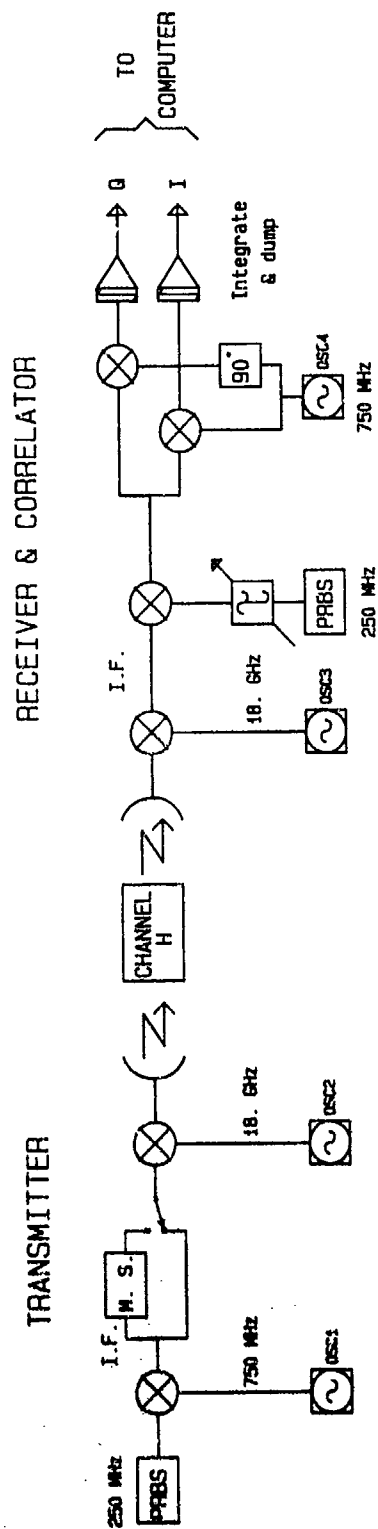


Figure A1 : PP/RAL wideband experimental system



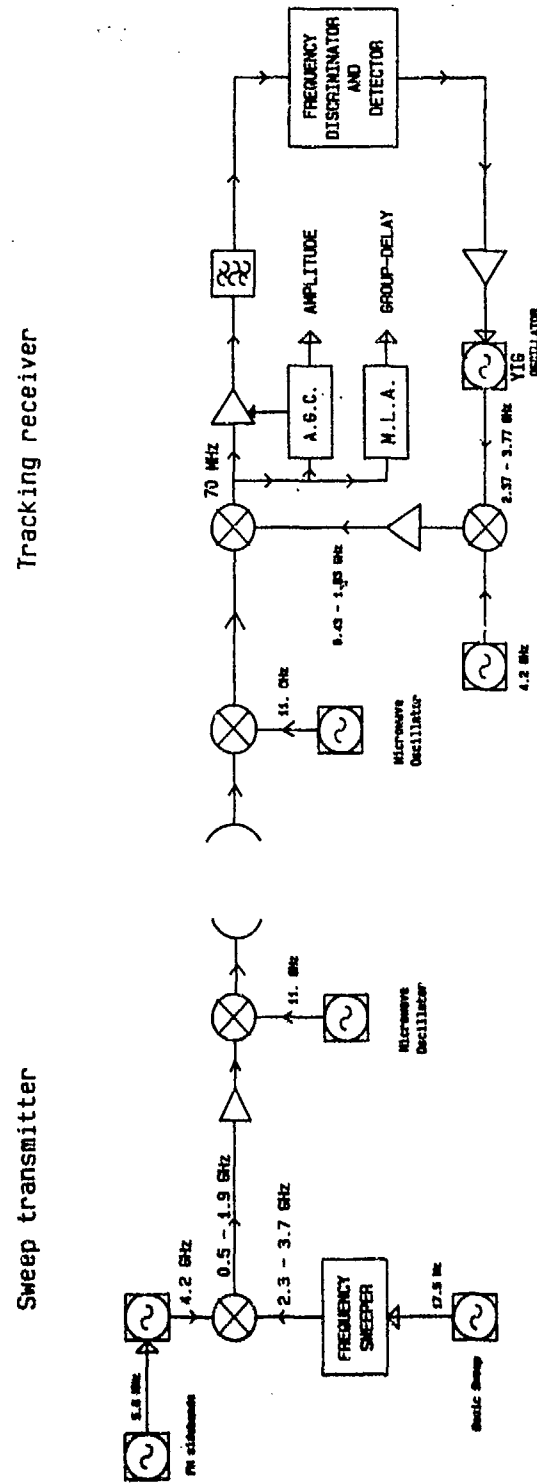


Figure B1 : CNET measurement system

## DISCUSSION

**L.B.Felsen**

The Prony algorithm is usually best suited to analysing signals with smooth oscillatory behaviour. But here, you seem to be using it for dealing with impulse events, which are not well handled in this manner. Could you clarify?

**Author's Reply**

The impulsiveness is in the assumed time-domain impulse response model. In the frequency domain this manifests as periodicities and it is the frequency-domain measurements that we are processing using the Prony algorithm.

**R.Valentin**

In Figures 4 and 5 you presented examples of amplitude and group delay responses showing rapid oscillations. What is the reason for this? Could it be caused by long waveguides connecting the antennas and the trans/receiver so that a mismatch at the ends of the waveguides can produce echoes with large delay?

**Author's Reply**

I do not think so. The waveguide runs used in our 18 GHz experiment are typically only 2 metres long. It is more likely to be due to noise, etc., in the correlator.

**R.L.Olsen**

I find it interesting that your results indicate the presence of a reflection. Could you please expand on your explanation as to why the Prony method does not handle this basely.

**Author's Reply**

Specular reflections do not present any problems, but diffuse reflections are less tractable. The reason for this is that a diffuse reflection is not well-approximated by the time domain delta-functions assumed by the Prony algorithm, although a grouping of multiple delta-functions may work or they may not. We are still investigating this subject area.



# COINDICE DE REFRACTION, METEOROLOGIE ET AFFAIBLISSEMENTS SUR LES TRAJETS EN VISIBILITE

L. MARTIN

CNET/LAB/MER  
Route de Trégastel  
22301 LANNION  
FRANCE

R.L. OLSEN

COMMUNICATIONS RESEARCH CENTRE  
Department of Communications  
P.O. Box 11490, Station H  
OTTAWA, Ont.  
CANADA K2H 8S2

T. TJELTA

NORWEGIAN TELECOMMUNICATIONS ADMINISTRATION  
Research Establishment  
P.O. Box 83  
N-2007 KJELLER  
NORWAY

## RESUME

Dans la mise au point d'une méthode de prévision fiable des affaiblissements à fréquence fixe, applicable, à l'ensemble d'un réseau de faisceaux hertziens, il est devenu indispensable de tenir compte des conditions radioclimatiques propres à chaque région occupée par un tel réseau hertzien. On propose une méthode purement météorologique pour le calcul d'un facteur géoclimatique, utilisé dans une formule de prévision des affaiblissements à fréquence fixe applicable au mois le plus défavorable. Cette méthode est basée sur l'étude simultanée du climat et des conditions de propagation sur deux couples de liaisons situées dans deux régions climatiques différentes.

## 1 - INTRODUCTION

Dans l'étude des relations entre les phénomènes météorologiques en air clair et les perturbations qu'ils entraînent dans la propagation des ondes radioélectriques sur les liaisons en visibilité, on peut distinguer deux types de démarche. L'une consiste à rechercher la concordance étroite entre une situation météorologique observée et les variations de champ reçu mesurées simultanément sur une liaison à fréquence fixe, bande étroite ou large bande. Cette concordance est en général recherchée par le calcul en usant de l'optique géométrique. Dans ce cas, une connaissance détaillée du profil vertical du coindice de réfraction,  $N$ , est nécessaire; il paraît indispensable de connaître aussi la variation horizontale de ce profil vertical. On fait l'hypothèse que la variation horizontale est faible, et à l'aide d'une radio sonde montée sur un ballon ou bien d'une tour instrumentée en plusieurs points on établit aussi finement que possible le profil vertical du coindice à chaque instant. Une telle démarche ne peut être appliquée à long terme du fait de son caractère coûteux. Or, les études statistiques de cette correspondance entre les affaiblissements et la météorologie pour la mise au point de méthodes de prévisions de ces affaiblissements sont nécessairement des études à long terme. L'autre démarche dans l'analyse des variables radio-météorologiques sera dans ce cas appliquée. Elle consiste à n'effectuer que des mesures météorologiques en deux points espacées verticalement de plusieurs dizaines de mètres, méthode simple mais qui peut être appliquée durant plusieurs années. On ne recherchera alors dans cette étude que les relations statistiques entre les variables météorologiques et les affaiblissements pour des durées d'analyse parfois grande, telle que le mois par exemple. On montre ci-après la validité d'une telle démarche appliquée à la recherche des conditions radioclimatiques à l'échelle du réseau hertzien d'un pays.

## 2 - QUELQUES ETUDES ANTERIEURES

### 2.1 - Etudes de l'indice de réfraction radioélectrique de l'atmosphère

Les premiers chercheurs qui ont étudié la propagation des signaux aux fréquences élevées sur des liaisons en visibilité directe ont très rapidement tiré la conclusion que les affaiblissements qu'ils observaient étaient dus à des structures verticales particulières de l'indice de réfraction radioélectrique. Ces structures donnaient soit des conditions d'infra-réfraction, soit le plus souvent des conditions de super-réfraction favorables à la génération de trajets multiples (CRANFORD et JAKES, 1952). A peu près à la même époque d'autres chercheurs conclurent aussi à l'importance des discontinuités de l'indice de réfraction de l'air dans la diffusion des ondes et leur propagation au-delà de l'horizon.

Les fluctuations spatiales et temporelles de l'indice de réfraction furent alors l'objet d'études intensives dans plusieurs pays. Nous nous limiterons volontairement à quelques unes d'entre elles. CRAIN (1953) a observé que des fluctuations rapides de l'indice de quelques unités  $N$  peuvent être mesurées jusqu'à 3 km d'altitude. Les dimensions verticales des discontinuités ne sont que de quelques pieds

quand on les mesure au niveau du sol, mais de plusieurs centaines de pieds à des altitudes supérieures à 300 mètres. UGAI (1959) fit aussi des études approfondies sur le sujet en utilisant une tour instrumentée et des radio sondes montées sur ballons. Il montre par exemple que le gradient  $dM/dh$  du coindice modifié tend vers sa valeur standard quand la vitesse du vent au sol augmente. De plus,  $dM/dh$  semble atteindre ses valeurs les plus faibles entre les vitesses de 0,5 et 1,5 m/s. Mais toutes les études de l'indice de réfraction faites jusqu'en 1961 semblent avoir été en relation avec l'étude de la diffusion troposphérique (LANE, 1961) et non avec les conditions de propagation sur les liaisons horizontales.

## 2.2 - Conduits atmosphériques et variations du niveau du signal radioélectrique

L'une des premières études sur les relations pouvant exister entre les discontinuités verticales de l'indice de réfraction et le champ radioélectrique reçu à l'extrémité de deux liaisons en visibilité semble avoir été celle conduite par IKEGAMI, et autres, (1959, 1966, 1967). Les auteurs utilisèrent pour leur expérience, qui dura 15 jours, un pylône instrumenté de 312 m de hauteur. Ils observèrent qu'environ la moitié des conduits sont des conduits de surface. Les conduits dont la hauteur moyenne se situe à environ 100 mètres du sol sont les plus intenses. Au-delà de cette hauteur, leur intensité décroît. On peut raisonnablement conclure qu'une liaison sera d'autant moins perturbée qu'elle sera bien dégagée par rapport au sol moyen. Dans cette expérience, l'une des liaisons est pratiquement horizontale, l'autre présente une inclinaison de 0,2°, les deux ayant la même longueur de 54,8 km. Sur la liaison horizontale, les variations à court terme les plus importantes du niveau du signal se produisent quand la hauteur moyenne du conduit est voisine de la hauteur de la liaison. Sur la liaison oblique, ces mêmes variations à court terme sont les plus importantes quand la hauteur moyenne du conduit se situe au voisinage de l'extrémité la plus basse de la liaison. Ceci semble montrer que les mesures météorologiques, qui seraient faites à l'extrémité la plus basse d'une liaison inclinée dans le but d'être comparées au niveau du champ reçu, seraient parfaitement justifiées. IKEGAMI (1967) a aussi montré que des interférences entre rayons multiples pouvaient aussi se produire en présence de couches, situées au sol ou bien dans son voisinage, dans lesquelles le gradient du coindice modifié  $M$  est positif. Cet auteur montre enfin que les courbures particulières du profil vertical de  $M$  peuvent conduire à des effets de diminution du niveau du signal par divergence et de renforcement du niveau par effet de convergence. Mais il n'a pas considéré la réflexion d'un signal sur le sol (OLSEN et autres, 1986, dans ce volume).

## 2.3 - Influence des gradients verticaux de température et influence du vent

Le coindice de réfraction  $N$  et sa valeur modifiée  $M$  sont la combinaison de trois variables physiques. SCHIAVONE (1983) a ainsi étudié la relation entre le gradient vertical de température mesuré entre 38,1 et 93,3 mètres et le pourcentage des apparitions d'affaiblissement supérieurs à 10 et à 20 dB. Ce pourcentage varie presque linéairement avec l'intensité de l'inversion de température de 0,5°C/100 m à plus de 4°C/100 m. La valeur de 3°C/100 m, soit 30°C/km, qui a été choisie dans l'étude présentée ci-après paraît donc parfaitement justifiée. La liaison radioélectrique simultanément étudiée avait une longueur de 57 km dans une région boisée, entre OMAHA et PALMETTO. SCHIAVONE (1983) a aussi montré que la vitesse du vent à 4 heures du matin pouvait être un bon indicateur climatique de la variation mensuelle de la probabilité d'apparition des affaiblissements dus à la réfraction.

Les concordances satisfaisantes obtenues par SCHIAVONE entre les mesures d'affaiblissement et les mesures de différences de températures faites en deux points seulement semblent indiquer que cette méthode de mesures simplifiée peut parfaitement rivaliser, pour certaines études notamment statistiques, avec celle plus élaborée qui consiste à utiliser une radio-sonde sur ballon ou bien un mât instrumenté en plus de deux points.

## 2.4 - Les mesures en deux points espacés verticalement

L'incidence de la méthode de mesure des variables météorologiques en deux points espacés verticalement a été étudiée pour le gradient des coindices. ROUX et MON (1983) ont montré que la pente des distributions des gradients de coindice de réfraction  $N$  diminue d'une façon importante quand la différence de hauteur entre les deux points de mesure passe de 28 mètres à 56 mètres puis à 83 mètres. La valeur médiane de la distribution diminue aussi. Ceci implique que des résultats semblables seront obtenus dans les mesures des gradients de température et de tension de vapeur d'eau.

Pour pouvoir comparer les distributions des gradients verticaux de température et les distributions des gradients verticaux de tension de vapeur d'eau obtenues en des lieux géographiques différents, il sera nécessaire de normaliser les résultats par rapport à un espacement vertical de référence. De plus, les conduits atmosphériques les plus intenses et les plus nombreux étant situés dans les 100 premiers mètres au-dessus du sol, il paraît souhaitable que les mesures différentielles des variables météorologiques soient effectuées entre un point situé au voisinage du sol et un autre localisé dans ces 100 premiers mètres.

## 2.5 - Rôle de l'humidité

IKEGAMI, et autres, (1966) a aussi observé que la création d'un conduit est étroitement reliée à l'apparition simultanée d'une couche avec inversion de température et d'une décroissance importante de l'humidité relative dans cette couche. L'humidité relative en un point de température donnée est le rapport entre la tension de vapeur d'eau,  $e$ , en ce point à cette température et la tension de vapeur saturante,  $e_s$ , à la même température, soit

$$H_R = \frac{e}{e_s} \times 100$$

où  $e_s = 6, 1078.10^{E_x}$ , en mb

et  $E_x = 7,5 T_c / (T_c + 237,3)$

$T_c$  est la température Celsius (SVLVAIN, 1984)

La tension de vapeur saturante,  $e_s$ , croissant rapidement quand la température augmente, l'humidité relative  $H_r$  décroîtra rapidement aussi. Ce phénomène peut se produire sans variation importante de la tension de vapeur d'eau,  $e$ . Il est donc probable que la corrélation entre les situations de ducts, et donc aussi les situations d'affaiblissements, et les gradients négatifs verticaux de la tension de vapeur d'eau ne soit pas évidente. Néanmoins, les gradients verticaux de  $e$ , sont une variable météorologie importante à prendre en compte du fait de son rôle dans l'expression du coindice de réfraction  $N$ .

### 3 - UNE ETUDE NOUVELLE EN FRANCE

#### 3.1 - Généralités

Les études à long terme de l'affaiblissement à fréquence fixe en période d'air clair sur les liaisons en visibilité ont montré la grande variabilité des distributions d'un mois à l'autre sur une même liaison (TATTERSALL, et autres 1977 ; DERENNES, 1979). La comparaison de l'affaiblissement dépassé pour un pourcentage de temps donné du mois le plus défavorable sur deux bonds, dont les principaux paramètres (longueur du bond, rugosité du profil, fréquence, hauteur des antennes, inclinaison du faisceau radioélectrique...) sont égaux, ou presque égaux, fait apparaître des différences parfois importantes, supérieures à 5 dB. De telles différences, qui ne peuvent s'expliquer que par les conditions climatiques, ont amené les organismes chargés de la planification des réseaux hertziens dans certains pays à ajouter à la formule de prévision des affaiblissements à fréquence fixe pour le mois le plus défavorable un terme correcteur, variable d'une région à l'autre (CCIR, 1986). Ce terme peut prendre des valeurs différentes suivant la région macro-climatique considérée dont le climat est soit tropical, soit tempéré. Ainsi aux U.S.A. on considère qu'à pourcentage de temps égal, l'affaiblissement dépassé sera de 6 dB supérieur dans une région de climat tempéré méditerranéen ou côtier ou de climat à forte humidité et températures élevées par rapport à une région sèche de haute montagne (BARNETT, 1972, VIGANTS, 1975). Pour la GRANDE-BRETAGNE, située dans la partie climatique tempérée du Nord-Ouest de l'Europe, J. DOBLE a trouvé que ce terme géoclimatique pouvait varier de 7 dB (DOBLE, 1979). Enfin, les premières études qui ont été faites en FRANCE sur l'évaluation de ce même terme géoclimatique montrent qu'il peut varier aussi de plus de 8 dB (TJELTA, et autres, dans ce volume).

On doit donc s'interroger sur l'origine de cette influence du climat et sur la manière de la paramétrer. L'évaluation qui a été faite jusqu'à présent du terme géoclimatique repose sur les analyses des distributions des affaiblissements à fréquence fixe faites, par exemple par régression multiple, sur une banque de données de propagation d'un volume obligatoirement limité (MARTIN, et autres 1985). Une telle analyse est indispensable mais doit être prolongée par une estimation de ce terme sur des données purement climatiques. Pour atteindre un tel objectif, des mesures à long terme simultanées des affaiblissements et de certains paramètres climatiques sont indispensables sur plusieurs liaisons dans différentes régions climatiques. Cette étude est en cours en FRANCE dans 11 stations de faisceaux hertziens où l'on mesure les principaux paramètres climatiques et simultanément sur 19 bonds hertziens reliés à ces stations dont on enregistre les variations des niveaux reçus.

On se contentera ci-après de donner la définition des variables climatiques mesurées qui nous ont paru avoir une réelle influence sur les conditions de propagation. On trouvera dans les références (ARCHAMBAULT, et autres, 1982) des renseignements détaillés sur cette expérience. Dans chacune des 11 stations hertziennes surveillées, un dispositif d'acquisition de données donne toutes les 3 heures 50 minutes environ, les pourcentages de temps pendant lesquels trois affaiblissements à fréquence fixe, variables d'un bond à l'autre, ont été dépassés sur deux bonds hertziens, ainsi que les pourcentages de temps de dépassement de cinq valeurs du gradient de coindice de réfraction  $\Delta N_s/\Delta h$  mesurée entre le sommet et la base de la tour de la station hertzienne considérée, gradients qui sont de + 200, + 100, - 157, - 300, - 450 en unités N/km. Le niveau radioélectrique reçu est mesuré chaque 1/10 de seconde, et les coindices de réfraction sont calculées toutes les trois minutes. A chaque fin de période de 3 heures 50 minutes, le dispositif d'acquisition donne aussi les températures sèches et humides au sommet et à la base de la tour, la pression atmosphérique à la base, les vitesses minimale  $V_m$  et maximale  $V_M$  et la direction du vent au sommet. On connaît donc à chaque période la différence des coindices de réfraction  $\Delta N_T$ , la différence des températures sèches  $\Delta T_s$ , l'écart entre les vitesses du vent  $\Delta V = V_M - V_m$ . Dans tout le texte qui suit, les différences des coindices de réfraction  $\Delta N_T$  et les différences des températures sèches  $\Delta T_s$  sont les différences entre les valeurs mesurées au sommet et les valeurs mesurées à la base de la tour hertzienne. Les gradients en ont été déduits. Les tensions de vapeur d'eau au sommet et à la base de la tour sont calculées à partir des températures sèches et humides qui y ont été mesurées ; on en a déduit leurs gradients.

L'objection majeure que l'on peut faire à ce type d'expérience porte sur la façon dont sont faites les mesures des variables météorologiques. Les températures sèches et humides ne sont mesurées qu'en deux points espacés verticalement de quelques dizaines de mètres. Les gradients verticaux des variables ne sont pas connus avec la même précision que dans les expériences utilisant une radio-sonde sur ballon captif ou bien un pylône instrumenté disposant de plus de deux points de mesure. Néanmoins, on constatera ci-dessous que les résultats obtenus dans cette expérience sont très intéressants à plus d'un titre. Il faut ajouter que la différence de hauteur des deux psychromètres servant aux mesures de température varie d'une station à l'autre.

#### 3.2 - Relations entre les statistiques d'affaiblissement et les statistiques de certaines variables météorologiques

La station de mesure dont on présente ci-dessous les résultats est celle de MONT DE MARSAN. Ce choix, parmi les onze stations, n'est pas le fait du hasard. Il est dû à la position particulière de MONT DE MARSAN située dans une vaste région boisée et assez chaude de FRANCE sous forte influence océanique, où les conditions de propagation sont souvent assez mauvaises. Deux bonds hertziens sont raccordés à la station de MONT DE MARSAN (figure 1). L'un de 45 km, venant de MAILLAS, est désigné ci-après par MAILLAS. L'autre de 56 km, venant de LEMBEYE, est désigné par LEMBEYE. Le seuil d'affaiblissement dépassé, dont les pourcentages de dépassement seront comparés à ceux des variables météorologiques étudiées, est de 25 dB, affaiblissement toujours situé dans la queue de la distribution sur les deux bonds hertziens étudiés dans cette station.

### 3.2.1 - Les gradients de coindice de réfraction $\Delta N_s/\Delta h$ mesurée toutes les trois minutes

La distribution des gradients de coindice  $\Delta N_s/\Delta h$ , obtenues pour une séparation verticale de 64 mètres entre les deux psychromètres, est donnée sur la figure 2 pour le mois de février 1985 et celui de septembre 1985 qui est défavorable sur le bond, MAILLAS, que l'on a choisi comme référence dans cette station. Cette liaison de 45 km et de rugosité moyenne survole surtout des surfaces boisées. Ces distributions de  $\Delta N_s/\Delta h$  concernent les mois entiers. Le pourcentage de temps de dépassement de l'affaiblissement 25 dB a été en septembre 8,5 fois plus grand qu'en février. La distribution de  $\Delta N_s/\Delta h$  en septembre est aussi plus défavorable que celle de février.

Les pourcentages de temps de franchissement d'un affaiblissement de 25 dB sont comparés mois par mois à ceux de dépassement du gradient de coindice au-dessous du seuil de - 157 unités N/km (figure 3). Bien que nous ne disposions que de 16 mois de mesures correctes des coindices, et malgré la dispersion des points, il apparaît clairement qu'une relation existe statistiquement entre les gradients de coindice mesurés à une extrémité d'une liaison et les événements de propagation qui peuvent se produire le long de cette liaison.

Mais du fait de la dispersion des points sur la figure 3, le pourcentage de temps de dépassement des gradients de coindice apparaît comme un indicateur insuffisant pour prévoir les événements de propagation. D'autres variables météorologiques semblent avoir aussi une influence que nous allons tenter de découvrir.

### 3.2.2 - Les gradients des températures sèches

Ces gradients  $\Delta T_s/\Delta h$  sont mesurés une fois toutes les 3 heures 50 minutes environ et sont exprimés en °C/km. Pour en étudier la comparaison avec les affaiblissements, les gradients de température positifs ont été choisis, ceux-ci étant générateurs de situations de super-réfraction. Les pourcentages de dépassement des affaiblissements de 25 dB semblent relativement liés aux pourcentages de dépassement de  $\Delta T_s/\Delta h = 30^\circ\text{C/km}$ . Mais la relation moyenne que l'on pourrait établir entre ces deux catégories de pourcentages ne serait pas encore satisfaisante pour en faire une méthode de prévision des affaiblissements. La première raison semble être le fait que les variables météorologiques qui peuvent avoir une influence sur les conditions de propagation sont, en plus de la température, la tension de vapeur d'eau et la pression atmosphérique. Ces variables évoluant d'une façon assez peu dépendante, il apparaît que la comparaison mois par mois des résultats dans une même station, mais aussi la comparaison des stations entre elles, ne pourra être faite que si les températures et les tensions de vapeur d'eau sont rapportées à une même pression de référence.

### 3.3 - Variables potentielles

L'idée de modifier les variables météorologiques en fonction de la pression atmosphérique a été proposée par KATZ (CRAIG et autres, 1951 ; BEAN et DUTTON, 1966) qui propose de choisir une pression de référence  $P_0$ . La température absolue  $T$ , obtenue à la pression  $P$ , devient la température potentielle :

$$(1) T_p = T (P_0/P)^{0,286}, \text{ en } ^\circ\text{K}$$

De même, la tension de vapeur d'eau potentielle

$$(2) E_p = E (P_0/P), \text{ en mb}$$

où  $E$  est la tension de vapeur d'eau existante à la pression  $P$ .

Le coindice de réfraction potentiel sera alors

$$(3) N_p = \frac{77,6}{T_p} \left[ P_0 + 4810 \frac{E_p}{T_p} \right]$$

Prenons  $P_0 = 1000$  mbars, on peut écrire

$$(4) N_p = \frac{77,6}{T} \left[ \frac{1000}{P} \right]^{0,714} + 3,73 \cdot 10^5 \frac{E}{T^2} \left[ \frac{1000}{P} \right]^{0,428}$$

Les expressions (1), (2) et (4) ont été utilisées pour calculer les variables potentielles au bas de la tour en utilisant la pression atmosphérique  $P_B$  mesurée en ce point. La pression atmosphérique au sommet  $P_H$  est obtenue en soustrayant à la pression  $P_B$  en bas le poids de la colonne d'air. Les variables potentielles au sommet de la tour ont été calculées en utilisant la pression  $P_H$  au sommet et en prenant une pression de référence :

$$P_{OH} = 1000 - (P_B - P_H), \text{ en mb}$$

Ainsi la température potentielle au sommet est donnée par

$$(5) T_{pH} = T_H (P_{OH}/P_H)^{0,286}, \text{ en } ^\circ\text{K}$$

La tension de vapeur d'eau potentielle au sommet est alors donnée par :

$$(6) E_{pH} = E_H (P_{OH}/P_H), \text{ en mb}$$

Les variables potentielles sont indépendantes de la pression atmosphérique et donc aussi de l'altitude des stations. Elles peuvent donc servir à comparer les caractéristiques météorologiques des stations entre elles. Mais elles ont aussi le grand intérêt de permettre de comparer entre eux les différents mois de mesure dans une même station. Le coindice de réfraction au sommet est calculé en utilisant

la température potentielle donnée par (5) et la tension de vapeur d'eau donnée par (6).

### 3.3.1 - Les gradients des températures sèches potentielles

Les coefficients de réfraction potentiels sont calculés à chaque période de 3 heures 50 minutes. Les pourcentages de temps de dépassement de certaines valeurs des gradients de ces coefficients de réfraction potentiels présentent une corrélation insuffisante avec les pourcentages de temps de dépassement du seuil 25 dB d'affaiblissement. Les fractions du mois avec dépassement des gradients des températures sèches potentielles  $\Delta T_p/\Delta h$  et les fractions du mois avec dépassement du seuil 25 dB d'affaiblissement sont au contraire bien corrélées sur le bond hertzien de référence, MAILLAS, qui a été choisi à MONT DE MARSAN. Le seuil choisi pour les gradients de température est très nettement positif,  $\Delta T_p/\Delta h = 30^\circ\text{C/km}$ , parce qu'un tel gradient crée des situations de super-réfraction. On sait qu'il a été observé sur une liaison que les affaiblissements supérieurs à 10 dB étaient d'autant plus fréquents que la valeur de  $\Delta T/\Delta h$  était plus forte (SCHIAVONE, 1983) et au moins supérieur à  $5^\circ\text{C/km}$ . Sur la figure 4, chaque point représente un mois de mesures effectuées en 1984 ou bien en 1985. La courbe moyenne qui semble représenter le mieux cet ensemble de points a une équation de la forme :

$$(7) \log P_T = k_1 \log P_A + k_2$$

où  $P_T$  est la fraction du mois avec dépassement du seuil  $\Delta T_p/\Delta h = 30^\circ\text{C/km}$ ,  $P_A$  est la fraction du mois avec dépassement du seuil 25 dB d'affaiblissement,  $k_1 = 0,401$  et  $k_2 = 0,405$ .

Il est évident que le nombre de points de mesure est encore insuffisant pour affirmer que les valeurs choisies pour  $k_1$  et  $k_2$  sont les meilleures.

### 3.3.2 - Les gradients des tensions de vapeur d'eau potentielles

La figure 5 montre la relation qui peut exister entre les fractions du mois pour lesquels les gradients de tensions de vapeur d'eau potentiels sont plus petits ou égaux à  $-10 \text{ mb/km}$  et les fractions du mois avec dépassement de A plus grand ou égal à 25 dB pour un certain nombre de mois de mesure en 1984 et 1985 à MONT DE MARSAN. Les points sont bien plus dispersés que dans le cas des gradients de températures potentielles. Malgré cette dispersion une courbe moyenne représentative de la relation entre les phénomènes peut être tracée ; elle est de la forme :

$$(8) \log P_E = k_3 \log P_A + k_4$$

où  $P_E$  est la fraction du mois avec dépassement du seuil  $\Delta E_p/\Delta h = -10 \text{ mb/km}$ , ( $P_A$  a été défini ci-dessus) et  $k_3 = 0,218$  et  $k_4 = 0,389$ . On peut encore ajouter qu'un certain nombre de points de mesure supplémentaires s'impose pour affiner les termes numériques de cette relation (8). Les valeurs inférieures ou égales à  $-10 \text{ mb/km}$  ont été prises en compte parce qu'elles correspondent généralement à des situations de super-réfraction. Toutefois il est possible qu'une autre valeur soit mieux corrélée avec les affaiblissements. Les analyses futures des données permettront de le savoir.

### 3.4 - L'influence du vent

Durant chaque période de 3 heures 50 minutes les vitesses minimale et maximale atteintes par le vent sont mesurées. Il est intuitif de penser que les conditions les plus favorables à la création de couches réfractantes uniformes de grande étendue apparaissent avec un vent relativement stable en vitesse et en direction. La différence  $\Delta V$  entre la vitesse maximale et la vitesse minimale du vent a été utilisée comme critère de stabilité de la vitesse du vent. Les fractions du mois pour lesquels  $\Delta V = 5 \text{ m/s}$  ont été comparés aux fractions du mois avec dépassement de A 25 dB. Une relation évidente existe entre ces fractions du mois (figure 6). La courbe moyenne représentative des points de mesure est représentée par l'équation :

$$(9) \log P_V = k_5 \log P_A + k_6$$

où  $P_V$  est la fraction du mois avec dépassement du seuil  $\Delta V = 5 \text{ m/s}$ ,  $P_A$  a été défini ci-dessus, et  $k_5 = 0,136$  et  $k_6 = 0,227$ .

La stabilité de la direction du vent sera étudiée et publiée ultérieurement. Le choix de  $5 \text{ m/s}$  pour le seuil des variations de vitesse du vent est arbitraire. Il a été inspiré par les observations de UGAI (1969) sur l'importance des vents faibles dans l'apparition des faibles gradients verticaux des coefficients de réfraction.

### 3.5 - Corrélation entre les 3 variations météorologiques utilisées

Certains mois, à MONT DE MARSAN, en 1985 les gradients des températures potentielles sont relativement corrélés avec les gradients des tensions de vapeur d'eau potentielles. Le coefficient de corrélation moyen entre les variables  $\Delta T_p/\Delta h$  et  $\Delta E_p/\Delta h$ , pour les mois dont on peut garantir l'exactitude des données météorologiques, est de 0,296. Le coefficient de corrélation moyen  $\Delta T_p/\Delta h$  et  $\Delta V$  entre les gradients des températures potentielles et la variation de vitesse du vent est de -0,01285 ; le coefficient de corrélation moyen  $\Delta E_p/\Delta h$  et  $\Delta V$  est de -0,012. La dépendance évidente des gradients de température potentiels et des gradients des tensions de vapeur d'eau potentiels n'est pas suffisamment étroite pour condamner toute tentative de recherche des probabilités jointes de ces variables météorologiques.

### 3.6 - Probabilités jointes des variables météorologiques

Certains des coefficients de corrélation entre les variables  $\Delta T_p/\Delta h$ ,  $\Delta E_p/\Delta h$ , et  $\Delta V$  sont très faibles. On négligera donc dans ce qui suit la petite dépendance observée entre  $\Delta T_p/\Delta h$  et  $\Delta E_p/\Delta h$ . La probabilité jointe cumulée de dépassement des seuils  $\Delta T_p/\Delta h = 30^\circ\text{C/km}$ ,  $\Delta E_p/\Delta h = -10 \text{ mb/km}$  et  $\Delta V = 5 \text{ m/s}$  est donc égale à

(10)  $P_J = P_T \times P_E \times P_V$ ,  
d'où en utilisant (7), (8) et (9) :

$$\log P_J = (k_1 + k_3 + k_5) \log P_{AR} + (k_2 + k_4 + k_6)$$

soit

$$(11) \log P_J = k_7 \log P_{AR} + k_8$$

où

$$k_7 = 0,755, k_8 = 1,021.$$

et où  $P_{AR}$  concerne le bond de référence R. Nous devons rappeler que la relation (11) n'est vraie que pour la probabilité  $P_{AR}$  de dépasser un affaiblissement de 25 dB et que pour la liaison de référence ou bien toute liaison qui posséderait les mêmes caractéristiques géographiques et radioélectriques, quelle que soit le climat.

Le produit  $P_J$  des trois probabilités élémentaires pour différents mois de mesure de 1984 et 1985 sur le bond hertzien de référence est représentée sur la figure 7. La courbe moyenne calculée selon (11) y a été tracée. Cette courbe moyenne calculée ne semble pas être la meilleure courbe moyenne des valeurs de  $P_J$ . Ceci est sans doute dû à la dépendance de  $\Delta T_p / \Delta h$  et de  $\Delta E_p / \Delta h$ .

N'ont été représentés que les mois pour lesquels des mesures exactes des trois variables météorologiques ont pu être obtenues. Il est certain qu'un plus grand nombre de points de mesure serait nécessaire pour obtenir la courbe moyenne exacte et donc les valeurs numériques correctes de  $k_7$  et  $k_8$  dans l'équation (11).

### 3.7 - Normalisation par rapport à la liaison de référence

Il est connu que l'on peut représenter la queue de la distribution des affaiblissements à fréquence fixe du mois le plus défavorable, dont la pente est celle de la queue de la distribution de Rayleigh, par un produit de termes, caractérisant la liaison, élevés à certaines puissances (CCIR, 1986). Plusieurs auteurs ont cherché à rendre aussi précise que possible une telle expression en ajoutant à l'expression du CCIR d'autres facteurs, caractérisant l'influence possible du climat (MARTIN et autres, 1985) ; TUELTA et autres, dans ce volume). Ainsi la probabilité d'avoir un affaiblissement supérieur à  $A_0$ ,  $A_0$  étant situé dans la queue de la distribution peut être représentée par

$$(12) P_A = K \prod_i F_i(x_i) 10^{-A_0/10}$$

où  $x_i$  sont les variables qui caractérisent la liaison,  $F_i$  sont les fonctions de ces variables et  $K$  est le facteur qui caractérise, pour la propagation, le climat du mois le plus défavorable dans la région où se trouve le bond hertzien étudié. On ne doit pas oublier que la valeur de  $K$  peut dépendre aussi du nombre des variables  $x_i$  que l'on a choisi et du type des fonctions  $F_i$  de ces variables. Donc dans une expression telle que (12), ne pas tenir compte de certaines variables, qui ont une influence importante sur la probabilité de dépassement  $P_A$  aura pour effet de rendre  $K$  dépendant de ces variables.

Soit :

$$(13) P_{AR} = K_R \prod_i F_i(x_{Ri}) 10^{-A_0/10},$$

la probabilité de dépasser un affaiblissement quelconque  $A_0$  sur le bond de référence indicé R (MAILLAS). Soit aussi  $K_R$  le facteur qui caractérise le climat dans la région de référence choisie, à savoir MONT DE MARSAN.

Soit aussi

$$(14) P_{AL} = K_L \prod_i F_i(x_{Li}) 10^{-A_0/10},$$

la probabilité de dépasser un affaiblissement quelconque  $A_0$  sur un bond quelconque L situé dans une région de facteur climatique  $K_L$ . On peut écrire

$$(15) \frac{P_{AR}}{P_{AL}} = \frac{K_R}{K_L} F_N$$

$$F_N = \frac{\prod_i F_i(x_{Ri})}{\prod_i F_i(x_{Li})}$$

où

L'expression (15) peut aussi s'écrire :

$$(16) P_{ALN} = P_{AL} \cdot F_N = P_{AR} \cdot K_L / K_R$$

où  $P_{ALN}$  est la probabilité de dépasser l'affaiblissement  $A_0$  qui aurait été observée si le bond L avait les mêmes caractéristiques géographiques et radioélectriques,  $x_{Ri}$ , que le bond de référence R. Les différences entre  $P_{ALN}$  et  $P_{AR}$  ne seront dues qu'aux différences entre les climats.  $P_A$  est le facteur de normalisation qui permet de passer des caractéristiques géographiques et radioélectriques du bond L à celles du bond de référence R. L'équation (11) qui relie les statistiques sur les données de propagation aux statistiques sur les données météorologiques pour le bond de référence R peut alors aussi s'appliquer à  $P_{ALN}$  et aux données météorologiques du bond L.

Les probabilités  $P_A$  de dépassement d'un affaiblissement de 25 dB sur le deuxième bond étudié à MONT DE MARSAN, LEMBEYE, ont été normalisées, soient  $P_{ALN}$ , et représentées sur la figure 8 avec les valeurs du bond de référence R. Ces nouveaux résultats montrent que la courbe moyenne calculée selon l'expression (11) n'est pas vraiment satisfaisante. La courbe moyenne estimée la meilleure, tracée sur la figure 8, est obtenue avec les valeurs  $k_7 = 0,658$  et  $k_8 = 0,686$ . La dispersion des points autour de la courbe moyenne estimée semble montrer que d'autres variables météorologiques ont aussi une influence sur les affaiblissements. L'expression (11) est vraie pour la liaison de référence de MONT DE MARSAN et pour toute autre liaison dont on aura normalisé la valeur de  $P_A$  par rapport à la liaison de référence, quelque soit la région climatique choisie, où  $P_A$  est la probabilité de dépasser un affaiblissement de 25 dB.



### 3.8 - Les facteurs géoclimatiques absolu K et relatif G

L'expression (11) peut s'écrire :

$$(17) \quad P_{JR} = \left[ \frac{P_{JR}}{10^{k_8}} \right]^{1/k_7}$$

où  $P_{JR}$  est la probabilité jointe des variables météorologiques correspondant aux conditions climatiques les plus défavorables durant un mois dans la région de référence R. Pour le bond de référence de MONT DE MARSAN, et pour le mois le plus défavorable (septembre 1985), on peut écrire en utilisant (13) et (17) :

$$(18) \quad K_R = \frac{\left[ P_{JR}/10^{k_8} \right]}{\prod_i F_i(x_{Ri}) 10^{-25/10}}$$

pour  $A_0 = 25$  dB,

$K_R$  étant le facteur géoclimatique absolu du bond hertzien de référence R. La valeur de  $K_R$  dépend des variables géographiques et radioélectriques  $x_{Ri}$  et des fonctions  $F_i$  qui ont été choisies pour représenter la probabilité de dépassement d'un affaiblissement de 25 dB pour le mois le plus défavorable. Il est alors possible de calculer, pour les différentes régions climatiques occupées par un réseau hertzien, les écarts de la valeur de  $K_L$ , correspondant au mois le plus défavorable dans la L ième région climatique, par rapport à la valeur de référence  $K_R$  de la région climatique de référence.

D'après (14) on peut écrire :

$$(19) \quad K_L = \frac{P_{AL}}{\prod_i F_i(x_{Li}) 10^{-25/10}}$$

pour  $A_0 = 25$  dB.

D'après (16),

$$(20) \quad P_{AL} = P_{ALN}/F_N = P_{ALN} \frac{\prod_i F_i(x_{Li})}{\prod_i F_i(x_{Ri})}$$

D'après (11), on peut aussi écrire :

$$(21) \quad P_{ALN} = \left[ \frac{P_{JL}}{10^{k_8}} \right]^{1/k_7}$$

D'où en combinant les expressions (18), (19), (20) et (21) :

$$(22) \quad G_L = \frac{K_L}{K_R} = \left[ \frac{P_{JL}}{P_{JR}} \right]^{1/k_7}$$

où  $k_7 = 0,658$

$G_L$  est le facteur géoclimatique relatif de la région climatique L comparée à la région climatique de référence R. L'expression (22) a été établie sur la base de l'expression (11) : elle n'est donc valable que pour le produit  $P_J$  des probabilités des variables météorologiques utilisées, à savoir le gradient vertical de la température potentielle mesurée en deux points, le gradient vertical de la tension de vapeur d'eau potentielle en 2 points et la variation de vitesse du vent. De plus la valeur numérique de  $k_7$ , égale à 0,658 dans notre étude, dépend aussi des variables météorologiques utilisées et peut-être aussi de la profondeur d'affaiblissement (25 dB) utilisée comme seuil pour le choix de la probabilité  $P_A$ .

Ce facteur géoclimatique relatif  $G_L$  de la L ième région comparée à la région de référence R, peut être utilement représenté par son logarithme  $g$ . Il ne dépend que des variables météorologiques. Mais cette expression (22) n'est valable que si les variables différentielles  $\Delta T_p/\Delta h$  et  $\Delta e_p/\Delta h$ , rapportées au km, ont été mesurées sur des différences de hauteur égale. On sait en effet que la distribution des gradients de coefficients de réfraction varie avec cette différence de hauteur (ROUX, 1983). Il en est certainement de même des gradients de températures et des gradients de tension de vapeur d'eau. Dans le futur, on devra tenir compte de ces variations de différences de hauteur pour l'application de l'expression (22). Il sera souhaitable d'adopter pour cette différence de hauteur une valeur standard, 80 ou 100 mètres par exemple. La différence de hauteur des psychromètres est d'environ 64 m à MONT DE MARSAN et de 71,3 m à ORLÉANS. L'application de l'expression (22) donne un climat "radioélectrique" plus favorable à ORLÉANS, - 7,5 dB, par rapport à MONT DE MARSAN. Cette valeur est sans doute légèrement plus forte, l'écart des psychromètres étant plus grand à ORLÉANS. A LYON, la différence de hauteur est de 82,6 m, ce qui aura pour effet de diminuer aussi  $P_{JL}$ . Sans appliquer de correction, on trouve que le climat de LYON est aussi plus favorable qu'à MONT DE MARSAN, l'écart dépassant sans doute - 15 dB.

### 4 - CONCLUSION

Cette étude du climat n'en est qu'à son début et elle connaîtra encore bien des développements. Elle montre qu'une relation assez étroite existe entre des variables météorologiques mesurées à une extrémité d'un bond hertzien et les phénomènes de propagation en air clair apparaissant sur ce bond, qui peut avoir une longueur de plusieurs dizaines de kilomètres. Elle montre aussi que les sondages verticaux de l'atmosphère à l'aide d'un ballon captif, si coûteux en temps, en argent et en personnel ne s'imposent pas nécessairement pour des études statistiques de longue durée. Des méthodes de sondage plus simples,

que l'on effectue durant plusieurs années, sont suffisantes pour la connaissance du climat "radioélectrique". Une analyse plus approfondie de l'influence du gradient de coindice local et du vent devra aussi être conduite. Enfin, l'existence, dans une même banque, de données de propagation et de données météorologiques est extrêmement utile à la compréhension de certains phénomènes. On devrait pouvoir ainsi donner les raisons de l'apparition sur certains bords, dont le dégagement est faible, d'affaiblissements anormaux. Une telle étude a été conduite pour mieux connaître l'influence du climat sur les distributions des affaiblissements à fréquence fixe, sur une ou plusieurs fréquences. Cette étude ne peut donc pas remplacer celles qui ont été menées récemment pour la compréhension détaillée de l'influence du climat sur la sélectivité des évanouissements en air clair (SYLVAIN, 1983).

## BIBLIOGRAPHIE

C. ARCHAMBAULT, R. CLAVIER, L. MARTIN et R. PENAUD

Dispositif automatique d'acquisition et de traitement de données s'adaptant au système de collecte ARGOS, Colloque ADERA, BORDEAUX, 12-14 Octobre 1982, FRANCE

W.T. BARNETT

Multipath propagation at 4, 6 and 11 GHz,  
B.S.T.J. Vol. 51,2, pp 321-361, Février 1972, USA

B.R. BEAN et E.J. DUTTON

Radio Meteorology, Ed. US Department of Commerce, National Bureau of Standards Monograph 92, 1966, U.S.A.

CCIR

Rapport 338, Volume 5, 1986, U.I.T., GENÈVE, SUISSE

R.A. CRAIG, I. KATZ, R.B. MONTGOMERY, et P.J. RUBINSTEIN

Gradient of refractive modulus in homogeneous air, potential modulus, Livre, Propagation of Short Radio Waves, ed. D.E. KERR (Mc Graw Hill Book Co, Inc. New-York) 1951, U.S.A.

C.M. CRAIN, A.P. DEAN et J.R. GERHARDT

Measurement of Tropospheric Index of refraction fluctuations and profiles, Proceedings of the IRE, février 1953, pp 284-290, U.S.A.

A.C. CRAWFORD et M.C. JAKES

Selective fading of microwaves,  
B.S.T.J., Janvier 1952, pp 68-90, U.S.A.

J. PERENNES

Etudes statistiques relatives à la propagation par trajets multiples, Rapport interne ONET, NT/TCR/APH/60, mai 1979, FRANCE

J. DOOLE

Predictions of multipath delays and frequency selective fading of digital links in the U.K., I.E.E. Digest, 1979/62, U.K.

F. IKEGAMI, M. HAGA, Y. FUKUDA et H. YOSHIDA

Experimental studies on atmospheric ducts and microwave fading, Review of the E.C.L. - U.T.I., Vol. 18, n° 7-8, juillet - août 1966, pp 503-533, JAPON

F. IKEGAMI

Analyses of microwave fading due to irregular structure of the atmospheric refractive index, Review of the E.C.L. - U.T.I. Vol. 15, n° 7-8, juillet-août 1967, pp 438-506, JAPON

J.A. LANE

The radio refractive index gradient over the British Isles, Journal of Atm. and Terr. Physics, 1961, pp 157-166, U.K.

L. MARTIN, R.L. OLSEN et Y. TJEFTA

Initial analyses of multipath fading measurements for various geographical conditions in FRANCE, ISAP 1985 Symposium, KYOTO, août 1985, JAPON

R.L. OLSEN, Y. TJEFTA, L. MARTIN et J. DOOLE

Towards a more accurate method of predicting the distribution of multipath fading on terrestrial microwave links, Electron. Lett., Vol. 32, n° 17, pp 901-903, 1986

G. ROUX et J.P. MON

Propagation anomalies in a 4,7 and 11 GHz line of sight path, URSI Comm. F. Symposium, LOUVAIN (BELGIQUE), 9-15 Juin 1983, FRANCE

J.A. SCHIAVONE

Meteorological effects on diurnal and seasonal fading variations, Conference on Communications, ICC 83, C 2.2 pp 641-644, 1983, U.S.A.

J.A. SCHIAVONE

Planetary boundary layer effects on microwave propagation, Sixth Amer-Meteorol Soc. Symposium, BOSTON, mars 1983, U.S.A.

M. SYLVAIN, F. BAUDIN, C. KLAPISZ, J. LAVERGNAT, S. MAYRARGUE, J.P. MON, B. MUTTEN, M. ROORYCK

The PACEM experiment on line of sight multipath propagation, URSI Comm. F. Symposium, LOUVAIN (BELGIQUE), juin 1983, FRANCE

M. SYLVAIN

Etudes des trajets multiples sur les liaisons hertziennes en visibilité : synthèse bibliographique, Rapport interne CNET N.T/CRPE/133, juin 1984, FRANCE

R.L.O. TATTERSALL et J.E. CARTWRIGHT

Multipath propagation: data collected from tests on line of sight radio paths at 11,20 and 37 GHz during the period 1972-1975, Post office Research Department Report n° 594, 1977, U.K.

S. UGAI

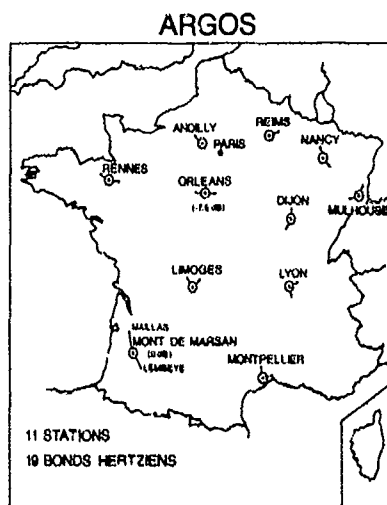
Statistical consideration of the structure of atmospheric refractive index, Reports of the E.C.L. - N.T.T., août 1959, pp 253-289, JAPON

A. VIGANTS

Space diversity engineering, B.S.T.J., vol 54, 1, pp 103-142, janvier 1975, U.S.A.

#### REMERCIEMENTS

Nous tenons à remercier toutes les personnes qui ont rendu possible la réalisation de cette étude nouvelle en FRANCE et toutes celles qui de près ou de loin ont participé à la collecte des données et à leur prétraitement.



#### IMPLANTATION DES BALISES

Figure 1  
Implantation des dispositifs d'acquisition de données en FRANCE

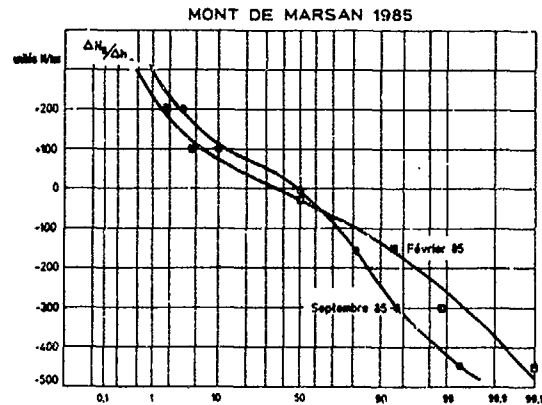


Figure 2  
Distributions des gradients de coindice de réfraction  $\Delta N_s$  mesuré chaque 3 minutes.

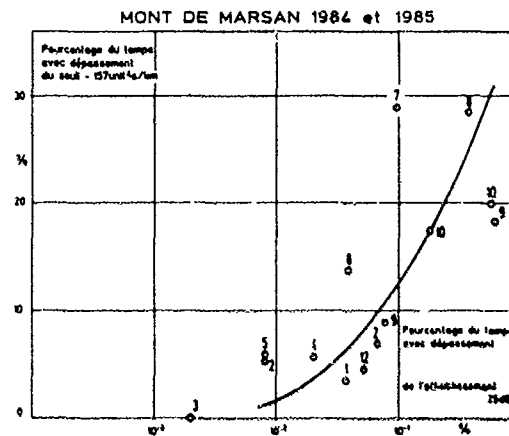


Figure 3  
Relation entre les pourcentages du temps avec dépassement d'un affaiblissement de 25 dB, d'une part et avec dépassement de la valeur  $\Delta N_s = -157$  N/km, d'autre part (chaque point représente un mois de mesure).

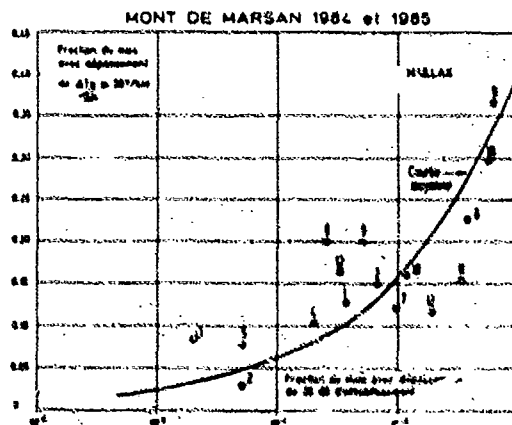


Figure 4  
Relation entre les fractions du mois avec dépassement d'un affaiblissement de 25 dB, d'une part et avec dépassement de la valeur  $\Delta N_s = -157$  N/km, d'autre part. (Chaque point représente un mois de mesure).

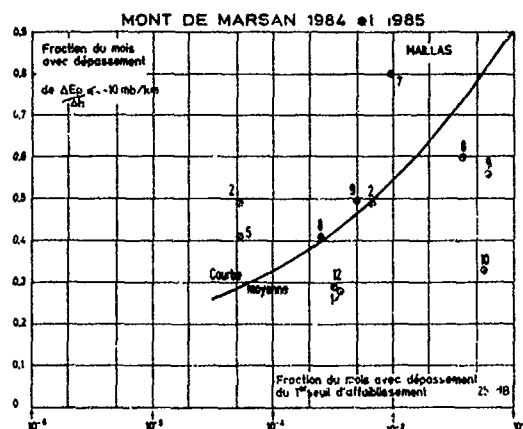


Figure 5

Relation entre les fractions du mois avec dépassement d'un affaiblissement de 25 dB, d'une part et avec dépassement de la valeur  $\Delta E_p \leq -10$  mb/km, d'autre part.

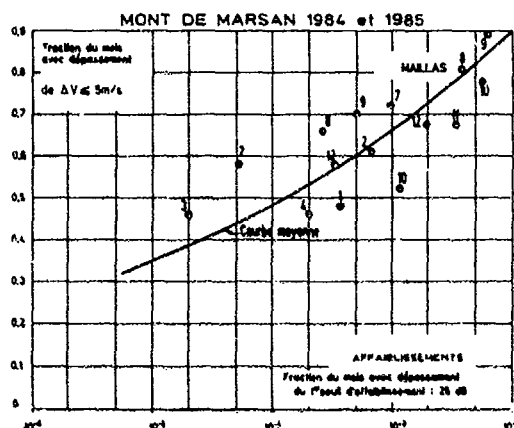


Figure 6

Relation entre les fractions du mois avec dépassement d'un affaiblissement de 25 dB, d'une part et avec dépassement de la valeur  $\Delta V = 5$  m/s, d'autre part.

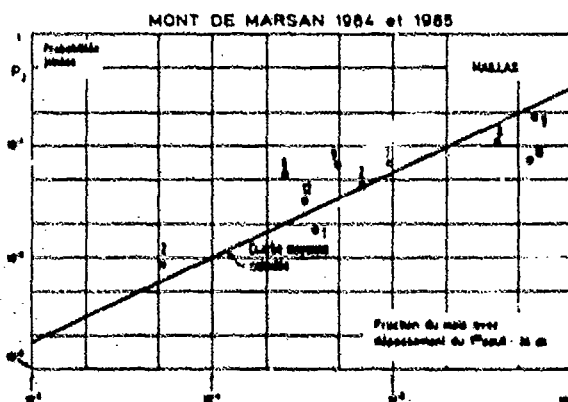


Figure 7

Relation entre les fractions du mois avec dépassement d'un affaiblissement de 25 dB et les probabilités jointes des variables météorologiques pour le bond de référence de MONT DE MARSAN.

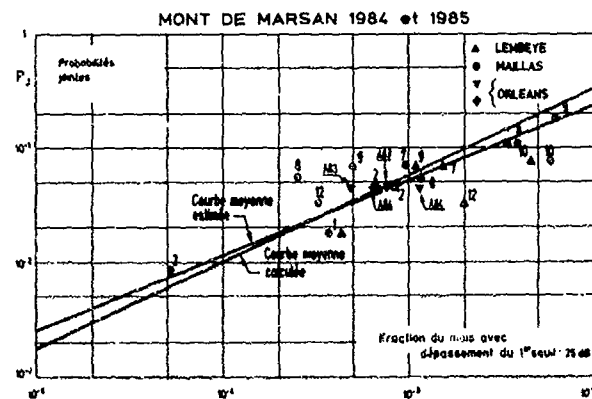


Figure 8

Relation entre les fractions du mois avec dépassement d'un affaiblissement de 25 dB et les probabilités jointes des variables météorologiques pour les deux bords de MONT DE MARSAN et pour les mois les plus défavorables des deux bords d'ORLEANS.

# **RADIO AND RADAR "HOLES" AND MULTIPATH ZONES: THE GLOBAL AND LOCAL INFLUENCES ON ATMOSPHERIC REFRACTIVE STRUCTURE AND RESULTING ADVERSE RADIO AND RADAR PERFORMANCE**

by

Owen R. Côté  
James F. Morrissey  
Yutaka Izumi

Air Force Geophysics Laboratory  
Hanscom AFB, MA 01731-5000  
USA

## **ABSTRACT**

With the increasing use of higher capacity digital radio systems on line-of-sight (LOS) and troposcatter (Tropo) radio paths, the role of atmospheric refractive structure as a cause of multipath or frequency selective fading becomes of an increasing importance in meeting long-term path performance standards. Results from recent USAF field testing of digital LOS and Tropo path performance, in which concurrent fine vertical resolution refractivity profiles were also made, show that multipath effects on LOS and TROPO complement each other both performance-wise and weather-wise. Maximum multipath delay is a clear propagation path related event in LOS and a heavy rain/thunderstorm related event in TROPO. Because radio holes and multipath zones occur concurrently, being produced by the same refractive ducting layer, LOS paths can be designed to minimize the occurrence of frequency selective fading at the possible expense of some increase in non-frequency selective fading under strong ducting conditions. Path length is less important in effecting path performance than ducting layer strength and geometry. The rule that maximum multipath delay goes as the third power of path length is not confirmed by measurements. Measured maximum delay on an LOS is better represented by a half-power dependence on path length.

Finally, the ray trace analysis coupled with fine resolution refractivity measurements obtained during the LOS and TROPO field tests can be applied to the geometry of an airborne radar emitter. Such a study also shows a pattern of radar holes and multipath zones. Performance measure for the three systems, digital LOS, digital Tropo, and airborne early warning radar based upon atmospheric refractive structure will be presented and related to atmospheric global weather patterns.

## **DISCUSSION**

### **E. Villar**

Considering the speed at which the nulls move across the bandwidth, could you please give us an indication about how fast we need to take a 'snapshot' of the channel to freeze it.

### **Author's Reply**

Estimates of the shape of the spectrum across the band, the impulse-response function, and bit-error-rate were computed once per second. "Notches" were observed to move across the band at about 3 MHz/sec. Hubbard, of ITS Boulder, believes that more dynamics will be observed over time periods shorter than one second. For the propagation test there is probably more information on this question in the bit-error-burst data and I refer you to Rob Hubbard at the Institute of Telecommunication Sciences, Boulder, Colorado.

# THE CORRELATION BETWEEN METEOROLOGICAL AND LOW-LEVEL ANGLE-OF-ARRIVAL MEASUREMENTS

J. Litva and P. Bauman  
Communications Research Laboratory  
McMaster University, Hamilton, Ontario, Canada

N.R. Fines

Communications Research Centre, Ottawa, Ontario, Canada

## SUMMARY

Although not widely appreciated, anomalous propagation can cause serious low-angle tracking errors. In fact, it may be argued that errors due to propagation, in particular propagation within evaporation ducts, are now as large, or even larger in some cases, than those caused by inaccuracies which are inherent to superresolution algorithms. The study of errors due to anomalous propagation forms the central thrust for this paper. In particular, this paper describes an investigation into the correlation between data from collocated radio and meteorological experiments.

The data analyzed and reported on in this paper have been recorded on the Ottawa River and consist of both radio and meteorological measurements. The measurements were carried out using a low-level beacon and a large synthetic aperture antenna, which is called a "vertical profiler". The primary radio parameters consist of the angles-of-arrival of the direct and multipath signals from the beacon. The primary meteorological parameters are relative humidity, temperature, and barometric pressure.

## 1. INTRODUCTION

### 1.1 The Low-Angle Propagation Problem

In recent years a considerable amount of research has been devoted to a near-classical problem which is commonly referred to as "low-angle radar tracking" [1]. It is primarily a multipath problem, wherein reflections from the sea surface enter the main beam of a shipborne tracking radar and seriously degrade its performance. The overriding objective therefore of the research has been to improve the performance of fire-control radars operating in multipath environments. Most of the work to date has been concentrated in the area of signal processing, wherein superresolution algorithms have been conceived, developed, tested and accepted or rejected based on their effectiveness in separating a target from its image and then providing an accurate estimate of the target's elevation. The state-of-the-art has now progressed to the point where other relevant factors must be considered, such as refraction effects associated with low-angle propagation.

It should be recalled that electromagnetic waves propagating within the earth's atmosphere do not travel along straight lines, but rather are generally bent or refracted. In ducts this effect is enhanced because the refractive index gradients are considerably greater than in a normal atmosphere. One effect of refraction is to extend the distance to the horizon, thus increasing the radar coverage. Again, in ducts this effect becomes greater, to the point that over-the-horizon propagation becomes possible. Another effect is the introduction of errors in the measurement of angle. This becomes particularly serious for low-angle targets because the propagation paths tend to be largely parallel to the earth's surface and are therefore more susceptible to tropospheric refraction.

It may be argued that the errors due to propagation, in particular propagation in evaporation ducts, are now as large, or even larger in some cases, than those caused by inaccuracies inherent to superresolution algorithms. This would suggest that a comparable effort to that devoted to radar signal processing is now warranted for investigating the effect of anomalous propagation on radar tracking, as well as developing techniques for reducing these errors.

With this in mind, the objectives for the research being reported on here are to analyze the Ottawa River data base. In particular, to investigate the correlation between radar angle-of-arrival and meteorological measurements by: (1) developing signal processing techniques for deriving deviations in angle-of-arrival of radar signals; (2) adapting a ray tracing program to provide radar parameters, such as angle-of-arrival or interference pattern null height for varying propagation conditions; and finally, (3) correlating measured radar parameters, synthesized using the ray tracing model, and measured refractivity gradients.

### 1.2 The Low-Angle Radar Multipath and Propagation Program

As part of a program to measure and model environmental phenomena which adversely affect the performance of maritime radars, the Communications Research Centre (CRC) in conjunction with McMaster University is carrying out a series of collocated meteorological and propagation trials. The first series of measurements were made on the Ottawa River, near Ottawa, Canada. Similar measurements have also been made on the Mediterranean, near Toulon, France. Since accurate angular estimation is central to low-angle tracking, the immediate objective is to develop a technique for measuring deviations in angle-of-arrival of radar signals, caused by anomalous tropospheric propagation, and to correlate these with meteorological parameters. A secondary objective

AD-P005 743



is to develop a data base for propagation at very low elevation-angles over sea. The final and overriding objective is to validate models and to develop techniques for predicting angle-of-arrival deviations from measured meteorological parameters.

Most of the measurements to date have been made on the Ottawa River. Recently, some additional data have been obtained from NATO radar trials which took place on the Mediterranean [2]. Although an understanding of North Atlantic propagation conditions is the ultimate goal, it is thought that the results from the Ottawa River will be useful for gaining insight into low-level propagation phenomena and developing techniques for making concurrent propagation and meteorological measurements. The data presented in this paper were recorded using a new instrument, which is called a vertical profiler. The profiler is a very large aperture antenna (17.3 m) which, in addition to making precise angle-of-arrival measurements, concurrently measures vertical profiles of tropospheric refractivity. This paper gives a description of the vertical profiler, as well as a review of the results from the Ottawa River [3]. In particular, it gives early results of angle-of-arrival measurements made in evaporation ducts.

Gradients in the tropospheric refractivity form the basis of the meteorological data. They are obtained by taking vertical samplings of temperature and relative humidity using meteorological sensors. The influence of atmospheric pressure is taken into account by applying a correction to the derived values for the gradient. The corrections are based on the assumption of changes in pressure with altitude occurring at a rate which is given for a standard atmosphere. The refractivity gradients which are derived from the meteorological data can in turn be used as inputs to a ray tracing program, from which are derived the angles-of-arrival of the direct and indirect signals emanating from the beacon. The degree of correlation found between the measured and calculated angles-of-arrival is used as an index for quantifying the correlation of the radio and meteorological measurements described in this paper.

## 2. LOW-LEVEL TROPOSPHERIC PROPAGATION

### 2.1 Refractivity

Radio waves travel in straight lines in free space. However, electromagnetic waves travelling in the earth's atmosphere do not travel in straight lines [4] but are generally bent or refracted. Bending, or refraction, of radio waves in the atmosphere is caused by the variation with altitude of the velocity of propagation, or the index of refraction, defined as the velocity of propagation in free space to that in the medium in question. A major detrimental effect of ray bending for radar trackers, particularly for low-angle targets, is the introduction of a discrepancy between the apparent and actual elevation angles of the target. These deviations can be particularly marked for angles less than one degree, which is the case for low-angle targets. In fact, typically, in low-angle scenarios, elevation angles can be as low as one-tenth of a degree, or less.

At microwave frequencies, the index of refraction  $n$  for air which contains water vapor is

$$(n-1)10^6 = N = 77.6 \frac{P}{T} + 3.73 \times 10^6 \frac{e}{T^2} \quad (1)$$

where,  $P$  = barometric pressure, millibars (1 mm Hg = 1.3332 millibars),  
 $e$  = partial pressure of water vapor, millibars, and  
 $T$  = absolute temperature, K.

Since the refractive index for air is typically 1.0003 a "scaled-up" index of refraction called refractivity is defined to be

$$N = (n-1)10^6. \quad (2)$$

This scaling results in numbers such as 300, which are considered to be more manageable. If, as is often the case, the water vapor content of the air is measured in terms of relative humidity (RH) the partial pressure  $e$  is obtained from

$$e = e_s \times RH \quad (3)$$

where,

$$e_s = 6.1 \exp\left(25.22 \frac{T-273}{T} - 5.31 \ln \frac{T}{273}\right) \quad (4)$$

Finally, if we assume a standard atmosphere,  $p = 1013$  mb, Eqn. (1) becomes

$$N = \frac{7.86 \times 10^4}{T} + 3.73 \times 10^6 \frac{e}{T^2} \quad (5)$$

### 2.2 Curvature and Effective Earth Radius Factor

The curvature  $C$  of a radio wave is given by

$$C = -\frac{1}{n} \frac{dn}{dh} \cos \theta \quad (5)$$

where  $\theta$  is the local elevation angle of the ray. It is customary for radio engineers to think in terms of effective earth radius factors. This convenient fiction makes straight

the actual curved path of a radio ray in the atmosphere by presenting it relative to an imaginary earth longer in radius by a factor  $k$  than the radius of the real earth,  $a$ , thus maintaining the relative curvature between the earth and the radio ray. This is expressed as

$$\frac{1}{a} + \frac{1}{n} \frac{dn}{dh} \cos \theta = \frac{1}{ka} + 0. \quad (7)$$

curvature of earth      curvature of radio ray      curvature of effective earth      curvature of straight line

Thus  $k$  is defined by

$$k = \frac{1}{1 + a \frac{dn}{dh} \cos \theta} \quad (8)$$

which, for rays tangential to the earth ( $\theta = 0$ ) and assuming  $n$  is unity, is approximated by

$$k = \frac{1}{1 + a \frac{dn}{dh}} \quad (9)$$

As indicated, the classical method of accounting for atmospheric refraction in computation is by replacing the actual earth of radius  $a$  ( $a = 3440$  nautical miles) by an equivalent earth of radius  $a_e = ka$  and then replacing the actual atmosphere by an homogeneous atmosphere in which electromagnetic waves propagate in straight lines rather than curved lines. In Fig. 1 are given examples of straight line propagation paths for effective earth models describing wide-ranging propagation conditions. In each instance the propagation paths for the actual earth are curved. For example, in (c) the real paths would have the same curvature as the surface of the true earth.

For a standard atmosphere  $dn/dh = -1/4a$ , wherein  $k = 4/3$ . Although very useful for engineering, the effective-earth's-radius model [5] is not a very good representation of actual atmospheric  $N$  structure. For typical  $N$ -versus-height distributions the  $4/3$  earth distribution has about the correct slope in the first kilometer above the earth's surface but is observed to decrease much too rapidly above that height. It appears that the success of the  $4/3$  earth model is due to its agreement with the average  $N$  structure near the earth's surface, which largely controls the refraction of radio rays at the small values of  $\theta$  common in long-range surface radars.

As indicated in Eqn. (6) the bending of an electromagnetic wave is proportional to the gradient of the refractive index. A number of different propagation regimes are defined by  $dn/dh$  or in terms of  $dn/dh$ , as indicated below

$$\frac{dn}{dh} = \begin{cases} > 0 & \text{(NU/km) subrefractive} \\ > -79 \text{ and } < 0 & \text{normal} \\ > -157 \text{ and } < -79 & \text{superrefractive} \\ < -157 & \text{ducting} \end{cases} \quad (10)$$

It is of interest here to note that the condition  $k = 4/3$  corresponds to a gradient of refractivity which is equal to  $-39$  NU/km. The effective-earth's-radius factor,  $k$ , for other values of  $dn/dh$  is given in Fig. 2. The factor  $k$  is quite variable and exhibits a singularity at  $dn/dh = -157$  NU/km. This singularity defines the beginning of trapping or ducting. Alternatively, by referring to Eqn. 7, the singularity can be described as corresponding to the condition where the radio-ray curvature becomes equal to the curvature of the earth. In other words, the effective-earth's-radius becomes infinite, i.e., for this one condition the curved earth model reduces to a flat earth model. For values of  $dn/dh < -157$ ,  $k$  assumes negative values.

In order to understand the significance of negative values for  $k$ , let us consider what happens as we move from right to left in Fig. 2. In the following discussion it is helpful as well to refer to Fig. 1. The factor  $k$  starts off being positive, with a magnitude less than one. This corresponds to subrefraction in propagation space and simply means that one models the propagation by using an effective earth's radius which is less than the actual earth's radius. As one moves to the left, the effective earth's radius increases, i.e., the effective earth starts to flatten out, until the effective earth's radius becomes equal to the earth's radius at  $dn/dh = 0$  and then goes on to exceed the earth's radius. At  $dn/dh = -157$ , as indicated earlier, the effective earth becomes flat, i.e.,  $ka = \infty$ . Finally, as one crosses the point of singularity and  $k$  assumes negative values, the effective-earth's-radius becomes negative. At this point the effective earth's surface becomes concave upwards, where previously it was concave downwards.

### 2.3 Evaporation Ducts

The evaporation duct is a typical feature [6] of the maritime boundary layer. This surface duct exists even at higher latitudes - in all, about 90 percent of the time. However, it should be noted that the thickness is often very small (especially during the winter time) and therefore no effect on radar wave propagation is found. During May to October the evaporation duct is the dominating propagation parameter with regard to cm-

and dm- waves.

Evaporation ducts lie just above the surface of the sea. They result from water vapor, or humidity, which evaporates from the sea surface. The air in contact with the sea is saturated with water vapor, with a saturation vapor content appropriate to the temperature of the sea surface. The air several meters above the sea is not usually saturated so there will be a gradual decrease in water vapor pressure from the surface value to the ambient value well above the surface. The thickness of the duct is defined to be equal to the height of the ambient value (where  $dN/dh$  becomes zero) above the surface of the water.

The evaporation duct heights vary generally between 0 to 40 metres with a long-term mean value of about 8 metres at northern latitudes and up to 30 metres at tropical latitudes [7]. The primary evaporation duct effects are to give extended ranges for surface-to-surface radio or radar systems operating about 3 GHz. The optimum frequency to achieve extended ranges via the evaporation duct appears to be around 18 GHz. Although the ducting effect extends beyond this frequency, absorption by atmospheric gases and extra attenuation due to a rough sea surface begin to counteract the benefits of the duct.

In a nonhomogeneous atmosphere, such as that found in an evaporation duct, where typically the index of refraction decreases with height, rays of sufficiently small initial elevation angle are refracted downward with a curvature proportional to the rate of decrease of the index of refraction with height. If the radius of curvature is less than the radius of the earth, such rays reach a maximum height and are confined, or trapped, between this height and the earth's surface. This process is referred to as trapping, and the region of the atmosphere within which it occurs is called a duct, because of the analogy to wave guide propagation.

### 3. THE PROFILER

#### 3.1 A Tool for Propagation Measurements

The profiler technique is based on synthesizing a large aperture antenna using a small antenna [2]. The small antenna samples the signals at  $N$  points over a large aperture. The data are recorded and then added together in such a way as to get the same result as one would have obtained using a large aperture antenna.

Because of the vertical profiler's large aperture, it can be used to resolve and accurately measure the angles-of-arrival of closely separated signals. In order to resolve the two signals it is necessary to measure at least one complete cycle of the field distribution pattern that is set up in space by interference between the signals. Since the scale size of the interference pattern is inversely proportional to the angular separation of the signals, a large aperture is required for closely separated signals. A diagram of a profiler in a typical measurement setup is given in Fig. 3. It consists of two antenna-receiver systems, one of which is stationary and acts as a reference and the other of which samples the profiler aperture distribution as it is transported vertically by means of a trolley. If the moveable receiver is phase locked with the reference receiver, one is able to measure both the amplitude and phase distributions which result from interference between the direct and indirect beacon signals.

##### 3.1.1 Digital Beamforming

It is well known from antenna theory that conventional beamforming consists of a Fourier transform of an antenna's aperture-distribution. In this case, sampling of the aperture distribution occurs at discrete points and beamforming is carried out by applying an FFT to the measured amplitude and phase. It is assumed that the samples do not vary during the sampling time, i.e., the source is stationary while the small sampling antenna goes through the  $N$  positions of the large antenna.

In addition to the conventional FFT-based beamforming there are a large number of non-linear or model-dependent beamforming techniques that might be considered for profiler signal processing. Perhaps the simplest of the nonlinear techniques that might be considered is one that treats the profiler as an interferometer. The technique is best implemented by using the height of a null in the profiler's interference pattern as a discriminant. For our purposes null height is a good choice because we know that the phase difference at that point on the profiler is 180 degrees. Usually in interferometry, the baseline separating the antennas, which comprise the interferometer, remains constant and one measures the phase difference between the signals at the two antennas. As an alternative implementation, one might conceive of maintaining a constant phase difference between the two antennas by adjusting the baseline and then measuring their separation. That is in effect the scheme that is being proposed here. Changes in the height of a null can be related to changes in the angles-of-arrival of the interfering signals. With a suitable model one can estimate the magnitude of these changes. It will be shown that the null height is sensitive to small changes in angles-of-arrival. Because of these advantages, the Ottawa River results will by and large be presented with the emphasis being placed on null height as a discriminant.

In addition to the antenna and receiver, the trolley, which runs on the vertical track, usually contains meteorological instrumentation. The meteorological data from these sensors is used to derive refractive index gradient profiles. With its full complement of radio

and meteorological equipment, the vertical profiler can make the following measurements:

- (i) Angles-of-arrival of the direct and indirect (multipath) signals emanating from a low-angle beacon or target,
- (ii) Very small variations in angle-of-arrival,
- (iii) Refractive index gradients,
- (iv) Ratios of the coherent to the incoherent components of the multipath signals, and
- (v) Characteristics of the diffuse components of the multipath signals (e.g. autocorrelation functions).

In addition to the above, the data recorded can be used for studies in high resolution spectral estimation.

### 3.2 Profiler Interference Pattern Nulls

In a multipath environment where we have two rays arriving at a receiving point from different directions a standing wave field is produced. The maxima and minima of the amplitude distribution in space are plane surfaces which are parallel to the bisector of the angle between the wave normals or rays [9].

Since profiler measurements are usually made using low-angle beacons, the ray paths followed by the direct and indirect signals are, to a first approximation, horizontal. Therefore the planes which represent the maxima and minima of the amplitude distribution in space are at right angles to the profiler aperture. The intersection of the profiler aperture with the planes for the minima define the location of the profiler nulls.

Unlike the maxima and minima of the amplitude distribution, the equiphase surfaces do not remain plane. They become corrugated or, if the two waves are of exactly equal strength, broken. On average, they are perpendicular to the wave normal of the stronger ray.

#### 3.2.1 Geometry

The geometry appropriate to the problem at hand is given in Fig. 4, where the profiler and the beacon are shown separated by the distance  $d$ . The angles-of-arrival, respectively, for the direct and indirect signals are  $\alpha_d$  and  $\alpha_i$ . Height  $h_1$  identifies a reference point 0 on the profiler aperture, which is usually taken to be its midpoint. The height of the beacon is given by  $h_2$ .

It should be noted that the multipath model depicted in Fig. 4 is incomplete because it assumes free-space propagation conditions, i.e., ray paths are straight lines. Propagation factors will be added to the model in the next section.

To solve problems based on a curved earth geometry we must first solve for  $d_1$ , i.e., we must find the point of reflection in Fig. 4. It is possible to find  $d_1$  and  $d_2$  if  $d$ ,  $h_1$ , and  $h_2$  are given, but to do so we must solve a cubic equation [8]. This equation has the formal solution

$$q = \frac{2}{\sqrt{3}} \left[ a (h_1 + h_2) + \left[ \frac{d}{2} \right]^2 \right]^{1/2} \quad (11)$$

where  $a$  = radius of the earth, in addition to:

$$\alpha = \cos^{-1} \left[ \frac{2 a (h_1 - h_2) d}{1} \right], \quad (12)$$

$$\text{and} \quad d_1 = \frac{d}{2} + q \cos \left[ \frac{\alpha + \pi}{3} \right]. \quad (13)$$

Another important parameter, when solving problems based on the curved earth geometry, is the curved earth correction factor  $J$ . With this factor we are able to adapt equations based on a flat earth geometry directly to a curved earth geometry. To calculate  $J$  we first introduce the dimensionless parameter

$$s_{1,2} = \frac{d_{1,2}}{[2 a h_{1,2}]^{1/2}} \quad (14)$$

where  $d_2 = d - d_1$ , and then substitute into

$$J = (1 - s_1^2)(1 - s_2^2). \quad (15)$$

The angles-of-arrival for the direct and the indirect rays can be derived by using an expression for the fall-off  $A_z$ , due to the curvature of the earth, at the position of the indirect ray's reflection point, as well as at the position of the beacon. The fall-

off is measured with respect to the profiler's horizon plane. An expression for  $\Delta z$  is derived using the sagitta equation from optics, i.e.,

$$\Delta z = \frac{t^2}{2a} \quad (16)$$

where  $t$  is respectively  $d_1$  and  $d$ . The reflection point for the indirect ray is obtained using Eqn. (13).

Expressions for  $a_d$  and  $a_1$  can now be written directly from an inspection of Fig. 4 and are given by

$$a_d = \tan^{-1} \left[ \frac{h_2 - d^2/2a - h_1}{d} \right] \quad (17)$$

$$a_1 = \tan^{-1} \left[ -\frac{h_1 + d_1^2/2a}{d_1} \right] \quad (18)$$

### 3.2.2 Propagation Model

In order to introduce propagation factors into our calculations we will need a propagation or ray tracing model. An appropriate model has been developed by Davies and Evans [10], which will henceforth be called the DE model. An example of a ray path diagram which was derived using the DE model is given in Fig. 5. In this diagram,  $dN/dh$  was constant and had a value equal to  $-450$  N/km. The rays from the beacon to the profiler are noticeably curved with a radius of curvature equal to  $2.27 \times 10^6$  m, which is considerably less than the radius of the earth, suggesting that Fig. 5 is representative of ducting conditions. To the right of the main diagrams are given the refractivity gradients. The modified refractivity,  $M$  is derived from  $N$  and is given by

$$M = N + 157 h \quad (19)$$

In addition to ray diagrams, the DE model provides received angles-of-arrival for the direct and indirect rays as a function of  $dN/dh$ , as well as the phase delay. The former is given in Fig. 6 and the latter in Fig. 7. The angle-of-arrival for the direct ray varies from  $-1$  to  $+3$  mradians over the indicated range of  $dN/dh$  values. The variation of the indirect ray is somewhat less than one mrad.

Another method for introducing propagation considerations into our multipath model is to use the effective earth model. It is shown [3] that this is a very powerful technique which allows one to dispense with ray tracing, at least for the propagation conditions of interest here, i.e., those that are typified by refractivity gradients which are linear. For tropospheric conditions where the refractivity gradients are more complex one will have to return to ray tracing. As was suggested by Fig. 1, if we wish to incorporate propagation conditions into our model, based on the effective earth methodology, we must first use an effective earth in place of the real earth and secondly, adjust the radius of the effective earth so as to reflect the effects of ray bending in the troposphere.

### 3.2.3 The Interference Pattern Null as a Discriminant

An expression for the height of the interference pattern null can best be written by first considering the spatial phase difference  $\phi$  between the direct and indirect signals along the profiler aperture. The quantity  $\phi$  is related to the angles-of-arrival of the direct and indirect signals, as well as the propagation phase delay, and is given by

$$\phi = \pi s (\sin a_d - \sin a_1) + x_p^T \quad (20)$$

where

- $\pi = 2\pi/\lambda$ ,
- $s$  = displacement along the profiler aperture w.r.t. the reference point 0 (usually the centre of the profiler),
- $h_1$  = altitude of the reference point 0,
- $h_2$  = altitude of the beacon
- $a_d$  = angle-of-arrival (elevation) of the direct signal,
- $a_1$  = angle-of-arrival of the indirect signal, and
- $x_p^T$  = total phase difference at the reference point 0.

The first term of Eqn. (20) gives the spatial variation along the profiler due to the inclination of the phase fronts of the direct and indirect rays with the profiler aperture. It is to be noted that because of the size of the profiler aperture these phase fronts must be considered as being curved, rather than planar. The latter is the conventional approximation used for smaller aperture antennas. Wave front curvature is not explicitly included in Eqn. (20) because the curved wave-front correction factor is nearly identical

for both the direct and indirect rays and therefore cancels. The quantity  $x_p^T$  takes into account all of the factors that contribute to the electrical path length difference between the direct and indirect signals at 0. It consists of three identifiable variables and can be written as

$$x_p^T = x_G + x_R + x_p \quad (21)$$

where,

- $x_G$  = phase due to the electrical path length difference, assuming propagation in free space
- $x_R$  = reflection phase (usually  $= \pi$ ), and
- $x_p$  = extra phase due to an incremental change in both path length and phase velocity which results from tropospheric refractive index gradients.

For free space propagation the first term in Eqn. (21) is given by

$$x_G = \beta \frac{2 h_1 h_2 J}{d} \quad (22)$$

It is common practice to combine  $x_G$  and  $x_p$  by forming their sum and setting it equal to the right hand of Eqn. (22), combined with the use of an effective earth radius factor in Eqns. (11) and (12) to account for refraction. Normal refractivity conditions are assumed, with the effective earth radius parameter  $k = 4/3$ . Other values of  $k$  are seldom, if ever, used; in particular, negative values for  $k$  are never used. With the theoretical development given by Litva and Bauman [3], though, all values of  $k$  can now be used, including negative values. It has been shown in Fig. 7, using the DE ray tracing program for a typical profiler geometry, that  $x_G + x_p$  increases monotonically as the vertical gradient of refractivity decreases.

The profiler nulls are defined by the condition

$$\phi_m = (2m + 1)\pi \quad (23)$$

where  $m = (\dots, -2, -1, 0, 1, 2, \dots)$

Let us assume that variable  $r = \text{residue } x_p^T \text{ (modulo } 2\pi \text{) for } dN/dh = 0$ . That is,  $r = x_p^T(0) - 2i\pi$ , where  $i$  is the smallest integer that satisfies the condition  $0 \leq r < 2\pi$  and the zero in brackets indicates  $dN/dh = 0$ . It follows from Eqn. (20) that the null heights are given by

$$s_m = \frac{(2m + 2i + 1)\pi - x_p^T}{\beta (\sin \alpha_d - \sin \alpha_1)} \geq 0 \quad (24)$$

where  $m = (\dots, -2, -1, 0, 1, 2, \dots)$

Although the location of the profiler nulls can be derived exactly using Eqn. (24), it is useful at times to consider an alternative expression which gives the separation of the nulls directly. The derivation of this expression is based on the brief discussion given at the beginning of Section 3.2, where the idea of a standing wave field was introduced. Hayden [9] has expanded on this and shown that if the angle between two rays in space is  $2\alpha$ , which in terms of the rays arriving at the profiler in Fig. 4 is given by  $\alpha_d + \alpha_1$ , then the separation of the planes defining the maxima or the minima in space is given by

$$s_{M-M} = s_{m-m} = \frac{\lambda}{2 \sin \alpha} \quad (25)$$

where

- $s_{M-M}$  = distance between the maxima, and
- $s_{m-m}$  = distance between the minima

It is to be noted that when  $2\alpha$  is small, Eqn. (25) reduces to the familiar expression giving the diffraction-limited resolution for an antenna, i.e.,  $\Delta s = \lambda/L$ . Based on this correspondence, it follows that the condition for the profiler's resolution of two signals, using digital beamforming, can be stated as follows: the profiler is able to resolve two signals only if the profiler aperture is equal to at least one cycle of the amplitude and phase distribution.

The attractiveness of using the null height given by Eqn. (24) as a discriminant lies in the fact that it is sensitive to small changes in  $\alpha_d$  and  $\alpha_1$ . To demonstrate this fact let us consider a small change in  $h_2$  in Fig. 4, leading to a change of  $\Delta \alpha_d$  in  $\alpha_d$ . Let us approximate the corresponding change in  $\alpha_1$  by  $-\Delta \alpha_d$ ; in other words, we assume a flat earth geometry. Let us also denote the resulting change in the null height by  $\Delta s$ . From Eqn. (24) it follows that

$$\Delta s = - \frac{\Delta \alpha_d (\alpha_d - \alpha_1)}{2 \beta \sin \alpha} \quad (26)$$

This equation can be given an alternate interpretation, i.e., it can be viewed as an expression that relates the minimum detectable change in the angle-of-arrival given by  $\delta\alpha$  to the error in measuring the null height,  $\delta s$ . From observations at the Ottawa River, we have established the following set of parameters:

$$\begin{aligned}\delta s &= 0.25 \text{ m} \\ s_m &= 10 \text{ m}\end{aligned}$$

$$\alpha_d - \alpha_i = 2 \times 10^{-3} \text{ radians.}$$

After substituting these parameters into Eqn. (26) we find that

$$\delta\alpha = 0.025 \text{ mrad.}$$

It should be noted that this resolution exceeds the classical diffraction-limited resolution of the profiler (given by  $\lambda/L = 0.0321/17.1 = 1.9 \text{ mrad}$ ) by almost two orders of magnitude. Also, the value of  $s_m$  used in Eqn. (26) is replaced by  $h_m$ , which is the distance from the base of the profiler to the interference null. The reason for using  $h_m$  here in place of  $s_m$  is that the problem that we are actually solving is an interferometer problem. In other words, the profiler must be treated as an interferometer with an effective aperture of  $2 h_m$ . In fact, this is the reason that the factor 2 appears in the denominator of Eqn. (26).

The sensitivity of the profiler technique to changes in  $dn/dh$  can be derived by taking the full differential of Eqn. (24). This turns out to be a fairly complex operation because  $x_p^T$ ,  $\alpha_d$  and  $\alpha_i$  are all functions of  $dn/dh$  and one must therefore bring the equations of Section 3.2.3 of Litva and Bauman [3] into the derivation. A simpler approach consists simply of plotting  $h = h_0 + s$  versus  $dn/dh$  (see Fig. 16) and then numerically finding the inverse gradient of the resulting curve. The result is given in Fig. 8 and consists of the ratio of the change in refractivity gradient to the corresponding change in null-height,

$$\text{i.e., } \left[ \frac{\partial h_0}{\partial (dn/dh)} \right]^{-1}, \text{ as a function of refractivity gradient.}$$

If, as before, we use  $\delta s = 0.25 \text{ m}$ , the sensitivity is seen to vary from 3 NU/km at  $dn/dh = 100$  to 15 NU/km at  $dn/dh = -500$ .

#### 4. THE UNDERLYING EXPERIMENT AND RESULTS

##### 4.1 The Experiment

The results reported in this paper were recorded on the Ottawa River at a test range located near Ottawa. A diagram of the Test-Range is given in Fig. 9. The measurements were made using a propagation path that ran down the centre of the section of the Ottawa River shown in the diagram. The experimental setup is given in Fig. 10. CW signals from a beacon mounted on a silo were recorded using a vertical profiler (traveller).

The profiler consists of a reference receiver fixed at a height of 19.5 m and a coherent receiver mounted on a vertical traveller (along with meteorological sensors), which samples the incoming fields over the height interval 1.7 to 20.3 m. The height of the beacon is 18 m; the distance between the beacon and the profiler, 11.53 km; and the height of the centre of the profiler, 12.3 m. All heights given here are measured with respect to the level of the water surface. The measurements were made at a frequency of 9.16 GHz.

Two types of data records were usually obtained at the Ottawa River - short term and long term. The short term measurements were about 1 minute in duration and consisted of a vertical sampling of the electromagnetic fields and meteorological parameters along the profiler aperture. The long term measurements consisted of data records that were usually at least 24 hours in duration. For the long term records the vertical traveller was fixed at a height of 11.8 m. The records consisted therefore of the amplitude measured at two points on the profiler aperture, i.e., at the heights of the traveller and the reference receiver. As well, meteorological data were recorded by the traveller's meteorological sensors.

##### 4.2 Short Term Results

Typical short-term vertical profiler results are given in Fig. 11 and 12. Figure 11 gives the radar measurements (electrical) and Figure 12 the corresponding meteorological (environmental) measurements. The combined data recorded by the profiler consist therefore of amplitude (for both the traveller and reference receiver), in-phase and quadrature-phase signals (for deriving the phase), temperature, atmospheric pressure and relative humidity. The amplitude profile in Fig. 11 shows one cycle of the spatial pattern that is generated by interference between the direct and indirect signals. There is a 22-dB null located at a height of 12.1 metres. Later it will be shown that  $h_0 = 12.1 \text{ m}$  corresponds to  $dn/dh = 155 \text{ NU/km}$ . In addition to the I and Q, the phase that is derived from these basic profiler measurements is also given. The environmental data given in Fig. 12 consist of temperature, pressure and relative humidity. Although not measured directly, a refractivity profile is also shown. It is derived from the meteorological data that are shown in the figure. The slope of the straight line fit to the refractivity gradient

has a value of  $-156.5$  NU/km, which agrees very nicely with the value corresponding to  $h_0 = 12.1$  m.

#### 4.2.1 Null-height as a Discriminant

In Fig. 13 are given a number of amplitude signatures which were recorded under representative propagation conditions. These conditions vary from: (a) subrefractive, (b) normal, (c) superrefractive, and (d) ducting. The null for (a) is situated near the top of the profiler; for (b) it is situated one-quarter of the way down from the top; for (c) near the centre of the profiler aperture; and for (d) the main null is near the bottom and a secondary null is about to appear near the top.

The result given in Fig. 13 demonstrates the variation in null height that was observed on the Ottawa River, as well as the ease of using null height as a discriminant for determining propagation conditions. In a later section a demonstration is given of the high degree of correlation observed between null-height and refractivity gradient. It will be seen to be consistent with the theory derived in Section 3.2.3 and the validity of using the null height as a propagation discriminant will thus have been established.

#### 4.2.2 Digital Beamforming Result

An example of digital beamforming carried out on short-term profiler data is given in Fig. 14(a). For purposes of comparison, a beamforming result based on synthetic data is given in Fig. 14(b) and there is reasonably good agreement between these two results. In particular, all of the sidelobes for the measured result are easily identifiable and they fall-off with angle in a manner similar to the synthetic data. The well-behaved sidelobes in Fig. 14(a) suggest that the amplitude and phase errors for the profiler measurements are relatively low [2]. The beamwidth in Fig. 14(a) is  $1.6$  mrad, which is consistent with  $0.88(\lambda/L) = 0.88(0.0321/17.1) = 1.65$  mrad.

The profiler amplitude and phase measurements that were used to obtain the beamforming results in Fig. 14(a) are given, respectively, in Figs. 15 (a) and (b). The synthetic amplitude and phase results that were used in deriving Fig. 14(b) are plotted on top of the corresponding measured results. Again one sees reasonably good agreement between the measured and synthetic data.

#### 4.2.3 Null Height and Refractivity Gradients

Figure 16 gives a plot of observed null height  $h_n$  versus refractive index gradient. This diagram is one of the principal results of this report and shows the high degree of correlation that has been observed between the radar and meteorological measurements on the Ottawa River. The solid curves give theoretically derived heights (using Eqn. 24 and  $h_n = h_1 + z_n$ ) for the first three interference nulls  $h_{-1}$ ,  $h_0$ , and  $h_1$ . Null  $h_{-1}$  is not observed because it is lower than the minimum profiler height, i.e.,  $1.7$  m. Null  $h_1$  is observed only when  $dn/dh < -150$ , null  $h_0$ , because of the geometry, is the predominantly observed null.

The data shown a good correlation with the theoretically derived curve for  $h_0$ . These data have been subjected to averaging; typically, each datum represents the average of about six profiler records. Although there is scatter observed in the individual datum because of the large variance in the measurements of the refractivity gradient, the average results given in Fig. 16 show good agreement with the theoretical curves. It follows from the agreement shown with the theory in Fig. 16, as represented by Eqn. 24, that the profiler null height is an effective discriminant for characterizing propagation conditions.

Based on observed null height, propagation statistics are given in Fig. 17. These results were derived using the short term profiler records for the period between Jan. 1984 to Oct. 1985. Most of the data were recorded during the summer months (July, August and September). The remainder were recorded during the winter months. (November, January, February and March). It should be pointed out that the data were not recorded in a highly systematic manner but rather as the opportunity presented itself. Nevertheless, Fig. 17 represents a fairly extensive data base.

In Fig. 17 two peaks are observed, one at  $-20$  NU/km, which is close to the value for a standard refractivity gradient, and the other at  $-45$  NU/km, which represents ducting conditions. The first peak encompasses most of the records observed during the winter months when the effects of water vapor are negligible. The second peak corresponds to summer propagation conditions when relative humidity plays a dominant role in defining propagation conditions.

#### 4.3 Long Term Results

An example of a long term result is given in Fig. 18(a). It consists of the amplitude measured at the traveller while it was fixed at a height of  $13.8$  m. In this example the time axis runs from 1200 hrs. on 23 Feb. 84 to 1000 hrs. on 24 Feb. 84.

The amplitude is observed to vary over the period of the record by up to  $17.5$  dB. Some of the variation appears to be quasi-periodic with periods as long as 34 minutes. These are attributed to atmospheric buoyancy waves [11]. If one assumes that the amplitude variations are caused by the vertical movement of the interference-pattern null, due to



refractivity gradient changes in the troposphere, one can convert the observed amplitude to equivalent null-height. Examples of interference pattern variations were given earlier in Fig. 13. Estimates of null-height are realized by using the standard interference pattern shown in Fig. 18(b). As can be seen from the diagram, there is a simple but ambiguous relationship between measured amplitude and null height. For the configuration shown, an increase in amplitude corresponds to a decrease in null height. Because the sides of the null can be approximated by straight lines, these parameters are virtually inversely related. If, on the other hand, the null is located above the traveller, the relationship becomes a linear one with an increase in amplitude corresponding to an increase in null height. The ambiguity can be resolved by either referring to the vertical profiler record taken immediately prior to the start of the long-term records or by referring to the amplitude of the fixed reference antenna.

The trace of null height is given in Fig. 19. It is based on the amplitude data given in Fig. 18(a) and the interference pattern in Fig. 18(b). Null-height is easily converted to  $dn/dh$  by using Fig. 16 and finally,  $dn/dh$  is converted to angle-of-arrival for the direct and indirect signals via Fig. 6. The  $dn/dh$  result is given in Fig. 19(b) and corresponding angle-of-arrival estimate in Fig. 19(c).

The peak variation observed in this long-term record was not the maximum of the values observed in the Ottawa River data set. In order to deduce values for the peak deviations, one must return to Fig. 16 and determine the angle-of-arrival variations that correspond to the observed variations in  $dn/dh$ . By comparing Figs. 16 and 6 it is seen that the peak variation for the direct signal was 2.7 mrad and for the indirect signal 0.7 mrad.

#### 5. CONCLUDING REMARKS

This paper gives results of propagation and multipath measurements carried out on the Ottawa River. Radar angle-of-arrival, as well as meteorological measurements were made concurrently and at the same location. The radar measurements were carried out using a very large-aperture synthetic aperture antenna, which is called a vertical profiler. When used as an interferometer, the resolution of the profiler was shown to be 0.025 mrad.

The objectives of this study were as follows:

- (i) To develop the vertical profiler as a multipath/propagation measurement tool.
- (ii) To investigate the correlation between angle-of-arrival variations with tropospheric refractivity gradients - the derivation of which are based on measured meteorological parameters.
- (iii) To develop techniques for correcting low-angle tracking errors which are caused by tropospheric propagation effects, in particular evaporation ducting.

The analytical tools to effectively use the profiler as a multipath/propagation measurement tool have been developed both in this paper and in a report by Litva and Bauman [2]. In this paper, emphasis has been placed on using the profiler as an interferometer, wherein its effective aperture becomes twice that of its physical aperture. This result can be improved upon even further by using superresolution techniques, wherein the effective aperture can be increased by a factor of from five to ten times its physical aperture. The application of superresolution techniques for enhancing the profiler's aperture will be described in future papers.

A very strong correlation is demonstrated between angle-of-arrival deviations and tropospheric refractivity based on data recorded using meteorological sensors. The meteorological measurements were carried out at one terminus of the propagation path. It was found also that there was a reasonably good correlation between integrated measurements over the total path, based on values derived from the profiler's null-height, with meteorological measurements at the profiler end-point of the propagation path. The sensitivity of the profiler for measuring  $dn/dh$  was found to vary between 3 and 15 NU/km, depending on the actual value of  $dn/dh$ .

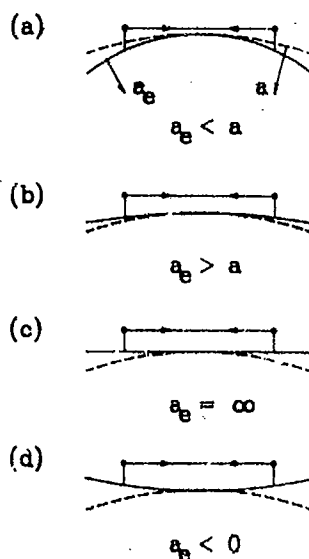
#### 6. ACKNOWLEDGEMENTS

This work was sponsored by the Department of National Defence, Ottawa, Canada.

#### 7. REFERENCES

1. Barton, D.K., "Low-angle tracking", Proc. IEEE, Vol. 62, No. 6, June 1974.
2. Litva J. and P. Bauman, "The Toulon NATO trials: report on the Canadian measurements", CRL Report No. 165, July 1986.
3. Litva, J. and P. Bauman, "Studies of correlation between meteorological and low-level angle-of-arrival measurements", CRL Report No. 174, November 1986.
4. Skolnik, M.I., Introduction to Radar Systems, McGraw-Hill Book Co., pp. 306-512, 1962.
5. Bean, B.R., E.J. Dutton and B.D. Warner, Radar Handbook, (Ed. M.I. Skolnik), McGraw-Hill Book Co., 1970.
6. -----, "Radar propagation due to low-level ducts over the sea", Final Report: NATO Research Study Group AC/245 (Panel III/RSG.6), December, 1977.

7. Eitner, H.U., J.H. Richter, R.A. Pappert, K.D. Anderson and G.B. Baumgartner, "Tropospheric radio propagation assessment", Proc. IEEE, Vol. 73, No. 2, Feb. 1985.
8. Kerr, D.E., Propagation of Short Radio Waves, (Ed. by D.E. Kerr - MIT Radiation Series), Dover Publications, Inc., 1965.
9. Hayden, E.C., "Propagation studies using direction-finding techniques", J. of Res. of the National Bureau of Standards, Vol. 65D, No. 3, May - June 1961.
10. Davies, W.S. and T.A. Evans, "Ray tracing on tropospheric ray paths", Australian Telecommunications Research, Vol. 15, No. 2, pp. 17-32, 1981.
11. Gossard, E.E. and W.H. Hooke, Waves in the Atmosphere, Elsevier Scientific Publishing Company, 1975.



propagation path —————  
 actual earth - - - - -  
 effective earth —————

Figure 1: Effective earth models for different propagation conditions. (a) Subrefractive (b) Normal (c) Transition between superrefractivity and ducting (d) Ducting

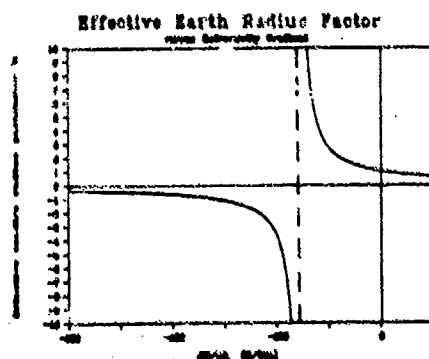


Figure 2: Effective earth's radius factor versus refractivity gradient.

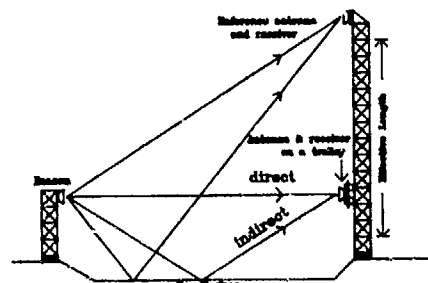


Figure 3: Profiler in a typical measurement setup.

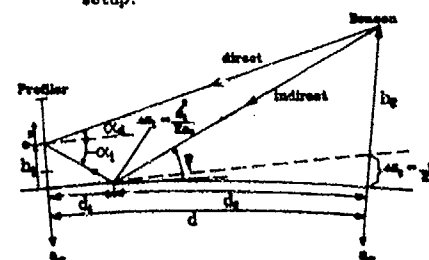


Figure 4: Profiler and curved earth geometry.

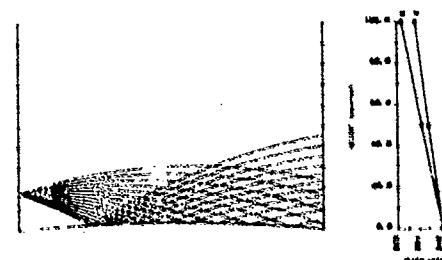


Figure 5: Examples of ray paths for  $dn/dh = -450$  N/km. The radius of curvature is equal to  $2.28 \times 10^6$  m.

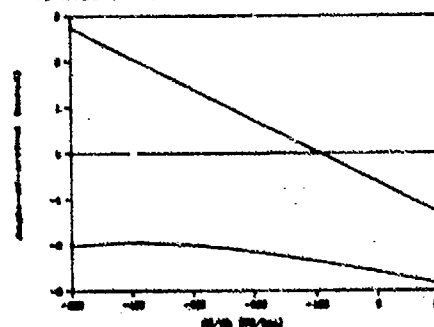


Figure 6: Angle-of-arrival for the direct and indirect rays versus refractivity gradient.

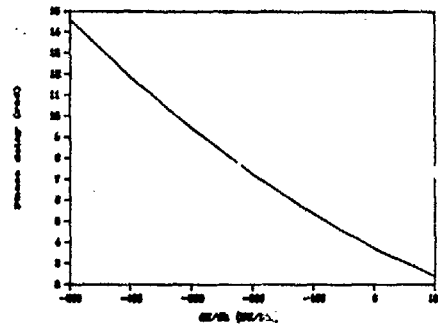


Figure 7: Phase delay as a function of refractivity gradient.

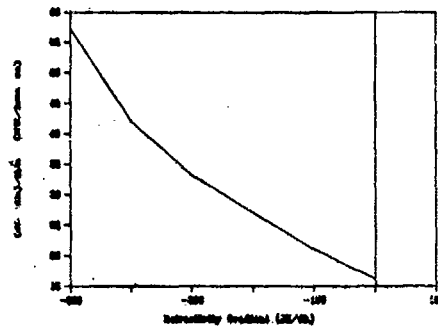


Figure 8: Ratio of the change in refractivity gradient to the corresponding change in null height as a function of refractivity gradient.

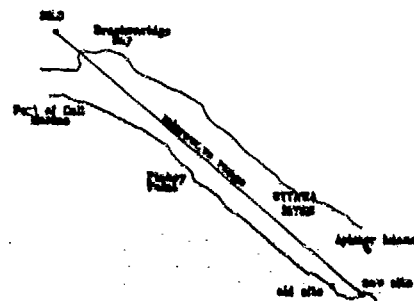


Figure 9: The Ottawa River test range.

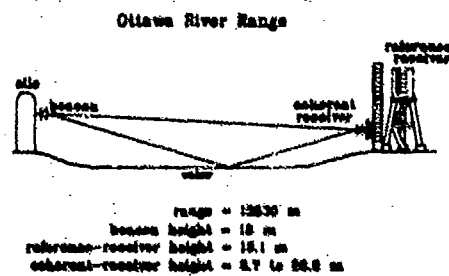


Figure 10: Actual Ottawa River test configuration with relevant geometrical parameters.

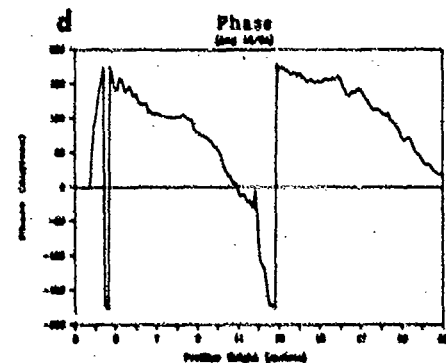
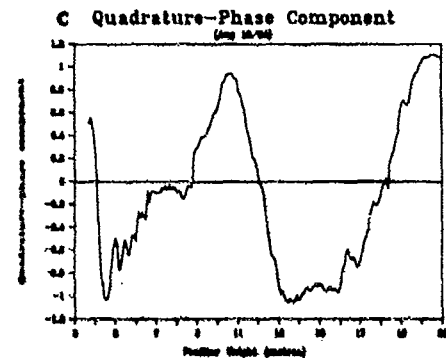
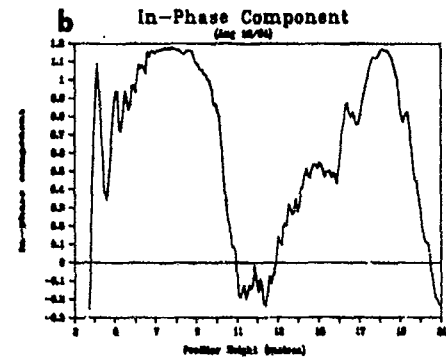
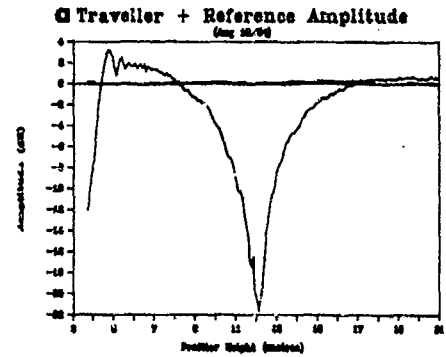


Figure 11: Profiler radar measurements. (a) Amplitude (b) In-phase signal (c) Quadrature-phase signal (d) Phase derived from (b) and (c).

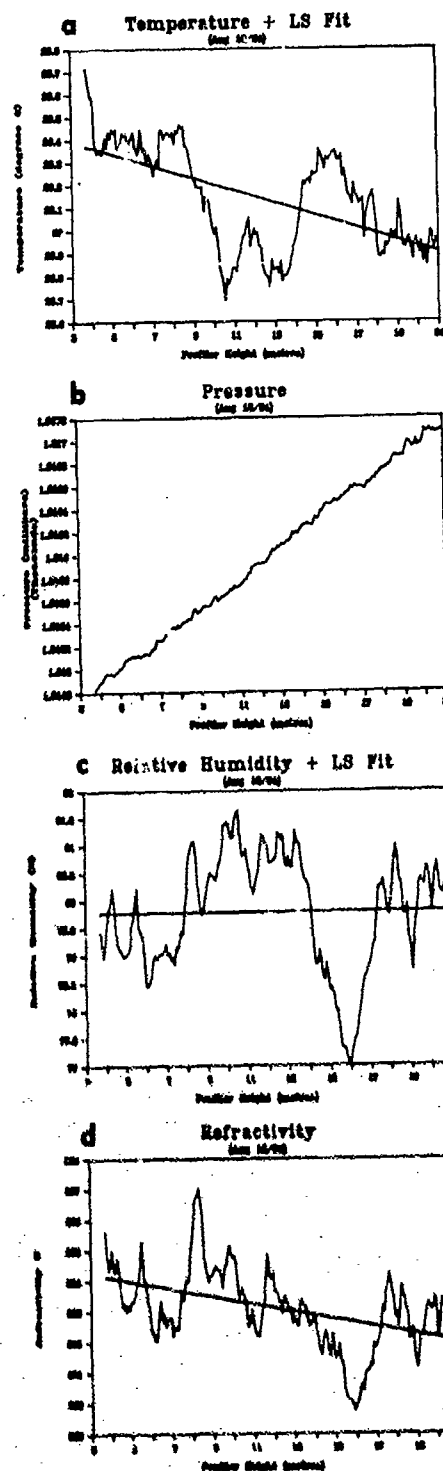


Figure 12: Profiler meteorological measurements. (a) Temperature (b) Barometric pressure (c) Relative humidity (d) Refractivity derived from measured parameters

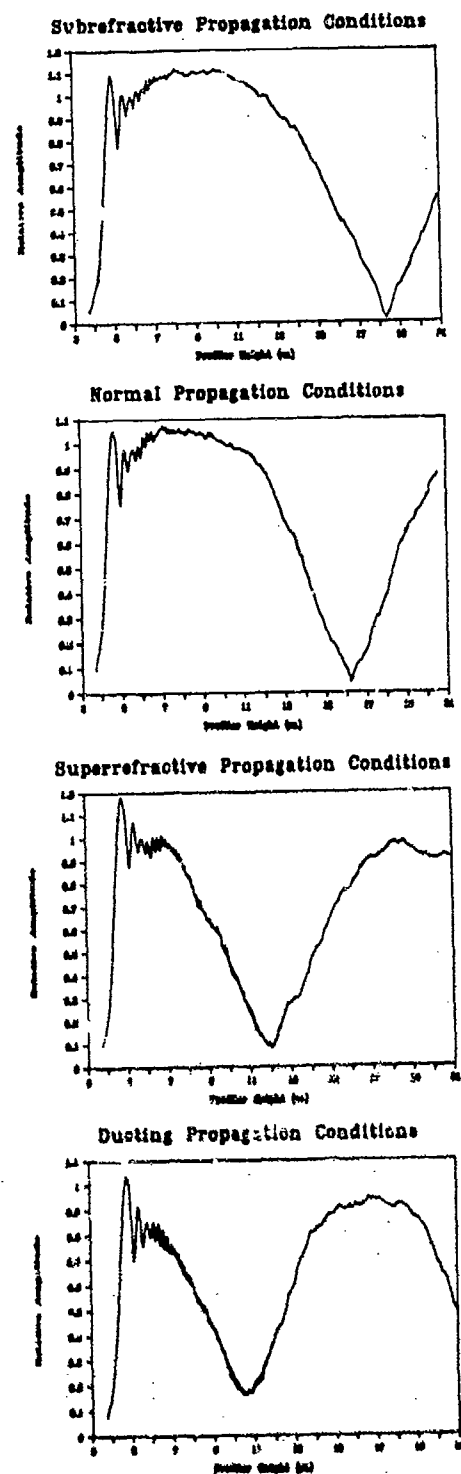


Figure 13: Profiler amplitude signatures recorded under varying propagation conditions

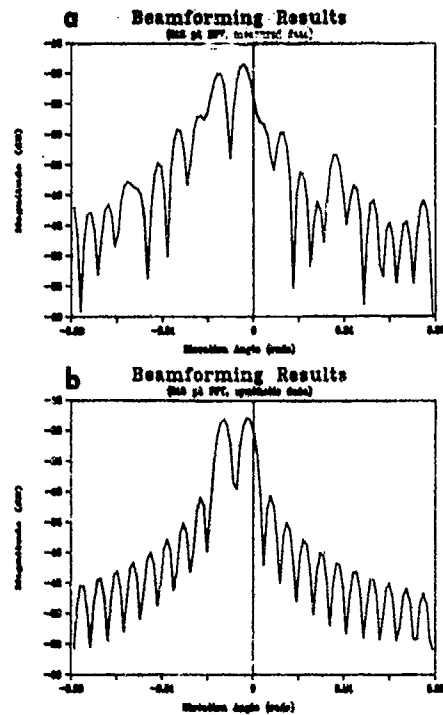


Figure 14: Comparison of digital beamforming with measured and synthetic aperture distributions. (a) Measured (b) Synthetic

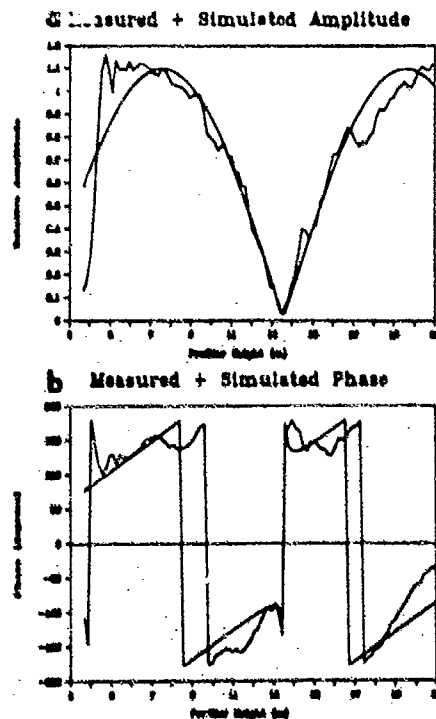


Figure 15: Comparison of measured and synthetic profiler aperture distribution. (a) Amplitude (b) Phase

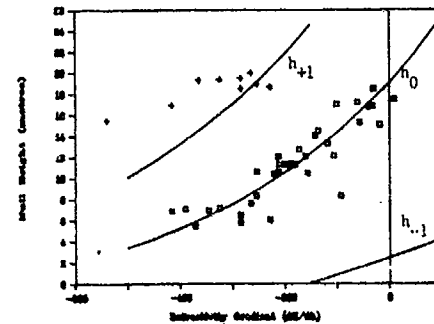


Figure 16: Null height versus refractivity gradient. Comparison of measured values of null height and refractivity gradient with theoretical curves.

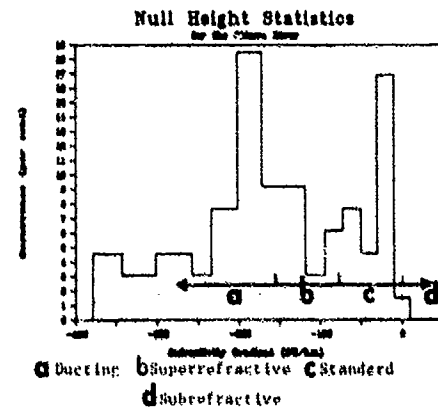


Figure 17: Propagation statistics derived from the Ottawa River data base.

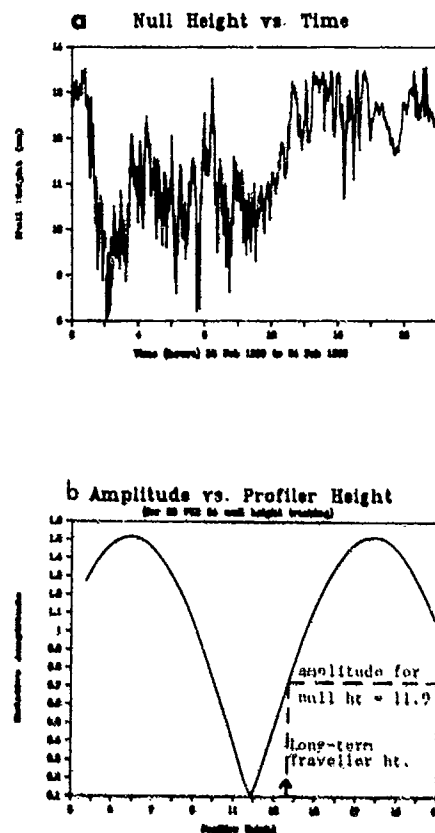


Figure 10: The basic components used in the data analysis of long-term profiler records. (a) Long-term amplitude record (b) Representative aperture distribution

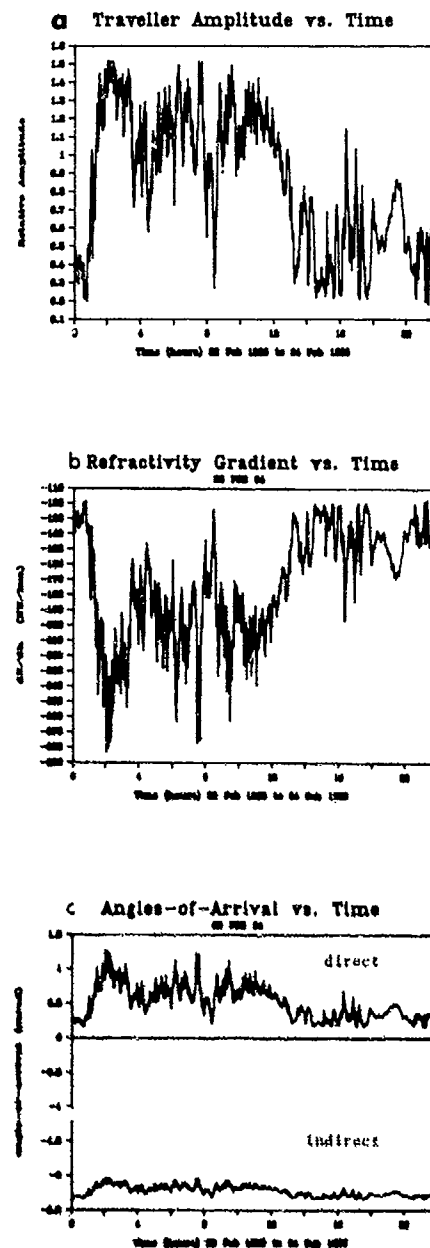


Figure 10: Estimates of long-term propagation parameters based on the assumption that recorded amplitude variations are caused by profiler null-height displacements. (a) Null height (b) Refractivity gradient (c) Angle-of-arrival

### SUMMARIZING DISCUSSION AFTER SESSIONS I TO III

In a general discussion (chaired by H.J.Albrecht) following the more propagation-oriented sessions I to III, some of the remaining discussion items were covered and added to the discussion remarks after the respective papers.

In addition, a more general exchange of views developed on the question of data bases and their use in system applications.

Questions such as standardization, resolution with particular regard to high frequencies, and reliability were dealt with in particular. In reply to a question on international standards by J.H.Whitaker, H.Kuschel referred to the D.L.M.S. model he used for his work (paper no. 7) and mentioned the US reference guide which is applied multinationally for the preparation of such data bases. He also pointed out that a D.L.M.S. version with 30 m intervals is being prepared. H.J.Albrecht added that, to his knowledge, a first topographic data base of general applicability had been used by the US Army in the late sixties and that models had been gradually improved; AGARD had covered the field in regular intervals with contributions and discussions on standardization and variability of input data. L.B.Felsen mentioned the importance of reliability of data and emphasized the need for a proper indication of all factors influencing the intended application.

AD-P005 744

16-1

## MM-WAVE PROPAGATION AND APPLICATION IN MILITARY COMMUNICATION SYSTEMS

by

Dr.-Ing. D.Rother

and

Dr.-Ing. E.Müller

Standard Elektrik Lorenz AG  
Pforzheim, Germany

### ABSTRACT

Tactical Communication is becoming more and more important in modern armies. After an improvement phase of Weapon- and Surveillance-Systems, emphasis is now on Command and Control and the optimization of the weapon efficiency. Hereby, communication is a dominant subsystem.

According to the electronic threat new requirements, i.e. Jam-resistance, security against Interception and Deception must be fulfilled; under conditions of a high degree of mobility.

Tactical communication in modern armies uses the VHF range from 30 MHz to 88 MHz. Advanced realizations, as they are operational or in introduction (Germany Army) now include digital transmission, voice and data capability and ECM-resistance by Frequency-Hopping methods and encryption. But the utilization of the VHF-band, including the traditional analog Fixed Frequency Communication (Interoperability) is strongly limited and not sufficient to meeting the Military Radio Net requirements. This is the reason for looking for new additional frequency ranges.

Possible solutions are offered by the mm-Waves in frequency bands higher than 30 GHz, which are free for use according to Frequency Planning. This paper investigates mm-Wave characteristics, propagation effects, i.e. atmospheric attenuation, shadowing, reflection, fading and its influence on radio links. System concepts for short range communication i.e. internal Command Post Communication are presented and discussed.

### 1. INTRODUCTION

Tactical VHF Radio Systems are in use in nearly all the armies of the world. This Communication System is the main instrument for information exchange and Command and Control on different levels of military organisations.

At Command Levels forward the brigade, Radio constitutes the primary means of communication. Besides the HF-links, which are used for long range operations, VHF-Communication is used in the battlefield by all ground forces.

This paper describes VHF-Radio Systems in use and according to the electronic threat, advanced Systems which will come into operation in the late eighties. For future improvements the application of mm-Waves has been investigated.

### 2. ARMY VHF-COMMUNICATION SYSTEMS

#### 2.1 Traditional Systems

VHF-Communication has been in use over some decades in Western armies. Well known examples are the US-Versions AN/PRC-77 and the VRC-12 Family, or the German SEM 25, SEM 35. These Tactical Radios operate in the frequency range from 30 MHz to 88 MHz. According to national frequency allocation, normally only some parts are usable. For the German Army, frequency range is limited to 80 MHz and some parts are restricted.

Radio communication in the VHF band is organized in the form of radio nets. A radio net consists of a certain group of participants, who should all receive information at the same time. This Simplex mode requires absolute radio discipline. Radio equipment is designed to transmit voice on fixed frequency. This fixed frequency is identical with one radio net.

Channel Spacing is realized in 50 KHz (older generations) and 25 KHz steps; this results in a maximum (not usable) number of ~ 2000, 2320 Channels, or independent radio nets.

Voice transmission is realized by Standard Analog Frequency Modulation (FM) including 150 Hz Tone Squelch. This



modulation is well adapted to the VHF radio channel characteristics (Fading, Multipath). An important matter is the NATO-Standardisation of this modulation and the relevant transmission parameters (STANAG) which allows real interoperability in the battlefield between NATO partners.

Tactical Radios are produced in different versions; man packs for short range communications up to 10 km with a maximum power of 5 W, and different vehicular stations which use power boosters of 40/50 W to communicate over distances of up to 30 km.

## 2.2 Electronic Threat

According to the importance of the VHF Radio System, the enemy has concentrated enormous activities to reduce and degrade the system performance. This electronic threat results in a number of Electronic Counter Measures (ECM), mainly in Interception and Jamming.

Traditional VHF communication is based on fixed frequency operation and a strong relation to a fixed radio net, including all partners of the net. A fixed frequency operation (one set-up) is normally active for a time between 5 sec to 12 sec. State of the art Surveillance Receiver Techniques are capable of surveying a total band of 30 MHz to 80 MHz in a time of 10 msec to 50 msec depending on the amount of equipment. Automatically switched on "Set-up Receivers" allow total surveillance of the VHF band. Based on this technical surveillance additional processing results in

- Information gathering of radio net specific communication
- Direction Finding and Position Locating
- Identification of radio net participants
- Identification of hierarchical structures, i.e. batteries, weapons, command post (Battalion, Brigade)
- Intelligence processing

Besides these passive surveillance and reconnaissance activities, active Counter Measures can follow:

- Jamming of important radio nets (at the right time)
- Deception of radio nets by transmitting false information; recording and retransmission
- and a number of more and more sophisticated actions.

It is obvious that the traditional fixed frequency radio is not secure enough to overcome the enemy's threat. That was realised in the middle of the 1970s and the US and German Military Authorities in particular started the development of new generations of Tactical VHF Radios [1, 2].

## 2.3 New Requirements

For this development a number of new requirements were defined according to the possible and future electronic threat:

- Security against
  - interception and Detection
  - Deception
  - Jamming
- Improvement and Upgrading of Communication Capacity
- Secure data transmission for Automatic Command, Control and Weapon Systems.

These tactical requirements resulted in investigation of new principles and new technical requirements for the equipment:

- digital transmission
- digital voice modulation
- secure coding methods
- Frequency economic methods
- Spread Spectrums application
- encryption

Finally the new generation should be realised with digital technologies and high integrated circuits (LSIs), to improve reliability, maintainability, and to reduce weight, volume and power consumption.

## 3. ADVANCED VHF-SYSTEMS

Since the late seventies, German Military Authorities sponsored the Development of a new VHF Radio Family, to overcome hostile electronic threat. This radio family, the FuGer A/VHF was designed and developed by SIEL. The main requirements and sub-tasks are discussed in the following paragraphs.

### 3.1 Digital transmission

Security against Interception and Detection can be achieved by encryption. Modern encryption methods with reasonable means require digital solutions, so it was necessary to find solutions for

- digital voice modulation
- digital transmission.

Voice modulation methods vary between traditional 64 kBit-PCM and advanced Vocoder principles with 2.4 KBit/sec. A large number of tests including military field test gave the result that 16 kBit/sec Deltamodulation is best suited for VHF-communication; even bit error to a rate of  $10^{-1}$  will give a sufficient quality of voice.

These 16 kBit/sec are well adapted to the radio channel and the channel spacing of 25 KHz, which must be used because of interoperability reasons with old equipment and a NATO-Standard. Binary Frequency Shift Keying (FSK-2) was selected as the modulation method, in accordance with traditional FM analog modulation.

VHF Radio Channels suffer from fading caused by multipath propagation. Bit error rates vary between  $10^{-1}$  and  $10^{-4}$ . For secure, high quality data transmission, it was necessary to incorporate the following principles:

- use of correlation marks for secure bit-synchronisation
- 24/36 block coding for error detecting and correcting
- multiple transmitting to reduce fading effects.

As a result, data transmission with bit-error rates less than  $10^{-4}$  is possible, related to a data rate of 2.4 KBit/sec, which is a standard in Command and Control applications.

Encryption has been realised with the 16 KBit/sec, according with the RF-bit rate, and the use of correlation technique resulted in a secure synchronisation.

### 3.2 Frequency Economic System

The German VHF frequency band is limited from 30 MHz to 80 MHz; some parts of the band are restricted. As a result the maximum number of channels (2000) is not available. In addition military staff require greater voice communication capacity. Overall, new services for data transmission, for Command, Control and Weapon Systems must use the VHF band. So it was necessary to find solutions for a better use of the frequency band.

In a fixed frequency operation, the channel is used by one radio net. Field tests and statistics showed, that even in case of high communication, the channel capacity is used only ~ 20% of time.

This fact allowed the design of a so called "Automatic Channel Selection" (ACS). A large number of Radio Nets are now sharing a bundle of frequencies (16). The Radio Net is defined by a digital number. In case of communication request, the transmitter searches a "free" frequency out of the bundle and transmits a selective call (Radio net number). All receivers (bundle) are scanning all 16 frequencies; if there is a call, they will detect their radio number and will stop scanning. After a time of some 100 msec, the transmitter and all authorized receivers will fix the same frequency and communication can be performed for the time necessary. At the end of the communication (timeout) all radios revert to the scanning mode.

The ACS works fully automatically; there is no difference to fixed frequency operation for the soldier. Figure 3.1 shows a schematic of the principle.

The ACS fulfills the requirement of a better use of VHF-Range and offers the user more communication capacity up to a factor of 10. It works for voice transmission, data transmission, in clear and in encrypted mode, made possible by digital principles. Besides, the ACS offers some ECM resistance because radio nets are not using the same fixed frequency and the ACS is automatically using the "best" channel.

### 3.3 Spread Spectrum Application

To achieve more ECM-resistance it is necessary to use Spread-Spectrum Principles. Hereby some essential functions must be fulfilled:

- Spreading the information over a broad, usable band
- method of spreading must guarantee a cryptological secure, authorized access
- Use of band must be frequency economic; great number of radio nets.

There are two principal methods, which fulfill these requirements to some extent:

- Direct Sequence Modulation (DS)
- Frequency Hopping (FH).

In case of DS-Modulation, the information is spread over the band (transmitter) by multiplying the information with a

defined high speed code sequence. The Spreading-Factor  $N$  as a relation between high speed code bandwidth and information bandwidth is a measure of jam-resistance. On the receiver side, using the identical code-sequence a de-spreading leads to the original information band. In case of jamming, only a small part ( $1/N$ ) of the jammer energy is finally within the information bandwidth (Figure 3.2.).

DS-Modulation offers a good anti-jam margin (1000 Channels = 30 dB). There are no possibilities for interception and deception, since the code-sequence is cryptologically secure and unique.

The main disadvantages are:

- only a limited number of code-sequences (Radio Nets) is available, which fulfill the requirement of orthogonality and cryptological security
- Code-Sequence synchronisation is very sensitive to jammers and to multipath effects (VHF)
- DS-Modulation is not a compatible method to existing VHF-Radio Standards.

Another possibility for Spread-Spectrum Application is Frequency Hopping. Hereby the information is formatted into data blocks; those blocks are transmitted on a defined sequence of frequencies. Hopping speed must be high enough to overcome fast surveillance receivers; ranges of so-called slow and medium Hoppers are in the range of 100 to 500 Hops/sec. Each radio net, is defined by a unique sequence of frequencies, which is generated by a cryptologically secure device (TRANSEC). A sufficient high number of different, statistically independent sequences (Radio Nets) is available.

FH-Systems offer a good anti-jam margin; by using frequencies (Hop-bundle) out of the total band, they come up to the same anti-jam margin as the DS-Modulation. (1000 Channels = 30 dB). In addition, frequencies to be used can be selected out of the band, so restricted areas and channels using traditional fixed frequency operation or ACS are not self-jammed as in case of DS-Modulation.

FH-realisation can use standard channel spacing and standard R/T equipment (filters, synthesizers). So the FH is compatible to existing VHF-Standards; it works with 16 KBit/sec transmission (FSK-2) and transmits voice or data in clear or encrypted mode.

The synchronisation of the Hop-sequence is realised by a clock-dependent algorithm, and does not suffer from jamming and hostile deception...

There is one principal disadvantage of FH-Systems. If on a bundle of frequencies ( $K$ ) a number of radio nets ( $N$ ) is active at the same time, there is a defined self-jamming (similar to DS-Modulation). Figure 3.3 shows a worst-case presentation. As an example with  $K = 256$  and  $N = 28$ , the resulting block error rate would be  $10^{-1}$  (bit error rate  $5 \cdot 10^2$ ) caused only by own radio nets.

This is a worst case consideration. In reality radio nets and related transmitters are distributed over the battlefield; then self-jamming is essentially reduced. Nevertheless, one should be conscious of the problem and carefully select FH-Radio Nets.

In order to get the best Anti-Jam margin, the Germany army is using a joint ACS-FH mode. FH is used by the specific radio net only in case of possible jamming; by that means an optimum Anti-Jam margin can be achieved.

### 3.4 Realisation

For the German Army, SEL has developed the FuGier A/VHF Radio Family. This radio system has now been in production since 1985. An ECCM version including Frequency Hopping will come into operation in the late eighties.

According to the new tactical requirements this radio system will overcome the hostile electronic threat. (Figure 3.4). Figure 3.5 shows a picture of a man pack and a vehicular version of the radio.

### 3.5 Future Development

It is obvious that after the introduction of ECM resistant radios, new activities for more sophisticated Counter Measures will come up. First concept-studies have been started with the objective of detecting DS-Modulation and Frequency-Hopping Systems. To be prepared, next generations of Army Communication Systems must be taken into consideration.

Possible solutions for the VHF-Radio could be

- Nullsteering Antenna Processor Systems to Jammer-Nulling
- Fast Hopping Systems, where Hopping Speed is in the range of Electromagnetic Wave Propagation speed

Even in the event that such systems are feasible and there are some doubts because of multipath effects, there is not possibility of offering more communication capacity in the VHF range. Since this is a main objective for the future, it is necessary to look for new possibilities, and that means other frequency ranges.

mm-Waves may be the solution.

## 4. MM-WAVE COMMUNICATION

### 4.1 General

For the selection of new frequency ranges to be used for army communications, some requirements must be fulfilled. Basically, those frequency bands must offer broadband capacity and high resistance against Interception and Jamming; full mobile, ground based application must be guaranteed.

Regarding possible free ranges, one comes up to ranges higher than 10 GHz. Figure 4.1 presents the propagation conditions of frequencies up to 400 GHz, where especially atmospheric attenuation is a main factor influencing propagation, besides free space attenuation. One can see that for some frequencies, resonator effects lead to high values of attenuation. There are some Maxima and Minima, where the ranges of 35 GHz, 60 GHz and 95 GHz are of special interest.

In the case of 60 GHz, atmospheric attenuation comes up to 15 dB/km; for 35 GHz (radio window) only 0.2 dB/km results. These additional attenuations essentially reduce propagation range. Assuming usual (realistic) system values for a transmission link,

|                                    |                      |
|------------------------------------|----------------------|
| $G_t = G_r = 7 \text{ dB}$         | Antenna Gain         |
| $P_t = 1 \text{ W}$                | Transmitted Power    |
| $P_{\text{min}} = -90 \text{ dBm}$ | Receiver Sensitivity |

the maximum range results in the values demonstrated in figure 4.2.

As an example of interest, the range for 35 GHz will be about 3300 m, and for 60 GHz only 650 m.

In addition, propagation is influenced by rainfall. While at 35 GHz, assuming a rate of 10 mm/h, range is reduced by a factor of two, 60 GHz are nearly insensitive against rain.

For the evaluation of ECM resistance of a radio system it is necessary to consider surveillance and jamming conditions. For surveillance receiving equipment, the following system parameters are realistic:

|                                    |                            |
|------------------------------------|----------------------------|
| $P_t = 1 \text{ W}$                | Transmitted Power          |
| $G_t = 7 \text{ dB}$               | Antenna Gain, Transmitter  |
| $G_r = 30 \text{ dB}$              | Antenna Gain, Surveillance |
| $P_{\text{min}} = -90 \text{ dBm}$ | Receiver sensitivity       |

Figure 4.3 shows the relation between surveillance ranges as a function of frequencies, including atmospheric attenuation. So 35 GHz can be detected over a distance of about 32 km; for 60 GHz this distance goes down to 2000 m. This means that under army battlefield conditions, 60 GHz communication is absolutely secure against interception and also jamming. The atmospheric attenuation of 15 dB/km at 60 GHz is an excellent means of achieving ECM-resistance. This is not the case for 35 GHz.

On the other side the 60 GHz communication range of ~ 1000 m, is not sufficient for the Army's tactical requirements (up to 30 km). But for some short range radio nets, e.g. Command Post internal Communication, 60 GHz are a potential solution.

The above-mentioned results are based on the assumption of free line-of-sight conditions and neglect distortions.

For a tactical application in the battlefield, this is not realistic. Shadowing effects, caused by houses, woods, vehicles as well as multipath propagation must be considered.

### 4.2 Effects of propagation

On valuation of possible assignments of a 60 GHz-System, we first consider the essential disturbing effects in a modelling manner. Those are:

- Shadowing and diffraction
- Reflections and fading.

#### 4.2.1 Shadowing and diffraction

For demonstrating the basic differences of a disturbed VHF- and mm-Wave respectively, a conducting vertical half-plane of height  $H$  is inserted between transmitter and receiver. (This model and the related formulas are shown in fig. 4.4). The diffraction attenuation is essentially affected by the height  $H$  and the frequency, resp. wavelength.

For example, the distance between the transmitter and the receiver is 500 m, the conducting half-plane is right in the middle of this distance and the height  $H$  is 1 m. From this, it follows for the attenuation at

|        |          |
|--------|----------|
| 60 MHz | : 6,5 dB |
| 60 GHz | : 18 dB  |

For a radio-system at 60 GHz with an operational coverage between 100 m and 1000 m, obstacles may totally interrupt the radio line.

#### 4.2.2 Reflections and fading

If the direct radio line is interrupted by an obstacle, there may be reflection. Depending on the angle of arrival, the quality and roughness of reflector, a part of the impact energy will be reflected to the receiver. As usual in wave propagation theory the roughness is defined by a normalized rms value. For a gaussian distributed change of height, this rms value is given by

$$\text{roughness (rms value)} = \delta_h \sin \frac{\psi}{\lambda},$$

where  $\psi$  is the angle of arrival,  $\lambda$  is the free space wavelength and  $\delta_h$  is the rms value of the distribution of height. It follows from this equation that the roughness is directly proportional to the frequency.

For a very small roughness, the impacting energy will be specularly reflected by the reflector. For increasing roughness, the amount of specularly reflected energy is decreasing while the diffusely scattered amounts are reaching the receiver. This behaviour may be described mathematically by two real diffraction coefficients,  $\rho_s$  and  $\rho_d$ , for the specular and the diffuse reflection respectively. Fig. 4.5 shows the run of  $\rho_s$  and  $\rho_d$ .

$\rho_s$  may be approximated by the equation [3]

$$\rho_s = e^{-1} I_0(z),$$

where  $I_0$  is the modified Bessel-function of the order zero and  $z$  is defined by

$$z = 2 \left( \frac{2\pi\delta_h \sin \psi}{\lambda} \right).$$

$\rho_d$  has a complicated dependence to  $\psi$ ,  $\delta_h$ ,  $\lambda$  and the cross-section of the reflector. It is nearly constant for values of roughness (rms value)  $> 0.15$  [3, 4]. The figure of 0.4 is a typical maximum value [4].

As a result, the reflected wave is the complex sum of two (uncorrelated) components

$$\begin{aligned} E_r &= E_{r,spec} + E_{r,diff} \\ &= E_{in} \rho_s + E_{in} \rho_d, \end{aligned}$$

where the reflection coefficient  $\rho$  is multiplied by  $\rho_s$  and  $\rho_d$  respectively. The (complex) reflection coefficient  $\rho$  is defined for specular reflection; it is different for vertically and horizontally polarized waves [3]. Furthermore  $\rho$  is dependent to the materials and frequency.

If there are no obstacles, but reflectors between transmitter and receiver, multipath reception occurs: depending on the roughness, the vector sum of the electrical field components is altered (increase or decrease (fading)).

For low antenna heights and distances less than 2000 m, fading is always to be taken into consideration in system development.

To render clear fading is simplest with a two-way model with one directly and one indirectly (reflected) received component of field strength (fig. 4.6). Fig. 4.7 shows the calculation of the normalized received power  $P_r/P_s$  in the case of two-way reception. For this consideration the vector sum was approximated by an algebraic sum. Because the diffuse and specular parts are uncorrelated, the total power is the sum of direct and diffuse power.

Two special cases are of particular interest: diffuse reflection and specular reflection at distances that are much larger than the heights of antennas. As depicted in fig. 4.8, in case of specular reflection and for path-length differences of

$$\Delta s = (D \pm 1) \lambda / 2 \approx 0, \pm \lambda / 2,$$

the received power is (approximately) zero. Between the nulls, there are maximas of 6 dB gain compared with the direct received power. At distances far from the last null (case  $n = 0$ ), the power is decreasing with  $1/d^4 \approx 1/10^{14} \text{ dB}$ , where  $s$  is the sum of atmospheric attenuation and rain attenuation in dB per kilometre.

In the case of diffuse reflection at 60 GHz and for roughnesses with a standard deviation greater than 20 mm, the fading effects are vanishing and the received power is slightly higher compared with the undisturbed case.

### 4.3 Experimental Results

#### 4.3.1 Test Equipment

In order to study the propagation conditions with small antenna heights ( $h_t = h_r = 2.7$  m) in real surroundings (streets, fields, woods) test equipment was built which works at 61 GHz, consisting of a transmitting and a receiving station. Figure 4.9 summarizes the main system parameters of the equipment, which was installed into two vehicles. For the measurement two antenna types, an omni-directional antenna ( $G = 5$  dB) and Horn-antenna (24 dB) were used. According to different antenna configurations, ranges between 150 m and 1500 m could be achieved.

Maximum transmitted power was  $2 \times 100$  mW; an injection locked oscillator (ILO) with a number of Gunn-Diodes were used. Transmitted power was shared by two carrier frequencies, with a spacing of 40 MHz.

Information data were generated by a shift-register of 16 bit, running at variable transmission rate between 0,125 MHz/sec up to 8 MHz/sec.

Receiver equipment was realised with variable IF-Filters and information LP-Filter; in addition it was possible to demodulate frequency diversity signals separate or continued (pre detection combining).

On the receiver side, local generated bitstream and transmitted bitstream were compared (after synchronisation). So bit-errors could be measured; intervals were between 10 msec and 15 min.

As a basis for interpretation of the channel characteristics and propagation effects, carrier to Noise Ratio C/N, and Bit error rate BER/time were measured and recorded. Two types of modulation, Binary Frequency Shift Keying (FSK) and Differential Phase Shift Keying (DPSK) have been tested and compared with theoretical figures [3, 4, 5, 6, 7].

#### 4.3.2 Test results

In the first test configuration both vehicles were on a street without special obstacles (line of sight). Driving one vehicle away from the other, variations of field strength were measured. Figure 4.10 and 4.11 show the theoretical and measured values. Measured Fading Depth was in the range of 20 dB to 25 dB. The larger the distance, variations become smaller and the distances between adjacent minima and maxima become larger. Measurements showed good coordination with theory.

Figures 4.12 and 4.13 show the results of BER measurements for FSK and DPSK at 8 MBit/sec transmission.

For comparison, theoretical values are outlined with a parameter  $c$ ,  $c$  is defined as the relation of direct received signal Energy  $A^2/s$  to the mean square value of all multipath signals, according to mathematical models of RICE-Fading [6].

This gives:

- $c = 0$  no direct signal
- $c = \infty$  no multipath signal

The measured BER (steady movement of one vehicle) shows the following results:

- Carrier/Noise Values are mainly concentrated in the range between 10 dB to 20 dB
- BER are in the range between  $10^{-2}$  and  $10^{-1}$
- for fixed C/N ratio, factor  $c$  varies tremendously (relation direct signal/ reflected sum)
- Measured values differ from theoretical limits ( $c = 0$ ) because of limited A/D-conversion accuracy
- DPSK results in better BER than FSK

In a second test configuration both vehicles were located on a field covered with grass. Test procedure was similar to the first one. One vehicle moved away from the other and C/N as well as BER was measured.

Figures 4.14 and 4.15 show the signal to noise ratio (C/N) as function of distance. According to the influence of grass, diffuse reflection is the main part of received signal, variations are very small.

For BER, measurement in Figure 4.16, (two carriers) and Figure 4.17 (one carrier) with FSK and 8 MBit/sec shows the following:

- Carrier/Noise Values are more concentrated
- BER are much better and in good accordance with theory
- Parameter  $c$  is nearly constant

A very important result is the fact that the use of Frequency-Diversity (two carriers 40 MHz Spacing) and pre-detection combining leads to a good BER performance.

#### 4.4 Problems and Solutions

Two examples of experimental results have been presented. A number of additional test configurations have been evaluated, i.e. shadowing in wooded areas, reflection between houses, influence of snow etc. As a main result one can say:

- communication with 60 GHz is feasible within short ranges
- Shadowing effects are the main problem; they can be solved on System level by
  - Relay concepts
  - TDMA with routing
- Fading problems can be reduced by
  - diversity
  - spread spectrum principles
- Intersymbol Interference can be reduced by coding methods

This 60 GHz experimental program is sponsored by the German MOD and will be continued in the next years by SEL. First application is planned for future command post internal communication.

#### 5. SUMMARY

This paper described the situation of Army Tactical Communication Systems, which traditionally are arranged in the VHF frequency band.

Advanced VHF generations, including ECM-resistance were presented and possible application of mm-Waves in the range of 60 GHz for future use were discussed.

#### References:

1. LTC H.P.Krause, D.Roth. Tactical VHF Radio Communications in the German Army. SIGNAL, November 1982
2. Col. E.R.Baldwin, Jr. The Army's New Frequency Hopping Jam Resistant Combat Net Radio. SIGNAL, November 1982.
3. Blake, Lamont V. Radar Range-Performance Analysis. Lexington Books, Lexington, 1980.
4. Barton, David K. Low-Angle Radar Tracking. Proc IEEE 62, 1974, No.6, pp 687—704
5. Proakis, John G. Digital Communications. McGraw-Hill, 1983
6. Whalen, Anthony D. Detection of Signals in Noise. Academic Press, 1971
7. Hagenauer, Joachim/Schweikert, Robert. Zukünftiger Satellitenmobilfunk — Datenverbindung mit Schiffen, Fahrzeugen und Flugzeugen. NTZ 27, 1984, No.2, pp 78—83

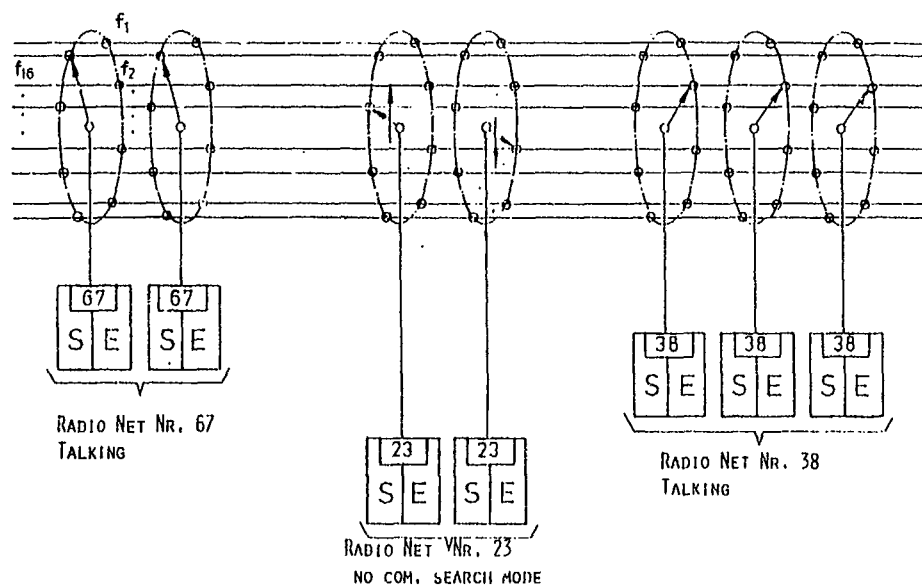


Figure 3.1: ACS: Frequency Bundle for common use

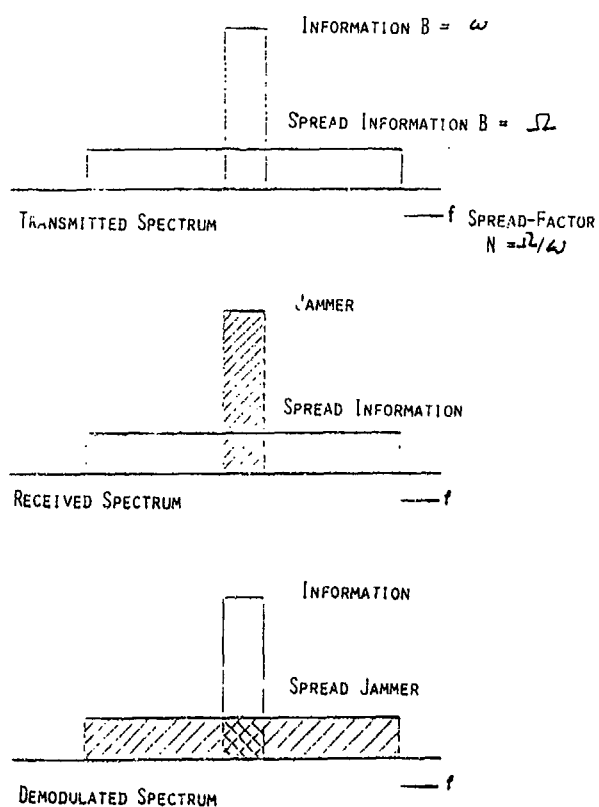


Figure 3.2: DS-Modulation



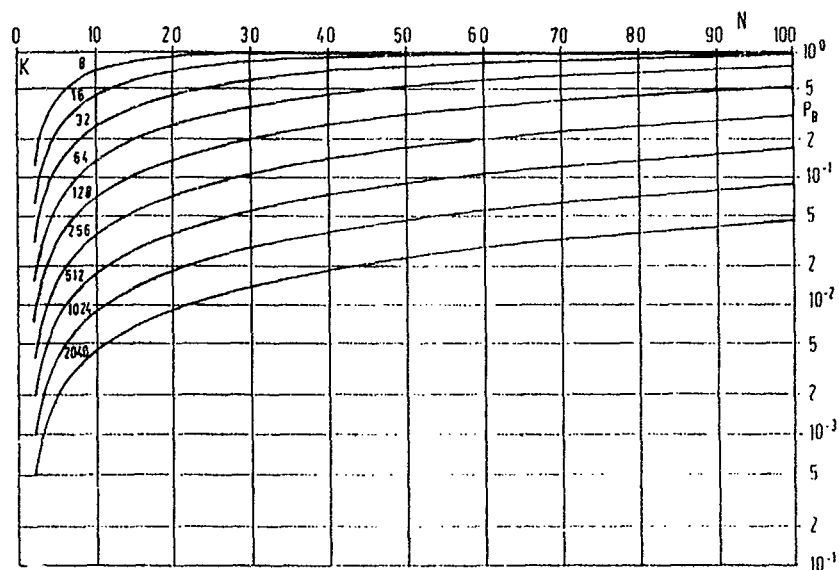


Figure 3.3: Frequency-Hopping/Self-Jamming

| NEW REQUIREMENTS   | SOLUTIONS  |
|--|--|
| • DATA TRANSMISSION                                      | • DIGITAL TRANSMISSION<br>16 KBIT/s; 2.4 KBIT/s                  |
| • SECURITY AGAINST<br>INTERCEPTION/DETECTION             | • ENCRYPTION 16 KBIT/s<br>VOICE, DELTAMODULATION                 |
| • FREQUENCY ECONOMY                                      | • AUTOMATIC CHANNEL SELECTION<br>FACTOR 6 ... 10 MORE RADIO NETS |
| • SECURE AGAINST<br>INTERCEPTION<br>DECEPTION<br>JAMMING | • FREQUENCY HOPPING<br>(PLUS ENCRYPTION)                         |

Figure 3.4: Advanced VHF-Systems

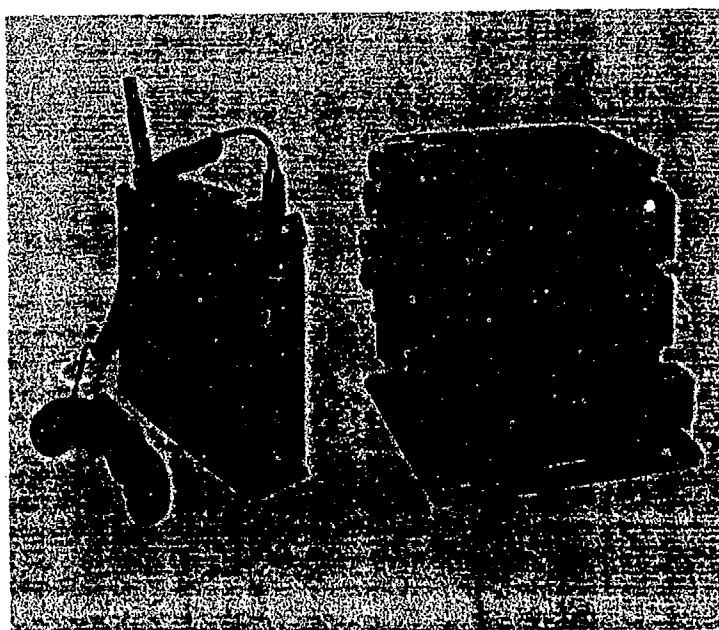


Figure 3.5: FuGer A/VHF Radio Family  
Manpack and Vehicular Station

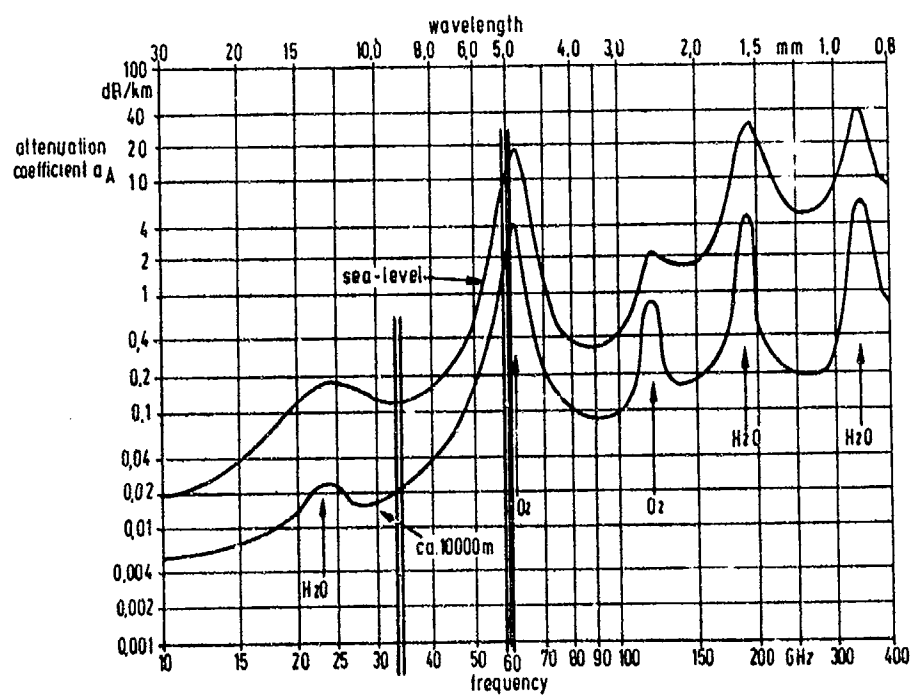


figure 4.1: atmospheric attenuation coefficient

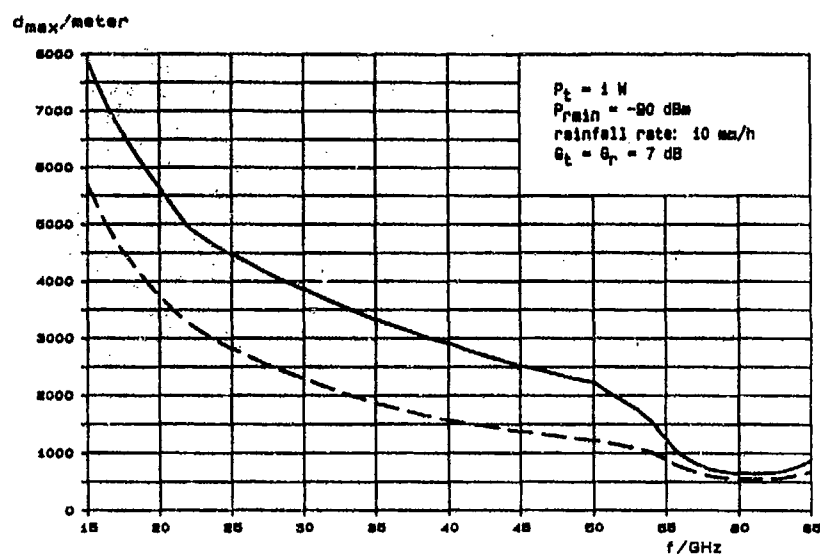


figure 4.2: maximum range without rain (—) and with rain (---)

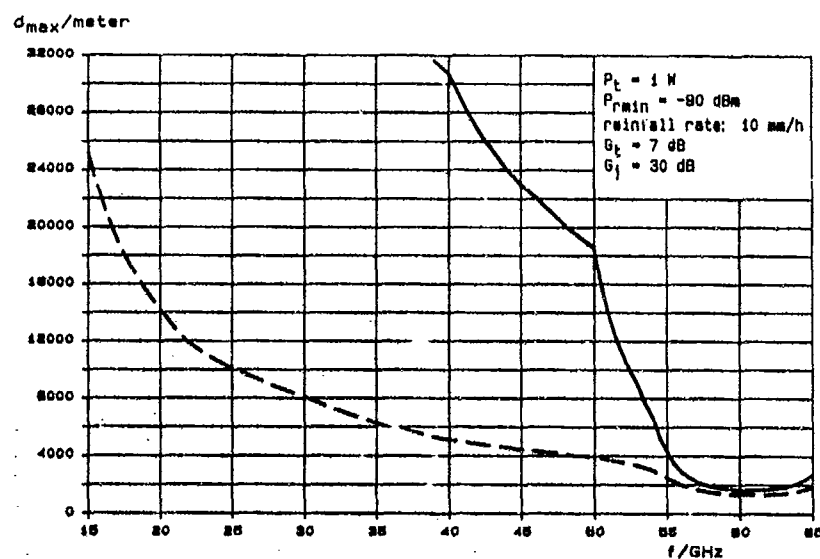
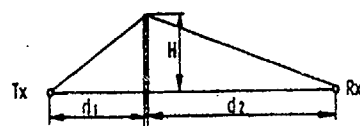


figure 4.3: maximum reconnaissance range without rain (—) and with rain (---)



diffraction attenuation

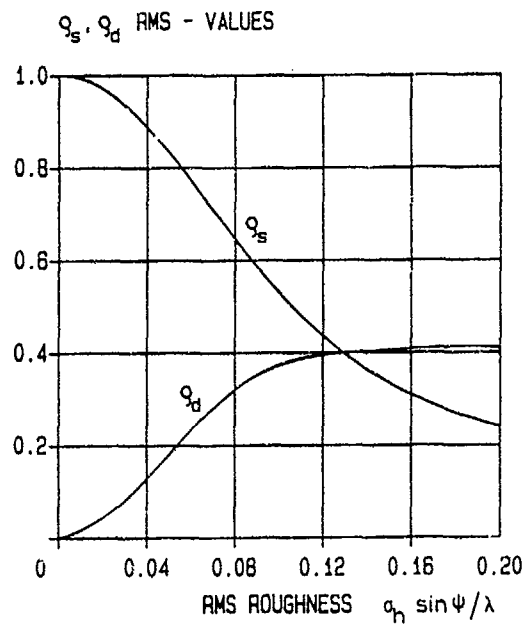
$$\begin{aligned} \frac{a_{\text{diff}}}{\text{dB}} &\approx 6 + 8.7 v & v < 1 \\ &= 13 + 20 \log(v) & v > 1 \end{aligned}$$

$$v = H \sqrt{\frac{2}{\lambda} \left( \frac{1}{d_1} + \frac{1}{d_2} \right)} \sim \sqrt{f}$$

example:

|   |   |
|---|---|
| $d_1 = d_2 = 250 \text{ m}$<br>$H = 1 \text{ m}$                          |   |
| $f = 60 \text{ MHz}$<br>$v = 0.056$<br>$a_{\text{diff}} = 6.5 \text{ dB}$ | $f = 60 \text{ GHz}$<br>$v = 1.77$<br>$a_{\text{diff}} = 18 \text{ dB}$ |
| <p>  </p> <p><u>line-of-sight-communication</u></p>                       |   |

figure 4.4: diffraction coefficient (model)



$$\rho_s \approx e^{-z} I_0(z)$$

$$z = 2(2\pi a_h \sin \psi / \lambda)^2$$

figure 4.5: scattering coefficients

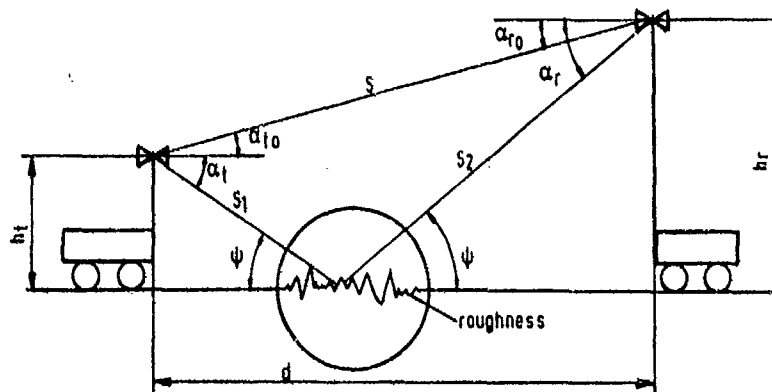


figure 4.6: two path model with rough reflecting surface

$$\frac{P_e}{P_0} = \left| f(\alpha_{to}) \cdot f(\alpha_{ro}) + k \rho_s \cdot \rho \cdot e^{j\varphi_s} \cdot e^{-j\Delta\varphi} \cdot f(\alpha_t) \cdot f(\alpha_r) \right|^2 + \left| k \cdot \rho_d \cdot \rho \cdot e^{j\varphi_s} \cdot e^{-j\Delta\varphi} \cdot f(\alpha_t) \cdot f(\alpha_r) \right|^2$$

$P_e$  = total received power

$P_0$  = direct received power (  $P_0 \sim 1/d^2 \cdot 1/10^{a \cdot d/\text{km}}$  ,  $a = a_A + a_R$  in dB/km )

$\rho_s$  = specular scattering coefficient (  $0 \leq \rho_s \leq 1$  )

$\rho_d$  = diffus scattering coefficient (  $0 \leq \rho_d < 0.5$  )

$\Delta\varphi$  = phase difference between direct and indirect (reflected) electric field component

$\rho e^{j\varphi_s}$  = complex (vertical or horizontal) reflection coefficient

$f(\alpha)$  = antenna voltage gain pattern

$k$  = additional attenuation due to the longer path (  $k \approx 1$  )

figure 4.7: received power for two path propagation

#### Special cases

$$h_r, h_t \ll d$$

$$f(\alpha) \approx 1$$

$$\rho \exp(j\varphi_s) = -1$$

#### o specular reflection

$$P_e/P_0 \approx 2 (1 - \cos \Delta\varphi) = 2 (1 - \cos \frac{2\pi \Delta s}{\lambda})$$

$$\text{with } \Delta s = (s_1 + s_2) - s \approx 2 h_r h_t / d$$

- fading effects (minima and maxima)

$$0 < P_e/P_0 < 4$$

#### o diffus reflection ( $f = 60 \text{ GHz}$ , $\sigma_h > 20 \text{ mm}$ )

$$P_e/P_0 \approx 1 + \rho_d^2 > 1$$

- no fading effects

figure 4.8: special cases for two path propagation

Test equipment

- o word generator
  - o pseudo-noise code
  - o length  $2^{15} - 1$
- o transmitter (two parts)
  - o frequency 61 GHz
  - o frequency-diversity (40 MHz)
  - o PSK- or FSK-modulation
  - o power  $2 \times 100 \text{ mW}$  (ILO)
  - o bitrate 0,125 - 8,0 Mbit/s
  - o antenna gain
    - o omnidirectional 5 dB ( $360 \times 20^\circ$ )
    - o horn 24 dB ( $30 \times 30^\circ$ )
- o receiver (two parts)
  - o variable nf-bandwidth
  - o variable if-bandwidth
  - o equal gain combining
  - o antennas like transmitter
- o bit error measuring equipment
- o data transfer and storage
  - o bit error rate at 2 frequencies
  - o received power+noise at 2 frequencies

figure 4.9: test equipment

M\_172 section 20 to 68

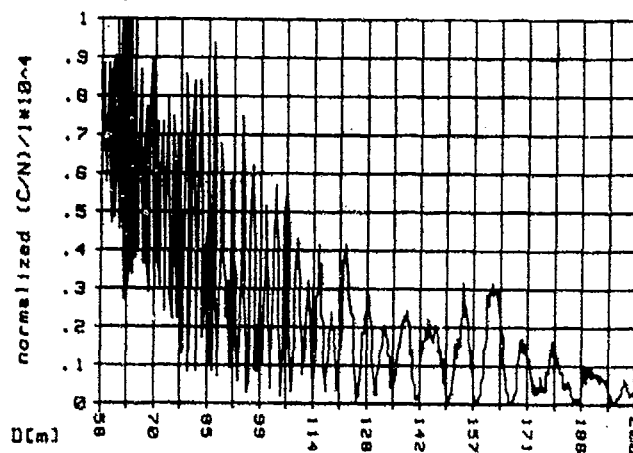


figure 4.10: normalized signal-noise-ratio as a function of distance

theoretical two path model

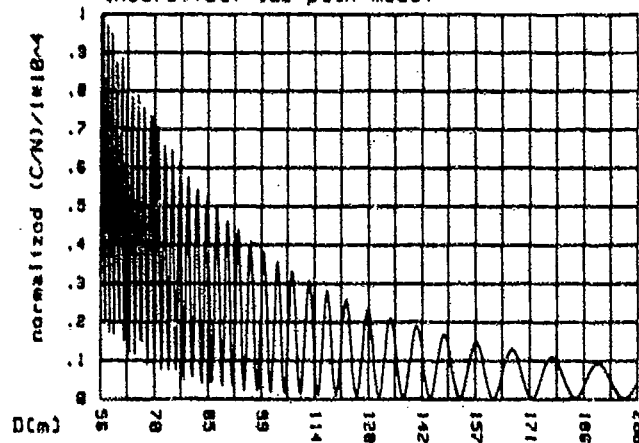


figure 4.11: normalized signal-noise-ratio as a function of distance



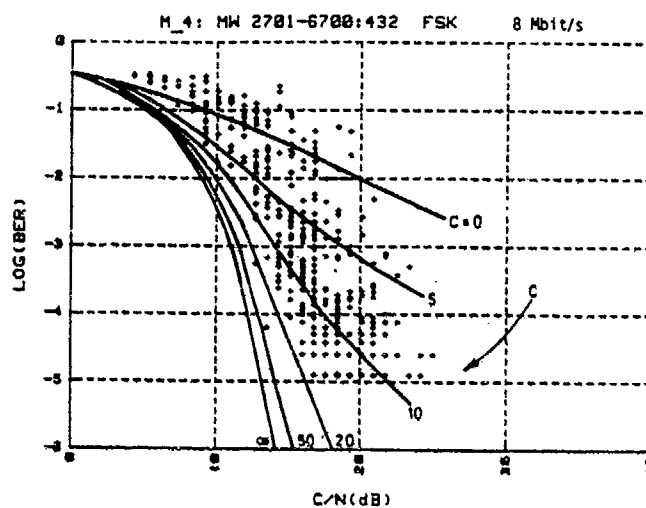


figure 4.12: theoretical and measured bit error rate

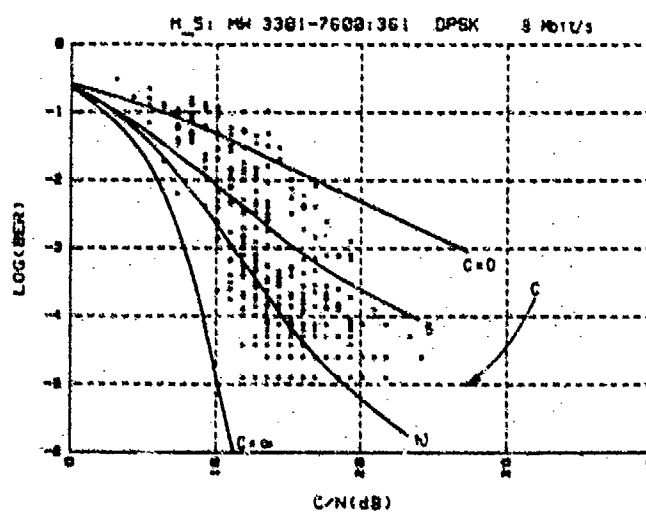


figure 4.13: theoretical and measured bit error rate

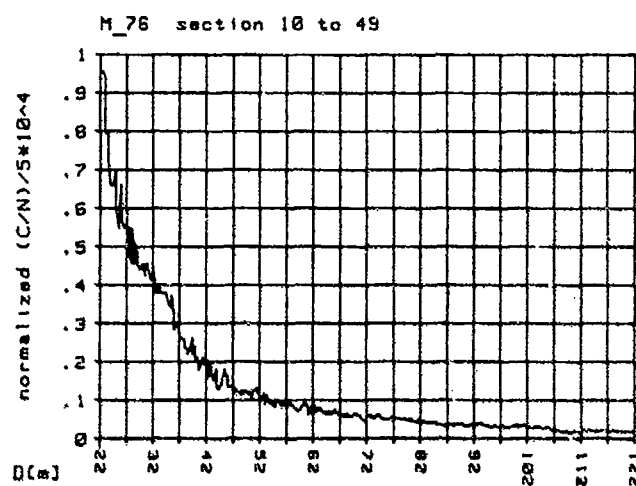


figure 4.14: normalized signal-noise-ratio as a function of distance

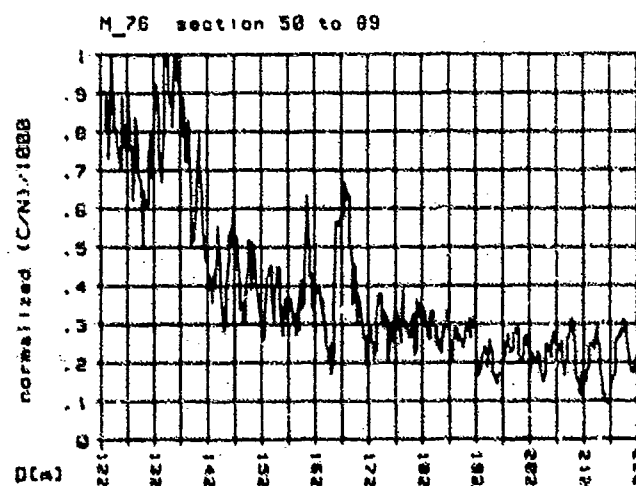


figure 4.15: normalized signal-noise-ratio as a function of distance

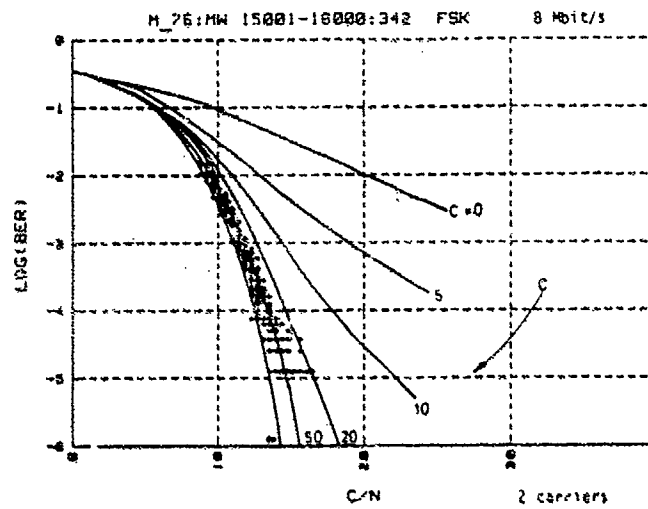


figure 4.16: theoretical and measured bit error rate

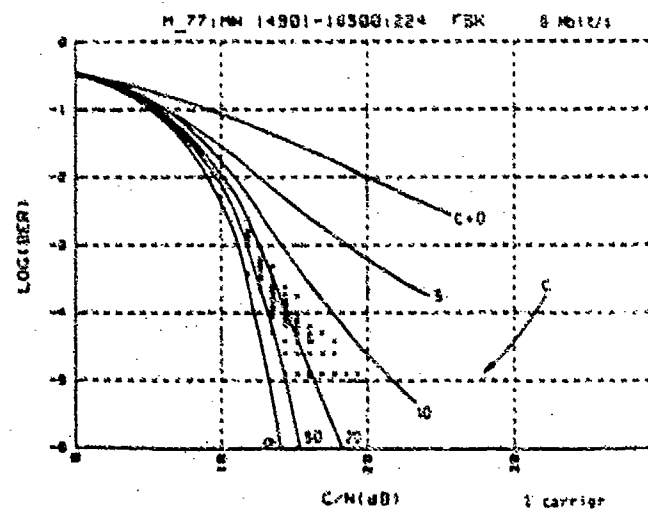


figure 4.17: theoretical and measured bit error rate

## DISCUSSION

**J. Snieder**

Remark: Differences between presented results of asphalt and grass will be explained in paper 22.

Question:

- (1) Have corrections for antenna gain been applied as a function of distance between the transmitter and receiver?
- (2) Has experimental value of forward reflection coefficient of asphalt been used in theoretical curve?

**Author's Reply**

- (1) Yes, see  $f(a)$  in the formula.
- (2) The theoretical curve is a rough approximation with the reflection coefficient of asphalt.

**A.N. Ince**

In a co-site operation how would you cope with the EMC problem that would arise when fixed and FH systems operate simultaneously; a situation which is likely to arise in the short and medium term?

**Author's Reply**

Problems can be solved by adequate frequency planning i.e. a bundle of frequencies as hop set. In statistical hopping there is always a "self jamming", so the mode of hopping should be used carefully.

**R. Holdway**

Have you addressed the issue of how to keep the costs of a MM wave communication system low enough to make it feasible for large scale use with the Army?

**Author's Reply**

A possible cost reduction could be possible by integration of receiver frontend in CMAA technology.

**E. Villar**

Have you considered adaptive equalization techniques to combat multipath and reduce your b.e.r.

**Author's Reply**

Up to now, we have no results.



## SPACE - DIVERSITY EFFECTS ON LINE-OF-SIGHT PROPAGATION PATHS

H.-G. Giloi, K. Metzger and R. Valentin

Forschungsinstitut der Deutschen Bundespost

6100 Darmstadt

Fed. Rep. of Germany

## SUMMARY:

This paper discusses the effects of space-diversity reception on the performance of analog and digital radio-relay systems. It reviews the existing results valid for analog systems and describes some single-frequency measurements of the dependence of the improvement factor on the vertical antenna separation. It was found that the prediction formula proposed by Hoasys gives a good approximation to the measured dependence.

The effect of the frequency-selectivity of the fading was taken into account for a performance estimation of digital radio links. Fading events measured in a 43-MHz bandwidth at 2.5 GHz with 3 antennas spaced 60 λ apart were described with an "effective" two-path model. Assuming maximum-power combining of the main and diversity branches the performance of 140-Mbit/s M-QAM systems (M = 16, 64, 256) were evaluated for a roll-off factor of α = 0.5. Results were obtained for idealized systems (no timing- and carrier phase jitter, perfect Nyquist filtering without channel distortions) optionally equipped with an adaptive transversal equalizer with 5 taps adjusted by the zero-forcing algorithm. A substantial improvement was obtained if both countermeasures were applied as compared to the case where either diversity or equalization was used. Furthermore, the improvement factor was reduced if the modulation scheme was changed from 16 QAM to 64 and 256 QAM keeping the transmitted power constant. This can be explained by the reduced flat fade margin and increased sensitivity of the higher-level modulation schemes to frequency selective fading.

## 1. INTRODUCTION

The performance degradation caused by propagation effects of radio relay systems can be significantly improved by diversity reception. A drawback is however involved because of increased expenses. Additional frequency bands (frequency diversity) and installation space for antennas (space diversity) is also needed. It is therefore desirable to have a good estimation of the improvement of the transmission performance dependent on parameters such as separation of space-diversity antennas, frequency separation etc. There exists already a lot of results on the improvement resulting from diversity reception in the case of analog FM/FDM radio-relay systems which are well documented and summarized in the CCIR-literature [1]. For the systems with diversity the improvement is mainly caused by an improvement of the signal-to-noise (S/N) ratio. Therefore, it is sufficient for a determination of outage to measure and describe the statistical distribution of the received power level at a single frequency with and without diversity. The improvement factor I defined by

$$I = \frac{Q_0(A_s > A_0)}{Q_d(A_d > A_0)} \quad (1)$$

is then a measure for the improvement in outage time for such systems.  $Q_0$  and  $Q_d$  are the probabilities that the attenuations  $A_0$  and  $A_d$  exceed a given threshold  $A_0$  without and with diversity, respectively. For high-capacity digital radio systems, however, the situation is more complicated because the outage is dependent on the statistical distribution of the S/N ratio and the extent of frequency selectivity of the fading. It is for this reason that also certain system parameters such as modulation scheme, transmitted bit rate, roll-off factor, equalization methods etc. will have a significant influence. The aim of this contribution is therefore to show how this problem can be tackled. First a short review and a refinement of already known results for analog radio systems will be presented.

## 2. DIVERSITY OPERATION IN ANALOG RADIO-RELAY SYSTEMS

The definition of the diversity improvement factor which is illustrated in Fig. 1 can further be evaluated if the statistical distribution of the received power level is known. For line-of-sight (LOS) paths very often a Rayleigh distribution is valid with a slope of 10 dB/decade as also shown in Fig. 1. Then the joint-probability density function of two correlated Rayleigh-distributed random variables can be expressed analytically and the improvement factor for deep fading is approximately given by [2]

$$I = \frac{1-K}{10^{-K/10}} \quad (2)$$

where K is the correlation coefficient of the received power.

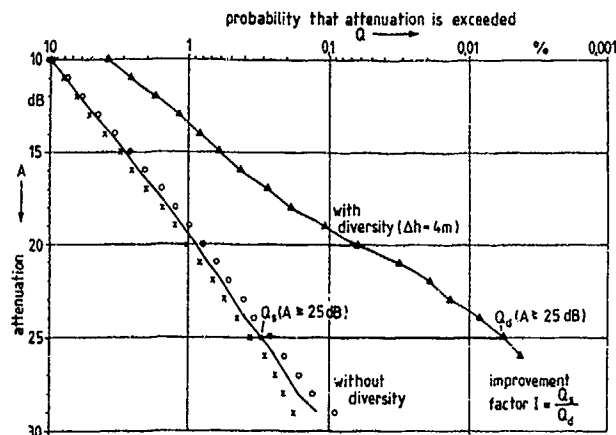


Fig. 1: Probability distribution for single reception and selector combining.

- x worst-month distribution of the attenuation measured at antenna 1
- o same for antenna 2  
(displaced in vertical direction by 4m relative to antenna 1)
- Δ distribution for diversity reception with selector combining

The dependence of the improvement on the attenuation is plotted in Fig. 2 for some correlation coefficients together with experimental results for a space diversity arrangement indicating a correlation coefficient of about 0.85 for the vertical antenna spacing of 4m ( $\Delta 120\lambda$ ).

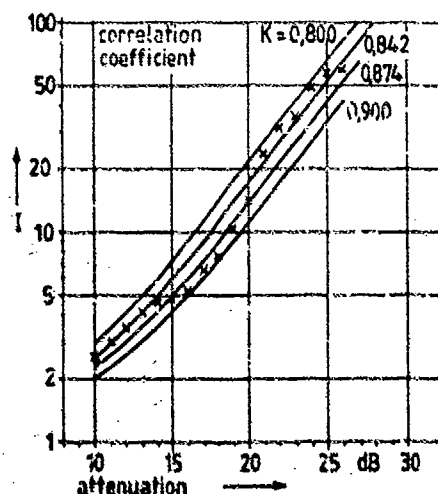


Fig. 2:

Improvement factor I versus fade depth for some correlation coefficients.

(x: experimental results for a space diversity arrangement with  $\Delta h = 4$  m ( $\Delta 120\lambda$ ) separation)

An important question in engineering space diversity equipment is how large the antenna separation should be to obtain a sufficient improvement. The existing formulas are sometimes contradictory as explained later. We have therefore carried out an experiment on a LOS path where 14 receiving antennas were mounted above each other with a spacing of 3 m corresponding to about 60λ at a transmission frequency of 9.3 GHz. For the time period of 1983-85 the improvement factor was determined from the statistical distribution of the attenuation as illustrated in Fig. 1 and the averaged correlation coefficient for the different antenna separations were obtained using the curves partly shown in Fig. 2. The results were compared with the values obtained from the CCIR prediction formula which is based on the work of Vigants [3]. As can be seen from Fig. 3 the results obtained from a fit to the Vigants formula

$$K = 1 - 0.0014 (\Delta h/m)^2 \quad (3)$$

remarkably deviate from the measured results. The best fit to our results was obtained with an expression proposed by Hosoya [2]:

$$K = \exp(-\alpha(\Delta h/m)^{\beta}) \quad (4)$$

with  $\alpha = 0.089$  and  $\beta = 1/2$ .

Thus the experiments indicate that the existing CCIR prediction method has to be used with caution only for a very limited range of antenna separations.

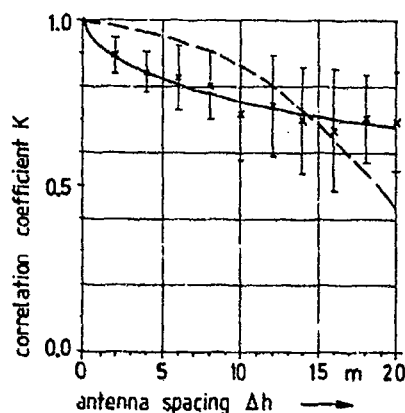


Fig. 3:  
Mean value  $\bar{x}$  and standard deviation  $\bar{s}$  of the correlation coefficient of two vertical separated space diversity antennas versus spacing  $\Delta h$ .  
(solid line: best fit to eq. 4  
dashed line: best fit to eq. 3.)

### 3. DIVERSITY OPERATION IN DIGITAL RADIO-RELAY SYSTEMS.

For high-capacity digital radio-relay systems the S/N-ratio and the frequency selectivity of the fading have to be known for determining both the system performance and the diversity improvement defined by

$$I = \frac{Q_s (BER_s > BER_0)}{Q_d (BER_d > BER_0)} \quad (5)$$

where  $Q_s$  and  $Q_d$  are the probabilities that the system exceeds a given BER-threshold  $BER_0$  without and with diversity, respectively. This improvement now depends on several parameters

- transfer functions  $H_{1,2}(f)$  of the propagation channels of the two diversity branches.
- the combining strategy for the two diversity signals
- system parameters such as bit rate, modulation scheme, roll-off factor  $\alpha$  and type of equalizer.

It is therefore difficult or impossible to find a general expression for a diversity improvement. Therefore an approach was developed consisting of

- propagation experiments conducted to measure the transfer functions of a space diversity arrangement.
- modelling of the radio system so that the system performance based on the actually measured fading events could be calculated by a computer.

#### 3.1 PROPAGATION EXPERIMENT

The data base of measured fading events was obtained on a 55-km propagation path (Fig. 4) in autumn 85. The amplitude and group-delay responses of the channel were measured in a 45 MHz bandwidth at 9.5 GHz for the main antenna by means of a Wawel & Goltzmann link analyser. Simultaneously the amplitude dispersion at a diversity antenna was recorded and stored. Another diversity antenna could be selected by a pin-diode switch so that during consecutive sweeps two different diversity configurations can be measured quasi-simultaneously as shown in Fig. 5. (In most of the cases the propagation conditions did not change very much if a sweep rate of 20 Hz was applied).

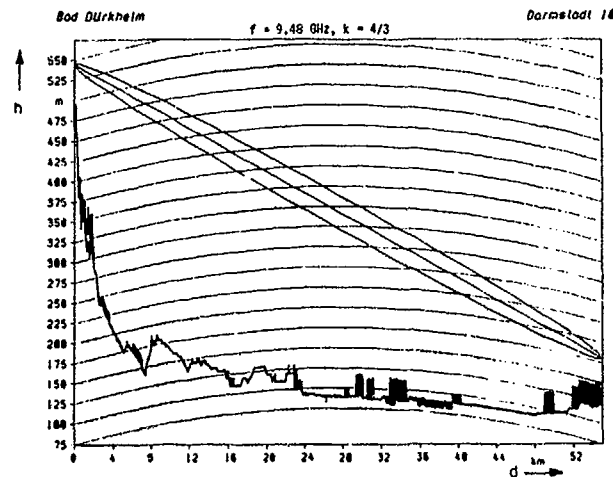


Fig. 4: Path profile for the wideband propagation experiment.

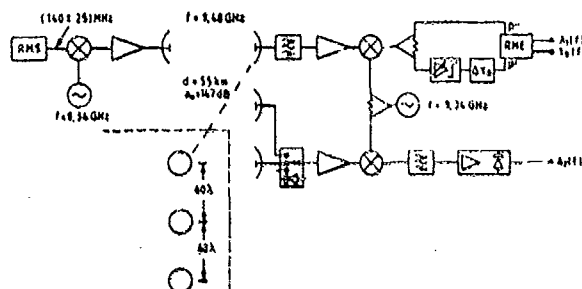


Fig. 5: Block diagram of the measuring set-up.

RMS: RME: transmitter and receiver unit of the Wandel & Goltermann link analyser.

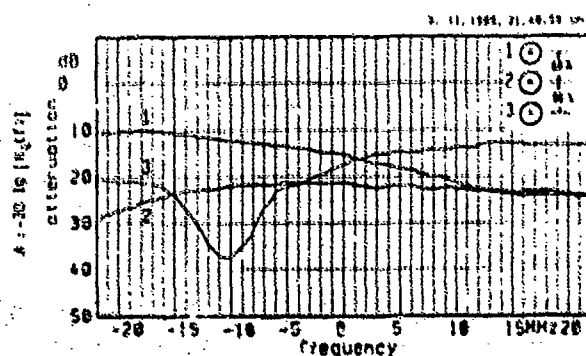


Fig. 6: Example of a measured fading event for a space-diversity set-up with 3 antennas  
(attenuation A is relative to free-space value of the link)



Fig. 6 shows an example of measured amplitude responses for three antennas mounted above each other with  $60 \lambda$  spacing. The parameters of the effective two-path model [4] were then fitted to the amplitude and group-delay dispersions:

$$H_i(t) = a_i \{1 - b_i \exp(-2\pi j(t - t_{oi}) \tau_i)\} ; i=1,2,3 \quad (6)$$

so that finally a set of parameters (or transfer functions) was available describing the measured fading events.

### 3.2 CALCULATION OF SYSTEM PERFORMANCE

The calculations of the degradations were performed on M-QAM systems being now introduced in many radio-relay networks. It was first assumed that the combiner adds up the two diversity signals so that maximum power is obtained at the output [5]. This means that the phase  $\theta$  in the diversity branch is continuously adjusted such that the expression

$$\int_B |H_d(f)|^2 df \quad (7)$$

is maximized. The integration in eq. (7) has to be performed over the channel bandwidth  $B$  where  $H_d(f)$  is given by

$$H_d(f) = \frac{1}{\sqrt{2}} (H_1(f) + H_2(f)e^{j\theta}) \quad (8)$$

The symbol-error rate was calculated for 16 QAM, 64 QAM and 256 QAM having a bit rate of 140 Mbit/s. For this purpose first the relevant parts of the system have to be modeled: the carrier recovery circuit was assumed to make use of the remodulation scheme. As outlined in Ref [6], this means that the imaginary part of the distorted impulse response of the system at the sampling point is zero, thus reducing the cross-channel interference. The modeled timing-recovery circuit consists of a non-linear device so that a spectral line at the timing frequency can be subtracted from the IF by subsequent bandpass filtering. The expressions for carrier phase and timing offset due to channel distortions were derived and published in Refs. [6,7].

If carrier-phase and timing offset  $t_0$  are known the sample of the impulse response at times  $nT + t_0$  ( $T$ : symbol duration) can be calculated assuming perfect Nyquist filtering for periods without fading. Then the symbol-error probability in the presence of both ISI and Gaussian noise can be obtained in principle by taking into account the  $2^n$  different symbol sequences. This direct method however is not applicable for high-level modulation schemes because of the excessive computational effort required. Therefore, a novel algorithm was applied which calculates the probability density function (pdf) of the ISI  $g(x)$  directly by the use of a recursion formula. If the pdf of ISI  $g(x)$  is known, the probability  $P_0$  that the random variable  $z = x + n$  ( $n$ : Gaussian noise with variance  $\sigma^2$ ) exceeds a given threshold  $t_0$  can easily be computed from

$$P_0 = \frac{1}{2} \int_{-\infty}^{+\infty} g(t) \operatorname{erfc} \left\{ \frac{t_0 - t}{\sqrt{2} \sigma} \right\} dt \quad (9)$$

For M-QAM modulation schemes the symbol-error probability is then given by

$$P_s \approx 4 \frac{\sqrt{M} - 1}{\sqrt{M}} P_0 \quad (10)$$

For all the fading events collected in autumn 1985 the error probabilities of 16, 64 and 256 QAM systems were calculated for single and diversity reception following the above procedure. For single reception the  $E_b/N_0$  ratio ( $E_b$ : energy per bit,  $N_0$ : one-sided noise power density) was assumed to be 40 dB and 50 dB under non-fading conditions giving flat fade margins of about 28 dB or 38 dB for 16 QAM. If the  $E_b/N_0$  ratio is constant this means that the transmitted power is constant for the different modulation schemes.

Fig. 7 shows as an example the results for a 16 QAM system calculated for the channel conditions observed at a space diversity arrangement with  $\Delta h = 2m \pm 60\lambda$ . The improvement factor is 2.8.

In Fig. 8 the improvement factor is plotted for different configurations. It may be noted that within the limited amount of investigated fading events no statistically significant increase of the improvement factor was obtained if the antenna spacing was changed from  $2m$  ( $60\lambda$ ) to  $4m$  ( $120\lambda$ ).

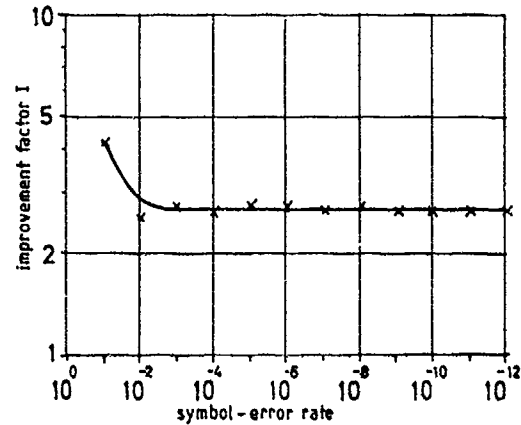
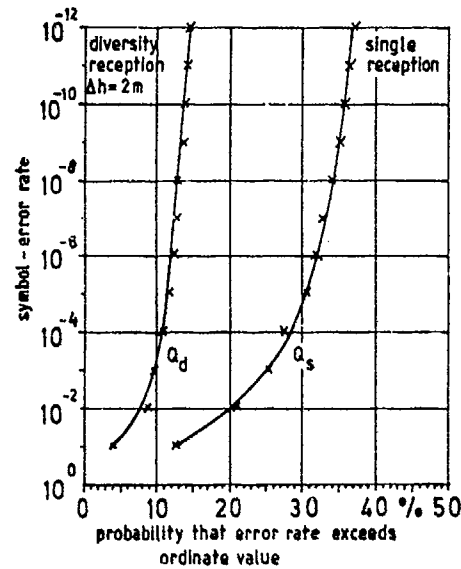


Fig. 7a: Symbol-error rate of a 16 QAM system versus percentage of observed channel conditions during which ordinate value is exceeded. (140 Mbit/s;  $\alpha = 0.5$ ,  $10 \lg E_b/N_0 = 50$  dB)

Fig. 7b: Improvement factor versus symbol-error rate for space diversity reception with an antenna spacing of  $\Delta h = 2 \text{ m} \pm 60\lambda$ .

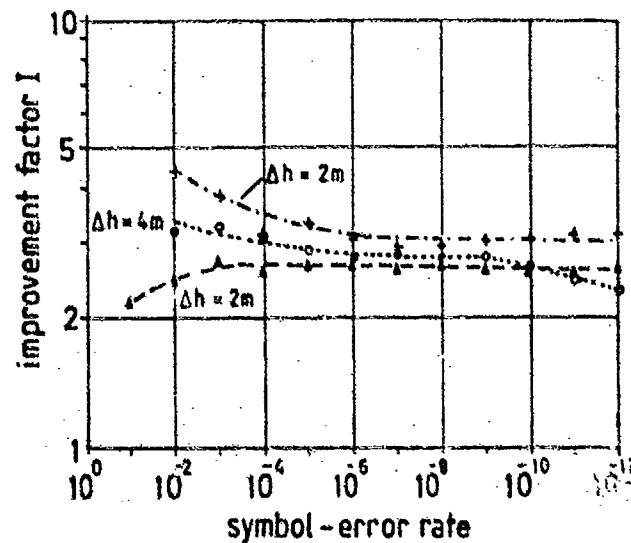


Fig. 8:  
Improvement factor I for different  
antenna configurations  
(140 Mbit/s; 16 QAM;  $\alpha = 0.5$ )

The effect of baseband equalization was also incorporated because it was expected that the combination of both methods would yield the maximum effect. One of the best equalization principles is based on a linear tap-delay line filter whose tap gains are adaptively adjusted so that series of the impulse response can be forced at timing instants  $kT$  ( $k = \pm 1, \dots, \pm N$ ), i.e. if the number of taps is  $2N + 1$  then  $N$  series are forced at the precursors and  $N$  series at the postcursor. That means that the overall impulse response  $h(t)$  has to be modified to

$$h_{eq}(t) = \sum_{k=-N}^{+N} a_k h(t + kT) \quad (11)$$

where the  $a_k$ 's are the complex tap gains which are adjusted to satisfy

$$h_{eq}(t_s + kT) = \delta_0^k \text{ for } k \leq N \quad (12)$$

with  $t_s$  denoting the sampling instant and  $\delta_0^k$  the Kronecker symbol.

The symbol-error rate can again be calculated with this modified impulse response using the above procedure. An equalizer with 5 taps ( $N=2$ ) was assumed and the results of the calculation are summarized in Table 1.

Table 1: Improvement factor for space diversity reception with  $\Delta h = 60\lambda$ ,  $10 \lg E_b/N_0 = 40\text{dB}$  for symbol-error rate  $10^{-8}$

| Improvement<br>for                             | modulation scheme |        |         |
|--|-------------------|--------|---------|
|  | 16 QAM            | 64 QAM | 256 QAM |
| single reception<br>with equalizer             | 8.9               | 6.7    | 3.7     |
| diversity<br>without equalizer                 | 2.9               | 1.6    | 1.2     |
| with equalizer                                 | 71.5              | 21.4   | 10.1    |
| relative to single reception without equalizer |                   |        |         |
| diversity<br>with equalizer                    | 8.0               | 3.2    | 2.8     |
| relative to single reception with equalizer    |                   |        |         |

It may be noticed that for a vertical space diversity arrangement alone the improvement is rather small. Only the additionally introduced equalizer in connection with diversity gives the desired results. Furthermore, for 256 QAM these countermeasures are not so efficient. This can be explained by the fact that we assumed constant transmitter power in all three cases so that the flat fade margin for 256 QAM is by 9.3 dB smaller than for 16 QAM. In the observed fading events the dispersion was always associated with a superimposed flat depression at all antennas. Then the equalizer is unable to do anything and the diversity reception can counteract the increased influence of thermal noise only to a limited extent. Combined with the increased sensitivity to dispersion this explains the moderate improvement.

#### REFERENCES

- /1/ Recommendations and Reports of the CCIR, 1982, Vol V (Propagation in non-ionized media), Genf: ITU, Rep. 328-4, pp. 279 - 314.
- /2/ Y. Hozoya: An investigation of the unified estimation method for the space diversity improvement CCIR Documents (1982 - 1986), IWP 5/2, Doc. 84/25
- /3/ A. Vignati: Space-Diversity Performance as a Function of Antenna Separation IEEE Trans. Comm., Vol. COM-16, No. 6, pp. 831-836, Dec. 1968
- /4/ W.D. Kummier, "A new selective fading model: Application to propagation data", Bell Syst. Tech. J., vol. 58, pp. 1037-1071, May-June 1979.
- /5/ P.D. Katabinis, "Maximum-Power and Amplitude-Equalizing Algorithms for Phase Control in Space Diversity Combining", Bell Syst. Tech. J. vol. 62, pp. 63-90, 1983
- /6/ L.J. Greenstein and B.A. Czekaj-Augus, "Performance comparison among digital radio techniques subjected to multipath fading", IEEE Trans. Commun., vol. COM-30 pp. 1184-1197, May 1982.
- /7/ K. Metzger and R. Valentin, "An Analysis of the Sensitivity of Digital Modulation Techniques to Frequency-Selective Fading", IEEE Trans. Commun., vol. COM-33, pp 986-992, Sept. 1985.

## DISCUSSION

**L. Boithias**

La décorrélation entre deux fréquences a deux aspects:

- (1) Si ces deux fréquences sont des porteuses, on a un effet de diversité de fréquence
- (2) Si ces deux fréquences appartiennent au même signal à large bande on a un effet d'évanouissement sélectif. Avez-vous étudié ce double aspect de la relation entre la diversité de fréquence et ces évanouissements sélectifs?

**Author's Reply**

This is an interesting question.


We have not studied these two aspects because our measurements were performed only in a medium bandwidth (typical for high bitrate radio relay systems). So experimental results were only available for the effect of frequency selectivity.

**A.N. Ince**

All radio channels, regardless of whether they carry analog or digital signals, are characterized in general by S/N and frequency selectivity. As we know the latter gives rise to intersymbol interference in digital systems whereas in analog systems it produces intermodulation. Diversity improves not only the signal amplitude but also the distortion IM and intersymbol interference (this is a partial answer to the previous question asked by Dr Olsen). Have you been able to separate these two effects?

**Author's Reply**

We used the transfer functions of the radio channel measured in our propagation experiment. Then we are able to calculate the diversity improvement for digital systems considering both the thermal noise *and* the intersymbol interference. We made no effort to separate the two effects because for outage calculations they have to be considered simultaneously.



# "SOME MEASUREMENTS OF HEIGHT GAIN AT V.H.F"

by

John Fairbrother  
Department of Trade and Industry  
Radio Regulatory Division  
Waterloo Bridge House  
LONDON  
United Kingdom

Kevin A Hughes, formerly of  
Department of Trade and Industry  
Radio Regulatory Division  
Waterloo Bridge House  
LONDON  
United Kingdom

Douglas M Holden  
GEC Research Limited  
Marconi Research Centre  
Great Baddow  
CHELMSFORD  
United Kingdom

Copyright (c) Controller HMSO, London 1986

## SUMMARY

This paper reviews some of the published work on antenna height gain and highlights limitations of the currently available information. Comparison is then made with the results of height gain experiments undertaken in South East England at frequencies of approximately 95 MHz and 200 MHz. The variation of height gain is investigated, as is a relationship between height gain and the location variability of received field strength within a given environmental area.

Experiments performed at about 95 MHz used vertical polarisation and path lengths varying from about 25 km to about 105 km. These paths were predominantly over land and were all obscured. The antenna employed was omnidirectional, and measurements were taken at many locations within each predetermined area at heights above local ground from 7 m to 30 m. Some measurements were also made on sloping ground to give effective heights of up to 60 m. The results are compared with some earlier measurements made at about 200 MHz over similar paths using a directional antenna at heights from 3 m to 10 m above local ground.

Further experiments at about 95 MHz used horizontal polarization and path lengths of about 200 km which were predominantly over the sea. In this case a directional antenna was deployed at heights from 7 m to 20 m above local ground. Since the received signal was fading, a simultaneous recording was made at each measurement location using a second antenna at a nominal 10 m above local ground. Height gain was derived from the difference between recordings from the two antennas.

It is suggested that within the range investigated height gain may be represented as  $n$  dB for each doubling of antenna height. The value of  $n$  varies with the local environment at the receiving site.

## 1 INTRODUCTION

Height gain is the term commonly used to describe variation of field strength with height. It may refer to the height of either the transmitting or the receiving antenna and is usually expressed as a gain (in dB) between two specific heights.

For unobstructed propagation paths, characterized by a flat or spherical earth profile, height gain may be readily determined by established theoretical methods.

For obstructed paths however, obscured by terrain, buildings and vegetation, height gain is generally derived empirically and it is for these cases that difficulties arise in its measurement and assessment.

In the planning of radio services in the VHF band, antenna height gain (transmitting and receiving) plays a significant role in the evaluation of received field strength, both for the wanted and interfering signal. A limited amount of height gain data for obstructed paths is available, for example in texts of the CCIR. This information generally applies only to the receiving antenna and values are given for particular antenna heights (often only two) as a function of frequency band, with perhaps some allowance for path length and environment type. The height gain data usually refer to antenna heights only for which available field strength prediction methods apply, eg 10 m for prediction methods for broadcasting services, 3 m for mobile services. There is nevertheless a requirement for height gain data to relate to other antenna heights in order to extend the application of prediction methods over a greater range of heights than hitherto. In addition, the data need to be sufficiently extensive so

AD-P005 746

as to reflect the influence of other propagation factors. Height gain cannot be considered in isolation and an appreciation of its relationship with other variables may lead to improvements in its measurement and in turn the accuracy of prediction methods in which the data are used. Principal amongst the factors to be considered are the environment local to the receiving antenna and the spatial variation of height gain within a specific area.

#### i) Variation with environment category

At distances beyond the horizon, height gain depends on the nature of the obstructions in the immediate vicinity of the receiving antenna and by inference, on the type of environment in which it is located. In a city, for example, multipath propagation would likely be the dominant mechanism and in some locations, it might be possible for two "spot" locations of the antenna to reveal zero or even negative height gain. By contrast, height gain in the rural environment might be expected to show far less variability, with the dominant propagation mode most likely being diffraction from nearby terrain irregularities.

In consequence, it is essential to ensure that an adequate distinction is made between categories of environment when measuring and presenting height gain data.

#### ii) Association with location variability

Height gain data not only need to be related to an environment category, but also require some degree of statistical averaging within the spatial area of interest. A possible method would be to acquire location variability distributions of received field strength using different heights of receiving antenna, as depicted in Figure 1. Differences between the distributions for given percentages of locations, correspond to values of height gain for the two antenna heights in question. The figure demonstrates that with  $h_1 > h_2$ , the distribution for the lower antenna height exhibits the steeper slope, as may perhaps be expected, due to the greater influence of local obstructions on the propagation paths. Consequently, height gain is itself a function of the percentage of locations. Presentations such as that shown in Figure 1 may therefore serve to express jointly location variability and height gain, both relating to one particular type of environment. However in order to present height gain as a function of some parameter other than location it is convenient to use the median (50%) location value ie that value of signal strength exceeded at 50% of locations within a given area.

The close association between location variability and height gain can be further illustrated in an example by considering the variation of received field strength in a town by moving the antenna from a height of 10 m to 30 m. The effect would be to remove many of the local obstructions (buildings) from the propagation path which in turn, could be likened to moving the antenna to a "good" site from a median or poor site, ie varying the location percentage associated with the receiving antenna.

Height gain data should reflect also any dependency on path length. As described in section 1.1 in connection with height gain information provided by the CCIN, there is uncertainty as to whether such a dependency exists. Additionally, a variation with frequency might be expected, inter-related with the influence of obstructions on the path and in particular those local to the receiving antenna. Differences revealed in the fading patterns of vertically and horizontally polarised signals would further suggest that height gain data should be referred to one or other polarisation state.

To supplement existing data, three sets of height gain measurements are presented in this paper and, within the limitations of the data, discussed in the light of the comments expressed above. Firstly though, a description is given of currently available information and of its limitations.

#### 1.1 BELL TELEPHONE COMPANY REPORT OF 1944

In 1944 The Bell Telephone Company produced a set of propagation curves for estimating received field strength for communication between aircraft and ground stations. Including the cases where both terminals were either airborne or on the ground. The series of curves cover frequencies from 200 MHz to 600 MHz, vertical and horizontal polarisation, antenna heights up to 12000 m, and path lengths up to 400 km over two types of soil and sea water. A smooth spherical earth of  $4/3$  true radius is assumed for the transition between line of sight and obscured paths. Provision is also made for diffraction loss over hills using a graphical method. There is some limited information on effective height and on the effects of local vegetation; buildings are only mentioned as acting as possible reflectors of the incoming signal.

Height gain curves have been derived from this report for the cases currently investigated, i.e.:-

|                         |           |         |
|-------------------------|-----------|---------|
| Vertical polarisation   | Land path | 200 MHz |
| Vertical polarisation   | Land path | 100 MHz |
| Horizontal polarisation | Sea path  | 100 MHz |

For antenna heights above 5 m all these curves show the classical gain of 6 dB for doubling the antenna height.

### 1.2 RECENT UK WORK

Certain United Kingdom mobile services employ frequencies of about 100 MHz, vertically polarised. In the planning of these services the need arose to quantify the potential interference from European FM broadcast transmissions sharing the same frequency band although with horizontal polarisation. To this end a series of measurements of field strength as received by a horizontally polarised antenna has been undertaken for several years at various locations in South East England. The receiving antennas are all at the standard height of 10 m, but at one receiving site located in the rural environment of Southminster some measurements were also taken at 3 m. A comparison of the data for the two antenna heights of 3 m and 10 m gives a mean height gain of 11 dB, equivalent to 6.4 dB per doubling of antenna height, for this rural location.

### 1.3 CCIR INFORMATION

Certain information on height gain appears in texts of the CCIR in association with field strength prediction methods. A well established and widely used prediction method for use at VHF is that given by CCIR Recommendation 370 which is primarily intended for the estimation of coverage areas of broadcasting stations. The method comprises sets of curves of field strength as a function of distance for various "effective" transmitting antenna heights. Sets of curves are provided for different percentages of time and a distinction is drawn between propagation paths over land and over sea. The curves represent values of field strength exceeded at 50 per cent of locations, adjusted for an erp of 1 kW and corresponding to a receiving antenna height of 10 m above local ground. Figure 2 shows an example for propagation paths over land for 50 per cent of the time.

In a discussion of height gain data associated with prediction methods such as that found in Recommendation 370, it is important to note the difference between the definitions of transmitting and receiving antenna height. Transmitting antenna height is an "effective" height, defined as the height over the average level of the ground between distances of 1 and 15 km from the transmitter in the direction of the receiver. On the other hand, receiving antenna height is defined simply as the height over local terrain.

Values of height gain relating to different transmitting antenna heights may be obtained by inspection of the field strength curves given in Recommendation 370, thereby providing a simple method of deriving height gain data for antennas above 17.5 m. However, because of the different definitions of transmitting and receiving antenna height, height gain data derived in this way would strictly apply only to changes in "effective" height and thus, in general, to transmitting antennas.

CCIR Recommendation 370 also provides data on height gain applicable to receiving antennas. The data are expressed as the reduction in field strength that may be expected by changing the receiving antenna height from 10 to 3 m above ground, and the values are presented according to the VHF broadcast bands I, II and III as follows:

Band I (41-68 MHz) and Band II (87.5-108 MHz): a reduction of 9 dB in hilly or flat terrain for both urban and rural areas;

Band III (162-230 MHz): a reduction of 7 dB for flat terrain in rural areas and 11 dB for urban or hilly terrain.

These values apply for distances up to 50 km. For distances in excess of 100 km the values should be halved, with linear interpolation for intermediate distances.

The receiving antenna heights of 10 and 3 m are traditionally accepted as appropriate for the planning of broadcast and mobile services respectively. Accordingly, propagation curves for use by the mobile services at VHF have been derived from those of Recommendation 370 by the direct application of the above height gain data. The curves are presented in CCIR Report 567, of which an example appears at Figure 1. The curves for transmitting antenna heights of 20 and 10 m are additional to those found in Recommendation 370 and were derived from the curve for 17.5 m by the application of theoretically derived distance dependent height gain correction factors.

The CCIR height gain data for receiving antennas quoted above indicate a distance dependence such that the values (in dB) for propagation path lengths over 100 km are half of those for path lengths less than 50 km, with linear interpolation in between. According to studies referred to in CCIR texts, the experimental evidence supporting this behaviour appears rather weak and some measurements have been reported which indicate that no such relationship exists. The basic curves in Recommendation 370 and Report 567 do however indicate some distance dependence in that they converge with distance but it must be borne in mind that height gain indicated by the curves relates to effective transmitting antenna heights and that a similar distance dependence may not be revealed in the case of receiving antenna heights.

A mechanism to explain a distance dependence of height gain must be a matter for conjecture and any evidence of such a relationship may arise from the influence of other factors such as the type of path and the environment local to the receiving antenna.

## 2 RECENT MEASUREMENTS

The preceding sections indicate that the current information on height gain is very limited. In many previous cases a set of data has been collected to solve a specific problem, and such results are almost always quoted as a gain, or loss, between the two specific antenna heights applicable to that problem. This paper aims to present the first results of a systematic study into height gain starting with frequencies around 100 MHz and 200 MHz and applying to typical obscured paths. A study of the bibliography will show very little information appertaining to the above parameters. Present knowledge is best summarised by the C.C.I.R. information (91.3). There is no indication if such results can be interpolated or extrapolated within specified limits or at all.

The following sections describe work that has been done to augment current knowledge on height gain and to extend the range of its applicability. The work should be of value to mobile services using these frequencies where it is likely that some of the base station antennas will be installed at the heights currently studied. The work was planned to include a range of common environment categories and topography.

The three series of measurements are described in the following subsections:

### 2.1 1983 SURVEY IN S E ENGLAND

Height gain tests were carried out in 1983 in S E England using transmissions from the Channel 9 transmitter at Croydon. The frequency monitored was the sound channel, 191.25 MHz, and the radiated power was about 22 kW. The transmission was vertically polarised. Seven regions within south east England were selected for the measurements, including urban, suburban and rural types of environment. The criteria for selecting measurement locations were that they should be 25 km from the transmitting site and that the radio path should be obstructed. In fact all paths showed attenuations of > 30 dB compared with the field strength that would have been predicted for a line of site path. In order to assess the location variability of height gain up to 100 measurements per square kilometre were made in each area (2 km x 1 km) surveyed. Within each region measurements of received field strength were made at spot locations based on a 100 m grid using antenna heights of 1, 5, 7 and 10 m above local ground. In this way a location variability distribution of the received field strength could be determined for each antenna height, and the results displayed as depicted theoretically in figure 1. In some cases it was not physically possible to take measurements in every square of the 100 m grid. The table below summarises the number of measurements actually taken in each region.

| Location     | Environment category | Distance from Tx | $\Delta h$ | Total number of measurements |
|--------------|----------------------|------------------|------------|------------------------------|
| Reading      | Urban                | 61 km            | 64 m       | 77                           |
| Widham       | Suburban             | 46 km            | 71 m       | 137                          |
| Crowthorne   | Suburban             | 49 km            | 52 m       | 100                          |
| Marlow       | Suburban             | 42 km            | 85 m       | 118                          |
| Chelmsford   | Suburban             | 53 km            | 71 m       | 109                          |
| Easters      | Rural                | 52 km            | 91 m       | 50                           |
| Manningfield | Rural                | 50 km            | 85 m       | 50                           |

The CCIR uses  $\Delta h$  as a statistical parameter which characterises the variations in ground height along part or all of a propagation path. In the case of broadcasting and for this study it is taken as the interdecile range of heights along the path between 10 km and 50 km from the transmitter.

The total number of measurements in each environment category was:-

|          |     |
|----------|-----|
| Urban    | 77  |
| Suburban | 494 |
| Rural    | 100 |

Figures 4 to 6 show families of location variability curves for urban, suburban and rural regions, respectively. For each antenna height a curve has been drawn showing the percentage of locations for which the signal strength exceeds the ordinate. Thus each curve shows the location variability for a particular antenna height and as the curves are plotted on a probability scale any difference from a normal distribution is shown by the deviation from a straight line. For a given percentage of locations the difference between curves corresponding to particular antenna heights gives the height gain not exceeded for that same percentage of locations. Each family of curves has been normalised to 0 dB at 10 m above ground level for a median (50%) location. It is quite evident from all three figures that the height gain at low signal strength is greater than for high signal strength, the slopes of the individual distributions decreasing with increasing antenna height. This is in direct agreement with the supposition depicted in figure 1 indicating increasing variability of the received signal with decreasing antenna height.

To summarise these results in terms of the received signal strength for a median location in each environment category, the height gains from 1 m to 10 m were found to be:-



|          |         |
|----------|---------|
| Urban    | 11.5 dB |
| Suburban | 12.0 dB |
| Rural    | 10.0 dB |

These results are within 2 dB of CCIR predictions or of gaining 6 dB for a doubling of the antenna height. However the rural figure was somewhat higher than had been expected. From previous studies a figure of between 6 and 7.5 dB had been measured but it was noted that in the 1983 tests discussed here there were frequently trees and tall hedgerows near the measurement locations whereas in the earlier tests only carefully selected open sites had been used. Therefore the height gain figure could be lower in other parts of the country with different agricultural practices.

## 2.2 1985 SURVEY IN ESSEX

Following the 1983 survey it was decided to collect further data using a range of antenna heights above the 10 m maximum of 1983. One objective was to obtain results with the receiving antenna raised above the local clutter and to consider an interpretation of the results in terms of effective antenna height as well as actual antenna height.

The measurements were obtained from monitoring transmissions in the band from 87.5 MHz to 100 MHz with obstructed paths ranging in distance from 29 km to 109 km. Measurements were made at the following heights: 7, 10, 12, 14, 16, 18, 20 m above local ground and some additional ones at 22, 24, 26 and 28 m at selected locations in Chelmsford. The four measurement areas are listed in the following table

| Site Name  | Terrain Type | Environment Category |
|------------|--------------|----------------------|
| Ilford     | Flat         | Urban                |
| Chelmsford | Flat         | Urban/Suburban       |
| Westcliff  | Sloping      | Suburban             |
| Althorne   | Sloping      | Rural                |

Various transmitting stations were used such that in each area three separate transmission paths were monitored. However care was taken in choosing the paths to ensure that all were obstructed. (See figure 7).

A summary of the height gain results referred to actual antenna height for 50% of locations is as follows:

|              | Ilford | Chelmsford | Westcliff | Althorne |
|--------------|--------|------------|-----------|----------|
| 7 m to 10 m  | 2.0 dB | 3.5 dB     | 3.0 dB    | 2.5 dB   |
| 10 m to 20 m | 9.5 dB | 8.0 dB     | 8.0 dB    | 6.5 dB   |

Figure 8 is a plot of height gain for 7 m to 10 m and 10 m to 20 m against distance for all paths and it can readily be seen that there is no distance dependence, contrary to information provided in CCIR texts.

The most interesting family of location variability curves derive from Chelmsford, figure 9, where there are a wide range of building types. It can be seen that for locations of low signal strength the height gain from 10 m to 20 m is 1.5 dB compared with 5 dB for areas of high received signal strength. For antenna heights greater than 20 m, or essentially above the local clutter, the height gain appears to be independent of received signal strength. ie There is no significant dependency on location variability.

In the hilly areas measurements were referred to effective antenna heights and the following height gains for 50% of locations were obtained.

|              | Westcliff | Althorne |
|--------------|-----------|----------|
| 20 m to 30 m | 2.0 dB    | 3.0 dB   |
| 30 m to 40 m | 3.0 dB    | 2.5 dB   |
| 40 m to 50 m | 2.0 dB    | 2.5 dB   |
| 50 m to 60 m | -         | 2.5 dB   |

The effective height gain was obtained by considering the height of the measurement location above the immediate foreground and adding the actual antenna height. For these results all readings were those from locations with a clear path towards the transmitter ie no antenna heights below 10 m or screened by taller buildings.

The regular increase in received signal strength with height is more clearly illustrated in figure 10 where the results of the Althorne measurements have been presented. With the exception of the 50 m curve at high values of received field strength, height gain remains fairly constant irrespective of field strength (percentage of locations). This agrees with the results shown in figure 9 for antenna heights above about 20 m, but contrasts with lower antenna heights. It should be noted that figure 9 is referred only to actual antenna heights above local ground. It is shown that an antenna operating above urban/suburban clutter exhibits the same reduced location variability as an antenna operating in an open rural environment. Therefore

in either of these cases an area could be surveyed with less spot measurements than would be required for an equal area with local clutter.

Following the above analysis some further measurements were taken to extend the range of antenna heights. These extra measurements used a similar antenna deployed at a series of heights below 10 m at the sites of Chelmsford, Westcliff and Althorne. These measurements were made at the same spots and receiving the same signals as for the main experiment. These additional readings extend the range of antenna heights to overlap with the 1983 experiment but at a different frequency. They are included in the Results section.

### 2.3 1986 SURVEY IN SOUTHMINSTER

To obtain height gain data for greater distances a series of measurements was undertaken using two distant VHF - FM radio stations. At a site in Southminster, a village some 65 km east-north-east of London, the DTI had been involved in the long term recording of signals transmitted from Aalter (Belgium) and Lopik (Netherlands). (See figure 11)

The relevant transmission characteristics are given below:

| Name   | Site Position | Frequency | Site Height | Antenna Height | Path Length |
|--------|---------------|-----------|-------------|----------------|-------------|
| LOPIK  | 05E03,52N01   | 92.6 MHz  | 0 m         | 280 m          | 292 km      |
| AALTER | 03E21,51N06   | 98.6 MHz  | 25 m        | 150 m          | 186 km      |

NOTE: Both stations use horizontal polarisation and an erp of 50 kW.

During preliminary measurements and the setting up of the equipment it was noted that the received signals were subject to fast and slow fading. It was decided therefore that simultaneous recordings should be made with a second mobile antenna deployed at a fixed height of 10 m, to which the measurements would be referenced. In this way the influence of fading on the results would be considerably reduced. The survey vehicle had two pneumatic masts 2.4 m apart and care was taken at all the measurement spots to ensure that the vehicle was positioned such that the incoming signals were at right angles to the axis between the two masts. It was agreed that meaningful comparisons could only be made during periods of slow fading but, in exceptional circumstances, peaks could be compared during periods of fast fading. Good correlation was found between fades at 10 m and at the other heights, but the only times when the two received signals were out of phase were when aircraft were flying across or along the path.

Within the village of Southminster some 18 locations were selected distributed over a square kilometre, and at these sites measurements of the two transmissions were taken at heights of 7, 10, 12, 14, 16, 18 and 20 m. The height gain was determined by comparing the received signal from the variable height antenna with that from the reference 10 m antenna. From the relatively small sample of 18 measurements figure 12 shows height gain as derived from the median (50%) location points of the family of location variability curves. The value of height gain relative to either transmitter increased regularly between heights of 7 m and 16 m, but increased at two separate, lower, rates above 16 m antenna height.

The data from these tests together with the 1983 survey have been added to those of figure 8 to extend the investigation of distance dependency of height gain. As can be seen in figure 13 (Note the logarithmic distance scale) no distance dependency is apparent.

### 3 RESULTS

The following table summarises the results that are available:

Range of Antenna Heights Deployed

| Approx Frequency<br>Polarisation<br>Path Type | Environment Category |                    |             |             |
|---|----------------------|--------------------|-------------|-------------|
|   | Urban                | Urban/<br>Suburban | Suburban    | Rural       |
| 200 MHz<br>Vertical<br>Land                   | 3 m to 10 m          |                    | 3 m to 10 m | 3 m to 10 m |
| 100 MHz<br>Vertical<br>Land                   | 7 m to 10 m          | 4 m to 20 m        | 4 m to 50 m | 4 m to 60 m |
| 100 MHz<br>Horizontal<br>Sea                  |                      |                    |             | 3 m to 20 m |

## NOTES:

1 The 4 m to 50 m and 4 m to 60 m ranges were obtained by combining the results of actual and effective heights on the sloping sites.

2 The 4 m to 28 m range all refers to actual heights and is included to show continuity over that range of heights. However due to the mixed nature of that site (Chelmsford centre) it has been allocated a special environment category (urban/suburban).

3 The 3 m to 20 m range was obtained by combining the results of the recent UK work §1.2 and the 1986 survey § 2.3.

In each case the raw data were represented in terms of location variability distributions as described in the introduction so as to reduce as far as possible the effects of any local peculiarities of the chosen sites. All the above results were plotted and in each case appeared to fit a logarithmic curve which may be expressed as the gain in decibels for doubling the height of the antenna. The results appear in figures 14 to 21 and are summarised in the following table:

Gain for Doubling Antenna Height

| Approx Frequency<br>Polarisation<br>Path Type | Environment Category |                    |          |        |
|---|----------------------|--------------------|----------|--------|
|   | Urban                | Urban/<br>Suburban | Suburban | Rural  |
| 200 MHz<br>Vertical<br>Land                   | 8.0 dB               |                    | 7.0 dB   | 5.5 dB |
| 100 MHz<br>Vertical<br>Land                   | 9.0 dB               | 8.0 dB             | 7.0 dB   | 6.5 dB |
| 100 MHz<br>Horizontal<br>Sea                  |                      |                    |          | 6.0 dB |

## 4 CONCLUSIONS

The data presented in this paper aim to augment the existing height gain information available in the technical literature. In particular, their applicability to heights above the urban clutter could be of benefit in the planning of mobile services as regards base station sites which are typically located at heights exceeding 20 m. Hitherto, no height gain data are readily available specifically addressing receiver antenna heights above 10 m.

Some of the height gain measurements have been presented in the form of location variability distributions, as discussed at the outset in the introduction to the paper. This has demonstrated the importance of recognising the variation of height gain with location, particularly at heights significantly influenced by local clutter. At greater heights, the dependence on location tends to disappear.

For convenience therefore, the main results are presented relative to a median location. They are displayed according to frequency and to environment category, and it is found that they may be quantified by a simple logarithmic relationship expressed in terms of the gain in decibels per doubling of height, irrespective of the actual antenna height concerned. As would be expected, lower values of height gain are obtained in the rural environment as compared with urban.

No significant dependency with frequency has been found and the results can probably be considered as appropriate for the VHF band as a whole. Moreover, the results reveal no distance dependency.

The results demonstrate that actual height gain and effective height gain may both be quantified by the same relationship provided that the effective heights have a clear path across the reference foreground.

It would be desirable to confirm and/or extend these results by performing further similar experiments in different environments and/or at different frequencies.

## ACKNOWLEDGEMENTS

The authors wish to thank The Technical Director of G E C Research Limited for permission to publish some of the information contained in this paper.

Thanks are also due to other members of the Department of Trade and Industry, Radio Regulatory Division who helped in the preparation of the paper and to the Monitoring Section who collected some of the data.

## BIBLIOGRAPHY

DATE 1986

AUTHORS Middleton, J

TITLE Field Strength Prediction Methods and Data Logging Techniques in Relation to Mobile Radio Services

DATE 1986

AUTHORS Sandell, R S; Lee, R W; Malcolm-Coe, J

TITLE Review of VHF Band 1 Field Strength Prediction

DATE 1982

AUTHORS Tewari, K K; Swarup, S; Roy, M N

TITLE An Empirical result for the height gain in Forest Medium

DATE 1981

AUTHORS Lau, E C W; MacDougall, J W

TITLE Height gain measurements of TV transmissions (530 MHz)

DATE 1979

AUTHOR Ott, R H

TITLE Ground wave propagation over irregular, inhomogeneous terrain: comparisons of calculations and measurements at frequencies from 121 kHz to 50 MHz.

DATE 1978

AUTHOR Kelly, K K

TITLE Flat suburban area propagation at 820 MHz

DATE 1978

AUTHORS Miya, K; Shimizu, K; Kojima, T

TITLE Oblique-incidence sporadic E propagation and its ionospheric attenuation

DATE 1977

AUTHOR Siremov, O

TITLE Measured VHF and UHF signal strength and spectrum occupancy versus antenna height

## FIGURES

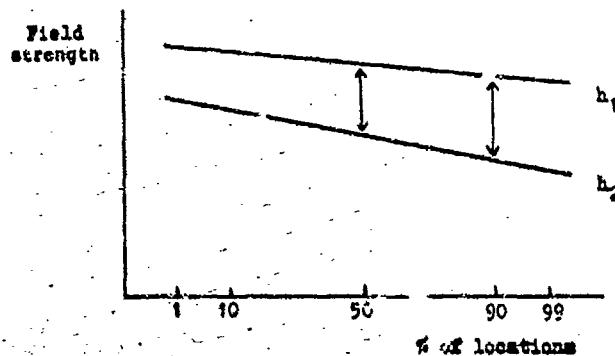


Figure 1

Location variability distributions for receiving antenna heights  $h_1$  and  $h_2$  ( $h_1 > h_2$ )

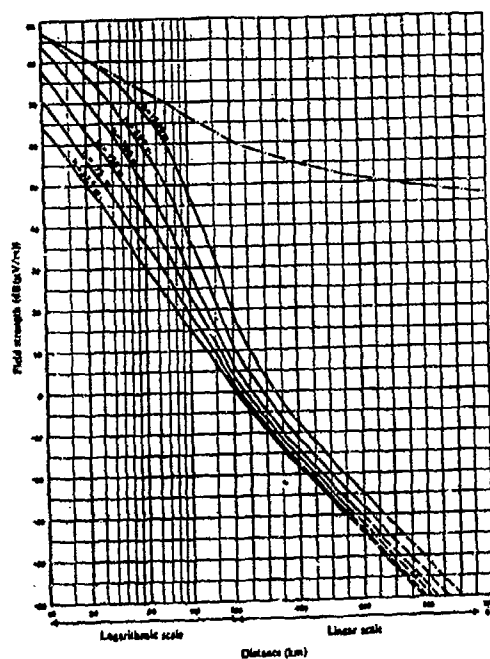


Figure 2 Field strength (dBμV/m) for 1 kW e.p.  
Frequency: 30 to 250 MHz (Bands I, II and III); Land; 50% of the time;  
50% of the locations;  $h_f = 10$  m;  $Q_d = 30$  m

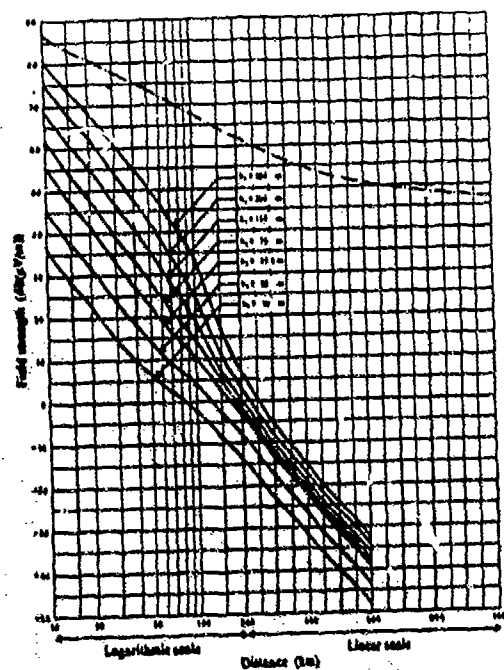


Figure 3 Field strength (dBμV/m) for 1 kW e.p.  
Frequency = 150 MHz, land, rural, 50% of the time; 50% of the locations;  $h_f = 3$  m

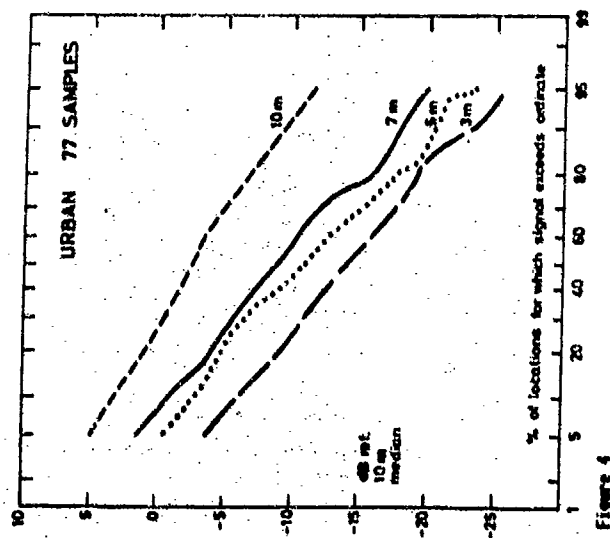


Figure 4

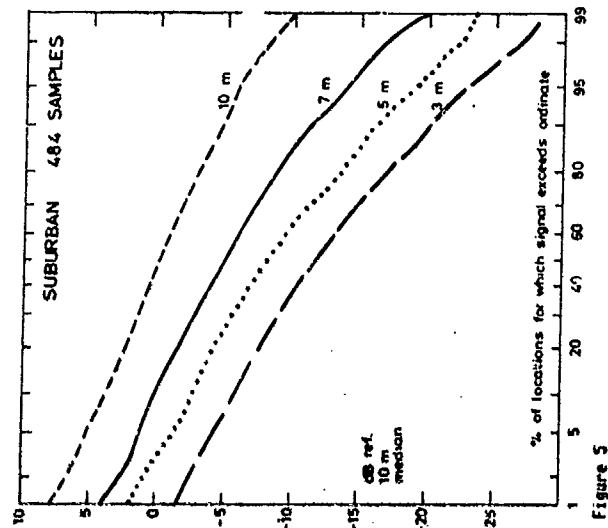


Figure 5

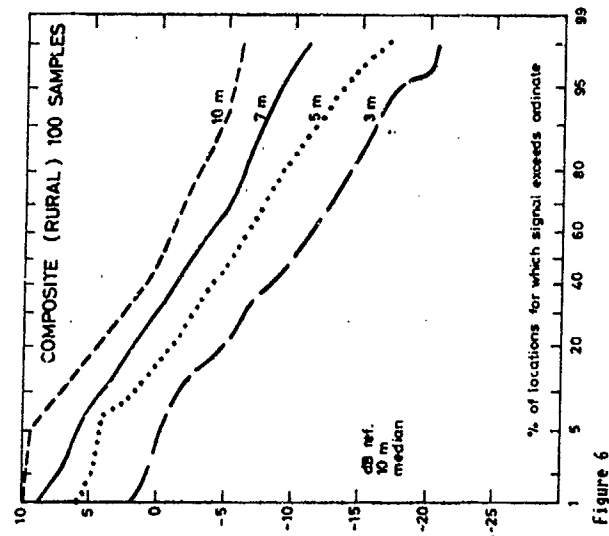
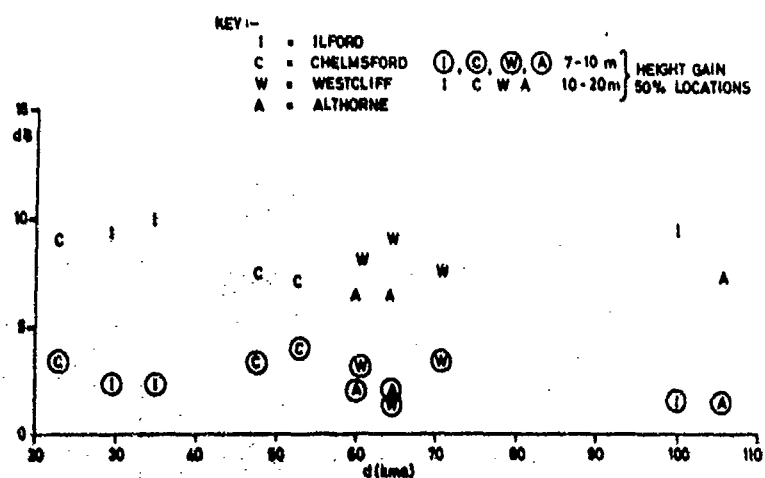
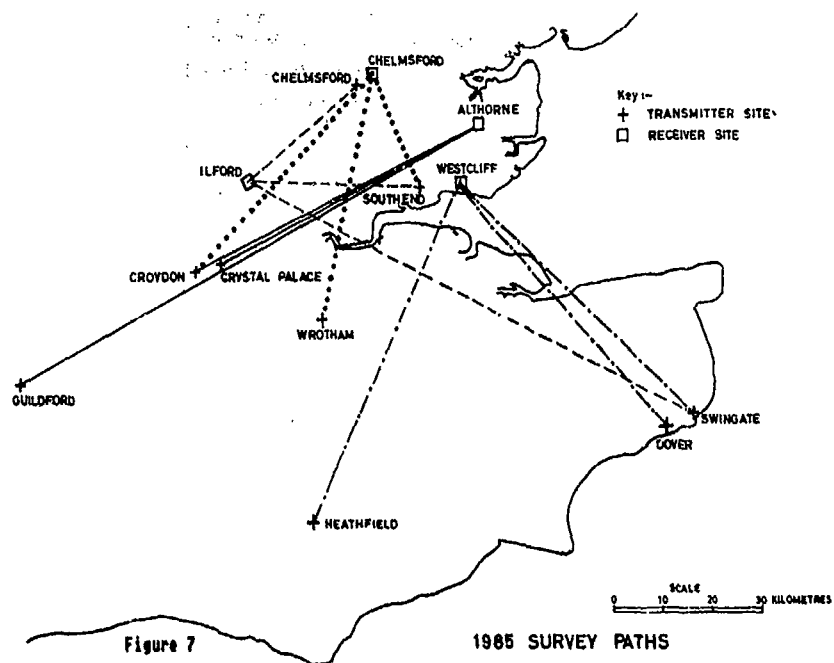


Figure 6



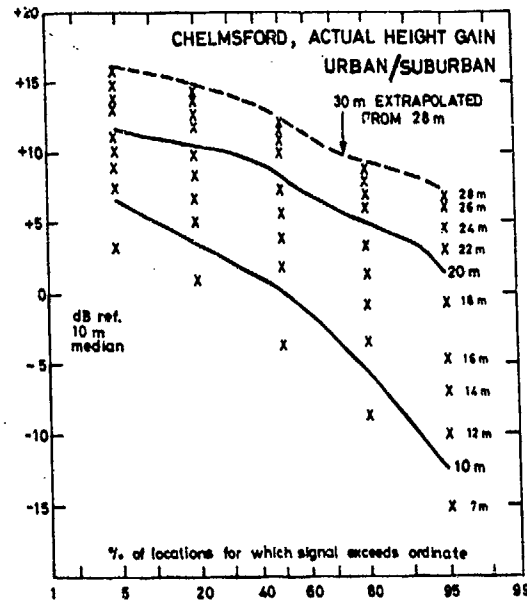


Figure 9

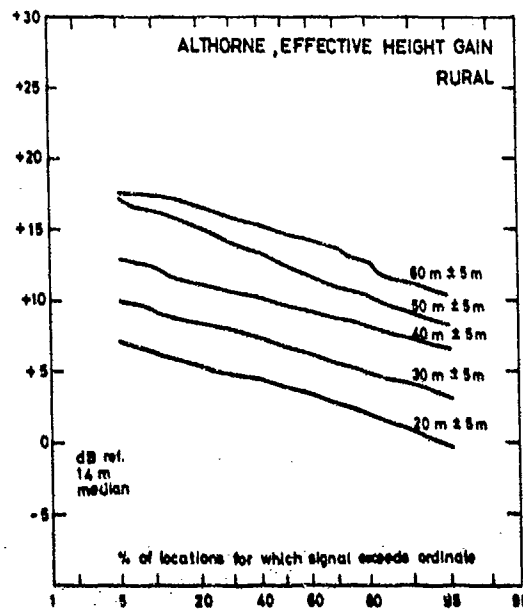


Figure 10



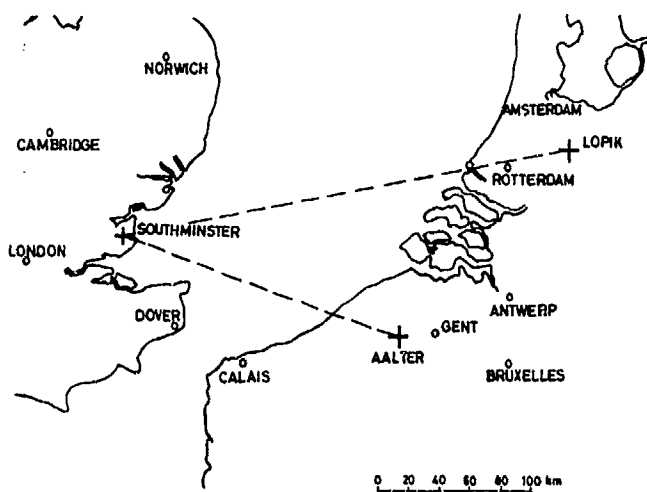


Figure 11

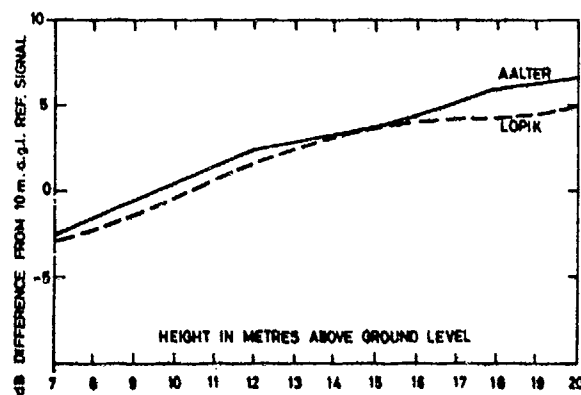
SOUTHMINSTER TEST PATHS

Figure 12

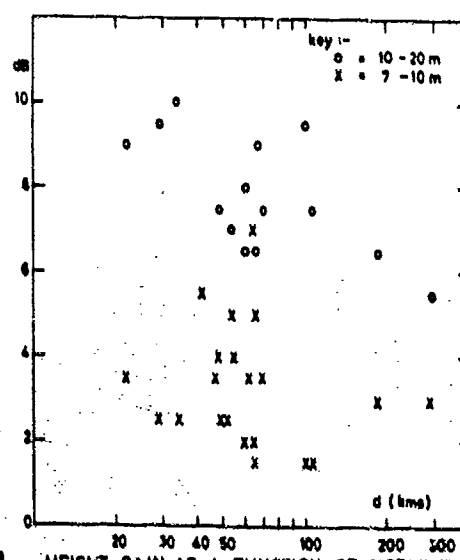
HEIGHT GAIN FOR LONG PATHS

Figure 13

HEIGHT GAIN AS A FUNCTION OF DISTANCE

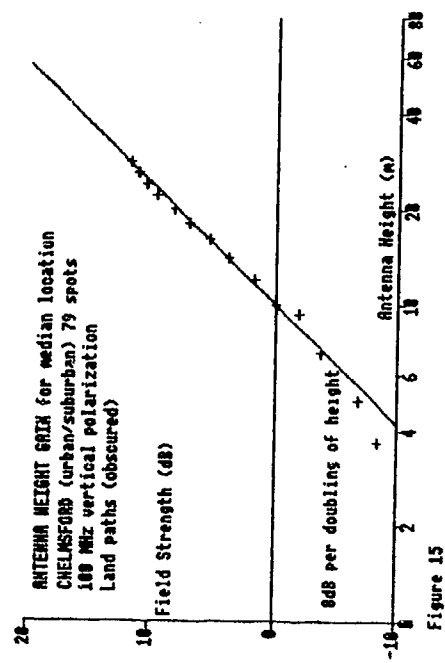


Figure 15

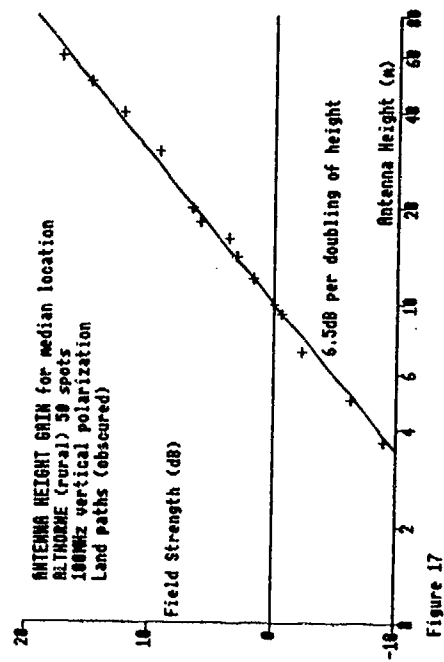


Figure 17

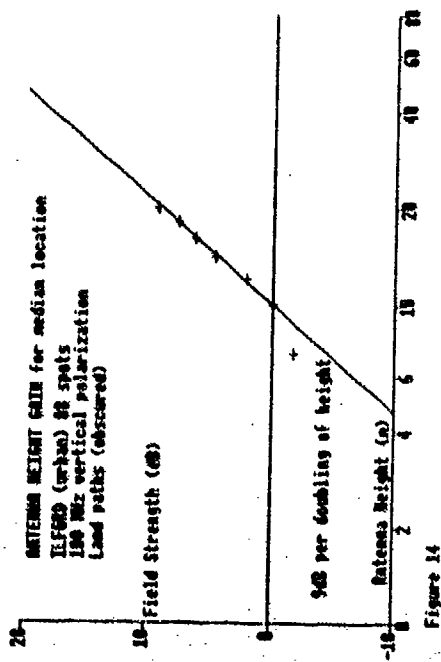


Figure 14

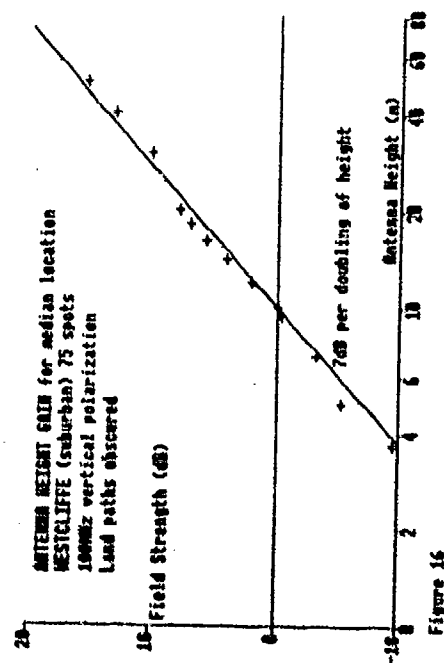
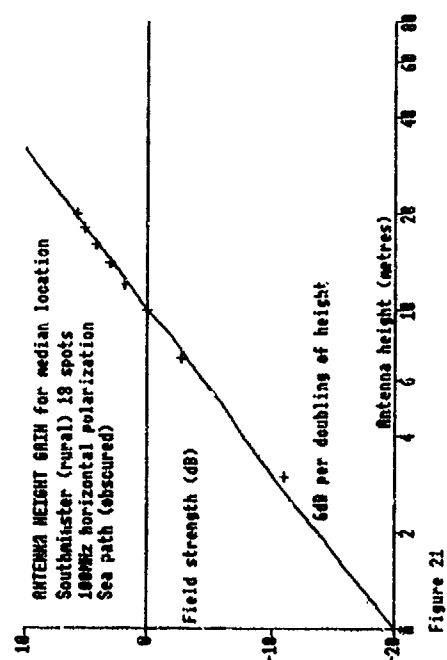
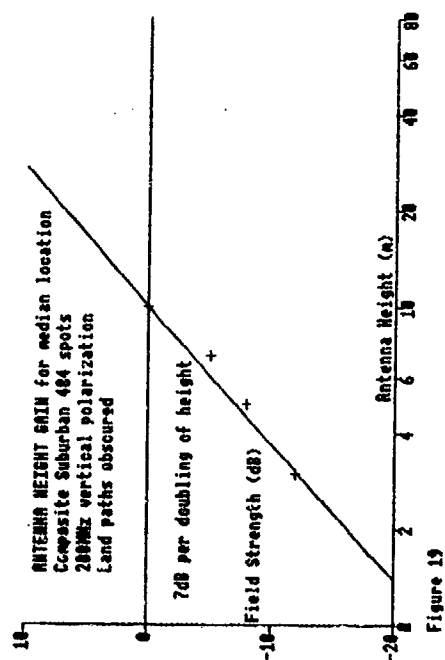
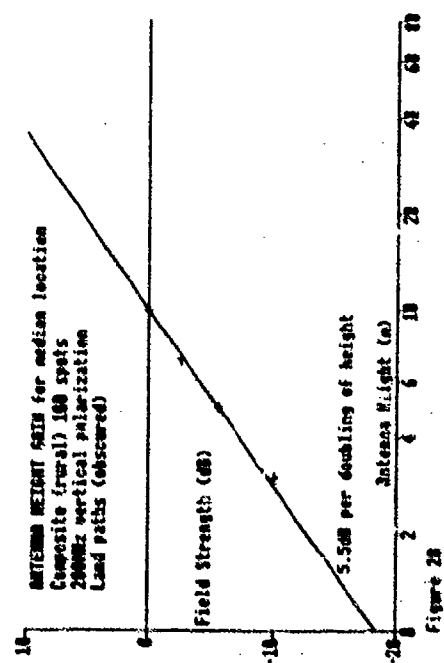
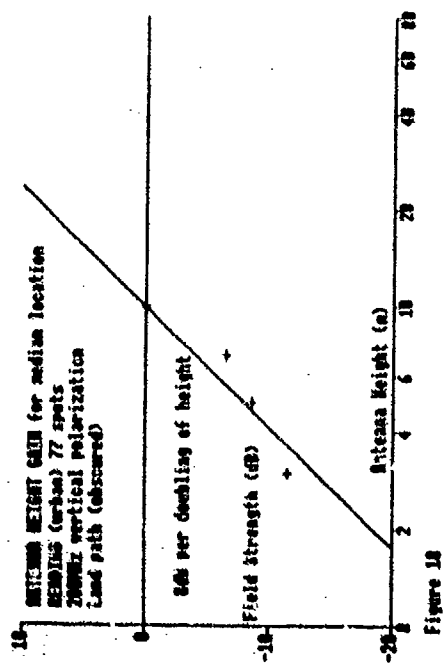


Figure 16



## DISCUSSION

**H.L.Bertoni**

You showed a 5%—95% variability of about 18 dB for low antennas for an urban/suburban area. How does this variability change when measurements are made in urban, suburban and rural areas?

**Author's Reply**

|            | Environment categories | Difference 5% to 95% | Number of spots |
|------------|------------------------|----------------------|-----------------|
| Ilford     | urban                  | 17.5 dB              | 88              |
| Chelmsford | urban/suburban         | 19.0 dB              | 79              |
| Westcliff  | urban                  | 12.5 dB              | 75              |
| Althorne   | rural                  | 15.0 dB              | 50              |

Antenna height 10 m in all cases.

**Note:**

For these fairly low numbers of spots the reliability of the tails of the curves (5% to 95%) is not very good.

**A.N.Ince**

Considering the considerable variability of field strength with location (10 dB) would you agree that before you consider doubling the antenna height you would look at your own location first; i.e. if you are in a favourable position you could be better off than someone in an unfavourable location with double the antenna height?

**Author's Reply**

The comment is valid, however the object of the work reported in the paper is to establish a relationship between received field strength and vertical movement of the antenna. The introduction of horizontal movement to different locations is an inevitable consequence of using an area for the receiving site. The relationships derived are for median locations. In the favourable positions height gain is less than the value for median, whereas in the unfavourable positions the height gain is greater. Future work is planned to investigate the effects of moving the antenna horizontally over a few tens of metres.

**L.Bolthias**

Dans les villes, définir la hauteur des antennes à partir du niveau du sol n'est pas toujours très réaliste car l'énergie radioélectrique se propage plutôt au dessus des toits. Il serait donc préférable de prendre comme référence le champ en un point dégagé et de corriger cette valeur en fonction du non dégagement de l'antenne. La correction serait donc toujours négative. Cette idée a été suggérée au CCIR et devrait être étudiée dans les prochaines années.

**Reponse d'Auteur**

Le commentaire est bon, mais il nous donne un autre problème. En effet pour suivre cette méthode nous devons trouver "le niveau radioélectrique" des toits. Si on peut préciser ce "niveau radioélectrique", on aura trouvé une valeur numérique pour décrire la différence entre les villes et la campagne. Je suis tout à fait d'accord que cette valeur sera très utile pour nos études à l'avenir.



AD-P005 747

# Envelope and Phase Statistics for Non-Gaussian Noise and Resulting Error Probabilities for Digital Communications Systems

J H ROBERTS  
PLESSEY ELECTRONIC SYSTEMS RESEARCH LIMITED  
ROKE MANOR, ROMSEY, HAMPSHIRE, SO51 0ZN

## Summary

It is becoming increasingly realised that the electromagnetic environment through which signalling is to be performed should be given serious attention from the point of view of its statistical characteristics when systems of communication, command, or control, are planned.

When data from a particular scenario is processed to produce a distribution of instantaneous noise amplitudes it is often observed that the statistics are non-Gaussian, with a slow fall-off in the distribution tail. The problem addressed here is how such noise affects the envelope and the phase of narrow-band transmissions operating in such scenarios, leading on to performance predictions for the standard digital modulation techniques.

In the paper statistical properties of the envelope and phase are first derived in a general manner. A new formula is given, for example, for the probability that a noise envelope sample exceeds a sample of the envelope of Signal + Noise. This is the basic statistic needed for assessing incoherently detected situations such as On-Ing or FSK.

In order to apply the results to specific noise types three kinds of non-Gaussian noise are studied which have intrinsic interest. These are:

- Cauchy noise,
- Quartic noise, and
- A mixture of Gaussian + Impulsive noise.

When comparisons against Gaussian noise are made on a S/N basis it is very clear that a non-Gaussian noise with a distribution having a long tail, can be very damaging to digital data. Diversity techniques or receiver design modifications with implications of extra size and cost may therefore call for serious consideration.

## 1. Introduction

In the spectral region below 100 MHz most man-made and natural electromagnetic interference is of a non-Gaussian nature. That is, its amplitude probability density function when determined from measured data for a time over which the statistics can be reasonably viewed as stationary, shows significant departure from

$$p(x) = \frac{1}{\sqrt{2\pi}\sigma} \exp(-x^2/2\sigma^2) \quad (1.1)$$

the well-known Gaussian form.

The departure in question is most often seen in the tail region of the density where a much slower fall-off occurs than the exponential change with  $x$  demonstrated by Eqn (1.1).

Since much electrical and electronic equipment is designed upon the assumption that it is Gaussian noise that is to be combatted and, it is suspected, the analysis of any other kind of noise is likely to prove difficult, it is of considerable interest to see how an analysis does proceed when a density differing from Eqn (1.1) is assumed, and to find that enormous complication need not be encountered.

While amplitude disturbances due to noise perhaps come to mind first, there are many situations in which important information lies in a phase angle or angular measurement (phase comparison radar (ref 1) or the interferometer principle widely exploited in fibre optic systems, for example) and, of course, these, equally, are victims to the attentions of any unwanted emissions that accompany a wanted signal at the receiver input.

Usually, angle data is derived from a narrow-band signal,  $x(t)$  say, having a representation as follows:-

$$x(t) = P(t)\cos\omega_c t - Q(t)\sin\omega_c t \quad (1.2)$$

Here  $P(t)$  and  $Q(t)$  are called the in-phase and the quadrature signal components and a pair of values  $P(t)$ ,  $Q(t)$  (where  $t$  is some sampling instant) can be viewed as Cartesian co-ordinates, so  $\theta = \tan^{-1}(Q(t)/P(t))$  gives the associated phase angle. The term 'narrow-band' means that the bandwidth of  $P(t)$  (and  $Q(t)$ ) is very much smaller than  $\omega_c$  the carrier, or

centre, frequency.

An example occurs in digital data transmission, and a modulation technique known as M-ary phase shift keying. The narrow-band signal leaving the transmitter is then:-

$$V(t) = A \cos[\omega_0 t + \alpha_m(t)] \quad (1.3)$$

In successive time intervals of length T secs the phase,  $\alpha_m(t)$ , may adopt one of M (supposed equally likely) values. The phase angles are:-

$$\alpha_m(t) = \frac{2\pi}{M} m \quad m = 1, 3, \dots, (M-1)$$

M is a power of two and, typically, has a value such as 8 or 16.

When narrow-band interference is added to Eqn (1.3) we wish to calculate the probability with which a device that examines phase will mistake a signaled member  $\Delta$ , from the phase set, for one of the other phase angles that could have been sent.

Alternatively, instead of phase the frequency can be used, so that one of M possible carrier frequencies is transmitted in each interval of length T secs (the symbol duration).

At the receiver, correspondingly, M filters are arranged in a bank, the filter outputs are envelope detected (this operation yields  $\sqrt{P(t)+Q(t)}$  in the case of Eqn (1.3)) and a search is made to associate the transmitted frequency with the detector output that least resembles an 'interference alone' envelope.

In the following both envelope and phase statistics are treated so that problems of the kind described above can be analysed. Attention is confined to narrow-band interferences but the theoretical approach to be described, which exploits the characteristic function of the interference distribution (the Fourier transform of the density), can be applied to low-pass situations as well.

Regarding notation, densities with argument x will refer to the instantaneous noise amplitude ( $- \infty < x < \infty$ ) while those with argument r will refer to the envelope of a narrow-band version of the noise ( $0 < r < \infty$ ). Densities with argument R ( $0 < R < \infty$ ) refer to the composite envelope when a sinusoidal signal accompanies the noise.

### 2. Three non-Gaussian Densities

There is a growing body of literature upon non-Gaussian interference (refs 2 - 5) and much of this follows Middleton in using a model constructed from the sum of a Gaussian component and an impulsive component. A flexibility is thereby enjoyed since the relative amounts of each component can be varied, and it has been reported (ref 5) that the density function that arises for the envelope can be made to fit measured data extremely closely.

When the impulse arrivals are assumed to follow the usual Poisson law (ref 7) the Gaussian + impulsive interference has an instantaneous amplitude density function given by:-

$$p_1(x) = \exp(-F) \sum_{k=0}^{\infty} \frac{F^k}{k!} \frac{1}{\sqrt{2\pi} \sigma_g} \exp\left(-\frac{x^2}{2\sigma_g^2}\right) \quad (2.1)$$

$$\text{where } \sigma_g^2 = \sigma_g^2 + k \sigma_i^2$$

Here  $\sigma_g$  is the r.m.s. value of the Gaussian component,  $\sigma_i$  that of a single impulse, while F gives the fraction of time occupied by impulses.

In the literature A is used rather than F for this over-lap parameter, but we reserve A for the amplitude of a sinusoidal signal, such as that shown in Eqn (1.3). The density, Eqn (2.1), is seen to be a sum of Gaussian densities, and the mean square value of  $x(t)$  is given by:-

$$\langle x^2(t) \rangle = \int x^2 p_1(x) dx = \sigma_g^2 + F \sigma_i^2 \quad (2.2)$$

This density is plotted on Fig 1 for F = 0.1.

The second and third densities to be examined have certain features in common.

$$\text{Let } p_2(x) = \frac{h(x)}{(x^2 + b^2)} \quad (2.3)$$

$$\text{and } p_3(x) = \frac{2b^3/\pi}{(x^2+b^2)^2} \quad (2.4)$$

Only a single parameter,  $b$ , is involved in specifying each of these, and it is seen that the tail of  $p_2(x)$  falls away as  $x^{-2}$  while that of  $p_3(x)$  follows  $x^{-4}$ .

The function  $p_2(x)$  is known as a Cauchy density (ref 8: it might also be termed 'parabolic' in view of the behaviour in the tail region) and the distribution has no finite moments. However, the parameter  $b$  fixes the amplitude bracket ( $2b$  volts) within which the noise spends 50% of its time.

An interference with the density  $p_3(x)$ , on the other hand, has  $b^2$  for its mean square value but, again, all higher moments are infinitely large. Interestingly, this somewhat pathological behaviour does not prevent us from obtaining the required density functions; we shall refer to  $p_3(x)$  as the Quartic density, and Fig 2 shows  $p_2(x)$  and  $p_3(x)$  in graphical form.

When a sinusoidal signal of amplitude  $A$  is added to Quartic noise a non-zero signal-to-noise power ratio exists, given by  $\rho = \frac{1}{2}A^2/b^2$ , and so, in the conventional manner, performance measures like error probability can be plotted against  $\rho$ .

This is not possible with Cauchy noise, however, since its mean square value is infinitely large but  $A+b$  can be viewed as a Signal-to-Noise voltage ratio ( $b$  is the voltage parameter specifying the Cauchy density) and, as will become evident, performance measures turn out to be expressible in terms of  $A+b$  (ref 9).

$p_2(x)$  and  $p_3(x)$  may be recognised as members of the Pearson Type VII or Student family (Chap 27, ref 10) and  $p_1(x)$ ,  $p_5(x)$ , etc approach the Gaussian form of Eqn (1.1) ever more closely.

### 3. The Characteristic Function

For a wide variety of signal in noise problems the working proceeds more smoothly if the characteristic function of the interference distribution is used, rather than the density function (ref 11). This characteristic function,  $\phi_N(u)$ , is the Fourier transform of a density  $p(x)$ , i.e.:-

$$\begin{aligned} \phi_N(u) &= \int_{-\infty}^{\infty} p(x) \exp(jux) dx \\ &= \langle \exp(jux) \rangle \end{aligned} \quad (3.1)$$

The pointed brackets,  $\langle \rangle$ , have already been used to indicate a long-term time average (see Eqn (2.2)) and we regard them as being equally applicable to ensemble averaging like that shown in Eqn (3.1).

Then, when  $x(t)$  has the narrow-band representation of Eqn (1.2), we can also write:-

$$\begin{aligned} \phi_N(u) &= \langle J_0[u\sqrt{p^2+q^2}] \rangle \\ &= \int_0^\infty J_0(zu) p(z) dz \end{aligned} \quad (3.2)$$

where  $p(z)$  is the probability density function of  $z = \sqrt{p^2+q^2}$ , that is, of the envelope of  $x(t)$ .

The Bessel function  $J_0(\ )$  can be thought of as deriving either from the  $\langle \rangle$  brackets referring to a time average, in which case only the low-frequency part of  $\exp[jux(t)]$  survives, or it comes from viewing the phase angle  $\tan^{-1}(q(t)/p(t))$  as being uniformly distributed over  $-\pi$  to  $+\pi$  (ref 12).

The characteristic functions of the three densities described in Sec 2 come out as follows:-

For the sum of Impulsive and Gaussian noises

$$\phi_1(u) = \exp\left\{-F \sum_{k=0}^{\infty} \frac{F^k}{k!} \exp\left(-\frac{u^2}{2} \sigma_k^2\right)\right\} \quad (3.3)$$

For Parabolic (Cauchy) noise

$$\phi_2(u) = \exp(-b|u|) \quad (3.4)$$

For Quartic noise

$$\phi_3(u) = \exp(-b|u|) \cdot [1 + b|u|] \quad (3.5)$$

Note that  $u$  is a dummy variable at our disposal, and bivariate forms of the characteristic function, such as:-

$$\phi_N(u_1, u_2) = \langle \exp(j(u_1 x(t) + u_2 x(t+T))) \rangle \quad (3.6)$$

involving two such variables, will appear in the following (see Sec 6).

It is instructive to note that the approach described above leads, in all cases, to the in-phase and quadrature components being random variables that have the density function of  $x(t)$ , but they are not independent. The only case in which these are independent processes is the familiar one of narrow-band Gaussian noise (ref 13).

On returning to Eqn (3.2) it can be recognised as being a Hankel transform (order zero; ref 14) and consequently:-

$$p(r) = r \int_0^\infty u J_0(ru) \phi_N(u) du \quad (3.7)$$

This is a form into which any characteristic function can be inserted in order to obtain the density of the corresponding envelope,  $p(r)$ , but this exercise is deferred until the next section (see Eqns (4.10) (4.11) and (4.12), or Figs 3a and 3b).

#### 4. The Envelope Density when a Signal is Present

When a sinusoidal signal of amplitude  $A$  accompanies the narrow-band interference the resultant envelope can be written:-

$$R(t) = \sqrt{[A + P(t)]^2 + Q^2(t)} \quad (4.1)$$

With signal and interference regarded as independent processes their characteristic functions multiply together, and so Eqn (3.7) can be immediately extended, to give:-

$$p(R) = R \int_0^\infty u J_0(Ru) J_0(Au) \phi_N(u) du \quad (4.2)$$

The cumulative distribution is then given by a very similar integral, viz:-

$$\int_0^R p(R) dR = R_1 \int_0^\infty J_1(R_1 y) J_0(Ay) \phi_N(y) dy \quad (4.3)$$

As a check on Eqn (4.2) suppose  $x(t)$  is Gaussian so

$$\phi_N(u) = \exp(-\frac{u^2}{2\sigma^2})$$

The integral then becomes a well-known result (p 718, ref 15) and we find:-

$$p(R) = \frac{R}{\sigma^2} \exp\left[-\frac{R^2 + A^2}{2\sigma^2}\right] I_0\left(\frac{RA}{\sigma^2}\right) = G(R, A, \sigma) \quad (4.4)$$

This, correctly, is the Rice-Nakagami density for the envelope of a signal in Gaussian noise.

Since Eqn (3.3) is merely a sum of Gaussian characteristic functions, the envelope density when a sinusoidal signal is added to the sum of impulses and Gaussian noise immediately follows from Eqn (4.2), and is:-

$$p_1(R) = \exp(-P) \int_0^\infty G(R, A, \sigma_k) \quad (4.5)$$

where  $G(\ )$  is defined by Eqn (4.4).

Upon inserting  $\phi_1(u)$  and  $\phi_3(u)$  into Eqn (4.2) the resulting integrals are not so easy to deal with. For the former case (ref 8):-



$$p_2(R) = R \int_0^{\infty} u J_0(Ru) J_0(Au) \exp(-bu) du \quad (4.6)$$

$$= \frac{2Rb}{\pi \sqrt{(R+A)^2 + b^2} \sqrt{(R-A)^2 + b^2}} \cdot E \left[ \frac{\sqrt{4RA}}{\sqrt{(R+A)^2 + b^2}} \right] \quad (4.7)$$

where  $E(\cdot)$  is the complete elliptic integral.

How Eqn (4.7) may be obtained is outlined in Appendix A, and to assist in achieving the corresponding result with  $\phi_3(u)$ , we note that for  $u > 0$ :-

$$\phi_3(u) = \phi_2(u) - b \frac{\partial \phi_2(u)}{\partial b} \quad (4.8)$$

Then, see Appendix A,

$$p_3(R) = \frac{2Rb^3}{\pi \sqrt{(R+A)^2 + b^2}^{3/2} \sqrt{(R-A)^2 + b^2}} \left[ 2 \left\{ \frac{(R+A)^2 + b^2}{(R-A)^2 + b^2} + 1 \right\} \times \right. \\ \left. E \left( \frac{\sqrt{4RA}}{\sqrt{(R+A)^2 + b^2}} \right) - K \left( \frac{\sqrt{4RA}}{\sqrt{(R+A)^2 + b^2}} \right) \right] \quad (4.9)$$

where  $K(\cdot)$  is a complete elliptic integral.

By placing  $A=0$  in Eqns (4.5) (4.7) and (4.9) we obtain the envelope densities for 'interference alone', and the respective results are:-

$$p_1(r) = \exp(-F) \sum_{k=0}^{\infty} \frac{F^k}{k!} \frac{r}{\sigma_k^2} \exp(-r^2/2\sigma_k^2) \quad (4.10)$$

$$p_2(r) = \frac{br}{(r^2 + b^2)^{3/2}} \quad (4.11)$$

$$p_3(r) = \frac{3rb^3}{(r^2 + b^2)^{5/2}} \quad (4.12)$$

These are plotted on Figs 3a and 3b.

Incidentally, the cumulative distribution of the envelope of signal and narrow-band Cauchy noise is given (see Eqn (4.3)) by:-

$$\int_0^R p_2(R) dR = R_1 \int_0^{\infty} J_1(R_1 y) J_0(Ay) \exp(-by) dy \quad (4.13)$$

This integral has received specific attention in the literature (ref 16) where it is shown that it can be expressed in terms of the elliptic integral  $K(\cdot)$  and Heuman's Lambda function (ref 17 p 595).

Figs 4a and 4b show plots of  $p_1(R)$ ,  $p_2(R)$  and  $p_3(R)$ . For large signal levels it is often adequate (as suggested by Eqn (4.1)) to use  $p_1(x)$ ,  $p_2(x)$  and  $p_3(x)$  with  $x = |A-R|$ , as replacements for these to simplify numerical work.

### 5. Performance Data

Having obtained general expressions for the envelope density, both with and without a signal present, we can apply our results to the analysis of an M-ary data transmission scheme like the one described in Sec 1.

A commonly adopted strategy is Or-ing in which the largest of the M envelope samples is accepted as the one that identifies the transmitted symbol. The probability of error,  $P_e(M)$ , can be expressed as:-

$$P_e(M) = 1 - \int_0^{\infty} p(R) \left[ \int_0^R p(r) dr \right]^{M-1} dR \quad (5.1)$$

where use of  $R$  indicates the presence of the signal, and use of  $r$  refers to interference alone.

$P_e(M)$  is always less than  $1-(1/M)$  and when  $(M-1)xP_e(2)$  is small (less than 0.1 say) a very useful approximation is:-

$$P_e(M) \approx (M-1) \cdot P_e(2) \quad (5.2)$$

A direct way of calculating  $P_e(2)$  is therefore valuable and, in Appendix B, it is shown that:-

$$P_e(2) = \frac{1}{2} [1 - A \int_0^\infty J_1(Au) \phi_N^2(u) du] \quad (5.3)$$

Eqn (5.3) is a new result into which any characteristic function can be inserted.

It may be seen that, essentially, a Hankel transform of unity order (ref 14) is involved thus the relationship can be inverted, should occasion demand, so that the  $\phi_N(u)$  that ensures a particular  $P_e(2)$  can be identified.

Note also that  $\phi_N^2(u)$  is the characteristic function pertaining to the sum of two independent interference samples from the same population. When such interference is made up from a Gaussian component (rms  $\sigma_g$ ) and an impulsive component (rms  $\sigma_I$ , overlap parameter  $F$ ) the addition provides a resultant interference having  $\sqrt{2}\sigma_g$ ,  $\sigma_I$  and  $2F$ . Thus, in this case,  $\phi_N^2(u)$  is given by Eqn (3.3) with  $2F$  for  $F$  and  $2\sigma_g^2$  for  $\sigma_g^2$ . Then:-

$$P_e(2) = \frac{1}{2} \exp(-2F) \sum_{k=0}^{\infty} \frac{(2F)^k}{k!} \exp\left[-\frac{1+\Gamma}{2} \frac{k}{k/2F+\Gamma}\right] \quad (5.4)$$

$$\text{where } \rho = \frac{A^2}{2(\sigma_g^2 + F\sigma_I^2)} \quad \text{and } \Gamma = \frac{\sigma_g^2}{F\sigma_I^2}$$

Thus  $\rho$  is the signal power-to-total interference power ratio, and  $\Gamma$  gives the power ratio of Gaussian noise to impulsive interference.

For Cauchy noise and Quartic noise  $P_e(2)$  is given by simple formulae, namely:-

$$P_e(2) = \frac{1}{2} \cdot \frac{1}{\sqrt{1+(A/2b)^2}} \quad (\text{Cauchy}) \quad (5.5)$$

$$P_e(2) = \frac{1}{2} \cdot \frac{[1 + \frac{1}{2}(A/2b)^2]}{[1 + (A/2b)^2]^{5/2}} \quad (\text{Quartic}) \quad (5.6)$$

Probabilities given by these results are shown on Fig 5, plotted against  $A/b$ . If  $A^2/2b^2$  is equated to  $\rho$  and a comparison is made against  $P_e(2) = \frac{1}{2} \exp(-0.5\rho)$  then it quickly becomes evident that a much poorer performance is achieved in Quartic noise than in Gaussian noise with the same  $\rho$ .

To gain some alleviation, time diversity, in which the message symbols are repeated several times before a decision about them is made, can be advantageous. With an odd number of repeats (such as three or five) a majority vote strategy can be implemented, and Fig 5 shows the performance achieved with three repeats and five repeats.

As is seen, three repeats or five repeats are effective in improving the error probability. With Gaussian noise, however, this error probability would lie at, or below,  $10^{-9}$  when the signal-to-noise ratio exceeds 12dB (in the case of Quartic noise,  $A/b$  is then 15dB).

## 6. Phase Statistics

In this section attention is focussed upon the M-ary phase shift keying modulation scheme described in Sec 1, and the probability of a symbol error is evaluated for our three types of non-Gaussian noise.

The basic analytical result needed for this exercise is stated below, and refs 11, 12, 18, and 21 give the background to its derivation.

With the received signal written as:-

$$V_R(t) = A \cos[\omega_0 t + \theta_m(t)] + N(t) = R_1(t) \cos(\omega_0 t + \theta_1(t)) \quad (6.1)$$

and the local reference against which  $V_R(t)$  is compared written as:-

$$V_R(t) = R_2(t) \cos(\omega_0 t + \theta_2(t)) \quad (6.2)$$

then the probability that  $\theta(t) = \theta_1(t) - \theta_2(t) \pmod{2\pi}$  lies in a range  $\alpha$  to  $\beta$ , is  $\int_{\alpha}^{\beta} p(\theta) d\theta$ , is given by:-

$$G(\beta) - G(\alpha)$$

$$\text{where } G(z) = \frac{z}{2\pi} - \frac{1}{2\pi} \iint_0^{2\pi} \frac{\partial \phi}{\partial z}(-u_1, u_2; z) \frac{du_1 du_2}{u_1 u_2} \quad (6.3)$$

The function  $\phi(-u_1, u_2; z)$  is a conditional joint characteristic function, defined by:-

$$\phi(-u_1, u_2; z) = \langle \exp[j(u_1 R_1 \cos(\omega_0 t + \theta_1) - u_2 R_2 \cos(\omega_0 t + \theta_2 + z))] \rangle \quad (6.4)$$

Two cases of practical interest are examined namely those of coherent detection and differentially coherent detection (DPSK). With the former  $R_2(t)$  is a constant and  $\theta_2(t) = \Delta$  the signalled phase is the local reference is locked, perfectly, in phase and frequency with the signal component of the receiver input.

With differentially coherent detection:-

$$R_2(t) = R_1(t-T) \quad \theta_2(t) = \theta_1(t-T)$$

so the reference is a delayed version of the receiver input. In this case noise is present on both the received signal and the reference, while coherent reception is disturbed only, we suppose, by the noise accompanying the received signal. In practice, noise samples  $N(t)$  and  $N(t-T)$  (with  $T$  the symbol duration) may not be independent but to account for this effect calls for detailed information regarding the higher order statistics of the non-Gaussian interferences in order for  $\phi(-u_1, u_2; z)$  (see Eqn (6.4)) to be evaluated. This problem is not addressed here and we assume  $N(t)$  and  $N(t-T)$  to be independent.

When it is supposed that all detected phases that fall within  $\pm \pi/M$  rad of  $\Delta$  a signalled phase (or phase change) are deemed to be correctly identified, the probability of error,  $P_e(M)$ , is given by:-

$$P_e(M) = 1 - G(\Delta + \pi/M) + G(\Delta - \pi/M) \quad (6.5)$$

where  $G(\cdot)$  is calculated from Eqn (6.3).

The calculation has been extensively studied for the Gaussian noise situation (refs 12, 18) and since, in the case of Gaussian + Impulsive interference the characteristic function Eqn (3.3) is a weighted sum of Gaussian characteristic functions the formulae for  $P_e(M)$ , needed here, can be written down as direct extensions of previously published results.

Thus, for coherent detection, use of Eqn (71) of ref 12 (or Eqn (3.18) of ref 18) leads to:-

$$P_e(M) = \exp -F \cdot \int_{-\pi/2}^{\pi/2 - \pi/M} \frac{F^k}{k!} \frac{1}{\pi} \int_0^{\pi} \exp[-\rho_k \sin^2(\pi/M \sec^2 \theta) d\theta] d\theta \quad (6.6)$$

$$\text{where } k = A^2 + 2\sigma_k^2.$$

In the differentially coherent case, Eqn 3.14 of ref 18 extends to:-

$$P_e(M) = \frac{\sin \pi/M}{2\pi} \exp -2F \int_0^{\pi} \int_{-\pi/2}^{\pi/2 - \pi/M} \frac{F^{1+k}}{1!k!} \frac{W(k,1) \exp -F(k,1;\theta)}{F(k,1;\theta)} d\theta \quad (6.7)$$

$$\text{where } F(k,1;\theta) = \left(a_k \frac{1+\rho_1}{2}\right) + \left(a_k \frac{1-\rho_1}{2}\right) \cos \theta - W(k,1) \cos \pi/M \cos \theta$$

$$\text{and } W(k,1) = \sqrt{\rho_k \rho_1}$$

In a differentially coherent case  $P_e(M)$  can also be written (ref 18) as:-

$$P_e(M) = 1 - \frac{1-2}{M} \sum_{m=1}^{M-1} m [H_m(A,N)]^2 \sin(m\pi/M) \quad (6.8)$$

$$\text{where } H_m(A, N) = \int_0^\infty \frac{J_m(Au)}{u} \phi_N(u) du \quad (6.9)$$

When  $\phi_N(u)$  has the simple form of Eqn (3.4) it is easy to arrive at:-

$$H_m(A, N) = \frac{1}{m} \left[ \sqrt{1 + \left(\frac{b}{A}\right)^2} - \frac{b}{A} \right]^m = \frac{B^m}{m} \quad (6.10)$$

and then to sum the series to give, for Cauchy noise:-

$$P_e(M) = 1 - \frac{1}{M} - \frac{2}{\pi} \tan^{-1} \left\{ \frac{B^2 \sin \pi/M}{1 - B^2 \cos \pi/M} \right\} \quad (6.11)$$

Interestingly, for the coherently detected situation and Cauchy noise, we find (ref 18)

$$P_e(M) = 1 - \frac{1}{M} - \frac{2}{\pi} \tan^{-1} \left\{ \frac{B \sin \pi/M}{1 - B \cos \pi/M} \right\} \quad (6.12)$$

To obtain the corresponding results for Quartic noise it is helpful to use Eqn (4.8). Then, for differentially coherent reception:-

$$P_e(M) = 1 - \frac{1}{M} - \frac{2}{\pi} \tan^{-1} \left\{ \frac{B^2 \sin \pi/M}{1 - B^2 \cos \pi/M} \right\} - \frac{2}{\pi} \frac{2b/a}{\sqrt{1 + (b/A)^2}} \cdot \frac{B^2 \sin \pi/M}{(1 - 2B^2 \cos \pi/M + B^4)} \\ - \frac{2}{\pi} \frac{(b/A)^2}{1 + (b/A)^2} \cdot \frac{B^2 \sin \pi/M (1 - B^4)}{(1 - 2B^2 \cos \pi/M + B^4)^2} \quad (6.13)$$

while, in the coherent case:-

$$P_e(M) = 1 - \frac{1}{M} - \frac{2}{\pi} \tan^{-1} \left\{ \frac{B \sin \pi/M}{1 - B \cos \pi/M} \right\} - \frac{2}{\pi} \frac{b/A}{\sqrt{1 + (b/A)^2}} \cdot \frac{B \sin \pi/M}{(1 - 2B \cos \pi/M + B^2)} \quad (6.14)$$

Coherent detection of M-ary PSK in non-Gaussian noise has received previous attention in the literature, notably in ref 20.

With  $M=4$ ,  $F$  small and  $\sigma=0$  we can compare a result given by Ziemer for operation in purely impulsive noise with our Eqn (6.6), which is then well approximated by:-

$$P_e(4) = \int_{-\pi/2}^{\pi/4} \exp[-\rho_1/2 \sec^2 \theta] d\theta \quad (6.15)$$

With the  $z$  of Ziemer's treatment equated to  $\sqrt{2\rho_1 + F}$  his Eqn (40) can be written:-

$$P_e(4) = \int_{-\pi/2}^{\pi/4} \operatorname{erfc}[\sqrt{\rho_1}/2 \sec \theta] d\theta \quad (6.16)$$

Remembering that for large argument  $\operatorname{erfc} x \approx e^{-x^2}/x\sqrt{\pi}$  it is evident that Eqn (6.15) and Eqn (6.16) behave rather similarly. A numerical check reveals that little more than 1dB separates predictions\* made from these formulae, and this is gratifying in view of the differing underlying assumptions.

Apart from remarking that Eqn (6.7) would appear to be a new result for DPSK, the Gaussian and impulsive type of interference is not examined further. Upon Fig 6, however, plots are given of the performance predicted for M-ary PSK and DPSK in Quartic noise.

---

\* Ziemer's result gives the smaller error probabilities.

---

## 7. Fading

Throughout the fore-going analysis it has been assumed that  $A$ , the signal amplitude, does not vary with time. This is far from being realistic in many situations and it is usual to ascribe a probability density to  $A(t)$  to model the so-called fast fading that is so

characteristic of HF links and mobile radio transmissions.

It is now common practice for the slow\* and fast fading behavior of particular links to be the subject of detailed study (ref 19), and a Rayleigh density is often anticipated for fast fading. This is not always observed in practice, however, and useful flexibility is introduced by using a suitable family of densities that can be fitted to measured data. Such a family is provided by Nakagami's m distribution (ref 11) and for this:-

$$p(A) = \frac{2m^m A^{2m-1}}{\Gamma(m)^m} \exp\left(-\frac{mA^2}{\Omega}\right) \quad (7.1)$$

Here m is a parameter that can be varied.

$$\Omega = \langle A^2(t) \rangle$$

$$\text{and } m = \frac{[\langle A^2 \rangle]^2}{\langle A^4 \rangle - [\langle A^2 \rangle]^2} \geq \frac{1}{2}$$

Results obtained on the assumption that A is constant can then be viewed as being conditional upon any A, and a further stage of averaging, using Eqn (7.1), is in order to achieve a final result averaged over all fast-fading amplitudes.

To illustrate, if this is carried out upon Eqn (5.3) the final outcome gives the probability that a sample of the envelope of narrow-band non-Gaussian noise exceeds an independently chosen sample of the envelope when the fading signal is present in the noise, and the fading law is given by Eqn (7.1). The result is:-

$$\langle P_e(2) \rangle = \frac{1}{2} \int_0^\infty \left(1 - \frac{\Omega}{2} u\right) {}_1F_1(m+1, 2; -\frac{u^2 \Omega}{4}) \phi_N^2(u) du \quad (7.2)$$

where  ${}_1F_1(,;)$  is the degenerate hypergeometric function (ref 15). Note that for m=1 Eqn (7.1) becomes a Rayleigh density and then:-

$$\langle P_e(2) \rangle = \frac{1}{2} \int_0^\infty u \exp\left(-\frac{u^2 \Omega}{4}\right) \phi_N^2(u) du \quad (7.3)$$

\* Slow fading is associated with topographical changes, and fast fading with multipath effects.

## 8. Conclusions

This paper has been concerned with the Amplitude and Phase perturbations introduced upon Angle Modulated Narrow-band signals when they are received in non-Gaussian noise.

General integrals are developed which refer to the envelope statistics of the Signal and Noise mixtures and, in particular, a new general formula (Eqn (5.3)) is given for the probability that a noise alone envelope sample exceeds an independently chosen sample of the envelope of Signal and Noise. The extension of this result with a fading signal is also given (Eqn (7.2)).

Of the three noise types considered the first (Gaussian plus Impulsive) has received earlier attention in the literature but the results for it given here, are thought not to have been presented before.

The other two noise types have intrinsic interest since their density functions fall away only as  $x^{-2}$  and  $x^{-4}$  in the tail region.

In general, therefore, high moments of their distributions are infinitely large, but the important second moment ( $\langle x^2 \rangle$ ) is finite for Quartic noise, and so a signal-to-noise power ratio can be defined and performance plotted against it.

Such performance is illustrated for all three noise types here, in both amplitude and phase cases, for some representative situations from among the many that may present themselves to the system analyst.

9. References

1. J H Roberts  
'Phase Comparison Monopulse Radar: Statistics of Phase Error'  
Electronics Letters  
26 April 1984, Vol 20, No 9, pp 382-3
2. D Middleton  
'Threshold detection in non-Gaussian interference environments: exposition and interpretation of new results for EMC applications'  
IEEE Trans on Electromagnetic Compatibility  
Vol EMC-26 1984, pp 19-28
3. J J Sheehy  
'Optimum detection of signals in non-Gaussian noise'  
J Acou Soc of America  
Vol 63, Jan 1978, pp 81-90
4. A M Maras, H T Davidson, A G J Holt  
'Resolution of Binary Signals for Threshold Detection in Narrow-band non-Gaussian Noise'  
IEE Proceedings, Vol 132, Pt F No 3, June 1985, pp 187-193
5. R F Dwyer  
'A Technique for improving Detection and Estimation of Signals contaminated by Under-ice Noise'  
Naval Underwater Systems Centre Report  
No NUSC-TD-6717, July 1982
6. A D Spaulding  
'Stochastic Modelling of the Electromagnetic Interference Environment'  
IEEE International Conference on Communications (ICC 77) Chicago 1977, pp 42.4-114-123
7. N B Chakrabarti, R Gangopadhyay  
'Error probabilities for ASK/PSK systems in additive mixture of Gaussian and Impulsive noise'  
Electronics Letters, 29 April 1976, Vol 12, No 9, pp 228-229
8. A Papoulis  
'Probability, Random Variables, and Stochastic Processes'  
Mc-Graw Hill 1965
9. J H Roberts  
'Envelope statistics of Narrow-band Cauchy noise'  
Electronics Letters, 5 December 1985, Vol 21, No 25/26, pp 1215-7
10. N L Johnson, S Kotz  
'Continuous Univariate Distributions - 2'  
Houghton Mifflin Co, Boston, 1970
11. J H Roberts  
'Angle Modulation'  
Peter Peregrinus, London 1977
12. R F Pawula, S O Rice, J H Roberts  
'Distribution of the Phase Angle between two vectors perturbed by Gaussian Noise'  
IEEE Trans on Communications, Vol COM-30, No 8, August 1982, pp 1828-1841
13. N H Lu, B A Eisenstein  
'Detection of Weak Signals in Non-Gaussian Noise'  
IEEE Trans on Information Theory, Vol IT-27, No 6, November 1981, pp 755-771
14. A Erdelyi et al  
'Tables of Integral Transforms Vol II'  
McGraw Hill 1954
15. I S Gradshteyn, I M Ryzhik  
'Tables of Integrals, Series and products'  
Academic Press 1965
16. H E Fettis  
$$\text{'Note on } \int_0^\infty \exp(-x) J_0(x/r) J_1(x/r) x^{-n} dx \text{'}$$
  
Mathematics of Computation, Vol 14, 1960, pp 372-374
17. M Abramowitz, I A Stegun  
'Handbook of Mathematical Functions'  
New York: Dover 1972
18. J H Roberts  
'A method of analysing Angle Modulation systems and its application to

phase-shift-keying'

Proceedings of Globe-Com '83,

IEEE Global Telecommunications Conference, San Diego, 28 November - 1 December 1983, pp 44.5.1-5

19. IEEE Proceedings F (Communications, Radar and Signal Processing) Vol 132, August 1985

20. R E Ziemer

'Character Error Probabilities for M-ary Signaling in Impulsive Noise Environments'  
IEEE Trans on Communication Technology, Vol COM-15, No 1, Feb '67, pp 32-44

21. R F Pawula

'A note on Roberts' Characteristic Function Method'

IEEE Trans on Communications, Vol COM-31, No 2, Feb 1983, pp 288-9

#### Appendix A: Envelope Densities

$$\text{With } p_2(R) = R \int_0^\infty u J_0(Ru) J_0(Au) \exp(-bu) du \quad (\text{A.1})$$

the product of Bessel functions can be replaced by:-

$$J_0(Ru) J_0(Au) = \frac{1}{\pi} \int_0^\pi J_0(u \sqrt{R^2 + A^2 + 2RA \cos \theta}) d\theta \quad (\text{A.2})$$

The u integration can then be performed easily, and:-

$$p_2(R) = \frac{2Rb}{\pi \sqrt{(R+A)^2 + b^2}} \int_0^{\pi/2} \frac{1}{(1 - k^2 \sin^2 \alpha)^{3/2}} d\alpha \quad (\text{A.3})$$

$$\text{where } k^2 = \frac{4AR}{(R+A)^2 + b^2}$$

The integral here is a special case of Elliptic Integrals of the Third Kind (p 599 entry 17.7.1, and p 600 entry 17.7.24 of ref 17) so:-

$$p_2(R) = \frac{2Rb}{\pi \sqrt{(R+A)^2 + b^2}} \frac{1}{((R-A)^2 + b^2)} E \left[ \sqrt{\frac{4AR}{(R+A)^2 + b^2}} \right] \quad (\text{A.4})$$

With  $\exp(-bu)$  replaced by  $\exp(-bu)(1+bu)$  in Eqn (A.1), we can use Eqn (4.8) of the text and differentiate Eqn (A.4) with respect to b, to obtain:-

$$p_3(R) = \frac{2Rb^3}{\pi [(R+A)^2 + b^2]^{3/2}} \frac{1}{[(R-A)^2 + b^2]} \left[ 2 \left\{ \frac{(R+A)^2 + b^2}{(R-A)^2 + b^2} + 1 \right\} x \right. \\ \left. E \left( \sqrt{\frac{4AR}{(R+A)^2 + b^2}} \right) - K \left( \sqrt{\frac{4AR}{(R+A)^2 + b^2}} \right) \right] \quad (\text{A.5})$$

#### Appendix B: Derivation of $P_e(2)$ (Binary FSK)

From Eqn (5.1)

$$P_e(2) = 1 - \int_0^\infty p(R) \left[ \int_0^\infty p(r) dr \right] dR \quad (\text{B.1})$$

where  $p(r)$  is given by Eqn (3.7) and  $p(R)$  by eqn (4.2).

By noting that:-

$$\int_0^\infty r J_0(vr) dr = R J_1(Rv) \quad (\text{B.2})$$

$P_e(2)$  can be written:-

$$P_e(2) = 1 + \iint_0^\infty u J_1(u) J_1(v) J_0(Au) \frac{\partial F(u,v)}{\partial v} du dv \quad (\text{B.3})$$

$$\text{where } F(u,v) = \int_0^\infty R J_0(Ru) J_0(Rv) dR \quad (B.4)$$

This integral can be interpreted in terms of a Dirac Delta function, however, (see ref 20) and:-

$$F(u,v) = \frac{\delta(u-v)}{uv} \quad (B.5)$$

Using this in equ (B.3), a follow-up integration by parts, gives:-

$$P_0(2) = \frac{1}{2} [1 - A \int_0^\infty J_1(Au) f_N^2(u) du] \quad (B.6)$$

#### Acknowledgement

The assistance provided by Miss Katy Dean and Miss N J Hulbert in preparing the manuscript, and by Mr Neil Martin regarding the figures, is most gratefully acknowledged.



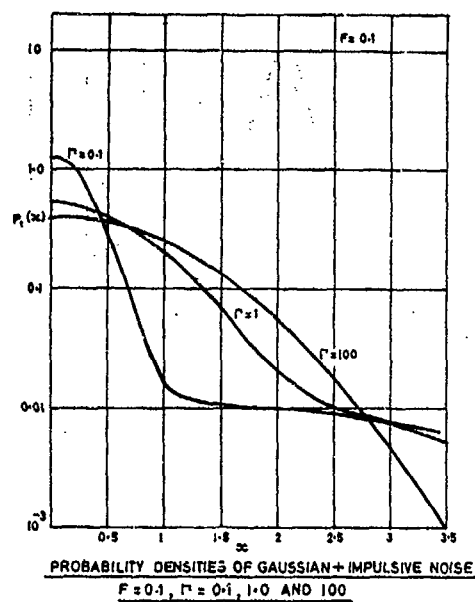


FIGURE 1

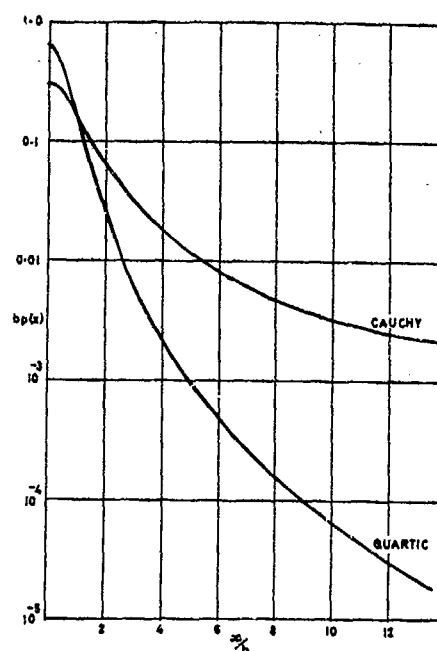


FIGURE 2

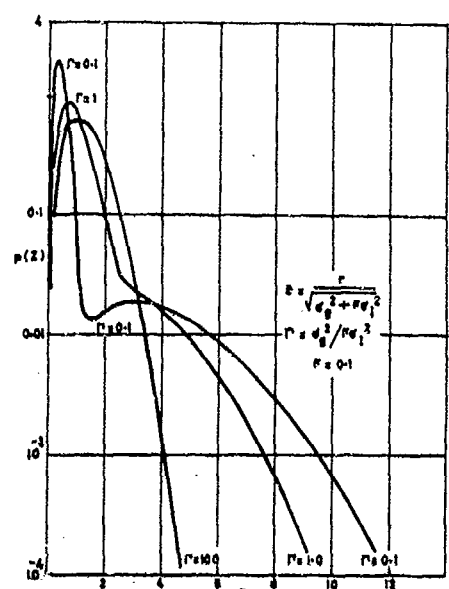


FIGURE 3a

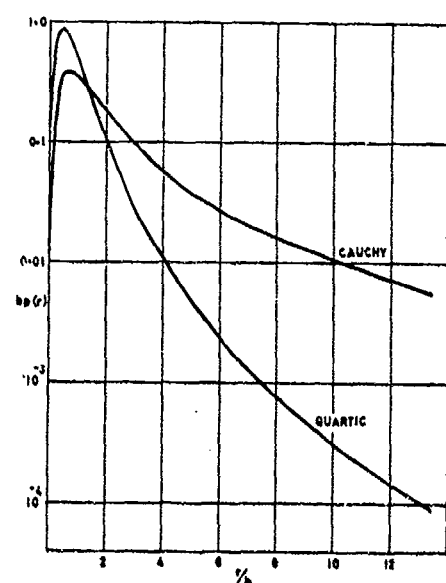
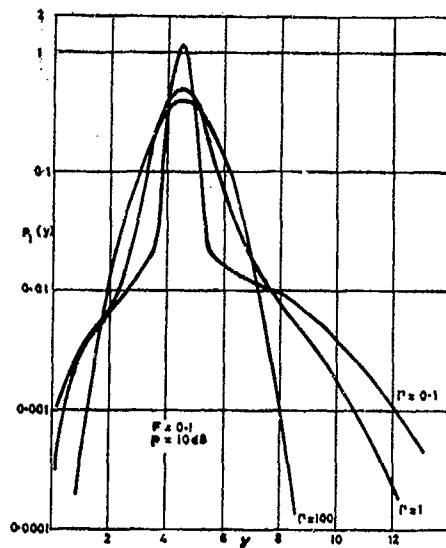
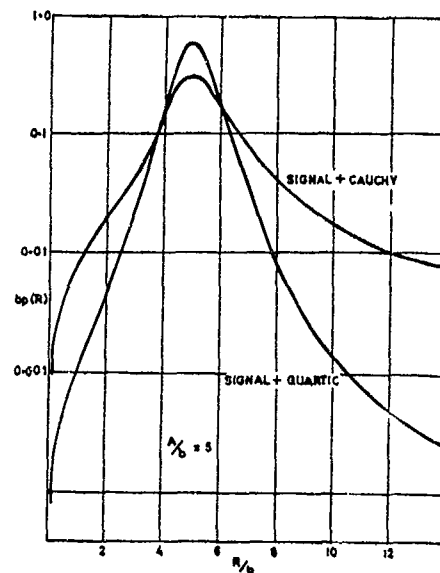


FIGURE 3b



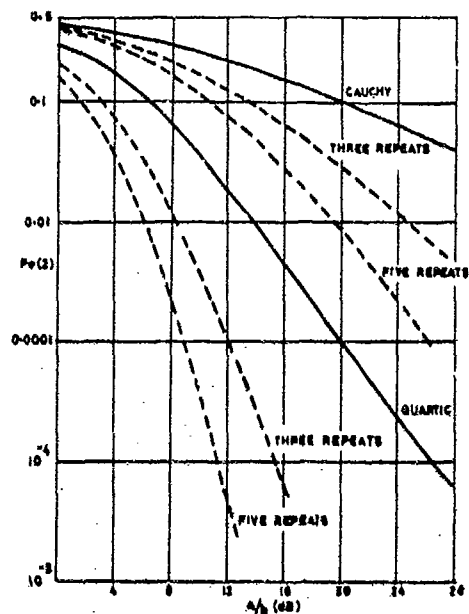
ENVELOPE DENSITIES FOR A SUM OF SIGNAL AND GAUSSIAN + IMPULSIVE NOISE:  $\rho = 0.1, 1.0$  AND  $100$

FIGURE 4a



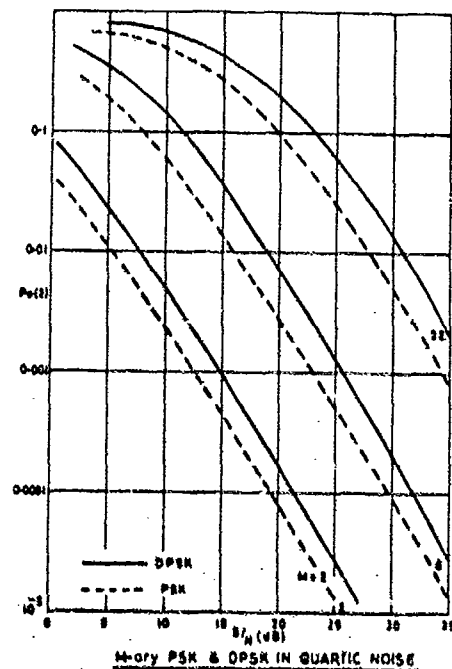
ENVELOPE DENSITIES FOR A SUM OF SIGNAL + CAUCHY NOISE AND A SUM OF SIGNAL + QUARTIC NOISE.

FIGURE 4b



PROBABILITY THAT ENVELOPE OF SIGNAL + CAUCHY NOISE LIES BELOW ENVELOPE OF CAUCHY NOISE ALONE, LIKEWISE FOR QUARTIC NOISE, & WITH MAJORITY VOTING RESULTS INCLUDED ALSO.

FIGURE 5



M-ary PSK & DPSK IN QUARTIC NOISE

FIGURE 6

## DISCUSSION

**A.N.Ince**

What physical mechanism gives rise to Cauchy type noise? At frequencies say above VHF how likely is it to have non-Gaussian noise? In cases where one has impulsive noise an efficient way of reducing errors would be to use ARQ if you have a return channel; do you agree?

**Author's Reply**

I concur with what you are saying. I think there are situations, as I understand, such as under-ice communication with submarines and so on, where the noise that affects the communication, the received signal, is more like Cauchy noise. I must confess I would like to see what these things look like, perhaps on an oscilloscope. I think what you are saying is correct about what one would call impulsive or spiky noise. Although Cauchy noise has a long tail, I do not think it would look quite as spiky, I do not quite know what it would look like. But it is difficult to confirm to say that it has a tail like that and that it does not have spikes. But it does not certainly have the same distribution as one gets if one builds a model of impulses.

**A.N.Ince**

What physical processes give rise to it?

**Author's Reply**

I think some noise with industrial background has been modelled with Cauchy noise. I think it is fairly often found in literature now that below a 100 MHz most man-made and most natural interference is said to be non-Gaussian. I have tried to give a shopping list of densities; if you come across one you could find one that would fit and you could try to formulate it.



AD-P0015748

## 6GHz PROPAGATION MEASUREMENTS OVER A 51 km PATH IN THE UK

J E Doble  
Technology Applications Department  
British Telecom Research Laboratories  
Martlesham Heath  
Ipswich IP5 7RE  
UK

## SUMMARY

For several years British Telecom has operated an experimental 6 GHz digital link over a 51 km path in the worst multipath environment in the UK. The aims of the experiment are to obtain detailed information on the way in which propagation effects degrade the performance of digital systems, with the ultimate aim of developing a system outage model firmly based on practical experience, and secondly to provide test facilities for the performance comparison of a variety of equipments employing different modulation systems, within a reasonably severe propagation environment.

Results from this link are discussed with particular emphasis being given to a previously unreported form of cross-polar-isolation (XPI) behaviour in which the XPI degrades with both frequency selective and flat components of fading. Such events occur only once or twice a year in the location of the experiment but emphasise the need for the development of interference cancellers if co-frequency cross-polar frequency plans are to become viable.

## 1. INTRODUCTION

For some years the British Telecom Research Laboratories (BTRL) have been running an experimental high-capacity (140 Mb/s) digital link over a 51km path in East Anglia. The purpose of this experiment was twofold - firstly to establish a test facility on which the performance capabilities of various digital equipments could be investigated within a real and comparatively severe propagation environment, and secondly to gain a real understanding of the propagation problems involved in wideband systems, with a view to the development of a system outage model firmly based on real propagation data. (Ref. 1)

The data collected during the life of this experiment has been undergoing analysis aimed at characterising the individual and joint statistics of flat and frequency selective fading, and to achieving a better understanding of the relationship between frequency selective fading and the degradation of Cross-Polar Isolation (XPI). This paper briefly describes the experimental link and then proceeds to discuss some results from the study with particular emphasis on anomalous XPI behaviour.

## 2. THE EXPERIMENTAL LINK

The test link was established in an area of the UK particularly prone to multipath fading as a result of a flat terrain coupled with a high liability to advection dusting arising from the proximity of the European land-mass and the North Sea. The system was initially set up to perform measurements on a 140 Mbit/s reduced bandwidth quadrature phase shift keyed (RBQPSK) equipment using a bandwidth of 66 MHz, but as interest in different modulation methods increased the experiment has been expanded to include 16 and recently 64 QAM systems.

The RBQPSK experiment runs in a co-frequency, cross-polar mode and is configured to permit the following measurements taken from the horizontally polarised receivers, all parameters being measured at one second intervals using an in-house designed computer controlled data collection system.

1. Wideband copolar attenuation.
2. Narrowband copolar attenuation within three 1 MHz slots equally spaced over 37 MHz about the channel centre.
3. Bit error ratio.
4. XPI.

These measurements are made for both non-diversity (Channel 2'VM1) and diversity (Channel 2'VM2 - phase aligned at RF) configurations, the spacing between main and diversity antennas being 13.5 metres. In addition a third channel (2'VM3) permits comparison between signal levels received at different antenna heights, a measurement not possible within the diversity receiver since the phase alignment is performed at RF.

The two vertically polarised receivers (2'VM1 & 2'VM2) permit the same group of measurements with the exception of the narrowband copolar attenuation. A block diagram of the receiver and data collection system is shown in Figure 1.

Traffic is simulated by the use of different pseudo-random patterns on each polarisation and the system XPI is measured using correlation techniques. The statistics of XPI behaviour built up over more than three years on a pseudo traffic carrying system is believed to be unique to British Telecom, and has led to some interesting results.

### 3. FADING DISTRIBUTIONS

#### 3.1 Analysis Method

The data derived from the agg lines of the receivers is that appertaining to the composite (flat plus frequency selective fading) signal in a 66 MHz wide channel. At the time the experiment was initiated, it was thought that system outage modelling would be based on wideband fading distributions, although with the fullness of time the modelling has followed the narrowband route. However, the implementation of narrow-band slot filters within the channel bandwidth enables either form of fading distribution to be made available.

In order to separate the flat and selective fading components, a time window is tracked across the database in order to determine the mean level within the window and hence the flat fade component. The difference between the flat fade and the total fade at the centre of the window allows the selective component at that instant to be determined. Initial tests of this method were carried out by comparing results for a selected nine-week database against those derived by a curve fitting exercise. These tests have shown the results of this method to be quite acceptable, and the distributions of flat and selective fading for the nine-week period, together with that of the composite fading, are shown in figure 2.

#### 3.2 Application of Results

Within the UK a general narrowband prediction model for composite multipath fading (Ref. 2) is in use, having the form:-

$$F_{0.1} = -28 + 35 \log d + 9.5 \log f - 14 \log r + G$$

where  $F_{0.1}$  is the fading exceeded for 0.1% of the Worst Month. (dB)

$d$  is the hop length in km

$f$  is the frequency in GHz

$r$  is the ground roughness in milliradians

and  $G$  is a geographic factor.

During the development of the outage model, we were faced with the question of whether the geographic term arose from changes to the flat, the selective, or both fading components. If it was the first of these then the impact on digital systems was not so significant since moderate flat fading has no great effect on the system signature. However, frequency selective fading is far more serious. A further aim of the BT study is therefore to identify the meaning of the geographic factor by installing data recorders on many links in the traffic-carrying network and analysing this fading data in the same way as that of the experimental link.

### 4. RELATIONSHIP BETWEEN XPI AND FREQUENCY SELECTIVE FADING

Drawing the equiprobable characteristic to a scattergram of XPI versus copolar attenuation results in the well known format of Figure 3. When studying the effect of multipath fading on system XPI, the inclusion of the flat fading components in the scattergram makes full comprehension of the XPI v selective fading relationship difficult. We expect that our understanding of the behaviour of XPI under fading conditions will be much improved by the ability to remove the flat fading components from the results.

### 5. ANOMALOUS XPI BEHAVIOUR

It is generally believed that the XPI of a system will not be degraded by flat fading, other than that to be expected as a result of interaction between offset arrival angles and the characteristics of the antennas. However, the capability of our experiment to record the XPI of a traffic carrying system at one second intervals over several years has revealed that this is not always so.

The BT experiment makes use of high XPI antennas that have been designed to avoid many of the problems of offset signal arrival angles (see Figure 4). Despite this precaution there have been several events recorded in which the non-frequency selective component of fading has been faithfully mirrored by XPI degradation. Events of this nature could have serious implications for any system that is designed to run in a co-frequency cross-polar mode, or which relies on maintaining a good working XPI value to reduce adjacent channel interference in an interleaved frequency plan.

An example of this anomalous behaviour is shown in Figure 5 & 6. Figure 5 shows the copolar fading recorded via the agg lines of the main (non-diversity) and diversity channels, and it can clearly be seen that the diversity reduces the multipath component but as would be expected, has no effect on the flat fading component. Figure 6 shows the XPI for the diversity channel and it can clearly be seen that the XPI degradation tends to follow the excursions of both components of fading over a period of some five hours. Several other such examples have been recorded and experience to date shows that events such as these may occur once or twice a year in this area of the UK.

An investigation has been instituted to try and determine the mechanism of these events, their frequency, and the area over which the effects are likely to be felt. To date, although the exact mechanism has not been established, there is evidence to suggest that such events take place as a result of interaction between a subsidence inversion and incoming frontal systems. This combination occasionally causes the inversion layer to descend from its usual height, of around 1 km, down to a height that can be as low as two or three hundred metres, and it is at these times that the anomalous events occur. Figure 7 is a contour plot of potential refractive index (PRI), derived from radiosonde data at a site 60km to the east of the experimental path, for a five day period centred on the event indicated by Figures 5 & 6. Although sonde data is not ideal for looking at thin inversion layers due to the fairly large height intervals at which information is relayed back to the ground, it nevertheless is indicative of abnormal situations. In this example it can be seen that the event for which the commencing and finishing times are indicated by the thick arrows, coincides with a period during which a super-refractive condition developed close to ground level. (The shaded zone lies between refractivity values of 310 and 290 N-units and is intended to draw attention to the relatively rapid change in the refractivity profile that took place).

The occurrence of these events, within the locality in which the experiment is being conducted, correlates well with unusual behaviour on a trans-horizon interference experiment operating between East Anglia and Holland. The received signal level on this experiment is normally at the forward scatter level, and is enhanced during ducting situations. The signal levels observed during the periods of anomalous XPI behaviour have suffered an abnormal degree of enhancement, and in addition have at times shown unusual diurnal distributions. The data from this experiment will thus provide useful evidence of likely frequency of occurrence of these events.

In order to determine the geographic extent of the anomalous behaviour, records from service links are being examined for any evidence of occurrence. Since measurement of XPI is not carried out on these links, records are being examined for evidence of flat fading of several hours duration coinciding with known events on the test link. In addition monitoring facilities are to be installed on a number of these service links, and may include rudimentary means of measuring XPD.

Enquiries amongst other administrations concerning these anomalous events elicited only one positive reply. However this was not unexpected since, with an event occurring only once or twice a year, constant monitoring of system XPI is essential if any occurrence is not to be overlooked.

## 6. CONCLUSIONS

The test facility set up by British Telecom has, in addition to providing the basic data required for the development of a propagation-based system outage model, provided the means of studying the behaviour of XPI under a wide range of propagation conditions, together with the improvement offered by height diversity. The long term database of XPI, gathered in a pseudo traffic carrying environment, is believed to be unique to BT and has revealed the presence of periods of anomalous behaviour. Although such behaviour is likely to prove infrequent, the duration of individual events, which can run into several hours, could prove troublesome for any system that relies on the maintenance of a minimum value of XPI.

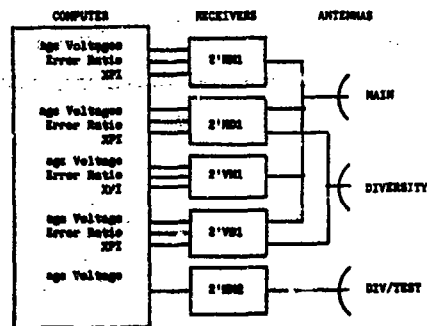
Since co-frequency cross-polar working is being considered by several manufacturers as a means of attaining high spectrum utilisation factors, the work reported in this paper points to the need to develop efficient low-cost interference cancellers if such systems are to meet the performance criteria demanded by system operators.

## 7. ACKNOWLEDGEMENT

Acknowledgement is made to the Director of Technology Applications Department, British Telecom Research Laboratories, for permission to publish this paper.

## 8. REFERENCES

1. DOBLE, J.E., A Flexible Digital Radio System Outage Model Based on Measured Propagation Data. European Conference on Radio Relay. November 1986.
2. DOBLE, J.E., Prediction of Multipath Delays and Frequency Selective Fading on Digital Links in the UK. 1979. IEE Digest, No. 62.

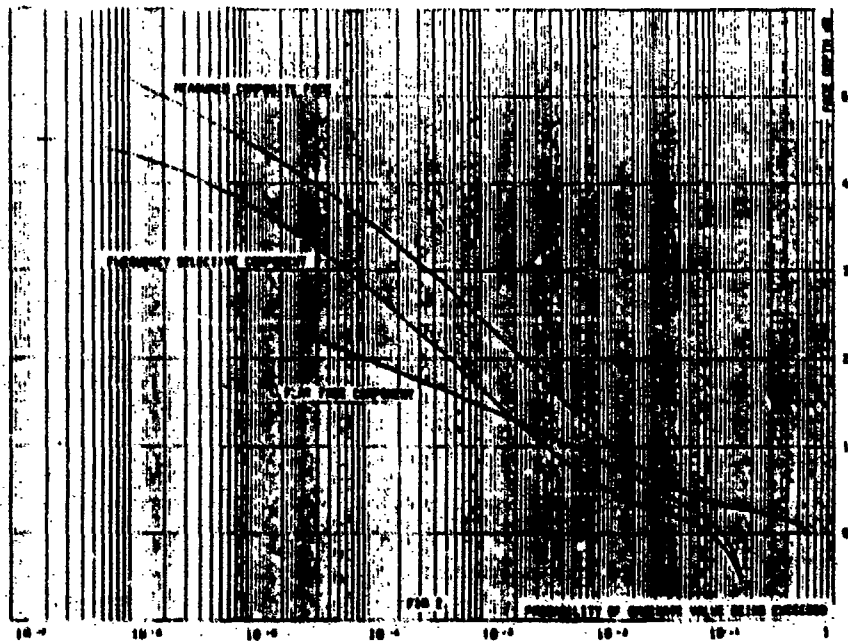


## RECEIVERS

- 2'RH1 Non-Diversity test channel (horizontal polarization), age voltages are for wideband system plus three 1 MHz slot filters at channel centre and  $\pm 10.5$  MHz.
- 2'RH2 Diversity version of the above.
- 2'RH3 Non-Diversity (co-frequency vertically polarized) channel. Measurement of age voltage is wideband only.
- 2'RH4 Diversity version of the above.
- 2'RH5 Wideband age measurement only. Used for comparison of signal level distributions for antennas with different ground clearances.

FIG 1

RECEIVERS AND DATA COLLECTION SYSTEM FOR THE RANPAC EXPERIMENT  
AT HONOLULU RADIO STATION



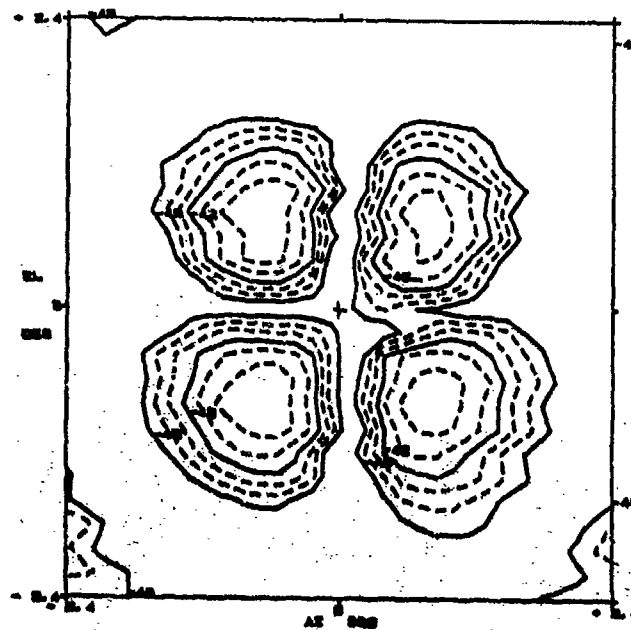
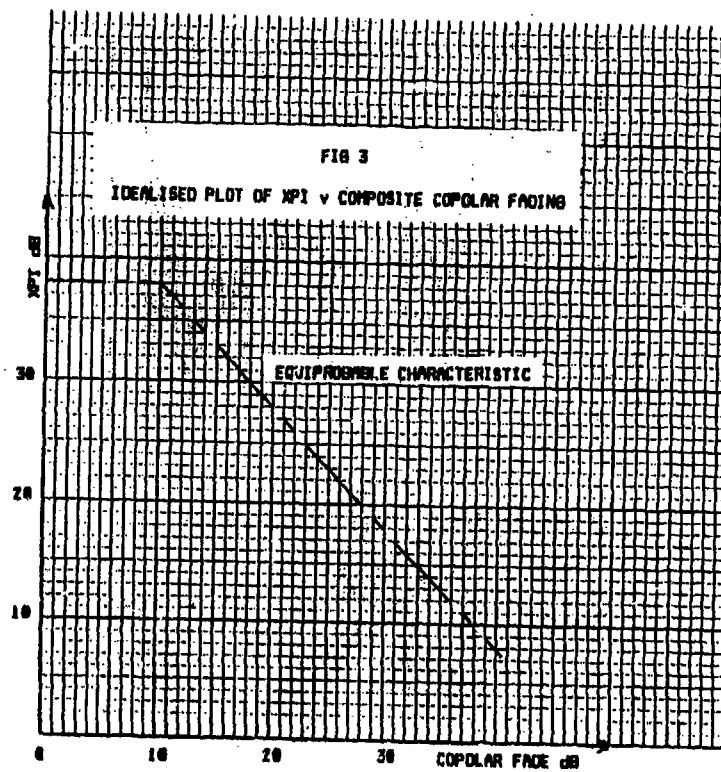


FIG 4.

CROSS-POLAR PATTERN OF HIGH XPI ANTENNA AT 8.137 GHz



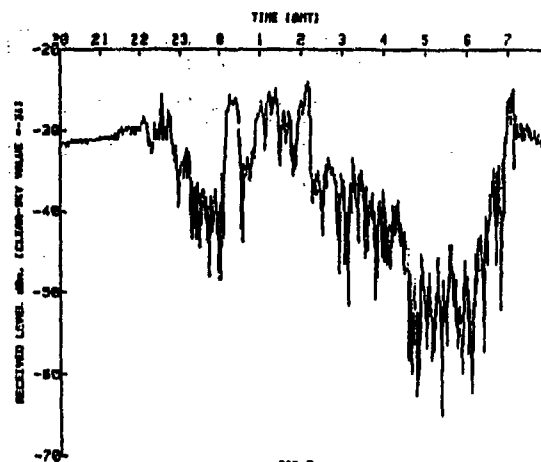
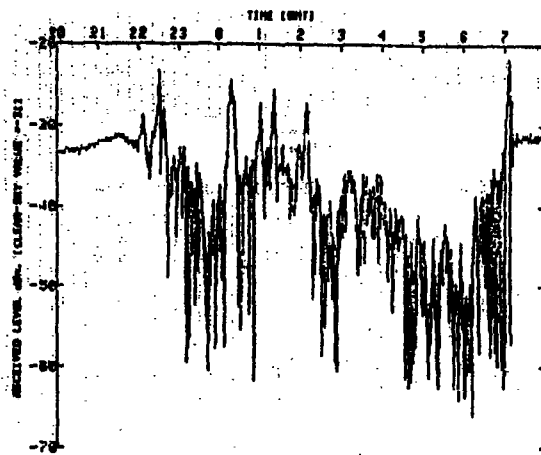


FIG 5.

COPOLAR RECEIVED LEVELS 2000hrs 25/4/84 - 0000hrs 26/4/84 FOR  
NON-DIVERSITY (UPPER TRACE) AND DIVERSITY (LOWER TRACE) RECEIVERS

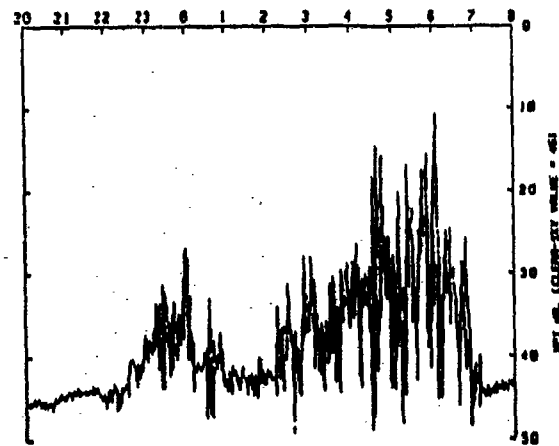
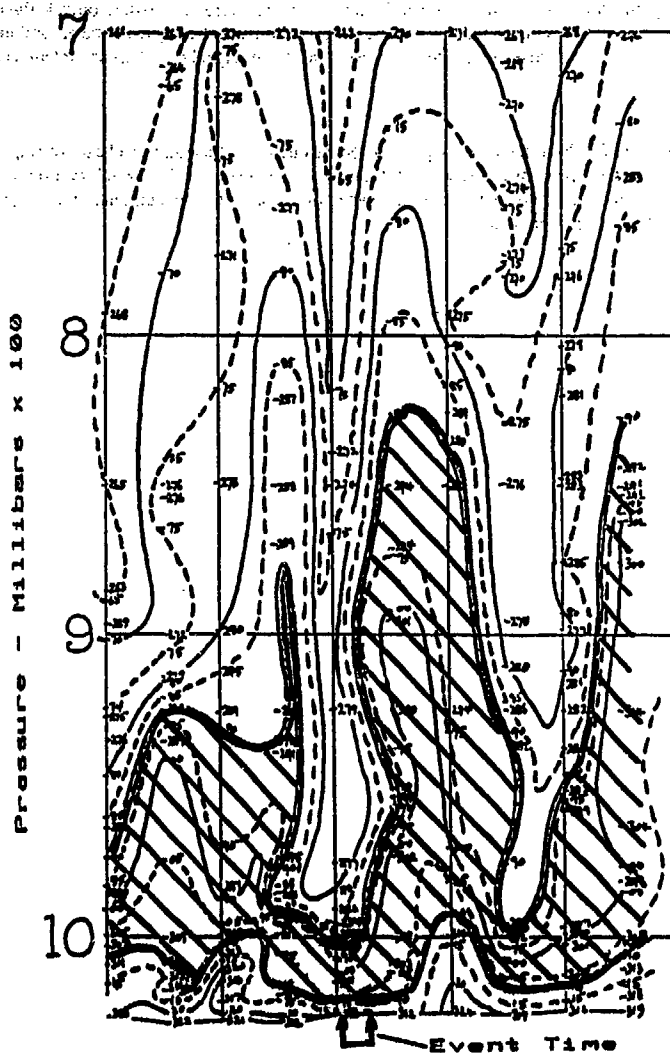


FIG 6.

RECEIVED LEVEL FOR THE DIVERSITY RECEIVER 2000hrs 25/4/84 - 0000hrs 26/4/84.

## Hemsby



24 25 26 27 28  
1984 April

FIG 7.  
POTENTIAL NR1 CONTOURS FOR HEMSBY (NORFOLK) 24th TO 28th APRIL 1984

## DISCUSSION

## R.L. Olsen

Having had several months to study your anomalous XPI data, I am satisfied that the events you have seen are real, and that system designers should take note accordingly. I can see that the cross-polar patterns of your antennas are excellent within a fairly large angular range. However, I wonder if you have measured the pattern outside the range indicated ( $\pm 2.4^\circ$ )? The reason I ask this is my concern about the effect of diffuse scattering from the ground in the foreground of the antennas. I think that large cross-polar side lobes, even those that might be well off the antenna axis, might favour this.

## Author's Reply

I have not seen patterns for the antenna cross-polar response outside of this range, so I cannot help you at this time. However, I will follow this up on my return to the UK and if extra data does exist, I will forward it to you. I am aware of your theory that our problem could be due to diffuse reflections from sidelobe illumination of the ground, and I agree that this could well be a viable explanation.



AD-P005 749

20A-1

## AN EHF TELECOMMUNICATION SYSTEM ENGINEERING MODEL

Kenneth C. Allen  
U.S. Department of Commerce  
NTIA/ITS.33  
325 Broadway  
Boulder, CO 80303-3328

### SUMMARY

An EHF Telecommunication System Engineering Model (ETSEM) has been developed as an aid in the design of line-of-sight (LOS) communication systems from 10 to 100 GHz. ETSEM provides tabulation of path geometry parameters and analyzes ray-path and Fresnel zone clearances to help the engineer design the path. ETSEM also predicts the performance (availability) of both digital and analog systems based on state-of-the-art EHF propagation models and equipment specifications. Attenuation by rain, clear-air absorption, and multipath are modeled. These are expected to essentially determine the statistics of link availability as limited by propagation impairments. Performance may be predicted for any interval of months of the year. A climatological data base for North America and Europe provides parameters for the propagation models. ETSEM has been implemented on a desk-top computer. Weaknesses and limitations of the model are discussed.

### 1. INTRODUCTION

The EHF Telecommunication System Engineering Model (ETSEM) was developed for the U.S. Army Information Systems Engineering Agency (USAISEA) to aid in the engineering design of line-of-sight (LOS) communication systems utilizing the radio spectrum from 10 to 100 GHz. The model predicts the performance (availability) of communication systems based on models of Extremely High Frequency (EHF) radio propagation and equipment specifications and provides other information useful for the design of such systems. The engineer is able to vary design parameters and see immediately the resulting change in the predicted performance of the system. This allows the engineer to efficiently examine tradeoffs to find economical designs that meet the communication requirements.

The model predicts the performance of both analog and digital communication systems. Performance is measured for digital systems by the bit error rate (BER) and for analog systems (FM/FDM) by the signal-to-noise ratio (S/N) in the worst channel. Performance may be predicted for any interval of months of the year. The ability to predict performance for periods as short as one month is important if accurate predictions of performance are to be made for short-term tactical installation.

The model has been implemented on an HP9825\* desk-top computer. The computer code is divided into modules for different tasks. These modules can be separated into three basic groups.

The first group of modules serves as an aid in the selection and design of the propagation path. Antenna heights and Fresnel-zone clearances as well as antenna azimuths and elevation angles are computed. These modules of the computer program are similar to the corresponding modules of ADSEM, a computer model for lower frequencies developed earlier by Hause and Wortendyke [1] at the Institute for Telecommunication Sciences (ITS).

The second group of modules combines the link equipment gain with the predicted cumulative distribution of propagation losses to produce a predicted cumulative distribution of the received signal level (RSL) from which the system performance can be determined.

The third group of modules is composed of models that predict the system performance based on the cumulative distribution of the RSL.

A climatological data base for North America and Europe is included in ETSEM. The parameters needed for the various propagation models are interpolated from this data base using the geographic coordinates of the midpoint of the path under study. This greatly reduces the amount of data required when analyzing a communication system. If desired, the climatological data can be manually entered.

### 2. SYSTEM INSTALLATION MODELS

#### 2.1 Earth Geometry Module

The purpose of the Earth Geometry Module is to provide tabulation of the following data:

- tower (or potential tower) designation,
- tower base elevations above mean sea level,
- tower location (latitude and longitude),
- the great circle distance between towers,
- azimuth from true north at each tower to the other tower,
- magnetic azimuths at each tower to the other tower,
- map crossing; i.e., the latitude and longitude of the points where the path crosses specified map boundaries,
- distances from map crossings to the towers.

The model used to compute earth geometry is unavoidably inexact but should be very satisfactory for engineering line-of-sight paths. The Earth Geometry Module defaults to the International Spheroid for these calculations but provision is made for the selection of other spheroids. Spheroids in use today include the Clark Spheroid of 1866, the Malayan Spheroid, the Bessel Spheroid, the Australian National Spheroid, and the International Spheroid.

The semi-major and -minor axes (in kilometers) of the different spheroids are contained in ETSEM. A map showing which areas of the world are based on the various spheroids is available [2]. Thus, for

\*The use of trade names is necessary to impart relevant information and does not imply a product endorsement.

greater accuracy, the applicable spheroid constants can be used in any particular area of the world. The spheroid used in preparing the maps from which the profile values are taken should be selected.

The model used for the computations is the one proposed by Thomas [3]. The initial point latitude, A, and longitude, B, as well as the terminal point latitude, X, and longitude, Y, are entered. The great circle path length (km), S; azimuth from the initial point, u; and azimuth from the terminal point, v, are computed. The program assumes positive values are north or east and negative values are south or west. The azimuth values are given in degrees east of north.

Map crossings are given as the latitude and longitude of the points where the path crosses the boundaries of maps as specified by the user. They are computed to aid in determining the terrain profile along the path from topological maps. The latitude or longitude of a map boundary is entered and the longitude or latitude, respectively, of the point where the path crosses the map boundary is computed. This enables the drawing of the path on individual topographical maps for the scaling of the path profile.

Map crossings are computed by successive approximations in which values of forward azimuth to the map crossing point are compared with the path forward azimuth to provide error values to measure convergence. If values of latitude, E, or longitude, F, of the map boundary are given, then F or E, respectively, are calculated.

## 2.2 Path Profile and Ray-Path Module

The purpose of the module is to help provide the designer with accurate information about the radio path. The goals are optimum selection of antenna heights and the preparation of foundation information to estimate the radio path reliability.

Several simple models are used to find parameters that are required in various steps of the system design. These models are needed to calculate ray path geometry, Fresnel zone clearance, minimum atmospheric layer penetration angle, mean atmospheric pressure along the ray path, and mean height of the ray path above ground.

In modeling ray paths, the earth and atmosphere are often idealized to a spherical system. A spherical earth is assumed and terrain heights are often given with respect to sea level. The atmosphere is treated as having a spherical structure concentric with the earth so that atmospheric parameters are a function of height only. It is convenient to further idealize our concepts and model the refractivity as proportional to height. Under these conditions a ray path follows the arc of a circle. If the geometry is then distorted so that the ray path becomes a straight line, the earth remains spherical but with a different radius. Thus we may conveniently imagine ray paths as straight lines so long as we are willing to imagine these ray paths over an earth with an "effective radius." The effective radius of the earth is found by multiplying the true radius by a constant called the k factor. The factor k is dependent on the proportionality factor of refractivity with height. The k factor is a common way of describing atmospheric conditions and has a typical value of about 4/3.

The geometry of the ray path is considered in section 4.2.15 of MIL-HDBK-416 [4] and the expression for the height of the ray path, h, in meters above mean sea level (msl) is computed as follows:

$$h = d^2/12.75k + d[(h_2 - h_1)/D - D/12.75k] + h_1 \quad (1)$$

where  $h_1$  = the antenna height in meters above msl where  $d = 0$ ,

$h_2$  = the antenna height in meters above msl where  $d = D$ ,

$d$  = the distance along the path in km,

$D$  = the length of the path in km,

$k$  = the Earth's radius factor.

Because the ray path depends on the k factor, some clearance over obstacles along the path should be included in the design of the path. This clearance is usually measured in Fresnel zones. In MIL-HDBK-416, section 4.2.13, [4] an equation is provided for calculating the nth Fresnel-zone radius,  $R_n$ , on a plane perpendicular to the path:

$$R_n = 17.3 \frac{n^{1/2}}{f} \sqrt{\frac{dD - d^2}{D}} \quad \text{m} \quad (2)$$

where  $f$  = frequency in GHz. The clearance, C, is the distance between the top of the obstacle directly beneath the ray path and the ray path in meters.

The number of Fresnel zones, n, that this clearance is equal to, is given by the following expression:

$$n = \frac{3.38 f C^2}{dD - d^2} \times 10^{-3} \quad (3)$$

For all entered values of d along the path, the clearance is calculated in units of the number of first Fresnel zones; i.e.,  $C/R_1$ , and the minimum value along with the corresponding value of d is noted.

Under some conditions layers form in the atmosphere and the resulting changes in refractivity with height can cause significant changes in ray paths. The direction of rays are more easily affected the shallower their angle of penetration through the layers. Some indication of how susceptible an installation may be to the effect of layers is given by computing the minimum angle of penetration with respect to a spherical atmosphere assuming some k factor, say 4/3.

The take off angle,  $\beta$ , is the angle between the horizontal plane and the tangent to the ray path in the great circle plane at an antenna. When  $d = 0$ ,

$$\beta_1 = \tan^{-1} \frac{h_2 - h_1}{1000 \times D} - \frac{D}{12750k} \quad (4)$$

when  $d = D$ ,

$$\beta_2 = -\tan^{-1} \frac{D}{12750k} + \frac{h_2 - h_1}{1000 \times D} \quad (5)$$

If  $\beta_1 < 0$  and  $\beta_2 < 0$ , i.e., the arrival angles at both ends of the path are below horizontal, then the minimum angle of penetration will be 0 at some point along the path. If  $|\beta_1| < |\beta_2|$ , the minimum angle

of penetration is  $|s_1|$  for  $k > 0$ . If  $|s_1| > |s_2|$ , the minimum angle of penetration is  $|s_2|$  for  $k > 0$ .

Atmospheric pressure is an important parameter in the computation of clear air absorption. To calculate the mean atmospheric pressure along the path, the expression for pressure,  $p$ , as a function of altitude,  $h$ , in meters above mean sea level provided in List [5], p. 266, is used:

$$p = 101.3(1 - 2.26 \times 10^{-5})^{5.2553} \quad (6)$$

where  $p$  is in kilopascals (kPa). One kilopascal equals 10 millibars. The mean pressure along the ray path is calculated by averaging 10 values calculated for equidistant points along the path for  $k = 4/3$ .

The tabular outputs of this module include, for various  $k$  factors input, the relevant path clearance values, the antenna heights necessary to meet specified minimum path clearance requirements, and a summary of the path profile.

An example of the graphical output available is shown in Figure 1. The path terrain profile is drawn and ray paths (and Fresnel zones) for entered  $k$  factors are plotted.

### 3. PROPAGATION MODELS

#### 3.1 Introduction

There are many propagation effects that may degrade the performance of LOS-EHF telecommunication systems. Fortunately, it is not necessary to model all of them in order to be able to predict the availability of the communication link. Only the propagation effects that essentially determine the cumulative distribution of the transmission loss need to be considered. In addition, since it is usually desired that the system be available more than 90 percent of the time, only the propagation effects that contribute to the greater levels of attenuation that are exceeded smaller percentages of the year need to be included. Thus, for example, although scintillation, which normally subsides during rain, often attenuates the signal by several decibels (dB), it does not contribute to the level of attenuation exceeded less than a few percent of the year, normally caused by rain, and therefore does not need to be included in order to predict availability.

All propagation models used predict cumulative distributions of the attenuation caused by individual propagation effects. These distributions are combined into a total cumulative distribution of transmission loss for small percentages of the year.

Three propagation effects were modeled because together they essentially determine the levels of EHF transmission loss exceeded small percentages of the time (less than 10 percent of the time). These propagation effects are rain on path, multipath, and clear-air absorption by oxygen and water vapor.

Attenuation by rain on path is the most significant threat to EHF telecommunication availability. Transmission losses in excess of 200 dB may occur. The accurate prediction of rain attenuation is by far the most essential ingredient in predicting the availability of EHF telecommunication systems. For many paths, predictions based on rain attenuation alone would be sufficient, with the error resulting from excluding the other propagation effects being much less than the normal year-to-year variation in rain attenuation. Dispersive effects by rain do not merit modeling for bandwidths less than 1 GHz [6].

The severity of multipath varies widely from path to path but generally the narrow beamwidths achievable and the tendency toward shorter paths at EHF's would decrease the amount of multipath expected. On the other hand, the shorter wave-lengths afford more opportunity for destructive interference. To date, there is not enough experience to evaluate the significance of the contribution of multipath to the overall cumulative distribution of transmission loss on EHF paths. Because of this and because multipath can result in fades in excess of 40 dB, it has been included as one of the propagation phenomena modeled.

In addition to causing fades, multipath also causes amplitude and phase dispersion. This effect of multipath has not been included in ETSEM because the multipath delay times expected for short paths and narrow beamwidths do not cause enough distortion to merit modeling for bandwidths less than 50 MHz.

Frequency and space diversity improvement for multipath fading have not been included. Because rain attenuation is expected to account for essentially all the outage time of high reliability EHF systems, diversity is not a cost effective way of increasing availability.

Clear air absorption by oxygen and water vapor ranges from less than 0.1 dB/km to more than 15 dB/km depending on frequency (10 - 100 GHz). Because the contribution to the total cumulative distribution of transmission loss can be large, a clear air attenuation model has been included in ETSEM. Clear air amplitude and phase dispersion do not need to be modeled for reasonable path lengths and bandwidths less than 1 GHz [8].

Although it has been shown that attenuation by clouds can add significantly to the cumulative distribution of transmission loss on earth-space paths for frequencies above 30 GHz [9], attenuation due to clouds and fog have not been included in the ETSEM. For most terrestrial LOS-EHF paths, cloud and fog attenuation should not effect the availability statistics. In addition, there is not a model available at this time that predicts the cumulative distribution of attenuation due to fog (or clouds on path) for EHF's as a function of path and climatological or geographic parameters.

However, there may exist paths in fog-prone areas such as parts of Germany or elevated paths between mountain tops that must penetrate a significant amount of cloud, for which the resulting attenuation does effect the availability statistics. It may be that fog and cloud models will need to be included in the ETSEM at some future time for such paths, especially at the upper end of the 10 to 100 GHz frequency range.

Attenuation by snow is so much less than attenuation by rain [6], that it does not need to be modeled for any path that is designed to operate reliably during intervals of time when rain is possible. For this reason attenuation by snow has not been included in ETSEM. Of course, snow attenuation sometimes should be considered for any path being designed to operate under conditions when rain is not possible or very unlikely and considerable snow is expected, such as winter months at high latitudes. However, snow is less of an attenuator than fog and therefore its threat to availability is not difficult to overcome in even the snowiest environment.

Obstruction fading is caused by the  $k$  factor (effective Earth radius factor) becoming so small that, in effect, the Earth bulges up and blocks the path so that it is no longer LOS for the radio waves. Obstruction fading can occur for SHF and EHF links. It has not been included in ETSEM because a link designed with adequate Fresnel-zone clearance (for an effective earth's radius factor equal to 2/3) should not suffer obstruction fading. An obstruction fading model is available [10, 11].

Antenna decoupling occurs when the  $k$  factor changes enough to cause the angle of departure or

arrival at the transmitting or receiving antennas to be outside the main lobe of the antenna pattern. These angles are the same for SHF and EHF radio waves; however, narrower beamwidths are more easily achieved for the shorter wave-length EHF waves. For beamwidths greater than about 0.04 deg per km of path length there should not be a decrease in availability due to antenna decoupling. For beamwidths near this value some caution should be exercised [12] to determine if further investigation of the threat of antenna decoupling to the link is necessary.

Defocusing occurs when the refractive index gradient is structured along the path in such a way as to cause the antenna beam to fan out, reducing the amount of power arriving at the receiving antenna [13]. Defocusing occurs for SHF and EHF frequencies. It should not affect availability but for an occasional problem path that is located near frequent and extreme atmospheric layering.

### 3.2 Rain Attenuation Module

There are three secondary models in the rain attenuation module. The first model predicts the cumulative distribution of point rain rate. The second model converts the cumulative distribution of rain rate into a cumulative distribution of attenuation for the path (point-to-path conversion) using the third model of raindrop size distribution.

The model of point rain rate distribution developed by Rice and Holmberg [14] was selected because it is the only model that gives the rain rate distribution in terms of commonly recorded climatological parameters. The Rice-Holmberg model gives the amount of time,  $T$ , in hours that the point rain rate,  $R$ , in mm/h is exceeded as

$$T = M [0.03 \exp(-0.03R) + 0.2(1-\beta) [\exp(-0.25\beta R) + 1.86 \exp(-1.63R)]] \quad (7)$$

where  $M$  is the total precipitation in mm for the time period and  $\beta$  is the thunderstorm ratio parameter that indicates what fraction of the rainfall is from convective storms. Because monthly predictions of performance are desirable for short term tactical deployments, monthly distributions of rain rate are needed.

Unfortunately, the Rice-Holmberg model gives  $\beta$  as a function of yearly statistics so that its original form cannot be used to predict monthly cumulative distributions of point rain rate. An alternate formulation for  $\beta$  is needed.

Dutton [15] used the intuitive formulation.

$$\beta = U/D \quad (8)$$

where  $U$  is the mean number of days with thunderstorms and  $D$  is the mean number of days with more than 0.01 inches of rain. Since  $U$  and  $D$  are available monthly statistics, (8) is a usable formulation to predict monthly cumulative distributions of  $R$ .

However, the question arises of how good an estimate is (8). This question was addressed by taking 18 cities located in the United States [16] and computing the yearly  $\beta$  according to the original Rice-Holmberg model. Using these values as "true" values, yearly values were calculated using (8) and compared. The standard deviation of these later values about the original ones was 129 percent. If only original values of  $\beta$  greater than 0.15 (13 cases) were used then the standard deviation was 93 percent. Thus the  $\beta$  values given in 8 differ significantly from the original Rice-Holmberg values.

It was noticed that the largest deviations occurred for cities with small  $M$ . Therefore a formulation that included  $M$  was tried with parameters that were adjusted to give the minimum standard deviation. The resulting formulation is given by

$$\beta = (M/1800 + 0.16)U/D. \quad (9)$$

The standard deviation for this latter formulation was 43 percent for all 18 cities and 31 percent for the 13 cities that had original  $\beta$  greater than 0.15. Thus the  $\beta$  values given by (9) are in better agreement with the Rice-Holmberg values than the values using Dutton's formulation (8).

Because rain is of utmost importance to EHF system availability, further study is indicated for the development of an estimate of  $\beta$  that uses commonly available monthly climatological statistics. Although it is uncertain at this time which formulation for  $\beta$  is best, Equation (9) was selected for use in ETSEM.

A model developed by Crane [17] is used for the point-to-path conversion of the point rain rate. This model was chosen because it is widely known, used by the CCIR, not too complex, and has been shown by Dutton [15] to be one of the better models.

It is usual to model the specific attenuation through rain by

$$A = \alpha R^{\beta} \quad (10)$$

where  $\alpha$  and  $\beta$  depend on the distribution of drop-sizes and on the radio wave frequency. Tables of these parameters have been computed by Olsen, Rogers and Hodge [18] for several of the more popular rain drop-size distributions.

The author compared measurements of the ratio of rain attenuation for 11.4 and 28.8 GHz on a 27 km path in Colorado [6] with the ratio of attenuation that would be expected for the different drop-size distributions using the parameters computed by Olsen et al. The ratios predicted for the distribution given by Joss, Thyams, and Waldvogel [19] for thunderstorms agreed best with the measured ratios. The parameters of Dutton et al. [20] that are given for five climate regions and were derived from a survey of measured drop-size distributions were also compared with the parameters of Olsen et al. Again, the Joss thunderstorm parameters showed the closest agreement, falling in about the middle of the range of values. Therefore the  $\alpha$  and  $\beta$  parameters for the Joss distribution are used in ETSEM for (10). This distribution also seems to be a good choice when it is realized that for many locations thunderstorms produce the high rain rates that are a threat to high availability links.

There is a range of more than a factor of 2 in EHF specific attenuation for the different drop-size distributions used by Olsen et al. and a range of a factor of 4 for the different climate regions used by Dutton et al. Thus there is a great uncertainty in EHF specific attenuation. This uncertainty is the most critical limitation to reliable prediction of EHF system availability is therefore the area of most pressing need for further research. It could well be that drop-size distributions dependent upon climate or type of rain will need to be developed before dependable predictions of the cumulative distributions of EHF attenuation can be made.

### 3.3 Clear-Air Absorption Module

The model of clear-air absorption can be broken into two parts. The first part is due to molecular oxygen and varies with time by only a few percent in dB. In the range of 10 to 100 GHz the absorption peaks at about 15 dB/km near 60 GHz and decreases to less than 0.1 dB/km outside the range of approximately 45 to 75 GHz.

The second part is due to water vapor and accordingly varies widely with time, season, and climate. Except for a slight increase near 22 GHz, the absorption increases from about 0.01 dB/km/g/m<sup>3</sup> at 10 GHz to nearly 0.1 dB/km/g/m<sup>3</sup> at 100 GHz in the lower atmosphere. At 22 GHz the absorption is approximately 0.04 dB/km/g/m<sup>3</sup>. Since the water vapor content of the atmosphere can exceed 50 g/m<sup>3</sup>, the attenuation at 100 GHz can be greater than 5 dB/km.

Oxygen absorption for frequencies between 10 and 100 GHz can be accurately modeled as the sum of more than 40 resonant absorption lines around 60 GHz and a nonresonant continuum [21]. This type of modeling is computation intensive, involving the summation of over 40 line contributions, and would require a prohibitive amount of computation time for ETSEM. A simpler model, good for altitudes below 4,570 m (15,000 ft.), that requires approximately two orders of magnitude less computation time was developed.

The model is an expansion in pressure and temperature of the specific attenuation with parameters that are frequency dependent contained in a table. The expansion for the specific attenuation,  $\alpha$ , in dB/km is

$$\alpha = \alpha_0 P^{\beta_1} \exp(\beta_2 P^2 + \beta_3 P), \quad (11)$$

where  $P$  is pressure and  $\theta$  is the relative inverse temperature given by  $\theta = 300/T$  with  $T$  in degrees Kelvin. The  $\alpha$ ,  $\beta_1$ ,  $\beta_2$ ,  $\beta_3$ , and  $\beta_4$  are parameters interpolated in frequency from the table. These parameters were found by fitting oxygen absorption predictions [21] for frequencies from 10 to 100 GHz. When the parameters are interpolated from the table, (11) gives specific attenuations that agree within 6.5 percent of those of Liebe [21].

The specific water vapor absorption model for frequencies from 10 to 100 GHz is simple. It consists of a water vapor continuum [21] and a single line at 22 GHz using a Lorentz line shape. The specific water vapor absorption,  $\alpha$ , in dB/km is given by

$$\alpha = 0.1820fN'' \quad (12)$$

where  $f$  is frequency in GHz and  $N''$  is the imaginary part of the complex refractive index. Now

$$N'' = N''_1 + N''_0 \quad (13)$$

where  $N''_1$  is the contribution by the 22 GHz line and  $N''_0$  is the contribution of the water vapor continuum (due to higher frequency lines).

Using the Lorentz line shape,

$$N''_1 = Sy^2 / [(1 - r)^2 + y^2] \quad (14)$$

where

$$S = 0.112 e^{0.35} \exp(2.143(1 - \theta)), \quad (15)$$

$$y = 28.1 (P_0^{0.8} + 4.8e0)10^{-3}, \quad (16)$$

$$r_0 = 22.23508, \quad (17)$$

and  $e$  is the partial water vapor pressure in kPa.

The water vapor continuum is given by

$$N''_0 = [1.4eP_0^{2.5} + 54.1e^{2.35}] r_0^{-6}. \quad (18)$$

The clear-air specific absorption is modeled in ETSEM as the sum of a constant dry-air term and a random water-vapor term for each month. This is a reasonable approach since the absorption by oxygen only varies by a few percent during a given month while the absorption by water vapor varies by a much larger percentage for most locations.

The constant for dry-air attenuation is found from the mean temperature and pressure for the month.

Bean and Cahoon [22] modeled the cumulative distribution of absolute humidity in g/m<sup>3</sup> by giving the humidity exceeded 10, 5, and 1 percent of the month in terms of the mean absolute humidity for the month. It was found that these levels corresponded closely to the levels that would be exceeded for a normally distributed random absolute humidity with standard deviation

$$\sigma = 0.0094\bar{p} + 2.05, \quad (19)$$

where  $\bar{p}$  is the mean absolute humidity for the month in g/m<sup>3</sup>. Thus, the absolute humidity was modeled as a normally distributed random variable with standard deviation as given in (19).

### 3.4 Multipath Fading Module

The multipath fading model of Crombie [23] was chosen for use in ETSEM. Crombie's model was developed specifically for frequencies above 10 GHz and, for the data base used to develop the model, the standard error of the estimated probability of multipath fading greater than 20 dB was 80 times smaller than that for the more widely known model of Barnett [24] used in ADSEM.

Like the Barnett model, Crombie's model is a worst month model. The author does not know of any method for scaling from the worst month to the other months of the year. Thus the model would be expected to normally overpredict the amount of multipath fading for an arbitrary interval of months.

The formulation of Crombie's model selected for ETSEM gives the percent,  $P$ , of the worst month that multipath attenuation,  $A$ , is exceeded as



$$P(A) = 100 \times 10^{(-A/10-0.997)} \times d^{2.49} \times f^{0.84} \times \theta^{1.19} \times h^{-2.44} \quad (20)$$

where

- d = path length (km),
- f = frequency (GHz),
- $\theta = \theta_T \times \theta_R$ ,
- h = average height at center of path (m),
- $\theta_T$  = beamwidth of transmitting antenna (mr), and
- $\theta_R$  = beamwidth of receiving antenna (mr).

### 3.5 Combined Cumulative Distribution Module

Once the cumulative distributions for the three propagation effects are determined, it is necessary to estimate the overall cumulative distribution of the RSL from them in order to predict the availability of the communication system.

Because the attenuation due to water vapor associated with rain can be quite significant, the water vapor and rain attenuation distributions were added together by adding the attenuations exceeded each percentage of the year. For example, to estimate the attenuation exceeded 1 percent of the time by the combined effects of rain and water vapor, the attenuation by rain exceeded 1 percent of the time is added to the attenuation by water vapor exceeded 1 percent of the time.

To find the total cumulative distribution of attenuation, the combined rain and water vapor attenuation distribution is combined with the multipath attenuation distribution. Because rain and multipath fading usually occur at different times, the distributions are combined by adding the amount of time each attenuation level is exceeded in each distribution. For example, the amount of time that 10 dB attenuation is exceeded for the total cumulative distribution is found by adding together the amount of time that multipath attenuation exceeds 10 dB and the amount of time that the combined rain and water vapor attenuation exceeds 10 dB.

The combined cumulative distribution of attenuation is used with the link gain to compute the cumulative distribution of received signal level (RSL).

### 3.6 Climatological Data Bases

The user of the model may input all the climatological parameters needed by the individual propagation models or may have them taken from the climatological data bases for North America and Europe included with the model.

The data bases contain the latitude, longitude and mean atmospheric pressure for selected meteorological observation stations and monthly mean statistics of:

- atmospheric temperature
- relative humidity or water vapor pressure
- total precipitation
- number of days with greater than 0.01 inch (or 0.25 mm) of precipitation
- number of days with thunderstorms.

Data from 132 and 150 stations are included in the North American and European data bases respectively [25-26].

When the data bases are used, the averages of the transmitter and receiver latitude and longitude are computed to estimate the latitude and longitude of the center of the path. These latitude and longitude are then used to "interpolate" from the data base.

The interpolation is done with the following procedure where all distances are measured in degrees as the square root of the sum of the squares of the difference in latitude and longitude.

1. The data base is searched for the closest two stations in each quadrant about the center of the path. Only stations within 8 deg latitude and longitude are considered.
2. For each meteorological parameter a weighted least squares fit is made using the weights  $1/r$  or  $1/r^2$  if  $r < 1$  where  $r$  is the distance of the station from the center of the path. If there are six to eight stations, a second-order bi-variate polynomial (six unknowns) is fit on longitude and latitude. A first-order polynomial (three unknowns) is used if there are only three to five stations. For one to two stations the value of the parameter for the closest station is used.

This method of interpolating from the data base was selected because of its simplicity. The weighting, order of the polynomial, and maximum distance of stations from the path were all examined and selected to give the minimum standard error when interpolating mean monthly precipitation.

## 4. SYSTEM PERFORMANCE MODELS

### 4.1 Introduction

In order to predict the performance of a communication system the cumulative distribution of the RSL level is used. It is determined from the cumulative distribution of transmission loss and the equipment gain. Models of the communication equipment performance as determined by the RSL are then used to predict the signal-to-noise ratio for analog (FM/FDM) systems and the bit error rate for digital systems.

### 4.2 Link Equipment Gain Module

The purpose of this module is to provide input to the program about the radio frequency equipment and to compute basic system parameters such as the antenna gains and free space RSL.

The following parameters are required input:

1. polarization
2. transmitter antenna diameter (parabolic assumed)
3. receiver antenna diameter
4. transmission line loss
5. diplexer and power splitter losses
6. receiver noise figure
7. receiver bandwidth
8. transmitter power

The free space transmission loss is calculated as

$$L_{fs} = 92.45 + 20 \log_{10}(fD) \quad (21)$$

where  $f$  is the frequency in GHz and  $D$  is the path length in km.

The antenna gains for parabolic antennas are calculated as

$$G = 10 \log_{10}(\eta \pi^2 d^2 / \lambda^2) \quad \text{dBi} \quad (22)$$

where  $\eta$  = aperture efficiency = 0.55

$d$  = antenna diameter

$\lambda$  = wavelength (same units as antenna diameter).

The antenna beamwidths for parabolic antennas are calculated using

$$B = 10(2.215 - G/20) \quad \text{deg} \quad (23)$$

where  $G$  is the antenna gain in dBi.

The free space RSL,  $S$ , is computed using

$$S = P_t + G_t + G_r - L_t - L_d - L_{fs} \quad \text{dBm} \quad (24)$$

Where  $P_t$  = transmitter power in dBm

$G_t$  = transmitter antenna gain in dBi

$G_r$  = receiver antenna gain in dBi

$L_t$  = transmission line (feeder) loss in dB

$L_d$  = diplexer, filter, and power splitter losses in dB

$L_{fs}$  = free space transmission loss.

The free space carrier-to-noise ratio (C/N) is computed using

$$C/N = S + 168 - 10 \log_{10}(B) - F \quad \text{dB} \quad (24)$$

where  $S$  = free space RSL in dBm

$B$  = the narrowest carrier or IF filter bandwidth in MHz

$F$  = receiver noise figure in dB.

#### 4.3 Analog Modulation Performance Modules

There are two analog modulation performance modules. The purpose of the first module is to compute the FM/FDM single-receiver transfer characteristic. The purpose of the second is to compute the availability of an FM/FDM system.

The quality of the FM/FDM system is evaluated in terms of the S/N in the worst channel (usually the highest baseband channel). From equipment parameters input by the user, noise components are calculated and added together to compute the worst-voice-channel S/N as a function of the RSL (transfer characteristic).

In general, the noise sources are thermal noise, (receiver front end noise), echo noise (echo-delayed signals due to transmission line impedance mismatched), and nonlinear noise (distortion due to nonlinearities in the modulator or demodulator and multipath effects). The sum of the total feeder echo noise and equipment intermodulation noise is called the time invariant noise since these noise components do not depend on path loss variability. This time invariant noise is normally the dominant contribution for the relatively high signal levels near the long-term median RSL for which the thermal noise is normally low.

The most significant parameter influencing analog radio link design is the voice channel S/N. It is defined as 10 times the common logarithm of the ratio of an RMS single-tone signal power (usually 1000 Hz and at such a level that the sine-wave voltage peaks are roughly equal to the voltage peaks in a signal developed by a telephone talker) to average noise power in a 300 to 3400 Hz bandwidth.

In a wideband communication system in which many voice channels are frequency-division multiplexed into a baseband signal that extends over a large spectrum, it is necessary to be able to analyze the performance of any voice channel in the band. However, only the channel occupying the highest frequency position in the baseband is usually analyzed since its quality is expected to be the poorest of the channels because of its lower modulation index, even with pre-emphasis.

Pre-emphasis is applied in most radio-relay systems to compensate for the higher noise power in the upper voice channels. The level of the upper frequencies of the baseband is increased while the level of the lower frequencies is decreased before modulation is effected. It is done in such a way that the mean power of the baseband signal is the same with or without pre-emphasis. The CCIR [28] has standardized the frequency characteristic of the pre-emphasis for all types of broadband systems. Between the lowest and highest voice channel, the pre-emphasis (i.e., the difference in level) is 8 dB.

For purposes of system noise calculations, thermal noise is defined as noise from all sources in a channel when there is no modulated signal present in any of the channels in the microwave system. By this definition, thermal noise includes atmospheric and cosmic noise, and all intrinsic and thermal noise produced in the equipment when no modulation is present. Thermal noise is measured in a channel with all modulation removed from all channels of the system.

The signal-to-thermal noise ratio in an FM/FDM system is related to path loss variability. As the path loss on a link becomes low, i.e., the received signal level becomes high, the baseband thermal noise is relatively quite low. As received signal level decreases toward FM threshold, the thermal noise becomes higher. Signal-to-thermal noise ratio,  $S/N_t$ , in a voice channel is proportional to received signal level,  $P_r$ , or carrier-to-noise ratio,  $C/N$ . In the region above FM threshold,  $S/N_t$  may be expressed in several forms [29], for example:

$$S/N_t = P_r + 20 \log_{10} \frac{f_c}{f_m} - 10 \log_{10}(kTb_0 \times 10^3) - F + I_E \quad (26)$$

$$S/N_c = C/N + 20 \log_{10} \frac{\Delta f}{f_m} + 10 \log_{10} \frac{B_{IF}}{b_u} + I_E \quad (27)$$

$$\Delta f = (\Delta f)(10^{PF/20})(10^{LF/20}) \quad \text{kHz} \quad (28)$$

$$LF = -10 + \log_{10}(n) \quad \text{dB} \quad (29)$$

where  $P_r$  = received carrier level in dBm  
 $\Delta f$  = rms per channel deviation in kHz  
 $f_m$  = highest modulating frequency in the baseband in kHz  
 $k$  = Boltzman's constant,  $1.3804 \times 10^{-20}$  millijoules/K  
 $T$  = antenna temperature taken to be 290 K  
 $b_u$  = usable voice channel bandwidth taken to be 3.100 kHz  
 $F_c$  = receiver noise figure in dB  
 $I_E$  = emphasis improvement (4 dB with emphasis and 0 without)  
 $C/N$  = predetection carrier-to-noise ratio in dB ( $N$  is the receiver front end thermal noise power in the same units as  $P_r$ )  
 $B_{IF}$  = receiver IF bandwidth in kHz =  $2(\Delta f + f_m)$   
 $\Delta f$  = peak carrier deviation in kHz  
 $LF$  = rms noise load factor in dB  
 $n$  = number of voice channels in baseband.  
 The value of  $P_r$  at which thermal noise threshold,  $TH$ , occurs is given by the equation:

$$P_r(TH) = -144 + 10 \log_{10}(B_{IF}) + F_c \quad (30)$$

The value of  $P_r$  at which FM threshold occurs,  $FMTH$ , is:

$$P_r(FMTH) = K_T + P_r(TH) \quad (31)$$

where  $K_T = 10$  without threshold extension and  $K_T = 3$  with threshold extension.

The terms of the right-hand side of (26) with the exception of  $P_r$  may be calculated for a given set of equipment parameters. This then becomes a constant--a figure of merit--and as  $P_r$  is allowed to vary, the voice channel  $S/N$  varies in proportion. Using this information, a receiver thermal noise transfer characteristic or "quieting curve" may be constructed, where its slope is uniquely determined by either (26) or (27) for conditions above FM threshold.

Equipment intermodulation noise, for the purpose of the system noise calculations, is defined as the total noise from all sources produced as a result of the presence of a modulated signal in the system except feeder echo noise. Intermodulation noise is measured in a channel with all modulation removed from the channel being measured, and with all remaining channels loaded with actual traffic or with an equivalent amount of white noise over a specific bandwidth. The intermodulation noise power in the channel is then equal to the measured total noise with modulation present, less the measured thermal noise with no modulation present.

The values of noise power ratio (NPR) in the channel having the worst  $S/N$  must be obtained from either equipment performance specifications or carefully controlled tests. The specific loading conditions and received signal level (RSL) must be known for each NPR value. Of particular importance, is the NPR value corresponding to the optimum RSL for a particular EHF radio.

If information is not available, an NPR value of 55 dB obtainable using new, quality equipment is probably the highest value that can be assumed for the initial estimate. A pre-emphasis improvement of 4 dB in the worst channel is usually assumed included in the NPR value.

The noise power ratio can be converted to an equivalent noise channel signal-to-equipment intermodulation noise ratio,  $S/N_e$ , and additionally to equipment intermodulation noise,  $N_e$ :

$$S/N_e = NPR + 10 \log_{10}(B_u/b_u) - LF \quad \text{dB} \quad (32)$$

$$N_e = 10^{(90 - S/N_e)/10} \quad (33)$$

$$B_u = f_u - f_l \quad (34)$$

where  $f_u$  = upper baseband frequency in kHz  
 $f_l$  = lower baseband frequency in kHz  
 $b_u$  = nominal voice channel bandwidth, 3.1 kHz  
 $LF$  = rms load factor in dB (see equation 29).

In these noise calculations flat-weighted noise will be used for ease in handling. If the designer desires to use other noise weightings, appropriate factors may be included at the conclusion of the design procedure.

If a transmission line many wavelengths long is mismatched at both the generator and load ends, its frequency-phase response is linear with a small sinusoidal ripple, and this leads to reflected waves in the line that cause distortion of an FPM signal. This type of distortion is more conveniently considered as being caused by an echo signal generated in a mismatched line, which results in intermodulation distortion. Significant levels of this type of intermodulation noise are reached when the waveguide lengths exceed approximately 20 meters per individual antenna, or 30 meters total per hop [4].

For EHF equipment it should seldom be necessary for waveguide lengths to exceed 1 meter. The resulting echo delay times of less than 6 nanoseconds should not contribute significant intermodulation noise for most bandwidths. Detailed information about waveguide type and velocities should therefore not be necessary except for wide bandwidths greater than approximately 50 MHz.

Feeder intermodulation noise,  $N_f$ , may be approximated given transmission line lengths, velocity of propagation in the lines, transmission system component voltage standing wave ratio's (VSWR) or return losses, transmission line losses, and directional losses. The calculations are performed separately for

each end of a link; i.e., transmitter and receiver, and the results are summed to determine the total hop contribution.

To calculate  $N_p$  in the worst channel, the echo delay time,  $T$  is first calculated from the transmission line length,  $L$ , in meters and the velocity of propagation,  $V$ , in meters/second using:

$$T = 2L/V \quad \text{seconds} \quad (35)$$

where reasonable default values for  $V$  are 195,000,000 and 225,000,000 for elliptical and rectangular waveguide, respectively.

The echo delay time is then converted to radian delay using:

$$\theta_0 = 2\pi f_m T \times 10^3, \quad (36)$$

where  $f_m$  is the highest modulating frequency in the baseband. The echo power,  $r$ , relative to the signal power is given by the expression [4]:

$$r = RL_e + RL_a + 2A_{cl} \quad (37)$$

where  $r$  = number of dB that echo is down from the signal power

$A_{cl}$  = transmission line loss in dB

$RL_e$  = return loss (dB) at the interface between the transmission line and either the transmitter or receiver as applicable

$RL_a$  = return loss (dB) at the interface between the transmission line and the antenna.

This model assumes that all discontinuities in the intermediate section of the transmission line between the transmitter or receiver and the antenna are negligible.

If parameters other than return loss are provided such as the VSWR or the voltage reflection coefficient,  $\rho$ , they can be converted to return loss,  $RL$ , using the following expressions:

$$\rho = \frac{VSWR - 1}{VSWR + 1} \quad (38)$$

$$RL = 20 \log_{10}(1/\rho). \quad (39)$$

The power in the echo cannot totally be considered as distortion power,  $D$ , unless the echo delay is large. To obtain the value of the signal-to-distortion ratio,  $S/D$ , a parameter  $A$  must be determined:

$$A = \frac{f_m^2}{f_c^2} \times 10^{\frac{L}{20}} \quad (40)$$

or alternatively,

$$A = \frac{f_m^2}{f_c^2} \times (n + 10)^{1/2} \quad (41)$$

where the variables have been defined earlier [see 26 and 27].

The signal-to-distortion ratio minus the echo power,  $(S/D - r)$ , can now be approximated [1] as the greater of  $F_1$  and  $F_2$  where:

$$F_1 = 7.17 - 8.23 \ln(A) + 40 \log(1/\theta_0) \quad (42)$$

$$F_2 = 9.412 - 54.64A + 113.2A^2 - 86.5A^3 + 31.52A^4 - 4.239A^5. \quad (43)$$

The calculations of echo attenuation (separately for transmitter and receiver) outlined above can now be converted to voice channel noise. To do this, the total echo attenuation,  $r$ , is added to the value of  $(S/D - r)$  obtained from (42) and (43) above. This results in the signal-to-distortion ratio,  $S/D$ , which must be corrected for the ratio of baseband to voice channel bandwidth and for the RMS load factor. The voice channel signal to feeder echo noise ratio becomes:

$$S/N_p = S/D \cdot 10 \log_{10} \frac{B_c}{B_v} - LF + I_R. \quad (44)$$

The conversion to flat-weighted noise is as follows:

$$S/N_p = 10^{(90 - S/N_p)/10} \quad \text{pW0.} \quad (45)$$

The foregoing feeder echo noise calculations are performed separately for each end of a hop and are summed to give a total link feeder echo noise contribution.

In the FM/FDM link availability model, the required performance level along with the single receiver transfer characteristic and the cumulative distribution of NBL are used to compute the availability of the link; i.e., the fraction of time that the  $S/N$  of the worst channel is above the required minimum.

On the basis of a hypothetical reference circuit, MIL-STD-185-300 [30] in paragraph 4.3.3.1.2 allocates a maximum of 3.33 pW0/mw median noise level in the noisiest voice channel due to radio equipment and propagation. This value translates to approximately 3.2 pW0/mw (flat weighting). In order to provide a design objective this value was selected as a standard of analog link quality. The 3.2 pW0/mw value seems to be consistent with CCIR [31] and industry standards for high performance links [32]. Most of this noise allocation is assigned to equipment noise since thermal noise is a small component of the median signal level. It should not be taken for granted that an individual link's median noise level does not fall within this noise allowance since it is the summation of the median noise values for all the links on a route that is important.

For short-term performance considerations, the maximum allowable flat weighted noise is 500,000 pW0 in the worst channel, MIL-STD-188-313, sec. 4.1.2.1.1.2 [33]. This value corresponds to a value of S/N in the worst channel of 33 dB. The S/N ratio is allowed to fall below 33 dB for no more than 10 minutes per year (approximately 2 min during the worst month [4]), which is equivalent to an average availability of 0.99998 of the year. The value of 0.99998 is used in ETSEM for all time periods.

The allowable long-term noise level in the worst channel is calculated using:

$$N = 3.2L \quad \text{pW0} \quad (46)$$

where L is the path length. The predicted long-term noise is calculated using:

$$N = N_t + N_g + N_f \quad \text{pW0} \quad (47)$$

where the long-term thermal noise is found from (26) using the long-term median RSL and  $N_g$  and  $N_f$  are found from (33) and (45).

The allowable short-term noise and availability are fixed as 500,000 pW0 and 0.99998 in accordance with the design objectives presented above. The predicted availability is found in the following manner using the combined cumulative distribution of RSL:

1. Using (47) and (26) the RSL corresponding to 500,000 pW0 of noise in the worst channel is found.
2. This RSL is used to compute the availability as follows:
  - a. If this RSL is greater than the greatest RSL in the combined distribution then the availability is less than the lowest availability of the distribution (about 0.9) and a message to this effect is included in the output.
  - b. If this RSL is less than the lowest RSL in the combined distribution then the availability is greater than 0.999999. In this case an availability of 0.999999 is taken and a new worst channel short-term noise level less than 500,000 pW0 is computed for the RSL from the distribution corresponding to an availability of 0.999999.
  - c. If neither condition in a or b is met, then the RSL is used to interpolate the availability from the combined distribution. Linear interpolation is applied to the common logarithm of the percentage of time the signal is below level.

The allowable fade margin is fixed at 30 dB as a design objective. The predicted fade margin is calculated as the long-term median RSL minus the RSL corresponding to the short-term noise level.

#### 4.4 Digital Modulation Performance Module

The purpose of this module is to predict the availability of digital links; i.e., the fraction of time that the bit error rate (BER) is less than some required performance standard. This is performed by assuming a standard shape for digital receiver transfer characteristics and adjusting the level according to equipment specifications. The RSL required to meet the performance specifications is then found from the specific digital receiver transfer characteristic. This RSL is then used to find the availability from the combined distribution of the RSL.

MIL-STD-188-322 [34] states that for the LOS digital microwave systems: "It is a design objective to have a 30 dB minimum fade margin on all paths. All radio links are required to have a minimum annual path availability of 0.99995 for maintaining a bit error rate of  $5 \times 10^{-9}$  for operation below 10 GHz. All radio links are also required to have a minimum annual path availability of 0.99998 for maintaining a bit error rate of  $1 \times 10^{-9}$ ."

In ETSEM these design objectives are extended to 100 GHz. Only the short-term requirement of a path availability of 0.99995 for BERs less than  $5 \times 10^{-9}$  has been included in ETSEM. Long-term or median path performance (for error rates substantially less than  $5 \times 10^{-9}$ ) are not meaningful since such low error rates are generally a function of equipment performance, not propagation effects.

Although the BER threshold will vary for various types of digital receivers, the shape of the transfer characteristic will generally remain the same in the presence of Gaussian noise [35] for systems using orthogonal modulation. The equation for the receiver transfer characteristic is:

$$\text{BER} = \frac{1}{2} \text{erfc} \left( k_0 \times 10^{\frac{P_r}{20}} \right) \quad (48)$$

where the constant,  $k_0$ , is equipment dependent. The error function complement,  $\text{erfc}$ , is found from

$$\text{erfc}(x) = 1 - \text{erf}(x) \quad (49)$$

where the error function is evaluated using an expansion [36].

The constant  $k_0$  is found from equipment specifications that give the BER at a reference RSL.  $P_r$ . ETSEM does this by iteratively adjusting  $k_0$  until (48) gives the reference BER for the reference RSL.

The allowable short-term BER and availability are fixed in ETSEM as  $5 \times 10^{-9}$  and 0.99995 in accordance with the design objectives presented above. The predicted availability is found in the following manner using the combined cumulative distribution of RSL:

1. The constant,  $k_0$ , is first found as discussed above.
2. The RSL corresponding to the allowable short-term BER is then found by iteratively solving (48) for  $P_r$ .
3. This RSL is then used to compute the availability in the same manner as described for analog systems above.

The allowable fade margin is fixed at 30 dB as a design objective. The predicted fade margin is calculated as the long-term median RSL minus the RSL corresponding to the short-term allowable BER as found in step 2 above.

#### 5. SUMMARY

ETSEM, RFV Telecommunication System Engineering Model, has been developed to aid in the engineering of line-of-sight telecommunication systems from 10 to 100 GHz. The model has been implemented on an HP 9825

desktop computer and uses equipment specifications and models of propagation effects to predict the performance (availability) of the link.

The cumulative distribution of the bit error rate for digital links and the cumulative distribution of the worst channel signal-to-noise ratio for FM-FDM links are predicted. These measures of performance are predicted for any interval of months out of the year.

The model includes several innovations and enhancements over previously existing models. One of these is the ability to predict monthly statistics of performance instead of just annual. This required the modification of the Rice-Holmberg model. Another feature is a new model of attenuation due to atmospheric oxygen in the form of an expansion in pressure and temperature.

Work is presently being done at ITS to install ETSEM on the IBM-AT computer and to add the following enhancements:

1. Extend the upper frequency range from 100 GHz to 300 GHz.
2. Extend the climatological data base to include the Middle East, South East Asia, Korea and Japan.
3. Add the capability to predict the performance of FSK modulated digital systems.
4. Add the capability to predict the performance of earth-space links.

#### 6. ACKNOWLEDGMENTS

The author would like to thank Dr. Hans Liebe for his helpful guidance on the development of a more computationally efficient algorithm for specific oxygen absorption. The author would also like to thank Greg Hand, who did the computer programming to develop the new oxygen absorption algorithm, and Dan Cronin, who did most of the programming of ETSEM. Thanks is also due to Larry Hause for his consistent help in explaining the ADSEM and WORLD programs, which are in some sense the parents of ETSEM.

#### 7. REFERENCES

- Hause, L.G. and D.R. Wortendyke, NTIA, Automated Digital System Engineering Model, 1979, Report No. 79-18.
- Dept. of the Army, Grid and Grid References, 1967, Technical Bulletin No. TM5-241-1.
- Thomas, P.D., USN, Spheroidal Geodesics, Reference Systems, and Local Geometry, US Naval Oceanographic Office, Washington, D.C. 1970.
- Dept. of Defense, Facility Design for Tropospheric Scatter, 1977, MIL-HDBK-417.
- List, R.J., Smithsonian Meteorological Tables, 6th Ed., Smithsonian Institution, Washington, D.C. 1951.
- Espeiland, R.H., E.J. Violette, and K.C. Allen, NTIA, Atmospheric Channel Performance Measurements at 10 to 100 GHz, 1984, Report 84-149.
- Webster, Alan R., Angles of Arrival and Delay Times of Terrestrial Line-of-Sight Microwave Links, IEEE Trans. Ant. Prop., AP-31, No. 1, 1983, pp. 12-17.
- Shanmugan, K.S., V.S. Frost, J.C. Holtzman, E.M. Friedman, and M. McKinley, USF, EMF Channel Modeling and Simulation, 1985, RADC Tech. Report 85-100.
- Allen, K.C., NTIA, Attenuation of Millimeter Waves on Earth-Space Paths by Rain Clouds, 1983, Report 83-132.
- Vigants, A., Microwave Radio Obstruction Fading, Bell Sys. Tech. J. 60, No. 6, 1981, pp. 785-801.
- Schiavone, J.A., Prediction of Positive Refractivity Gradients for Line-of-Sight Microwave Radio Paths, Bell Sys. Tech. J. 60, No. 6, 1981, pp. 803-822.
- Allen, K.C., NTIA, EMF Telecommunication System Engineering Model, 1986, Report 86-192.
- Allen, K.C., R. Ott, E.J. Violette, and R.H. Espeiland, Weight-Gain Study for 23 km Links at 9.6, 11.4, and 28.8 GHz, IEEE Trans. Ant. Prop. AP-30, No. 4, 1982, pp. 734-740.
- Rice, P.L. and N.R. Holmberg, Cumulative Time Statistics of Surface-Point Rainfall Rates, IEEE Trans. Comm., Vol. COM-21, No. 10, 1973, pp. 1131-1136.
- Dutton, E.J., NTIA, Microwave Terrestrial Link Rain Attenuation Prediction Parameter Analysis, 1984, Report 84-148.
- Allen, K.C., M.J. Liebe, and C.M. Rush, NTIA, Estimates of Millimeter Wave Attenuation for 18 United States Cities, 1983, Report 83-119.
- Cramer, R.K., Prediction of Attenuation by Rain, IEEE Trans. Comm. COM-28, No. 9, 1980, pp. 1717-1733.
- Gleason, R.L., D.V. Rogers, and D.B. Hodge, The aRb Relation in the Calculation of Rain Attenuation, IEEE Trans. Ant. Prop., AP-26, No. 2, 1978, pp. 318-329.
- Joss, J., J.C. Thoms, and A. Melvoge, The Variation of Rain Drop-Size Distribution at Locarno, Proc. Int. Cong. CL Physics, 1966, pp. 369-373.
- Dutton, E.J., C.E. Lewis, and F.K. Steele, NTIA, Climatological Coefficients for Rain Attenuation at Millimeter Wavelengths, 1983, Report 83-129.
- Liebe, M.J., NTIA, An Atmospheric Millimeter Wave Propagation Model, 1983, Report 83-137.

- Bean, S.R. and B.A. Cahoon, A Note on the Climatic Variation of Absolute Humidity, Bull. American Met. Soc., Vol. 38, No. 7, 1957, pp. 395-398.
- Crombie, D.D., Prediction of Multipath Fading on Terrestrial Microwave Links at Frequencies of 11 GHz and Greater, AGARD/NATO Conference Proc. No. 346, 1983.
- Barnett, W.R., Multipath Propagation at 4, 6, and 11 GHz, Bell System Technical Journal, Vol. 56, No. 2, 1972, pp. 321-361.
- Wallen, C.C., ed., Climates of Northern and Western Europe, World Survey of Climatology, Vol. 5, New York, Elsevier Scientific Publishing Co., 1970.
- Wallen, C.C., ed., Climates of Central and Southern Europe, World Survey of Climatology, Vol. 6, New York, Elsevier Scientific Publishing Co., 1977.
- Bryson, R.A. and F.K. Hare, ed., Climates of North America, World Survey of Climatology, Vol. 11, New York, Elsevier Scientific Publishing Co., 1974.
- CCIR, Pre-emphasis Characteristic for Frequency Modulation Radio-relay Systems for Telephone Using Frequency-division Multiplex, 1982, Vol. 9, Rec. 275-3, XV Plenary Assembly.
- Dept. of Defense, Facility Design for Tropospheric Scatter, 1977, MIL-HBDK-417.
- Dept. of Defense, Standards for Long Haul Communications - Systems Design/Standards Applicable to the Defense Communications System, 1971, MIL-STD-188-300.
- CCIR, Noise in the Radio Portion of Circuits to be Established over Real Radio-relay Links for FDM Telephony, 1978, Vol. 9, Rec. 395-2, XIV Plenary Assembly.
- Brodhage, H. and W. Hormuth, Planning and Engineering of Radio Relay Links, 7TH ED., Siemens & Halsk, 1968.
- Dept. of Defense, Subsystem Design and Engineering Standards and Equipment Technical Design Standards for Long-haul Communications Transversing Microwave LOS Radio and Tropospheric Scatter Radio, 1973, MIL-STD-188-313.
- Dept. of Defense, Subsystem Design/Engineering and Equipment Technical Design Standards for Long-Haul Line-of-Sight (LOS) Digital Microwave Radio Transmission, 1976, MIL-STD-188-312.
- Bell Telephone Laboratories, Transmission Systems for Communications, Winston Salem, N.C., Western Electric Company, 1970.
- Abramowitz, M. and I.A. Stegun, Handbook of Mathematical Functions, Washington, D. C., National Bureau of Standards, 1964, p. 299.

Figure 1. Example path profile and ray tracing plot of the terrain profile and ray path module.

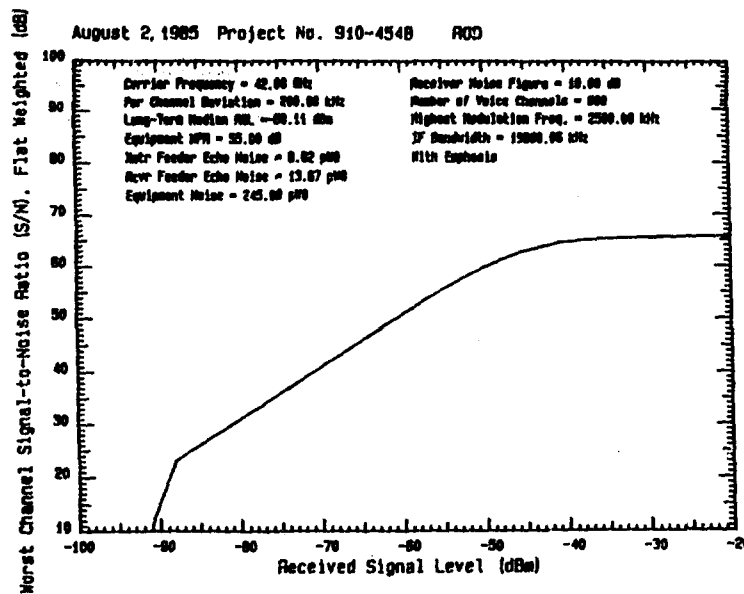
Table 1. Example Output of the Combined Distribution Module

Distribution of RSL and C/N  
Lee Hill to Receiver Path

|                              |       |           |
|------------------------------|-------|-----------|
| Time Period                  |       | Jun - Jun |
| Carrier Frequency            | (GHz) | 42.888    |
| Path Length                  | (km)  | 17.31     |
| Free Space Trans. Loss       | (dB)  | 149.68    |
| Free Space RSL               | (dBm) | -66.13    |
| Free Space C/N               | (dB)  | 42.86     |
| Median Clear Air Atten.      |       | 1.98      |
| Long-term Median Trans. Loss | (dB)  | 151.64    |
| Long-term Median C/N         | (dB)  | 49.88     |
| Long-term Median RSL         | (dBm) | -58.11    |

| Percent of Time<br>Below Indicated RSL | Time      | RSL         | C/N        |
|--|-----------|-------------|------------|
| 10.0426 %                              | 72.35 hr  | -59.11 dBm  | 46.06 dB   |
| 5.0426 %                               | 36.31 hr  | -59.11 dBm  | 46.06 dB   |
| 2.0399 %                               | 14.69 hr  | -59.39 dBm  | 46.60 dB   |
| 1.0024 %                               | 7.22 hr   | -62.92 dBm  | 28.43 dB   |
| 0.5003 %                               | 3.60 hr   | -72.29 dBm  | 18.79 dB   |
| 0.2000 %                               | 1.64 hr   | -87.17 dBm  | 3.02 dB    |
| 0.1000 %                               | 47.28 min | -97.95 dBm  | -6.96 dB   |
| 0.0500 %                               | 21.60 min | -110.60 dBm | -19.69 dB  |
| 0.0200 %                               | 8.64 min  | -143.06 dBm | -52.87 dB  |
| 0.0100 %                               | 4.32 min  | -166.20 dBm | -75.29 dB  |
| 0.0050 %                               | 2.16 min  | -189.20 dBm | -94.29 dB  |
| 0.0020 %                               | 91.84 sec | -206.94 dBm | -115.99 dB |
| 0.0010 %                               | 29.92 sec | -221.37 dBm | -130.10 dB |
| 0.0005 %                               | 12.96 sec | -234.60 dBm | -143.70 dB |
| 0.0002 %                               | 5.10 sec  | -250.99 dBm | -159.69 dB |
| 0.0001 %                               | 2.59 sec  | -267.38 dBm | -171.31 dB |





FM/FDM Equipment Transfer Characteristic  
Lee Hill to Receiver Path

Figure 2. Example output of the FM/FDM single-receiver transfer characteristic module.

Table 2. Example Output of the FM/FDM Link Performance Module

| FM/FDM Link Performance<br>Lee Hill to Receiver Path |       |                    |                       |
|--|-------|--------------------|-----------------------|
| System Type  |       | FM/FDM             |                       |
| Path Length  | (km)  | 17.3               |                       |
| Long-term Distribution Parameters:                   |       |                    |                       |
| Long-term Median C/N                                 | (dB)  | 40.9               |                       |
| Long-term Median RSL                                 | (dBm) | -90.1              |                       |
| Equipment Noise S/N                                  | (dB)  | 66.11              |                       |
| Xtr Feeder Echo S/N                                  | (dB)  | 80.64              |                       |
| Rcvr Feeder Echo S/N                                 | (dB)  | 78.64              |                       |
| Thermal S/N - C/N                                    | (dB)  | 28.00              |                       |
| Excess Improvement                                   | (dB)  | 4.0                |                       |
| P(FHFN) - P(TH)                                      | (dB)  | 3.00               |                       |
| Link Performance                                     |       |                    |                       |
| Long-term Noise                                      | (μW)  | Allowable<br>55.40 | Calculated<br>1067.00 |
| Short-term Noise                                     |       | 500000.0           | 500000.0              |
| Availability   |       | 0.999980           | 0.996494              |
| Fade Margin  | (dB)  | 30.0               | 20.0                  |

## DISCUSSION

E. Villar

Your model does not include scintillation-type of fading. I submit to you that large scintillations occur in mm-wave propagation, and that there are now both experimental results and long-term modelling (IEEE Trans AP Aug. 86). They should be included in your model. Could you please comment? Thank you.

Author's Reply

Well, there are several effects which we realize may need to be included at some point. We were not sure how to model some of these effects. In the case of scintillations we left it out because of our observations. On the 27 km-path, when we were observing on 30.3 GHz, we would see, on bad scintillation days, peak-to-peak scintillations of 10 dB. But in order to have a reasonable reliability for the system, we knew, we had more than 10 dB of fade margin. We have made observations at 96 GHz on a 17 km path in Alabama where we have seen peak-to-peak scintillations of 20 to 30 dB. Now that occurred in August this year; this is fairly recent information for us. We know now from that combination of information that, probably below the 60 GHz absorption band, we would not have to model scintillation for any system that is being designed for a great deal of reliability. We did on occasion see these scintillations large enough to cause some bit errors but they did not significantly affect the overall distribution of the bit-error rate. We had roughly a 10 dB fade margin on the 27 km link. So we did sometimes see some bit-error rates that were caused by scintillations. Those bit errors did not depart from the signal-to-noise curve defined by the complimentary error function. They were not dispersive, they were basically power fading. We are just not aware at this time of how to make predictions of accumulated distribution of the scintillation effect based on path parameters, like the average temperature and the humidity for the month and the path length, and frequency. If we knew that dependence it appears that we would need to include that at frequencies higher than the 60 GHz absorption band, like 96 GHz. But I would also mention that on that 27 km path we saw variations due just to the background change in the amount of water vapour in the air, the diurnal variation, of 20 dB in signal level, just due to changes in clear absorption. I think I am aware of the paper that you are talking about, but only of its existence. I did not look at it close enough to see whether we could include it in our model or not. I intend to go back if we decided to model scintillation and see whether there are parameters that we could easily get from the data base or make reasonable estimates of.

A. Hewitt

What factors which have been neglected for tropospheric links do you expect to need to include for earth-space links?

Author's Reply

One is, we neglected the effect of fog. On an earth-space path, the amount of attenuation due to clouds becomes significant at some point. I have done some calculations that indicated, maybe around 90 to 100 GHz, that, for small percentages of the year, the amount of attenuation that is due to clouds is as great as that due to rain. So that in heavy thunderstorms there is a great deal of liquid water content in the clouds. At roughly 90 GHz and above, there can be as much attenuation due to the clouds as due to the rain. There again, it is difficult to model at this time. Otherwise I think that the only problem in going to the earth-space path is to be getting some of the statistics on the distribution of water vapour in height; it varies with time.

A. N. Ince

Would you not take into account increase in noise level due to precipitation in earth-space paths?

Author's Reply

No, we have not taken it into account. I suppose we will have to take it into account for the earth-space path. On a space path, we would need to take into account the noise-temperature of clouds and rain.



# UNE CAMPAGNE DE PROPAGATION EN MILIEU MARITIME, UTILISANT UN SYSTÈME NUMÉRIQUE À 36 GHZ

Yvonick MURTAUD  
Département Antennes - UA 83/ CNRS  
UNIVERSITÉ de RENNES I  
Avenue du général Leclerc  
35042 - RENNES CEDEX

et

Alain JUNCHAT  
groupe "Analyse des Signatures et Rayonnements  
électromagnétiques - Environnement"  
CENTRE D'ELECTRONIQUE DE L'ARMEMENT  
35170 - BRUZ

## SUMMARY

Within the framework of the NATO study group AC.243 (Panel 3/RSG.8), a propagation campaign in a maritime environment, took place at the end of 1984 on the French Atlantic coast, near LORIENT.

A 8.448 Mbit/s system, working at 36 GHz was used by the French Delegation.

A transmitter and a receiver were fixed at a few ten meters height, at each end of a line of sight (LOS) of 9.7 Km, fully above the sea level. The received field came from the addition of the direct field and the reflected field.

Among others, this experimentation was to study the attenuation at 36 GHz which was caused by rain and the behaviour of the digital link in function of the surrounding conditions.

Met and oceanographic sensors were placed along the path. Rain-data were measured, on the transmitter site by an ordinary tipping - bucket rain gauge and on the reception site by a spectropuviometer. This optical rain gauge which has been created recently, gave double histogram of the number of drops per diameter and velocity class.

In order to know the sea state, a buoy with a swell sensor was anchored close to the line of sight (LOS). It provided regularly the significant height of waves.

The study of the distribution of the rain-drop size measured by the spectropuviometer, shows the good agreement of these data with the distributions of Marshall Palmer or Joss and al. .

From these distributions and using the Mie theory, the specific attenuation is calculated.

On selected periods, the whole attenuation on the link is forecast and compared to the experimental values. The digital transmission analysis reveals that the link quality strongly depends on the sea state.

When the sea is quiet, the reflection of a part of the incident energy on the water, disturbs the link with the tide.

In case of rain, the data transmission can be very disturbed and even stopped during a few minutes.

## 1 - INTRODUCTION (N.U.)

Les applications navales des télécommunications, de la poursuite ou du guidage, offrent un certain nombre de perspectives intéressantes notamment dans le domaine centimétrique ou millimétrique.

Les systèmes utilisés dans ces applications rayonnent généralement avec une faible incidence par rapport à la surface de la mer. Dans ces conditions particulières, la présence de double trajets, dus à la réflexion d'une partie de l'énergie incidente sur la mer, et l'action des hydrométéores ont des influences déterminantes sur la propagation en milieu maritime.

Afin d'étudier ces phénomènes deux campagnes de mesures organisées par le sous-groupe propagation du RSG.8, commission 3, AC.243, se sont déroulées d'octobre à janvier 81-82 et 84-85. Pour des raisons scientifiques, logistiques et tactiques une base de mesure située entre la presqu'île de CAVRES et l'île de GROIX a été utilisée. Cette zone de la côte atlantique, au sud de la Bretagne, est localisée à une vingtaine de kilomètres au sud-est de LORIENT.

La longueur des liaisons entre le site d'émission situé sur l'île de GROIX et le site de réception à CAVRES est de 9.7 km. Les matériels de mesure utilisés étaient placés respectivement à 48.2 m et 13.2 m de hauteur par rapport au niveau zéro des cartes marines.

Durant la campagne 84-85, le centre d'électronique de l'armement (CELAR), a mis en oeuvre :

- un système numérique fonctionnant à 36 GHz,
- un pluviomètre optique, aussi appelé spectropuviomètre,
- une station météorologique classique,
- une bouée équipée d'un capteur permettant de mesurer les caractéristiques de la houle.

Ces matériels sont décrits en détail dans le paragraphe 2.

Ils ont permis :

- de déterminer de façon expérimentale l'affaiblissement d0 à la pluie,
- d'étudier le comportement de la liaison numérique, en fonction des conditions d'environnement.

Ces deux points sont examinés successivement dans les paragraphes 3 et 4.

## 2 - DESCRIPTION DES MATÉRIELS UTILISÉS (N.U.)

### 2.1. LA LIAISON NUMÉRIQUE A 36 GHz

La liaison hertzienne à 36 GHz mise en place pour cette campagne, a été fabriquée par THOMSON-CSF. Elle permet la transmission d'informations sous forme numérique. Ces principales caractéristiques apparaissent dans le tableau 2.1.

|                              |                                      |
|------------------------------|--------------------------------------|
| Puissance de l'émetteur      | 50 mW                                |
| Gain des antennes            | 42 dB                                |
| Polarisation                 | linéaire, orientée à 45°             |
| Ouverture du faisceau à 3 dB | 1.5 degré                            |
| Dynamique du récepteur       | environ 60 dB                        |
| Modulation numérique         | MDP2 (modulation de phase à 2 états) |
| Débit numérique              | 8.448 Mbit/s                         |

TABEAU 2.1.

Durant la campagne le niveau du champ reçu à l'entrée du récepteur, était obtenu à la cadence de 1 Hz à partir de la mesure de la tension de C.A.G. et d'une courbe d'étalonnage (tension - niveau).

Pour l'étude spécifique de la qualité de la liaison, un générateur de bits WANDEL et GOLTERMANN était utilisé à l'émission. Un détecteur de même marque comptait le nombre d'erreurs, indiquait les dépassements de capacité de comptage et les pertes de synchronisation à la réception.

### 2.2. SPECTROPLUVIOMETRE

Ce capteur a été conçu pour mesurer de façon précise, sans contact, les précipitations pluvieuses. Un traitement de ses données fournit un double histogramme en diamètre (de 0 à 5 mm) et en vitesse (de 0 à 10 m/s) des gouttes de pluie.

Le classement est effectué sur 16 classes de même largeur [1].

#### 2.2.1. Principe de la mesure

Une diode électro-luminescente, émettant dans l'infrarouge, forme à travers une lentille convergente et un diaphragme rectangulaire horizontal, un faisceau parallélépipédique (figure n° 2.1.). Ce faisceau est focalisé sur une photodiode. Le courant délivré par celle-ci est constant lorsque le faisceau n'est pas occulté. Lorsqu'une goutte de pluie traverse le faisceau, l'intensité de lumière décroît par rapport à sa valeur nominale. Après suppression de la composante continue, inversion et amplification, le signal est constitué d'impulsions dont la hauteur et la largeur sont fonction respectivement de la taille des gouttes de pluie et de leur vitesse de chute.

L'amplitude maximale de l'impulsion est proportionnelle à la section efficace verticale de la goutte. Le diamètre d'une goutte, supposée sphérique, est donc déduit de cette valeur.

#### 2.2.2. Calcul de l'intensité de la pluie

Afin de limiter les erreurs dues aux effets de bord, un pré-traitement permet d'éliminer les gouttes de pluie dont la vitesse diffère de plus de 50 % des valeurs de GUNN et KINZER [2].

La distribution des gouttes  $n(D, v)$  par  $m^3$  et par intervalle de diamètre et de vitesse est obtenue à partir du nombre,  $C(D, v)$ , de gouttes comptées dans chaque classe de diamètre et de vitesse. La distribution est telle que :

$$n(D, v) = C(D, v) / (S \cdot \Delta t \cdot v(D)), \quad (1)$$

expression dans laquelle :

- $S$  est la surface de captation du pluviomètre ( $10^{-2} m^2$ ),
- $\Delta t$  est le temps d'échantillonnage.

La vitesse  $v$  et le diamètre des gouttes  $D$  sont pris par rapport à la valeur centrale de chaque classe.

Pour chaque échantillonnage, la concentration en gouttes, ( $m^{-4}$ ) et la vitesse moyenne  $v(D)$  sont déduites de :

$$N(D) = \sum_v n(D, v) \quad (2)$$

$$V(D) = [\sum_v n(D, v) \cdot v] / N(D) \quad (3)$$

L'intensité de la pluie peut être calculée à partir de (2) et (3) et s'écrit :

$$R \text{ (mm/h)} = 3.6 \cdot 10^6 \cdot \frac{\pi}{6} \sum_D N(D) \cdot V(D) \cdot D^3 \quad (4)$$

#### 2.2.3. Incertitude de mesure

Les mesures de diamètre et de vitesse de chute des gouttes de pluie sont entachées d'erreurs. Trois causes principales sont responsables de cette incertitude :

- le pas d'échantillonnage,
- l'instrument, par construction,
- les conditions d'environnement.

Les erreurs introduites par l'échantillonnage sont dues au comportement statistique des averse. Pour une période de 60 s, typiquement utilisée pendant cette campagne, l'erreur est d'environ 8 % sur des intensités de 1 mm/h et de 4 % sur des intensités de 100 mm/h.

La forme du capteur génère deux types d'erreur. Le premier est dû aux effets de bord : une goutte peut tomber le long d'une des deux grandes parois verticales du faisceau. Le second intervient lorsqu'il y a multiplicité des gouttes : plus d'une goutte est alors présente dans le faisceau. Ces deux effets combinés conduisent à une erreur globale inférieure à 10 % dans les tailles 0.8 - 4.5 mm. L'erreur sur l'intensité de la pluie reste toutefois inférieure à 1 % pour les valeurs n'excédant pas 30 mm/h.

Enfin, des causes externes telle que la non-sphéricité des gouttes et l'existence de vent à composante horizontale forte peuvent nuire également à la précision des mesures.

#### 2.3. PLUVIOMETRE A AUGET

Cet appareil de conception classique donne une estimation de la durée et de l'intensité des précipitations pluvieuses. La surface de son collecteur est de 1000 cm<sup>2</sup>. La quantité d'eau nécessaire à un basculement de l'auget est de 20 g, soit 0.2 mm de pluie.

L'acquisition du taux de pluie s'effectuant toutes les 6 mn, le pas élémentaire de mesure est donc de 2 mm/h.

#### 2.4. BOUÉE DE MESURES DE VAGUES

Une bouée était mouillée à proximité de la ligne de visée. Elle procurait, toutes les demi-heures, la vitesse et la direction du vent, la hauteur significative  $H_{1/3}$  et la période  $T_{1/3}$  des vagues.

Ces deux derniers paramètres résultent d'un traitement des variations instantanées du niveau de la mer, enregistrées pendant 10 mn. Ces données élaborées étaient ensuite transmises à une station terrestre par liaison hertzienne et à un satellite relié au système ARGOS.

### 3 - ÉTUDE EXPÉRIMENTALE DE L'AFFAIBLISSEMENT PAR LA PLUIE (N.U.)

Dans le but d'étudier l'influence de la pluie sur la propagation des ondes à 36 GHz, une analyse de l'atténuation a été effectuée de deux manières complémentaires :

- à partir des données de pluviométrie,
- à partir du niveau de champ reçu.

Avant de présenter en détail les méthodes de traitement utilisées et les résultats s'y rapportant, quelques rappels sont donnés ci-après.

Les données de pluviométrie mesurées pendant la campagne 84-85 et qui seront utilisées dans cette étude, sont également présentées.

### 3.1. RAPPELS CONCERNANT L'ATTENUATION PAR LA PLUIE DES ONDES MILLIMETRIQUES

#### 3.1.1. Atténuation linéique

Connaissant la distribution  $N(D)$  de la taille des gouttes de pluie, l'atténuation linéique peut en être déduite par l'expression classique :

$$A \text{ (dB/km)} = 4.343 \cdot 10^{-3} \int_0^{\infty} N(D) Q(D) dD \quad (5)$$

Dans cette formule :

- $D$  représente le diamètre de la goutte de pluie en mm,
- $N(D) dD$  est le nombre de gouttes dans la classe  $[D, D + dD]$ , par unité de volume ( $\text{m}^{-3} \cdot \text{mm}^{-1}$ ),
- $Q(D)$  est la section efficace d'extinction en  $\text{mm}^2$ .

En supposant que les gouttes de pluie ont une forme sphérique,  $Q(D)$  peut être calculé à partir de la théorie de Mie :

$$Q(D) = \frac{\lambda^2}{2\pi} \sum_{n=1}^{\infty} (2n+1) \text{Re}(a_n + b_n) \quad (6)$$

où :

- $\lambda$  est la longueur d'onde incidente,
- $a_n$  et  $b_n$  sont les coefficients de Mie exprimés à partir des fonctions de Ricatti-Bessel  $y_n$  et de Hankel  $h_n$ . Ces fonctions ont pour paramètres  $\frac{mD}{\lambda}$  et  $m \frac{mD}{\lambda}$  ( $m$  est l'indice de réfraction de l'eau).

#### 3.1.2. Distributions de taille des gouttes de pluie

Comme il apparaît dans l'expression (5), le calcul de l'atténuation linéique passe par la connaissance de la distribution de la taille des gouttes de pluie. De telles mesures ont été réalisées pour la première fois, en 1943, par LAWS et PARSONS [3]. Les résultats se présentaient alors sous une forme tabulée assez difficile à employer. Dès 1948, MARSHALL et PALMER [4] proposent de représenter les distributions sous une forme littérale plus facilement exploitable. Cette écriture, affinée par JOSS et al. en 1968 [5], utilise la fonction suivante :

$$N(D) = N_0 e^{-\gamma D} \quad (7)$$

$$\text{avec } \gamma = \alpha R^{-0.21} \quad (8)$$

$N_0$  et  $\alpha$  sont des variables dépendant des distributions (tableau n° 3.1.). Dans (8),  $R$  est le taux de pluie en mm/h.

| Type de distributions     | $N_0$<br>mm <sup>-3</sup> | $\alpha$<br>mm |
|---------------------------|---------------------------|----------------|
| Marshall - Palmer         | 8 000                     | 4.1            |
| Joss et al. Bruine        | 30 000                    | 5.7            |
| Joss et al. pluie moyenne | 7 000                     | 4.1            |
| Joss et al. orage         | 1 400                     | 3.0            |

TABLEAU 3.1.

### 3.2. DONNEES DE PLUVIOMETRIE MESUREES PENDANT LA CAMPAGNE 84-85

Les diverses situations météorologiques rencontrées durant l'expérience ont permis d'acquérir une base de données pluviométriques couvrant les types de pluie les plus fréquemment observés en automne et en hiver sur les côtes de l'atlantique nord. Pour les différents types de pluie, les distributions mesurées avec le spectropluviomètre ont été comparées aux distributions usuelles de MARSHALL-PALMER ou JOSS et al., à taux de pluie identique.

#### 3.2.1. Pluies bruineuses

La bruine est une pluie fine dont l'intensité est inférieure à quelques dixièmes de mm/h. C'est une pluie que l'on rencontre souvent sur les côtes bretonnes et qui dure généralement plusieurs heures. L'examen des figures de distributions (fig. 3.2.1. a, b) montre que seules les 3 ou 4 premières classes sont différentes de 0 (diamètre inférieur à 1.2 mm). La distribution calculée de "Joss bruine" est en accord avec les mesures, sauf pour la première classe où le nombre de gouttes est surestimé.

Par son principe, le spectropluvionètre mesure ce type de pluie, alors que les pluviomètres classiques comme le pluviomètre à auget, y sont insensibles.

### 3.2.2. Pluies moyennes

Les distributions mesurées (fig. 3.2.2. a, b) sont en bon accord avec les distributions de MARSHALL-PALMER ou "Joss-moyenn". Ces distributions surestiment, néanmoins, le nombre de gouttes dans les petites classes. Pour les grandes classes, les valeurs mesurées sont souvent au-dessus de celles données par les distributions exponentielles.

Des gouttes pouvant atteindre un diamètre de 4 mm ont été mesurées.

### 3.2.3. Pluies fortes

Des pluies fortes, pour la région, d'une durée de quelques minutes ont été relevées simultanément par le spectropluvionètre, à CAVRES, et le pluviomètre à auget à GROLX. Durant ce type d'événement, le taux de pluie a parfois excédé 30 mm/h. Les distributions correspondantes (fig. 3.2.3. a, b) s'apparentent aux distributions de "Joss-orage". Celles-ci ont tendance à surestimer le nombre de gouttes dans les classes extrêmes et à sous-estimer les classes moyennes.

## 3.3. CALCUL DE L'ATTÉNUATION À PARTIR DES DONNÉES DE PLUVIOMÉTRIE

### 3.3.1. Atténuation linéique

À partir de l'équation (5), un programme de calcul de l'atténuation linéique dans le domaine des diamètres compris entre 0 et 5 mm a été mis en place.

Les données d'entrée de ce programme sont :

- la fréquence,
- la distribution de taille de gouttes de pluie (mesurée ou calculée),
- la température ambiante.

Un sous-programme permet de calculer l'indice de réfraction de l'eau à partir du modèle de Ray [6].

Ce programme a été appliqué à la distribution théorique (de Marshall-Palmer ou Joss et al.) et à la distribution expérimentale (mesurée par le spectropluvionètre).

Dans les figures 3.3 a et b, l'atténuation calculée à partir des distributions théoriques apparaît en pointillés, tandis que l'atténuation calculée à partir des distributions expérimentales est représentée par un nuage de points. La droite des moindres carrés correspondant à cet ensemble discret est un trait plein. Elle exprime l'atténuation linéique sous la forme bien connue :

$$A_r \text{ (dB/km)} = a R^b \quad (9)$$

où :

- a et b sont déterminés par la méthode des moindres carrés
- R est le taux de pluie
- L'indice r est relatif aux mesures effectuées par le spectropluvionètre situé au site récepteur (r).

L'analyse des cas d'événements (illustrés par les figures 3.3 a et b), montre que les points de mesures concordent généralement bien avec les droites théoriques. Néanmoins, lorsque le taux de pluie dépasse quelques mm/h, il apparaît que les atténuations calculées à partir des distributions expérimentales sont souvent au-dessus des atténuations théoriques. Cet écart est dû à la forme de la distribution qui présente un nombre de gouttes plus important dans les classes intermédiaires et parfois grandes (voir figures 3.2.3.).

### 3.3.2. Atténuation sur la liaison

En supposant la structure granulométrique de la pluie homogène de part et d'autre de la liaison, l'atténuation au site émetteur peut être déduite de (9) et s'écrit :

$$A_e \text{ (dB/km)} = a R_e^b \quad (10)$$

Dans cette expression  $R_e$  est le taux de pluie relevé par le pluviomètre à auget.

L'atténuation globale sur la liaison est donc prise comme étant la moyenne arithmétique des atténuations linéiques à l'émission et à la réception :

$$A_t \text{ (dB)} = 9.7 \left( \frac{A_e + A_r}{2} \right) \quad (11)$$

### 3.4. CALCUL DE L'ATTENUATION DEDUITE A PARTIR DU CHAMP RECU

#### 3.4.1. Modélisation du phénomène de double trajet

La composition du champ dû au rayon direct et du champ réfléchi par la mer conduit à une figure d'interférence dont les affaiblissements, périodiques, sont d'autant plus profonds que la mer est calme. Pour étudier dans son ensemble l'atténuation causée par la pluie, la méthode consiste, bien entendu, à soustraire le signal mesuré, (donc avec pluie), du signal théorique équivalent sans pluie.

Ce signal est calculé à partir d'un modèle prenant en compte :

- l'indice de réfraction de l'air avec l'altitude,
- la rotondité de la terre,
- le diagramme de rayonnement des antennes,
- le coefficient de réflexion dans la direction spéculaire.

Pour le calcul de ce dernier coefficient, c'est l'expression de Miller et Brown [7] qui a été retenue. En effet, dans les situations de mer agitée, elle présente une meilleure concordance avec les mesures effectuées, que l'expression de Beckmann et Spizzichino.

$$\rho = \exp [-2 (2 \pi z)^2] I_0 [2 (2 \pi z)^2] \quad (12)$$

où  $z$  est la rugosité de la mer et  $I_0(\cdot)$  la fonction de Bessel modifiée d'ordre 0.

Les paramètres d'entrée du programme de calcul correspondant sont la hauteur de la marée et la hauteur  $H$  1/3 des vagues.

Il s'avère difficile en se basant sur cette méthode de reproduire les variations temporelles du niveau de champ reçu avec suffisamment de précision.

Cette difficulté est due principalement :

- à la méconnaissance de la structure de l'indice de réfraction de l'air,
- aux incertitudes de mesures des hauteurs de vagues et de marée.

#### 3.4.2. Reconstitution du niveau de champ reçu

On suppose que le signal reçu n'est pas perturbé par la pluie et que les variations périodiques du champ sont seulement dues à la marée. On s'assure en examinant les conditions météorologiques que l'on ne se situe pas dans un cas pouvant engendrer des variations d'indice de réfraction de l'air.

Pour certaines positions du niveau de la mer le niveau de champ reçu passe par un extremum (un ellipsoïde de Fresnel est alors tangent à la surface).

Le principe de la méthode utilisée est donc de repérer sur le signal reçu les instants pendant lesquels les ellipsoïdes de Fresnel sont tangents à la surface et de leur associer, dans le cas d'une atmosphère standard, la hauteur de mer correspondante calculée à l'aide du programme décrit au § 3.4.1. Les variations instantanées de la mer sont ensuite interpolées puis lissées.

La connaissance du profil de marée et des variations du coefficient de réflexion spéculaire permet de reconstituer le niveau de champ reçu.

En l'absence de pluie, la figure 3.4.1. montre que les variations des signaux mesurés et calculés par cette méthode sont très proches.

Par temps de pluie, le traitement est plus délicat car le positionnement des instants de tangence des ellipsoïdes de Fresnel avec la mer peuvent ne plus correspondre avec les extréma. La reconstitution du profil de la marée s'appuie alors sur les extréma dus aux trajets doubles. Dans ce cas, la position de ces points est interpolée en tenant compte du profil sinusoïdal de la marée. Pour un certain nombre de cas correspondant à des pluies moyennes ou fortes, les atténuations déduites du champ reçu ont été comparées à celles calculées à partir des données de pluviométrie (figures 3.4.2 et 3.4.3).

Sur l'ensemble des cas traités, il apparaît une bonne concordance entre les atténuations mesurées et les atténuations calculées. Néanmoins, on remarque quelquefois, à un instant donné, des écarts plus ou moins importants. Ils viennent en fait essentiellement des hypothèses faites sur la cellule de pluie. En effet la zone pluvieuse ne présente pas toujours un profil uniforme tel que celui défini dans le modèle. En outre les seules données de pluviométrie aux extrémités de la liaison ne permettent pas de connaître les variations du taux de pluie sur l'ensemble du trajet et donc de déterminer l'atténuation sur la liaison à chaque instant.

En revanche, les courbes de probabilités cumulées des atténuations mesurées et calculées sont très proches l'une de l'autre (figure n° 3.4.4). Ces courbes ont été tracées à partir de 2 dB (à 0.2 dB/km) à cause des incertitudes de mesures entachant les faibles atténuations ; elles tendent à prouver la validité de la méthode retenue.



Lorsqu'il pleut simultanément aux deux extrémités d'une liaison hertzienne d'une dizaine de kilomètres, ou moins, la fréquence d'occurrence des atténuations dans le domaine millimétrique peut être évaluée correctement à partir de la distribution de taille des gouttes de pluie relevée à une extrémité de la liaison et du taux de pluie mesuré à l'autre extrémité.

#### 4 - COMPORTEMENT DE LA LIAISON NUMÉRIQUE EN FONCTION DES CONDITIONS MÉTÉOROLOGIQUES ET OCÉANOGRAPHIQUES (N.U.)

##### 4.1. PRÉSENTATION - GÉNÉRALITÉS

La mise en œuvre, dans le cadre de cette expérience d'une liaison à déport numérique d'informations a permis d'évaluer la qualité de transmission de données, en atmosphère maritime dans le domaine millimétrique.

Les paramètres caractéristiques de la liaison :

- taux d'erreur,
- indicateur du dépassement de comptage,
- indicateur de perte de synchronisation,

ont été enregistrés toutes les 12 secondes pendant toute la durée de la campagne.

Les deux derniers indicateurs sont activés quand le taux d'erreur est au moins supérieur à  $10^{-3}$ . Dans ce cas précis, la liaison peut alors être considérée comme coupée. Du fait de la faible altitude des antennes, l'état de la mer influe de façon importante sur le niveau de champ reçu. L'étude du comportement de la liaison numérique a donc porté sur les situations de mer calme et de mer agitée. Les cas de pluie, engendrant de fortes atténuations, ont été également analysés.

Pour ces différents cas, la courbe des probabilités cumulées du niveau de champ moyenné sur 12 secondes et la courbe de probabilités cumulées du taux d'erreur ont été tracées (figures 4.2.1.1, 4.2.1.2). La durée des événements où la liaison est coupée (taux d'erreur supérieur à  $10^{-3}$ ) a aussi été relevée.

##### 4.2. ANALYSE DES RÉSULTATS

###### 4.2.1. Situations de mer calme

(États de la mer 1, 2, 3 de l'échelle de Douglas ;  $H 1/3 < 1.2$  m).

Lorsque la mer est calme ou peu agitée, le champ reçu s'affaiblit périodiquement en fonction de la hauteur du niveau de la mer. Les variations du taux d'erreur correspondantes s'opposent à celles du niveau de champ. La transmission des données est meilleure sur les maxima. Elle se dégrade quand le niveau de champ diminue. Sur les minima de champ, la liaison est généralement coupée pendant quelques dizaines de secondes. La plus longue interruption relevée a été de 4 minutes environ. On note aussi que la durée maximale pendant laquelle la liaison numérique a fonctionné sans discontinuer est d'à peu près 4 heures. Afin de quantifier ces observations une analyse statistique portant sur 140 heures a été effectuée. Des figures n° 4.2.1. représentant les probabilités cumulées, on déduit le tableau 4.1. suivant :

| Taux d'erreur ( $T_E$ ) | Pourcentage de temps durant lequel le taux d'erreur est inférieur à $T_E$ | Marge brute correspondante |
|-------------------------|---|----------------------------|
| $1,1 \cdot 10^{-5}$     | 50  | - 36 dB                    |
| $1 \cdot 10^{-4}$       | 91  | - 43,5 dB                  |
| $1 \cdot 10^{-3}$       | 96,8  | - 46 dB                    |

TABLÉAU 4.1.

Pendant 3,2 % du temps de fonctionnement, la liaison était coupée.

###### 4.2.2. Situations de mer agitée

(États de la mer 4, 5, 6 de l'échelle de Douglas ;  $H 1/3 > 1,5$  m).

Quand l'état de la mer augmente, les affaiblissements périodiques deviennent de moins en moins prononcés pour disparaître à l'état 5. Le niveau de champ est alors quasiment constant (- 40 dB) et le taux d'erreur se situe en moyenne vers  $10^{-5}$ . On n'observe plus de coupure dans la transmission des données.

Les résultats d'une analyse statistique portant sur 102 heures sont représentés figures n° 4.2.1. et résumés dans le tableau n° 4.2. ci-après.

| Taux d'erreur ( $T_E$ ) | Pourcentage de temps durant lequel le taux d'erreur est inférieur à $T_E$ | Marge brute correspondante |
|-------------------------|---|----------------------------|
| $1.1.10^{-5}$           | 50  | - 38 dB                    |
| $3.10^{-5}$             | 99  | - 41.5 dB                  |
| $7.10^{-5}$             | 99.9  | - 43 dB                    |
| $1.10^{-4}$             | 99.95   | - 43.5 dB                  |

TABLEAU 4.2.

Quel que soit l'état de la mer, il apparaît dans les tableaux 4.1. et 4.2. que la marge brute pour un taux d'erreur de  $10^{-4}$  est de 44 dB environ.

#### 4.2.3. Situations avec pluie

Les chutes de pluie ont causé, parfois, des affaiblissements profonds et durables. Elles ont coupé la liaison numérique pendant plusieurs minutes. Des coupures de plus de 20 minutes ont été relevées.

L'action des pluies importantes est illustrée par la figure 4.2.3. qui représente le cas d'une mer agitée avec pluie moyenne puis forte. En l'absence de précipitation, la liaison transmet les données avec un taux d'erreur moyen de  $10^{-5}$ . Sous l'action d'une pluie moyenne le taux d'erreur varie de  $10^{-5}$  à  $6.10^{-3}$ . Enfin, sous l'effet d'une pluie forte, la liaison est alors coupée pendant 10 mn.

### 5 - CONCLUSIONS (N.U.)

La campagne d'expérimentation conduite par le sous-groupe propagation du RSC.8 - commission 3 - AC.243 a fourni une importante base de données radiodélectriques, et de pluviométrie, représentative des conditions météorologiques et océanographiques de la côte atlantique bretonne.

La contribution française à cette campagne s'est axée sur deux thèmes :

- l'atténuation par la pluie,
- l'étude du comportement d'une liaison numérique.

#### 5.1. ATTENUATION PAR LA PLUIE

La sensibilité du spectropluviomètre a permis de mesurer précisément les distributions de taille de gouttes de pluie. Elles apparaissent dans l'ensemble conformes aux distributions proposées par Marshall-Palmer et Jones et al.

A partir de ces données, l'atténuation globale sur la liaison a été calculée et comparée avec l'atténuation mesurée. Compte tenu de la longueur de la liaison et la présence de trajet double, la prédiction en pourcentage de temps des atténuations par la pluie à partir des seules données de pluviométrie apparaît satisfaisante.

#### 5.2. COMPORTEMENT DE LA LIAISON NUMÉRIQUE

La qualité de la transmission numérique est directement liée au niveau de champ reçu. A conditions météorologiques identiques, la transmission numérique est d'autant meilleure que la mer est agitée.

La pluie, et le phénomène de réflexion sur la mer, atténuent de façon uniforme le signal dans toute la bande de transmission. Des taux d'erreur anormalement élevés, et qui seraient engendrés par des trajets multiples atmosphériques, (cause d'affaiblissements sélectifs en fréquences), n'ont pas été observés.

# RÉFÉRENCES

- [1] Hauser D., Ameyenc P., Mutton B., Waldeufel P., "A new optical instrument for simultaneous measurement of raindrop diameter and fall speed distributions", Journal of Atmospheric and Oceanic technology, Vol. 1, Sept. 1984.
- [2] Gunn R., Kinser G.D., "The terminal velocity of fall for water droplets in stagnant air", J. Meteor., Vol. 6, pp. 243 - 248, 1949.
- [3] Laws J.O., Parsons D.A., "The relation of raindrop size to intensity", Trans. Amer. Geophys. Union, Vol. 24, pp. 452 - 460, 1943.
- [4] Marshall J.S., Palmer W. M.C.K., "The distribution of raindrops with size", J. Meteor., Vol. 5, pp. 165 - 166, Aug. 1948.
- [5] Jones J., Thoms J.C., Waldvogel A., "The variation of raindrop size distributions at Locarno", Proc. Conf. Cloud Physics, pp. 368 - 173, 1968.
- [6] Ray P.S., "Broadband complex refractive indices of ice and water", Applied Optics, Vol. 11, n° 8, Aug. 1972.
- [7] Miller A.R., Brown R.M., Vagh E., "New derivation for the rough - surface reflection coefficient and for the distribution of sea - wave elevations", IEE Proceedings, Vol. 131, Pt. M, n° 2, April 1984.

# REMERCIEMENTS

Les auteurs remercient les différentes personnes qui ont collaboré à divers titres à ces expérimentations. En particulier :

- le CNET/CEPE qui a prêté et mis en oeuvre son spectropluviomètre,
- le CMM de l'IFREMER et l'EPSON qui ont respectivement fourni et mis en place la bouée de mesure de vagues.

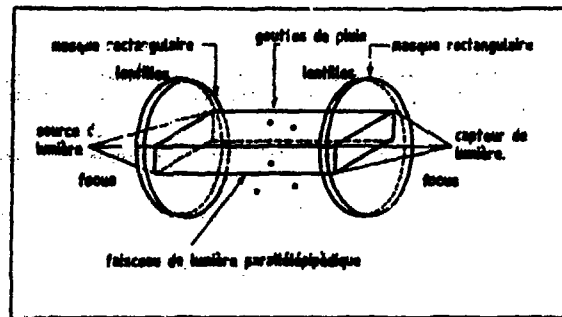
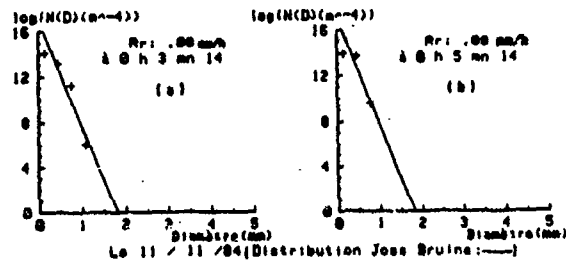
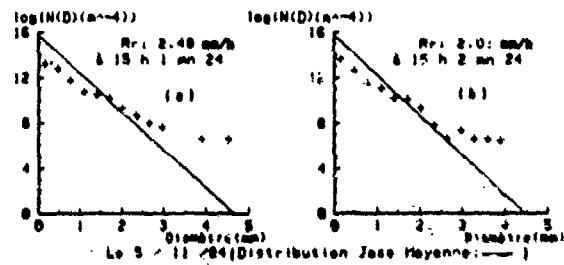


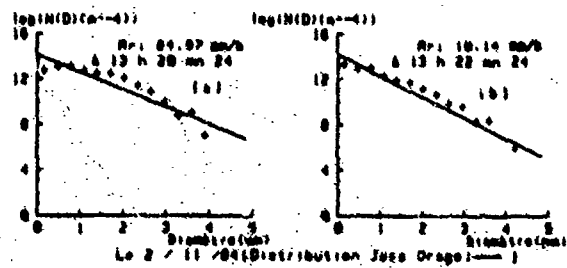
Figure 2.1. : Schéma de principe du spectrophotomètre



Figures 3.2.1.

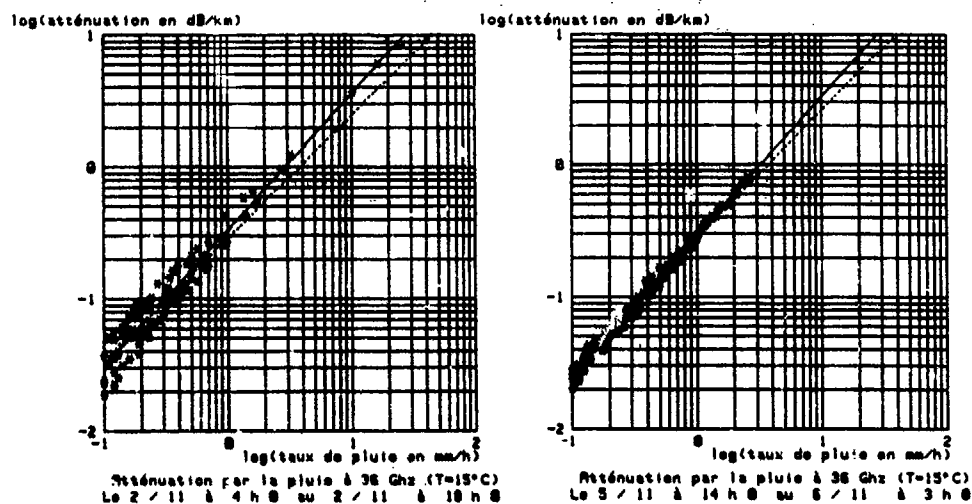


Figures 3.2.2.



Figures 3.2.3.

Distributions mesurées de taille de gouttes de pluie (+)



Figures 3.3. a et b : Calcul de l'atténuation linéique à partir des distributions mesurées et théoriques.

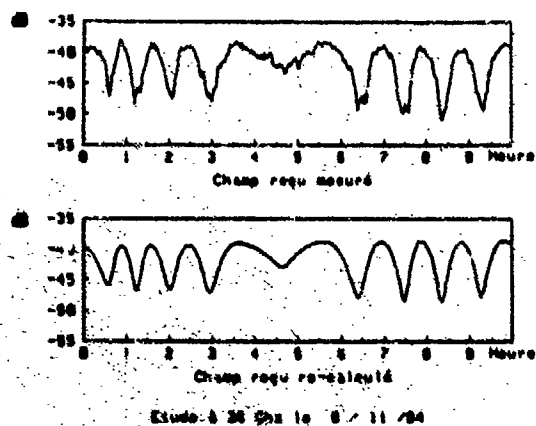


Figure 3.4.1. : Reconstitution du niveau de champ reçu

Etude expérimentale de l'atténuation par la pluie à 36 GHz  
 Le 2 / 11 / 84 de 9 h 8 à 15 h 8  
 Valeurs moyennées sur 120 s

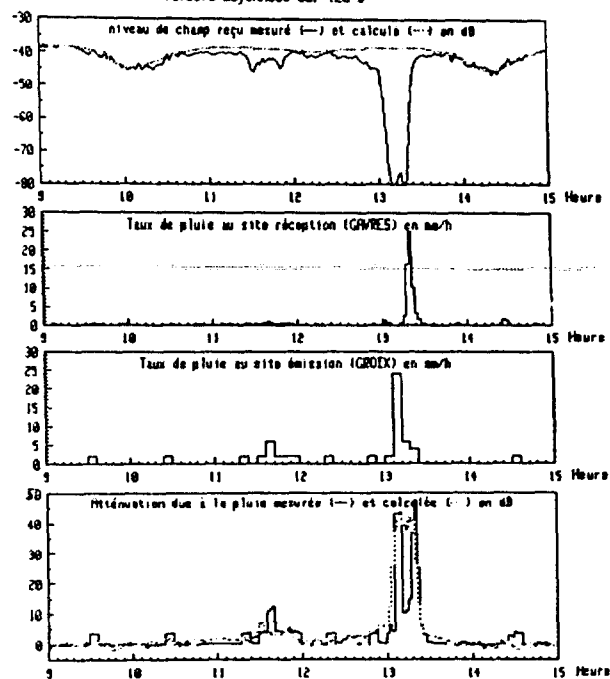


Figure 3.4.2.

Etude expérimentale de l'atténuation par la pluie à 36 GHz  
 Le 5 / 11 / 84 de 17 h 8 à 21 h 8  
 Valeurs moyennées sur 120 s

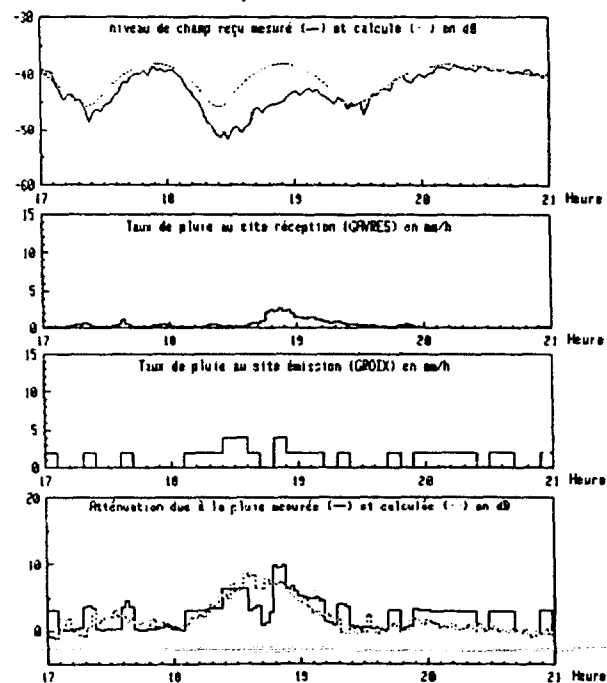


Figure 3.4.3.

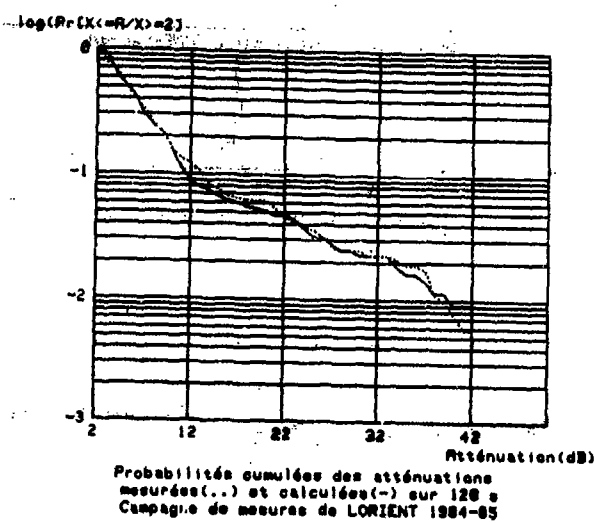
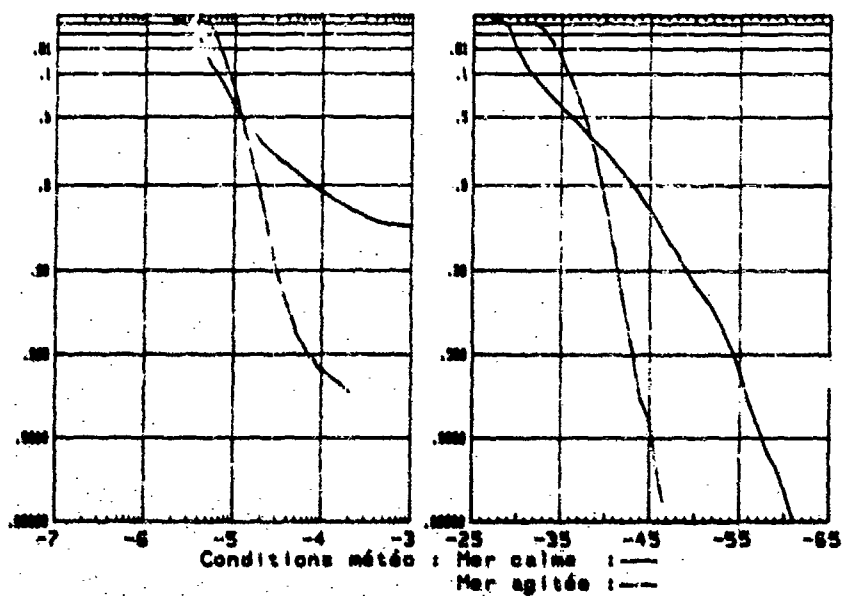


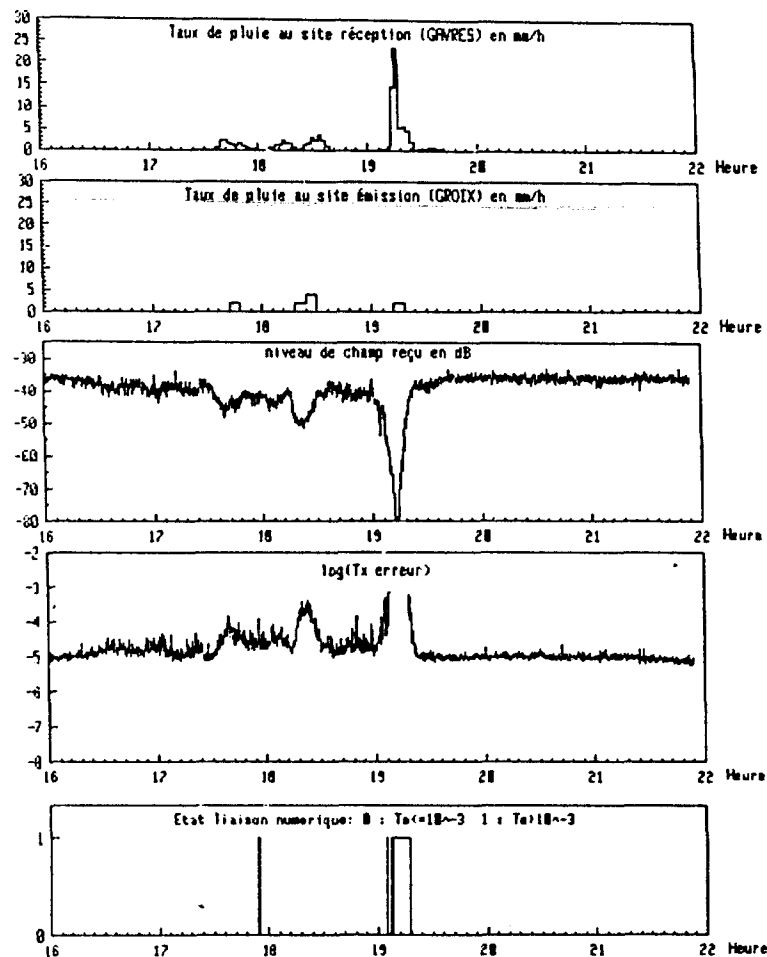
Figure 3.4.4.

Probabilités cumulées du taux d'erreur  
Etude sur 12 secondes

Probabilités cumulées du niveau de champ reçu (dB)



Figures 4.2.1. 1 et 1



Figures 4.2.3. : Influence de la pluie sur la transmission numérique.  
(le 14.12.1984)

## DISCUSSION

**L.Boithias, FR**

Avez vous essayé d'appliquer des méthodes générales de calcul d'affaiblissement par la pluie, déjà publiées, et en particulier celle du CCIR, pour étudier la précision de ces méthodes?

**Réponse d'Auteur**

Nous n'avons pas encore envisagé de faire des statistiques mais cela pourrait être fait effectivement.

**C.Goutelard, FR**

Les mesures des taux d'erreurs moyens sur des périodes de 12 secondes sont très intéressantes. Cependant, il serait nécessaire de les compléter par des lois de distribution si vous envisagiez d'élaborer des codages correcteurs.

De toute façon cette information serait utile en tant que données pour les spécialistes de traitement de l'information.



| REPORT DOCUMENTATION PAGE     |  |                      |  |                         |                      |                |                        |              |                        |
|-------------------------------|--|----------------------|--|-------------------------|----------------------|----------------|------------------------|--------------|------------------------|
| 1. Recipient's Reference      | 2. Originator's Reference  | 3. Further Reference | 4. Security Classification of Document |                         |                      |                |                        |              |                        |
|                               | AGARD-CP-407   | ISBN 92-835-0434-8   | UNCLASSIFIED                           |                         |                      |                |                        |              |                        |
| 5. Originator                 | Advisory Group for Aerospace Research and Development<br>North Atlantic Treaty Organization<br>7 rue Ancelle, 92200 Neuilly sur Seine, France  |                      |  |                         |                      |                |                        |              |                        |
| 6. Title                      | TERRESTRIAL PROPAGATION CHARACTERISTICS IN MODERN<br>SYSTEMS OF COMMUNICATIONS, SURVEILLANCE, GUIDANCE AND<br>CONTROL  |                      |  |                         |                      |                |                        |              |                        |
| 7. Presented at               | the Electromagnetic Wave Propagation Panel Specialists' Meeting held in Ottawa,<br>Canada, 20-24 October 1986.   |                      |  |                         |                      |                |                        |              |                        |
| 8. Author(s)/Editor(s)        | Various  |                      | 9. Date                                |                         |                      |                |                        |              |                        |
|                               |  |                      | November 1987                          |                         |                      |                |                        |              |                        |
| 10. Author's/Editor's Address | Various  |                      | 11. Pages                              |                         |                      |                |                        |              |                        |
|                               |  |                      | 282                                    |                         |                      |                |                        |              |                        |
| 12. Distribution Statement    | This document is distributed in accordance with AGARD<br>policies and regulations, which are outlined on the<br>Outside Back Covers of all AGARD publications.   |                      |  |                         |                      |                |                        |              |                        |
| 13. Keywords/Descriptors      | <table border="0"> <tr> <td>Terrestrial propagation</td> <td>Guidance and control</td> </tr> <tr> <td>Communications</td> <td>Ground characteristics</td> </tr> <tr> <td>Surveillance</td> <td>Tropospheric interface</td> </tr> </table>  |                      |  | Terrestrial propagation | Guidance and control | Communications | Ground characteristics | Surveillance | Tropospheric interface |
| Terrestrial propagation       | Guidance and control   |                      |  |                         |                      |                |                        |              |                        |
| Communications                | Ground characteristics   |                      |  |                         |                      |                |                        |              |                        |
| Surveillance                  | Tropospheric interface   |                      |  |                         |                      |                |                        |              |                        |
| 14. Abstract                  | <p>Modern system development requires serious attention to the operational environment and variations it experiences due to natural and artificial influences. Applications based on propagation in the vicinity of the earth surface predominantly depend on characteristics of the near-ground propagation medium as well as on its lower boundary, the ground-surface, or on the "terrestrial propagation characteristics".</p> <p>Research work carried out during the last few decades has resulted in data banks and other information on average behaviour of parameters concerned, such as ground profiles, vegetation and electrical characteristics. An efficient operation of modern systems of communication, surveillance, guidance and control requires more and more details of ground data and, particularly, of their deviation from average values on account of anthropogeneous effects in addition to seasonal and diurnal variations.</p> |                      |  |                         |                      |                |                        |              |                        |

|  |   |  |   |
|--|---|--|---|
| AGARD Conference Proceedings No.407<br>Advisory Group for Aerospace Research and Development, NATO<br><b>TERRESTRIAL PROPAGATION CHARACTERISTICS IN MODERN SYSTEMS OF COMMUNICATIONS, SURVEILLANCE, GUIDANCE AND CONTROL</b><br>Published November 1987<br>282 pages<br><br>Modern system development requires serious attention to the operational environment and variations it experiences due to natural and artificial influences. Applications based on propagation in the vicinity of the earth surface predominantly depend on characteristics of the near-ground propagation medium as well as on its lower P.T.O | AGARD-CP-407<br><br>Terrestrial propagation<br>Communications<br>Surveillance<br>Guidance and control<br>Ground characteristics<br>Tropospheric interface | AGARD Conference Proceedings No.407<br>Advisory Group for Aerospace Research and Development, NATO<br><b>TERRESTRIAL PROPAGATION CHARACTERISTICS IN MODERN SYSTEMS OF COMMUNICATIONS, SURVEILLANCE, GUIDANCE AND CONTROL</b><br>Published November 1987<br>282 pages<br><br>Modern system development requires serious attention to the operational environment and variations it experiences due to natural and artificial influences. Applications based on propagation in the vicinity of the earth surface predominantly depend on characteristics of the near-ground propagation medium as well as on its lower P.T.O | AGARD-CP-407<br><br>Terrestrial propagation<br>Communications<br>Surveillance<br>Guidance and control<br>Ground characteristics<br>Tropospheric interface |
| AGARD Conference Proceedings No.407<br>Advisory Group for Aerospace Research and Development, NATO<br><b>TERRESTRIAL PROPAGATION CHARACTERISTICS IN MODERN SYSTEMS OF COMMUNICATIONS, SURVEILLANCE, GUIDANCE AND CONTROL</b><br>Published November 1987<br>282 pages<br><br>Modern system development requires serious attention to the operational environment and variations it experiences due to natural and artificial influences. Applications based on propagation in the vicinity of the earth surface predominantly depend on characteristics of the near-ground propagation medium as well as on its lower P.T.O | AGARD-CP-407<br><br>Terrestrial propagation<br>Communications<br>Surveillance<br>Guidance and control<br>Ground characteristics<br>Tropospheric interface | AGARD Conference Proceedings No.407<br>Advisory Group for Aerospace Research and Development, NATO<br><b>TERRESTRIAL PROPAGATION CHARACTERISTICS IN MODERN SYSTEMS OF COMMUNICATIONS, SURVEILLANCE, GUIDANCE AND CONTROL</b><br>Published November 1987<br>282 pages<br><br>Modern system development requires serious attention to the operational environment and variations it experiences due to natural and artificial influences. Applications based on propagation in the vicinity of the earth surface predominantly depend on characteristics of the near-ground propagation medium as well as on its lower P.T.O | AGARD-CP-407<br><br>Terrestrial propagation<br>Communications<br>Surveillance<br>Guidance and control<br>Ground characteristics<br>Tropospheric interface |

|   |   |
|---|---|
| <p>boundary, the ground-surface, or on the "terrestrial propagation characteristics".</p> <p>Research work carried out during the last few decades has resulted in data banks and other information on average behaviour of parameters concerned, such as ground profiles, vegetation and electrical characteristics. An efficient operation of modern systems of communication, surveillance, guidance and control requires more and more details of ground data and, particularly, of their deviation from average values on account of anthropogeneous effects in addition to seasonal and diurnal variations.</p> <p>ISBN 92-835-0434-4</p> | <p>boundary, the ground-surface, or on the "terrestrial propagation characteristics".</p> <p>Research work carried out during the last few decades has resulted in data banks and other information on average behaviour of parameters concerned, such as ground profiles, vegetation and electrical characteristics. An efficient operation of modern systems of communication, surveillance, guidance and control requires more and more details of ground data and, particularly, of their deviation from average values on account of anthropogeneous effects in addition to seasonal and diurnal variations.</p> <p>ISBN 92-835-0434-8</p> |
| <p>boundary, the ground-surface, or on the "terrestrial propagation characteristics".</p> <p>Research work carried out during the last few decades has resulted in data banks and other information on average behaviour of parameters concerned, such as ground profiles, vegetation and electrical characteristics. An efficient operation of modern systems of communication, surveillance, guidance and control requires more and more details of ground data and, particularly, of their deviation from average values on account of anthropogeneous effects in addition to seasonal and diurnal variations.</p> <p>ISBN 92-835-0434-3</p> | <p>boundary, the ground-surface, or on the "terrestrial propagation characteristics".</p> <p>Research work carried out during the last few decades has resulted in data banks and other information on average behaviour of parameters concerned, such as ground profiles, vegetation and electrical characteristics. An efficient operation of modern systems of communication, surveillance, guidance and control requires more and more details of ground data and, particularly, of their deviation from average values on account of anthropogeneous effects in addition to seasonal and diurnal variations.</p> <p>ISBN 92-835-0434-8</p> |